The Controls on Vanadium, Iron and Zinc Stable Isotope Fractionation in Upper Crustal Plutons

MADELEINE ANN STOW

The Controls on Vanadium, Iron and Zinc Stable Isotope Fractionation in Upper Crustal Plutons

Madeleine Ann Stow

This thesis is submitted in partial fulfilment of the requirements for the degree of Doctor of Philosophy at Durham University

Department of Earth Sciences

July 2022

Abstract

Chemically diverse plutonic rocks make up most of the upper continental crust, but the exact crystal-liquid segregation processes and physical conditions in solidifying mush bodies are debated. Transition metal stable isotopes are increasingly used to investigate magmatic processes, but knowledge of their specific behaviour in plutonic settings is lacking. Better understanding of the cause(s), magnitudes and directions of isotope fractionation in relatively simple, closed system plutons is required to assess the efficacy of transition metal stable isotopes at investigating mush processes.

This thesis investigated the calc-alkaline Boggy Plain Zoned Pluton, SE Australia, and the tholeiitic Red Hill Intrusion, Tasmania. This was the first time that the Fe-V-Zn isotopic composition of whole rock powders and mineral separates from closed system suites have been interpreted in combination with detailed textural observations, which provided a more comprehensive understanding of the controls of isotope fractionation in plutonic settings.

Fractional crystallisation was the major control on Fe and V isotopic trends, whereas Zn isotopic fractionation was mostly driven by fluids. It was observed that the isotopic composition of powders from coarse-grained, cumulative rocks does not necessarily represent a true melt composition, questioning the assumptions and modelling approaches of many previous studies of intrusive rocks. Instead, a focus on mineral separates was more informative, and enabled derivation of the first temperature-dependent mineral-melt fractionation factors for calc-alkaline magmas, and development of a new method for calculating melt composition from mineral separate data, which will be useful for future studies. The magnitudes of fractionation factors were overwhelmingly influenced by temperature, whereas changing fO_2 had no resolvable effect. Hence, accurate temperature estimates and temperature-dependent fractionation factors are vital for future work on plutonic settings. The isotopic variability observed on the pluton-scale highlights the significant isotopic heterogeneity of the upper crust in general. This has implications for how accurately clastic sediments record changes in ‘average’ crustal isotopic composition over geological timescales, and thus understanding temporal changes in the isotopic compositions of the crust and oceans.

Declaration

I declare that this thesis, which I submit for the degree of Doctor of Philosophy at Durham University, is my own work, and is not substantially the same as any which has previously been submitted at this or any other university.

Madeleine Stow
July 2022

Acknowledgements

First and foremost, I would like to thank my supervisors Julie Prytulak, Madeleine Humphreys and Geoff Nowell. I could not have hoped for a better supervisory team, especially over the course of a PhD which has been impacted by a global pandemic! Thanks to Julie and Madeleine for all their encouragement and guidance throughout the project, for always being so open and available to talk to, for such detailed feedback on writing, and for supporting me throughout my time at Durham. I have learnt so much from both of you. Thank you to Geoff for teaching me all about mass spectrometry, for answering my endless questions about the Neptune and for not getting too annoyed when I promised multiple times that this was definitely my final batch of samples! Thanks also to Kevin Burton and the group at the university of Iceland for allowing me to work on the lavas from the 2021 Fagradalsfjall eruption, which was a great opportunity to look at such freshly erupted, chemically interesting samples.

Thanks to other members of the Durham Isotope Group for fun times in the clean labs over the years, most notably Sophie Page, Bryony Rogers, Mathieu Dellinger, and Marie-Anne Ancellin. The biggest thanks go to Sophie; it was great to have someone to rant with about the challenges of Fe isotope measurements on the Neptune!

This work was funded by the Natural Environment Research Council (NERC) IAPETUS Doctoral Training Partnership [Grant number NE/L002590/1], and I gratefully acknowledge this funding and the associated training opportunities. I am also thankful for the extra 4 months funded extension for Covid disruption, which allowed me to make up on missed lab time and complete this work.

When the pandemic hit in the second year of my PhD, I had only measured a few batches of samples and did not have enough data to even start to write a chapter. I thought this was going to completely change my lab-based project. So huge thanks must go to the Earth Sciences Health and Safety committee for their hard work in getting us back into the lab as soon as possible. Even though only one of us was allowed in each area of the lab at a time, it made a huge difference to me not be stuck at home all the time, and to be able to make some progress with work. Thanks also to Paolo Sossi and John Foden for allowing me to work on the Red Hill samples, which was hugely beneficial when my originally planned Scottish fieldwork was derailed by Covid.

Thanks to Sam Hammond at the Open University for carrying out the trace element analysis for the Boggy Plain magnetite separates. Within the department, thanks to Ian Chaplin and Sophie Edwards for help with thin section and sample preparation.

Thanks to the postgrad community (past and present) at Durham for fun away weekends, regular pub trips and the daily 10.30 am tea break. Special thanks go to Emma Ownsworth, Katharine Groves, Eloise Bretagne, Katy Burrows, Chris Ward, Tim Armitage, Bob Elliot, Josh Brown, Miles Wilson and Jack Lee.

One of the biggest thanks goes to Olly Sanford, for all his support and encouragement over the last three and a half years. Thanks for putting up with living at opposite ends of the country for longer than either of us first thought, and for always being there to cheer me up when things were stressful in the lab.

The final thanks go to my Mum and Dad, for always believing in me and supporting me in everything I do. I wouldn't be where I am today without you.

August 2022: Thank you to my examiners Marc-Alban Millet and Andy Aplin for an enjoyable viva.

Contents

Abstract iii

Declaration iv

Acknowledgements v

Contents vii

List of Figures xii

List of Tables xiv

Chapter 1: Introduction 1

1.1 Thesis Rationale 1

1.2 Stable Isotope Theory 3
1.2.1 Equilibrium Fractionation 4
1.2.2 Kinetic Fractionation 8

1.3 Iron Stable Isotopes 8
1.3.1 Chemical Characteristics 8
1.3.2 *Ab Initio* and Spectroscopic Studies 9
1.3.3 Iron Isotopes in Terrestrial Samples 10

1.4 Zinc Stable Isotopes 14
1.4.1 Chemical Characteristics 14
1.4.2 Zn Isotopes in Terrestrial Samples 15

1.5 Vanadium Stable Isotopes 17
1.5.1 Chemical Characteristics 17
1.5.2 Vanadium Isotopes in Terrestrial Samples 18
1.5.3 Vanadium Isotopes and Oceanic Redox State 21

1.6 Thesis Outline 22

Chapter 2: Methods 24

2.1 Introduction 24

2.2 Materials 25

2.3 Sample Digestion 26

2.4 Ion-Exchange Column Chromatography 27
2.4.1 Background 27
2.4.2 Column 1: Separation of V, Fe and Zn 29

2.4.3 Further V separation 32
2.4.3.1 Column 2: Removal of Ti 34
2.4.3.2 Column 3: Main V-Cr Separation 35
2.4.3.3 Column 4 and 5: Clean-up Columns 36

2.5 MC-ICP-MS Methodology 37
2.5.1 Background 37
2.5.2 Iron MC-ICP-MS Methodology 40
2.5.2.1 Background Principles and Considerations 40
2.5.2.2 Instrumentation and Measurement Protocol 41
2.5.2.3 Quality Control and Assurance 47
2.5.2.4 Iron Specific Considerations 55
2.5.3 Zinc MC-ICP-MS Methodology 59
2.5.3.1 Background Principles and Considerations 59
2.5.3.2 Instrumentation and Measurement Protocol 61
2.5.3.3 Quality Control and Assurance 64
2.5.4 Vanadium MC-ICP-MS Methodology 73
2.5.4.1 Background Principles and Considerations 73
2.5.4.2 Instrumentation and Measurement Protocol 74
2.5.4.3 Quality Control and Assurance 78

2.6 Strontium and Neodymium Isotope Analysis 82
2.6.1 Ion Exchange Column Chromatography 82
2.6.2 Sr Isotope Ratio Measurements 83
2.6.3 Nd Isotope Ratio Measurements 84

Chapter 3: Integrated Petrological and Fe-Zn Isotopic Modelling of Plutonic Differentiation 86

3.0 Abstract 86

3.1 Introduction 87

3.2 Geological Background 91
3.2.1 Boggy Plain Zoned Pluton 91
3.2.2 Whole rock chemical variations 92

3.3 Sample Selection and Petrography 94

3.4 Analytical Methods 98
3.4.1 Chemical isolation 99
3.4.2 Isotope Ratio Measurement 100

3.5 Results 102
3.5.1 Iron isotopic data 102
3.5.1.1 Mineral-mineral fractionation factors 104
3.5.2 Zinc Isotopic Data 104

3.6 Drivers of Fe-Zn isotopic variation in the Boggy Plain Zoned Pluton 109
3.6.1 Impact of crustal assimilation and fluid exsolution on Fe-Zn isotopic compositions 109
3.6.2 Fe isotopic fractionation during fractional crystallisation 111
3.6.3 Controls on Inter-Mineral Fractionation Factors in the BPZP 112

3.7 Modelling Fe isotopic variations in plutonic settings 118
3.7.1 Step 1: Estimating initial magma composition ($\delta^{56}Fe_{initial}$) 118
3.7.2 Step 2: Estimating fraction of Fe remaining (*f*Fe) 119
3.7.3 Step 3: Calculating mineral-melt fractionation factors 119

3.7.4 Step 4: Deriving a bulk mineral-melt fractionation factor ($\Delta^{56}Fe_{min\text{-}melt}$) 123
3.7.5 Model Comparisons 125

3.8 Implications 127

3.9 Conclusions 129

3.A1 Neodymium Isotopic Analyses 131
3.A1.1 Methodology 131
3.A1.2 Results 131

3.A2 Iron-Zinc Isotopic variations 133

3.A3 Rhyolite-MELTS Modelling 134

Chapter 4: Vanadium Isotopic Behaviour in the Continental Crust 137

4.0 Abstract 137

4.1 Introduction 138

4.2 Geological Background and Samples 141
4.2.1 Overview 141
4.2.2 Magnetite Petrography 143

4.3 Methods 144
4.3.1 Vanadium Isotope Analysis 144
4.3.2 Magnetite Trace Element Analysis 146
4.3.3 Magnetite Major Element Estimation 147

4.4 Results 148
4.4.1 Vanadium Isotopic Compositions of Whole Rock and Mineral Separates 148
4.4.2 Magnetite Trace Element Data 152

4.5 Causes of V isotopic variations in the Boggy Plain Zoned Pluton 156
4.5.1 Explaining the scatter in WR $\delta^{51}V$ values 157
4.5.2 Indistinguishable $\delta^{51}V$ of biotite, magnetite, and hornblende primocrysts in the same sample.. 158
4.5.3 Drivers of the increase in $\delta^{51}V$ with differentiation 161
4.5.4 Trends in mineral separate V isotopic composition 162

4.6 Models of V Isotopic Variation 166
4.6.1 Rayleigh models and reconstruction of melt isotopic composition 166
4.6.2. Smaller variation in modelled $\delta^{51}V_{melt}$ of the BPZP compared to extrusive lavas 170

4.7 Pluton-scale isotopic heterogeneity and implications for the average isotopic composition of the continental crust 172

4.8 Conclusions 174

Chapter 4 Appendix 175

Chapter 5: The influence of Fe-Ti Oxide mineralogy and crystallisation on V isotopic trends: comparison of a calc-alkaline and tholeiitic intrusion 176

5.0 Abstract 176

5.1 Introduction 177

5.2 Geological Background 181
5.2.1 The Red Hill Intrusion, SE Tasmania 181
5.2.2 Whole Rock Chemical Variations 183
5.2.3 Sample Petrography 185
5.2.4 Oxide and Sulphide Petrography 187

5.3 Methods 192
5.3.1 Iron, Zinc and Vanadium Isotopic Compositions 192
5.3.2 Strontium and Neodymium Isotopic Analyses 193

5.4 Results 193
5.4.1 Vanadium Isotopes 193
5.4.2 Iron Isotopes 196
5.4.3 Zinc Isotopes 202
5.4.4 Strontium and Neodymium Isotopes 205

5.5 Discussion 208
5.5.1 Radiogenic Sr-Nd values in the Red Hill intrusion 208
5.5.2 Zinc Isotopes in the Red Hill intrusion 209
5.5.3 Assessing the attainment of inter-mineral isotopic equilibrium 211
5.5.4 Vanadium isotope trends in the Red Hill Intrusion 214
5.5.5 Modelling V isotope behaviour in calc-alkaline and tholeiitic magmas 215
5.5.6 Discussion of model results 221

5.6 Complications and considerations for future work 222

5.7 Conclusions 225

Chapter 6: Synthesis and Future Work 227

6.1 Synthesis and Conclusions 227
6.1.1 Advances in understanding the controls on Fe, V and Zn isotope fractionation in intrusive settings 227
6.1.2 Complications with investigating isotopic variations in intrusive settings 232
6.1.3 Implications for the composition of the continental crust 235

6.2 Future Work 237
6.2.1 Determining accurate mineral-melt fractionation factors 237
6.2.2 Future investigations in intrusive settings 238
6.2.3 New approaches for modelling isotopic trends 239

References 241

Appendix 1: Preliminary Fe-Zn Isotope Data from the Fagradalsfjall Eruption, 2021 263

A1.1 Introduction 263

A1.2 Fe and Zn isotope fractionation during mantle melting 265

A1.3 Results 266

A1.4 Preliminary Conclusions 269

A1.5 References 270

Appendix 2: Copy of Stow et al. (2022) 272

Appendix 3: Contents of Electronic Appendices 298

List of Figures

1.1 Compilation of force constants for Fe-O bonds in minerals and melt, from NRIXS and *ab initio* studies …… 10
1.2 Range in $\delta^{56}Fe$ values measured in chondrites and terrestrial igneous lithologies ……....11
1.3 Range in $\delta^{56}Fe$ values measured in chondrites and terrestrial igneous lithologies ……..….15
1.4 Range in $\delta^{51}V$ values measured in chondrites and terrestrial igneous lithologies ……..... 19
2.1 Flowchart illustrating the full column chromatography procedure used in this study …….... 29
2.2 Flowchart outlining the process to separate Fe, V and Zn in Column 1 ……30
2.3 Iron partitioned to the AG1-X8 resin during the 6M HCl wash step……..31
2.4 Flowcharts describing the four stages of ion exchange chromatography used in this study for quantitative separation of V ……33
2.5 Main V-Cr separation column ……..……36
2.6 Schematic of Neptune MC-ICP-MS ……39
2.7 Typical shape of a Fe peak scan at medium resolution ($m/\Delta m \approx 4000$) ……41
2.8 Long term reproducibility of Romil Fe standard ……..53
2.9 Long term reproducibility of USGS reference material GSP-2 ……54
2.10 Iron isotopic composition of the synthetic magnetite powder against mass dissolved ……..……58
2.11 Long term reproducibility of the *Romil Zn* in-house standard ……..70
2.12 Long term reproducibility of the IRMM-3702 certified reference material ..70
2.13 Long term reproducibility of the BDH solution standard……..…...81
3.1 Map of the Berridale and Kosciuszko batholiths in the SE of the Lachlan Fold Belt, and the Boggy Plain Zoned Pluton …….. 92
3.2 Chemical variations in the BPZP ……..93
3.3 Petrographic textures in the BPZP ……97
3.4 Typical textures and morphologies of Fe-Ti oxides in the BPZP …… 98
3.5 Three-isotope plots for Fe ($\delta^{56}Fe$ vs $\delta^{57}Fe$) and Zn ($\delta^{66}Zn$ vs $\delta^{68}Zn$) ……102
3.6 Iron isotopic composition of whole rocks and mineral separates against WR MgO and SiO_2 content ……..… 103
3.7 Zinc isotopic compositions of whole rock and mineral separates against WR MgO and SiO_2 content …….. 106
3.8 Variation in magnetite-biotite fractionation factors with WR SiO_2, WR $Fe^{3+}/\Sigma Fe$ and biotite $Fe^{3+}/\Sigma Fe$ …….……... 114
3.9 Measured $\Delta^{56}Fe_{mag\text{-}bt}$ for the BPZP samples against crystallisation temperature …..……. 115
3.10 Change in $\delta^{56}Fe$ of a magma undergoing fractional crystallisation, modelled using the Rayleigh equation at constant $\Delta^{56}Fe_{min\text{-}melt}$ …… 120

3.11 Determinations of modal abundances, bulk $\Delta^{56}Fe_{min\text{-}melt,}$ and resulting magma $\delta^{56}Fe$ from three Rayleigh models ……..……. 124
3.S1 Measured εNd and age corrected εNd_i values against WR MgO content for the BPZP whole rock samples ……132
3.S2 Zinc vs Iron isotopic compositions for the BPZP whole rock samples …..133
3.S3 Rhyolite-MELTS models of major element variations in the BPZP magma ……135
3.S4 Determinations of modal abundances, bulk $\Delta^{56}Fe_{min\text{-}melt}$ and resulting magma $\delta^{56}Fe$ using Rhyolite-MELTS ……..…… 136
4.1 Fe and V variations in the BPZP ……142
4.2 Variation in WR $\delta^{51}V$ with WR MgO and SiO_2 content ……149
4.3 Variation in mineral separate $\delta^{51}V$ with WR MgO and SiO_2 content ……150
4.4 Inter-mineral fractionation factors in the BPZP ……..150
4.5 Trace element variations in magnetite measured by ICP-QQQ-MS …….. 153
4.6 Ti-Nr-Cr magnetite discrimination diagram …….. 156
4.7 Variation in biotite V isotopic composition and chemistry ……... 162
4.8 Variation in magnetite V isotopic composition and chemistry …….. 163
4.9 Vanadium isotopic composition of magnetite mineral separates plotted against WR $Fe^{3+}/\Sigma Fe$ ……..164
4.10 The $\delta^{51}V$ evolution of a melt undergoing fractional crystallisation …….167
4.11 Calculation of the $\delta^{51}V$ of the BPZP melt from magnetite mineral separate data …… 169
4.12 A comparison of the reconstructed BPZP melt and extrusive lava suites …172
5.1 Variation in WR $\delta^{51}V$ of extrusive lava suites ……..……..180
5.2 Geological Map of the Red Hill Intrusion …… 182
5.3 Chemical variations in the Red Hill Intrusion …… 184
5.4 Petrography of the Red Hill intrusion …… 186
5.5 Oxide and sulphide petrography in the Red Hill intrusion ……. 189
5.6 Schematic illustrating the method used to calculate bulk titanomagnetite TiO_2 concentration …… 190
5.7 V isotopic composition of whole rock and mineral separates against WR MgO content ……... 194
5.8 Comparison of Fe isotope data from this study and Sossi et al. 2012 ….....197
5.9 Three-isotope plot for Fe ($\delta^{56}Fe$ vs $\delta^{57}Fe$) …… 198
5.10 Zn isotopic composition of whole rock and mineral separates against WR MgO content ……...……... 202
5.11 Initial Sr and Nd isotopic compositions in the Red Hill intrusion ……. 206
5.12 Measured $\Delta^{56}Fe_{mag\text{-}px}$ for the Red Hill samples against crystallisation temperature …… 213
5.13 Comparison of melt isotopic evolution in the Red Hill intrusion and Boggy Plain Zoned Pluton …… 220
6.1 Summary diagram of concepts discussed in this thesis and ideas for future work ……... 240
A1.1 Temporal chemical variations in the Fagradalsfjall basalts ……264
A1.2 Iron isotopic composition of the Fagradalsfjall basalts …… 266
A1.3 Zinc isotopic composition of the Fagradalsfjall basalts …… 269

List of Tables

1.1 Bonding environments of Fe, V and Zn in melt and minerals relevant to this work 6-7
2.1 The cup configuration and resistors used for Fe isotopic measurements at Durham University 42
2.2 Iron isotopic compositions of the test batch of USGS reference materials..... 48
2.3 Literature compilation of Fe isotopic compositions of USGS reference materials ..... 50 - 51
2.4 Iron isotopic compositions of USGS reference materials processed with each batch of samples 52
2.5 Long term reproducibility of the Romil Fe standard 53
2.6 Total procedural Fe blanks for each batch of samples processed.....55
2.7 Iron isotopic composition of the synthetic magnetite powder aliquots 58
2.8 Iron isotopic compositions of 3 magnetite mineral separates 59
2.9 The cup configuration and resistors used for Zn isotopic measurements at Durham University 62
2.10 Zinc isotopic compositions of the test batch of USGS reference materials ...65
2.11 Literature compilation of Zn isotopic compositions of USGS reference materials 67-68
2.12 Zinc isotopic composition of USGS reference materials processed with each batch of samples 69
2.13 Zinc isotopic composition of the IRMM-3702 certified reference material from previous studies relative to the JMC-Lyon and AA-ETH standards 71
2.14 Total procedural Zn blanks for each batch of samples processed 71
2.15 The cup configurations and resistors used for V isotopic measurements at Durham University 75
2.16 Average $\delta^{51}V_{AA}$ values for the Ti and Cr-doped BDH solutions before corrections, and the β factor used for mass bias correction 78
2.17 Vanadium isotopic compositions of USGS reference materials processed with each batch of samples 79
2.18 Literature compilation of V isotopic compositions of USGS reference materials 80
2.19 Total procedural V blanks for each batch of samples processed 82
3.1 Iron and Zinc isotopic composition of BPZP whole rock samples and USGS reference materials 107
3.2 Iron and Zinc isotopic composition of BPZP mineral separates 108
3.3 Temperature determinations for the BPZP 113
3.S1 Neodymium isotopic composition of BPZP samples.....133
3.S2 Starting magma composition and parameters used to model magma fractional crystallisation with Rhyolite-MELTS 134
4.1 Vanadium isotopic composition of BPZP whole rock powders 151

4.2 Vanadium isotopic composition of BPZP mineral separates …….. 152
4.3 Transition metal concentrations of magnetite mineral separates measured by ICP-QQQ-MS ……. 154
4.4 Transition metal concentrations of the synthetic magnetite powder measured by ICP-QQQ-MS …… 154
4.5 Structural formula and most likely V substitutions for magnetite, biotite and hornblende …….. 160
4.S1 Magnetite trace element data measured by ICP-QQQ-MS ……. 175
5.1 Titanomagnetite TiO_2 concentrations calculated using the mass balance approach and measured using EDS coarse rasters ……. 190
5.2 Sulphide compositions measured by EDS …….. 191
5.3 Vanadium isotopic compositions of whole rock and mineral separates from the Red Hills Intrusion …… 195
5.4 Whole Rock Fe isotopic compositions from this study, compared to values from Sossi et al. (2012) …….. 199 - 200
5.5 Iron isotopic compositions of pyroxene mineral separates from this study, compared to values from Sossi et al. (2012) …… 201
5.6 Iron isotopic compositions of magnetite mineral separates from this study, compared to values from Sossi et al. (2012) …… 201
5.7 Zinc isotopic compositions of whole rock and mineral separates from the Red Hills Intrusion …… 203 - 204
5.8 Neodymium isotopic composition of the Red Hills samples ……207
5.9 Strontium isotopic composition of the Red Hills samples …….. 207
A1.1 Iron isotope data for the Fagradalsfjall basalts relative to the NRM524 standard …….. 268
A1.2 Zinc isotope data for the Fagradalsfjall basalts relative to the AA-ETH standard ……...267

Chapter 1: Introduction

1.1 Thesis Rationale

Formation of a chemically evolved continental crust through subduction and arc magmatism is a unique process on Earth that is not observed elsewhere in the solar system (e.g. Taylor, 1989). The continental crust is largely constructed from intrusive plutonic bodies which form when magmas cool and crystallise within crustal reservoirs, rather than erupting at the Earth's surface. The continental crust is reworked over time by numerous metamorphic and melting events, and consequently the crust is extremely chemically and lithologically diverse, and an important record of past geological activity (e.g. Rudnick and Gao, 2003). Variations in the elemental and isotopic compositions of crustal rocks, and the sediments eroded from them, have previously been used as evidence for global scale processes during Earth evolution, such as the start of modern-day plate tectonics (see reviews by Condie, 2018 and Hawkesworth et al., 2020) and the oxygenation of the atmosphere (e.g. Bucholz et al., 2018). From an economic standpoint, the concentration of critical metals in the continental crust during magmatic processes (e.g. Groves and Bierlein, 2007) is vital for our modern day technologies.

However, to fully understand the continental crust rock record, it is necessary to understand the magmatic processes which occur in the plutonic bodies that solidify to form large proportions of the crust. It is now understood that most crustal magma storage occurs in crystal rich mushy regions rather than in large liquid dominated magma chambers (e.g. Bachmann and Bergantz, 2004; Cashman et al., 2017; Sparks et al., 2019). However, the exact chemical conditions and petrogenetic processes which occur in these mushy regions when plutonic bodies cool and crystallise are still uncertain (e.g. Sparks et al., 2019). Therefore, there is a requirement for chemical tracers which can track both intensive parameters (e.g. T, fO_2) and differentiation processes (e.g. fractional crystallisation, melting, diffusion, fluid exsolution) in these settings.

One possibility is the use of "non-traditional" transition metal stable isotope systems (TMSI; e.g. Fe, V, Zn, Cu, Ti). Since equilibrium stable isotope fractionation is theoretically driven by differences in bonding environment and redox state between

phases, and varies inversely with temperature (e.g. Urey, 1947; Schauble, 2004), TMSIs have the potential to provide information about both physical conditions and processes during magmatic differentiation (e.g. see review in Teng et al., 2017). Since the early 2000s, analytical developments have enabled high precision measurements of the small variations in isotopic compositions found at high temperatures for a huge range of isotope systems. For example, isotope systems which have previously been used to investigate processes during magmatic differentiation include Fe (e.g. Dauphas et al., 2017 and references therein), Ti (e.g. Deng et al., 2019; Hoare et al., 2020), Zn (e.g. Chen et al., 2013; Moynier et al., 2017), Zr (e.g. Inglis et al., 2019), Cr (e.g. Shen et al., 2020), V (e.g. Prytulak et al., 2013; Prytulak et al., 2017).

To date, the majority of studies of TMSIs in magmatic systems have focused on fine grained, nearly aphyric lavas, such as those erupted from Hekla volcano, Iceland. Most of the current knowledge of isotopic behaviour in magmatic systems is based on variations in the isotopic compositions of whole rock powders from cogenetic lava suites. Lavas are fundamentally different from the intrusive rocks which make up most of the continental crust. Lavas represent an instantaneously quenched magma, whereas intrusive rocks can be coarse grained, modally heterogeneous, and composed of both crystals and trapped interstitial melt that may have changed in their relative proportions compared with a parental magma (e.g. by extraction or exchange of interstitial melt from a crystal mush, or physical segregation of crystals from melt; Irvine, 1982; Chappell and Wyborn, 2004). Therefore, a whole rock composition may not represent the isotopic composition of the evolving melt (e.g. Chappell and Wyborn, 2004; Vernon and Collins, 2011). Intrusive rocks also cool and crystallise over hundreds to millions of years timescales (e.g. Paterson et al., 2011), leading to potential for isotopic fractionation at sub-solidus conditions due to isotopic exchange between phases during sub-solidus exsolution. However, some isotopic studies of intrusive rocks analyse the isotopic composition of whole rock powders, often without due consideration of the textural and petrological complexities of the samples, and/or compare samples from separate, genetically unrelated intrusions (e.g. Poitrasson and Freydier, 2005; Heimann et al., 2008; Telus et al., 2012; Foden et al., 2015; Gajos et al., 2016; He et al., 2017; Wu et al., 2017; Wu et al., 2018).

In this work, we use an integrated chemical and petrological approach for investigating the behaviour of transition metal stable isotope systems in intrusive settings. Three

isotope systems are chosen, which show contrasting behaviours in magmatic systems: Iron (Fe), Zinc (Zn) and Vanadium (V). Two case studies are investigated: the calc-alkaline Boggy Plain Zoned Pluton, Australia (Wyborn, 1983) and the tholeiitic Red Hill intrusion, Tasmania (McDougall, 1962). For both systems, petrological examination of samples is combined with Fe-V-Zn isotopic analysis of mineral separates and whole rock powders. The aims of this study are to:

1. Identify the main cause(s), magnitudes and directions of Fe, V and Zn isotope fractionation in intrusive settings.
2. Determine the effect of varying mineralogy, magma chemistry, fO_2 and temperature on Fe, V and Zn isotope fractionation. Assess the potential for Fe, V and Zn isotopes to be used as proxies for physical parameters or conditions during magmatic differentiation.
3. Develop methods for modelling isotopic variations in intrusive samples, based on the petrological understanding obtained from examination of crystal textures.
4. Extrapolate the findings from plutonic bodies to broader implications for the isotopic composition of the continental crust, and sediments eroded from it, over larger spatial and temporal scales.

Sections 1.2 to 1.5 summarise our current understanding of Fe, Zn and V isotopic fractionation in igneous settings. An outline of the contents of the thesis is given in Section 1.6.

1.2 Stable Isotope Theory

Stable isotope fractionation is the preferential partitioning of the heavier and lighter isotopes of an element between two phases. Stable isotopes can be fractionated by both mass dependent (i.e. the ratios of the different isotopes scale with the difference in mass between the isotopes) and mass independent processes (e.g. Dauphas and Schauble, 2016). In natural samples, mass independent fractionations are found in extra-terrestrial material, generated by processes during the formation of the solar system (e.g. Clayton et al., 1973), or in samples from the Early Earth resulting from UV photolysis of gases in

an oxygen poor atmosphere (e.g. Farquhar et al., 2000). In this work, only mass dependent stable isotope fractionation is considered.

The fractionation of stable isotopes between two phases can be expressed by Equation 1.1, where α is the fractionation factor between the two phases and R is the ratio of the heavy/light isotopes in the phase. Fractionation factors can also be expressed using delta notation (Equation 1.2; e.g. Dauphas et al., 2017; Faure and Mensing, 2005).

$$\alpha_{A-B} = R^A/R^B \qquad [1.1]$$

$$\Delta_{A-B} = \delta_A - \delta_B \approx 1000(\alpha_{A-B} - 1) \approx 1000 ln\alpha_{A-B} \qquad [1.2]$$

1.2.1 Equilibrium Fractionation

The theoretical calculations for predicting equilibrium stable isotope fractionation between phases were originally presented by Urey (1947) and Bigeleisen and Mayer (1947), based on the vibrational energies of molecules. These equations were developed to explain mass dependent fractionation of the "traditional" low mass stable isotopes (H, C, N, O, S), but are also applicable to the growing group of "non-traditional" stable isotopes which are now being routinely analysed (e.g. Fe, V, Zn, Ti, Cr, Zr, Si). From these calculations, there are several basic rules which govern equilibrium isotope fractionation between phases (Bigeleisen and Mayer, 1947; Urey, 1947; Schauble, 2004).

- The magnitude of equilibrium isotope fractionation decreases with temperature, roughly proportional to $1/T^2$. Therefore, in the high temperature magmatic settings studied in this work, isotopic fractionation is predicted to be small compared to variations in surface environments such as rivers and sediments.
- The magnitude of isotope fractionation scales inversely with mass i.e. lighter elements show larger fractionation. Therefore, all else being equal, the transition metal stable isotopes studied in this work (Fe, V and Zn) are predicted to show smaller fractionations than lighter stable isotopes (e.g. H, C, O).

- At equilibrium, heavy isotopes are concentrated in the materials with the highest bond force constants (stiffer, shorter and stronger bonds), which tend to form in substances with:

    1. High oxidation state. In the context of this work, this means that for the multi-valent elements Fe and V, heavier isotopes are predicted to concentrate in phases with the highest valence state (e.g. for Fe, magnetite with high $Fe^{3+}/\Sigma Fe$ is predicted to have a heavier isotopic composition than other minerals; Sossi and O'Neill, 2017).
    2. Low coordination number. For example, Zn^{2+} can be held in IV-fold coordination in melt, and VI-fold coordination in minerals, which might explain enrichment in heavy Fe in the melt phase during partial melting (Sossi et al., 2018).
    3. Covalent bonds with similar electronegativities. In this work, the metal cations bond to oxygen anions in minerals and melt, which typically form ionic bonds. However, Fe-S bonds in sulphides have a more covalent character.

The bonding environments of Fe, V and Zn in the phases relevant to this work are summarised in Table 1.1.

Table 1.1. Bonding environments of Fe, V and Zn in melt and minerals relevant to this work.

Phase	Fe Bond Lengths (Å)	Fe Bonding Environment	V Bonding Environment	Zn Bonding Environment
(Titano)magnetite: **$^{IV}(Fe^{3+})^{VI}(Fe^{3+}, Fe^{2+})O_4$** (pure magnetite) Ti substitutes following the reaction: $^{IV}Fe^{3+} + {}^{VI}Fe^{3+} = {}^{IV}Fe^{2+} + {}^{VI}Ti^{4+}$ (e.g. Wechsler et al., 1984; Bosi et al., 2009)	Magnetite: ^{VI}Fe-O = 2.068 ^{IV}Fe-O = 1.873 (Sossi and O'Neill, 2017) Ti substitution leads to longer tetrahedral and shorter octahedral bonds; Bosi et al. 2009).	In end member magnetite, Fe^{2+} on VI-fold site, Fe^{3+} substituted evenly between IV and VI-site (Wechsler et al., 1984).	V^{3+} and V^{4+} on VI sites (O'Neill and Navrotsky, 1984; Toplis and Corgne, 2002).	Normal spinel, $^{IV}Zn^{2+}$ substituting for $^{IV}Fe^{2+}$ (Marshall and Dollase, 1984) Uncertain in inverse spinel (magnetite), $^{VI}Zn^{2+}$ for $^{VI}Fe^{2+}$ may be energetically unfavourable (Yang et al., 2021).
Biotite: **$I\,M_{2\text{-}3}\,\square_{1\text{-}0}T_4O_{10}A_2$** M = VI-fold (Li, **$Fe^{3+}$**, **$Fe^{2+}$**, Mg, Mn, **Zn**, Al, Cr, **V**, Ti) T = IV-fold (Be, Al, B, Fe^{3+}, Si) I = Cs, K, Na, NH_4, Rb, Ba, Ca A = Cl, F, OH, O, S $\square$ = vacancy (Rieder et al., 1999)	Annite: ^{VI}Fe-O = 2.109 (Nie et al., 2021)	Fe^{2+} and Fe^{3+} in VI-fold coordination on the M layer (Rieder et al., 1999)	Most likely as V^{3+} substituting for $^{VI}Fe^{3+}$in the M layer (Zheng et al., 2019)	Most likely as Zn^{2+} substituting for $^{VI}Fe^{2+}$ in the M layer (Rieder et al., 1999)
Hornblende: **$AB_2C_5T_8O_{22}W_2$** B= VI- to VIII-fold (Na, Ca, Mn^{2+}, **Fe^{2+}**, Mg, Li)	Synthetic Amphibole: M_2-O = 2.107 M_3-O = 2.115 (Redhammer and Roth, 2002)	Fe^{2+} can be found on B and C sites, Fe^{3+} is found on C sites (Oberti et al., 2007)	Most likely V^{3+} substituting for Fe^{3+} on VI-fold C sites (Oberti et al., 2007).	Most likely as $^{VI}Zn^{2+}$ substituting for $^{VI}Fe^{2+}$ (Oberti et al., 2007)

C = VI-fold M1, M2 and M3 sites (Mg, **Fe^{2+}**, Mn^{2+}, Al, **Fe^{3+}**, Mn^{3+}, Ti^{4+}, Li) A = Na, K, Ca, Pb, Li T = IV-fold (Si, Al, Ti^{4+}, Be W = OH, F, Cl, O) (Hawthorne et al., 2012)				
Pyroxene: **$M_1M_2T_2O_6$** M_1 = VI-fold (Mn^{2+}, **Fe^{2+}**, Mg, **Fe^{3+}**, Al, Cr, Ti) M_2 = distorted VI -fold (Na, Ca, Mn^{2+}, **Fe^{2+}**, Mg, Li) T = IV-fold (Si, Al) (Cameron and Papike, 1981; Morimoto, 1988)	Fe-O bonds in various pyroxenes: Augite M_1 = 2.163 Augite M_2 = 2.050 Hedenbergite M_1 = 2.152 Diopside M_1 = 2.146 Enstatite M_1 = 2.149 (Rabin et al., 2021)	Fe^{2+} on M_1 and M_2 sites, Fe^{3+} on M_1 sites (Cameron and Papike, 1981; Morimoto, 1988)	Most likely V^{3+} for $^{VI}Fe^{3+}$ and V^{4+} for $^{VI}Ti^{4+}$ (Toplis and Corgne, 2002)	Most likely as $^{VI}Zn^{2+}$ substituting for $^{VI}Fe^{2+}$ (Cameron and Papike, 1981; Morimoto, 1988)
Silicate Melt		Fe^{3+} and Fe^{2+} in IV- to V-fold coordination (Wilke et al., 2005).	Redox dependent - minor V^{3+}, higher abundances of V^{4+} and V^{5+} in IV- and V-fold coordination (Giuli et al., 2004; Sutton et al., 2005; Righter et al., 2006).	Most likely IV-fold Zn^{2+} because Zn^{2+} has no octahedral site preference energy (e.g. Sossi et al., 2018a).

1.2.2 Kinetic Fractionation

Stable isotopes can be fractionated by kinetic processes, with chemical and Soret (thermal) diffusion being the most relevant for igneous systems (e.g. Dauphas et al., 2017). In chemical diffusion, as elements diffuse from high to low concentrations, the lighter isotopes diffuse faster (e.g. Richter et al., 2003). Diffusive exchange of Fe and Mg isotopes between olivine and melt is known to drive spatial variations in Fe and Mg isotopes within olivine grains (e.g. Sio et al., 2013). In Soret diffusion, diffusion occurs along a thermal gradient, with heavier isotopes preferentially enriched at the cold end (e.g. Richter et al., 2008). Soret diffusion has been proposed to explain large scale isotopic variations in granitoids (e.g. Zambardi et al., 2014; Gajos et al., 2016), although this is not well accepted (Müntener and Baumgartner, 2019).

These processes are not thought to cause resolvable Fe-V-Zn isotope fractionation in this work, as discussed in the context of specific sample sets in subsequent chapters. The current understanding of Fe, V and Zn stable isotopes in igneous systems is summarised below.

1.3 Iron Stable Isotopes

1.3.1 Chemical Characteristics

Iron is a redox sensitive element which exists in 3 oxidation states: metallic (Fe^0), ferrous (Fe^{2+}) and ferric (Fe^{3+}). These species are stratified through the earth with metallic iron in the core, ferrous iron dominant in the mantle and ferric iron present in oxygenated surface environments and waters (e.g. McCammon, 2005; Dauphas et al., 2017).

Iron has four stable isotopes; ^{54}Fe, ^{56}Fe, ^{57}Fe and ^{58}Fe with abundances of 5.845%, 91.754%, 2.119% and 0.292% respectively (Lodders, 2003). Isotope ratios are expressed as $\delta^{56}Fe$ or $\delta^{57}Fe$ values, relative to the IRMM-014 standard (Equation 1.3). The IRMM-014 standard is no longer commercially available, so delta values can also be expressed relative to the NRM-524 standard, which is isotopically indistinguishable from IRMM-014 (Craddock and Dauphas, 2011). Assuming only mass dependent fractionation occurs, $\delta^{57}Fe \approx 1.5 \times \delta^{56}Fe$.

$$\delta^{5X}Fe = [\frac{(^{5X}Fe/^{54}Fe)_{sample}}{(^{5X}Fe/^{54}Fe)_{IRMM-014}} - 1] \times 1000 \qquad [1.3]$$

In magmatic systems, variation in $\delta^{56}Fe$ is driven by Fe isotope fractionation between minerals, melts and fluids. Iron can be present in a variety of oxidation states and coordination environments in magmatic systems. Silicate melts contain both Fe^{3+} and Fe^{2+} in IV- to V-fold coordination (Wilke et al., 2005). For this work, the key minerals to consider are magnetite and the silicate phases biotite, hornblende and pyroxene. Magnetite ($^{IV}Fe^{3+}\ ^{VI}(Fe^{2+}, Fe^{3+})\ O_4$) hosts Fe^{3+} in VI- and IV-fold coordination, and Fe^{2+} in the VI site. In the silicate phases, Fe^{2+} and Fe^{3+} are typically found in VI-fold coordination (Leake et al., 1997; Rieder et al., 1999; Cameron and Papike 1981). Therefore, Fe isotopic fractionation can be driven by both variations in redox state and coordination environment, but deconvolving the two effects is complex.

1.3.2 *Ab Initio* and Spectroscopic Studies

There are several methods which can be used to predict the magnitude of equilibrium Fe isotopic fractionation between phases during magmatic differentiation. Firstly, *ab initio* calculations based on the electronic structure of minerals using either density functional theory (e.g. Blanchard et al., 2009; Nie et al., 2021; Rabin et al., 2021) or other theoretical approaches (Sossi and O'Neill, 2017) can be used to calculate reduced partition function ratios (β factors) for Fe in different minerals. Alternatively, spectroscopic approaches such as nuclear resonance inelastic X-ray scattering (NRIXS; Dauphas et al., 2012; Dauphas et al., 2014; Roskosz et al., 2015; Nie et al., 2021; Roskosz et al., 2022) or Mössbauer spectroscopy (Polyakov and Mineev, 2000; Mineev et al., 2007; Polyakov et al., 2007) can be used to calculate β factors. The β factors can then be used to derive bond force constants for different phases. The bond force constants for some common minerals are shown in Figure 1.1. Minerals generally follow the order of heavy Fe isotope enrichment predicted by theory, with heavier isotopes concentrating in phases with higher Fe^{3+} content, lower bond coordination, and shorter Fe-O bonds. However, the nature of cations surrounding the Fe ions can also exert a control (Rabin et al., 2021).

In melt, Fe^{2+} and Fe^{3+} have different bond force constants, so that the overall force constant for Fe in the melt increases with $Fe^{3+}/\Sigma Fe$ (Dauphas et al., 2014; Roskosz et al.,

2022). Additionally, the force constant for Fe^{2+} is higher in alkali-rich, high silica magmas, most likely due to a decrease in the average bond coordination of Fe^{2+} in melts with high alkali content (Dauphas et al., 2014; Roskosz et al., 2022). The fractionation factor of Fe between mineral-mineral or mineral-melt phases at equilibrium can then be calculated using Equation 1.4 (Dauphas et al., 2014). As seen in Figure 1.1, the bond force constants of most minerals are smaller than in melt, which drives an increase in δ^{56}Fe in melt during fractional crystallisation.

$$\Delta^{56}Fe_{A-B} = 2853 \times \frac{<F_A> - <F_B>}{T^2} \qquad [1.4]$$

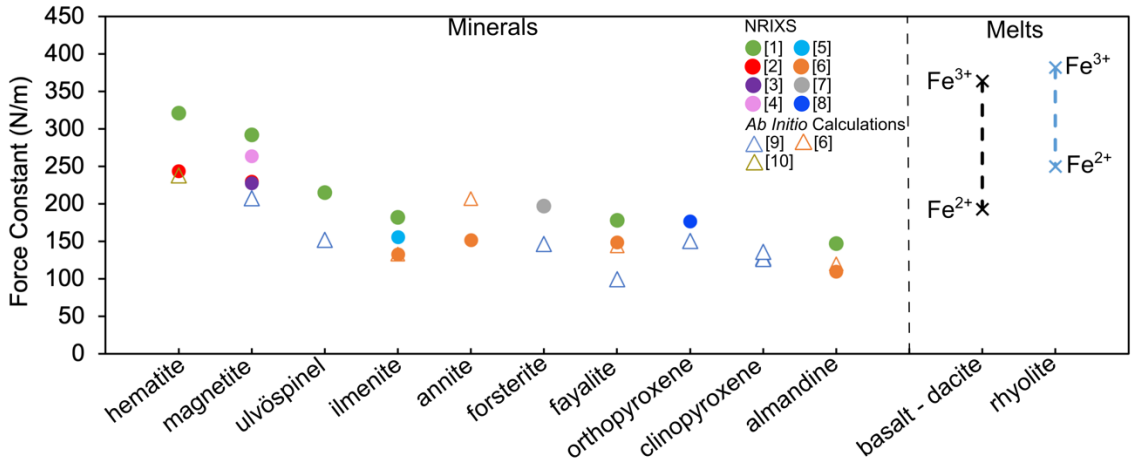

Figure 1.1. Compilation of force constants for Fe-O bonds in minerals and melt, from NRIXS and *ab initio* studies. Circles are data from NRIXS studies. Triangles are values using *ab initio* calculation approaches. For melt, the values for the Fe^{2+}-O and Fe^{3+}-O end members for basaltic to dacitic and rhyolitic melts are given (Roskosz et al., 2022). The average force constant for melt will lie between these values depending on $Fe^{3+}/\Sigma Fe$ ratio. Mineral species to the left of the figure typically have higher $Fe^{3+}/\Sigma Fe$, lower Fe-O bond coordination and shorter bonds, resulting in higher bond force constant. References: [1]Sossi and O'Neill, 2017 [2]Dauphas et al., 2012 [3]Polyakov et al., 2007 [4]Roskosz et al., 2015 [5]Williams et al., 2016 [6]Nie et al., 2021 [7]Dauphas et al., 2014 [8]Jackson et al., 2009 [9]Rabin et al., 2021 [10]Blanchard et al., 2009.

1.3.3 Iron Isotopes in Terrestrial Samples

Iron is the most extensively studied transition metal stable isotope (see review in Dauphas et al., 2017). Currently, the Fe isotopic compositions of most terrestrial lithologies have been measured. However, most studies measure the isotopic composition of whole rock

powders, and to date, a greater number of studies have focussed on extrusive lavas rather than intrusive plutonic rocks. Therefore, much of the current understanding about Fe (and other transition metal) isotopes in magmatic systems is based on extrusive lavas and may not necessarily be directly applicable to intrusive settings.

Typical ranges of the Fe isotopic compositions of terrestrial lithologies are illustrated in Figure 1.2.

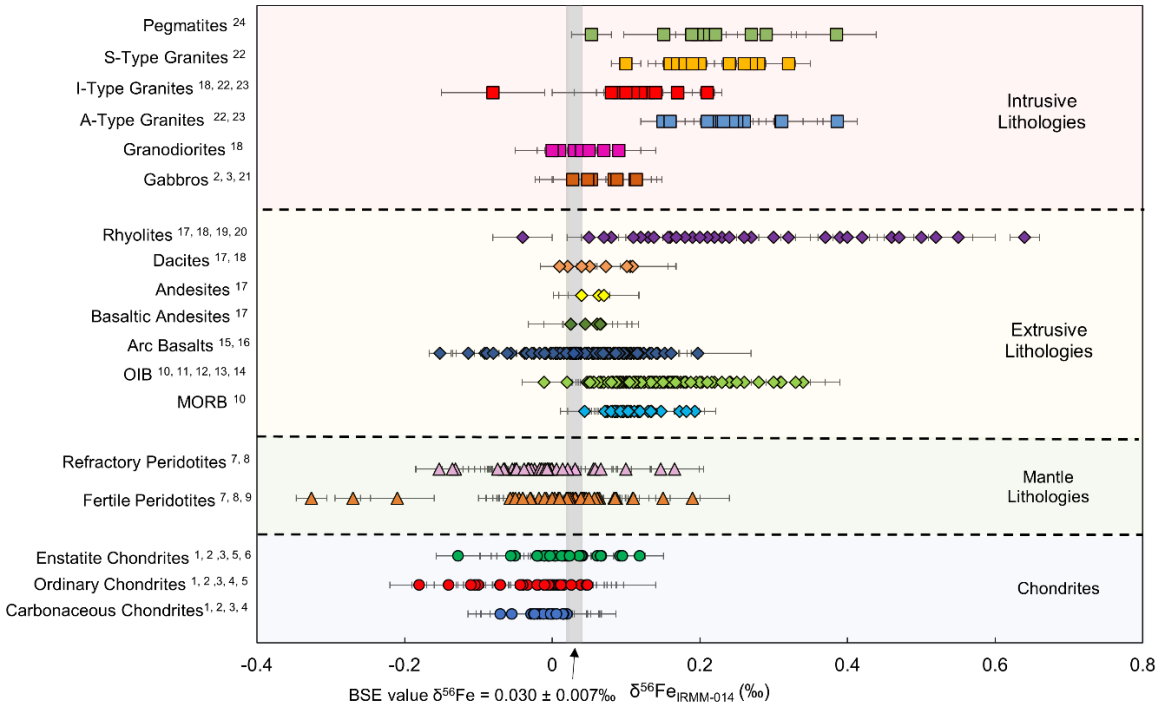

Figure 1.2. Range in δ^{56}Fe values measured in chondrites and terrestrial igneous lithologies. Data from [1]Craddock and Dauphas, 2011, [2]Poitrasson et al., 2005, [3]Schoenberg and von Blanckenburg, 2006, [4]Wang et al., 2013, [5]Needham et al., 2009, [6]Wang et al., 2014, [7]Weyer and Ionov, 2007, [8]Poitrasson et al., 2013, [9]Huang et al., 2011, [10]Teng et al., 2013, [11]Konter et al., 2016, [12]Nebel et al., 2019, [13]Gleeson et al., 2020, [14]Soderman et al., 2021, [15]Dauphas et al., 2009a, [16]Foden et al., 2018, [17]Schuessler et al., 2009, [18]Heimann et al., 2008, [19]Du et al., 2017, [20]Xia et al., 2017, [21] Su et al., 2015, [22]Foden et al., 2015, [23]Poitrasson and Freydier, 2005, [24]Telus et al., 2012. An estimate of the Fe isotopic composition of the Bulk Silicate Earth (BSE) from Sossi et al. (2016) is shown by the grey vertical band.

The Bulk Silicate Earth

The Fe isotopic composition of mantle peridotites is generally influenced by two processes, melt extraction and metasomatism. Metasomatized peridotites can show extremely variable Fe isotopic compositions depending on the nature of the metasomatizing fluid or melt, and values often reflect disequilibrium Fe isotope fractionation during melt/fluid percolation (e.g. Weyer and Ionov, 2007; Poitrasson et al., 2013; Zhao et al., 2015). In contrast, unmetasomatized peridotites which have experienced high degrees of melt extraction show light $\delta^{56}Fe$ values (Weyer and Ionov, 2007). On average, unmetasomatized peridotites ($\delta^{56}Fe$ = 0.033 ± 0.027, 2SD, n=60; Sossi et al., 2016) have lighter isotopic composition than average MORB ($\delta^{56}Fe$ = 0.105 ± 0.039‰, 2SD, n=43; Teng et al., 2013), which is used to suggest that isotopic fractionation on the order of 0.1‰ occurs during mantle partial melting. Some mantle derived basalts show distinct $\delta^{56}Fe$ values from the MORB average, which is attributed to the melting of different mantle sources with distinct isotopic compositions. Arc basalts are isotopically lighter than average MORB, which, whilst debated, can be interpreted as melting of an already depleted mantle source in the presence of oxidised fluids (Nebel et al., 2015; Sossi et al., 2016). Some ocean island basalts show isotopically heavy $\delta^{56}Fe$ values, which, whilst again debated, can be interpreted as the contribution of an isotopically heavy pyroxenite in the mantle source (e.g. Williams and Bizimis, 2014; Konter et al., 2016; Nebel et al., 2019; Soderman et al., 2021).

Iron Isotope Fractionation in Magmatic Systems

There is no resolvable change in $\delta^{56}Fe$ with increasing SiO_2 content in mafic and intermediate rocks (e.g. Beard et al., 2003; Poitrasson et al., 2004; Schuessler et al., 2009; Figure 1.2). However, studies on high silica samples show a clear increase in $\delta^{56}Fe$ values in rocks with >70 wt. % SiO_2 (e.g. Poitrasson and Freydier, 2005). High $\delta^{56}Fe$ values have been measured in both intrusive (Schoenberg & Von Blanckenburg, 2006; Heimann et al., 2008; Telus et al., 2012) and extrusive (Du et al., 2017; Xia et al., 2017) silicic rocks, up to a maximum $\delta^{56}Fe_{IRMM\text{-}014}$ value of + 0.64‰ in a rhyolite from the Hailar Basin, NE China (Xia et al., 2017).

The two most common interpretations for the increase in $\delta^{56}Fe$ in high silica samples are exsolution of isotopically light fluids (e.g. Poitrasson and Freydier, 2005; Heimann et al., 2008; Telus et al., 2012), and/or fractional crystallisation driving the evolving magma to higher $\delta^{56}Fe$ values (e.g. Sossi et al., 2012; Foden et al., 2015). Additionally, the increase in the force constant of Fe^{2+} in high silica, alkali rich melts may also partly explain this increase in $\delta^{56}Fe$ at high SiO_2 (Dauphas et al., 2014; Roskosz et al., 2022). It is likely that all processes contribute to the increase in $\delta^{56}Fe$, with the variable relative importance of each dependent on the specific setting. However, one reason for the uncertainty in interpreting the heavy $\delta^{56}Fe$ values in high silica intrusive rocks is that the studies analysed whole rock samples, making it difficult to distinguish the possible effects of mineral-mineral and mineral-melt isotopic fractionation. Therefore, more recent studies have begun to examine the Fe isotopic composition of mineral separates in order to provide more insight.

Teng et al. (2008) initially showed that accumulation of isotopically light olivine in Kilauea Iki Lava Lake causes an increase in the $\delta^{56}Fe$ of the residual melt. Sossi et al. (2012) examined the mineralogical control on whole rock Fe isotopic composition in intrusive settings at the Red Hill intrusion, Tasmania (explored in Chapter 5). In this low fO_2, tholeiitic magma, initial crystallisation of isotopically light Fe^{2+} bearing pyroxene causes melt $\delta^{56}Fe$ and $Fe^{3+}/\Sigma Fe$ to increase. When the magma reaches magnetite saturation, crystallisation of this isotopically heavy, Fe^{3+}-bearing phase causes melt $\delta^{56}Fe$ to decrease (Sossi et al., 2012). Other empirical studies have shown that mineral separates can have a wide range of isotopic compositions in igneous rocks (e.g. Heimann et al., 2008; Schoenberg et al., 2009; Telus et al., 2012; Chen et al., 2014; Bilenker et al., 2017; Wu et al., 2017; Bai et al., 2021). However, all the previous studies on granitic plutons present mineral separate data from separate, genetically unrelated intrusions, without any petrological context (Heimann et al., 2008; Telus et al,. 2012; Wu et al., 2017).

The only study to date of mineral separates within a closed system intrusive pluton is of the Red Hill intrusion (Sossi et al., 2012). There have been no other systematic investigations of mineral separates in closed system intrusive suites with different chemistry and mineralogy. This is especially important because the tholeiitic Red Hill intrusion may not be representative of the majority of the continental crust, which generally forms from calc-alkaline magma (e.g. Jagoutz and Kelemen, 2015; Chin et al.,

2018; Collins et al., 2020). Therefore, one aim of this study is to investigate Fe isotope fractionation in a closed system, calc-alkaline pluton with a focus on analysis of mineral separates, in order to better understand the behaviour of Fe in intrusive settings (Chapter 3).

1.4 Zinc Stable Isotopes

1.4.1 Chemical Characteristics

Zinc is a monovalent, lithophile element present only as Zn^{2+} in terrestrial minerals and aqueous complexes. Zinc is mildly incompatible in minerals during magmatic differentiation but is present in silicate minerals at hundreds of µg/g. Zinc has 5 stable isotopes, with the following natural abundances: ^{64}Zn (48%), ^{66}Zn (28%), ^{67}Zn (4%), ^{68}Zn (19%) and ^{70}Zn (0.6%) (e.g. Böhlke et al., 2005). Traditionally, isotope ratios are expressed as $\delta^{66}Zn$ values, relative to the JMC-Lyon standard (Equation 1.5).

$$\delta^{66}Zn = \left[\frac{(^{66}Zn/^{64}Zn)_{sample}}{(^{66}Zn/^{64}Zn)_{JMC-Lyon}} - 1\right] \times 1000 \qquad [1.5]$$

However, since the JMC-Lyon standard is no longer available, Zn values in this work are expressed relative to the AA-ETH standard, where $\delta^{66}Zn_{JMC\text{-}Lyon} = \delta^{66}Zn_{AA\text{-}ETH} + 0.28$ (Archer et al., 2017). If fractionation is mass dependent, $\delta^{67}Zn \approx 1.5 \times \delta^{66}Zn$, and $\delta^{68}Zn \approx 2 \times \delta^{66}Zn$, where $\delta^{67}Zn$ and $\delta^{68}Zn$ values are expressed using the $^{67}Zn/^{64}Zn$ and $^{68}Zn/^{64}Zn$ ratios respectively.

Zinc predominantly exists in octahedral coordination in silicate minerals (e.g. Moynier et al., 2017). Octahedrally coordinated Zn^{2+} has an ionic radius of 0.74Å, therefore most likely substitutes for VI-fold Fe^{2+} (0.78Å) and Mg^{2+} (0.72Å) due to their similar ionic radii (Shannon, 1976). In normal spinels ($^{IV}A^{2+}\,{}^{VI}B^{3+}{}_2O_4$), Zn^{2+} and other divalent cations are found in tetrahedral sites (Marshall and Dollase, 1984; Yang et al., 2021). The substitution of Zn^{2+} in inverse spinel like magnetite ($^{IV}A^{3+}\,{}^{VI}(B^{2+}, B^{3+})\,O_4$) is less clear, because although Zn^{2+} could substitute for Fe^{2+} on the VI-site, this may be energetically unfavourable (Yang et al., 2021). In silicate melt, Zn^{2+} is most likely IV-fold coordinated, because Zn^{2+} has no octahedral site preference energy (e.g. Sossi et al., 2018a).

1.4.2 Zn Isotopes in Terrestrial Samples

Figure 1.3 shows the Zn isotopic compositions of a range of terrestrial samples. As with Fe, most measurements of Zn isotopes in terrestrial igneous rocks have focussed on extrusive lavas.

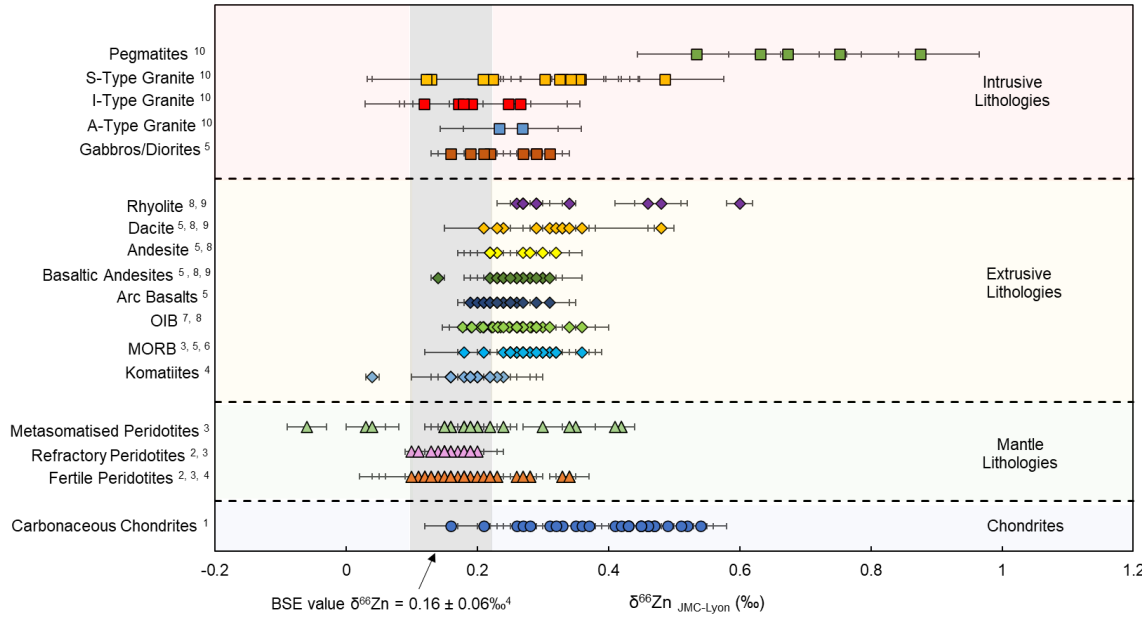

Figure 1.3. Range in δ^{66}Zn values measured in chondrites and terrestrial igneous lithologies. Data from: [1]Luck et al., 2005, [2]Doucet et al., 2016, [3]Wang et al., 2017, [4]Sossi et al., 2018a, [5]Huang et al., 2018, [6]Huang et al., 2016, [7]McCoy-West et al., 2018, [8]Chen et al., 2013, [9]Xia et al., 2017 and [10]Telus et al., 2012. The Bulk Silicate Earth (BSE) value of 0.16 ± 0.06‰ (2SD) is shown by the vertical grey band (Sossi et al., 2018a).

The Bulk Silicate Earth

Mantle peridotites, extrusive and intrusive igneous rocks all cluster within the range of $\delta^{66}Zn_{JMC\text{-}Lyon}$ from 0.1 to 0.3‰. Using fertile peridotites and komatiites, Sossi et al. (2018a) estimated that the Zn isotopic composition of the Bulk Silicate Earth is $\delta^{66}Zn_{JMC\text{-}Lyon}$ = 0.16 ± 0.06‰ (2SD).

Due to its monovalent character, equilibrium isotope fractionation of Zn in magmatic settings is driven by changes in coordination environment between minerals and melt. The controls on Zn isotope fractionation during mantle melting are still debated, but the

magnitude of fractionation is interpreted in the context of differential degrees and depths of melting (Doucet et al., 2016; Wang et al., 2017; Huang et al., 2018; Sossi et al., 2018a). Zinc exists in IV-fold coordination in silicate melts and spinel (Sossi et al., 2018a), and VI-fold co-ordination in other silicate minerals. Consumption of isotopically heavy spinel during mantle melting would therefore generate an isotopically heavier melt and leave a lighter residual mantle, which may explain the ~0.1‰ difference between refractory peridotites and MORB (Figure 1.3; Wang et al., 2017). However, it is still debated if melting in the garnet stability field fractionates Zn isotopes, because garnet peridotites and ocean island basalts have similar isotopic compositions (Doucet et al., 2016; Wang et al., 2017).

Zinc Isotope Fractionation in Magmatic Systems

Mid Ocean Ridge Basalts have an average $\delta^{66}Zn_{JMC\text{-}Lyon}$ of 0.27 ± 0.06‰ (2SD, n=13; Wang et al., 2017; Huang et al., 2018), and mantle derived basalts generally have Zn isotopic compositions within this range. Anomalously heavy $\delta^{66}Zn$ values in a small subset of basalts have been explained by recycling of isotopically heavy C-bearing phases into the mantle source, although the exact form of this carbon is debated (Liu et al., 2016; Beunon et al,. 2020; Liu et al., 2022).

Chen et al. (2013) first demonstrated that fractional crystallisation alone causes negligible Zn isotope fractionation of <0.1‰. In the Kilauea Iki lava lake, samples spanning an SiO_2 range from 44.63 – 57.07 wt.% and MgO range from 2.37 – 25.83 wt.% show a slight increase in WR $\delta^{66}Zn_{JMC\text{-}Lyon}$ from 0.26‰ to 0.36‰ during differentiation. This increase is predicted to be due to the crystallisation of isotopically light Fe-Ti oxides and olivine (Chen et al., 2013). Samples from Hekla volcano spanning a SiO_2 range from 46.42 - 72.07 wt.% and MgO range from 0.54 – 5.57 wt.% show a similar range in $\delta^{66}Zn$, but there is no correlation between isotopic composition and indices of magmatic differentiation (Chen et al., 2013). There has been no investigation into Zn isotope fractionation in a closed system intrusive suite thus far, but there is no difference in Zn isotopic composition between diorites (average $\delta^{66}Zn_{JMC\text{-}Lyon}$ of 0.25‰, n=7; Huang et al., 2018) and granites (average $\delta^{66}Zn_{JMC\text{-}Lyon}$ of 0.26‰, n=19; Telus et al., 2012), which suggests that fractional crystallisation in intrusive settings also causes negligible Zn isotope fractionation.

Some evolved samples, including rhyolites, granites and pegmatites, show heavier $\delta^{66}Zn$ values than mantle derived basalts, up to $\delta^{66}Zn_{JMC\text{-}Lyon} \sim 0.8‰$ (Telus et al., 2012; Xia et al., 2017; Doucet et al., 2018; Wang et al., 2020). The heavy $\delta^{66}Zn$ of samples is most commonly attributed to the exsolution of isotopically light fluids from high silica polymerised melts (Telus et al., 2012; Wang et al., 2020), but could also be caused by enrichment of heavy Zn in the melt during partial melting of crustal lithologies (Doucet et al., 2018; Sossi et al., 2018a; Xu et al., 2019). Therefore, Zn stable isotopes are a useful tracer of fluid exsolution processes which could affect other isotope systems. Zinc isotopes are also an informative system to study alongside Fe and V isotopes, because Zn is found in a single redox state (Zn^{2+}) so will not be fractionated by changes in redox state.

To date, there have been no studies of Zn isotopes in whole rock samples or mineral separates from closed system intrusive suites. The only published mineral separate data for crustal rocks are for biotite, hornblende and magnetite separates in one melanosome from the Dabie Orogen, China (Xu et al., 2019). This work significantly enhances our current knowledge of Zn isotopic fractionation in intrusive settings by studying the Zn isotopic composition of WR powders and mineral separates from two closed system intrusive suites (Chapters 3 and 5).

1.5 Vanadium Stable Isotopes

1.5.1 Chemical Characteristics

Vanadium is a moderately incompatible lithophile element. It can exist in multiple oxidation states, and is predominantly found as V^{3+}, V^{4+} and V^{5+} in terrestrial environments (e.g. Huang et al., 2015). Vanadium partitioning is strongly redox dependent, and V compatibility in silicates and oxides decreases with increasing fO_2 due to the greater compatibility of V^{3+} compared to V^{4+} and V^{5+} (e.g. Canil, 1997; Toplis and Corgne, 2002).

In crustal rocks, the highest concentrations of V are found in Fe-Ti oxide minerals such as magnetite. Magnetite hosts both V^{3+} and V^{4+} in VI-fold coordination (O'Neill and

Navrotsky, 1984; Balan et al., 2006). Silicate minerals can also contain considerable concentrations of V (hundreds of μg/g). Most V in silicate phases is found as V^{3+}, which can substitute for Fe^{3+} on VI-fold sites due to their similar ionic radii (0.645Å and 0.64Å respectively; Shannon, 1976). However, there is also potential for $^{VI}V^{4+}$ to substitute for $^{VI}Ti^{4+}$ in Ti-bearing phases (ionic radii of 0.58Å and 0.605Å respectively; Shannon, 1976).

In silicate melt, V is present at a higher redox state (minor V^{3+}, higher abundances of V^{4+} and V^{5+}) and in IV- and V-fold coordination (Giuli et al., 2004; Sutton et al., 2005; Righter et al., 2006). Therefore, in a similar manner to Fe, V isotope fractionation is driven by both variations in redox state and coordination environment during fractional crystallisation. *Ab initio* calculations for aqueous species demonstrate that heavy ^{51}V concentrates in phases where V is present in a higher valence state, lower coordination and shorter V-O bond lengths (Wu et al., 2015), as predicted based on stable isotope fractionation theory (e.g. Urey, 1947; Schauble, 2004). However, to date there have been no *ab initio* studies considering V isotope fractionation between minerals and melt.

Vanadium has two isotopes, ^{50}V and ^{51}V with abundances of 99.76% and 0.24% respectively. Isotope ratios are expressed as $\delta^{51}V$ values relative to the AA standard (Nielsen et al., 2011; Equation 1.6).

$$\delta^{51}V = \left[\frac{(^{51}V/^{50}V)_{sample}}{(^{51}V/^{50}V)_{AA}} - 1\right] \times 1000 \qquad [1.6]$$

1.5.2 Vanadium Isotopes in Terrestrial Samples

At this time, V isotope systematics are less well studied compared to the Fe and Zn isotope systems. Development of a method for high precision V isotope ratios lagged behind other transition metal isotope systems due to the analytical challenges of measuring two isotopes present in vastly different abundances ($V^{51}/V^{50} \sim 420$) with direct isobaric interferences (^{50}Ti and ^{50}Cr on ^{50}V; Nielsen et al., 2011; Prytulak et al., 2011; see discussion in Chapter 2, Section 2.5.4).

Figure 1.4 shows V isotopic compositions of terrestrial and chondritic samples. Thus far, only the V isotopic composition of mantle peridotites and extrusive lavas have been

investigated. At the time of writing there are no published measurements of $\delta^{51}V$ in either intrusive WR samples or mineral separates.

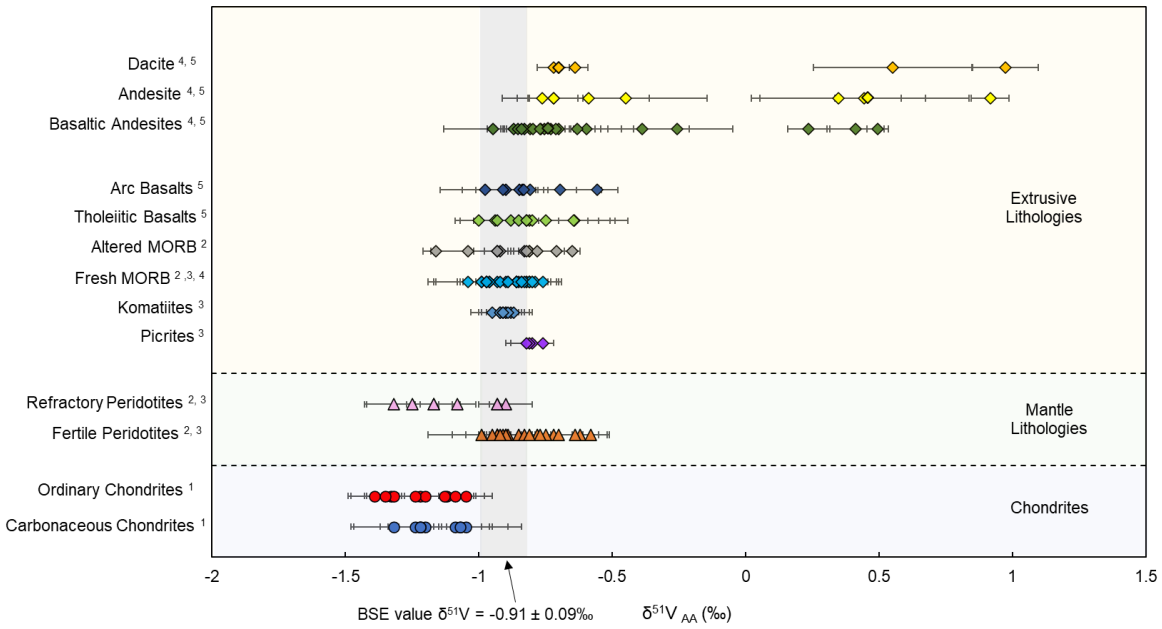

Figure 1.4. Range in $\delta^{51}V$ values measured in chondrites and terrestrial igneous lithologies. The grey vertical band is the Bulk Silicate Earth (BSE) value of -0.91 ± 0.09‰ (2SD) from Qi et al., 2019. Data from [1]Nielsen et al., 2019, [2]Prytulak et al., 2013, [3]Qi et al., 2019, [4]Wu et al., 2018 and [5]Prytulak et al., 2017.

Prytulak et al. (2013) presented the first measurements of V isotopes in terrestrial samples for peridotites (range in $\delta^{51}V$ from -0.62‰ to -1.17‰), basalts (-0.88 ± 0.27‰, 2SD, n=35) and MORB glasses (-0.95 ± 0.13‰, 2SD, n=6). After improvements in analytical methods, recent studies have determined broadly similar values for mafic lavas, with smaller uncertainties. For example, Wu et al. (2018) determined the average V isotopic composition of MORB as $\delta^{51}V$ = -0.84 ± 0.10‰ (2SD, n=22), and Qi et al. (2019) found an average $\delta^{51}V$ for komatiites of -0.91 ± 0.05‰ (2SD, n=10). It is not yet clear whether V isotopes are fractionated during partial melting of the mantle. Fertile spinel lherzolites show identical isotopic composition to komatiites (Qi et al., 2019), and there is <0.1‰ difference between average estimates for MORB and mantle peridotites, which is within typical analytical uncertainty. Improvements in analytical precision and further studies of mantle peridotites and mantle derived basalts are necessary to resolve this.

Large variations in WR $\delta^{51}V$ of up to 2‰ are observed during fractional crystallisation in lavas from Hekla, Anatahan and Kilauea Iki (Prytulak et al., 2017; Ding et al., 2020). This increase is attributed to the crystallisation of Fe-Ti oxides such as titanomagnetite and ilmenite. Vanadium is highly compatible in Fe-Ti oxides (e.g. Toplis and Corgne, 2002), so a high proportion of the V in the system can be hosted in these phases. Vanadium in oxides is primarily found as VI-fold coordinated V^{3+} (O'Neill and Navrotsky, 1984). Fe-Ti oxides are theoretically predicted to be isotopically lighter than coexisting melt where V is present in higher redox state and lower coordination (Prytulak et al., 2017). This has also been proven experimentally in V isotope partitioning experiments between magnetite and melt in a Ti-free system at P-T-fO_2 conditions relevant to granitic systems (Sossi et al., 2018b). The partitioning experiments also demonstrated that the fractionation factor between magnetite and melt ($\Delta^{51}V_{mag\text{-}melt}$) varies with magma fO_2, increasing in magnitude by approximately 0.05‰ per log unit increase of fO_2. This is expressed by the relationship $\Delta^{51}V_{mag\text{-}melt} = -0.045(\Delta FMQ) - 0.70$ (Sossi et al., 2018b).

Lavas from Hekla, Anatahan and Kilauea Iki display distinct trends of WR $\delta^{51}V$ with WR MgO content, which is thought to be due to variation in the timing of Fe-Ti oxide saturation and the exact species of Fe-Ti oxides crystallising (Ding et al., 2020). Ding et al. (2020) hypothesised that Ti-rich ulvöspinel and ilmenite may have smaller $\Delta^{51}V_{oxide\text{-}melt}$ values than magnetite, but this has not yet been investigated in natural Fe-Ti oxide mineral separates.

One of the major challenges in interpreting V isotope data is that there are currently no published mineral-melt fractionation factors for silicate and oxide phases, apart from the experimentally derived magnetite-melt fractionation factors from Sossi et al. (2018b). The fractionation factors from Sossi et al. (2018b) may not be directly applicable to natural systems because they were conducted in a Ti-free environment. There is potential for variation in the Ti content of magnetite to influence its V isotopic composition because of changes in the bonding environment and average redox state of V, as documented for Fe and Ti isotopes (e.g. Rabin et al., 2021; Hoare et al., 2022).

It is also not yet clear what effect the crystallisation of silicate phases could have on V isotopic compositions in an evolving magma. Silicate minerals also host VI-fold V^{3+}, so should also be isotopically lighter than coexisting melt. Phases such as biotite, pyroxene

and hornblende can have V concentrations up to several hundred μg/g and exist in significant proportions in intrusive granites. Mineral-melt fractionation factors for silicate and oxide phases at conditions relevant to terrestrial magmas are necessary for accurate modelling V isotopic variations during magmatic differentiation.

Therefore, an aim of this thesis is to investigate the controls on V isotope fractionation during magmatic differentiation in intrusive settings. Studying V isotopes in WR powders and mineral separates in two chemically distinct, closed system plutonic suites will permit examination of the controls of mineralogy, chemical composition, temperature and fO_2 on V isotope fractionation. A greater understanding of the fundamental mineralogical controls on V isotope fractionation is still required before V isotopes can be used to understand more complex magmatic processes, such as Fe-Ti oxide and sulphide saturation, and the formation of economic ore bodies.

1.5.3 Vanadium Isotopes and Oceanic Redox State

One promising application of the V isotope system is to track ocean palaeoredox variations by measuring the V isotopic composition of shales (Schuth et al., 2019; Wu et al., 2019; Nielsen, 2020; Wu et al., 2020; Fan et al., 2021). Initial studies suggest that the magnitude of V isotopic fractionation between seawater and sediments varies with the oxygen content of bottom waters. The largest magnitude of V isotope fractionation occurs in oxic settings, and the magnitude decreases in anoxic and euxinic settings (Nielsen et al., 2020; Wu et al., 2020). This difference is most likely due to changes in the phases which scavenge V from seawater, and are deposited in the sediments, in these different environments (Wu et al., 2020).

However, in order to use the V isotopic composition of shales to trace variations in ocean redox state through time, the V isotopic composition of seawater through time must also be known. The major source of V to the oceans is from the weathering of upper crustal silicate rocks and transport of this material via rivers (Shiller and Mao, 2000; Schuth et al., 2019), hence it is vital to understand the V isotopic composition of the continental crust, and any variations in composition over geological time. However, there is currently no published data on the V isotopic composition of the intrusive rocks which make up a large proportion of the upper crust. Therefore, the range and variability of $\delta^{51}V$ in the upper crust is not known at this time. By studying two plutonic suites in this work, we

can gain a better understanding of the V isotopic composition of the crust, and the sediments eroded from it.

1.6 Thesis Outline

As summarised above, Fe, V and Zn isotopes have the potential to trace different processes during magmatic differentiation but there are a lack of studies focussing specifically on intrusive systems which make up the majority of the continental crust. Therefore, an investigation of isotopic behaviour in intrusive systems is the focus of this thesis. Two intrusive suites, with contrasting mineralogy, both of which evolved by approximately closed system fractional crystallisation, are examined. These are the calc-alkaline Boggy Plain Zoned Pluton, Australia (Chapters 3 and 4) and the tholeiitic Red Hill Intrusion, Tasmania (Chapter 5). For each suite, detailed petrological examination of samples is combined with Fe-V-Zn isotopic analysis of both whole rock powders and mineral separates. This detailed approach provides information about how best to investigate isotopic variations in intrusive samples, the specific drivers of Fe, V and Zn isotope fractionation in intrusive settings, and implications for the isotopic composition of the continental crust in general.

Chapter 2 describes the ion exchange chromatography procedures used to separate the elements of interest (Fe-V-Zn) from a single sample digestion, and the methods refined at Durham for accurate and precise Fe, V and Zn isotope ratio measurements by Multi Collector Inductively Coupled Plasma Mass Spectrometry (MC-ICP-MS).

Chapter 3 investigates Fe and Zn isotopic variations in mineral separates and whole rock powders during differentiation of the calc-alkaline Boggy Plain Zoned Pluton. This is the first combined study of Fe and Zn isotopes in a closed system plutonic suite, which allows a detailed investigation into the processes which drive Fe and Zn isotopic fractionation in intrusive settings, and the best approaches for modelling these variations. Note that this chapter has recently been published in Geochimica et Cosmochimica Acta with co-authors Julie Prytulak, Madeleine Humphreys and Geoff Nowell (Stow et al, 2022). A pdf version of the paper can be found in Appendix 2.

Chapter 4 examines V isotope variations in the Boggy Plain Zoned Pluton using the baseline knowledge obtained from the Fe-Zn study in Chapter 3. This is the first study of

V isotopes in whole rock samples and mineral separates from intrusive igneous rocks. This approach allows us to investigate inter-mineral V isotope fractionation between silicate and oxide minerals, and the drivers of V isotope fractionation in intrusive settings. More generally, we explore implications for the V isotopic composition of the continental crust, and the clastic sediments eroded from it, and implications for V mass balance between different geological reservoirs.

Chapter 5 is a combined Fe-V-Zn isotope study of the tholeiitic Red Hill intrusion, Tasmania, with the primary goal of examining V isotopic fractionation in a tholeiitic intrusive setting for the first time. We compare this work to data from the Boggy Plain Zoned Pluton (Chapter 4) to examine V isotopic behaviour in two intrusive systems with contrasting chemistry, Fe-Ti oxide mineralogy and fO_2 conditions.

Chapter 6 presents a synthesis of the main findings of the thesis, and suggestions for future work.

The **Appendix** contains preliminary data from an investigation of the Fe-Zn isotopic compositions of basalts from the 2021 Fagradalsfjall eruption in Iceland. This work was not originally planned as part of this thesis, but the eruption provided the opportunity to join a global collaboration investigating temporal elemental and isotopic variations in the lavas which erupted between March and September 2021. In contrast to the rest of the thesis, a whole rock approach is appropriate for these fine grained, aphyric glassy lavas, which do not have the same textural complexities as the intrusive samples investigated in the rest of this work.

Chapter 2: Methods

2.1 Introduction

This chapter discusses the chemical procedures required to separate and purify Fe, V and Zn from whole rock and mineral separate powders, and the protocols developed at Durham University for isotopic analysis by Multi-Collector Inductively-Coupled-Plasma Mass-Spectrometry (MC-ICP-MS). The chapter covers details of the materials used for all chemical procedures (Section 2.2) and the methods for sample digestion (Section 2.3). Section 2.4 then discusses the ion exchange column chromatography procedures used to separate Fe, V and Zn from a single sample digestion. In Section 2.5, the three protocols for Fe, V and Zn analysis by MC-ICP-MS are outlined.

Three established ion exchange column chromatography procedures (Nielsen et al., 2011; Sossi et al., 2015; Wu et al., 2016) are combined to allow collection of all three elements from the same sample digestion. The benefit of recovering all three elements from a single digestion is that it reduces the volume of material required, which is an important consideration when hand picking mineral separates. Additionally, for coarse grained intrusive rocks which can be heterogeneous at the decimetre scale, it allows direct comparison of the three isotopic systems from the same sample aliquot.

The method from Sossi et al. (2015), previously used for Fe, Zn and Cu separation, is used to initially separate Fe, Zn and V. One complication is that in typical silicate samples, V and Zn concentrations are of the order of 100 μg/g, yet Fe is present at weight percent levels. Iron concentrations are highest in Fe-Ti oxides. Tests with a synthetic magnetite powder were conducted to assess the maximum oxide mass that can be processed using this procedure without overloading the Fe column capacity, and while still obtaining enough Zn and V for analysis. The results are discussed in Section 2.5.2.4.

In the combined method, Fe and Zn are collected directly from the first column. For Zn, this column procedure is repeated once to ensure full removal of all matrix elements, which is necessary for obtaining mass dependent isotope ratios. A second column is also necessary for mineral separates with high Fe content, such as magnetite and pyroxenes.

The V fraction is collected with other matrix elements. Four further columns are required to fully separate and purify the V, with care taken to quantitatively remove Cr and Ti which are direct isobaric interferences on ^{50}V. These latter columns follow methods in Nielsen et al. (2011) and Wu et al. (2016).

The measurement protocols developed to achieve accurate and precise Fe, V and Zn isotopic analysis by MC-ICP-MS are discussed in Section 2.5. For each isotope system, the instrumentation and measurement protocol, method of mass bias corrections and data quality and assurance checks are covered, in addition to any details specific to that isotope system. Total analytical uncertainties (as 2SD of the mean of at least 3 measurements of a sample) are typically below ± 0.05‰ for Fe and Zn, and below ± 0.1‰ for V.

The development of these methods makes it possible to measure the isotopic composition of trace (V and Zn) and major (Fe) elements from a single digestion of silicate whole rock powders, silicate mineral separates, or oxide mineral separates.

Ion exchange column chromatography procedures and protocols for strontium (Sr) and neodymium (Nd) isotope ratio measurements by MC-ICP-MS are described in Section 2.6.

2.2 Materials

All sample digestion, column chromatography and MC-ICP-MS analysis was carried out at the Arthur Holmes Isotope Geology laboratory, Department of Earth Sciences, Durham University.

All acids used in sample digestion and column chromatography (HCl, HNO_3 and HF) were purified by sub-boiling distillation in either two-bottle or Savillex DST1000 Teflon stills; once distilled, these acids are prefixed TD (Teflon Distilled). All dilutions used ultra-pure 18.2MΩ cm grade water from a MilliPore Element water purification unit (MQ H_2O). Romil UpA H_2O_2 (30%) was used as purchased and refrigerated in a light proof bottle between uses to avoid decomposition into water and oxygen.

Savillex PFA beakers were used for all sample digestions and sample collection. These beakers were cleaned extensively between uses with a sequence of reagent grade HNO_3 and HCl acid baths and refluxed in TD 7M HNO_3 before use.

Savillex PFA columns were used for ion exchange column chromatography procedures where Zn blanks needed to be reduced to a minimum (Section 2.5.3.3). These columns were heated in weak TD HNO_3 between uses. For other procedures, quartz glass columns and miniature Teflon columns (100µl resin volume) were used.

Exchange resins (anion resin AG1-X8 and cation resin AG50W-X12) were pre-cleaned by agitating the resin alternately with TD 6M HCl and MQ H_2O. To reduce Zn total procedural blanks, the AG1-X8 resin was further cleaned using a large BioRad Econo-Pac column with 250ml reservoir fitting to an in-house designed vacuum box. To clean 20 ml of resin, a sequence of 200 ml TD 3M HCl, 200 ml MQ H_2O, and 200 ml TD 3M HNO_3 was eluted 3 times (Section 2.5.3.3).

Teflon autosampler vials were used for Zn isotopic analysis only, to reduce Zn blanks (Section 2.5.3.3). These autosampler vials were cleaned with TD HNO_3 between uses. Firstly, vials were refluxed with TD 7M HNO_3 on a hotplate overnight, then heated at 100 °C in a PFA pot with TD 1M HNO_3.

2.3 Sample Digestion

All whole rock samples and mineral separates were digested in powder form. Silicate powders (mass < 70 mg) were dissolved in a 3:1 mixture of 3 ml TD 29M HF and 1 ml TD 16M HNO_3 in tightly capped Teflon beakers on a hotplate at 160 °C for > 48 hours. Samples were then evaporated on a hotplate at 130 °C to incipient dryness until a sticky white residue remained. This process leads to the loss of all SiO_2 from the sample via the reaction of HF and SiO_2 to gaseous SiF_4 (e.g. Mann et al., 1997), reducing the sample mass by about 50%. Sufficient TD 16M HNO_3 was added with a dropper bottle to just cover the residue, which was then evaporated at 180 °C until fully dry. This step was repeated until the residue was a dark brown colour, indicating the destruction of insoluble fluorides. TD 6M HCl was added to samples then evaporated to dryness to convert all ions to chloride form. Samples were refluxed in 1 ml 6M HCl loading solution and visually inspected to ensure complete dissolution had occurred.

Oxide mineral separates often contained inclusions or coatings of silicate material after magnetic separation. For this reason, powders were digested in TD 6M HCl instead of the HF-HNO_3 procedure described above. This allowed full dissolution of the oxides and the remaining insoluble silicates were separated by centrifugation. Masses up to 200 mg (though typically <50 mg) were fully dissolved in approximately 5 ml TD 6M HCl in tightly capped Teflon beakers on a hotplate at 120 °C for > 48 hours. Samples were evaporated at 130 °C until fully dry and refluxed in 1 ml TD 6M HCl. Samples were centrifuged for 5 minutes at 4000 rpm to remove the solid residue, and the supernatant was loaded directly onto the first ion exchange column.

For samples which required trace element analysis (method described in Chapter 4, section 4.3.2), a 50 µl aliquot was taken from the 1 ml solution at this stage before the sample was loaded onto the first column.

2.4 Ion-Exchange Column Chromatography

2.4.1 Background

To ensure accurate isotopic analyses, the element(s) of interest need to be separated from each other and from the sample matrix. For stable isotope analysis this is for two reasons. Firstly, to remove elements that form isobaric interferences on the analyte, and secondly to remove matrix which induces variable mass bias (e.g. Schoenberg and von Blanckenburg, 2005).

There are two main types of isobaric interferences: atomic (isotopes with the same mass) or molecular species (argide, oxide and nitride species formed in the plasma). In most cases, atomic interferences originate from the sample matrix and since they cannot be resolved from the analyte they must be quantitatively removed by column chemistry, or reduced to a level where they can be corrected for algebraically (e.g. Schoenberg and von Blanckenburg, 2005). Molecular isobaric interferences are formed in the plasma of the MC-ICP-MS and generally derived from the plasma gas (Ar) combined with light elements from the sample solution (H, N, O, C etc.) (e.g. Belshaw et al., 2000). These molecular interferences are removed through chemistry and can also be reduced by choice of acid that samples are analysed in (e.g. Belshaw et al., 2000) and sample introduction system (e.g. Weyer and Schwieters, 2003). Additionally, the analyte can be resolved from

isobaric interferences by measuring at medium-high mass resolution (e.g. Weyer and Schwieters, 2003). This is because the analyte and interference do not have the exact same mass due to nucleon mass defect (e.g. Sleno, 2012). In the case of Fe, Zn and V the molecular interferences all lie to the high mass side of the analyte (see Figure 2.7). Reducing interferences is especially important for low abundance isotopes. For example ^{50}V makes up only 0.24% of the natural abundance of V, so is present in very low concentrations, but has several potential atomic isobaric interferences including ^{50}Ti and ^{50}Cr (Nielsen et al., 2011), so the ^{50}V abundance cannot be measured accurately if these interferences are present.

The presence of matrix elements has also been shown to increase the instability of instrumental mass bias (e.g. Dauphas et al., 2009b for Fe isotopic measurements). Stable mass bias is necessary when correcting by standard sample bracketing (Albarède et al., 2004), which is used in this study. Hence, it is necessary to quantitatively separate the analyte from other matrix elements.

Numerous methods have been published for the individual extraction of Fe, V and Zn from geological samples using different exchange resins and acids. The specific ion exchange chromatography procedure developed in this study combines three previous methods (Nielsen et al., 2011; Sossi et al., 2015; Wu et al., 2016) to separate and purify the elements of interest (Fe, V and Zn) from the same sample digestion. This reduces the amount of material which needs to be processed, which is important when picking low abundance mineral separates.

An overview of the procedure used is shown in Figure 2.1. In the first column step, Fe, Zn and V are separated from each other and most other matrix elements following the method in Sossi et al. (2015). Following this column, the Fe and Zn fractions are quantitatively separated from matrix elements. This column is repeated for the Zn fractions, and for the Fe fractions from mineral separates with exceptionally high concentrations of Fe (e.g. magnetite). Samples are then ready for analysis by MC-ICP-MS. However, the V fraction is eluted with most of the remaining matrix elements and a further 4 columns are necessary to fully separate and purify V. Initially, V is separated from matrix elements (Ti, Al, Ca and Mn), some Cr, and any remaining Fe following the procedure in Wu et al. (2016). Remaining matrix elements and Cr are removed following the main V separation procedure in Nielsen et al. (2011). Clean up columns to remove

remaining traces of Ti and Cr are repeated as necessary to reduce isobaric interferences on ^{50}V, following the procedure in Nielsen et al. (2011).

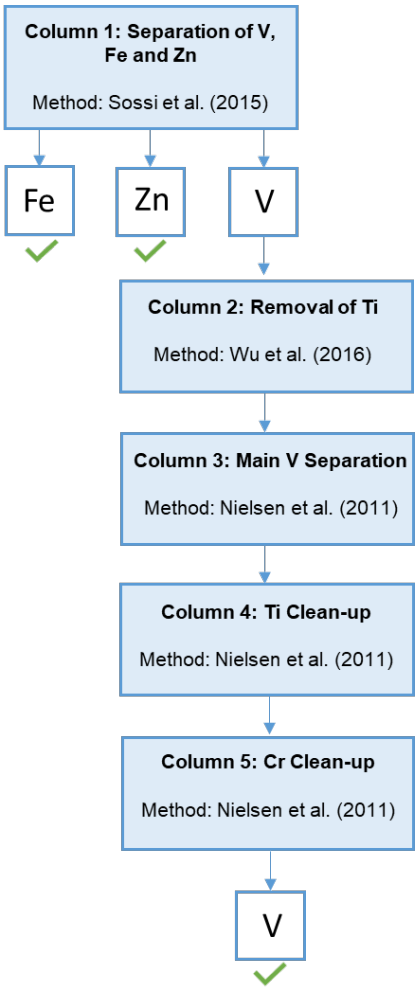

Figure 2.1. Flowchart illustrating the full column chromatography procedure used in this study.

2.4.2 Column 1: Separation of V, Fe and Zn

The first column separation procedure is modified from Sossi et al. (2015) and is illustrated in Figure 2.2. The column is based on the principle that V, Fe and Zn have distinct partition coefficients with anion exchange resins at specific molarities of HCl and HNO_3 (e.g. Nelson et al., 1964; van der Walt et al., 1985). For example, in 6M HCl on the Dowex 50 X-4 anion resin, K_D values for Fe^{3+} are $>10^2$ but <1 for V^{4+} (Nelson et al., 1964). Therefore, Fe and Zn partition to the resin in TD 6M HCl whereas V and other matrix elements do not. During the procedure, V is immediately eluted from the column in 6M HCl and separated from Fe and Zn. Iron and Zn are then separated from one another

because Fe is released at low molarities of HCl, while Zn is retained. Zinc is released from the column only by switching to TD 3M HNO_3. Therefore, the column separates elements based on an 'on-off' affinity for the resin, rather than by a chromatographic separation requiring a calibrated elution with a certain volume of titrated acid. It is not necessary to accurately titrate acids used in this separation.

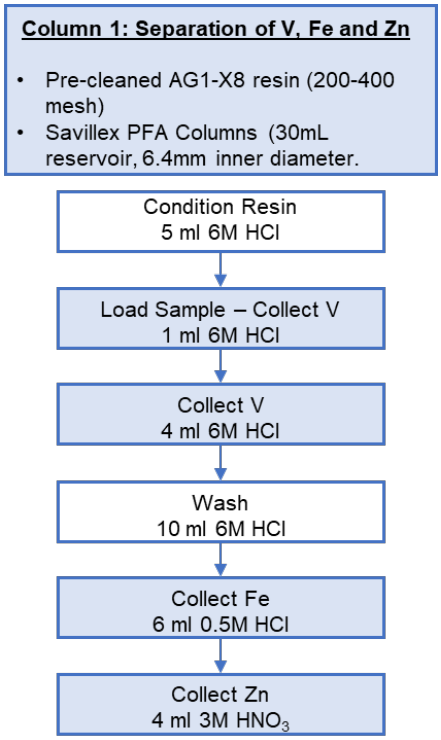

Figure 2.2. Flowchart outlining the process to separate Fe, V and Zn in Column 1

Pre-cleaned BioRad AG1-X8 resin (200-400 mesh) was loaded into Savillex PFA columns (30 ml reservoir volume) with PTFE frits. The columns have a high aspect ratio of 0.64 cm diameter by 6.5 cm length, which Sossi et al. (2015) found to yield optimal Fe-Zn-Cu separation. It is particularly important to use PFA columns for this step to minimise Zn procedural blanks (Section 2.5.3.3), which would be elevated by alternate column material such as polypropylene or quartz glass (e.g. Wilkes et al., 2010).

Vanadium was collected as the sample is loaded and with the first 4 ml TD 6M HCl. After a 10ml TD 6M HCl wash, Fe was collected in 6ml TD 0.5M HCl and Zn was collected in 4ml TD 3M HNO_3. An advantage of this column is that Fe is visible as a brown-orange colour when retained on the column, and if Fe is eluted from the column in HCl, the acid

is yellow. Therefore, it is visibly apparent if the resin reaches its capacity for Fe and Fe is prematurely lost (Figure 2.3).

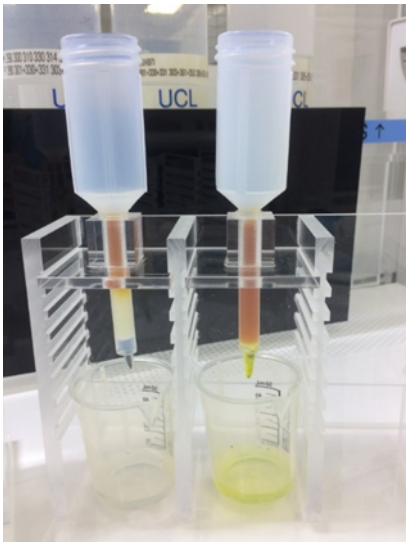

Figure 2.3. Iron partitioned to the AG1-X8 resin during the 6M HCl wash step. When Fe is partitioned to the resin it is a brown colour. If the column is overloaded and Fe is lost dissolved in the 6M HCl, it will be a yellow colour (right hand column).

The Zn fractions from the separation were passed through the column a second time. This was necessary to remove all matrix and obtain mass dependent Zn isotope ratios. The Fe fractions were passed through the column a second time for samples containing high masses of Fe (e.g. magnetite and silicate mineral separates). The entire procedure takes on the order of 8 hours.

After this first column, Fe and Zn separation is complete. The resulting fractions were evaporated at 130 °C, and the residue was covered with TD 16M HNO_3 and evaporated twice at 160 °C to destroy any organic resin which had passed through the frits. Samples were then refluxed in TD 3% HNO_3 before mass spectrometry; Zn fractions were dissolved in 1ml TD 3% HNO_3 and Fe fractions in 10ml TD 3% HNO_3. The V fraction was evaporated at 130 °C, then TD 16M HNO_3 was added to cover the residue and evaporated at 160 °C to destroy any resin-derived organics that were present. The residue was then dissolved and fluxed in TD 1M HNO3 at 100-130 °C for at least 12 hours before it was loaded onto the next column.

2.4.3 Further V separation

Vanadium is eluted with the majority of matrix elements from column 1 (except Fe, Zn and Cu; Sossi et al., 2015). Vanadium poses extra analytical challenges compared to Fe and Zn, which is why the development of a method for V separation and precise isotopic analysis lagged behind other transition metals (e.g. Fe, Cu, Zn in the early 2000s). In addition to the analytical difficulties involved in measuring a system with only two stable isotopes, and with direct isobaric interferences on the minor isotope (Section 2.5.4.1), it is also difficult to separate V from its matrix whilst maintaining 100% yield, which is necessary to avoid column-induced isotope fractionation during the separation procedure (Nielsen et al., 2011).

The V separation procedure is adapted from Nielsen et al. (2011) and Wu et al. (2016). The underlying principle, first used by Nielsen et al. (2011), is that V^{5+} forms anionic V-peroxide complexes with hydrogen peroxide (H_2O_2) in mildly acidic solutions, which will partition strongly onto anion exchange resins such as AG1-X8. Most V should be present as V^{5+} because strongly oxidising acids, such as HNO_3, are used during sample digestion. However, Fe and Ti must be removed before H_2O_2 can be used. This is because Fe and Ti catalyse the dissociation of H_2O_2 to water and oxygen, causing loss of V because V-peroxide complexes can no longer form. Additionally, the presence of H_2O_2 causes Ti-oxides to precipitate when the sample is loaded onto the resin, so as further acids are added, Ti will be eluted and collected with the V fraction (Nielsen et al., 2011).

Because Fe is quantitatively separated from the V fraction by column 1 (Section 2.4.2), the function of column 2 (see section 2.4.3.1), adapted from Wu et al. (2016) is to remove most of the Ti. Subsequently, H_2O_2 can be used in column 3 (Section 2.4.3.2) to remove V from remaining matrix elements (Nielsen et al., 2011). Columns 2 and 3 each take around 8 hours to complete. Columns 4 and 5 (Section 2.4.3.3) are small resin volume columns designed to remove any remnant traces of Ti and Cr respectively. They take approximately 3-4 hours to complete. These columns can be repeated as necessary, depending on the composition of the samples. For example, Ti-rich titanomagnetite samples, such as those from the Red Hills intrusion (Chapter 5), require at least 3 Ti clean-up columns, but only 2 Cr clean-up columns. These clean-up columns are critical because both Cr and Ti have a mass 50 isotope which interferes directly on the minor ^{50}V. Near complete separation of V from Ti and Cr is required to avoid large corrections and errors

on V isotopic measurements. The entire procedure used for V separation is shown in Figure 2.4.

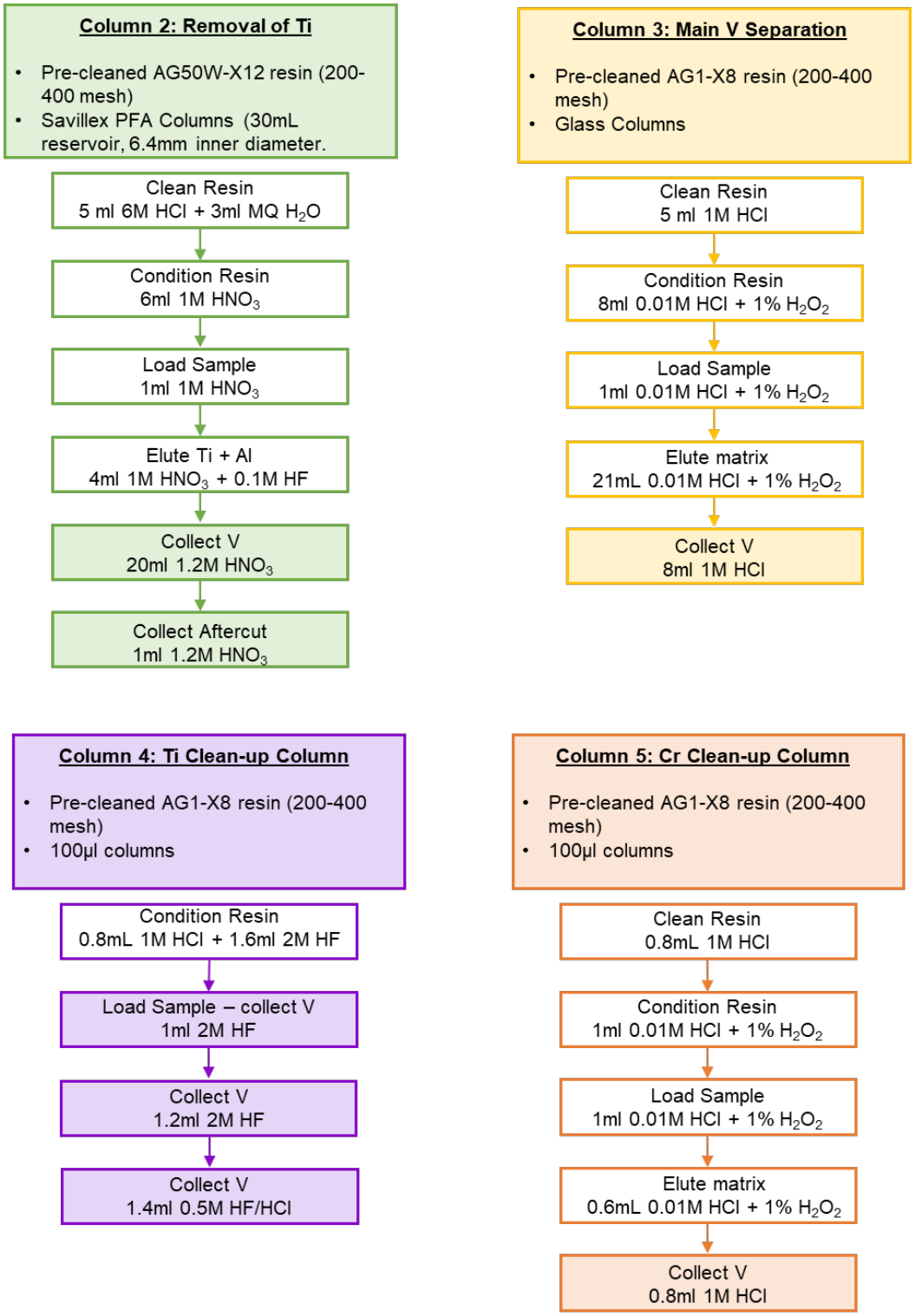

Figure 2.4. Flowcharts describing the four stages of ion exchange chromatography used in this study for quantitative separation of V.

2.4.3.1 Column 2: Removal of Ti

Column 2 is adapted from Wu et al. (2016), and separates V from matrix elements such as Ti, Al, Ca and Mn. It also separates some Cr and any remaining Fe from the V fraction. Wu et al. (2016) repeat the column twice to ensure all Fe and Ti was removed, but because we use the anion exchange column from Sossi et al. (2015) as the first separation, only one pass of column 2 is necessary. By starting with the Sossi et al. (2015) column, we are also able to collect the Fe and Zn fraction from the same digestion as V, which is not straightforward using the Wu chemistry alone.

Column 2 requires TD 1M and 1.2M HNO_3 to separate V from Ti. Because of the sensitivity of the V K_D value on the resin to different molarities of HNO_3 (Strelow et al., 1965) a 5M, 1M and 1.2M stock were titrated with 1M NaOH to be used during the procedure.

The AG50W-X12 cation resin (200-400 mesh) was pre-cleaned by shaking alternately with MQ and TD 6M HCl in a Teflon bottle. 2ml resin was loaded into the same Savillex PFA columns used for column 1 (30ml reservoir volume, 6.4mm capillary inner diameter). In principle, quartz glass columns can be used because they do not contribute significantly to the V procedural blank. However, the bulb headed columns (Figure 2.5) dripped very slowly, which extended the length of the procedure, so these were not used. Samples were loaded in 1ml TD 1M HNO_3. 4ml TD 1M HNO_3 + 0.1M HF was used to elute Ti and Al. Vanadium was then collected in 20ml TD 1.2M HNO_3. Most matrix elements (Ca, Mn, Cr) remained partitioned to the resin at this stage (Wu et al., 2016). The V fractions were evaporated overnight, then covered with TD 16M HNO_3 and evaporated to dryness twice at 160 °C. TD 6M HCl was added to the residues and evaporated at 130 °C before samples were refluxed in 1ml TD 0.01M HCl ready for loading onto column 3.

Wu et al. (2016) state that there should be 100% recovery for V if no more than 10 μg V is loaded onto the column. A further 1ml TD 1.2M HNO_3 was collected after the V fraction to test that V was quantitatively removed in the main collection. The after-cuts were evaporated, then covered with TD 16M HNO_3 and evaporated twice at 160 °C. 1ml TD 3% HNO_3 was added, and the V concentration was measured during MC-ICP-MS sessions. After-cuts typically contained less than 2 ng V and were always negligible

relative to the amount of V processed (>1000 ng). Given that typical total procedural blanks for V were of a similar magnitude, this confirms that there was no quantitative V loss during column 2.

Wu et al. (2016) also separately collect the first 1 ml after switching to 1.2M HNO_3 to monitor V loss. However, we collected this 1 ml with the main V fraction. This is because any V lost at this stage is eluted with other matrix elements (e.g. Na). When the concentrations of the pre-cuts were measured by MC-ICP-MS, high concentrations of other matrix elements damaged the sample and skimmer cones. However, if the pre-cut is collected with the main V fraction, the remaining columns will remove any matrix and ensure no V loss at this stage.

2.4.3.2 Column 3: Main V-Cr Separation

After removal of Fe and Ti, column 3 was used to separate V from other matrix elements, and was designed to focus on effective V-Cr separation. The procedure was identical to that described in Nielsen et al. (2011). Quartz columns (diameter 5-6mm) were fitted with quartz wool or polypropylene frits and filled with 1ml of AG1-X8 resin (200-400 mesh). The resin was cleaned with 5ml TD 1M HCl then conditioned with 8ml TD 0.01M HCl + 1% v/v H_2O_2. The H_2O_2 was refrigerated in a light proof container when not in use. 33 µl of 30% H_2O_2 (1% v/v) was added to cool samples immediately prior to loading, causing the immediate formation of V-peroxide complexes. At this stage, if the samples contained high concentrations of V, a yellow colour could be seen at the top of the resin bed (Figure 2.5A). Most matrix elements were then eluted by 21 ml TD 0.01M HCl + 1% v/v H_2O_2 while V remains partitioned to the resin. Vanadium was collected with 8 ml TD 1M HCl; at this stage, the resin turned a red-orange colour if V was present (Figure 2.5B), caused by reduction of V.

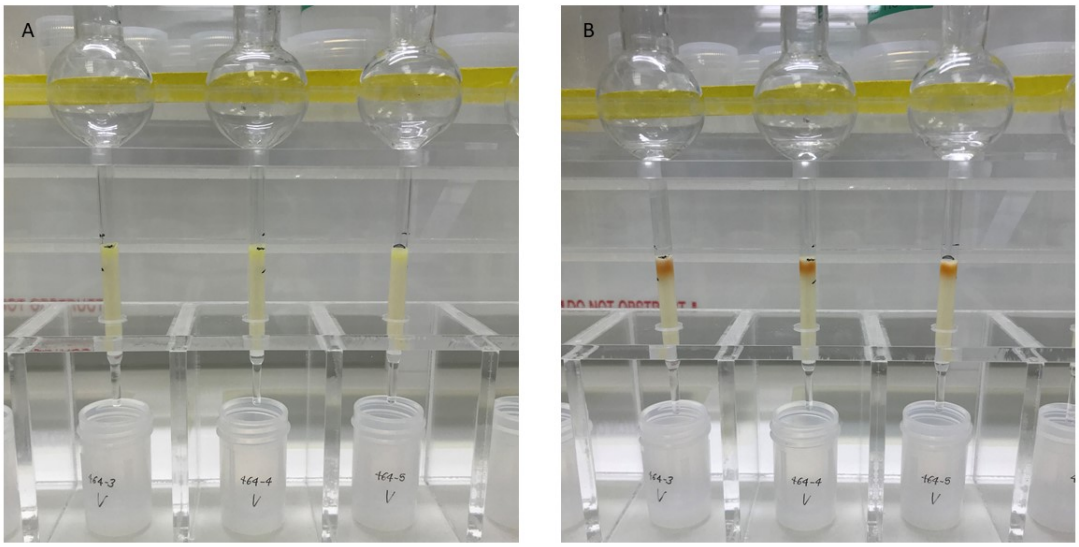

Figure 2.5. Main V-Cr separation column. A: Yellow colour observed at the top of the resin bed when V samples dissolved in 0.01M HCl + 1% v/v H_2O_2 are loaded. B: Orange/red colour observed when V is eluted by 1M HCl.

Vanadium fractions were evaporated at 130 °C and covered with TD 16M HNO_3 and evaporated twice at 160 °C to destroy any resin-derived organics present. Around 100 µl TD 2M HF was added to the residues and evaporated at 130 °C. Samples were then refluxed overnight in 1ml TD 2M HF at < 120 °C before the Ti clean up column (Column 4).

2.4.3.3 Column 4 and 5: Clean-up Columns

Columns 4 and 5 were used to remove small amounts of residual Ti and Cr still present after columns 2 and 3, to reduce interferences of ^{50}Ti and ^{50}Cr on the minor ^{50}V isotope during mass spectrometry. The method is adapted from Nielsen et al. (2011). For both procedures, Teflon columns (100 µl resin volume) and AG1-X8 resin (200-400 mesh) were used.

The Ti clean-up column is based on the differential partitioning of V and Ti to an anion exchange resin in HF; this method is used to separate Ti from silicate matrices for mass

spectrometry because Ti will remain partitioned to the resin in HF, while V, and several other matrix elements, will be eluted immediately after loading (Makishima et al., 2002, Nielsen et al., 2011). Samples were loaded in 1 ml 2M HF. Vanadium was collected as the sample was loaded, and with 1.2ml TD 2M HF and 1.4 ml TD 0.5M HF/HCl mixture. Residues were evaporated at 130 °C, covered with TD 16M HNO_3 and evaporated twice at 160 °C, then refluxed in TD 2M HF if repeating the column or TD 0.01M HCl if proceeding to the Cr clean-up column.

The Cr clean up column is a $1/10^{th}$ scaled-down version of column 3 (Section 2.4.2.2) because almost all matrix has been removed and there is now a smaller amount of material remaining. It works following the same theory that V-peroxide complexes will partition to the resin in weak HCl (Nielsen et al., 2011). 33 µl 30% H_2O_2 was added to cooled samples immediately prior to loading. After a 0.6 ml wash of TD 0.01M HCl + 1% v/v H_2O_2, V was collected in 0.8 ml TD 1M HCl. The red-orange colour change (Figure 2.5) was also be observed at this stage. Vanadium cuts were evaporated at 130 °C, treated twice with TD 16M HNO_3 at 160°C, then TD 6M HCl at 130 °C, then refluxed in 1ml TD 0.01M HCl if the column was repeated.

After the Cr clean-up column, samples were evaporated, treated twice with 200 µl TD 16M HNO_3 and 20 µl H_2O_2 at 160 °C to destroy any resin present, then fluxed in 1ml TD 3% HNO_3 for measurement by MC-ICP-MS. If samples still showed high ^{53}Cr or ^{49}Ti ($^{53}Cr/^{51}V$ and $^{49}Ti/^{51}V$ >0.00001; Nielsen et al., 2011) during mass spectrometry, further Cr and/or Ti clean up columns were performed as necessary.

2.5 MC-ICP-MS Methodology

2.5.1 Background

All isotope ratio measurements were performed on Thermo Fisher Scientific Neptune and/or Neptune Plus Multi-Collector Inductively-Coupled-Plasma Mass Spectrometers (MC-ICP-MS) at Durham University.

The Neptune and NeptunePlus are double focusing multiple collector ICP-MS. A schematic is shown in Figure 2.6. Sample aerosol is ionised by an inductively coupled Ar plasma within the torch and the positively charged ions are accelerated by a -2kV

potential through Ni sample and skimmer cones into the instrument. The ion beam is reshaped by the quad lenses. A variable resolution slit tongue with slits of different widths is located before the electrostatic analyser. This allows the mass resolution (MR) to be changed between low resolution (MR ~400), medium resolution (MR ~7000-8000) and high resolution (MR ~8000-10000). Mass resolution is defined as m/Δm, where Δm is the difference between the masses measured at 95% and 5% of the maximum signal intensity on the peak shoulder. The maximum resolution that can be attained with the medium or high MR slits gradually decreases over time as the width of the slit increases due to ablation from ions passing through the slit.

After passing through the slit, positively charged ions are further accelerated and focused for energy variation in the electrostatic analyser (ESA; Figure 2.6). Ions of the same mass but different energy enter the magnet pole at different positions, such that after the magnet separates on charge/mass ratio and energy, the mass and energy focal planes are coincident with the collector array. The collector array comprises nine Faraday cups, of which the axial is fixed, and the remaining eight collectors are movable and can be aligned with the ion beams for the separated masses. This allows simultaneous measurement of multiple masses/isotopes, which is a fundamental requirement for high precision isotope ratio measurements. The Faraday detectors are connected to a series of amplifiers through a relay matrix, which allows any Faraday cup to be connected to any amplifier. There are 9 amplifiers with $10^{11}\Omega$ resistors and 1 with a $10^{10}\Omega$ resistor. The 'standard' amplifier with $10^{11}\Omega$ resistor has a maximum dynamic range of 50 V (it can measure a maximum signal of 50V), while this is 500V for the amplifier with a $10^{10}\Omega$ resistor. This enables simultaneous analysis of isotopes whose abundances vary over orders of magnitude.

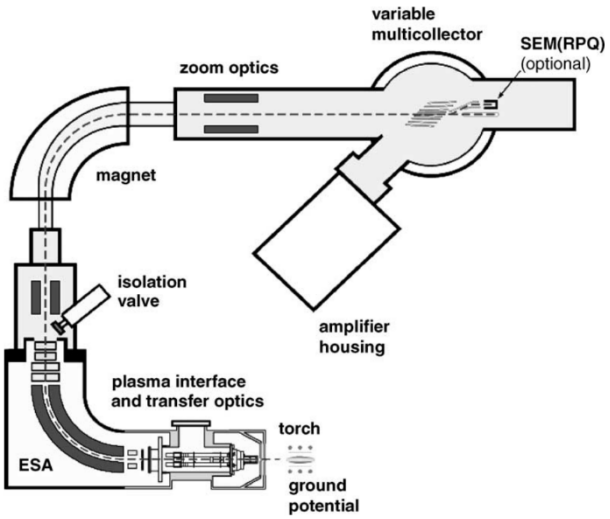

Figure 2.6. Schematic of Neptune MC-ICP-MS. From Weyer and Schwieters (2003).

With MC-ICP-MS, preferential extraction and transmission of heavier ions in the instrument introduces an instrumental mass bias (e.g. Albarède et al., 2004). For radiogenic isotope ratio measurements this instrumental mass bias can be corrected for by measuring a ratio of an unradiogenic pair of isotopes of known ratio and applying a correction, using either a power or exponential law (e.g. Rehkämper et al., 2000). This approach is not possible for stable isotope systems (e.g. Fe, Zn) or elements with only two isotopes (e.g. V), although there are other approaches that can allow the mass bias to be corrected (e.g. standard-sample bracketing, external doping or double spike; Dauphas et al., 2017).

One advantage of MC-ICP-MS is that mass bias changes only slightly over short time periods, so it can be assumed that mass bias during sample measurements is the same as for the bracketing standards of known composition. Drift in mass bias can therefore be corrected using standard sample bracketing (SSB), where the average of the bracketing standard either side of a sample is used to correct for drift. For example, to calculate a δ^{56}Fe value relative to the IRMM-524 certified reference material, Equation 2.1 would be used.

$$\delta^{56}Fe = \left[\frac{(^{56}Fe/^{54}Fe)_{sample}}{(^{56}Fe/^{54}Fe)_{IRMM-524\ average}}\right] \times 1000 \qquad [2.1]$$

The protocols for Fe, Zn and V isotope ratios measurements are described in detail in Sections 2.5.2, 2.5.3 and 2.5.4 respectively.

2.5.2 Iron MC-ICP-MS Methodology

2.5.2.1 Background Principles and Considerations

Iron isotope variability in terrestrial samples was first measured by Thermal Ionisation Mass Spectrometry (TIMS) (Beard and Johnston, 1999). However, this method could only resolve differences in $\delta^{56}Fe$ in low temperature sedimentary environments where biological processes were occurring, while the Fe isotopic compositions of igneous samples were identical within errors of 0.1-0.3‰. TIMS also has the disadvantage of irregular time-dependent instrumental mass fractionation during analysis, and Fe has a low ionization efficiency (e.g. Beard et al., 2003).

At this time, high precision measurements of other transition metal stable isotopes (Zn and Cu) were being made by MC-ICP-MS with analytical uncertainties of ±0.04‰ at the 95% confidence level (Maréchal et al., 1999). A major obstacle in the use of MC-ICP-MS for Fe isotopic measurements is that Ar-O and Ar-N species produce molecular interferences on Fe; $^{40}Ar^{14}N$ on ^{54}Fe, $^{40}Ar^{16}O$ on ^{56}Fe and $^{40}Ar^{16}OH$ on ^{57}Fe (Table 2.1 and Belshaw et al., 2000). These interferences are particularly abundant because an Ar based plasma is used for sample ionisation, and because O and N are present in the atmosphere and in the weak HNO_3 in which samples are commonly dissolved. Techniques to minimise these interferences in early studies included using desolvating nebulizers to reduce oxide interferences and boost analyte signal (Anbar et al., 2000; Belshaw et al., 2000), dissolving samples in HCl (Belshaw et al., 2000), using high concentrations of Fe to overwhelm the interferences (Belshaw et al., 2000), using a collision cell with H_2 to break apart these molecules (Beard et al., 2003), and running in cold plasma (running at lower power; 600W compared to 1200W) to avoid Ar-O and Ar-N formation (Kehm et al., 2003).

The development of the Neptune MC-ICP-MS allowed measurements to be made in in high resolution mode (MR=8000-10000), resulting in improved accuracy of Fe isotope analysis. At this resolution, the Fe peaks can be partially resolved from the argide interferences as flat-topped shoulders on the low mass side of the peak (Weyer and Schwieters, 2003; Figure 2.7). A resolution of at least 2500 is necessary to resolve the interferences (Weyer and Schwieters, 2003).

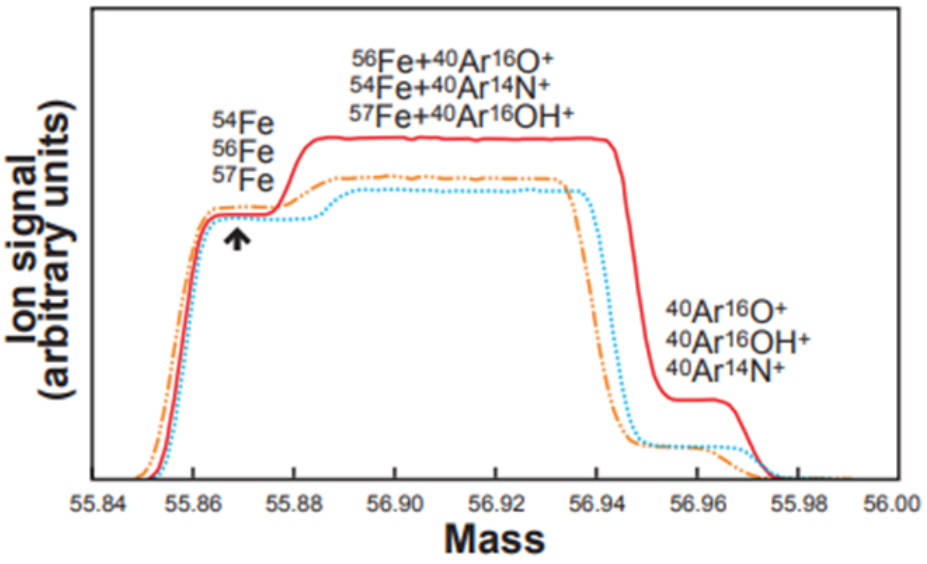

Figure 2.7. Typical shape of a Fe peak scan at medium resolution (m/Δm ≈ 4000). Fe can be resolved from the interferences on the flat shoulder on the low mass side of the peak. The peak centre (black arrow) is manually selected. Figure from Dauphas et al., 2017.

Mass bias can be corrected by standard sample bracketing with either the IRMM-014 or isotopically indistinguishable IRMM-524 standards (e.g. Belshaw et al., 2000; Craddock and Dauphas, 2011). Initially the IRMM-014 standard was used for this work, but this standard is no longer commercially available. From October 2020 onward, IRMM-524B was used as the bracketing standard. Recently, there has been some debate about whether more accurate mass bias correction can be achieved by the use of a double spike (e.g. Millet et al., 2012) or Ni doping (e.g. Poitrasson and Freydier, 2005; Dauphas et al., 2009b; Sossi et al., 2015). A compilation by Zhu et al. (2018) showed that Ni doping or using a Fe double spike were more effective at correcting for short term fluctuations in mass bias, but SSB is sufficient if the drift is stable. The correction methods used in this study are discussed in Section 2.5.2.2.

2.5.2.2 Instrumentation and Measurement Protocol

Iron isotope measurements were carried out on the Neptune and NeptunePlus MC-ICP-MS instruments at Durham University. The method has evolved significantly over the

last 3 years as the instrumental setup and mass bias correction techniques were refined to yield the most precise and reproducible values.

Prior to analysis, the concentration of Fe in the fractions from column 1 was measured. Concentrations were determined by comparing the ^{56}Fe signal of a 2ml sample aliquot to a solution of known Fe concentration. After column 1, Fe fractions were dissolved in 10ml TD 3% HNO_3. A 2ml aliquot containing 10 µl of the stock solution and 1990 µl TD 3% HNO_3 was used for the concentration tests. When the Fe measurement protocol at Durham was first being established, samples were diluted with TD 3% HNO_3 to a concentration of 2 µg/g Fe, resulting in a signal of 10-20V on ^{56}Fe. However, over time it was observed that measurement accuracy and reproducibility increased when samples were run at higher Fe concentrations. It was then standard procedure to dilute all samples and standards to a concentration of 10 µg/g Fe, to ensure we measured a signal >50V on ^{56}Fe (see Section 2.5.2.4). The concentrations of the samples and the bracketing standard were always matched to within ±10% (e.g. Schoenberg and von Blanckenburg, 2005; Dauphas et al., 2009b).

Seven isotopes were measured simultaneously using the cup configuration listed in Table 2.1 (^{53}Cr, ^{54}Fe, ^{56}Fe, ^{57}Fe, ^{58}Fe, ^{60}Ni and ^{61}Ni). A $10^{10}\Omega$ resistor was connected to cup L1 to measure signals over 50V on ^{56}Fe. $10^{11}\Omega$ resistors were used on all other cups.

Table 2.1. The cup configuration and resistors used for Fe isotopic measurements at Durham University. Cr and Ni isotopes in italics are those used for interfering element corrections (Section 5.2.2). Also shown are the main polyatomic interferences on Fe. The Fe signal is resolved from these interferences using medium mass resolution slits.

Element/ polyatomic species	**Faraday Cup**								
	L4	**L3**	**L2**	**L1**	**C**	**H1**	**H2**	**H3**	**H4**
Amplifier	$10^{11}\Omega$		$10^{11}\Omega$	$10^{11}\Omega$ or $10^{10}\Omega$	$10^{11}\Omega$	$10^{11}\Omega$	$10^{11}\Omega$		$10^{11}\Omega$
Fe			^{54}Fe	^{56}Fe	^{57}Fe	^{58}Fe			
Cr	*^{53}Cr*		^{54}Cr						
Ni						^{58}Ni	*^{60}Ni*		*^{61}Ni*
Main polyatomic species			$^{40}Ar^{14}N$	$^{40}Ar^{16}O$	$^{40}Ar^{17}O$ $^{40}Ar^{16}O^{1}H$	$^{40}Ar^{18}O$			

The sample introduction system consisted of a Savillex PFA Concentric Flow nebuliser with 50µl/min uptake rate (CF50) coupled to either a quartz Stable Introduction System from Elemental Scientific Incorporated (ESI SIS) or a borosilicate glass Cinnabar micro-cyclonic spray chamber from Glass Expansion. Standard Ni sample and skimmer cones were used. With this setup, typical sensitivity for Fe was approximately 6-9V/ppm on ^{56}Fe at an uptake rate of 50µl/min.

Measurements were performed in medium resolution mode to allow the Fe peaks to be resolved from the argide interferences (e.g. Weyer and Schwieters, 2003). The peak centre (centre of the shoulder) was selected manually before each sequence. Mass resolution was typically between 5500-8000 depending on the age and degradation of the resolution slit, and tuning conditions on the day.

All measurement sequences were run using an autosampler, because identical time spacing between every sample analysis is necessary when correcting for mass bias using standard sample bracketing. Isotope ratios were measured in static multi-collection mode where an individual measurement was comprised of 1 block of 50 cycles with an integration time of 4.194s per cycle; total analysis time around 3.5 minutes. Approximately 2 µg of Fe was consumed during one analysis at a concentration of 10 µg/g. Uptake and washout times of 45 s and 120 s respectively were used, with TD 3% HNO_3 used as the wash acid.

Two in house standards, *Romil Fe* (diluted from a 1000 µg/g Fe ROMIL Reference Solution) and *Fe Wire* (a solution made by dissolving an iron wire) were measured throughout sessions to assess machine performance and stability.

Interfering Element Corrections

^{53}Cr was monitored during all measurements and used to correct for the isobaric interferences of ^{54}Cr on ^{54}Fe (Table 2.1). This correction assumes a true $^{53}Cr/^{54}Cr$ ratio of 4.017336 and uses an exponential mass fractionation law to calculate the measured ^{54}Cr, on the assumption that Cr and Fe share the same mass bias (e.g. Schoenberg and von Blanckenburg, 2005).

Previous studies have argued that the effect of the interference from Cr on measured Fe isotope ratios cannot be resolved if the $^{54}Cr/^{54}Fe$ ratio is above 0.01 to 0.1 (Schoenberg and von Blanckenburg, 2005; Dauphas et al., 2009b). Column 1 should separate most Cr from Fe, so only trace amounts should be present (Sossi et al., 2015). Consequently, samples and USGS standards typically had $^{54}Cr/^{54}Fe$ ratios from 10^{-6} to 10^{-5} which was much lower than published thresholds, and this correction typically changed the $\delta^{56}Fe$ value by less than 0.005‰, considerably less than the method reproducibility (±0.05‰).

The in-house *Romil Fe* solution standard measured throughout sessions has around 100 times higher Cr than samples, giving a signal of 10^{-3}V on ^{53}Cr, compared to the 10^{-5} or 10^{-6}V measured for samples. This corresponds to a $^{54}Cr/^{54}Fe$ ratio of 10^{-4} which is still below the threshold for obtaining accurate delta values. However, there is around 0.1‰ difference between the $\delta^{56}Fe$ value for the Romil solution before and after the internal interference corrections are applied (e.g. $\delta^{56}Fe$ values of approximately 0.05‰ and 0.16‰ respectively). This highlights the importance of trying to achieve quantitative removal of Cr from samples during column chemistry. However, since the Romil solution is only used to assess instrument stability during sequences, obtaining an absolute value is not necessary, it is more important that the value is reproducible.

Since $\delta^{56}Fe$ and $\delta^{57}Fe$ together can be used to demonstrate mass dependence, the $\delta^{58}Fe$ ratio was not reported, so it was not necessary to use ^{60}Ni to correct for interferences of ^{58}Ni on ^{58}Fe. Additionally, from November 2021, we began to correct for mass bias using Ni doping (see below), so no Ni correction was applied.

Mass Bias Corrections

1. Standard Sample Bracketing Only (October 2018 – November 2021)

From October 2018 to November 2021, mass bias was corrected only by standard sample bracketing (SSB). During this time, the long-term reproducibility for the *Romil Fe* solution standard was around 0.050‰ (2SD) (See section 2.5.2.3). This is comparable to values obtained by Zhu et al. (2018) comparing SSB, Ni doping and double spike. Therefore, SSB seems to be sufficient to correct for drift in mass bias when the drift is stable. The IRMM-014 certified reference material was initially used as the bracketing

standard. However, the supply of this standard is now exhausted. Therefore, from October 2020 onward, the IRMM certified reference material EC-NRM 524B was used as the bracketing standard. The EC-NRM 524 standard (hereafter referred to as IRMM-524B) is a metal wire used as a neutron dosimetry reference material. The IRMM-014 standard was made directly from these metal wires (Craddock and Dauphas, 2011; Dauphas et al,. 2017), hence IRMM-524B should be isotopically identical to IRMM-014. We obtained the IRMM-524B standard as a metal wire and dissolved the entire wire in 5M HNO_3. The concentrated stock was then stored in a Teflon bottle in TD 3% HNO_3.

Craddock and Dauphas (2011) and de Vega et al. (2020) report that the reference material IRMM- 524A has an identical isotopic composition to IRMM-014. However, no other studies have reported if IRMM-524B is also isotopically identical to IRMM-014. Over the course of this work, the average isotopic composition of the Romil Fe in-house standard was 0.160 ± 0.064‰ (2SD, n=317) when bracketed with the IRMM-014 standard, and 0.172 ± 0.057‰ (2SD, n=250) when bracketed with the IRMM-524B standard. Note that this is considering all data, irrespective of the method of mass bias correction, see Section 2.5.3.2). These two long term averages are within error of each other, although may indicate there is a minor isotopic offset (~0.010-0.020‰) between IRMM-014 and IRMM-524B. This offset is smaller than our typical reproducibility of 30-40ppm (2SD) on samples and standards. A thorough, inter-lab calibration of IRMM-524B would be required to determine if there really is an offset, but this is not possible within the timeframe of this work. However, even if the absolute values of samples measured relative to IRMM-524B are offset, variation in Fe isotopic composition between samples will still be preserved.

2. Standard Sample Bracketing and Ni Doping (November 2021 Onward)

From November 2021, we began to correct for mass bias using both SSB and external element doping with Ni. Samples and standards were doped to a concentration of 8 µg/g Ni using a pure Ni solution (1000µg/g Ni ROMIL Reference Solution), ensuring the Fe/Ni ratio in samples and standards was matched to within 10%. This change occurred after other members of the Durham Isotope Group found that Ni doping significantly improved the accuracy and reproducibility of measurements of high Mg boninite lavas, which perhaps have more complex matrices than other whole rock samples. Although Ni doping

did not significantly improve the long-term reproducibility of solution standards (SSB Only 2SD = 0.064‰, n=317; SSB and Ni Doping 2SD = 0.056‰, n=150), it was extremely beneficial during periods of mass bias instability. When mass bias was corrected using SSB alone, a considerable amount of data from each Fe measurement session was rejected because it was measured during periods of mass bias instability. However, Ni doping was an effective method of mass bias correction during these periods of instability.

The mass bias corrections are calculated automatically on the Neptune software, and the theory is as follows. For the Ni dopant, the mass discrimination between ^{60}Ni and ^{61}Ni can be written using the exponential mass fractionation law (Equations 2.2 and 2.3, from Poitrasson and Freydier, 2005).

$$R_T = R_M \times (m_1/m_2)^{\beta} \qquad [2.2]$$

$$\left(\frac{^{61}Ni}{^{60}Ni}\right)_T = \left(\frac{^{61}Ni}{^{60}Ni}\right)_M \left(\frac{mass^{61}Ni}{mass\ ^{60}Ni}\right)^{\beta_{Ni}} \qquad [2.3]$$

T and M denote the mass bias corrected ratio and the ratio measured by MC-ICP-MS respectively and β is the fractionation factor. For the dopant, R_T is the known ratio in the solution used, and for Ni we use the natural abundance of ^{61}Ni/^{60}Ni, i.e. 1.1399/26.2231 (Lodders, 2003). B_{Ni} was calculated by rearranging Equation 2.3.

$$\beta_{Ni} = \ln\left[\frac{\left(\frac{^{61}Ni}{^{60}Ni}\right)_T}{\left(\frac{^{61}Ni}{^{60}Ni}\right)_M}\right] / ln\left(\frac{mass^{61}Ni}{mass\ ^{60}Ni}\right) \qquad [2.4]$$

The mass bias corrected Fe ratio ((^{56}Fe/^{54}Fe)$_T$) is then calculated using the exponential mass fractionation law for Fe with the β_{Ni} fractionation factor.

$$\left(\frac{^{56}Fe}{^{54}Fe}\right)_T = \left(\frac{^{56}Fe}{^{54}Fe}\right)_M \left(\frac{mass^{56}Fe}{mass\ ^{54}Fe}\right)^{\beta_{Ni}} \qquad [2.5]$$

2.5.2.3 Quality Control and Assurance

Data Quality Control

Iron isotope ratios were reported as δ^{56}Fe values relative to the IRMM-014 or IRMM-524B standard, where:

$$\delta^{56}Fe = \left[\frac{(^{56}Fe/^{54}Fe)_{sample}}{(^{56}Fe/^{54}Fe)_{IRMM\ 014/524B\ average}}\right] \times 1000 \qquad [2.6]$$

Several criteria were developed during this study to help determine whether data should be accepted or rejected. These criteria are:

1. The concentration of sample and bracketing standard must be matched within 10%.
2. Acceptable values for USGS standards and in house *Romil Fe* and *Fe Wire* standards must be measured within the sequence.
3. Samples must have mass dependent δ^{56}Fe and δ^{57}Fe. An expected δ^{57}Fe is calculated from measured δ^{56}Fe ($\delta^{57}Fe_{calc} \approx$ 1.5 x δ^{56}Fe) and this is compared to the measured δ^{57}Fe. The values must agree to within 20%. Mass dependent values show that there are no unresolved isobaric interferences. Note that this relationship breaks down when δ^{56}Fe values are near zero.
4. The within-run relative standard error (RSE) for each individual sample analysis must be <30. This considers the standard error in the measurement of ^{56}Fe/^{54}Fe over 50 integrations, compared to the average ^{56}Fe/^{54}Fe:

$$RSE = \frac{standard\ error\ in\ \frac{^{56}Fe}{^{54}Fe}}{average\ \frac{^{56}Fe}{^{54}Fe}} \times 1000000 \qquad [2.7]$$

5. The relative standard deviation (RSD) of the ^{56}Fe/^{54}Fe ratio of the bracketing standards is calculated from:

$$RSD = \frac{standard\ deviation\ of\ \frac{^{56}Fe}{^{54}Fe}\ of\ bracketing\ STDs}{average\ \frac{^{56}Fe}{^{54}Fe}\ of\ bracketing\ STDs} \times 1000000 \qquad [2.8]$$

The RSD check can be used to highlight two possible problems. Firstly, it is a measure of how the mass bias is drifting. When this number is constant, it indicates that there is a regular drift in mass bias, which can be corrected by standard sample bracketing. If the RSD is high (e.g. >100) this indicates that the

mass bias is drifting very quickly which can indicate machine instability. Additionally, a fluctuating RSD value indicates there is not a regular drift in mass bias. A jump in RSD can also show that the standard has been affected by the matrix of the preceding sample. If this is the case, the RSD value will return to normal for the next standard. The measurements of samples which affect the bracketing standard afterwards are rejected. For these reasons, RSD values must remain approximately constant (±30) through the periods of a run where data is taken from, and must be <100.

Reference Materials

Several USGS reference materials were digested and processed through chemistry as described in Section 4, prior to processing of any samples. This was to ensure that there was no isotopic fractionation during the procedure and that the accepted $\delta^{56}Fe$ values were measured. The results are summarised in Table 2.2.

The USGS reference materials used in this study were the BHVO-2, BCR-2 and BIR-1a basalts and the GSP-2 granodiorite. The Fe (and V and Zn) isotopic compositions of these reference materials have been measured in numerous studies, so there is a good database on which to compare our results. For Fe, this data is summarised in Table 2.3. The reference materials also span a wide range in SiO_2 content from 47.96% to 66.6% (e.g. Raczek et al., 2007; Fourny et al., 2016) similar to the samples measured in this study. The GSP-2 standard is the most silicic and has the most similar composition and matrix to the Boggy Plain and Red Hills whole rock samples.

Table 2.2. Iron isotopic compositions of the test batch of USGS reference materials. Duplicates of BIR-1a and GSP-2 were dissolved. Errors quoted as 2 Standard Deviations of the mean of at least 3 measurements. Ranges and average literature $\delta^{56}Fe$ values are from Table 2.3.

USGS Standard	$\delta^{56}Fe_{IRMM-014}$ (‰)	2SD	n	$\delta^{56}Fe_{IRMM-014}$ Literature Range (‰)*	$\delta^{56}Fe_{IRMM-014}$ Literature average (‰)*	n*
BCR-2	0.050	0.049	3	0.040 – 0.110	0.084 ± 0.034 (2SD)	17
BIR-1a (1)	0.034	0.019	3	0.050 – 0.062	0.056 ± 0.010 (2SD)	13
BIR-1a (2)	0.037	0.041	6			
GSP-2 (1)	0.136	0.036	6	0.150 – 0.173	0.158 ± 0.015 (2SD)	8
GSP-2 (2)	0.138	0.022	3			

In the case of Fe, all the reference materials run as part of this procedural test were within error of values reported in the literature (Table 2.3), although consistently light by approximately 0.020‰. However, these measurements were carried out while the Fe measurement protocol was still being established at Durham. Samples were run at 2 μg/g, yielding a signal of only 11V and 0.7V on ^{56}Fe and ^{54}Fe respectively. Therefore, the ^{54}Fe measurement would be more sensitive to the presence of Cr. The $\delta^{56}Fe$ and $\delta^{57}Fe$ values were also non mass dependent. It is highly likely that if these samples had been measured with a signal of >40V ^{56}Fe, their $\delta^{56}Fe$ values would be closer to the literature values.

This possibility is supported by a comparison between values in Table 2.2 with those in Table 2.4. Table 2.4 lists the $\delta^{56}Fe$ values for the USGS reference materials processed with every batch of samples throughout this work. These samples were run at higher ^{56}Fe beam intensities (>50V) and are within error of literature values. The *Synth. Mag* standard is an in-house synthetic magnetite powder (>96.8 wt.% Fe_3O_4; Inoxia.ltd) digested with batches of magnetite mineral separates. It was also used to test the maximum Fe which could be loaded on the columns without overloading them (see Section 2.5.2.4).

Table 2.3. Literature compilation of Fe isotopic compositions of USGS reference materials. Errors are quoted as stated in the literature; [1]2SD, [2]2SE, [3]95% confidence interval.

Reference Material BHVO-2			Reference Material BCR-2		
$\delta^{56}Fe_{IRMM-014}$ (‰)	Quoted error	Reference	$\delta^{56}Fe_{IRMM-014}$ (‰)	Quoted error	Reference
0.114	0.011[3]	Craddock and Dauphas (2011)	0.079	0.047[1]	Weyer et al. (2005)
0.128	0.019[1]	Millet et al. (2012)	0.087	0.023[3]	Dauphas et al. (2009a)
0.104	0.043[2]	Sossi et al. (2012)	0.091	0.011[3]	Craddock and Dauphas (2011)
0.120	0.052[3]	Telus et al. (2012)	0.098	0.025[1]	Millet et al. (2012)
0.121	0.049[1]	Liu et al. (2014)	0.091	0.034[2]	Sossi et al. (2012)
0.112	0.021[1]	He et al. (2015)	0.090	0.040[1]	Chen et al. (2014)
0.100	0.030[1]	Nebel et al. (2015)	0.107	0.025[1]	Liu et al. (2014)
0.131	0.052[2]	Wu et al. (2017)	0.080	0.024[1]	He et al. (2015)
0.080	0.030[1]	Xia et al. (2017)	0.060	0.090[1]	Bilenker et al. (2017)
0.100	0.060[1]	Foden et al. (2018)	0.093	0.017[1]	Zhu et al. (2018)
0.095	0.029[1]	McCoy-West et al. (2018)	0.088	0.040[1]	Cao et al. (2018)
0.114	0.019[1]	Zhu et al. (2018)	0.070	0.040[1]	Chen et al. (2019)
0.128	0.035[1]	Cao et al. (2019)	0.110	0.080[1]	Du et al. (2019)
0.080	0.050[1]	Chen et al. (2019)	0.080	0.040[1]	Gong et al. (2020)
0.130	0.050[1]	Du et al. (2019)	0.080	0.040[1]	Soderman et al. (2021)
0.116	0.007[3]	Peters et al. (2019)	0.040	0.030[1]	Chen et al. (2021)
0.110	0.040[1]	Soderman et al. (2021)	0.100	0.020[2]	Deng et al. (2022)
0.111	0.030[1]	Wagner et al. (2021)			
0.110	0.040[1]	Chen et al. (2021)			
0.130	0.020[2]	Deng et al. (2022)			

Reference Material BIR-1a			Reference Material GSP-2		
$\delta^{56}Fe_{IRMM-014}$ (‰)	Quoted error	Reference	$\delta^{56}Fe_{IRMM-014}$ (‰)	Quoted error	Reference
0.050	0.039[1]	Weyer et al. (2005)	0.159	0.013[3]	Craddock and Dauphas (2011)
0.051	0.046[1]	Schoenberg and von Blanckenburg (2006)	0.173	0.031[1]	Liu et al. (2014)
0.053	0.047[1]	Schuessler et al. (2009)	0.154	0.012[1]	He et al. (2015)
0.053	0.015[3]	Craddock and Dauphas (2011)	0.156	0.033[2]	He et al. (2017)
0.050	0.014[1]	Millet et al. (2012)	0.163	0.027[1]	Foden et al. (2018)
0.060	0.042[1]	Liu et al. (2014)	0.150	0.030[2]	Wu et al. (2018)
0.062	0.010[1]	Williams and Bizimis (2014)	0.156	0.024[1]	Zhu et al. (2018)
0.061	0.045[1]	El Korh et al. (2017)	0.150	0.040[1]	Gong et al. (2020)
0.060	0.020[1]	Inglis et al. (2017)			
0.054	0.039[1]	McCoy-West et al. (2018)			
0.060	0.040[1]	Williams et al., (2018)			
0.050	0.040[1]	Soderman et al. (2021)			
0.053	0.011[1]	Wagner et al. (2021)			

Table 2.4. Iron isotopic compositions of USGS reference materials processed with each batch of samples. Errors quoted as 2 Standard Deviations of the mean of at least 3 measurements. Literature Range from table 2.3 (*).

Batch	USGS Standard	$\delta^{56}Fe_{IRMM-014}$ (‰)	2SD	n	$\delta^{56}Fe_{IRMM-014}$ Literature Range (‰)*
430	GSP-2	0.150	0.033	13	0.150 – 0.173
456	BHVO-2	0.119	0.066	8	0.080 – 0.131
475	GSP-2	0.171	0.055	4	0.150 – 0.173
497	BIR-1a	0.034	0.016	4	0.050 - 0.062
525	BIR-1a	0.070	0.065	4	0.050 - 0.062
532	BIR-1a	0.057	0.051	3	0.050 - 0.062
534	BIR-1a	0.065	0.043	6	0.050 - 0.062
537	BCR-2	0.095	0.018	3	0.040 – 0.110
539	Synth. Mag	0.107	0.085	3	n/a

Long Term Reproducibility

In-house Fe standard *Romil Fe* and USGS reference materials were used to assess long term reproducibility and accuracy. Throughout this study, both the bracketing standard (IRMM-014 to IRMM-524B) and method of mass bias correction (SSB only to SSB with Ni doping) have been changed. The average Fe isotopic composition of the *Romil Fe* standard during the periods where these different measurement protocols were used is summarised in Table 2.5 and shown in Figure 2.8. For an individual analytical session, errors are given as two standard deviations of at least 3 measurements and are typically between 0.040-0.060‰, which we take as the best estimate for the long-term reproducibility of Fe measurements.

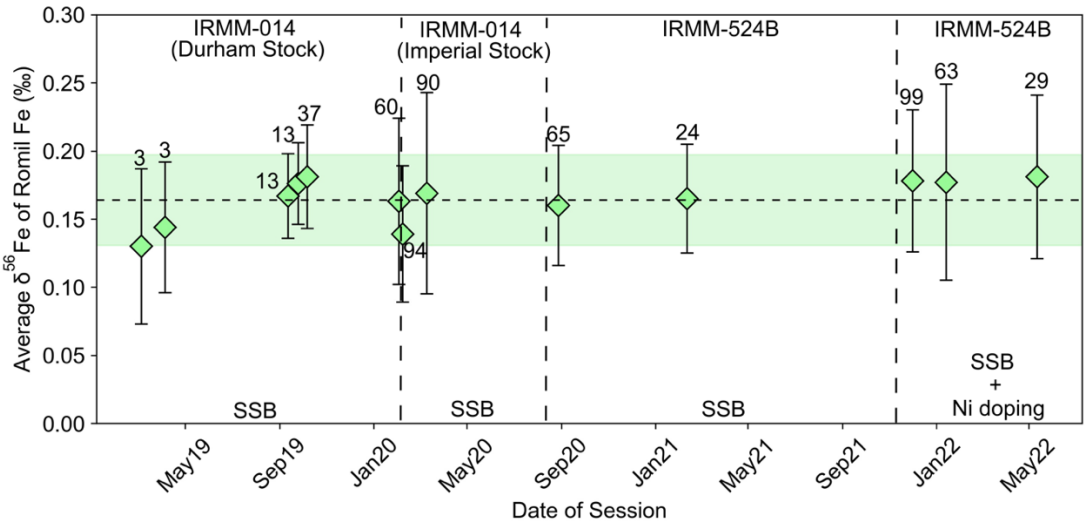

Figure 2.8. Long term reproducibility of Romil Fe standard. The green diamonds show the average δ^{56}Fe for the Romil Fe standard in an individual measurement session. The number of analyses is noted beside each measurement. The changes in bracketing standards and method of mass bias correction are labelled (see text for more information). The dotted line and green shaded area is the average of all the session values; 0.164 ± 0.033‰ (2SD, n=13).

Table 2.5. Long term reproducibility of the Romil Fe standard. The average δ^{56}Fe for all measurements of Romil Fe using the different measurement protocols are listed. Errors are 2SD.

Date	**Bracketing Standard**	**Mass Bias Correction**	**δ^{56}Fe (‰) of Romil Fe**	**n**
March 2019 – February 2020	IRMM-014 (Durham Stock)	SSB Only	0.169 ± 0.053	134
February 2020- March 2020	IRMM-014 (Imperial Stock)	SSB Only	0.152 ± 0.063	182
October 2020 – February 2021	IRMM-524B	SSB Only	0.162 ± 0.043	89
November 2021 - Present	IRMM-524B	SSB and Ni Doping	0.178 ± 0.060	191

We replaced the stock of IRMM-014 throughout this study from the "Durham" stock to one sourced from Imperial College London ("Imperial"). Previous studies have demonstrated that different IRMM-014 stocks have homogeneous isotopic composition (Dauphas et al., 2004; Dauphas et al., 2009b). The long-term average δ^{56}Fe value for the Romil Fe standard varies by 0.017‰ when the different stocks are used as the bracketing standard (Table 2.5), but values are still within error. It is also important to note that the

method was still being refined at this time, and different combinations of nebulisers and spray chambers were also used during these sessions.

IRMM-524B was used as the bracketing standard from October 2020 onward, and Ni doping was used from November 2021 onward. As mentioned in Section 2.5.2.2, the $\delta^{56}Fe$ values for Romil Fe are higher when using the IRMM-524B bracketing standard but are within error of values obtained when bracketing with IRMM-014. This suggests there may be an isotopic offset of around 0.01 – 0.02‰ between IRMM-014 and IRMM-524B, but a thorough inter-lab calibration would be needed to confirm this.

The GSP-2 granodiorite standard dissolved with Batch 430 was repeatedly analysed to assess long term accuracy of Fe isotope measurements. The average $\delta^{56}Fe_{IRMM\text{-}014}$ of GSP-2 measured in 8 different Fe analytical sessions (0.151 ± 0.048, 2SD, n=8) agrees with published literature values (Figure 2.9; Table 2.3).

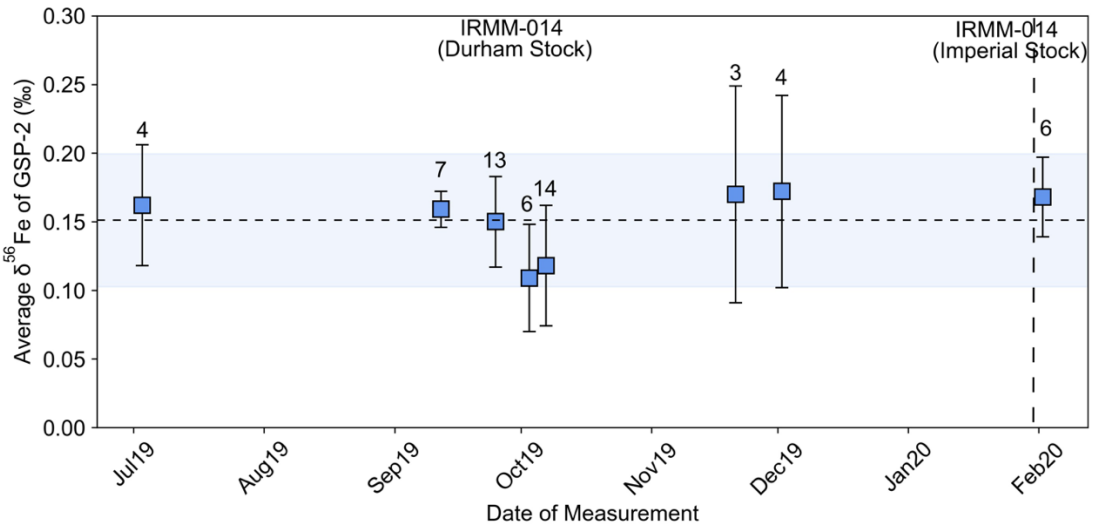

Figure 2.9. Long term reproducibility of USGS reference material GSP-2. The number of analyses is noted beside each measurement. The dotted line and blue shaded area represents the long term average $\delta^{56}Fe_{IRMM\text{-}014}$ = 0.151 ± 0.048‰ (2SD, n=8).

Total Procedural Blanks

For every batch of samples analysed, one beaker was left empty and processed through the column chemistry procedure as if it was a sample. After the full procedure, the concentration of that element in 1ml TD 3% HNO3 was measured to give a Total

Procedural Blank (TPB). Total procedural Fe blanks are listed in Table 2.6. Given that Fe is a major element (weight percent concentrations) in all silicate and oxide samples, these blanks are negligible compared to the total Fe processed (typically over 5 mg).

Table 2.6. Total procedural Fe blanks for each batch of samples processed. Note, batch numbers in Durham are used by all laboratory users, so are not consecutive numbers.

Laboratory Batch Number	Total Procedural Blank Fe (ng)
411	20
415	28
430	17
456	28
464	25
497	21
525	39
532	74
534	92
537	27
539	55

2.5.2.4 Iron Specific Considerations

Introduction System

As the Fe analysis method was refined, some observations were made about the effect of different sample introduction systems on the accuracy and reproducibility of measurements.

As mentioned in Section 2.5.2.2, two different spray chambers were used in the course of the study; a quartz dual cyclonic-Scott Double Pass spray chamber from ESI and a borosilicate glass micro-cyclonic spray chamber. No difference was found in the measured isotopic composition of our standard solutions when using either chamber. From March 2019 to March 2020, the Romil Fe standard had an average of $\delta^{56}Fe_{IRMM\text{-}014}$ = 0.179 ± 0.036 (2SD, n=55) using the cyclonic spray chamber and $\delta^{56}Fe_{IRMM\text{-}014}$ = 0.158 ± 0.064 (2SD, n=179) with the ESI SIS spray chamber, using the CF 50µl/min nebuliser in both cases.

Two different nebulisers were also used during the initial set up of the Fe measurement protocol; a PFA MicroFlow nebuliser from ESI (PFA 50) and a PFA Concentric Flow

nebuliser from Savillex (CF 50), both with 50 µl/min uptake rate. It was observed that the nebuliser choice had a strong influence on beam stability. For example, over 50 integrations of the IRMM standard, the ^{56}Fe signal had a standard deviation of >0.5V when using the PFA 50 nebuliser, but <0.2V using the CF 50 nebuliser.

The nebuliser choice had a minor effect on the precision of measurements. For example, the Romil standard had a value of $\delta^{56}Fe_{IRMM\text{-}014} = 0.152 \pm 0.071‰$ (2SD, n=77) using the PFA nebuliser, and precision improved to 0.144 ± 0.043‰ (2SD, n=77) using the CF nebuliser. This data was taken from the same analytical session where the resolution was the same, and the ^{56}Fe beam size was between 30-40V. Two-sample t-tests show that the PFA and CF mean are not statically different.

However, both nebulisers were used to measure oxide mineral separates. The measurements with the CF nebuliser were consistently lighter by approximately 0.050‰. Two-sample t-tests indicate that the measurements made with the PFA 50 and CF 50 nebulisers were statistically different. This was possibly due to the beam instability when the PFA nebuliser was used, which may have more of an effect for oxide samples which have a different matrix to silicate samples. For this reason, the CF nebuliser was used in all further analytical sessions.

Solution Concentrations

Since the start of this study in 2019, samples have been diluted to different Fe concentrations for analysis. For those analyses where the ^{56}Fe signal was below 20V, $\delta^{56}Fe$ and $\delta^{57}Fe$ values were not mass dependent, as predicted theoretically ($\delta^{57}Fe \approx \delta^{56}Fe$ x 1.5), suggesting that there was an unresolved interference on one or several of the isotopes. Results typically had poor reproducibility, and incorrect values for USGS and solution standards were obtained.

By increasing the signal of ^{56}Fe to over 40V these unidentified interferences were overwhelmed, and mass dependent $\delta^{56}Fe$ and $\delta^{57}Fe$ values were measured. Since Fe concentrations were not limited in any samples, Fe fractions from column 1 were diluted to yield a signal of at least 40-50V on ^{56}Fe, which normally equated to around 8-10 µg/g Fe. Since the standard amplifier with $10^{11}\Omega$ resistor can only measure a signal up to 50V,

a $10^{10}\Omega$ resistor was used on the L1 amplifier when measuring a larger signal (up to 500V) on ^{56}Fe.

Magnetite Fe Overloading Tests

The ion exchange column chromatography method described in Section 2.4.2 was developed and calibrated for silicate whole rock samples. However, this procedure was used to separate Fe, V and Zn from Fe-Ti oxide mineral separates for this work. For column chromatography to be successful, it is necessary for elements to remain partitioned to the resin until they are eluted. This becomes problematic when processing oxide minerals. They have very high Fe concentrations and sample digestions must be sufficiently large to yield enough V and Zn for analysis, which are only present at the µg/g level. All the Fe must remain partitioned to the resin in 6M HCl while the V fraction is eluted. Non-quantitative recovery can result in isotopic fractionation (e.g. Maréchal and Albarède, 2002).

To test the maximum mass of Fe-Ti oxides which could be processed without loss of Fe and subsequent column-induced Fe isotope fractionation, masses of a synthetic magnetite powder (>96.8 wt.% Fe3O4; Inoxia.ltd) varying from 10-200 mg were dissolved, as detailed in Section 2.3, and passed through column 1. The aim was to follow the normal procedure and determine what mass of powder would overload the Fe column capacity, causing premature Fe loss before 0.5M HCl was added to purposefully elute the Fe fraction. This can be visually detected because Fe is a brown/orange colour when bound to the resin, and the HCl containing dissolved Fe is a yellow colour (Figure 2.3; Section 2.4.2). The results are summarised in Table 2.7 and Figure 2.10.

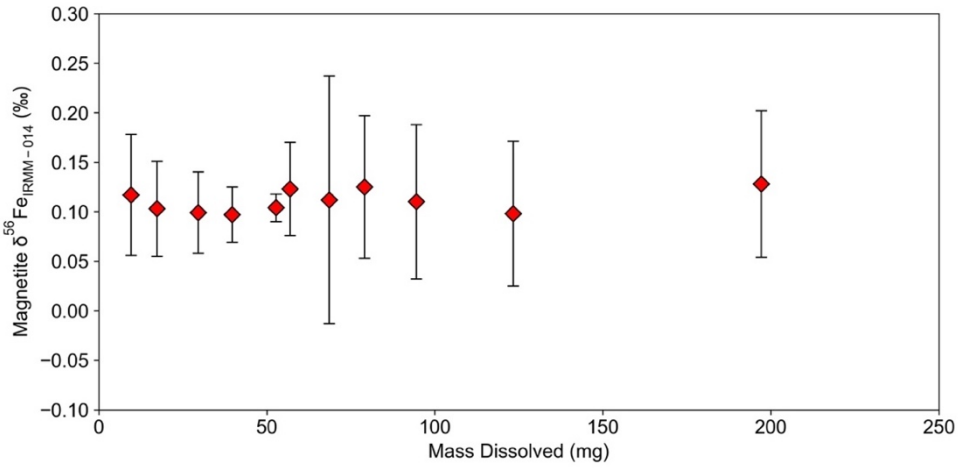

Figure 2.10. Iron isotopic composition of the synthetic magnetite powder against mass dissolved. Errors are 2SD of the mean of three measurements.

Table 2.7. Iron isotopic composition of the synthetic magnetite powder aliquots. Errors are 2SD of the mean of three measurements.

Synthetic magnetite mass (mg)	$\delta^{56}Fe_{IRMM-014}$ (‰)	2SD	n
9.6	0.117	0.061	3
17.4	0.103	0.047	3
29.6	0.099	0.041	3
39.7	0.097	0.029	3
52.8	0.108	0.027	3
57.0	0.123	0.047	3
68.6	0.112	0.124	3
79.1	0.126	0.073	3
94.6	0.110	0.077	3
123.4	0.098	0.072	3
197.2	0.128	0.073	3
Overall Average	0.111	0.023	11

During the 6M HCl step of the column chemistry procedure (Section 2.4.2), Fe should remain bound to the resin. However, a yellow-coloured acid was eluted from the columns containing the samples with masses over 50 mg (Figure 2.3). This may indicate Fe loss from the column, but accurate yields could not be calculated due to the errors propagated when making numerous dilutions of the Fe cuts from column 1, and errors in the weight

of the powder. However, despite this possible Fe loss, the Fe isotopic composition of all samples were identical within error. The average isotopic composition of the 11 aliquots was $\delta^{56}Fe_{IRMM\text{-}014} = 0.111 \pm 0.023$ (2SD, n=11). This confirmed that up to 200 mg of oxide powder can be loaded onto column 1 without fractionating Fe. This is a considerably larger mass than is necessary; normally under 30 mg was dissolved.

Three real magnetite powders were also dissolved in duplicate and processed through chemistry to test the robustness of the method for real mineral separates. Iron isotopic compositions are shown in Table 2.8. The Fe isotopic compositions of both digestions were identical within error for each sample and indicate that the Fe isotopic composition of oxide mineral separates can be measured accurately using this method.

Table 2.8. Iron isotopic compositions of 3 magnetite mineral separates. SA917 is a magnetite of igneous origin from the Bushveld intrusion, South Africa. AM NZ is a magnetite from New Zealand and AM Shet is a hydrothermally precipitated magnetite from Shetland (Muxworthy, 1998).

Sample	$\delta^{56}Fe_{IRMM\text{-}014}$ (‰)	2SD	n
SA917 (1)	0.465	0.033	3
SA917 (2)	0.466	0.025	3
AM NZ (1)	0.059	0.026	3
AM NZ (2)	0.040	0.014	3
AM Shet (1)	0.137	0.026	2
AM Shet (2)	0.158	0.034	2

2.5.3 Zinc MC-ICP-MS Methodology

2.5.3.1 Background Principles and Considerations

The first MC-ICP-MS method for high precision Zn isotope measurements used a magnetic sector instrument in low resolution mode (Marèchal et al., 1999). They generated flat topped peaks and used multiple collectors to remove the effect of signal fluctuations due to plasma instability. Results had reproducibility of ± 0.04‰ at the 95% confidence interval. Although many variations in measurement protocols have since been published, the level of analytical precision obtained by Marèchal et al. (1999) is

comparable to that obtained by recent methodologies (e.g. errors of ± 0.06‰ 2SD; Sossi et al., 2015).

In comparison to Fe and V (Sections 2.5.2 and 2.5.4), Zn can be measured in low resolution mode on flat peak tops because the isotopes have no (or negligible) molecular interferences. In the Zn mass range, the only atomic isobaric interference is ^{64}Ni on ^{64}Zn, which can be corrected for by monitoring ^{62}Ni. The molecular species $^{40}Ar^{14}N_2^+$ and $^{40}Ar^{14}N^{16}O^+$ interfere on masses 68 and 70 respectively (e.g. Zhu et al., 2015) but are not a problem if the $\delta^{68}Zn$ value is not of direct interest. There may be HNO_3 related species at masses 64 ($^1H_2{}^{14}N^{16}O_3^+$) and 66 ($^1H_2{}^{14}N^{16}O_2{}^{18}O^+$), but these can be corrected using an on-peak zero subtraction (Mason et al., 2004).

Similar to Fe, there are a number of ways to correct for instrumental mass bias during Zn isotope measurements. Marèchal et al. (1999) used external element normalisation to correct for instrumental mass bias by doping all samples with Cu. This correction assumes that Cu and Zn have similar mass bias. Zn mass bias can also be corrected using standard sample bracketing (e.g. Paniello et al., 2012; Chen et al., 2013, Chen et al., 2016, Huang et al., 2018). Often a combination of external element normalisation with Cu addition and standard-sample bracketing is employed.

Some studies have employed a Zn double spike to correct for mass bias in seawater and other samples with complex matrices (e.g. Bermin et al., 2006; Arnold et al., 2010) but calibrating an accurate double spike is time-consuming, and the long-term reproducibility of $\delta^{66}Zn$ values using double spike is similar to Cu doping alone (e.g. Moynier et al., 2017). For these reasons, standard sample bracketing combined with external element normalisation was used to correct for mass bias in this study.

Zinc isotopic ratios are conventionally reported in delta notation relative to the JMC Lyon standard, introduced by Marèchal et al. (1999) before widespread, certified standards for 'non-traditional' isotope systems were available. Unfortunately, the supply of JMC Lyon has been exhausted. Currently, the certified isotope reference material IRMM-3702 or the AA-ETH Zn solution (Archer et al., 2017) are commonly used as bracketing standards. The AA-ETH solution (made by dissolving a pure Alfa Aesar Zn foil) has been shown to be isotopically indistinguishable from IRMM-3702 (Archer et al., 2017). JMC-Lyon has an isotopic composition of $\delta^{66}Zn = 0.28 \pm 0.02$‰ relative to AA-ETH Zn and IRMM-

3702 (Archer et al., 2017). Therefore, $\delta^{66}Zn$ values are measured relative to either ETH Zn or IRMM-3702 and recast by +0.28‰ for reporting relative to JMC-Lyon Zn standard.

2.5.3.2 Instrumentation and Measurement Protocol

Zinc isotope measurements were carried out on either the Neptune or NeptunePlus MC-ICP-MS instruments at Durham University, using an approach similar to Marèchal et al. (1999).

Prior to analysis, the concentration of the Zn fractions from column 1 was determined. The Zn fractions were dissolved in 1 ml TD 3% HNO_3 after column 1. Concentrations were determined by comparing the ^{66}Zn signal of aliquots containing 20 µl of this solution and 980 µl TD 3% HNO_3 to a solution of known Zn concentration. Savillex PFA autosampler vials were used exclusively for Zn analyses to reduce Zn blanks (Section 2.5.3.3). The autosampler vials were cleaned with TD HNO_3 and MQ H_2O between uses.

For analysis, all samples and standards were diluted with TD 3% HNO_3 to a concentration of 750 ng/g Zn. The Zn aliquots and standards were doped with a 1000 µg/g Cu ROMIL Reference Solution to 375 ng/g Cu, giving a 2:1 Zn:Cu ratio. Sample Zn and Cu concentrations were always within 10% of the concentration of the bracketing standards (e.g. Chen et al. 2016), but this concentration matching is less important when an external element spike, such as Cu, is used (Sossi et al. (2015).

Seven masses were measured simultaneously using the cup configuration as listed in Table 2.9 (^{62}Ni, ^{63}Cu, ^{64}Zn, ^{65}Cu, ^{66}Zn, ^{67}Zn and ^{68}Zn). Amplifiers with $10^{11}\Omega$ resistors were used on all Faraday cups.

The sample introduction system consisted of a Savillex PFA Concentric Flow nebuliser with 50µl/min uptake rate (CF 50) and coupled to either a glass quartz ESI SIS or a borosilicate glass Cinnabar micro-cyclonic spray chamber from Glass Expansion. Standard Ni sample and skimmer cones were used. Average sensitivity was 5-6V/ppm on ^{64}Zn at an uptake rate of 50µl/min.

Table 2.9. The cup configuration and resistors used for Zn isotopic measurements at Durham University. Ni isotopes in italics are used for interfering element corrections. Cu isotopes in bold are used for mass bias corrections. The main polyatomic species are also shown (Mason et al., 2004).

Element / Polyatomic Species	**Faraday Cup**								
	L4	**L3**	**L2**	**L1**	**C**	**H1**	**H2**	**H3**	**H4**
Amplifier		$10^{11}\,\Omega$	$10^{11}\,\Omega$	$10^{11}\,\Omega$	$10^{11}\,\Omega$	$10^{11}\,\Omega$	$10^{11}\,\Omega$	$10^{11}\,\Omega$	
Zn				^{64}Zn		^{66}Zn	^{67}Zn	^{68}Zn	
Cu			**^{63}Cu**		**^{65}Cu**				
Ni		*^{62}Ni*		^{64}Ni					
Main Polyatomic Species				$^{1}H_2{}^{14}N^{16}O_3$		$^{1}H_2{}^{14}N^{16}O_2{}^{18}O$		$^{40}Ar^{14}N_2$	

Measurements were carried out in low resolution (MR ~400) and as such an automatic peak centre routine was used to set the centre cup mass at the start of an analytical session.

All measurement sequences were run using an autosampler, because identical time spacing between every sample analysis is necessary when correcting for mass bias using standard sample bracketing. Isotope ratios were measured in static multi-collection mode where an individual measurement was comprised of 1 block of 30 cycles with an integration time of 4.194s per cycle; total analysis time approximately 2 minutes. Approximately 150 ng of Zn was consumed during an analysis at a concentration of 750 ng/g. Uptake and washout times of 45 s and 120 s respectively were used, with TD 3% HNO_3 used as the wash acid. The certified isotope reference material IRMM-3702 and an in house standard *Romil Zn* (diluted from a 1000 μg/g Zn ROMIL Reference Solution) were measured during all sequence to assess machine performance.

Interfering Element Corrections

For the Zn cup configuration used in this study, the only atomic interference on Zn is from ^{64}Ni on ^{64}Zn. As with the interference of ^{54}Cr on ^{54}Fe, this is an important correction as ^{64}Zn is used as the denominator isotope. The ^{64}Ni interference can be corrected for using an exponential law, by monitoring ^{62}Ni and assuming a ^{64}Ni/^{62}Ni ratio of 0.25671. However, since Ni is almost quantitatively removed during chemistry (e.g. Sossi et al., 2015), and ^{64}Ni only accounts for around 0.9% of the natural abundance of Ni (e.g. Lodders, 2003), the ^{64}Ni signal was approximately 4 orders of magnitude smaller than the ^{64}Zn signal (10^{-4}V). Therefore, this correction was negligible, typically changing the δ^{66}Zn value by 0.005‰, considerably less than the method reproducibility (±0.040‰). Previous studies have also shown the ^{64}Ni contribution is negligible (e.g. Petit et al., 2008).

Mass Bias Corrections

Mass bias was corrected by a combination of external element doping and standard sample bracketing with the AA-ETH Zn solution (Archer et al., 2017).

Copper was added as an external spike to correct for drift in mass bias due to matrix effects (Marèchal et al., 1999, Archer and Vance, 2004 and Sossi et al., 2015). This assumes that Cu isotopes are affected by mass bias in the same manner as Zn. These corrections are calculated automatically on the Neptune software. The theory is as follows.

For the Cu dopant, the mass discrimination between ^{65}Cu and ^{63}Cu can be written using the exponential mass fractionation law (Equations 2.9 and 2.10, adapted from Marèchal et al., 1999).

$$R_T = R_M \times (m_1/m_2)^{\beta} \qquad [2.9]$$

$$\left(\frac{^{65}Cu}{^{63}Cu}\right)_T = \left(\frac{^{65}Cu}{^{63}Cu}\right)_M \left(\frac{mass\,^{65}Cu}{mass\,^{63}Cu}\right)^{\beta_{Cu}} \qquad [2.10]$$

T and M denote the mass bias corrected ratio and the ratio measured by MC-ICP-MS respectively and β is the fractionation factor. For the dopant, R_T is the known ratio in the

solution used, and for Cu we use the natural abundance of $^{65}Cu/^{63}Cu$, i.e. 30.826/69.174 (Lodders, 2003). β_{Cu} was calculated by rearranging Equation 2.10.

$$\beta_{Cu} = \ln\left[\frac{\left(\frac{^{65}Cu}{^{63}Cu}\right)_T}{\left(\frac{^{65}Cu}{^{63}Cu}\right)_M}\right] / ln\left(\frac{mass\,^{65}Cu}{mass\,^{63}Cu}\right) \quad [2.11]$$

The mass bias corrected Zn ratio ($(^{66}Zn/^{64}Zn)_T$) is then calculated using the exponential mass fractionation law for Zn with the β_{Cu} fractionation factor.

$$\left(\frac{^{66}Zn}{^{64}Zn}\right)_T = \left(\frac{^{66}Zn}{^{64}Zn}\right)_M \left(\frac{mass\,^{66}Zn}{mass\,^{64}Zn}\right)^{\beta_{Cu}} \quad [2.12]$$

Standard sample bracketing with the AA-ETH Zn standard was used to further correct for mass bias.

2.5.3.3 Quality Control and Assurance

Data Quality Control

Zinc isotope ratios were calculated as $\delta^{66}Zn$ values relative to the AA-ETH Zn standard, where

$$\delta^{66}Zn = \left[\frac{(^{66}Zn/^{64}Zn)_{sample}}{(^{66}Zn/^{64}Zn)_{AA-ETH-Zn\ average}} - 1\right] \times 1000 \quad [2.13]$$

The $\delta^{66}Zn_{AA}$ values were recast by +0.28‰ and reported relative to the JMC Lyon standard (Archer et al., 2017).

Several criteria were developed during this study to help determine whether data should be accepted or rejected. These criteria are:

1. The concentration of sample and bracketing standard (AA-ETH Zn) must be matched within 10%.
2. Acceptable values for USGS standards, in-house *Romil Zn* standard, and certified isotopic reference material IRMM-3702 must be measured within the sequence.
3. Samples must have mass dependent $\delta^{66}Zn$ and $\delta^{67}Zn$. An expected $\delta^{67}Zn$ is calculated from measured $\delta^{66}Zn$ ($\delta^{67}Zn_{cal} \approx 1.5 \times \delta^{66}Zn$) and this is compared to

the measured $\delta^{67}Zn$. The values must agree to within 20%. Mass dependent values show that there are no unresolved isobaric interferences. Note that this relationship breaks down when $\delta^{66}Zn$ values are near zero.

4. The within-run relative standard error (RSE) of a sample must be <30 (see Section 2.5.2.3).
5. The relative standard deviation (RSD) of the bracketing standards must remain approximately constant (±30) through periods of a run where data is taken from and must be <100 (see Section 2.5.2.3).

Reference Materials

Several USGS reference materials were digested and processed through chemistry as described in Section 4, prior to processing of any samples. This was to ensure that there was no isotopic fractionation during the procedure and that the accepted $\delta^{66}Zn$ values were measured. These were the same digestions from which the $\delta^{56}Fe$ values in Section 2.5.2.3 were determined. The results are summarised in Table 2.10.

Table 2.10. Zinc isotopic compositions of the test batch of USGS reference materials. Duplicates of BIR-1a and GSP-2 were dissolved. Errors quoted as 2 Standard Deviations of the mean of several measurements in different analytical sessions. *Ranges and Average for literature $\delta^{66}Zn$ values from Table 2.11.

USGS Standard	$\delta^{66}Zn_{JMC\text{-}Lyon}$ (‰)	2SD	n	$\delta^{66}Zn_{JMC\text{-}Lyon}$ Literature Range (‰)*	$\delta^{66}Zn_{JMC\text{-}Lyon}$ Literature average (‰)*	n*
BCR-2	0.237	0.019	4	0.200 - 0.330	0.273 ± 0.079	19
BIR-1a (1)	0.204	0.023	4	0.200 – 0.310	0.247 ± 0.063	9
BIR-1a (2)	0.212	0.054	4			
GSP-2 (1)	1.840	0.074	4	1.030 - 1.070	1.050 ± 0.040	3
GSP-2 (2)	1.052	0.015	4			

In the case of Zn, all the reference materials run as part of this procedural test were within error of values reported in the literature (Table 2.10), with the exception of one GSP-2 digestion. A possible reason for this may be that this reference material has a heterogeneous Zn isotopic composition. Heterogeneous isotopic compositions have been reported for other standards made from coarse grained intrusive rocks (e.g. Tl isotopic heterogeneity in the G-2 granite; Brett et al., 2018). There are only four published values for GSP-2 ranging from $\delta^{66}Zn_{JMC\text{-}Lyon}$ of 1.00‰ to 1.07‰ (Chen et al., 2016; Deng et al.,

2017; Doucet et al., 2018; Jeong et al., 2021), so this heterogeneity may not be apparent yet. The GSP-2 standard was also digested with samples in batch 439 and 475 (see Table 2.12). These values are also outside the range of previously published values, which is further evidence for possible isotopic heterogeneity in the GSP-2 standard.

Table 2.11. Literature compilation of Zn isotopic compositions of USGS reference materials. Errors are quoted as stated in the literature; [1]2SD, [2]2SE, [3]95% confidence interval.

Reference Material BHVO-2			Reference Material BCR-2		
$\delta^{66}Zn_{JMC\text{-}Lyon}$ (‰)	Quoted error	Reference	$\delta^{66}Zn_{JMC\text{-}Lyon}$ (‰)	Quoted error	Reference
0.29	0.09[1]	Herzog et al. (2009)	0.20	0.09[3]	Archer and Vance (2004)
0.21	0.09[1]	Moynier et al. (2010)	0.29	0.12[1]	Chapman et al. (2006)
0.48	0.13[1]	Moeller et al. (2012)	0.33	0.09[1]	Herzog et al. (2009)
0.29	0.09[3]	Telus et al. (2012)	0.25	0.02[1]	Moynier et al. (2011)
0.33	0.04[1]	Chen et al. (2013)	0.33	0.13[1]	Moeller et al. (2012)
0.27	0.06[1]	Sossi et al. (2015)	0.25	0.01[1]	Sossi et al. (2015)
0.31	0.03[1]	Chen et al. (2016)	0.25	0.04[1]	Chen et al. (2016)
0.35	0.02[1]	Doucet et al. (2016)	0.28	0.06[1]	Pons et al. (2016)
0.32	0.05[1]	Pons et al. (2016)	0.25	0.02[1]	Deng et al. (2017)
0.31	0.04[1]	Wang et al. (2017)	0.27	0.03[1]	Wang et al. (2017)
0.33	0.01[1]	Xia et al. (2017)	0.25	0.08[1]	Araujo et al. (2018)
0.25	0.10[1]	Araujo et al. (2018)	0.23	0.04[1]	Huang et al. (2018)
0.34	0.01[1]	Doucet et al. (2018)	0.33	0.06[1]	Little et al. (2019)
0.33	0.04[1]	Huang et al. 2018	0.25	0.04[1]	Liao et al. (2020)
0.31	0.02[1]	McCoy-West et al. (2018)	0.31	0.03[1]	Beunon et al. (2020)
0.28	0.06[1]	Sossi et al. (2018a)			
0.39	0.07[1]	Little et al. (2019)			
0.34	0.01[1]	Beunon et al. (2020)			
0.32	0.04[1]	Liao et al. (2020)			

Reference Material BIR-1a			Reference Material GSP-2		
$\delta^{66}Zn_{JMC\text{-}Lyon}$ (‰)	Quoted error	Reference	$\delta^{66}Zn_{JMC\text{-}Lyon}$ (‰)	Quoted error	Reference
0.26	0.09[1]	Herzog et al. (2009)	1.07	0.06[1]	Chen et al. (2016)
0.31	0.04[1]	Chen et al. (2013)	1.05	0.03[1]	Deng et al. (2017)
0.23	0.05[1]	Chen et al. (2016)	1.03	0.04[1]	Doucet et al. (2018)
0.2	0.04[1]	Sossi et al. (2015)	1.05	0.04[1]	Zhu et al. (2019)
0.25	0.05[1]	Wang et al. (2017)	1.00	0.20 (1SE)	Jeong et al. (2021)
0.27	0.03[1]	Huang et al. (2018)			
0.25	0.03[1]	McCoy-West et al. (2018)			
0.27	0.04[1]	Little et al. (2019)			
0.24	0.04[1]	Zhu et al. (2019)			

Following these initial tests, at least one USGS sample was processed with every batch of samples, summarised in Table 2.12. With the exception of the GSP-2 standards, these are within error of literature values given in Table 2.11.

Table 2.12. Zinc isotopic composition of USGS reference materials processed with each batch of samples. All $\delta^{66}Zn$ values are quoted with respect to JMC Lyon. Literature range of $\delta^{66}Zn$ from Table 2.11. As in Section 2.5.2.3, Synth. Mag. is an in-house synthetic magnetite standard.

Batch	USGS Standard	$\delta^{66}Zn_{JMC\text{-}Lyon}$ (‰)	2SD	N	$\delta^{66}Zn_{JMC\text{-}Lyon}$ Literature Range (‰)*
430	GSP-2	0.956	0.059	3	1.030 - 1.070
464	*Synth. Mag.*	0.304	0.014	3	n/a
475	GSP-2	1.126	0.022	3	1.030 - 1.070
497	BIR-1a	0.288	0.040	6	0.200-0.310
525	BIR-1a	0.268	0.036	4	0.200-0.310
532	BIR-1a	0.234	0.010	3	0.200-0.310
534	BIR-1a	0.247	0.010	3	0.200-0.310
537	BCR-2	0.241	0.019	3	0.200 – 0.330
539	*Synth. Mag.*	0.356	0.025	3	n/a

Long Term Reproducibility

In-house Zn standard *Romil Zn* and the certified isotopic reference material IRMM-3702 were used to assess long term reproducibility and accuracy. The average $\delta^{66}Zn_{AA\text{-}ETH}$ of *Romil Zn* is identical within error in all measurement sessions across a 3-year time period (Figure 2.11).

Previous studies have measured the certified reference material IRMM-3702 relative to the JMC-Lyon and/or AA-ETH standards (Table 2.13). The average $\delta^{66}Zn_{AA\text{-}ETH}$ of IRMM-3702 measured in all 8 Zn analytical sessions agrees with the published literature values (Figure 2.12).

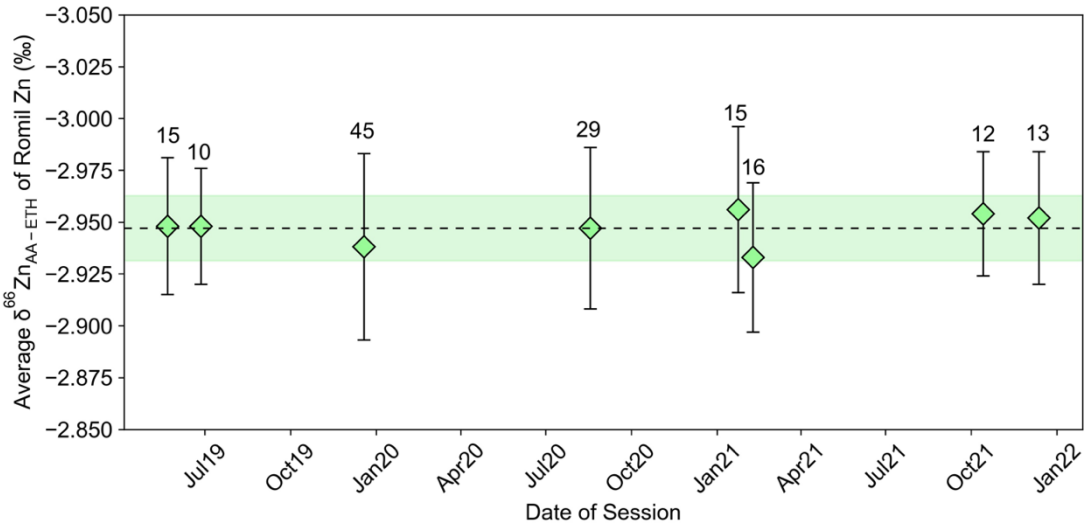

Figure 2.11. Long term reproducibility of the *Romil Zn* in-house standard. The diamonds show the average δ^{66}Zn values for *Romil Zn* in an individual measurement session, and the number of analyses is listed beside the symbol. The dashed line and green shaded area is the average of all the session values; δ^{66}Zn = -2.947 ± 0.016 (2SD, n=8).

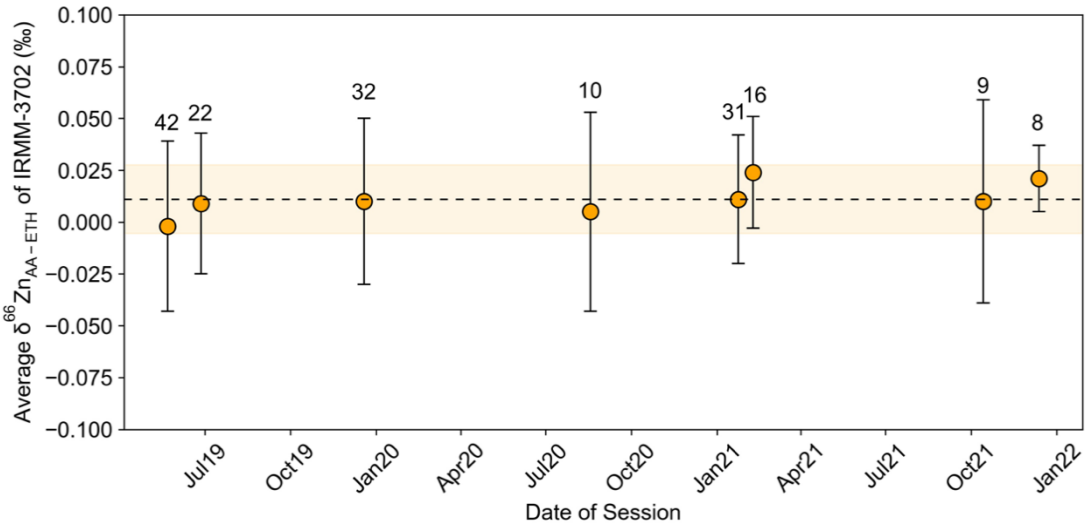

Figure 2.12. Long term reproducibility of the IRMM-3702 certified reference material. The circles show the average δ^{66}Zn values for IRMM-3702 in an individual measurement session, and the number of analyses is listed beside the symbols. The dashed line and shaded area is the average of all the session values; δ^{66}Zn = 0.011± 0.017 (2SD, n=8).

Table 2.13 Zinc isotopic composition of the IRMM-3702 certified reference material from previous studies relative to the JMC-Lyon and AA-ETH standards. *If the $\delta^{66}Zn$ value is only given with respect to JMC-Lyon, a $\delta^{66}Zn_{AA\text{-}ETH}$ value is calculated using the correction of -0.28‰ from Archer et al. (2017).

Reference	$\delta^{66}Zn_{JMC\text{-}Lyon}$ (‰)	$\delta^{66}Zn_{AA\text{-}ETH}$ (‰)	2SD
Borrok et al. (2010)	0.27	-0.01*	0.07
Moeller et al. (2012)	0.29	0.01*	0.05
Petit et al. (2012)	0.32	0.04*	0.03
Archer et al. (2017)	0.28	0.02	0.02
Sossi et al. (2015)	0.30	0.02*	0.02
Doucet et al. (2016)	0.27	0.01*	0.02
Wang et al. (2017)	0.27	0.01*	0.03
Doucet et al. (2018)	0.28	0.00*	0.02
Beunon et al. (2020)	0.28	0.00*	0.04

Total Procedural Blanks

Total Procedural Blanks (TPB; Section 2.5.2.3) for Zn for every batch of chemistry are listed in Table 2.14.

Table 2.14. Total procedural Zn blanks for each batch of samples processed. The modified resin cleaning procedure described below was adopted after Batch 430.

Laboratory Batch Number	Total Procedural Blank Zn (ng)
415	28
430	45
456	5
464	6
475	11
497	15
525	27
532	4
534	6
537	5
539	9

Zinc is more prone to blank issues than Fe or V. There are two reasons for this. Firstly, Zn is present at μg/g level concentrations in all samples, which makes it more susceptible to contamination than elements such as Fe which are present in higher concentrations. Secondly, Zn is commonly found in the lab environment. Zinc is involved in the

production of plastic bottles, centrifuge tubes, pipette tips, and gloves (Wilkes et al., 2010; Bryan et al., 2015). Zinc is also present in low concentrations in acids and resins used during ion exchange chromatography.

Therefore, special care was taken to reduce Zn blanks. Initial steps adopted to reduce Zn blanks were to use dedicated PFA Teflon beakers for all sample dissolutions, a dedicated set of PFA columns instead of quartz glass for column 1, and dedicated PFA autosampler vials for mass spectrometry measurements.

During the first few Zn analytical sessions, TPB began to increase; Table 2.14 shows that the first batch of Zn samples processed had a Zn TPB of 28ng and the second batch had a Zn TPB of 45ng. Two column blanks performed after the high TPB values were measured (following the same procedure as column 1 but with 1mL 6M HCl loaded instead of a sample) contained 50 and 51ng Zn. Such high blanks are problem for Zn, because the typical amount of Zn recovered from a sample is ~2 μg, so a column blank of 50 ng would account for 2.5% of the total Zn.

To address this problem, the PFA Teflon columns used for column 1 were cleaned by wiping the inside of the stem with a sontara wipe and acetone. The columns were placed in a PFA pot with weak (1-2M) TD HNO_3 and heated at 100 °C for over 24 hours. Before chemistry, the columns were rinsed with full reservoirs of TD 6M HCl and TD 1M HNO_3. However, a repeat column blank yielded 32ng Zn.

Reagent blanks were checked by taking 1ml of each acid used in column 1 (TD 6M HCl and TD 3M HNO_3), evaporating them and re-dissolving in TD 3% HNO_3. The measured reagent blanks were 0.6 ng/g and 0.2 ng/g for TD 6M HCl and TD 3M HNO_3 respectively. Whilst these blanks seem low, the volume of 6M HCl used in the column 1 prior to collecting Zn (see Figure 2.2) is 26 ml, which amounts to 15.6ng of potential Zn blank. This Zn will bind to the resin until collected in 4 ml 3M HNO3, adding another ~1ng Zn. Nevertheless, this potential total reagent blank of ~17ng still fails to account for the high TPB (Table 2.14) or column blanks (See above).

Since the source of Zn was not from columns or reagents, a probable source was the AG1-X8 resin itself and/or from the polypropylene bottle in which it was cleaned. It had only been cleaned by shaking alternately with MQ H_2O and TD 6M HCl. Since Zn partitions

to this resin in 6M HCl (e.g. Sossi et al., 2015) this was not effectively removing Zn. To improve the resin cleaning procedure specifically for Zn, the resin was further cleaned using the vacuum box and 3M HNO_3 in which Zn is released from the resin, as described in Section 2.2. Two column blanks using resin cleaned with this modified procedure were 3.3 ng and 10. 3 ng total Zn, while the column blank for uncleaned resin processed at the same time was 83.4 ng. Subsequently, the resin was always pre-cleaned with this modified cleaning procedure before use in column 1. Total procedural blanks have generally remained below 10ng Zn since this improved cleaning procedure was adopted (Batch 456 onward, Table 2.14), and now routinely account for less than 1% of the Zn in the sample.

2.5.4 Vanadium MC-ICP-MS Methodology

2.5.4.1 Background Principles and Considerations

Early studies measuring V isotopes using Thermal Ionisation Mass Spectrometry (TIMS) had analytical uncertainties on the order of 1% (Balsiger et al., 1969; Pelly et al., 1970). A combination of issues slowed the development of high precision V isotope mass spectrometry relative to other transition metal isotope measurements:

- Since V only has two isotopes, the double spike method cannot be used to correct for instrumental mass bias.
- The natural $^{51}V/^{50}V$ ratio is around 420. Therefore, amplifiers with different resistance are required to enable simultaneous measurement of the high and low abundance masses.
- There are many interferences present within the mass range of V; both Argon-based molecular interferences ($^{40}Ar^{13}C^{+}$, $^{36}Ar^{16}O^{+}$, $^{38}Ar^{14}N^{+}$ etc.) and sample-derived atomic interferences (e.g. ^{50}Cr and ^{50}Ti).

The first protocol for the measurement of V isotopes via MC-ICP-MS was published in Nielsen et al. (2011). This work, and other recent studies, typically quote errors below 0.2‰ 2SD (e.g. Prytulak et al., 2011; Prytulak et al., 2013; Nielsen et al., 2014; Wu et al., 2016; Prytulak et al., 2017; Sossi et al., 2018b; Nielsen et al., 2019). This improvement in the precision and accuracy of V isotopic measurements is due to a combination of:

- The development of an effective chromatography procedure (e.g. Nielsen et al., 2011; Wu et al., 2016), which reduces the Cr and Ti interferences to levels where they can be corrected for algebraically.
- Developments in amplifier and resistor technology for MC-ICP-MS increasing the dynamic range of Faraday detectors, allowing measurements of low and high abundance isotopes simultaneously with an adequate beam intensity on the minor isotope.
- Developments in sample introduction systems. Running in dry plasma reduces molecular interferences from argide and oxide species and gives a higher sensitivity. Nickel X-skimmer cones were also used to provide higher sensitivity (e.g. Nielsen et al., 2011).
- Availability of MC-ICP-MS with variable resolution image slits that permit isotope ratio measurements at pseudo-high resolution so that molecular interferences can be resolved from the analyte isotope.

The protocol from Nielsen et al. (2011) measured at low mass resolution on a Nu Plasma instrument at a concentration of 5 μg/g V, which was large enough to overwhelm the molecular interferences. However, measuring at higher resolution ($\Delta M/M > 4000$) can resolve V from the molecular interferences. Vanadium can then be measured on the narrow shoulder on the lower mass side of the peaks (Nielsen et al., 2016; Wu et al., 2016). Although running at medium-high resolution leads to a reduction of signal by about 90% compared to low resolution, the increase in the analyte/interference ratio on the peak shoulder means that it is possible to analyse smaller quantities of V. For example, the isotopic composition of samples with concentrations as low as 500 ng/g V can now be measured (e.g. Hopkins et al., 2019). This has allowed measurement of the V isotopic composition of materials with low V concentrations, for example the silicate mineral separates in this study.

2.5.4.2 Instrumentation and Measurement Protocol

Vanadium isotope measurements were carried out on the Neptune MC-ICP-MS instrument at Durham University, based on the protocol of Wu et al. (2016).

Prior to analysis, the concentration of the V fractions was measured. After the final clean up column, the V fractions were dissolved in 1ml TD 3% HNO_3. Concentrations were determined by comparing the ^{51}V signal of aliquots containing 10 µl of this solution and 990 µl TD 3% HNO_3 to a solution of known V concentration. For analysis, all samples and standards were diluted with TD 3% HNO_3 to concentrations of 500 ng/g V or 1 µg/g V, dependent on the V content of the sample. The concentrations of the samples and the bracketing standard were always matched to within ±10%.

Six isotopes were measured simultaneously using the cup configuration listed in Table 2.15 (^{48}Ti, ^{49}Ti, ^{50}V, ^{51}V, ^{52}Cr and ^{53}Cr). The Neptune amplifier housing contains one amplifier with a $10^{10}\Omega$ resistor which was connected to the centre Faraday cup to permit measurement of a >50V signal on ^{51}V. This allowed samples to be measured at higher concentrations, thereby improving the signal on the minor ^{50}V isotope. At concentrations of 1 µg/g V, signals were typically 200-300mV on ^{50}V and ~100V on ^{51}V. All other Faraday cups used standard $10^{11}\Omega$ resistors.

Table 2.15. The cup configurations and resistors used for V isotopic measurements at Durham University. Ti and Cr isotopes in italics are those used for interfering element corrections. Also shown are the main polyatomic interferences on V. The V signal is resolved from these interferences using medium mass resolution slits.

Element/ Polyatomic Species	**Faraday Cup**								
	L4	**L3**	**L2**	**L1**	**C**	**H1**	**H2**	**H3**	**H4**
Amplifier	$10^{11}\Omega$		$10^{11}\Omega$	$10^{11}\Omega$	$10^{10}\Omega$	$10^{11}\Omega$		$10^{11}\Omega$	
V				^{50}V	^{51}V				
Cr						^{52}Cr		^{53}Cr	
Ti	^{48}Ti		^{49}Ti						
Main Polyatomic Species	$^{36}Ar^{12}C$		$^{36}Ar^{13}C$	$^{36}Ar^{14}N$	$^{36}Ar^{15}N$	$^{36}Ar^{16}O$ $^{38}Ar^{14}O$ $^{40}Ar^{12}C$		$^{40}Ar^{13}C$	

The sample introduction system consisted of a PFA Concentric Flow nebuliser with a 50µl/min uptake rate, coupled to an Aridus 3 Desolvating Nebuliser System. A desolvating nebuliser system was used to increase sensitivity. Nickel sample cones and

X-skimmer cones were used. With this setup, the typical sensitivity for V was 100-120V/ppm on ^{51}V and 250-300mV/ppm on ^{50}V at an uptake rate of 50µl/min.

Measurements were made in medium resolution mode to allow the V peaks to be resolved from the molecular interferences (Wu et al., 2016). The peak centre (centre of the shoulder on the low mass side of the peak) was selected manually before each sequence. Mass resolution was typically between 6000-8000, depending on the degradation of the resolution slit, and tuning conditions.

All measurement sequences were run using an autosampler, because identical time spacing between every sample analysis is necessary when correcting for mass bias using standard sample bracketing. Isotope ratios were measured in static multi-collection mode where an individual measurement was comprised of 1 block of 50 cycles with an integration time of 4.194s per cycle; total analysis time around 3.5 minutes. Approximately 0.3 µg of V was consumed during an analysis for a concentration of 1 µg/g. Uptake and washout times of 45 s and 120 s respectively were used, with TD 3% HNO_3 used as the wash acid.

The V standard BDH (from BDH Chemicals; first characterised by Nielsen et al., 2011) was measured throughout sessions to assess machine performance and stability. Mass bias was corrected by standard sample bracketing with the AA (Alfa Aesar Specpure) V solution (Nielsen et al., 2011).

Interfering Element Corrections

To obtain accurate $\delta^{51}V$ values, it is vital to correct for isobaric atomic interferences on the minor ^{50}V isotope. Following Nielsen et al. (2011), these interferences were corrected by monitoring ^{49}Ti and ^{53}Cr in cups L2 and H3 respectively, then calculating the beam size of ^{50}Ti and ^{50}Cr on mass 50 using the exponential mass fractionation law. For Ti, this is described by Equation 2.14.

$$\left(\frac{^{50}Ti}{^{49}Ti}\right)_T = \left(\frac{^{50}Ti}{^{49}Ti}\right)_M \times \left(\frac{m_{50}}{m_{49}}\right)^{\beta} \quad [2.14]$$

A value of 0.972537 was used for the true $^{50}Ti/^{49}Ti$ ratio. Equation 2.14 is rearranged to find $^{50}Ti_M$.

$$^{50}Ti_M = \frac{(\frac{^{50}Ti}{^{49}Ti})_T}{(\frac{49.94479}{48.94787})^{\beta}} * {}^{49}Ti_M \quad [2.15]$$

Equation 2.14 can be re-written to describe Cr (Equation 2.16).

$$(\frac{^{53}Cr}{^{50}Cr})_T = (\frac{^{53}Cr}{^{50}Cr})_M \times (\frac{m_{53}}{m_{50}})^{\beta} \quad [2.16]$$

Equation 2.16 is rearranged to calculate the measured ^{50}Cr using a value of 2.18665 for the true $^{53}Cr/^{50}Cr$ ratio.

$$^{50}Cr_M = \frac{(\frac{52.94065}{49.94646})^{\beta}}{(\frac{^{53}Cr}{^{50}Cr})_T} * {}^{53}Cr_M \quad [2.17]$$

The true intensity of ^{50}V is then calculated by subtracting $^{50}Ti_M$ and $^{50}Cr_M$ from the ^{50}V value measured in cup L1. This is then used to calculate a corrected $^{51}V/^{50}V$ ratio for each sample or standard in the sequence, which is used when calculating $\delta^{51}V$ values in Equation 2.18.

Initially, a β value of -2 was used to describe the mass fractionation of both Ti and Cr (Equations 2.14 and 2.16) as in Nielsen et al. (2011), because the samples cannot be doped with Ti or Cr, it was impossible to determine the true β factor. However, the accuracy of the correction can be improved by measuring the $^{50}Ti/^{49}Ti$ and $^{50}Cr/^{53}Cr$ ratios of two doped BDH solutions containing 1 µg/g V + 1 ng/g Ti, and 1 µg/g V + 1 ng/g Cr respectively during every sequence, after Wu et al. (2016). This allows the true β factors for Ti and Cr to be calculated, to be used in these equations. Prior to correction, the doped solutions have very different $\delta^{51}V_{AA}$ compared to the long-term average isotopic composition of BDH measured during this work ($\delta^{51}V_{AA}$ = -1.23 ± 0.10 ‰, 2SD, n=397), as summarised in Table 2.16. The β factors in equations 2.14 and 2.16 are varied iteratively until the resulting $\delta^{51}V$ value of the doped solution matches the long-term average value from Wu et al. (2016) (-1.23 ± 0.08‰, 2SD, n=197). These optimal β factors are then used in equations 2.15 and 2.17 to correct all the data from that

measurement sequence. The doped BDH solutions are measured during every sequence. For Ti, average β values range from -1.1 to -1.50, and between -1.0 to -1.25 for Cr (Table 2.16). All corrections are performed manually offline.

Table 2.16: Average $\delta^{51}V_{AA}$ values for the Ti and Cr-doped BDH solutions before corrections, and the β factor used for mass bias correction. The doped standards are measured during every sequence of samples and a β factor is derived for every sequence. The table reports the average $\delta^{51}V$ and β factor for the entire analytical session.

Session	Ti doped BDH Solution				Cr doped BDH Solution			
	$\delta^{51}V_{AA}$ (‰)	2SD	n	β factor	$\delta^{51}V_{AA}$ (‰)	2SD	n	β factor
November 2019	-1.82	0.09	7	-1.1	0.33	0.10	7	-1.0
March 2020	-1.81	0.17	11	-1.1	0.30	0.12	8	-1.0
September 2020	-1.88	0.08	5	-1.2	0.58	0.05	5	-1.0
December 2020	-1.89	0.15	4	-1.15	0.56	0.20	4	-1.25
May 2021	-1.89	0.04	3	-1.4	0.17	0.07	3	-1.1
August 2021	-1.69	0.08	4	-1.15	0.31	0.10	4	-1.05
February 2022	-1.73	0.03	4	-1.15	0.30	0.09	4	-1.15
March 2022	-1.87	0.06	6	-1.50	0.23	0.12	6	-1.1

2.5.4.3 Quality Control and Assurance

Data Quality Control

Vanadium isotope ratios were reported as $\delta^{51}V$ values relative to the AA (Alfa Aesar Specpure) V solution. The V standard BDH was measured between each unknown sample, in the sequence … AA, AA, unknown, AA, AA, BDH, AA, AA, unknown…

The $\delta^{51}V$ value is then calculated using Equation 2.18, where $^{51}V/^{50}V_{AA}$ average is the average of the four AA measurements bracketing the sample.

$$\delta^{51}V = \left[\frac{(^{51}V/^{50}V)_{sample}}{(^{51}V/^{50}V)_{AA\ average}} - 1\right] \times 1000 \qquad [2.18]$$

Several criteria were developed to decide whether data should be accepted or rejected.

1. The concentration of sample and bracketing standard (AA) must be matched within 10%.
2. The $^{49}Ti/^{51}V$ and $^{53}Cr/^{51}V$ ratios of the samples must be < 0.00001, after Nielsen et al. (2011). As a first approximation, concentrations of Cr and Ti in the samples

must be of the same magnitude or lower than those in the undoped AA and BDH standards.

3. Acceptable values for USGS standards and the BDH standard must be measured between each sample and/or during each sequence.
4. The signal on the minor ^{50}V isotope must be above 100mV.
5. The within-run Relative Standard Error (RSE; Section 2.5.2.3) of the $^{51}V/^{50}V$ ratios for each sample analysis must be consistent throughout the sequence. RSEs for 1 µg/g and 0.5 µg/g concentrations are typically under 20 ppm and 40 ppm respectively.
6. The Relative Standard Deviation (RSD; Section 2.5.2.3) of the $^{51}V/^{50}V$ ratio on the 4 bracketing standards must remain approximately constant for the periods of a sequence data is taken from, and must be <100.

Reference Materials

As with Fe and Zn analyses, at least one USGS sample was processed with every batch of samples, as summarised in Table 2.17. The range of $\delta^{51}V_{AA}$ values reported in the literature are summarised in Table 2.18 for comparison. All $\delta^{51}V_{AA}$ values measured in this study are within error of literature values.

Table 2.17 Vanadium isotopic compositions of USGS reference materials processed with each batch of samples. Errors quoted as 2 standard deviations of the mean of at least 3 measurements. $\delta^{51}V_{AA}$ literature range from Table 2.18 (*).

Batch	USGS Standard	$\delta^{51}V_{AA}$ (‰)	2SD	n	$\delta^{51}V_{AA}$ Literature Range (‰)*
430	GSP-2	-0.58	0.06	4	-0.76 - -0.62
456	BHVO-2	-0.79	0.17	6	-1.05 - -0.83
464	*Synth. Mag.*	-0.96	0.07	3	n/a
475	GSP-2	-0.69	0.09	3	-0.76 - -0.62
484	*Synth. Mag.*	-0.86	0.06	10	n/a
489	BIR-1a	-0.98	0.08	4	-1.05 - -0.89
497	BIR-1a	-0.79	0.05	7	-1.05 - -0.89
523	BIR-1a	-0.90	0.04	5	-1.05 - -0.89
532	BIR-1a	-0.98	0.06	5	-1.05 - -0.89
539	*Synth. Mag.*	-0.85	0.08	4	n/a
540	BIR-1a	-0.97	0.08	5	-1.05 - -0.89

Table 2.18. Literature compilation of V isotopic compositions of USGS reference materials. Errors are quoted as stated in the literature; [1]2SD, [2]2SE, [3]95% confidence interval.

Reference Material BHVO-2			Reference Material BCR-2		
$\delta^{51}V_{AA}$ (‰)	Quoted error	Reference	$\delta^{51}V_{AA}$ (‰)	Quoted error	Reference
-0.89	0.08[1]	Prytulak et al. (2011)			
-0.88	0.10[1]	Prytulak et al. (2013)	-0.95	0.16[1]	Prytulak et al. (2011)
-0.83	0.09[1]	Wu et al. (2016)	-0.92	0.16[1]	Prytulak et al. (2013)
-1.05	0.14[1]	Sossi et al. (2017)	-0.78	0.08[1]	Wu et al. (2016)
-0.86	0.12[1]	Hopkins et al. (2019)	-1.03	0.09[1]	Schuth et al. (2017)
-0.91	0.08[1]	Ding et al. (2020)	-1.11	0.08[1]	Sossi et al. (2018b)
			-0.74	0.05[1]	Wu et al. (2018)
			-0.85	0.26[1]	Hopkins et al. (2019)
			-0.79	0.15[1]	Nielsen et al. (2019)
			-0.75	0.05[1]	Qi et al. (2019)
			-0.81	0.03[1]	Ding et al. (2020)

Reference Material BIR-1a			Reference Material GSP-2		
$\delta^{51}V_{AA}$ (‰)	Quoted error	Reference	$\delta^{51}V_{AA}$ (‰)	Quoted error	Reference
-0.94	0.15[1]	Prytulak et al. (2011)	-0.63	0.10[1]	Prytulak et al. (2011)
-0.92	0.16[1]	Prytulak et al. (2013)	-0.62	0.07[1]	Wu et al. (2016)
-0.92	0.09[1]	Wu et al. (2016)	-0.76	0.15[1]	Nielsen et al. (2019)
-1.05	0.22[1]	Sossi et al. (2018b)			
-0.96	0.03[1]	Wu et al. (2018)			
-0.89	0.23[1]	Hopkins et al. (2019)			
-0.90	0.09[1]	Qi et al. (2019)			
-1.01	0.05[1]	Ding et al. (2020)			

Long Term Reproducibility

Long term reproducibility is assessed by repeated measurement of the BDH standard. Previous studies have reported long-term average $\delta^{51}V$ values of -1.19 ± 0.12‰ (2SD, n= 600; Nielsen et al., 2011) and -1.23 ± 0.08‰ (2SD, n =197; Wu et al., 2016). The average $\delta^{51}V_{AA}$ values from each analytical session are shown in Figure 2.13, and are within error of the long term averages from previous studies.

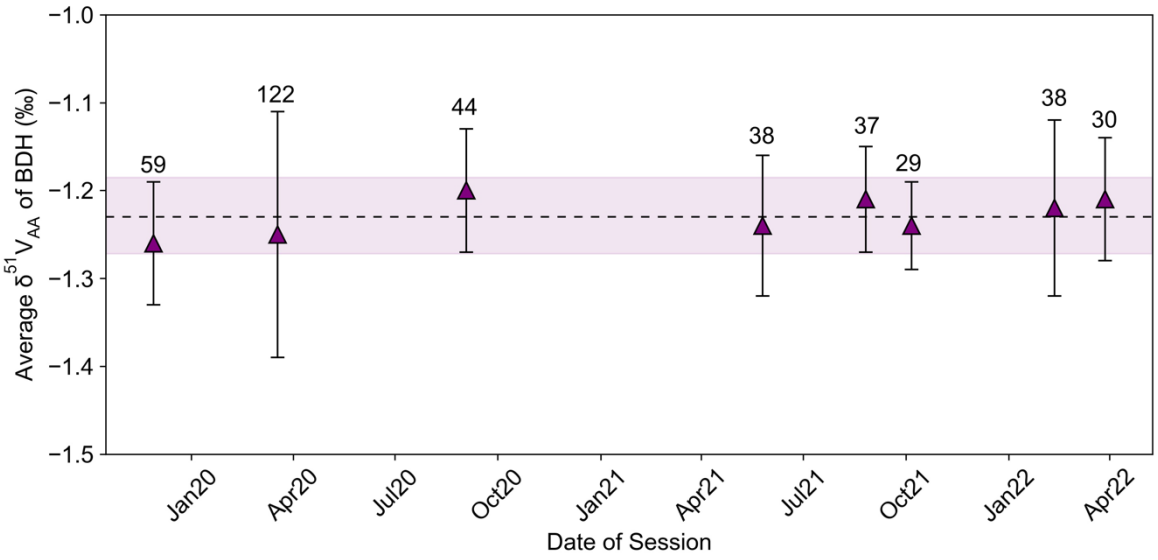

Figure 2.13. Long term reproducibility of the BDH solution standard. The triangles are the average $\delta^{51}V_{AA}$ values for BDH in an individual measurement session. The dashed line and shaded area is the average of all the session values; $\delta^{51}V$ = -1.23 ± 0.04‰ (2SD, n=8).

Total Procedural Blanks

Total Procedural Blanks (TPB; Section 2.5.2.3) for V for each batch of samples are listed in Table 2.19. Given that the mass of V processed was typically > 2 µg, these are negligible.

Table 2.19. Total procedural V blanks for each batch of samples processed.

Laboratory Batch Number	Total Procedural Blank V (ng)
430	1.5
456	2.0
464	2.0
475	1.3
484	2.7
497	1.5
523	8.5
525	1.4
532	1.5
539	3.0
540	1.5

2.6 Strontium and Neodymium Isotope Analysis

2.6.1 Ion Exchange Column Chromatography

Chemical purification and Sr and Nd isotopic analyses were conducted at the Arthur Holmes Isotope Geology Laboratory, Durham University. Approximately 50 mg of the whole rock powder was dissolved in 3 ml of TD (Teflon Distilled) 29M HF and 1 ml of TD 16M HNO_3 in Savillex beakers on a hotplate at 160 °C for >48 hours. Samples were dried down before being re-dissolved in 1ml TD 16M HNO_3 overnight. The samples were again dried down and taken up in 1 ml TD 3M HNO_3 in preparation for column chemistry.

Three column chromatography procedures were necessary to fully purify and separate Sr and Nd from sample matrices. The first column used a 1ml micro-column containing 120 µl Eichrom Sr resin. The columns were cleaned with 1 column volume (cv) MQ H_2O, 1cv TD 6M HCl and 1cv MQ H_2O before the resin was loaded. The resin was then cleaned with 1cv TD 6M HCl and 2cv MQ H_2O and then conditioned with 0.5cv 3M HNO_3. Samples were centrifuged before loading, and the supernatant was loaded onto the columns. The fraction containing Nd was collected as the sample was loaded and with a further 500µl TD 3M HNO_3. The Sr was then collected in 500 µl MQ H_2O. Before measurement of Sr isotope ratios, 22µl TD 16M HNO_3 was added to the Sr fractions to acidify them. Full details of the procedure are found in Font et al. (2008).

Following the Sr column, further separation and purification of Nd from the matrix fraction requires two additional column chromatography steps. The first column uses Bio-Rad Poly-prep columns with 1.4 ml of AG50W-X8 cation resin. This column separates a bulk rare earth element (REE) cut from other matrix elements. The resin was pre-cleaned with 10 ml TD 6M HCl, and conditioned with 1 ml TD 1M HCl before samples were loaded on the column in 1 ml TD 1M HCl, and washed into the resin with a further 1 ml TD 1M HCl. Matrix elements were eluted in 7 ml TD 1M HCl, before a bulk REE fraction was collected in 6.5 ml TD 6M HCl. The resin was cleaned after use with 2 ml MQ H_2O, 10 ml TD 4M HNO_3, 2 ml MQ H_2O, 10 ml TD 6M HCl and 10 ml MQ H_2O.

The bulk REE fraction was evaporated at 120°C, then re-dissolved in 200 µl TD 0.185M HCl. Neodymium was separated from the other REE using the Eichrom Ln-Spec resin in Savillex columns (5 ml reservoir volume, 6cm length and 3.2mm internal diameter). Prior to sample loading, the resin was cleaned with 5 ml TD 6M HCl and the packing loosened by backflushing with MQ H_2O, before being pre-conditioned with 2 ml TD 0.185M HCl. Samples were loaded in 200 µl TD 0.185M HCl, and washed into the resin with 300 µl TD 0.185M HCl. The REE were eluted with 8 ml TD 0.185M HCl, and Nd was collected with 5 ml TD 0.185M HCl. The resin was cleaned after use with 5 ml TD 6M HCl and 5 ml MQ H_2O. The final Nd fractions were evaporated at 120°C and then dissolved in 0.5ml TD 3% HNO_3 prior to measurement.

2.6.2 Sr Isotope Ratio Measurements

The methods for measuring Sr and Nd isotope ratios use similar sample introduction systems and measurement protocols. For Sr, measurements were made on a Neptune MC-ICP-MS in low resolution mode ($m/\Delta m \sim 400$). An automatic peak centre was selected at the start of each session. Masses ^{82}Kr, ^{83}Kr, ^{84}Sr, ^{85}Rb, ^{86}Sr, ^{87}Sr and ^{88}Sr were measured on Faraday cups L4, L3, L2, L1, C, H1 and H3, using standard $10^{11}\Omega$ resistors. Samples were introduced using a ESI PFA nebuliser coupled to a Glass Expansion borosilicate glass Cinnabar microcyclonic spray chamber. Typical sensitivity was 58V/ppm total Sr, at an uptake rate of ~90µl/min. Measurements were made in one block of 50 cycles, with a 4.19s integration time per cycle, total analysis time around 3.5 minutes.

Prior to analysis, the concentration of the samples was tested by taking 50 µl of the sample and diluting this with 950µl TD 3% HNO_3. The signal on ^{86}Sr in this aliquot was

compared to a solution of known Sr concentration. These tests were done to ensure that the signal on ^{88}Sr (the most abundant isotope) did not exceed maximum dynamic range of the $10^{11}\Omega$ resistors of 50V.

Instrumental mass bias was corrected internally, using an exponential law and a $^{88}Sr/^{86}Sr$ ratio of 2.375209. Interference corrections on Sr arising from Kr in the Ar gas and any residual Rb remaining after sample chemistry were corrected for by monitoring the ^{82}Kr, ^{83}Kr and ^{85}Rb. The samples were run at ^{88}Sr beam intensities varying from 24 – 47V. Beam intensities ranged from 0.38 – 0.43 mV for ^{83}Kr and 1.1 – 18.8mV for ^{85}Rb. The $^{85}Rb/^{88}Sr$ ratio varied from 0.00004 – 0.0005. The maximum value is an order of magnitude lower than the $^{85}Rb/^{88}Sr$ value of doped NBS987 standards which are measured occasionally, and still have an $^{87}Sr/^{86}Sr$ ratio indistinguishable from pure NBS987.

The certified reference material NBS987 was measured during each analytical session. The average $^{87}Sr/^{86}Sr$ for NBS987 obtained in this work was 0.710273 ± 0.000013 (2SD, n=8). All data were normalized to a NBS987 value of 0.71024 (Thirlwall, 1991).

2.6.3 Nd Isotope Ratio Measurements

Measurements were made on a Neptune MC-ICP-MS in low resolution mode ($m/\Delta m \sim 400$). An automatic peak centre was selected at the start of each session. Masses ^{142}Nd, ^{143}Nd, ^{144}Nd, ^{145}Nd, ^{146}Nd, ^{147}Sm, ^{148}Nd, ^{149}Sm and ^{150}Nd were measured on Faraday cups L4, L3, L2, L1, C, H1, H2, H3 and H4 respectively, with $10^{11}\Omega$ resistors connected to all cups. Samples were introduced using a ESI PFA nebuliser coupled to a Glass Expansion borosilicate glass Cinnabar microcyclonic spray chamber. Typical sensitivity was 60V/ppm total Nd, at an uptake rate of ~90µl/min. Samples were run from a beam size of 19 – 119V total Nd. Measurements were made in one block of 50 cycles, with a 4.19s integration time per cycle, total analysis time around 3.5 minutes.

Measured Nd isotope ratios were corrected for instrumental mass bias using the exponential law, and a $^{146}Nd/^{145}Nd$ ratio of 2.071943 (equivalent to the more commonly used $^{146}Nd/^{144}Nd$ ratio of 0.7219). The $^{146}Nd/^{145}Nd$ ratio was used for mass bias correction because Nd is typically measured at Durham on a bulk REE cut, where there is a Sm isobaric interference on ^{144}Nd, and the same method file was used for this study. ^{147}Sm

was monitored throughout each analysis to apply a correction for the isobaric interference on ^{144}Nd, ^{148}Nd and ^{150}Nd using $^{144}Sm/^{147}Sm$, $^{148}Sm/^{147}Sm$ and $^{150}Sm/^{147}Sm$ ratios of 0.20504, 0.74970 and 0.49213 respectively. These 'true' ratios would normally be corrected for mass bias prior to applying the interference correction, but given the extremely small Sm beams (range from 0.03 – 0.23mV, average of 0.075mV on ^{147}Sm) the correction is very insensitive to whether the ratios are corrected or not. The JNdi standard was measured throughout analytical sessions to check machine performance. The average $^{143}Nd/^{144}Nd$ for JNdi obtained in this work was of 0.512104 ± 0.000014 (n=8, 2SD).

Chapter 3: Integrated Petrological and Fe-Zn Isotopic Modelling of Plutonic Differentiation

A version of this chapter has been published in Geochimica et Cosmochimica Acta:
Stow, M.A., Prytulak, J., Humphreys, M.C.S. and Nowell, G.M. (2022) Integrated Petrological and Fe-Zn Isotopic Modelling of Plutonic Differentiation. Geochimica et Cosmochimica Acta, 320, 366-391.
Author Contributions: The work for this chapter and manuscript are my own, and were conducted with the help, guidance and expertise of my co-authors that would be usual of a supervisory team.
A copy of the paper is provided in Appendix 2.

3.0 Abstract

The upper continental crust is formed from chemically diverse granitic plutons. Active debate surrounds the range of physical conditions (P-T-X-fO_2) and differentiation processes which occur in mush bodies that solidify to form plutons. Transition metal stable isotopes are increasingly employed to trace magmatic processes in both extrusive lavas and intrusive plutonic suites, with a focus on analysis of whole rock powders. However, studies of plutonic suites often overlook the complex textures represented within coarse grained samples, and how these will influence whole rock isotopic compositions.

Here we examine the calc-alkaline Boggy Plain Zoned Pluton, SE Australia, which closely approximates closed system behaviour during magmatic differentiation. We combine petrological examination with Fe and Zn isotopic analysis of biotite, hornblende and magnetite mineral separates and whole rock powders. Whole rock Fe isotopic composition (as $\delta^{56}Fe$) increases from 0.038‰ to 0.171‰ with decreasing MgO content, while mineral separates display heavy Fe isotope enrichment in the order magnetite > biotite = hornblende > pyroxene. A lack of correlation between whole rock Fe and Zn isotopic compositions suggests that the Fe isotopic variation is predominantly driven by closed system fractional crystallisation: specifically by the balance between crystallisation of isotopically heavy magnetite, and isotopically light silicates. To

demonstrate this quantitatively, temperature dependent mineral-melt fractionation factors were derived from the mineral separate data ($\Delta^{56}Fe_{mag\text{-}melt} = 0.17x10^6/T^2$ and $\Delta^{56}Fe_{bt/hbd\text{-}melt} = -0.12x10^6/T^2$) and used to construct models that successfully reproduce the observed Fe isotopic variation during fractional crystallisation. These fractionation factors are compared to theoretical and empirical estimates from previous studies. We highlight that accurate determinations of temperature and modal mineralogy are critical when modelling Fe isotopic variations in plutonic suites. Successful interpretation of equilibrium Fe isotopic fractionation in a relatively simple calc-alkaline suite like the Boggy Plain Zoned Pluton paves the way for Fe isotopes to be used to investigate more complex mush bodies.

3.1 Introduction

It is now generally accepted that many crustal magma reservoirs are not melt-dominated systems, but instead are crystal-rich mushy regions where high melt fractions are present only transiently (e.g. Bachmann and Bergantz, 2004; Hildreth, 2004; Cashman et al., 2017; Sparks et al., 2019). The conceptual shift away from traditional melt-rich magma 'chambers' has generated new questions about storage conditions and differentiation processes in plutonic settings (e.g. Sparks et al., 2019). In melt dominated reservoirs, closed system in-situ fractional crystallisation was the intuitive differentiation mechanism to form chemically and lithologically zoned plutons (e.g. Tindle and Pearce, 1981; Wyborn et al., 1987). However, there is debate about how efficient crystal-liquid segregation processes are in evolved crystal mushes with a more viscous, low-density melt (Holness, 2018; Bachmann and Huber, 2019). Other processes such as magma recharge, mixing, assimilation and/or reactive porous flow (Jackson et al., 2018; Weinberg et al., 2021) may also be important controls on chemical variability. Despite these conceptual developments, chemical trends in plutonic suites are commonly modelled as the liquid line of descent of a liquid magma body undergoing fractional crystallisation and/or assimilation (e.g. Burton-Johnson et al., 2019), even though this may not be realistic.

The stable isotope variations of transition metals such as Fe are well established tracers of magmatic processes (e.g. see review in Dauphas et al., 2017). Equilibrium stable isotope fractionation in magmatic systems is fundamentally driven by differences in bond strength between minerals, melts and fluids. With Fe a major element constituent of melts and minerals, Fe isotopes can be a powerful tool to investigate processes such as partial melting (e.g. Williams et al., 2005; Weyer and Ionov, 2007; Williams and Bizimis, 2014; Xia et al., 2017; Xu et al., 2017), fractional crystallisation (e.g. Teng et al., 2008; Schuessler et al., 2009; Sossi et al., 2012; Du et al., 2017; He et al., 2017; Williams et al., 2018; Du et al., 2019) and fluid exsolution (e.g. Heimann et al. 2008; Telus et al., 2012). In minerals, Fe^{3+} preferentially enters tetrahedral sites whereas larger Fe^{2+} ions tend to be octahedrally coordinated. Tetrahedral Fe-O bonds are shorter and stiffer, and preferentially incorporate heavy Fe isotopes (Schauble, 2004). Variation in Fe oxidation state and coordination environment is thought to control the order of heavy Fe isotope enrichment in common rock forming minerals, such that: feldspar>magnetite> biotite, hornblende > pyroxene, olivine > ilmenite (Polyakov et al., 2007; Dauphas et al., 2012; Sossi et al., 2012; Sossi and O'Neill, 2017; Wu et al., 2017; Cao et al., 2019). In the coexisting melt, bond strength increases with $Fe^{3+}/\Sigma Fe$ ratio, and is greatest in high silica, polymerised, alkali rich melts (Dauphas et al., 2014). Fractionation factors (i.e. the difference in isotopic composition between phases) are also inversely proportional to T^2. Hence, equilibrium fractionation factors are controlled by mineral and melt chemistry, but also by intrinsic parameters such as temperature and fO_2. Taken together, this means that Fe isotopes could in principle address many important questions in petrology such as the relationship between melt redox state, crystallising assemblage and differentiation pathway. Conversely, processes such as additions of new batches of magma (Nebel et al., 2020), thermal diffusion (Zambardi et al., 2014; Gajos et al., 2016) and/or fluid exsolution (Poitrasson and Freydier, 2005; Heimann et al., 2008; Telus et al., 2012) may overprint these equilibrium isotopic fractionations.

Zinc and Fe isotopic compositions can be combined to further constrain magmatic processes and test the significance of possible overprinting processes. In contrast to Fe, Zn has relatively simple behaviour in magmatic systems (Telus et al., 2012; Moynier et al., 2017; Xia et al., 2017; McCoy-West et al., 2018). Zinc is a monovalent trace element present only as Zn^{2+}, so isotopic fractionation is not driven directly by changes in redox conditions. Numerous studies have demonstrated that negligible Zn isotope fractionation

(<0.1‰) occurs during fractional crystallisation alone (Chen et al., 2013; Doucet et al., 2018; Huang et al., 2018). However, some high silica rhyolites, S-type granites and pegmatites have Zn isotopic compositions up to 0.6‰ heavier than mantle derived basalts (Telus et al., 2012; Xia et al., 2017; Doucet et al., 2018; Wang et al., 2020). Exsolution of isotopically light fluids (Telus et al., 2012; Wang et al., 2020) and/or enrichment of heavy Zn in the melt during partial melting (Doucet et al., 2018; Sossi et al., 2018a; Xu et al., 2019) are proposed to explain heavy Zn isotopic compositions in these evolved samples. Furthermore, extreme Zn isotopic compositions can be generated by chemical and/or thermal diffusion processes (e.g. McCoy-West et al., 2018). Doucet et al. (2020) discussed the principle of the coupled isotope systematics of Fe and Zn. Theoretically, since Fe and Zn are fractionated by different processes, Fe and Zn isotopes can be decoupled by interaction with fluids or sediments, and fO_2 variations during differentiation. However, a correlation between Fe and Zn isotopes in the same samples would imply that both are fractionated by the same processes. Hence, we employ a paired Fe-Zn approach in this study in order to better identify the causes of both Fe and Zn isotope fractionation in the BPZP.

Previous work on plutonic rocks has employed the isotopic composition of homogenous whole rock powders, in the absence of key information on petrographic textures (e.g. Poitrasson and Freydier, 2005; Schoenberg and von Blanckenburg, 2006; Heimann et al., 2008; Telus et al., 2012; Foden et al., 2015; Gajos et al., 2016; He et al., 2017; Du et al., 2019; Nebel et al., 2020). These types of studies make the implicit assumption that the whole rock composition is analogous to the evolving liquid composition. This may be valid for lavas, but is less appropriate for samples from coarse-grained, texturally complex plutonic suites. Plutonic rocks are typically formed of primocrysts surrounded by interstitial phases crystallised from trapped melt, so neighbouring phases in solidified samples were not necessarily in chemical equilibrium with each other. If chemical trends are generated by fractional crystallisation, samples have also experienced some degree of crystal-melt segregation. Therefore, whole rock composition of plutonic rocks is generally not equivalent to the melt composition at the time of crystallisation (Chappell and Wyborn, 2004; Vernon and Collins, 2011; Barnes et al., 2019).

It is crucial to consider this petrographic complexity when constructing geochemical models for plutonic suites. For example, it is common practice to choose the sample with

the highest MgO content as the 'parental' magma composition for fractional crystallisation models of co-genetic lava suites, or to back-calculate a 'parental' magma composition from the most mafic sample in a suite (e.g. Sossi et al., 2016). However, this approach is problematic in plutonic settings where the most MgO rich samples are cumulates which do not represent real liquid compositions. Further, the competing controls on Fe isotope fractionation are generally difficult to distinguish using whole rock analyses alone. For example, a trend to increasingly heavy Fe isotopic composition with SiO_2 content is observed in a global compilation of igneous whole rocks, irrespective of tectonic setting. This variation has been ascribed to disparate processes such as fluid exsolution (Poitrasson and Freydier, 2005; Heimann et al., 2008; Telus et al., 2012), thermal diffusion (Zambardi et al., 2014; Gajos et al., 2016), fractional crystallisation and subsequent fO_2 variations (Sossi et al., 2012; Foden et al., 2015) and changing melt structure (Dauphas et al., 2014). It is critical to incorporate petrologic information, and, wherever analytically feasible, analyse individual mineral phases to help determine the cause of isotopic variation in a suite of related rocks.

Although intermediate to silicic plutons dominate the upper continental crust, only four previous studies have reported Fe isotopic compositions of mineral separates from granitoids (Heimann et al., 2008; Sossi et al., 2012; Telus et al., 2012; Wu et al., 2017). Of these, only Sossi et al. (2012) present mineral separates from a co-genetic plutonic suite (the low fO_2, tholeiitic Red Hills intrusion, Tasmania): there, fractionation of isotopically light pyroxene initially drives the residual magma to increasingly heavy Fe isotopic values. Upon saturation of isotopically heavy magnetite, the Fe isotopic composition of the residual magma decreases. However, these results are not necessarily directly applicable to the intermediate-silicic plutons which make up the majority of the continental crust. The continental crust is dominantly formed of I-type plutons, which crystallise from high fO_2 magmas derived from igneous protoliths, and crystallise mineral assemblages dominated by phases like biotite, hornblende and magnetite (e.g. Chappell and White, 2001).

Here, we present an integrated Fe and Zn isotope investigation of mineral separates and whole rocks from the I-type Boggy Plain Zoned Pluton, SE Australia, in order to unpick the controls on transition metal isotope fractionation in hydrous granites. The Boggy Plain Zoned Pluton formed via closed system fractional crystallisation of a calc-alkaline parent

magma (Wyborn, 1983; Wyborn et al., 1987; Ickert, 2010). We combine textural and petrographic examination with Fe-Zn isotopic analysis of both whole rock powders and mineral separates for the main hosts of Fe and Zn (i.e. biotite, hornblende and magnetite). We construct temperature dependent models of isotopic fractionation that also take into account the effects of variation in modal mineralogy and fractionation factors. We consider how realistic different modelling approaches are in plutonic environments and provide a framework for further modelling of Fe isotopic variations in more complex mush settings.

3.2 Geological Background

3.2.1 Boggy Plain Zoned Pluton

The Boggy Plain Zoned Pluton (BPZP) is a type example of a concentrically zoned pluton formed by closed system fractional crystallisation of a calc-alkaline magma (Wyborn, 1983; Wyborn et al., 1987; Hoskin et al., 2000; Wyborn et al., 2001; Chappell and Wyborn, 2004; Ickert, 2010; Ickert et al., 2011; Chappell et al., 2012; Park et al., 2013; Iles, 2017). The pluton outcrops over an area of 36km^2 in the northern region of the Kosciuszko batholith in the Lachlan Fold Belt, SE Australia (Figure 3.1A), and crystallised at 417 ± 2Ma (Ickert, 2010). The BPZP is concentrically zoned, from minor gabbroic and dioritic cumulates at the rim, through granodiorite to granite, with lithologies becoming progressively more felsic towards the centre of the pluton. The granite is cut by late-stage aplitic dykes (Wyborn, 1983; Figure 3.1B). Towards the centre of the pluton, there is increasing bulk rock and mineral Fe^{3+}/Fe^{2+}, decreasing proportions of ilmenite and increasing proportions of magnetite, all of which are evidence supporting an increase in magma fO_2 of >1 log unit during differentiation (Wyborn, 1983; Czamanske and Wones, 1973). Temperature estimates from two-pyroxene and biotite-apatite geothermometry give crystallisation temperatures ranging from 900 °C in the diorite to 700 °C in the felsic lithologies (Wyborn, 1983).

The continuous chemical trends in the BPZP were generated by *in situ* fractional crystallisation of a single body of intermediate magma in an upper crustal magma chamber (Wyborn, 1983; Wyborn et al., 1987). Recent isotopic studies (Nd, Hf, U-Pb, O; Ickert, 2010; Ickert et al., 2011; Iles, 2017) suggest minor amounts (10-20%) of crustal

assimilation (consistent with our ancillary data, see Section 3.A1 and later discussion). However, decoupling between major element and isotopic trends suggests this assimilation probably occurs prior to upper crustal magma differentiation (Ickert, 2010) which is the focus of our study. Therefore, we consider the Boggy Plain pluton to be as representative a candidate for closed system fractionation as is feasible in nature.

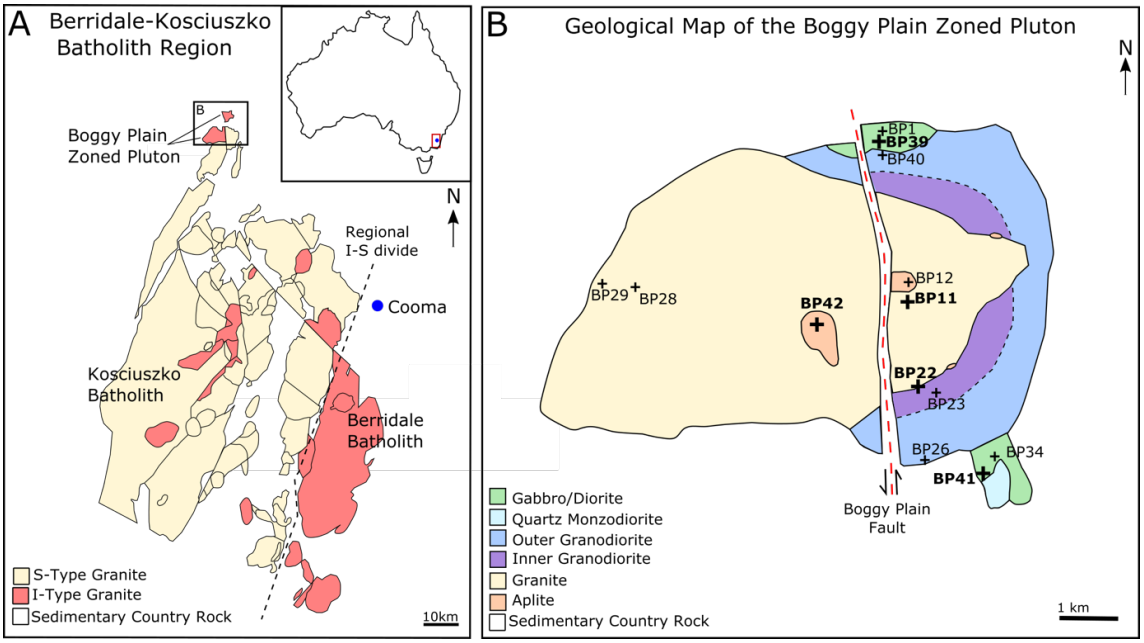

Figure 3.1. (A) Map of the Berridale and Kosciuszko batholiths in the SE of the Lachlan Fold Belt (adapted from Ickert, 2010). The Boggy Plain Zoned Pluton is located in the North of the batholith. The sedimentary country rock is mostly Silurian-Ordovician aged turbidites and shales (Wyborn, 1983). (B) Geological map of the Boggy Plain Zoned pluton showing the concentric zonation from a gabbroic rim to a granitic core (adapted from Wyborn, 1983). The geological map is a reconstruction after subtracting 4.9km left lateral strike slip motion on the Boggy Plain Fault (Wyborn et al., 1987). The black dashed line shows the boundary between the inner and outer granodiorite. Sample localities are indicated by crosses; those in bold are ones from which mineral separates were picked.

3.2.2 Whole rock chemical variations

Major and trace element compositions of whole rock samples typically show smooth, continuous trends with SiO_2 or MgO content, consistent with fractional crystallisation of a single parent magma (Wyborn, 1983; Figure 3.2). Whole rock concentrations of highly incompatible elements (e.g. Rb) increase with differentiation, and concentrations of

elements compatible in the crystallising bulk assemblage decrease with differentiation (e.g. Sr, compatible in plagioclase).

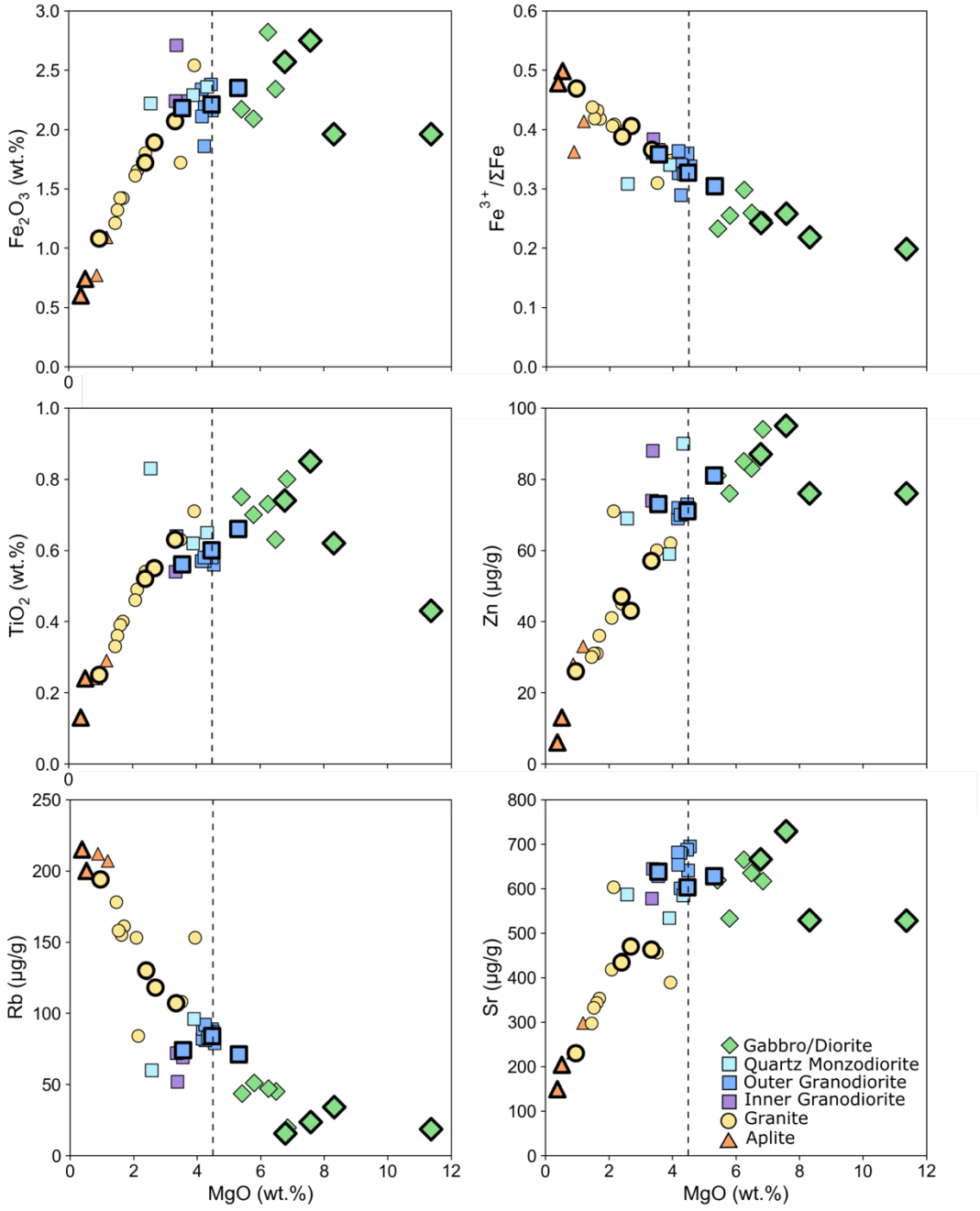

Figure 3.2. Chemical variations in the BPZP. Whole rock compositional data from Wyborn (1983). Large symbols with bold outlines are those chosen for isotopic analysis in this study. The dashed line approximates the separation of liquids (<4.5 wt.% MgO) from cumulate rocks (>4.5 wt. % MgO; see text). The line also corresponds to the composition of sample BP26, which is used as the parental melt composition in subsequent models. The scatter in the granodiorite data (blue and purple squares) is attributed to the compositional zoning in the granodiorite.

To understand the behaviour of Fe isotopes, the causes of variations in Fe concentration within the suite must first be understood. Variations in whole rock Fe_2O_3 and $Fe^{3+}/\Sigma Fe$ are plotted against MgO content in Figure 3.2. Fe_2O_3 concentrations are scattered in samples with MgO >4.5 wt.%. These higher MgO samples are petrographically identified as cumulates due to the presence of framework forming primocrysts and interstitial phases. Here "cumulate" is taken to mean that samples have experienced a concentration of crystals and/or crystal-melt segregation (e.g. Chappell and Wyborn, 2004). Therefore, the scatter in whole rock compositions of samples with MgO >4.5 wt.% is likely due to variability in the modal mineralogy and amount of trapped interstitial melt, rather than representing variation in liquid composition. For Fe_2O_3 the scatter is dictated by the proportion of interstitial magnetite, biotite and hornblende. Similar scatter is observed for TiO_2, Zn and Sr. Below 4.5 wt.% MgO, the Fe_2O_3 trend is smooth, reflecting crystallisation of magnetite, biotite and hornblende as part of the near-liquidus mineral assemblage. The whole rock compositions are therefore more representative of the fractionating magma when MgO is below 4.5 wt.%. Whole rock $Fe^{3+}/\Sigma Fe$ increases with differentiation, and together with increasing $Fe^{3+}/\Sigma Fe$ in both biotite and hornblende in more evolved samples is thought to reflect an increase in the magma fO_2 during differentiation (Wyborn, 1983).

3.3 Sample Selection and Petrography

Based on major and trace element variations, samples or sampling localities from Wyborn (1983) were carefully selected to represent the complete range of lithologies observed in the BPZP. Samples were either those originally collected by Wyborn (1983), or from a field campaign in 2013 that resampled the same locations from Wyborn (1983).

We examined every sample petrographically, building on observations in Wyborn (1983) and Hoskin et al. (2000). A full description of all samples is given in Electronic Appendix 3. Two distinct textural groups of minerals were identified, primocrysts (i.e. euhedral crystals which likely crystallised unconfined from the magma) and interstitial phases (with anhedral morphologies which crystallised in confined spaces from the interstitial melt). In the context of the stable isotopic evolution of a cogenetic suite undergoing fractional crystallisation, we assume that only primocryst crystallisation will influence

the isotopic composition of the evolving residual magma. However, the modal abundance of both primocryst and interstitial phases regulates the whole rock isotopic composition.

The lithologies in the BPZP progress from gabbro to monzodiorite to granodiorite to granite (Figure 3.1). This is typical of a calc-alkaline differentiation sequence in showing early magnetite saturation and crystallisation of hydrous phases such as biotite and hornblende, interpreted as the result of high initial H_2O content and high fO_2 (e.g. Sisson and Grove, 1993a; Zimmer et al., 2010). Gabbros and diorites form the outer rim of the pluton and are only exposed over an area of <2km^2 (Figure 3.1). Samples BP41 (gabbro) and BP39 (diorite) contain framework-forming primocrysts and interstitial phases, a texture typical of cumulate rocks (e.g. Irvine, 1982). In the gabbro, the main framework forming primocryst phases are plagioclase (An_{60}) (55%), clinopyroxene (15%), orthopyroxene (10%) and minor olivine (<10%) (Figure 3.3A). Anhedral biotite (5%) occupies interstitial sites (Figure 3.3B). Titanomagnetite (here referred to as magnetite) and ilmenite are rare (<1%) and found as inclusions within pyroxenes and as discrete grains associated with biotite in interstitial sites. In the diorite, the abundance of clinopyroxene is higher, and hornblende can be found with biotite in interstitial sites and as rims surrounding pyroxene crystals (Figure 3.3C), suggesting that both biotite and hornblende crystallised from melt films and trapped interstitial melt. Magnetite is almost exclusively associated with biotite and is therefore interpreted as an interstitial phase.

In more evolved samples, those with >58 wt. % SiO_2 and <4.5 wt.% MgO, biotite and hornblende replace orthopyroxene and clinopyroxene as the main ferromagnesian primocryst phases. Sample BP40 (5.32 wt.% MgO) shows the transition between the two textural regimes (Figure 3.3D). Pyroxenes (20%) have irregular crystal habits whereas hornblende (15%) and biotite (5%) begin to show more prismatic shapes. Oxides (1%) are predominantly magnetite and exist mostly as inclusions within biotite and hornblende. Plagioclase (35%) remains a primocryst phase, and there is the first appearance of interstitial orthoclase (often poikilitic) (15%).

In the granites (BP11, BP22, BP28 and BP29), euhedral biotite (10%) and hornblende (15%) are the main ferromagnesian primocryst phases (Figure 3.3E), interpreted to have fully replaced the pyroxenes. Quartz (20%), plagioclase (35%) and orthoclase (20%) are the most abundant phases. There is 1% magnetite and minor interstitial titanite (<1%).

A fine-grained aplite (BP42 and BP12) is found in the core of the pluton. Quartz, orthoclase and plagioclase make up over 95% of the modal mineralogy, with minor biotite and magnetite (<5% by volume; Figure 3.3F). There is no hornblende present in the aplite. Biotite commonly shows a green colour along cleavage planes from chloritization by Cl-rich fluids.

Fe-Ti oxide minerals such as titanomagnetite can host a large proportion of the Fe in the system. Low temperature oxyexsolution of titanomagnetite is common during slow cooling, resulting in exsolution of ilmenite (Frost and Lindsley, 1991). Exsolved ilmenite can occur as lamellae along {111} planes of the magnetite host (both thin trellis-type and thicker sandwich-type) or as anhedral granules on the edge of magnetite grains (Frost and Lindsley, 1991). The exchange of Fe and Ti between magnetite and ilmenite during oxyexsolution can alter the Fe isotopic composition of the oxide minerals (e.g. Dziony et al., 2014; Chen et al., 2014; Cao et al., 2019). In the mafic cumulates, there is evidence for low temperature re-equilibration of interstitial magnetite grains. Granular exsolution and trellis and sandwich exsolution lamellae of ilmenite are only present in the mafic diorites (Figure 3.4 A and B). In the more evolved samples, primocryst titanomagnetite only shows very fine trellis-type exsolution lamellae (Figure 3.4C and D). There is no variation in exsolution style with grain size. The bulk magnetite separates were handpicked from a 125-250 μm size fraction following an initial magnetic separation. This size fraction is much larger than the scale of exsolution features (Figure 3.4), which permits sampling of magnetite grains in bulk with their hosted ilmenite lamellae. We are therefore confident that our approach allows us to determine the isotopic composition of bulk titanomagnetite at the time of crystallisation.

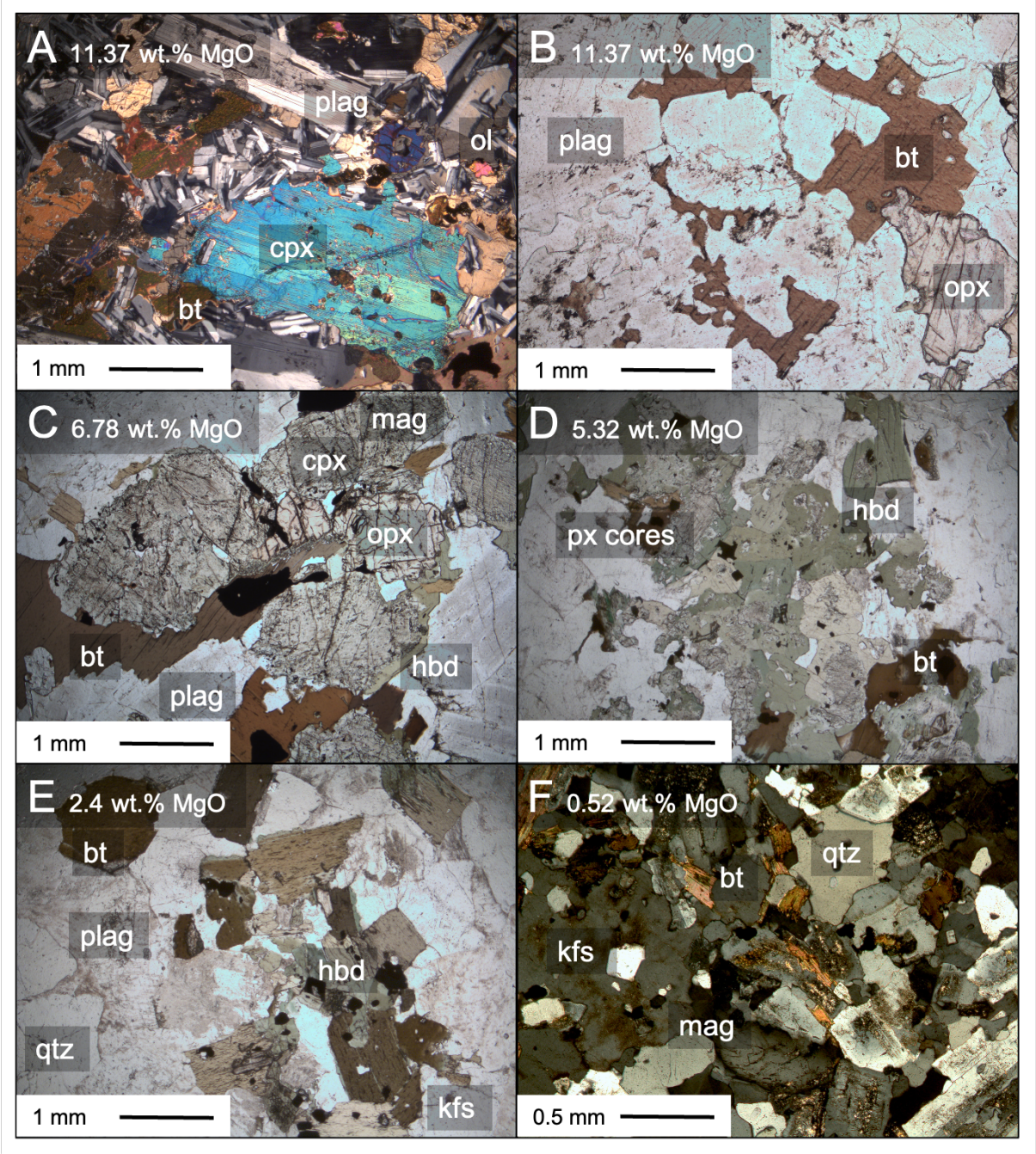

Figure 3.3. Petrographic textures in the BPZP. (A) BP41 showing a typical cumulate texture, containing euhedral primocrysts of pyroxene and plagioclase, and minor interstitial biotite. (B) BP41 showing anhedral morphologies of interstitial biotite. (C) BP39 containing euhedral pyroxene primocrysts with biotite and hornblende rims. (D) BP40 transitional textures. Pyroxene cores surrounded by hornblende and biotite. (E) BP28 containing euhedral biotite and hornblende primocrysts, and no pyroxene present. (F) BP12 showing fine grained aplitic texture. Abbreviations opx = orthopyroxene, plag = plagioclase, ol= olivine, bt= biotite, hbd = hornblende, mag=titanomagnetite, kfs= K-feldspar. The BPZP samples are very coarse grained and therefore photomicrographs can show small scale features, but do not effectively demonstrate larger scale textural information. Full thin section scans are provided in Electronic Appendix 2.

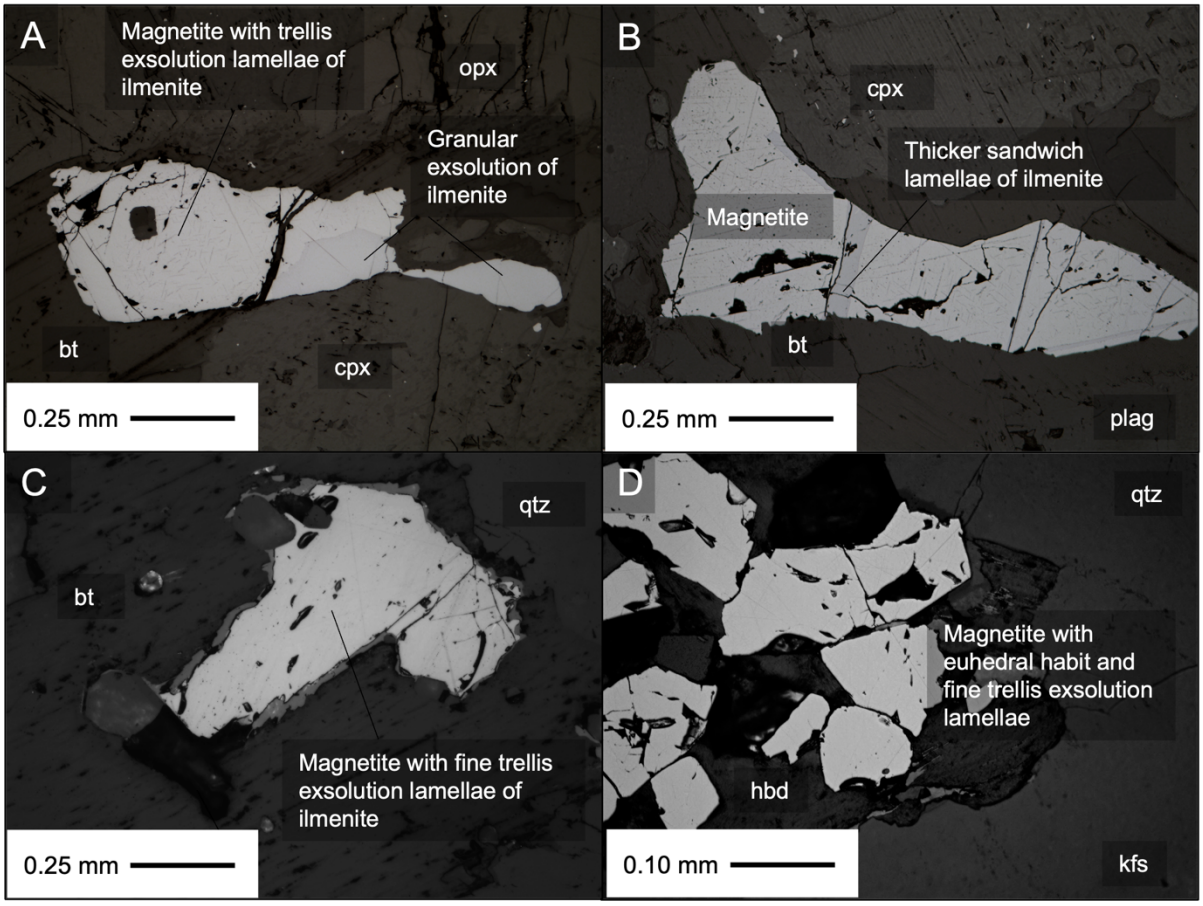

Figure 3.4. Typical textures and morphologies of Fe-Ti oxides in the BPZP. (A) and (B) BP39 diorite, containing interstitial magnetite grains (white/yellow colour) with anhedral morphologies, showing granular exsolution of ilmenite and trellis exsolution of ilmenite (grey/brown colour). (C) and (D) BP22 granodiorites contain small, euhedral grains with very fine trellis exsolution lamellae. This is typical of magnetite grains in samples with WR MgO < 4.5 wt.%.

3.4 Analytical Methods

Twelve whole rock samples, along with biotite, hornblende and magnetite mineral separates from five of the samples, were measured for Fe-Zn isotopic compositions. Biotite, hornblende and magnetite separates were chosen because they host the majority of Fe and Zn in the system, with modal proportions varying over the differentiation sequence. Mass balance calculations show that approximately 30% of total Fe is hosted in magnetite, and the remainder distributed equally between biotite and hornblende. In contrast, <5% of the total Zn is hosted in magnetite, but up to 80% is hosted in biotite. Chemical purification and isotopic analysis were conducted at the Arthur Holmes Isotope Geology Laboratory, Durham University. Iron and Zn fractions were obtained from the same digestion. This reduces the amount of material required for isotopic analyses, which

is beneficial when picking mineral separates. Since Fe is present at weight percent concentrations in all rock forming minerals, and Zn is a trace element with maximum concentrations of several hundred μg/g, the Zn concentration of mineral separates and whole rock powders dictated the mass of sample required for analysis. Biotite and hornblende mineral separates have Zn concentrations from 138-292 μg/g (Wyborn, 1983). Mass balance considerations based on whole rock and mineral separate Zn concentrations in Wyborn (1983) show that magnetite should contain 50-150 μg/g Zn. Approximately 1.5 μg total Zn is required to make at least three Zn isotopic measurements. Therefore, a minimum of 10-20 mg biotite and hornblende and 30-40mg magnetite were handpicked under binocular microscope from a 125-250μm size fraction, avoiding crystal fragments containing obvious inclusions. For whole rock analyses (9-95 μg/g Zn; Wyborn, 1983), approximately 50-70 mg of powder was required. The Nd isotopic compositions of four whole rock samples were also analysed in order to verify the absence of significant crustal assimilation (Ickert, 2010), as described in Section 3.A1.

3.4.1 Chemical isolation

Mineral separates and whole rock samples were ground to homogenous powders using a Fritsch Pulverisette 0 agate motor and ball. Whole rock powders and silicate mineral separates were dissolved in 3 ml of Teflon Distilled (TD) 29M HF and 1 ml of TD 16M HNO_3 in Savillex beakers on a hotplate at 160 °C. The magnetite separates frequently contained silicate inclusions, which potentially have distinctive Fe and Zn isotopic compositions. Therefore, magnetite samples were dissolved in 5 ml TD 6M HCl in Savillex beakers on a hotplate at 120 °C. This allowed full dissolution of the oxides, and the remaining insoluble silicates were separated by centrifugation.

Samples were refluxed in 1 ml TD 6M HCl before being loaded onto anion exchange columns containing 2 ml Bio-Rad AG1-X8 resin (200-400 mesh) following the method of Sossi et al. (2015). The resin was initially pre-cleaned by shaking with TD 6M HCl and MQ H_2O. Following this initial fines removal and pre-clean step, 20 ml of resin was further cleaned using a BioRad Econo-Pac column with 250 ml reservoir connected to a vacuum box. Cleaning involved eluting a sequence of 200 ml each of MQ H_2O, TD 3M HCl, MQ H_2O, TD 3M HNO_3, MQ H_2O. This was repeated three times. The cleaning steps were necessary to reduce Zn procedural blanks to below 20 ng total Zn.

Most matrix elements were eluted with 14 ml TD 6M HCl, followed by Fe collection in 6 ml TD 0.5M HCl, and finally Zn collection in 4 ml TD 3M HNO_3. The isolated Zn fractions were passed through the same column procedure a second time. Column yields were consistently >95% for Fe and Zn, in agreement with Sossi et al. (2015). Total procedural blanks ranged from 10-30ng for Fe and 10-20ng for Zn during the course of the study.

3.4.2 Isotope Ratio Measurement

Iron isotopic measurements were carried out on a Neptune MC-ICP-MS in medium resolution mode ($m/\Delta m \sim 6000$-8000) to resolve Fe from isobaric molecular oxide and nitride interferences. Masses ^{53}Cr, ^{54}Fe, ^{56}Fe, ^{57}Fe, ^{58}Fe, ^{60}Ni and ^{61}Ni were measured on Faraday cups L4, L2, L1, C, H1, H2 and H4 respectively. ^{53}Cr was monitored in order to correct for the atomic interference of ^{54}Cr on ^{54}Fe. $10^{11}\Omega$ resistors were used on all cups with the exception of L1, where a $10^{10}\Omega$ resistor was connected to allow measurement of >50V signals on ^{56}Fe. Standards and samples were run at a concentration of 8-10 µg/g Fe. Typical sensitivity with wet plasma in medium resolution was ~5V/ppm on ^{56}Fe using a Savillex CF50 concentric flow nebuliser with 50µl/min uptake rate connected to a Glass Expansion borosilicate glass Cinnabar microcyclonic spray chamber. An individual measurement was comprised of 1 block of 50 cycles with an integration time of 4.194s per cycle, total analysis time around 3.5 minutes. Approximately 2 µg of Fe was consumed during one analysis at a concentration of 10 µg/g. Mass bias and instrument drift was corrected by standard sample bracketing with the IRMM-014 Fe standard and/or the isotopically indistinguishable IRMM-524 standard (Craddock and Dauphas, 2011).

Iron isotopic data are reported in delta notation relative to the IRMM-014 standard, where $\delta^{X}Fe = [(^{X}Fe/^{54}Fe)_{sample}/(^{X}Fe/^{54}Fe)_{IRMM\text{-}014} - 1] \times 10^3$ and X is mass 56 or 57. All samples show mass dependent behaviour (Figure 3.5A). Samples were measured a minimum of three times, and errors are reported as 2SD of all individual measurements of the sample. USGS reference materials GSP-2, BHVO-2 and BIR-1a were processed and analysed alongside all unknowns, giving $\delta^{56}Fe$ values within the range of previous measurements (e.g. Craddock and Dauphas, 2011; Liu et al., 2014; Table 3.1). Long term reproducibility for Fe isotopic measurements was ±0.050‰ (n=148, 2SD) based on measurement of an internal lab standard '*Romil Fe'* over the course of the study.

Zinc isotopic measurements were carried out on a Neptune Plus MC-ICP-MS in low resolution mode (m/Δm ~ 400). Masses ^{62}Ni, ^{63}Cu, ^{64}Zn, ^{65}Cu, ^{66}Zn, ^{67}Zn and ^{68}Zn were measured in Faraday cups L3, L2, L1, C, H1, H2 and H3 respectively, with $10^{11}\Omega$ resistors connected to all cups. ^{62}Ni was monitored to correct for the isobaric interference of ^{64}Ni on ^{64}Zn. ^{63}Cu and ^{65}Cu were used for mass bias corrections. Samples were run at concentrations of 0.750 µg/g Zn and doped with 0.375 µg/g Cu. Typical sensitivity with wet plasma was ~4V/ppm on ^{66}Zn using the same introduction setup as for Fe. Mass bias and instrument drift was corrected by a combination of external element doping with Cu, and standard sample bracketing with the AA-ETH Zn solution (Archer et al., 2017). Data in this study is reported relative to AA-ETH, where $\delta^{X}Zn = (^{X}Zn/^{64}Zn)_{sample}/(^{X}Zn/^{64}Zn)_{AA\text{-}ETH} - 1] \times 10^3$ and X is mass 66, 67 or 68. All samples show mass dependent behaviour (Figure 3.5B).

The AA-ETH Zn solution has an isotopic composition indistinguishable from the certified isotopic reference material IRMM-3702, while its δ^{66}Zn value is offset relative to the commonly used reference standard JMC 3-0749 L, also known as JMC Lyon Zn (Maréchal et al., 1999) by +0.28 ± 0.02‰ (Archer et al., 2017). The majority of previous studies report data relative to JMC Lyon, but the standard is no longer available. Data from this study is recast relative to JMC-Lyon for comparison, using the correction of Archer et al. (2017). The IRMM-3702 Zn standard was measured regularly throughout this study, giving an average isotopic composition of $\delta^{66}Zn_{AA\text{-}ETH}$ = 0.015 ± 0.035‰ (n=83, 2SD), in agreement with Archer et al. (2017). Several USGS reference materials were processed and analysed alongside unknowns, giving δ^{66}Zn values which agree with previous measurements (e.g. Sossi et al., 2015; Chen et al., 2016; Table 3.1).

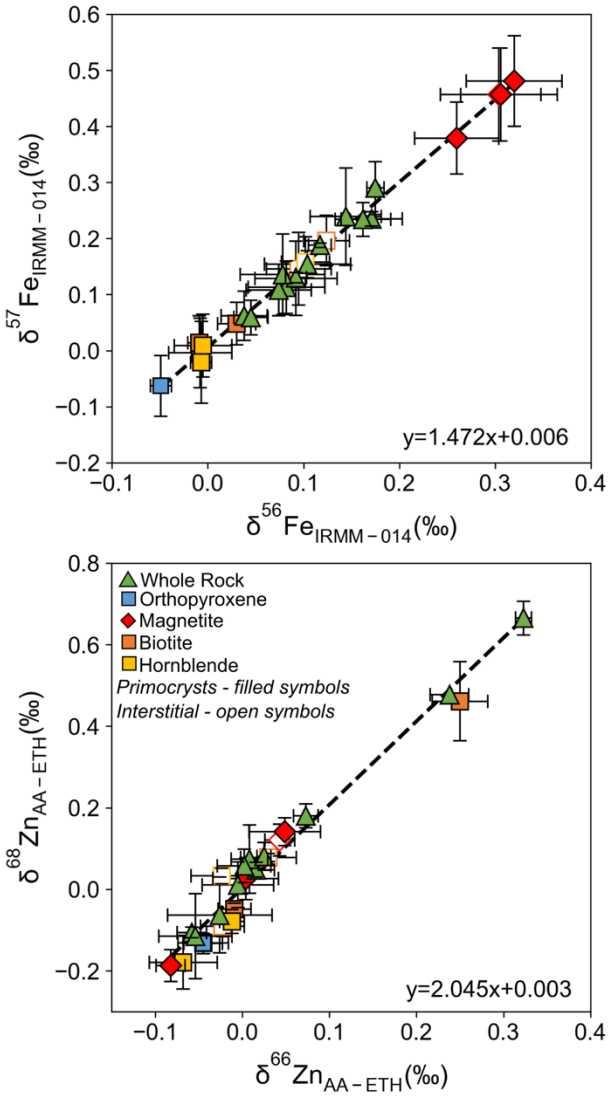

Figure 3.5. Three-isotope plots for (A) Fe (δ^{56}Fe vs δ^{57}Fe) and (B) Zn (δ^{66}Zn vs δ^{68}Zn). The slopes of the linear regressions are 1.47 and 2.01 respectively, which are consistent with the gradients predicted by mass dependent fractionation laws (i.e. ~1.5 and 2; Young et al., 2002).

3.5 Results

3.5.1 Iron isotopic data

Iron isotopic data for whole rock and mineral separates are shown in Tables 3.1 and 3.2. Major and trace element compositions for whole rocks and mineral separates are from Wyborn (1983).

The whole rock δ^{56}Fe values vary with whole rock MgO content. δ^{56}Fe values increase from 0.038 ± 0.024‰ (2SD) in the most mafic samples to a maximum value of 0.171 ±

0.032‰ (2SD) at 0.52 wt.% MgO / 73.07 wt.% SiO_2 (Figure 3.6). This range is similar to values previously measured in other I-type granitoids, which typically show maximum $\delta^{56}Fe \sim 0.21$‰ with differentiation (Foden et al., 2015).

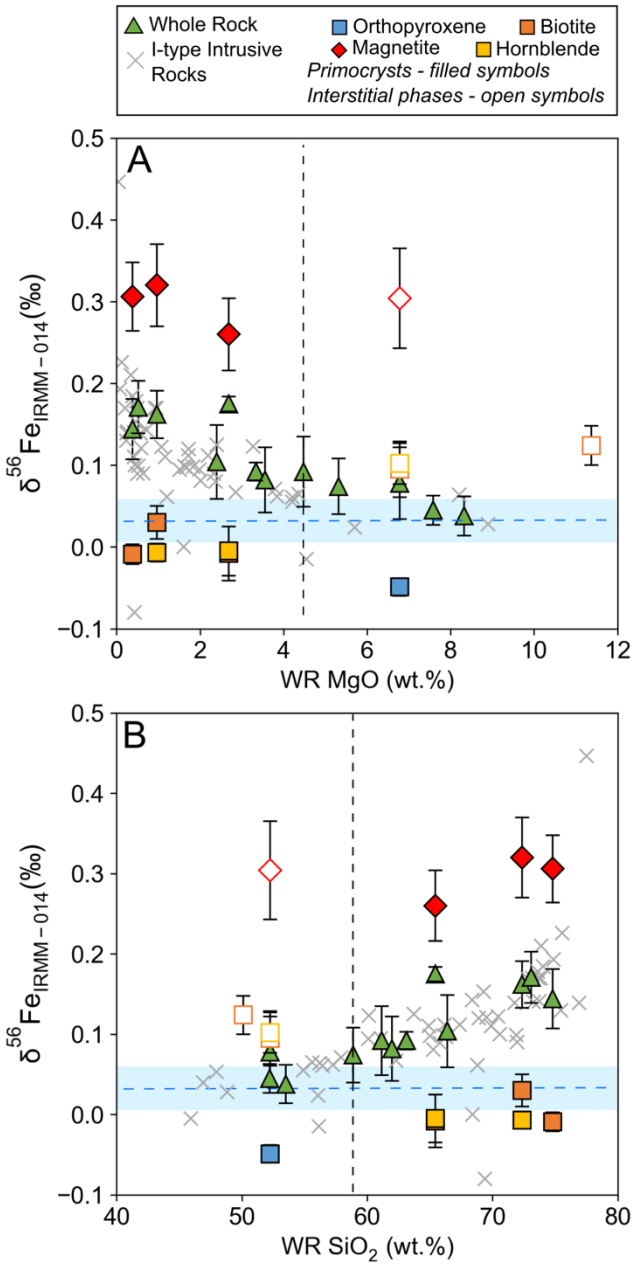

Figure 3.6. Iron isotopic composition of whole rocks and mineral separates against WR MgO (A) and SiO_2 (B) content. Errors are plotted as 2SD of at least 3 individual measurements of each sample. A compilation of data from other plutonic I-type rocks is shown by the grey crosses (Poitrasson and Freydier, 2005; Schoenberg and von Blanckenburg, 2006; Heimann et al., 2008; Telus et al., 2012 and Foden et al., 2015). The vertical dashed line shows the divide between cumulate samples and liquids as in Figure 3.2. The blue shaded area is the estimate for the Bulk Silicate Earth from Sossi et al. (2016) of $\delta^{56}Fe = 0.033 \pm 0.027$‰.

3.5.1.1 Mineral-mineral fractionation factors

The Fe isotopic composition of the mineral separates is shown in Table 3.2. As expected, the mineral separates are enriched in ^{56}Fe relative to ^{54}Fe in the order magnetite > biotite = hornblende > orthopyroxene, in agreement with previous studies (e.g. Heimann et al., 2008; Sossi et al., 2012; Wu et al., 2017). This order of isotopic enrichment also supports observations from NRIXS and Mössbauer spectroscopy that β factors, and consequently $\delta^{56}Fe$ values, increase with $Fe^{3+}/\Sigma Fe$ (Polyakov and Mineev, 2000; Polyakov et al., 2007; Schoenberg et al., 2009).

The isotopically lightest mineral separate measured is the orthopyroxene, which contains octahedrally coordinated ferrous iron ($\delta^{56}Fe$ = -0.049 ± 0.011‰; 2SD, n=3). Magnetite ($^{IV}Fe^{3+}\ ^{VI}(Fe^{2+},Fe^{3+})\ O_4$) is the isotopically heaviest mineral phase measured. Magnetite $\delta^{56}Fe$ values are approximately constant across the differentiation sequence, varying from 0.260‰ to 0.320‰. Biotite and hornblende mineral separates have $Fe^{3+}/\Sigma Fe$ and $\delta^{56}Fe$ values between these extremes, consistent with a combination of Fe^{2+} and Fe^{3+} ions typically found in VI-fold coordination (e.g. Leake et al., 1997; Rieder et al., 1998). Biotite mineral separates span a range of $\delta^{56}Fe$ from -0.009‰ to 0.124‰ and hornblende separates from -0.007‰ to 0.102‰. Biotite and hornblende have identical isotopic compositions to each other in individual samples, with an average $\Delta^{56}Fe_{bt\text{-}hbd}$ of 0.009‰. However, biotite and hornblende separates from interstitial phases have heavier isotopic composition than primocrysts.

3.5.2 Zinc Isotopic Data

Zinc isotopic data for whole rock and mineral separates is presented in Tables 3.1 and 3.2. The Zn isotopic data is reported relative to the AA-ETH standard (Archer et al., 2017). With the exception of aplite samples BP12 and BP42, whole rock Zn isotopic compositions fall between $\delta^{66}Zn_{AA\text{-}ETH}$ of -0.058 ± 0.017‰ (2SD) and 0.073 ± 0.014‰ (2SD) (Figure 3.7). This is comparable to whole rock samples from the Hekla cogenetic lava suite ($\delta^{66}Zn_{AA\text{-}ETH}$ of -0.06‰ to +0.05‰; Chen et al. (2013)). With the exception of the aplites, samples are all within error of the average Zn isotopic composition of mantle derived magmas from Chen et al. (2013) of $\delta^{66}Zn_{AA\text{-}ETH}$ = 0.01 ± 0.08‰.

The silicate and oxide mineral separates from samples BP41, BP39, BP22 and BP11 have isotopic compositions within error of the average isotopic composition of basaltic magmas in Chen et al. (2013). Given that Zn^{2+} (0.74Å) has a similar ionic radius to Fe^{2+} (0.78Å) (Shannon, 1976), Zn^{2+} most likely substitutes for VI-fold coordinated Fe^{2+} in biotite, hornblende and magnetite. Silicate and oxide primocrysts from the same sample have Zn isotopic compositions that are indistinguishable within error, which is consistent with these theoretical considerations of bonding environment. Xu et al. (2019) also measured identical $\delta^{66}Zn$ in biotite, hornblende and magnetite separates from one melanosome from the Dabie Orogen, central China.

However, in the aplite sample (BP42), the magnetite has an isotopic composition within error of the other separates, but the biotite has a significantly heavier $\delta^{66}Zn_{AA\text{-}ETH}$ of 0.250 ± 0.032‰ (2SD). The whole rock isotopic composition plots between the isotopic composition of biotite and magnetite, at a value of 0.238 ± 0.022‰ (2SE). The other aplite sample (BP12) also has a heavy whole rock isotopic composition of $\delta^{66}Zn_{AA\text{-}ETH}$ = 0.323 ± 0.009‰ (2SD).

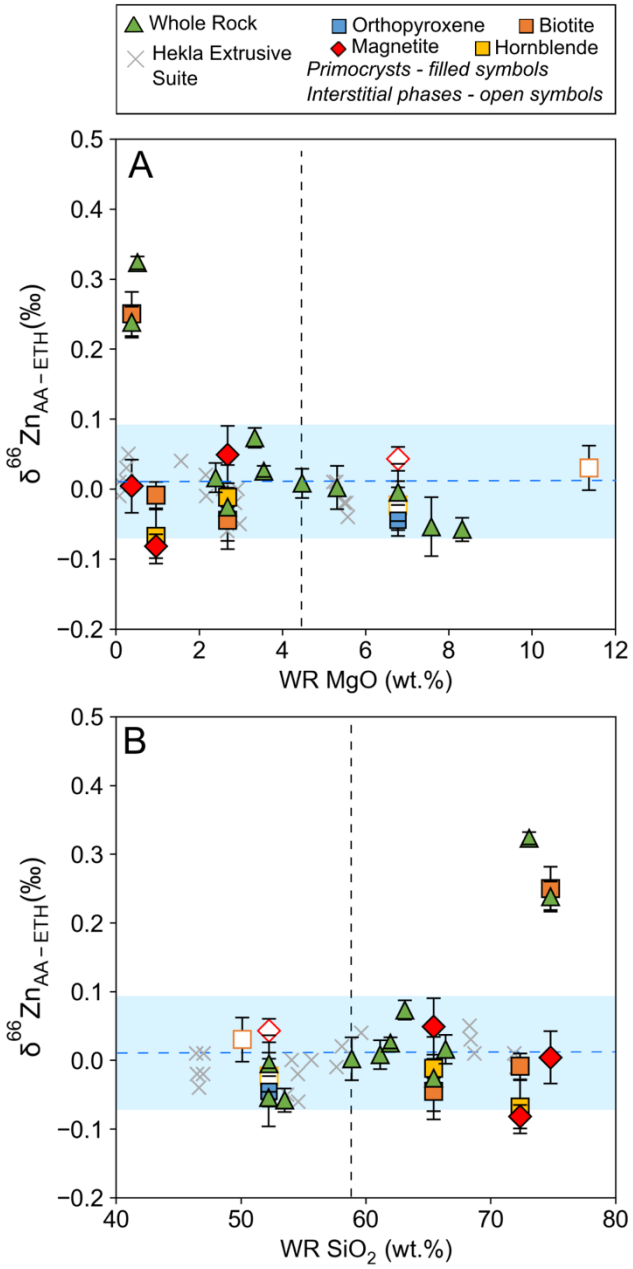

Figure 3.7. Zinc isotopic compositions of whole rock and mineral separates against WR MgO (A) and SiO_2 (B) content. Errors are plotted as 2SD of at least 3 individual measurements of each sample. Grey crosses are co-genetic lavas from Hekla, Iceland (Chen et al., 2013). The vertical dashed line shows the divide between cumulate samples and liquids as in Figure 3.2. Given that the pristine and depleted mantle have distinct Zn isotopic composition, and that heavy Zn isotopes can become concentrated in the melt during mantle partial melting (e.g. Wang et al., 2017; Huang et al., 2018; Sossi et al., 2018a), the average isotopic composition of mantle derived magmas from Chen et al., 2013 ($\delta^{66}Zn_{AA\text{-}ETH}$ of 0.01 ± 0.08‰) is shown by the blue shaded area for comparison.

Table 3.1. Iron and Zinc isotopic composition of BPZP whole rock samples and USGS reference materials. Whole rock (WR) MgO content from Wyborn (1983). Iron isotopic ratios are quoted relative to the IRMM 014 standard. Zinc isotopic ratios were measured relative to the AA-ETH standard. These are recast relative to the JMC-Lyon standard using the correction of +0.280‰ (Archer et al., 2017). Errors are quoted as 2 standard deviations of the mean of all measurements of the sample. If <3 analyses could be made, errors are reported as 2SE (+).

Sample	Rock Type	WR MgO (wt. %)	δ^{56}Fe IRMM-014 (‰)	2SD	δ^{57}Fe IRMM-014 (‰)	2SD	n	δ^{66}Zn JMC-Lyon (‰)	$\delta^{66}Zn_{AA\text{-}ETH}$ (‰)	2SD	$\delta^{68}Zn_{AA\text{-}ETH}$ (‰)	2SD	n
BP34	Diorite	8.32	0.038	0.024	0.062	0.044	3	0.222	-0.058	0.017	-0.106	0.013	3
BP1	Diorite	7.58	0.045	0.018	0.059	0.031	3	0.226	-0.054	0.042	-0.115	0.104	3
BP39	Diorite	6.78	0.078	0.044	0.136	0.072	3	0.275	-0.005	0.041	0.011	0.056	3
BP40	Granodiorite	5.32	0.074	0.034	0.108	0.046	4	0.282	0.002	0.031	0.057	0.041	3
BP26	Granodiorite	4.48	0.092	0.043	0.129	0.066	5	0.288	0.008	0.021	0.074	0.084	3
BP23	Granodiorite	3.56	0.082	0.040	0.113	0.047	3	0.305	0.025	0.008	0.081	0.034	3
BP29	Granite	3.34	0.092	0.011	0.130	0.009	3	0.353	0.073	0.014	0.180	0.029	3
BP22	Granite	2.69	0.175	0.009	0.290	0.047	6	0.254	-0.026	0.060	-0.063	0.093	4
BP28	Granite	2.40	0.104	0.045	0.154	0.024	4	0.296	0.016	0.021	0.048	0.018	3
BP11	Granite	0.96	0.162	0.029	0.234	0.030	4						
BP12	Aplite	0.52	0.171	0.032	0.253	0.013	3	0.603	0.323	0.009	0.665	0.041	3
BP42	Aplite	0.38	0.144	0.037	0.239	0.087	4	0.518	0.238	0.022^{+}	0.477	0.025^{+}	2
	Replicate		0.117	0.012	0.188	0.004	3						
USGS reference Materials													
GSP-2			0.150	0.033	0.217	0.034	13	0.956	0.676	0.059	0.954	0.104	3
BHVO-2			0.139	0.031	0.221	0.042	8						
BIR-1a			0.034	0.016	0.048	0.024	4	0.288	0.008	0.040	0.052	0.104	6

Table 3.2. Iron and Zinc isotopic composition of BPZP mineral separates. For mineral textures, I denotes interstitial phases, and P primocrysts. Iron isotopic ratios are quoted relative to the IRMM 014 standard. Zinc isotopic ratios were measured relative to the AA-ETH standard. These are recast relative to the JMC-Lyon standard using the correction of +0.280‰ (Archer et al., 2017). Errors are quoted as 2 standard deviations of the mean of all measurements of the sample.

Sample	Mineral Phase	Texture	$\delta^{56}Fe$ IRMM-014 (‰)	2SD	$\delta^{57}Fe$ IRMM-014 (‰)	2SD	n	$\delta^{66}Zn$ JMC-Lyon (‰)	$\delta^{66}Zn$ AA-ETH (‰)	2SD	$\delta^{68}Zn$ AA-ETH (‰)	2SD	n
BP41	Biotite	I	0.124	0.024	0.196	0.045	3	0.310	0.030	0.032	0.078	0.010	3
BP39	Orthopyroxene	P	-0.049	0.011	-0.063	0.054	4	0.235	-0.045	0.022	-0.133	0.025	3
	Biotite	I	0.095	0.034	0.146	0.065	8	0.257	-0.023	0.025	-0.091	0.025	3
	Hornblende	I	0.102	0.025	0.158	0.045	3	0.256	-0.024	0.035	0.033	0.019	3
	Magnetite	I	0.304	0.061	0.457	0.083	3	0.323	0.043	0.017	0.121	0.039	3
BP22	Biotite	P	-0.008	0.033	-0.004	0.062	7	0.235	-0.045	0.029	-0.132	0.018	3
	Hornblende	P	-0.005	0.030	0.009	0.056	3	0.268	-0.012	0.014	-0.079	0.029	3
	Magnetite	P	0.260	0.044	0.379	0.064	5	0.329	0.049	0.041	0.141	0.034	3
BP11	Biotite	P	0.030	0.020	0.048	0.038	3	0.271	-0.009	0.019	-0.049	0.015	3
	Hornblende	P	-0.007	0.011	-0.021	0.073	4	0.212	-0.068	0.039	-0.179	0.066	3
	Magnetite	P	0.320	0.050	0.481	0.081	4	0.198	-0.082	0.017	-0.187	0.039	3
BP42	Biotite	P	-0.009	0.012	0.014	0.048	4	0.530	0.250	0.032	0.461	0.097	3
	Magnetite	P	0.306	0.042	0.457	0.083	4	0.284	0.004	0.038	0.026	0.051	3

3.6 Drivers of Fe-Zn isotopic variation in the Boggy Plain Zoned Pluton

Previous geochemical and petrographic work on the BPZP indicates that its evolution very closely approximates closed system fractional crystallisation (Wyborn, 1983; Wyborn, 1987; Wyborn et al., 2001). Fractional crystallisation is commonly proposed as the dominant control on Fe isotopic variation in both extrusive (e.g. Teng et al., 2008; Schuessler et al., 2009; Du et al., 2017; Xia et al., 2017) and plutonic (e.g. Telus et al., 2012; Sossi et al., 2012; Foden et al., 2015; Du et al., 2019) suites. However, Fe isotopes can be fractionated by multiple other processes, which are often difficult to distinguish using whole rock analyses alone (e.g. Soderman et al., 2020). In contrast, fractional crystallisation is thought to cause <0.1‰ Zn isotopic fractionation (e.g. Chen et al., 2013; Doucet et al., 2018; Huang et al., 2018), but there is the potential for larger magnitudes of Zn isotopic fractionation by fluid alteration (e.g. Telus et al., 2012; Wang et al., 2020). In this section we first exclude processes that do not contribute to Fe-Zn isotopic variations in the BPZP, then assess the controls on inter-mineral isotopic fractionation factors necessary for developing internally consistent, fully quantitative models of Fe isotopic variations in calc-alkaline magmas during fractional crystallisation.

3.6.1 Impact of crustal assimilation and fluid exsolution on Fe-Zn isotopic compositions

Although the observed isotopic variation could, in part at least, reflect source mantle heterogeneity (e.g. Williams and Bizimis, 2014; He et al., 2017; Gleeson et al., 2020) or crustal contamination (e.g. Schoenberg and von Blanckenburg, 2006; Hiebert et al., 2016), we infer that these processes have had a negligible impact on the BPZP magma. Age-corrected whole rock εNd_i measured in this study show less than 2 epsilon unit variation (Table 3.S1; Figure 3.S1), with values very similar to Ickert (2010) that are typical of magmas derived from an upper mantle source. The Nd isotopic data would be consistent with either the source of the BPZP being contaminated with ~10% crustal material or the parent magma from a homogenous source assimilating approximately 10% crustal material, with the exposed Ordovician-Silurian aged sedimentary country rock proposed as a possible assimilant (Ickert, 2010). However, irrespective of whether the Nd

isotopic composition is inherited from a contaminated source or early assimilation of crust, the magma appears to subsequently evolve via closed system fractional crystallisation, without further assimilation. Therefore, the effect of crustal assimilation on the variation of Fe-Zn isotopic compositions within the BPZP magma is likely to be negligible.

There is variation in both Fe and Zn whole rock isotopic compositions across the BPZP differentiation sequence (Figures 3.6 and 3.7). However, for Zn, this range is exaggerated by the presence of two isotopically heavy aplite samples. The remaining whole rock samples fall within a 0.13‰ range, with similar $\delta^{66}Zn$ values to the Hekla extrusive suite (Chen et al., 2013). Biotite, hornblende and magnetite separates also fall within this range. The mafic cumulates have the lightest $\delta^{66}Zn$ values, which may be due to the accumulation of isotopically light pyroxene which hosts the majority of Zn in these samples. There is no systematic variation in whole rock $\delta^{66}Zn$ with MgO content for the samples with <4.5 wt.% MgO, which are interpreted to be representative of evolving magma composition. This suggests that Zn isotopes are not significantly fractionated during fractional crystallisation of the BPZP, agreeing with the findings of previous studies (e.g. Chen et al., 2013; Huang et al., 2018).

The heavy Zn isotopic composition of the aplites is most likely due to fluid alteration. Zn can be mobilised as chloride complexes in magmatic fluids (e.g. Zajacz et al., 2008). Zn-chlorides are predicted to be enriched in ^{64}Zn (Fujii et al., 2014), and exsolution of isotopically light Zn bearing fluids may therefore explain the heavy Zn isotopic compositions up to $\delta^{66}Zn_{AA\text{-}ETH}$ = 0.60‰ observed in some rhyolites and pegmatites (Telus et al., 2012; Xia et al., 2017; Doucet et al., 2020). Chloritized biotite present in the most felsic lithologies of the BPZP indicates the presence of Cl-rich fluids during late-stage crystallisation. Hence, the heavy $\delta^{66}Zn$ values for the aplites and the biotite separates from BP42 are most likely caused by loss of isotopically light Zn during the chloritization of the biotite grains.

Iron isotopes can also potentially be fractionated by fluids. Fluid exsolution has been invoked to explain the heavy Fe isotopic compositions of some granites and pegmatites (Poitrasson and Freydier, 2005; Heimann et al., 2008; Telus et al., 2012). Ferrous iron is predicted to complex strongly with chloride ions in magmatic fluids; the fluid should

therefore be isotopically lighter than Fe^{3+} bearing silicate minerals and melt (Fujii et al., 2014). However, both aplite samples have whole rock $\delta^{56}Fe$ values similar to the other whole rock samples. Hence, we are confident that late-stage fluid exsolution or alteration has not led to fractionation of Fe isotopes in the BPZP.

In addition, there is no correlation between whole rock $\delta^{56}Fe$ and $\delta^{66}Zn$ in the BPZP (Figure 3.S2). The existence of coupled Fe-Zn isotope signatures in cratonic and mantle samples has previously been proposed to demonstrate that Fe and Zn isotopes are fractionated by the same processes during continental crust formation (Doucet et al., 2020). However, that co-variation is likely due to initial partial melting processes, rather than fractionation during magmatic evolution. Therefore, a lack of correlation supports the interpretation that Fe and Zn are not fractionated by the same processes in the BPZP.

Having interpreted the heavy Zn isotopic signatures as a consequence of fluid alteration, and given that there is no significant variation in $\delta^{66}Zn$ in the remainder of the whole rock data, we focus only on the Fe isotopic variations in the BPZP in the following sections.

3.6.2 Fe isotopic fractionation during fractional crystallisation

As demonstrated above, the Fe isotopic variation in the BPZP is not significantly influenced by source heterogeneity, crustal contamination or fluid exsolution. We therefore infer that the observed trend in whole rock $\delta^{56}Fe$ is driven by fractional crystallisation. The variation in magma $\delta^{56}Fe$ during fractional crystallisation is dependent on the fractionation of Fe between the melt and the crystallising assemblage. Fractionation factors are influenced primarily by temperature, Fe oxidation state and coordination environment (Polyakov and Mineev, 2000; Polyakov et al., 2007; Dauphas et al., 2014; Sossi and O'Neill, 2017), with the nature and number of surrounding cations exerting a minor control (Rabin et al., 2021).

In order to evaluate quantitatively the isotopic fractionation resulting from fractional crystallisation, we require accurate knowledge of mineral-melt fractionation factors. For the BPZP, we specifically require values for hydrous phases like biotite and hornblende, which host the majority of the Fe in the system. Fractionation factors can be determined experimentally (e.g. Shahar et al., 2008; Sossi and O'Neill, 2017) or empirically from mineral separates (e.g. Sossi et al., 2012; Wu et al., 2017; Ye et al., 2020; Nie et al., 2021).

Alternatively, reduced partition function ratios (β factors) in relevant phases can be derived using spectroscopic techniques (e.g. Mössbauer and nuclear resonance inelastic X-ray scattering (NRIXS)), and used to theoretically determine bond force constants (<F>) and fractionation factors (e.g. Polyakov et al., 2007; Dauphas et al., 2012; Roskosz et al., 2015; Dauphas et al., 2014; Nie et al., 2021). In addition, β factors and force constants can also be obtained from first principle calculations based on density functional theory (e.g. Blanchard et al., 2009; Rabin et al., 2021).

The strength of our BPZP dataset is that we report isotopic variations in mineral separates across a single closed system differentiation sequence, for which temperature and fO_2 estimates already exist. These mineral separate data can be used to derive accurate and internally consistent mineral-mineral and mineral-melt fractionation factors, as outlined below. These are reflective of natural variation in T-X-fO_2 conditions in calc-alkaline settings and include the first measurements for biotite and hornblende across a differentiation sequence within a single cogenetic pluton.

3.6.3 Controls on Inter-Mineral Fractionation Factors in the BPZP

Inter-mineral fractionation factors are expressed in the form $\Delta^{56}Fe_{min\text{-}min} = A \times 10^6/T^2$. Hence, accurate crystallisation temperature estimates are critical, given the temperature dependence of fractionation ($\Delta \propto 1/T^2$; Urey, 1947; Schauble, 2004). Crystallisation temperatures can be difficult to define given the wide solidus-liquidus interval for granites, and difficulty in determining the true composition of coexisting liquids. Ickert et al. (2011) calculated zircon crystallisation temperatures between 750-850°C in all zones of the BPZP. However, given that zircon is one of the last phases to crystallise, these temperatures are not equivalent to the crystallisation temperatures of the Fe bearing primocrysts. We estimated primocryst crystallisation temperatures for the BPZP samples using multiple geothermometers (Table 3.3). These results indicate a 200 °C temperature range between the most primitive and evolved samples.

Biotite, hornblende and magnetite separates are divided into two textural groups: crystals with euhedral morphologies (primocrysts) assumed to crystallise from the main magma body, and anhedral crystals crystallised from trapped interstitial melt. Biotite, hornblende and magnetite are present as interstitial phases in the mafic cumulates, whereas they are primocrysts in samples with MgO <4.5 wt.%. This is important for understanding isotopic

fractionation because we assume that crystallisation of primocrysts will drive changes in the composition of the residual magma, whereas crystallisation of trapped interstitial melt will only drive local changes. Additionally, interstitial phases crystallised from isolated melt pockets may not have crystallised in chemical or isotopic equilibrium with each other, or the main magma body. Thus, mineral-mineral fractionation factors for interstitial phases may not reflect isotopic equilibrium.

Since primocryst biotite and hornblende have identical isotopic compositions in individual samples, and because biotite is present over a wider SiO_2 range than hornblende in the BPZP, we focus on variations in the magnetite-biotite fractionation factor ($\Delta^{56}Fe_{mag\text{-}bt}$) and assume this to be equal to $\Delta^{56}Fe_{mag\text{-}hbd}$. Within a cogenetic suite, variations in mineral-mineral fractionation factors can be controlled by variation in mineral composition, Fe coordination environment and/or temperature (e.g. Schauble, 2004). In the BPZP the $\Delta^{56}Fe_{mag\text{-}bt}$ increases with $Fe^{3+}/\Sigma Fe$ of biotite (values given in Wyborn, 1983), and this coincides with increasing SiO_2 content, increasing WR $Fe^{3+}/\Sigma Fe$ and decreasing crystallisation temperature (Figures 3.8 and 3.9).

Table 3.3. Temperature determinations for the BPZP. Calculations from [1]Putirka (2008, Eq. 27b at 1.5kbar); [2]Holland and Blundy (1994, Edenite-richerite thermometer at 1.5kbar); [3]Ludington (1978); [4]Wells (1977). Values using 3 and 4 are given in Wyborn (1983). All mineral chemistry is from Wyborn (1983). +A crystallisation temperature was then chosen by only considering estimates where phases were present as primocrysts. *Uncertainty estimates for the thermometers are given as quoted in the literature. Given the typical uncertainties for each thermometer, each chosen temperature has an uncertainty estimate of approximately ±50°C. Mineral abbreviations as in Figure 3.3.

Sample	Primocryst Mineralogy	Temperature Estimates (°C)				Chosen Temperature (°C)+
		Two-Feldspar[1]	Hornblende-Plagioclase[2]	Biotite-Apatite[3]	Two-Pyroxene[4]	
BP39	opx, cpx, plag		751		865	865
BP22	plag, cpx, bt, hbd	806	724			724
BP11	plag, bt, hbd, kfs, qtz	769	648	674		697
BP42	Plag, bt, qtz, kfs			695		695
Uncertainty (°C)*		± 30	± 35-40	n/a	± 70	

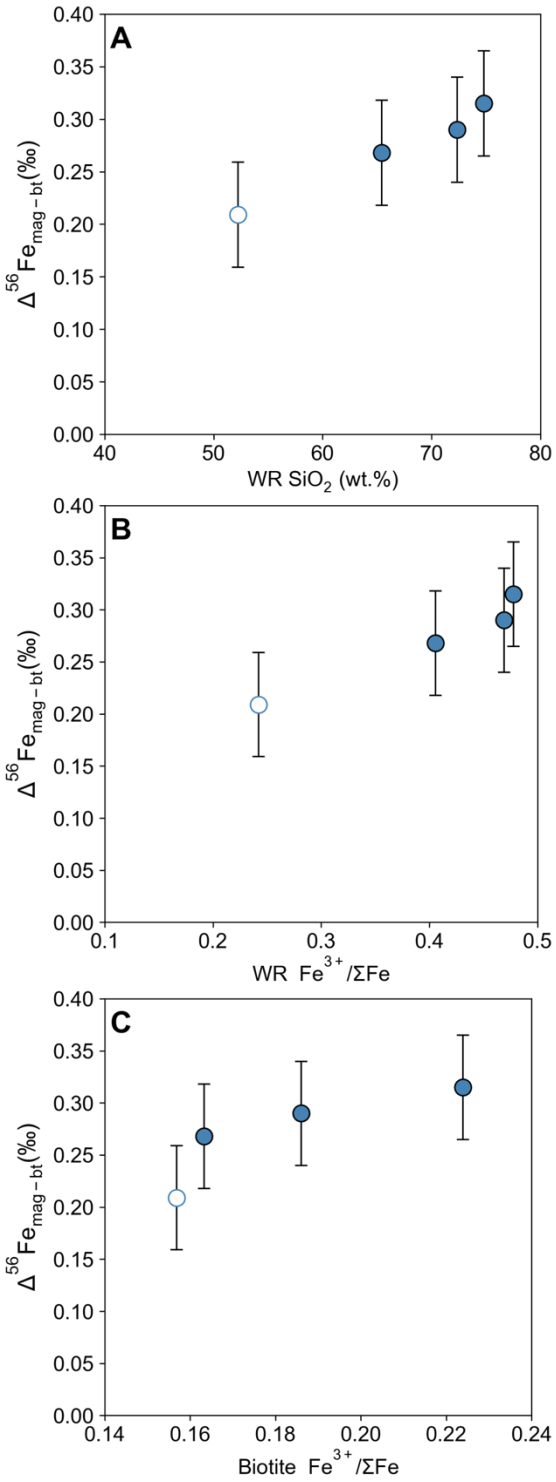

Figure 3.8. Variation in magnetite-biotite fractionation factors with (A) WR SiO_2, (B) WR $Fe^{3+}/\Sigma Fe$ and (C) biotite $Fe^{3+}/\Sigma Fe$. Shaded symbols are when biotite and magnetite are both primocrysts. Open symbols are when biotite and magnetite are present as interstitial phases. Errors are the long term analytical uncertainty of ±0.05‰ (2SD) from measurement of solution standards.

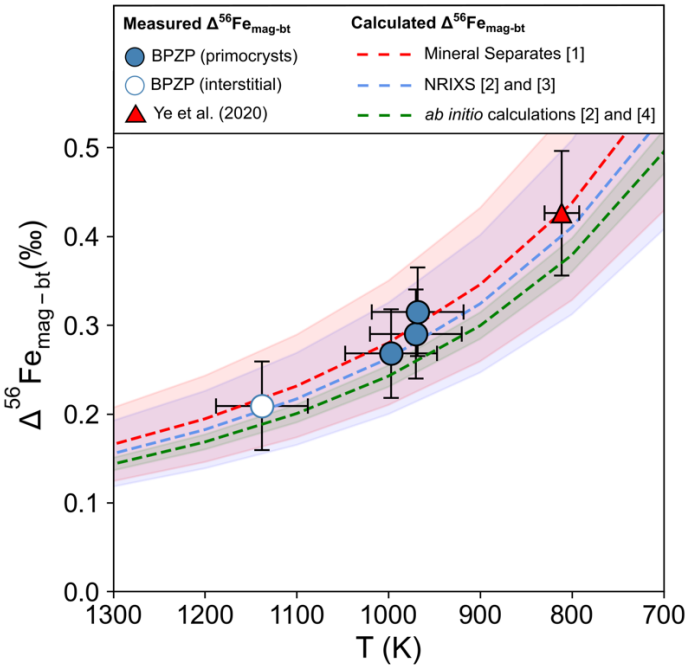

Figure 3.9. Measured $\Delta^{56}Fe_{mag-bt}$ for the BPZP samples against crystallisation temperature (K). Filled circles are for primocryst biotite and hornblende. Open circles are interstitial biotite and hornblende. Errors in $\Delta^{56}Fe_{mag-bt}$ are given as ±0.05‰, the long-term analytical uncertainty for Fe. Errors in T as ±50K, as discussed in the Table 3.3 caption. The red triangle shows the measured $\Delta^{56}Fe_{mag-bt}$ from a metamorphosed ironstone in Ye et al. (2020) [1]. The red line and shaded area show the relationship $\Delta^{56}Fe_{mag-bt} = 0.28 (\pm 0.07) \times 10^6/T^2$ from Ye et al. (2020) [1]. The blue line and shaded area show a theoretical estimate of $\Delta^{56}Fe_{mag-bt}$ calculated using NRIXS data, using Equation 1 after Dauphas et al. (2014). Values of 172 ± 16 N/m (Nie et al., 2021 [2]) and 264 ± 6 N/m (Roskosz et al., 2015 [3]) are used for the force constants of biotite and magnetite respectively, as discussed in the text. The green line and shaded area show a theoretical estimate of $\Delta^{56}Fe_{mag-bt}$ determined using values from *ab initio* calculations. Values of 207 N/m (Nie et al., 2021 [2]) and 292 N/m (Sossi and O'Neill, 2017 [4]) are used for the force constants of biotite and magnetite respectively, as discussed in the text. The error envelope considers a 5% error in the *ab initio* calculations.

Figure 3.9 shows the variation in $\Delta^{56}Fe_{mag-bt}$ of the BPZP samples with temperature, using the temperature estimates given in Table 3.3. Here we compare these values to temperature dependent biotite-magnetite fractionation factors derived by three different methods in previous studies. The red area represents the relationship derived by Ye et al. (2020) of $\Delta^{56}Fe_{mag-bt} = 0.28 (\pm 0.07) \times 10^6/T^2$, from measurements of biotite and magnetite separates in a banded iron formation metamorphosed at a temperature of 538 ± 39 °C. The blue and green lines show $\Delta^{56}Fe_{mag-bt}$ derived theoretically using bond force constants

(<F>) obtained from NRIXS and *ab initio* studies respectively, following the method of Dauphas et al. (2014) (Equation 3.1).

$$\Delta^{56}Fe_{A-B} = 2853 \times \frac{<F_A>-<F_B>}{T^2} \qquad [3.1]$$

Thus far, only Nie et al. (2021) have determined values for the bond force constant of biotite (<F_B>). These values are for the biotite Fe endmember annite, and were determined by both NRIXS (188 ± 16 N/m) and DFT calculations (207 N/m). There are several published values for the bond force constant of magnetite (<F_A>), ranging from 198 ± 15 N/m to 292 N/m (Polyakov et al., 2007; Mineev et al., 2007; Dauphas et al., 2012; Roskosz et al., 2015; Sossi and O'Neill, 2017; Rabin et al., 2021). The reason for this wide range of values is partly due to systematic variations between values derived using NRIXS, Mössbauer and *ab initio* calculations, as previously reported (e.g. Blanchard et al., 2009; Roskoz et al., 2015; Rabin et al., 2021). Hence, to accurately compare inter-mineral fractionation factors, it is more appropriate to use force constants determined by the same technique (Rabin et al., 2021), since it is the offset between, rather than the absolute force constant values, which will control the magnitude of Fe isotope fractionation.

The blue shaded area shows the $\Delta^{56}Fe_{mag\text{-}bt}$ calculated using force constants determined by NRIXS. For <F_B> in this equation, we correct the value of 188 ± 16 N/m (Nie et al., 2021) for the Fe^{3+} content on the BPZP biotite ($Fe^{3+}/\Sigma Fe \sim 0.18$; Wyborn, 1983) as described in Nie et al. (2021), giving a value of 172 ± 16N/m. For consistency, we also chose a value for magnetite (<F_A>) determined by NRIXS using the same analytical and processing procedures. Dauphas et al. (2012) and Polyakov et al. (2007) derived values of 230 ± 6 N/m and 228 ± 15 N/m respectively for the magnetite force constant. However, this data was collected over a smaller energy range than in more recent studies, which may have led to underestimation of <F> (Roskosz et al., 2015). Therefore, we chose to use the value of 264 ± 6 N/m for magnetite, derived from a regression of Al-bearing spinel (Roskosz et al., 2015).

The green shaded area shows $\Delta^{56}Fe_{mag\text{-}bt}$ calculated using force constants determined from *ab initio* calculations. Errors for force constants derived through *ab initio* calculations are thought to be on the order of ±5% (Rabin et al., 2021). The value of 207 N/m is used for

biotite (Nie et al., 2021). Choosing an appropriate value for magnetite is more difficult, because the two studies which give *ab initio* values for the force constants of magnetite and ulvöspinel use different calculation approaches, resulting in different force constant values (292 N/m and 207.5 N/m for magnetite and 215 N/m and 151.8 N/m for ulvöspinel respectively; Sossi and O'Neill, 2017 and Rabin et al., 2021). However, the force constant for magnetite of 207.5 N/m from Rabin et al. (2021) is identical to that of biotite from Nie et al. (2021). Given the large $\Delta^{56}Fe_{mag\text{-}bt}$ measured in the BPZP mineral separates, and difference in valence state and coordination environment between the two phases, it is unlikely that the force constants for biotite and magnetite are the same. Instead, this is likely an artifact of differences in the calculation method used. Hence, we chose to use the value of 292 N/m from Sossi and O'Neill (2017) for magnetite. To further support this choice, Nie et al. (2021) and Sossi and O'Neill (2017) calculate similar values for fayalite (178 N/m and 144 N/m) compared to the lower value of 99.6 N/m in Rabin et al. (2021), so the two studies are more directly comparable. We also chose to use values for magnetite rather than ulvöspinel, given the low Ti content of the BPZP magnetite (<0.7 wt.% TiO_2; Wyborn, 1983).

It is remarkable that an expression describing variation in $\Delta^{56}Fe_{mag\text{-}bt}$ with temperature, determined from ironstones metamorphosed <550 °C (red line), coincides with values for biotite and magnetite crystallising from the BPZP magma when extrapolated to temperatures >690°C. These samples have experienced vastly different P-T-X-fO_2 conditions throughout their formation; for example, the biotite separates have different $Fe^{3+}/\Sigma Fe$ content: 0.13-0.22 for the BPZP (Wyborn, 1983) and 0.26-0.31 for the metamorphosed ironstone (Ye et al., 2020). The fractionation factors obtained from NRIXS data and *ab initio* calculations (blue and green lines) also show good agreement with the BPZP data. These findings demonstrate that temperature has a critical control on inter-mineral fractionation factors, in addition to variations in chemistry and/or fO_2. This highlights that accurate temperature estimates are essential when modelling Fe isotopic fractionation, especially in plutonic settings where temperature variations can be large.

3.7 Modelling Fe isotopic variations in plutonic settings

In this section, we use our petrographic observations and mineral separate data to produce accurate and internally consistent models of Fe isotopic fractionation during fractional crystallisation of the BPZP. The whole rock samples with MgO > 4.5 wt.% consist of accumulated crystals and variable proportions of trapped interstitial melt, thus do not approximate a true melt composition. Hence, we chose to model only the $\delta^{56}Fe$ evolution of the BPZP below 4.5 wt.% MgO. From this point, whole rock isotopic composition approximates evolving magma composition. The mineral-mineral fractionation factors defined above are used to mathematically derive mineral-melt fractionation factors ($\Delta^{56}Fe_{min\text{-}melt}$). Fractional crystallisation is modelled incrementally using the Rayleigh equation (Equation 3.2, after Sossi et al. (2012)) as the amount of residual Fe (*f*Fe) in the system decreases:

$$\delta^{56}Fe = \delta^{56}Fe_{initial} + (\Delta^{56}Fe_{min\text{-}melt} \times \ln fFe) \qquad [3.2]$$

For this calculation, the Fe isotopic composition of the parent magma ($\delta^{56}Fe_{initial}$) must be known, and a bulk mineral-melt fractionation factor ($\Delta^{56}Fe_{min\text{-}melt}$) and fraction of Fe remaining (*f*Fe) estimated for each model step. A series of models was produced to demonstrate how variations in modelling approaches, specifically estimates of mineral-melt fractionation factors, predict vastly different $\delta^{56}Fe$ trends in the residual magma.

3.7.1 Step 1: Estimating initial magma composition ($\delta^{56}Fe_{initial}$)

In lavas, the $\delta^{56}Fe$ of the most mafic sample is typically used to represent the isotopic composition of the parental magma ($\delta^{56}Fe_{initial}$). However, in plutonic settings like the BPZP, the most mafic samples are often cumulates (e.g. Chappell and Wyborn, 2004). The average $\delta^{56}Fe$ value of the mafic cumulates is 0.065‰. However, this value is most likely to reflect accumulation of isotopically light pyroxene, rather than reflect a primary melt composition. We therefore take the parental magma to be the most mafic granodiorite containing both primocryst biotite and hornblende (BP26; $\delta^{56}Fe$ = 0.092‰), as this is assumed to be more representative of a liquid composition. Alternatively, if we assume that the interstitial biotite and hornblende in the mafic cumulates crystallised from trapped interstitial melt, it would also be appropriate to use the average isotopic

composition of these interstitial phases (0.107 ± 0.030‰) as the parental melt composition.

3.7.2 Step 2: Estimating fraction of Fe remaining (*f*Fe)

To estimate the fraction of Fe remaining (*f*Fe), we calculate the Fe content of the evolving magma (C) using Equation 3.3, where C_0 is the initial FeO_{tot} concentration, F is the melt fraction, and D is the bulk mineral-melt partition coefficient for Fe.

$$C = C_0 \times F^{D-1} \qquad [3.3]$$

The bulk partition coefficient for Fe was defined by modelling the major element trends for the BPZP whole rocks (e.g. MgO and FeO_{tot}) and selecting a bulk partition coefficient value which best reproduces the whole rock compositions (D_{MgO} =2 and D_{FeOtot} = 1.8). The model was carried out over twenty steps, as F was varied in increments of 0.05. The fraction of Fe remaining at each model step is then calculated by *f*(Fe) = (F x C)/C_0.

3.7.3 Step 3: Calculating mineral-melt fractionation factors

Inter-mineral fractionation factors determined directly from measurements of mineral separates (Section 3.6.3) are not directly used when modelling Fe isotopic evolution of a magma. Instead, mineral-melt fractionation factors are necessary to describe isotopic fractionation between the crystals and residual melt. Temperature dependent mineral-melt fractionation factors can be estimated using the Rayleigh equation (Equation 3.2), by iteratively selecting the $\Delta^{56}Fe_{min\text{-}melt}$ value which best fits the data (e.g. Sossi et al., 2012). Many studies use this method to estimate the bulk $\Delta^{56}Fe_{min\text{-}melt}$ which describes the entire isotopic evolution of the system rather than estimate mineral-melt fractionation factors for specific phases. For the BPZP, a bulk $\Delta^{56}Fe_{min\text{-}melt}$ of approximately -0.03‰ can describe the Fe isotopic evolution of the residual melt until 2% Fe remains (Figure 3.10). However, this value does not capture the true variations in the mineral assemblage during the fractionation sequence.

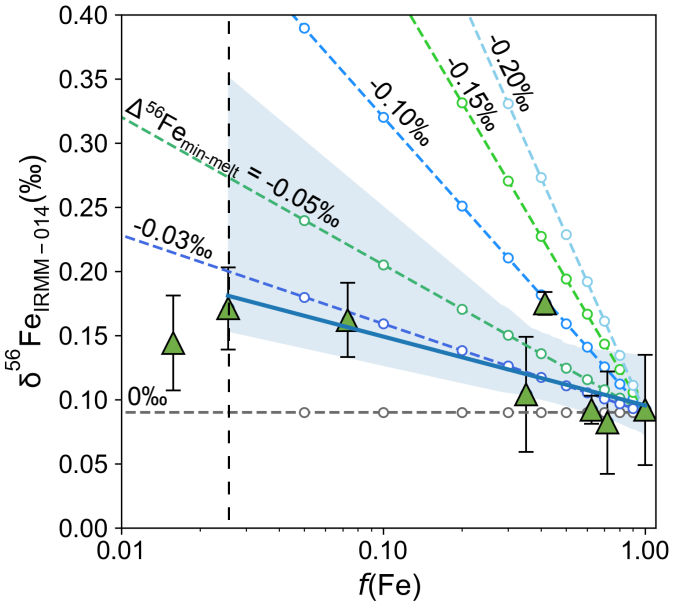

Figure 3.10. Change in $\delta^{56}Fe$ of a magma undergoing fractional crystallisation (dashed lines), modelled using the Rayleigh equation ($\delta^{56}Fe = \delta^{56}Fe_i + (\Delta^{56}Fe_{min\text{-}melt} \times \ln f(Fe))$ at constant $\Delta^{56}Fe_{min\text{-}melt}$. BP26 was used as the starting magma composition. For the BPZP whole rock data (green triangles), *f*(Fe) is calculated based on changing MgO and FeO_{tot} content as described in the text. Previous studies have used the variation in concentration of incompatible elements (e.g. Rb, Th, U) to estimate F. However, concentrations of incompatible elements will also vary depending on the amount of trapped interstitial melt in the samples, so this method was not used. The blue shaded area is a weighted linear regression of the BPZP data from the start of the calculation until 2% Fe remains. This shows that the isotopic evolution for this part of the fractionation sequence can be described by a bulk $\Delta^{56}Fe_{min\text{-}melt}$ of approximately -0.03‰.

However, a strength of the BPZP data set is that temperature dependent fractionation factors for all the individual phases in the fractionating assemblage can be calculated using the mineral separate data. Fractionation factors for each mineral are expressed in the form $\Delta^{56}Fe_{min\text{-}melt} = A \times 10^6/T^2$.

The bulk mineral-melt fractionation factor can be expressed by weighting (W) the fractionation factors for each mineral phase (p) by their Fe content ($[FeO_{tot}]$) and modal abundance (M).

$$\text{Bulk } \Delta^{56}Fe_{min\text{-}melt} = \Sigma(\Delta^{56}Fe^{p}_{min\text{-}melt} \times W^{p}) \qquad [3.4]$$

$$\text{where } W^{p} = (M^{p} \times [FeO_{tot}]^{p})/\Sigma(M^{p} \times [FeO_{tot}]^{p}) \qquad [3.5]$$

For the BPZP, this gives the expression:

$$\text{Bulk } \Delta^{56}Fe_{min\text{-}melt} = (\Delta^{56}Fe_{mag\text{-}melt} \times W_{mag}) + (\Delta^{56}Fe_{bt\text{-}melt} \times W_{bt}) + (\Delta^{56}Fe_{hbd\text{-}melt} \times W_{hbd}) \quad [3.6]$$

Biotite and hornblende have identical isotopic composition to each other across the differentiation sequence, so $\Delta^{56}Fe_{bt\text{-}melt} = \Delta^{56}Fe_{hbd\text{-}melt}$.

$$\text{Bulk } \Delta^{56}Fe_{min\text{-}melt} = (\Delta^{56}Fe_{mag\text{-}melt} \times W_{mag}) + (\Delta^{56}Fe_{bt\text{-}melt} \times W_{bt}) + (\Delta^{56}Fe_{bt\text{-}melt} \times W_{hbd}) \quad [3.7]$$

The expression can therefore be expressed in terms of the relative weighting of silicate ($W_{sil} = W_{bt} + W_{hbd}$) and oxide phases ($W_{mag}$).

$$\text{Bulk } \Delta^{56}Fe_{min\text{-}melt} = (\Delta^{56}Fe_{mag\text{-}melt} \times W_{mag}) + (\Delta^{56}Fe_{bt\text{-}melt} \times W_{sil}) \quad [3.8]$$

For the BPZP, considerations of the modal abundances and FeO_{tot} concentrations of the fractionating assemblage show that $W_{sil} \sim 0.72$ and $W_{mag} \sim 0.28$ until 20% Fe remains. Therefore, $W_{sil} \sim 2.6 \times W_{mag}$.

$$\text{Bulk } \Delta^{56}Fe_{min\text{-}melt} = W_{mag} (\Delta^{56}Fe_{mag\text{-}melt} + 2.6\Delta^{56}Fe_{bt\text{-}melt}) \quad [3.9]$$

Substituting in the Bulk $\Delta^{56}Fe$ value of -0.03‰ obtained from Equation 3.2 (Figure 3.10), and the W_{mag} value of 0.28 gives the equation:

$$-0.107 = \Delta^{56}Fe_{mag\text{-}melt} + 2.6\Delta^{56}Fe_{bt\text{-}melt} \quad [3.10]$$

A second equation can be generated using the mineral separate data. Since at equilibrium, $\Delta_{a\text{-}c} = \Delta_{a\text{-}b} + \Delta_{b\text{-}c}$, then for the BPZP we can express the biotite-magnetite fractionation factor as:

$$\Delta^{56}Fe_{mag\text{-}bt} = \Delta^{56}Fe_{mag\text{-}melt} + \Delta^{56}Fe_{melt\text{-}bt} \quad [3.11]$$

This can be rearranged to:

$$\Delta^{56}Fe_{mag\text{-}bt} = \Delta^{56}Fe_{mag\text{-}melt} - \Delta^{56}Fe_{bt\text{-}melt} \quad [3.12]$$

Thus, using the magnetite-biotite fractionation factors at known temperatures (Figure 3.9), we can then solve the values of $\Delta^{56}Fe_{mag\text{-}melt}$ and $\Delta^{56}Fe_{bt\text{-}melt}$ simultaneously, using

Equations 3.10 and 3.12. The following values are calculated using the $\Delta^{56}Fe_{mag\text{-}bt}$ values for BP22, BP11 and BP42. A conservative error estimate is ±0.03‰, which is the average of the 2SD values reported for whole rock and mineral separate measurements.

- $\Delta^{56}Fe_{bt/hbd\text{-}melt} = -0.12 \times 10^6/T^2$ [3.13]
- $\Delta^{56}Fe_{mag\text{-}melt} = +0.17 \times 10^6/T^2$ [3.14]

The fractionation factors derived here do not explicitly consider the possible change in the bond force constant of ferrous iron in high silica melts (Dauphas et al., 2014), or variation in fractionation factor with mineral and melt chemistry. However, they are representative of T-fO_2 conditions in a calc-alkaline suite.

The only silicate mineral-melt fractionation factors for comparison are those from Sossi et al. (2012) for the tholeiitic Red Hills plutonic suite. Sossi et al. (2012) give a $\Delta^{56}Fe_{px\text{-}melt}$ value of $-0.17 \times 10^6/T^2$. The biotite-melt and hornblende-melt fractionation factors derived here are smaller ($\Delta^{56}Fe_{bt/hbd\text{-}melt} = -0.12 \times 10^6/T^2$). This supports theoretical considerations of valence and coordination environment. Biotite, hornblende and pyroxene all contain Fe in VI-fold coordination. However, the hydrous silicates have higher $Fe^{3+}/\Sigma Fe$. Therefore, Fe-O bonds should be stronger in hydrous silicates than pyroxenes, and thus there should be a smaller isotopic offset between hydrous silicates and coexisting melt at equilibrium. Additionally, the $\Delta^{56}Fe_{bt/hbd\text{-}melt}$ expression is similar to a $\Delta^{56}Fe_{bt\text{-}melt}$ value of -0.1‰ estimated from measurements of biotite separates and whole rock powders in Du et al. (2017).

Perhaps surprisingly, the $\Delta^{56}Fe_{mag\text{-}melt}$ value calculated for the BPZP is within error of the value of Sossi et al. (2012) for the Red Hills suite ($+0.13 \times 10^6/T^2$). Magma fO_2 in the calc-alkaline BPZP suite is higher than in the tholeiitic Red Hills suite (Wyborn, 1983; Sossi et al., 2012). Theoretically, differences in melt $Fe^{3+}/\Sigma Fe$ and subsequent variation in primary magnetite composition should lead to variation in $\Delta^{56}Fe_{mag\text{-}melt}$ values between the BPZP and Red Hills. The fact that $\Delta^{56}Fe_{mag\text{-}melt}$ values are within error in both suites suggest that bonding environment and temperature exert a more dominant control on Fe isotopic fractionation factors than melt redox state.

3.7.4 Step 4: Deriving a bulk mineral-melt fractionation factor ($\Delta^{56}Fe_{min\text{-}melt}$)

Deriving a bulk mineral-melt fractionation factor ($\Delta^{56}Fe_{min\text{-}melt}$, Equation 3.4) requires knowledge of the fractionating mineral assemblage. The variation in modal proportions of the fractionating assemblage over the differentiation sequence was approximated using a linear regression of the modal abundance of primocryst phases against sample MgO content. A bulk $\Delta^{56}Fe_{min\text{-}melt}$ value is then derived at each model step by multiplying the mineral-melt fractionation factors by a Fe weighting factor for each phase (Equations 3.4 and 3.5). We use the mineral-melt fractionation factors calculated above for biotite, hornblende and magnetite, and the value of $\Delta^{56}Fe_{px\text{-}melt} = -0.17 \times 10^6/T^2$ for pyroxene, from Sossi et al. (2012). Temperature estimates were calculated based on a linear regression of the temperature estimates for the BPZP samples (Table 3.3) against MgO content.

The parameters discussed above were used to model the $\delta^{56}Fe$ of the residual magma using the Rayleigh equation (Equation 3.2). Calculated magma $\delta^{56}Fe$ is shown by the black solid line in Figure 3.11. The blue shaded area shows the range in magma $\delta^{56}Fe$ when uncertainties of ±0.03‰ for the mineral-melt fractionation factors are considered. We consider this level of uncertainty to be intrinsic to such modelling and emphasise that errors in fractionation factors will always be amplified in the most silicic samples.

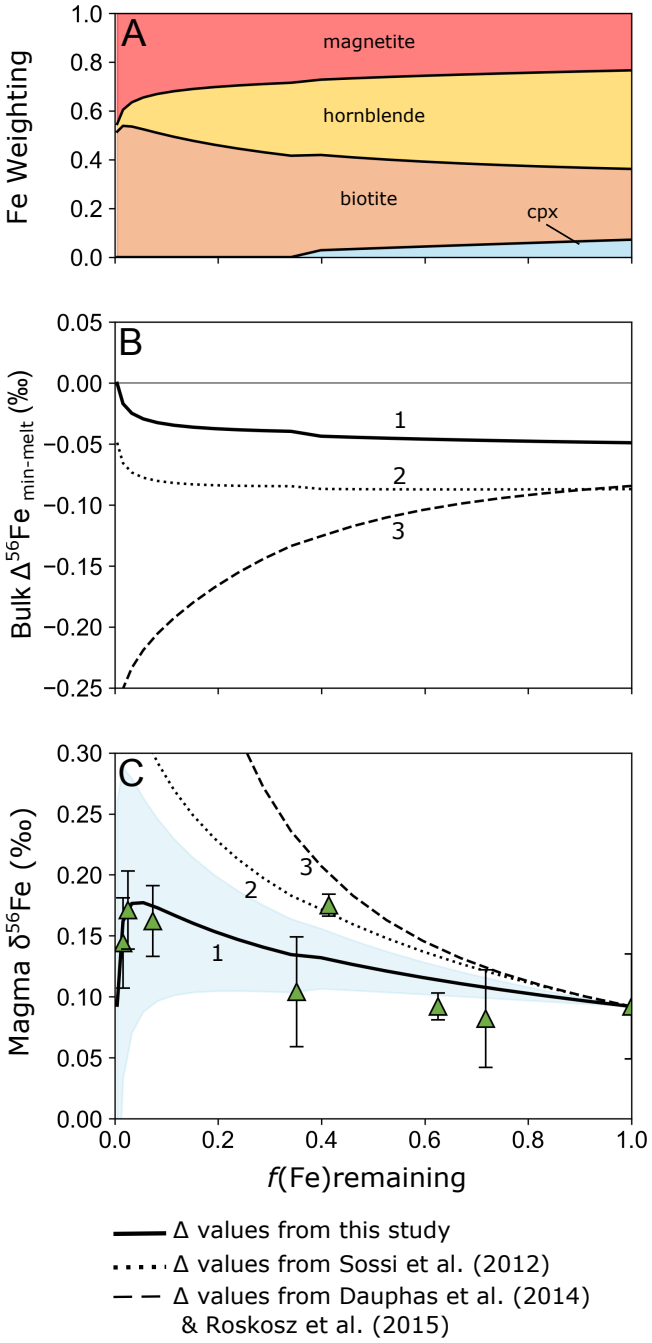

Figure 3.11. Determinations of modal abundances (A), bulk $\Delta^{56}Fe_{min\text{-}melt}$ (B), and resulting magma $\delta^{56}Fe$ (C) from three Rayleigh models. Green triangles show the isotopic composition of the BPZP WR samples. *f*(Fe) is calculated as described in the text. The blue error envelope shows magma $\delta^{56}Fe$ considering an error of ±0.03‰ on the fractionation factor expressions.

3.7.5 Model Comparisons

Several studies use the thermodynamic modelling software Rhyolite-MELTS (Gualda et al., 2012; Ghiorso and Gualda, 2015) to model variation in Fe isotopic composition during fractional crystallisation (e.g. Dauphas et al., 2014; Foden et al., 2015; He et al., 2017; Xia et al., 2017). However, MELTS cannot accurately reproduce the stability of hydrous silicates like biotite and hornblende in calc-alkaline magmas (Gualda et al., 2012). Given that these are the main Fe bearing silicate phases in the BPZP and similar systems, the evolving magma chemistry and Fe isotopic composition cannot be accurately modelled this way (See Figures 3.S3 and 3.S4). We therefore recommend that for I-type granites, modal abundances of the fractionating assemblage should be determined from petrographic observations, considering only the modal proportions of primocrysts and not interstitial phases. However, the choice of selected fractionation factors remains important.

Model 1 (Figure 3.11) uses the fractionation factors calculated in this study (Equations 3.13 and 3.14). For the first part of the differentiation sequence, isotopically light phases like biotite and hornblende host the majority of Fe in the system, causing an increase in the $\delta^{56}Fe$ of the evolving magma. However, below 1 wt.% MgO, when fFe < 0.1, magnetite becomes the dominant Fe host and causes a decrease in $\delta^{56}Fe$ of the most silicic magma.

In contrast, using fractionation factors for the tholeiitic Red Hills complex ($\Delta^{56}Fe_{mag\text{-}melt}$ = +0.13 x $10^6/T^2$ and $\Delta^{56}Fe_{min\text{-}melt}$ = -0.17 x $10^6/T^2$ for all silicate phases; Sossi et al., 2012), generates bulk $\Delta^{56}Fe_{min\text{-}melt}$ values of approximately -0.09‰ (Model 2; Figure 3.11). The calculated increase in magma $\delta^{56}Fe$ in Model 2 is therefore larger than Model 1 and does not match the BPZP whole rock data. This reinforces the notion that fractionation factors for anhydrous silicates from a tholeiitic suite are not applicable to calc-alkaline settings where hydrous phases like biotite and hornblende are present.

Finally, we calculated fractionation factors using bond force constants (Model 3; Figure 3.11). An average force constant (<F>) was calculated for the melt and minerals at each step of the model, following the method in Dauphas et al. (2014). Given the scarcity of force constant measurements for biotite and hornblende, <F> values for silicate minerals

were calculated as in Dauphas et al. (2014): a force constant for each mineral was calculated by weighting the force constants for ferrous (197N/m) and ferric (255N/m) Fe in olivine and glasses by mineral $Fe^{3+}/\Sigma Fe$. For example, biotite with a $Fe^{3+}/\Sigma Fe$ of 0.18 has a calculated <F> of 207N/m. For magnetite, a force constant of 264 ± 6 N/m was adopted, the value determined by Roskosz et al. (2015). The bulk force constant for the minerals ($<F_{min}>$) was calculated by multiplying the force constants for each phase by their Fe weighting (Equation 3.5). For the melt, the force constant for Fe^{2+} was calculated from $F^{Fe2+}=199+41/(1+e^{34-SiO2/2})$, and Fe^{3+} assigned a value of 351N/m (Dauphas et al., 2014). $<F_{melt}>$ was then calculated by weighting these force constants by the $Fe^{3+}/\Sigma Fe$ of the melt. Bulk $\Delta^{56}Fe_{min\text{-}melt}$ was then calculated using Equation 3.1. The bulk $\Delta^{56}Fe_{min\text{-}melt}$ values calculated in this way (Model 3) are always negative. This is because the force constant estimates for Fe-O bonds in the melt (351N/m for Fe^{3+} and between 200-240 N/m for Fe^{2+}) are always larger than in minerals. The bulk mineral-melt fractionation factor becomes more negative as the bond force constant of Fe^{2+} increases at high silica content (Dauphas et al., 2014), which drives an increase in $\delta^{56}Fe$ of the melt at more felsic compositions. However, the BPZP whole rock samples do not show this magnitude of $\delta^{56}Fe$ increase during differentiation. This suggests that there are uncertainties with extrapolating bond force constants measured in orthosilicates and glasses (Dauphas et al., 2014) to Fe^{3+} bearing silicates with more complex structures, like biotite and hornblende. This is demonstrated by the discrepancy between the bond force constant measured directly in biotite Fe endmember annite by NRIXS (188±16N/m at $Fe^{3+}/\Sigma Fe = 0.32$; Nie et al., 2021) and that calculated based on biotite $Fe^{3+}/\Sigma Fe$ content as above (216N/m at $Fe^{3+}/\Sigma Fe = 0.32$). Additionally, this approach also assumes that force constants only vary with mineral $Fe^{3+}/\Sigma Fe$. However, variation in mineral composition and/or subsequent changes in Fe-O bond length will also affect force constants (Roskosz et al., 2015; Sossi and O'Neill, 2017; Rabin et al., 2021). Therefore, further work is needed to define force constants in hydrous silicates in order to accurately model fractional crystallisation in hydrous, I-type magmas in this way.

We conclude that there are several requirements for accurate modelling of Fe isotopic evolution in co-genetic plutonic settings, which differ from modelling of co-genetic extrusive lavas.

1. Accurate modal abundances. Only the modal abundance of primocryst phases crystallising from the main magma body will influence magma $\delta^{56}Fe$ and Fe content. Interstitial phases crystallised from trapped melt will influence bulk rock $\delta^{56}Fe$ but not magma $\delta^{56}Fe$ evolution. Modal abundance estimates from observations of samples are more accurate than those estimated from Rhyolite-MELTS, especially in I-type systems.
2. Accurate estimation of parental melt composition. In contrast to extrusive suites, the most mafic samples in plutonic bodies are often cumulates and do not reflect a true liquid or parental melt composition, so should not be used as such.
3. Temperature dependent mineral-melt fractionation factors. The use of temperature dependent fractionation factors is vital in plutonic settings where temperature variations can be large. It must also be considered that fractionation factors derived from *ab initio* calculations or NRIXS studies are not necessarily directly applicable to the specific chemistry and $Fe^{3+}/\Sigma Fe$ of the minerals in the suite being studied. Therefore, empirically derived fractionation factors at similar X-fO_2 conditions may be more appropriate.

Rayleigh models like those above assume perfect closed system fractional crystallisation. Although in practice the differentiation processes occurring in plutonic settings are more complex (e.g. Janoušek and Moyen, 2020), this straightforward approach can accurately reproduce the Fe isotopic trends in the BPZP.

3.8 Implications

I-type granitoids like the BPZP are the most abundant granite type in the upper continental crust (e.g. Kemp et al., 2007). In the BPZP, whole rock $\delta^{56}Fe$ is controlled by the balance between crystallisation of isotopically light silicates (biotite and hornblende) and isotopically heavy magnetite. Crystallisation drives a muted increase in $\delta^{56}Fe$ with differentiation, as demonstrated mathematically using the Rayleigh equation. Hence, this is the extent of Fe isotopic fractionation to be expected in a simple calc-alkaline system undergoing fractional crystallisation in the absence of additional processes (i.e. crustal contamination, fluid alteration, addition of new batches of magma). The restricted range

in whole rock $\delta^{56}Fe$ observed and modelled in the BPZP matches the observation that I-type granitic rocks globally have low $\delta^{56}Fe$ values <0.2‰ (Foden et al., 2015).

Although the BPZP is interpreted to form by progressive fractional crystallisation of a liquid body of magma, it is likely that such liquid-dominant bodies of magma are rare in the crust. Instead, magma reservoirs are recognised to be "mushy" regions composed of non-eruptible crystal frameworks and interstitial melt (Bachmann and Bergantz, 2004; Hildreth, 2004). There remain questions surrounding the exact crystal-melt segregation and differentiation processes (e.g. Bachmann and Bergantz, 2004; Holness, 2018) and temperature regimes (e.g. Barboni et al., 2016; Rubin et al., 2017) in these mushes. However, if we consider that the larger, more complex mush bodies are formed of smaller plutonic units where magmatic processes are similar to the BPZP, this study provides a necessary baseline understanding of the behaviour of Fe isotopes to enable future investigation of more complex mushes.

A key finding from this study is that the $\Delta^{56}Fe_{mag\text{-}bt}$ values measured in the BPZP at temperatures >690 °C show close agreement with temperature dependent expressions derived from NRIXS and *ab initio* data (Figure 3.9). Additionally, the $\Delta^{56}Fe_{mag\text{-}bt}$ values measured in the BPZP match temperature dependent expressions derived from mineral separates in a banded iron formation metamorphosed at 538°C (Ye et al., 2020; Figure 3.9). Hence, the BPZP study demonstrates the validity of these expressions when extended to higher temperatures. Mineral separates from a metamorphosed ironstone and an I-type granite will have experienced different P-T-X-fO_2 conditions during crystallisation. Therefore, the agreement between $\Delta^{56}Fe_{mag\text{-}bt}$ values from two vastly different geological settings suggests that inter-mineral fractionation factors between the same mineral pair in different samples is overwhelmingly controlled by temperature, rather than variations in chemical composition and/or fO_2.

The similarity between inter-mineral fractionation factors from a range of geological settings, temperatures, compositions and fO_2 conditions demonstrates the wide applicability of Fe isotopes to addressing problems in igneous geology. Specifically, in crystal mushes, inter-mineral fractionation factors between phases at equilibrium could be used to provide information about magma storage temperatures. This is especially useful in plutonic settings because of the lack of appropriate geothermometers when

coexisting liquid composition cannot be easily determined (e.g. Putirka, 2016). If crystallisation temperature is known, inter-mineral fractionation factors can also be used to test for isotopic equilibrium between phases. Although the BPZP mineral separates obtain Fe isotopic equilibrium during fractional crystallisation, differentiation processes in larger mush bodies are thought to be more complex. Mush regions are often open systems, and if processes such as magma recharge, mixing, reactive porous flow and crustal assimilation occur, crystal scale isotopic disequilibrium may be expected. Therefore, the application of stable isotopic compositions to the investigation of more complex mushy systems to determine features like the range of storage temperatures and the extent of isotopic (dis)equilibrium during differentiation is a promising avenue of future research.

As Fe is present in multiple redox states, previous studies have investigated the potential link between Fe isotopic composition of mineral separates and/or whole rock powders and magma fO_2 during magmatic differentiation (e.g. Williams et al., 2005; Sossi et al., 2012; Foden et al., 2015). Although magma fO_2 will control the fractionating mineral assemblage, leading to distinct trends in whole rock $\delta^{56}Fe$ for I-, A- and S-type granites (Foden et al., 2015), this study has demonstrated that variation in mineral $Fe^{3+}/\Sigma Fe$ does not have a resolvable effect on Fe isotope fractionation factors between specific mineral pairs, suggesting limited use of Fe isotopes in mineral phases as a direct fO_2 proxy. A problem with Fe is that it is present as a major element in all silicate and oxide phases, and Fe isotopes are fractionated by a multitude of processes. However, the isotopic composition of trace elements concentrated in only one mineral may have potential as fO_2 proxies. A possibility is vanadium isotopes, where experimental studies suggest relationship between magnetite-melt V fractionation factors and magma fO_2 (Sossi et al., 2018b). Therefore, combining a well-studied isotope system of a major element like Fe with isotopes of a trace element like V may provide further understanding about P-T-X-fO_2 conditions during magmatic differentiation.

3.9 Conclusions

The Boggy Plain Zoned Pluton is a useful natural system for investigating Fe isotope fractionation during closed system fractional crystallisation of an I-type magma. This is the first time that the Fe isotopic composition of mineral separates have been measured

in a closed system I-type suite. This has permitted the derivation of new mineral-melt fractionation factors which are representative of the X-T-fO_2 conditions in calc-alkaline settings.

1. In the BPZP, whole rock $\delta^{56}Fe$ increases from 0.038‰ to 0.171‰ with decreasing MgO content. Whole rock $\delta^{66}Zn$ is not affected by fractional crystallisation, but fluid alteration may cause the heavy $\delta^{66}Zn$ signal observed in aplite samples. A lack of coupling between $\delta^{56}Fe$ and $\delta^{66}Zn$ strongly suggests that Fe isotopes are not fractionated by fluid exsolution, thus Fe isotopic variation is dominantly controlled by fractional crystallisation.
2. Minerals show heavy Fe isotope enrichment in the order magnetite > biotite = hornblende > orthopyroxene. Mineral separates display inter-mineral Fe isotopic equilibrium. Inter-mineral fractionation factors match previous empirical and theoretical estimates from a range of P-T-X-fO_2 conditions.
3. Mineral separate data can be used to derive temperature dependent fractionation factors for magnetite and hydrous silicates in calc-alkaline settings: $\Delta^{56}Fe_{mag\text{-}bt} = 0.28x10^6/T^2$, $\Delta^{56}Fe_{mag\text{-}melt} = 0.17x10^6/T^2$ and $\Delta^{56}Fe_{bt/hbd\text{-}melt} = -0.12x10^6/T^2$. These are used to construct internally consistent, temperature dependent models of Fe isotopic fractionation during fractional crystallisation of a calc-alkaline magma.
4. The strong temperature dependence on equilibrium Fe isotopic fractionation highlights future avenues of research for the use of Fe isotopes in investigating petrogenetic processes and physical conditions in crystal mush bodies.

Chapter 3 Appendix

An electronic appendix of supplementary material was included when this chapter was submitted as a paper. A modified version of this appendix is included below. Petrographic descriptions and scans of the thin sections in plane polarized light are included in the thesis Electronic Appendices 2 and 3.

3.A1 Neodymium Isotopic Analyses

3.A1.1 Methodology

Chemical separation of Nd was conducted at the Arthur Holmes Isotope Geology Laboratory, Durham University, following the ion exchange column chromatography procedure described in Chapter 2 Section 2.6.1. Neodymium isotopic measurements were made on a Neptune MC-ICP-MS following the method described in Chapter 2 Section 2.6.2. All isotopic ratios are expressed relative to the average $^{143}Nd/^{144}Nd$ ratio of the JNdi standard measured throughout the session, 0.512104 ± 0.000014 (n=8, 2SD). The BCR-2 standard gave a $^{143}Nd/^{144}Nd$ of 0.512633 ± 0.000012 (2SE), which agrees extremely well with published values (e.g. Weis et al., 2006; Jweda et al., 2016) and is identical to the average of all published values (minus two obvious outliers) reported on the GeoRem database.

Present and initial epsilon values (εNd and εNd_i) were calculated using values of 6.54 x 10^{-12} for $\lambda^{147}Sm$ (Begemann et al., 2001) and values of 0.512630 and 0.1960 for the $^{143}Nd/^{144}Nd$ and $^{147}Sm/^{144}Nd$ of the chondritic uniform reservoir (CHUR) (Bouvier et al., 2008). The full age correction calculations are shown in Electronic Appendix 1.

3.A1.2 Results

The measured εNd values and age corrected εNd_i values for the BPZP whole rock samples are shown in Table 3.S1 and Figure 3.S1. The Sm and Nd concentrations used for the age correction calculations are given in Table 3.S1. These concentrations were determined using Neutron Activation Analysis (Wyborn, 1983). However, these measurements were made on different whole rock powders than used in this study. Assuming a ±10% uncertainty in Sm and Nd concentrations due to both the analytical uncertainties associated with the Neutron Activation Analysis measurements and variations in Sm and Nd concentrations between powder aliquots, an error estimate of ±0.60 is given for the calculated εNd_i values, as shown by the error bars on Figure 3.S1.

There is a <2 ε unit variation in the initial Nd isotopic composition of the BPZP samples, assuming a crystallisation age of 417.2Ma (Ickert et al., 2011). The εNd values measured here are similar to those measured on a different set of samples by Ickert (2010) (Figure

3.S1). However, there is an offset between the age corrected εNd_i values calculated in each study. The studies measure whole rock powders created from different whole rock samples, so this offset could be due to heterogeneity in sample Sm and Nd concentrations and isotopic composition.

There is a slight positive correlation between MgO content and εNd_i (Figure 3.S1). This suggests that crustal material may have been assimilated into either the mantle source of the BPZP magma, or into the magma reservoir itself during fractional crystallisation. A possible assimilant is the Ordovician-Silurian age sedimentary country rock surrounding the BPZP (Wyborn, 1983). Similar sedimentary rocks in the region have εNd values from -9.5 to -10.5 (McCulloch and Woodhead, 1993). Simple AFC models demonstrate that approximately 10% assimilation of this sedimentary material can account for these isotopic compositions (Ickert, 2010). However, the magma then appears to evolve via closed system fractional crystallisation without further assimilation. Therefore, it is unlikely crustal assimilation is the cause of the variation in Fe-Zn isotopic compositions within the BPZP.

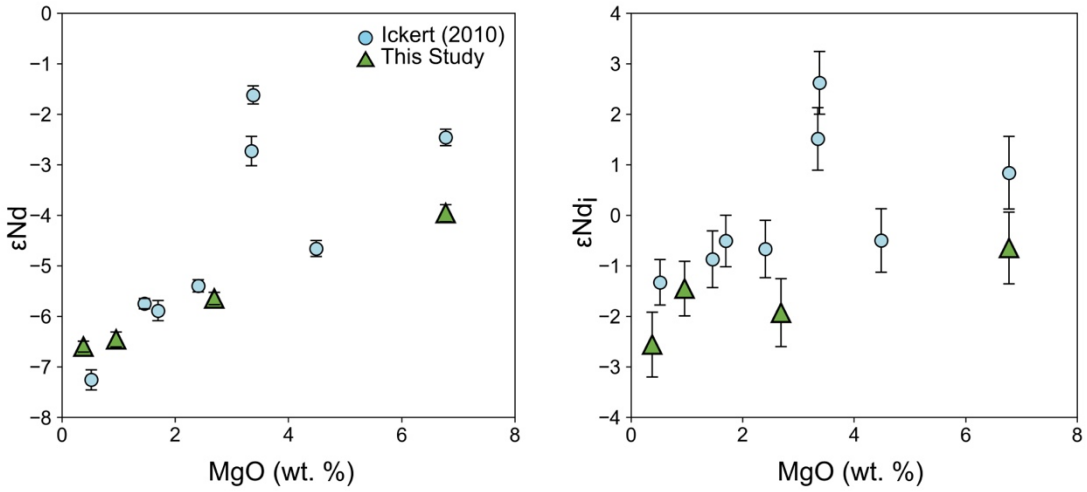

Figure 3.S1. Measured εNd and age corrected εNd_i values against WR MgO content for the BPZP whole rock samples from this study (green triangles) and Ickert (2010) (blue circles). Errors in εNd are 2SE of the measured $^{143}Nd/^{144}Nd$ ratio. Errors in εNd_i represent propagation of a ±10% uncertainty in Sm and Nd concentrations.

Table 3.S1. Neodymium isotopic composition of BPZP samples. Errors are 2SE. *Sm and Nd concentrations are measured by Neutron Activation Analysis, given in Wyborn (1983). $^{143}Nd/^{144}Nd_i$ and εNd_i are calculated using the parameters listed in the text.

Sample	Lithology	Nd (µg/g)*	Sm (µg/g)*	$^{143}Nd/^{144}Nd$	2SE	$^{143}Nd/^{144}Nd_i$	εNd_i	2SE
BP39	Diorite	15.8	3.5	0.512427	0.000009	0.512061	-0.65	0.17
BP22	Granite	32.6	6.8	0.512340	0.000006	0.511996	-1.93	0.12
BP11	Granite	24.3	4.1	0.512299	0.000008	0.512020	-1.45	0.15
BP42	Aplite	17.1	3.4	0.512292	0.000006	0.511964	-2.56	0.11

3.A2 Iron-Zinc Isotopic variations

Figure 3.S2 shows the relationship between whole rock $\delta^{56}Fe$ and $\delta^{66}Zn$ for the BPZP samples. With the exception of the fine grained, late crystallising aplites (blue triangles), there is no relationship between $\delta^{56}Fe$ and $\delta^{66}Zn$. A lack of correlation between $\delta^{56}Fe$ and $\delta^{66}Zn$ is evidence that Zn and Fe isotopes are not fractionated by fluid exsolution during differentiation of the BPZP, as discussed in the main text.

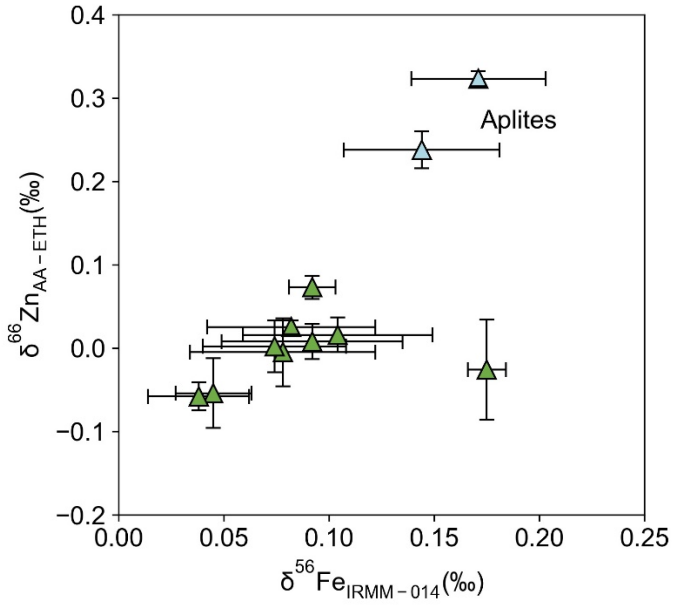

Figure 3.S2. Zinc vs Iron isotopic compositions for the BPZP whole rock samples. The aplite samples are represented by the blue triangles. Errors are plotted as 2SD of at least 3 individual measurements of each sample.

3.A3 Rhyolite-MELTS Modelling

The thermodynamic modelling software Rhyolite-MELTS (Gualda et al., 2012; Ghiorso and Gualda, 2015) was used to model variation in Fe isotopic composition during fractional crystallisation of the BPZP magma, following the method of previous studies (Dauphas et al., 2014; Foden et al., 2015; He et al., 2017).

The parameters used in the models are listed in Table 3.S2. The composition of sample BP26 is chosen as the initial magma composition. The BPZP major element trends are best reproduced during fractional crystallisation with fO_2 buffered between FMQ+2 and FMQ+3 at 1.5kbars (Figure 3.S3; blue and yellow dashed lines). However, the major element trends can be better reproduced using the Rayleigh equation (Equation 3.3) with appropriate partition coefficient values. This is likely because there is a lack of appropriate thermodynamic data for modelling the crystallisation of hydrous silicates like biotite and hornblende (Gualda et al,. 2012), so their crystallising proportions are typically underestimated. This means that the concentrations of elements compatible in these phases are incorrectly estimated in the evolving magma.

Table 3.S2. Starting magma composition and parameters used to model magma fractional crystallisation with Rhyolite-MELTS to produce the models shown in Figure 3.S2.

Starting Composition BP26 (QFM+2)		**Model**	**Initial fO_2 $\log_{10}$**	**Buffer**	**Initial $Fe^{3+}/\Sigma Fe$**	**P (bars)**	**Liquidus T (°C)**
SiO_2	61.37	1	-8.61	unbuffered	0.15	1500	1163
TiO_2	0.60	2	-8.61	FMQ	0.15	1500	1163
Al_2O_3	13.70	3	-5.98	unbuffered	0.31	1500	1155
Fe_2O_3	2.10	4	-5.98	FMQ+2	0.31	1500	1159
FeO	4.21	5	-4.50	FMQ+3	0.40	1500	1184
MnO	0.11						
MgO	4.50						
CaO	6.28						
Na_2O	2.55						
K_2O	2.58						
P_2O_5	0.20						
H_2O	1.60						

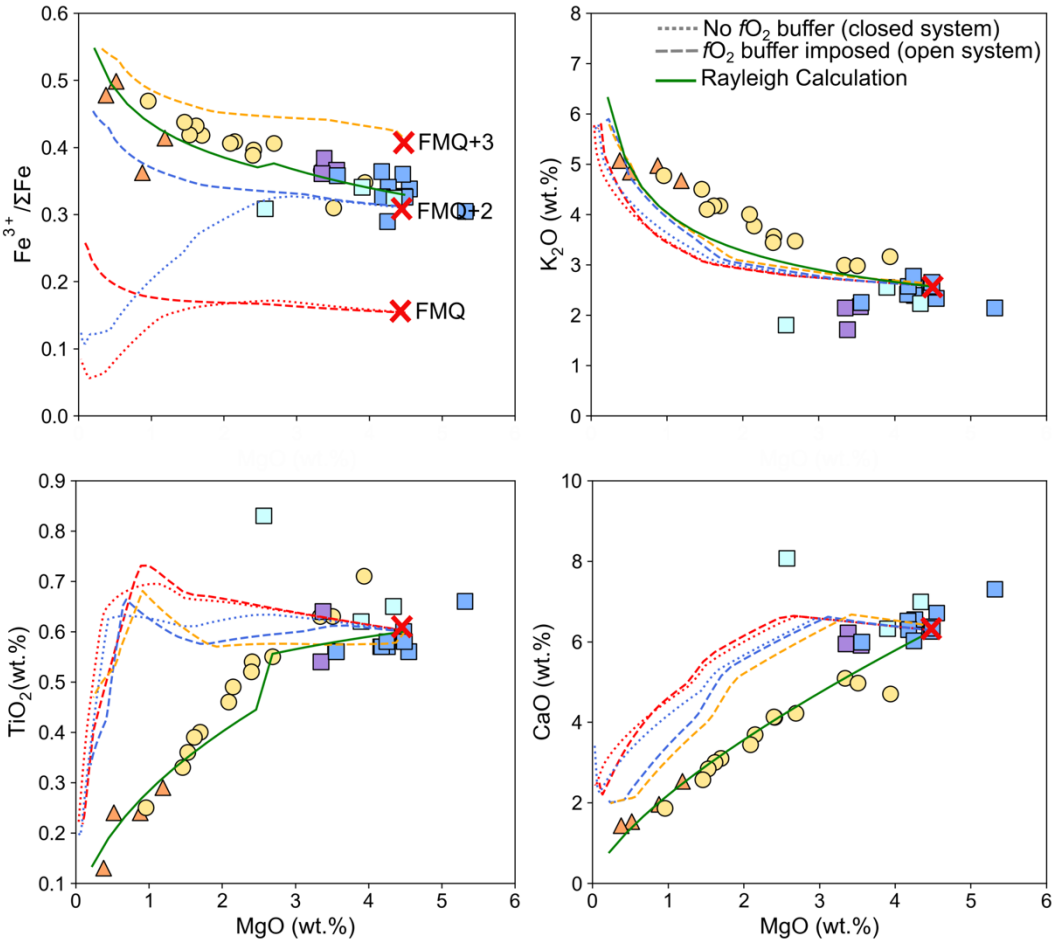

Figure 3.S3. Rhyolite-MELTS models of major element variations in the BPZP magma. The dotted lines are with no fO_2 buffer imposed. The dashed lines are with a fO_2 buffer imposed. The solid line is our Rayleigh model. Red crosses show the starting magma composition in the models (BP26). Symbols as for Figure 3.2.

Rhyolite-MELTS predicts that the main Fe bearing minerals which will crystallise from the BPZP parental magma are clinopyroxene, orthopyroxene, and magnetite. Magnetite is predicted to make up over 60% of the Fe budget for most of the crystallisation sequence. Biotite is only predicted to crystallise above 70 wt.% SiO_2, and no hornblende crystallises (Figure 3.S4A). This does not reflect the true modal mineralogy of the BPZP, where the observed modal abundances indicate that biotite, hornblende and magnetite host approximately equal proportions of the Fe in the system.

Since magnetite is predicted to be the dominant Fe bearing phase in the system, and $\Delta^{56}Fe_{mag\text{-}melt}$ values from this study and Sossi et al. (2012) are positive, the calculated bulk

$\Delta^{56}Fe_{min\text{-}melt}$ values are also positive (Figure 3.S4B, solid and dotted lines). A positive bulk $\Delta^{56}Fe_{min\text{-}melt}$ value would lead to a decrease in magma $\delta^{56}Fe$ with differentiation. This is not seen in the BPZP whole rock samples. This highlights that Rhyolite-MELTS should not be used to support modelling of Fe isotopic evolution in I-type systems, because there is a lack of appropriate thermodynamic data for modelling the crystallisation of hydrous silicates like biotite and hornblende (Gualda et al,. 2012). Therefore, the proportions of crystallising hydrous silicates are underestimated. Given that these are the main Fe bearing silicate phases in the BPZP, the evolving magma Fe isotopic composition cannot be accurately modelled this way.

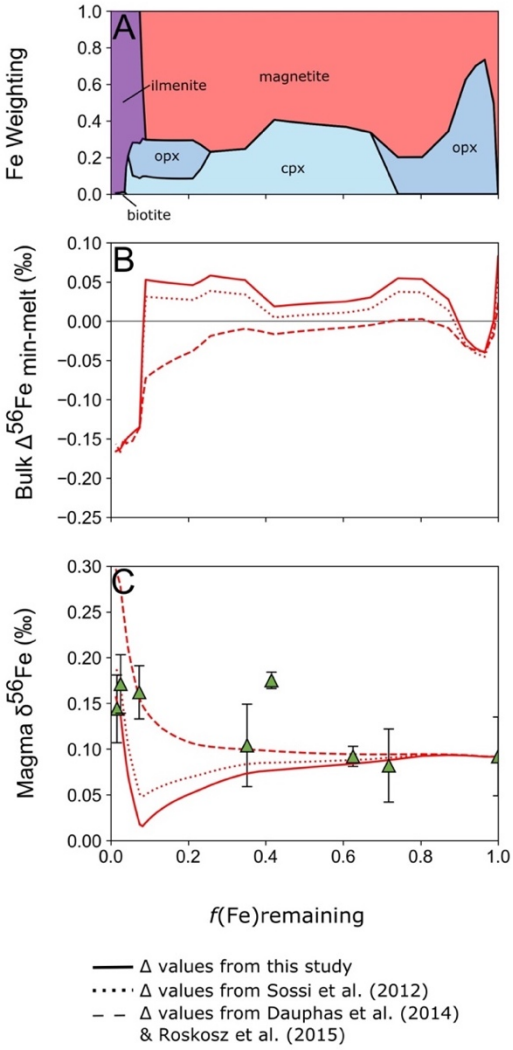

Figure 3.S4. Determinations of modal abundances (A), bulk $\Delta^{56}Fe_{min\text{-}melt}$ (B) and resulting magma $\delta^{56}Fe$ (C) using Rhyolite-MELTS as described in the text. Green triangles show the isotopic composition of the BPZP WR samples. *f*(Fe) is calculated as described in the text.

Chapter 4: Vanadium Isotopic Behaviour in the Continental Crust

4.0 Abstract

The intermediate to felsic intrusive rocks that make up the upper continental crust can host significant quantities of vanadium (V), but their V isotopic composition has yet to be investigated. Analyses of intrusive crustal rocks are necessary for both understanding V isotope behaviour during plutonic differentiation, and for accurately interpreting the V isotopic record of clastic sediments eroded from the continents over geological time, both of which have implications for V isotope mass balance between geological reservoirs.

Here we present the first investigation into the V isotopic composition of an upper crustal granite and its mineral separates, using samples from the calc-alkaline Boggy Plain Zoned Pluton. WR samples and mineral separates both show increases in $\delta^{51}V$ of around 0.6‰ during magmatic differentiation. However, WR $\delta^{51}V$ is scattered, reflecting variations in modal mineralogy of samples, rather than a true melt composition. Mineral separates show more well-defined trends in $\delta^{51}V$. The increase in $\delta^{51}V$ during differentiation is caused by crystallisation of isotopically light magnetite, biotite and hornblende which drive the residual magma, and later crystallising minerals, to a heavier isotopic composition. A new approach is developed to reconstruct the V isotopic composition of the evolving melt from the mineral separate data, to overcome the complications with interpreting WR analyses in intrusive settings.

The fact that V isotopic compositions of WR samples and their mineral separates vary by 0.6‰ within a single plutonic body undergoing magmatic differentiation highlights that the upper continental crust can have extremely heterogeneous V isotopic composition over small geographic areas. Therefore, the average V isotopic composition captured by clastic sedimentary deposits such as diamictites and loess is unlikely to reflect the true isotopic complexity present. This leads to uncertainties in estimating variations in the isotopic composition of the crust and the riverine input of V to the oceans over geological

time, which has implications for the interpretation of the V isotope record in marine shales for studies of oceanic redox variations.

4.1 Introduction

The upper continental crust is a significant reservoir of Vanadium (V), with a concentration of approximately 100 µg/g (Rudnick and Gao, 2003; Huang et al., 2015). The weathering of upper crustal silicate rocks and transport of this material via rivers is the major source of V to the oceans (Shiller and Mao, 2000; Schuth et al., 2019). Therefore, a knowledge of the V isotopic composition of the continental crust is critical for constraining the isotopic mass balance of V between different geological reservoirs on a planetary scale. Additionally, it is important to understand any temporal variation in the isotopic composition of the continental crust. A promising application of the V stable isotope system is to track palaeoredox variations in the oceans by measuring the isotopic composition of shales (Schuth et al., 2019; Wu et al., 2019; Nielsen, 2020; Wu et al., 2020; Fan et al., 2021). However, the V isotopic composition of a shale will partly depend on the isotopic composition of the ocean at the time of deposition, in addition to the magnitude of V isotope fractionation during deposition (Nielsen, 2020; Wu et al., 2020). Therefore, it is vital to understand if the isotopic composition of the major source of V to the oceans has changed over geological time.

There are two principal ways to calculate the composition of the upper continental crust. The first method is to sample large numbers (hundreds to thousands) of upper crustal rocks spanning a wide area and calculate an average composition based on the abundance of each rock type (e.g. Shaw et al., 1986; Gao et al., 1998) Alternatively, average crustal composition can be estimated from the fine grained, terrigenous sediments which have been eroded from the continent. Examples include loess, glacial diamictites and oceanic shales (e.g. Taylor et al., 1983; Condie, 1993; Gaschnig et al., 2016; Greber and Dauphas, 2019).

Recently, the isotopic compositions of various transition metal stable isotopes (e.g. Ti, Zr, Mo) in clastic sedimentary deposits of different ages have been measured, in order to estimate the average isotopic composition of the continental crust through time (e.g. Greber et al., 2017; Greaney et al., 2020; Klaver et al., 2021; Tian et al., 2021). For

example, temporal variations in isotopic composition have been interpreted to reflect the onset of plate tectonics and first formation of silicic crust by 3.5 Ga (Ti isotopes; Greber et al., 2017), and the initiation of oxidative weathering 2.9 Ga (Mo isotopes; Greaney et al., 2020). This approach could potentially also be useful for V isotopes, particularly because alteration or chemical weathering processes do not produce resolvable V isotope fractionation (Prytulak et al., 2013; Schuth et al., 2019; Qi et al., 2022). Thus, clastic sedimentary rocks should in theory record the average V isotopic composition of the continental crust. However, there are uncertainties with using clastic sediments to calculate an average crustal composition. Hydrodynamic sorting of heavy minerals during transport, for example zircon and Fe-Ti oxides which can have distinct isotopic compositions, can concentrate these phases in coarser fractions and bias results (Klaver et al., 2021). Additionally, preferential weathering of less resistant mineral phases could also influence the isotopic composition of clastic sediments. Therefore, an understanding of the V isotopic composition of typical upper crustal rocks and their minerals is necessary before these sedimentary records can be accurately interpreted.

Vanadium is a moderately incompatible trace element which exists in multiple redox states in terrestrial environments. Vanadium has two stable isotopes, ^{50}V and ^{51}V with proportions of 0.24% and 99.76% respectively. Isotope ratios are reported as $\delta^{51}V$ values relative to the AA standard (Nielsen et al., 2011). Most previous work on the V isotopic composition of terrestrial igneous rocks has focused on mantle derived basalts (Prytulak et al., 2013; Prytulak et al., 2017; Wu et al., 2018; Qi et al., 2019; Novella et al., 2020; Ding et al., 2020). There appears to be minor V isotope fractionation during low degree mantle partial melting, with isotopic variation of <0.1‰ between mantle peridotites (-0.91±0.06‰, 2SD, n=8; Qi et al., 2019) and MORB (-0.84±0.02‰, 2SE, n=22; Wu et al., 2018), although values are within typical analytical uncertainties. Larger degrees of V isotopic fractionation are observed during magmatic differentiation (Prytulak et al., 2017; Wu et al., 2018; Ding et al., 2020). Variations in WR $\delta^{51}V$ of up to 2‰ were observed in lavas undergoing fractional crystallisation at Hekla and Anatahan volcanoes (Prytulak et al., 2017). Kilauea Iki lavas also show an increase in $\delta^{51}V$ of around 0.5‰ during differentiation (Ding et al., 2020). Increases in WR $\delta^{51}V$ are attributed to fractional crystallisation of isotopically light Fe-Ti oxides such as magnetite. Vanadium is highly compatible in magnetite (Toplis and Corgne, 2002), and is most likely hosted as octahedrally co-ordinated V^{3+} (O'Neill and Navrotsky, 1984). Given that V is found in

higher oxidation state and lower co-ordination in silicate melts (Giuli et al., 2004; Sutton et al., 2005; Righter et al., 2006), magnetite is theoretically predicted to be isotopically lighter than the melt from which it crystallises. The experimental study of Sossi et al. (2018b) confirmed that magnetite is isotopically lighter than coexisting melt for V. The study also demonstrated a larger magnitude of V isotope fractionation is predicted between magnetite and melt ($\Delta^{51}V_{mag\text{-}melt}$) at higher magma fO_2.

Although the general increase in WR $\delta^{51}V$ is accepted to be due to fractional crystallisation of Fe-Ti oxides, variations in the magnitude and timing of this increase are attributed to variation in the chemistry of Fe-Ti oxides and the timing of oxide saturation. For example, Ti-rich magnetite is the main oxide phase to crystallise at Hekla and Anatahan (Baldridge et al., 1973; deMoor et al., 2005; Schuessler et al., 2009), while both magnetite and ilmenite crystallise at Kilauea Iki (Helz, 1987; Helz and Thornber, 1987). Based on the WR $\delta^{51}V$ trends, Ding et al. (2020) proposed that there is a smaller increase in WR $\delta^{51}V$ during fractional crystallisation at Kilauea Iki because there is a smaller fractionation factor between ilmenite and coexisting melt compared to magnetite and coexisting melt. However, these variations have not yet been measured in mineral separates or linked to differences in V bonding environment and redox state between the different mineral phases. The implication is that Fe-Ti oxides, which host the majority of V in the system, potentially have extremely variable $\delta^{51}V$, which will influence the average crustal composition calculated using clastic sediments.

Studying the behaviour of V isotopes in extrusive lavas may not be directly applicable to understanding the V isotopic composition of the continental crust. Most of the upper continental crust is formed by intermediate to silicic plutonic rocks. To date, there have been no published studies on the V isotopic composition of intrusive crustal rocks or their mineral separates. It is therefore unknown how V isotopes behave in intrusive settings, which have slowly crystallised over a large temperature range. For example, there is the potential for the V isotopic composition of Fe-Ti oxides to be altered by low temperature oxyexsolution (e.g. Frost and Lindsley, 1991). It is also unknown if felsic intrusive rocks will show similar heavy $\delta^{51}V$ values to evolved lavas, given that plutonic rocks may be cumulative and WR compositions are not necessarily analogous to the composition of the evolving melt (e.g. Chappell and Wyborn, 2004). Therefore, before determining temporal variations in the average V isotopic composition of the upper continental crust, the range

and controls on V isotopic composition in typical upper crustal rocks and mineral separates must be understood.

Here, we examine the V isotopic composition of whole rock samples and V-rich mineral separates (biotite, hornblende and magnetite) from the Boggy Plain Zoned Pluton (BPZP; Wyborn, 1983; Wyborn et al., 1987). The Fe-Zn isotopic study in Chapter 3 (Stow et al., 2022) indicated that elemental and isotopic trends in the pluton can be approximated by closed system fractional crystallisation. Hence, this is an ideal simple system to investigate V isotopic behaviour in intrusive settings. The aims of this study are to:

1. Determine the range of $\delta^{51}V$ in whole rock samples and mineral separates in a typical upper crustal pluton
2. Understand the controls on V isotopic fractionation in intrusive settings, and compare this to our knowledge of extrusive systems
3. Extrapolate these data to investigate the V isotopic composition of the upper continental crust in general, and V isotope mass balance between terrestrial reservoirs over geological time.

4.2 Geological Background and Samples

4.2.1 Overview

The Boggy Plain Zoned Pluton (BPZP) is a concentrically zoned calc-alkaline pluton formed by closed system fractional crystallisation of a single parent magma (e.g. Wyborn, 1983; Stow et al., 2022). A detailed geological history of the BPZP and petrographic descriptions of samples are given in Chapter 3 (Stow et al., 2022), Section 3.2 and 3.3. The samples analysed for V isotopic composition are the same as those analysed for Fe and Zn isotopic composition in Chapter 3 (Stow et al., 2022). In most cases, Fe, V and Zn isotopic compositions were determined from the same sample digestion.

The BPZP is an ideal case study for the first investigation of the behaviour of V isotopes in an intrusive setting. Firstly, work on the more established Fe and Zn isotope systems indicated that neither source heterogeneity, crustal assimilation, nor fluid exsolution could explain isotopic trends, and all Fe and Zn isotopic variation was caused by approximately closed system fractional crystallisation (Stow et al., 2022; Chapter 3).

Trends of V concentration in the BPZP (Figure 4.1) are similar to the variations in Fe concentration discussed in Chapter 3 (Stow et al., 2022). In the mafic cumulate samples (WR MgO >4.5 wt.%), V concentrations are scattered, reflecting variable proportions of cumulus minerals and trapped interstitial melt. Below 4.5 wt.% MgO, WR V concentrations shows a smooth, continuous decrease with WR MgO content, most likely driven by the crystallisation of titanomagnetite (herein referred to as magnetite), biotite and hornblende as the near-liquidus mineral assemblage. Hence, V isotope trends can be interpreted within the same framework as Fe isotopes in Chapter 3 (Stow et al., 2022).

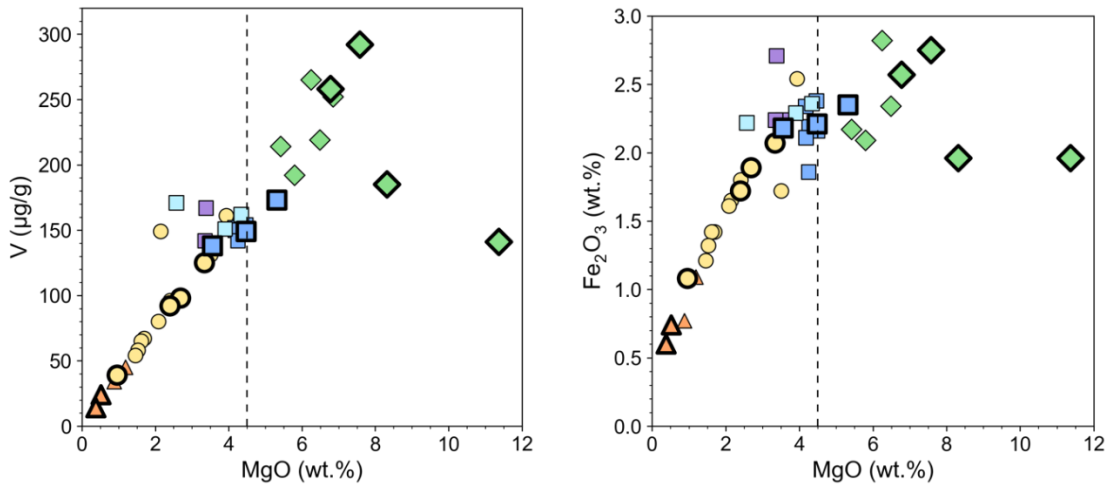

Figure 4.1. Fe and V variations in the BPZP. Whole rock compositional data from Wyborn (1983). Large symbols with bold outlines are those chosen for isotopic analysis in this study. The dashed line approximates the separation of liquids (<4.5 wt.% MgO) from cumulate rocks (>4.5 wt. % MgO).

A major unknown is whether the V isotopic composition of magnetite varies with melt fO_2 in real samples, since a positive correlation between melt fO_2 and the magnitude of $\Delta^{51}V_{mag\text{-}melt}$ has been observed in partitioning experiments (Sossi et al., 2018b). In the BPZP, magnetite is present in all lithologies across a wide WR SiO_2 range. It is proposed that magma fO_2 increased during fractional crystallisation, evidenced by increasing magnetite:ilmenite ratio and increasing Fe^{3+}/Fe^{2+} of silicate phases towards the centre of the pluton (Wyborn, 1983). However, it is difficult to quantitatively estimate magma fO_2 in intrusive rocks. Many oxybarometers require the coexistence of mineral-mineral or mineral-melt pairs at equilibrium, and also require that Fe-Ti oxide compositions are

unaffected by subsolidus reactions during slow cooling, for example the magnetite-ilmenite (Buddington and Lindsley, 1964; Ghiorso and Evans, 2008), biotite-K-feldspar-magnetite (Wones, 1981), and magnetite-melt (Arató and Audétat, 2017) oxybarometers. These conditions are unlikely to be fulfilled in intrusive settings. However, we can still test if the V isotopic composition of the BPZP magnetite samples reflect a qualitative increase in magma fO_2.

4.2.2 Magnetite Petrography

The petrographic context of samples must be understood to interpret V isotopic compositions of magnetite. A major challenge with chemical analysis of Fe-Ti oxide minerals in intrusive rocks is that oxides are susceptible to subsolidus re-equilibration during slow cooling. In magnetite, this results in low temperature oxyexsolution of ilmenite as lamellae or granules (Frost and Lindsley, 1991). This can alter the isotopic composition of oxide minerals, as has been reported previously for both Fe (e.g. Dziony et al., 2014; Chen et al., 2014; Cao et al., 2019) and Mg isotopes (Chen et al., 2021) in layered mafic intrusions. Given that V concentrates in magnetite relative to ilmenite (Schuiling and Feenstra, 1980), exsolution of ilmenite lamellae could increase the concentration of V in the magnetite host. However, it is still uncertain if magnetite and ilmenite would have different V isotopic composition (Ding et al., 2020), so the effect of subsolidus equilibration on V isotope ratios is unknown.

However, as discussed in Chapter 3 (Stow et al., 2022), only magnetite in the mafic cumulates (sample BP39) shows evidence of low temperature re-equilibration and exsolution of ilmenite lamellae and granules. Samples BP40, BP22, BP11 and BP42 have only extremely fine trellis-type exsolution lamellae (see Chapter 3, Figure 3.4). Therefore, magnetite host grains and their exsolution features can be sampled in bulk by hand-picking whole oxide grains from a 125 -250 μm size fraction.

The trace element concentrations of the magnetite separates are also measured prior to isotopic analysis to determine the 'purity' (e.g. Ti, Cr content) of the magnetite separates (Section 4.3.2). This combined petrographic and chemical approach confirms that the bulk oxide mineral separate fraction is recording the isotopic composition of magnetite at the time of crystallisation. This allows V isotopic data to be interpreted with confidence.

4.3 Methods

4.3.1 Vanadium Isotope Analysis

Sample Preparation and Digestion

Chemical separation of vanadium, and V isotopic analysis of biotite, hornblende and magnetite mineral separates and whole rock powders was conducted in the Arthur Holmes Isotope Geology Laboratory, Durham University. Biotite and hornblende separates were hand-picked under binocular microscope from a 125 – 250 μm size fraction, avoiding crystals with obvious inclusions or alteration features where possible. The magnetite separates were initially separated from silicate material using a hand magnet, and then further hand-picked under binocular microscope to exclude other phases. Mineral separates were ground into powders by hand using an agate pestle and mortar, which was cleaned with low Fe quartz sand between each sample. To make at least three V isotopic measurements, approximately 2 μg total V is required. Biotite and hornblende contain 200 – 800 μg/g V (Wyborn, 1983), and magnetite separates contain 1000 – 5000 μg/g V (Section 4.4.2), so approximately 20 – 30 mg material was digested. For the whole rock samples (14 – 292 μg/g V; Wyborn, 1983), approximately 50 – 70 μg of powder was digested.

The whole rock powders and silicate mineral separates were digested in a 3:1 mixture of Teflon distilled (TD) 29M HF and TD 16M HNO_3 in sealed Teflon beakers on a hotplate at 160 °C for at least 48 hours. Samples were evaporated at 120 °C to incipient dryness, then TD 16M HNO_3 was added and evaporated at 180 °C until the residues were a dark brown colour. This is to destroy any fluorides formed during the digestion step. The magnetite separates were digested in 5 ml TD 6M HCl on a hotplate at 120 °C for 48 hours. This is because after hand-picking, magnetite grains sometimes contained small silicate inclusions, or silicate material attached to the margins of grains. Although silicate material typically contains an order of magnitude lower V concentration than magnetite (see mineral separate V concentrations above), they may have distinct V isotopic compositions. However, using 6M HCl permits full digestion of the oxide grains and the insoluble silicates can be separated by centrifugation. Samples were evaporated at 120 °C

then taken up in 1 ml TD 6M HCl for column chromatography. A 20 µl aliquot of the magnetite samples was taken at this stage for trace element analysis.

Column Chromatography

Five separate column procedures are necessary to ensure complete V separation from matrix elements. The V separation procedure is adapted from Nielsen et al. (2011) and Wu et al. (2016). The underlying principle, first used by Nielsen et al. (2011), is that V^{5+} forms anionic V-peroxide complexes with hydrogen peroxide (H_2O_2) in mildly acidic solutions, which will partition strongly onto anion exchange resins such as AG1-X8. However, Fe and Ti must be removed before H_2O_2 can be used, because Fe and Ti catalyse the dissociation of H_2O_2 to water and oxygen, causing loss of V because V-peroxide complexes can no longer form. Additionally, the presence of H_2O_2 causes Ti-oxides to precipitate when the sample is loaded onto the resin, so as further acids are added, Ti will be eluted and collected with the V fraction (Nielsen et al., 2011). Column 1 removes Fe and column 2 removes Ti, and subsequently H_2O_2 can be used in Column 3 to separate V from other matrix elements. The minor ^{50}V isotope has direct isobaric interferences from ^{50}Cr and ^{50}Ti. Columns 4 and 5 (both repeated twice) are clean-up columns designed to remove trace Cr and Ti, necessary for accurate isotopic analysis. Full details of the column procedure can be found in Chapter 2, Section 2.4.

Vanadium Isotopic Analysis

Vanadium isotopic compositions were measured on a Neptune MC-ICP-MS, following the protocol outlined in Wu et al. (2016). A full summary is found in Chapter 2, Section 2.5.4. Measurements were made in medium resolution mode ($m/\Delta m$ = 6000-8000), allowing V to be resolved from isobaric interferences on the shoulder on the low mass side of the peak. Masses ^{48}Ti, ^{49}Ti, ^{50}V, ^{51}V, ^{52}Cr and ^{53}Cr were measured in cups L4, L2, L1, C, H1 and H3 respectively. A $10^{10}\Omega$ resistor was connected to the centre cup to measure signals >50V on ^{51}V. This allows samples to be measured at higher concentrations, thereby increasing the signal on the minor ^{50}V isotope (the natural $^{51}V/^{50}V$ ratio is ~ 420).

Standards and samples were run at concentrations of 1 ug/g V. The sample introduction system consisted of a PFA Concentric Flow nebuliser coupled to an Aridus 3 Desolvating

Nebuliser System. Typical sensitivity was >100V/ppm on ^{51}V. Mass bias and instrument drift was corrected by standard sample bracketing with the AA standard (Nielsen et al., 2011). Vanadium isotopic compositions are reported in delta notation relative to the AA standard: $\delta^{51}V = [(^{51}V/^{50}V)_{sample}/(^{51}V/^{50}V)_{AA} -1] \times 10^3$. The BDH V solution (Nielsen et al., 2011) was measured throughout analytical sessions to assess machine precision and accuracy. The long-term average was $\delta^{51}V = -1.23 \pm 0.10‰$ (2SD, n=397), which is within error of values from other studies (e.g. Nielsen et al., 2011; Wu et al., 2016; Schuth et al., 2019; Wu et al., 2019). USGS Reference Materials were processed with each batch of chemistry (Table 4.1), and $\delta^{51}V$ values agree with previously published values (e.g. Prytulak et al., 2011; Wu et al., 2016; Qi et al., 2019).

^{48}Ti, ^{49}Ti, ^{52}Cr and ^{53}Cr were used to correct for interferences of ^{50}Ti and ^{50}Cr on ^{50}V, using the exponential law ($R_T = R_M \times (m_1/m_2)^{\beta}$ .Two BDH solutions were doped with 100ppb Ti and Cr respectively, and measured in every sequence in order to determine β values for Cr and Ti, after Wu et al. (2016), as described in Section 2.5.4.

4.3.2 Magnetite Trace Element Analysis

Trace element concentrations of the magnetite mineral separates were obtained from the same aliquots used for isotopic measurements. A 20 µl aliquot was taken from the sample dissolved in 1ml TD 6M HCl before it was loaded onto the first column. This bulk analysis approach was preferred to in-situ analysis (e.g. by LA-ICP-MS) because it allows magnetite grains and any ilmenite that may have exsolved during cooling to be sampled together. Therefore, the trace element concentration of the original titanomagnetite grains at the time of crystallisation can be determined.

It is difficult to analyse oxide minerals by solution ICP-MS given the overwhelming concentration of Fe compared to other trace elements, and lack of suitable calibration standards. An additional concern is that magnetite samples were weighed then digested in TD 6M HCl to avoid digestion of any silicate inclusions. Hence, the exact mass of magnetite digested is not known. For these reasons, the trace element concentrations determined here will be minimum values. However, accurate trace element ratios are obtained.

Trace element analysis of the oxide mineral separates was conducted at the Open University, UK, using an Agilent 8800 ICP-QQQ-MS inductively coupled plasma mass spectrometer. Samples were dried down and taken up in 2% HNO_3 to make a 4000-fold dilution. These dilutions were aspirated into the mass spectrometer using a quartz microflow nebuliser with uptake rate 500µl/min. The Agilent 8800 contains two quadrupoles and a collision/reaction cell (Octopole Reaction System; ORS) which can be operated in three configurations: 'no gas', 'He gas' or 'O_2 mass shift'. Most elements were measured in 'no gas' mode, except for the Rare Earth Elements (La to Lu) where O_2 gas was used to shift the mass by 16. The first quadrupole controls the masses which enter the ORS, and the second quadrupole is used in either mass-shift or on-mass mode depending on whether a gas is used in the reaction cell (e.g. Wei et al., 2017; Brett et al., 2018). Calibration standards of known concentration were run at the start of each measurement session. An in-house synthetic magnetite powder *Synth. Mag.* (>96.8 wt. % Fe_3O_4) from Inoxia Ltd was measured before and after the BPZP magnetite samples. Errors are reported as the within run RSD of each individual analysis. For the first-row transition metals which were the focus of this work, RSDs were typically <5% (see Table 4.S1).

4.3.3 Magnetite Major Element Estimation

In addition to trace element data, the major element chemistry of the magnetite was also estimated. Since magnetite grains were separated from the bulk crushate using a hand magnet, there was potential for oversampling magnetite vs exsolved ilmenite. This approach also allowed an estimate of magnetite $Fe^{3+}/\Sigma Fe$ to be calculated stoichiometrically, following the approach in Droop (1987). Major element chemical data for magnetite mineral separates was measured by energy dispersive X-ray spectroscopy (EDS) using a Hitachi SU70 SEM at Durham University. Oxide separates were picked and mounted in resin. The resin blocks were polished, and carbon coated to a thickness of approximately 20nm, and examined at a working distance of approximately 15mm. The SEM uses an acceleration voltage of 15kV and a 46µA emission current. A representative selection of crystals were analysed, by selecting individual points on the crystals to measure, using an acquisition time of 30 seconds. Typical 1σ errors based on counting statistics were 0.15 – 0.25 wt.% for Fe and 0.10 – 0.15% for Ti. It is important to note that the EDS is intermittently calibrated using Co metal, but no calibration

standards were run in the session where this EDS data was obtained, so chemical compositions are approximate values. The data were only used to quantify variations in the Fe and Ti content of titanomagnetite and ilmenite to assess how 'pure' the bulk oxide (magnetite) fraction was.

4.4 Results

4.4.1 Vanadium Isotopic Compositions of Whole Rock and Mineral Separates

The V isotopic composition of the whole rock powders and mineral separates are shown in Tables 4.1 and 4.2. The data represents the first V isotopic measurements reported thus far for silicate and oxide mineral separates from granites.

There is an overall increase in whole rock $\delta^{51}V_{AA}$ from -1.15 ± 0.04‰ (2SD) to -0.56 ± 0.06‰ (2SD), with decreasing WR MgO and increasing WR SiO_2 content (Figure 4.2), although the data are scattered. For several samples, the isotopic composition of a separate digestion of the same powder was measured. For samples BP12 and BP23, the $\delta^{51}V$ values of the two digestions agree within error. However, the $\delta^{51}V$ values for the two digestions of BP40 and BP28 do not match (labelled on Figure 4.2). Replicate digestions of mineral separates were also made, which involved picking new mineral grains from the remaining sample crushate and making a new powder. The $\delta^{51}V$ values for the replicate digestions of mineral separates all reproduce within error (Table 4.2).

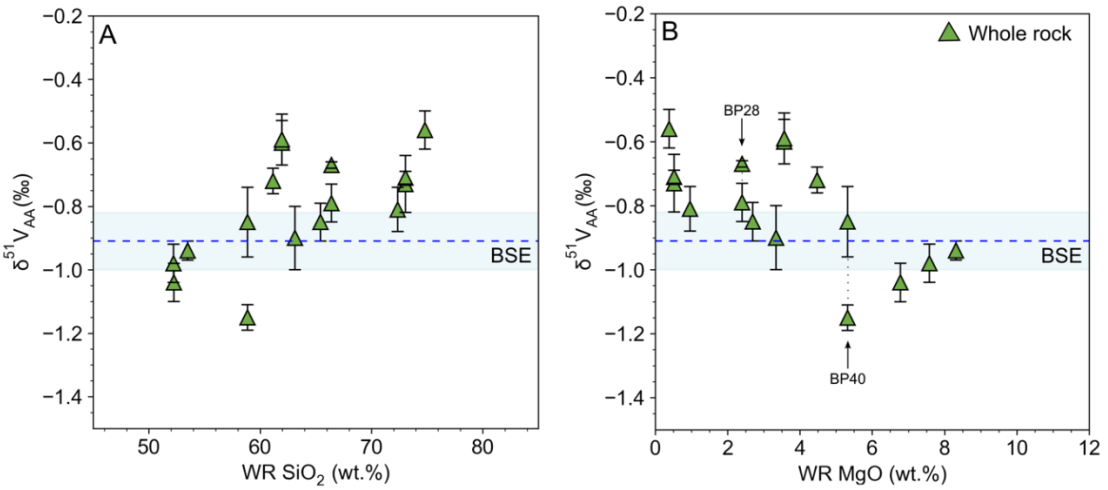

Figure 4.2. Variation in WR $\delta^{51}V$ with WR MgO (A) and SiO_2 (B) content. Whole rock SiO_2 and MgO data are from Wyborn (1983). The blue shaded area is the estimate for the BSE from Qi et al (2019) of 0.91 ± 0.09‰ (2SD, n=18). Errors are plotted as 2SD of at least 3 individual measurements of each sample. When <3 analyses were made, errors are reported as the internal 2SE of an individual measurement, see Table 4.1. Samples BP40 and BP28 are labelled. Replicate digestions of these samples did not reproduce, see Table 4.1.

Magnetite, biotite and hornblende mineral separates show trends of increasing $\delta^{51}V$ with decreasing WR MgO and increasing WR SiO_2 (Figure 4.3). These trends are well defined compared to WR values. Primocryst biotite and magnetite from the same sample have $\delta^{51}V$ values within error. Primocryst biotite is always approximately 0.1‰ heavier than primocryst hornblende from the same sample. Inter-mineral fractionation factors ($\Delta^{51}V_{mag\text{-}bt}$ and $\Delta^{51}V_{bt\text{-}hbd}$) for primocryst phases show no relationship with temperature, or parameters of differentiation (Figure 4.4; filled symbols). Note that although at first glance $\Delta^{51}V_{mag\text{-}bt}$ appears to show trends, the trend is exaggerated by the $\Delta^{51}V_{mag\text{-}bt}$ value for interstitial biotite and magnetite in sample BP39, which likely did not crystallise in isotopic equilibrium. If this value is ignored, primocryst $\Delta^{51}V_{mag\text{-}bt}$ values are all approximately zero.

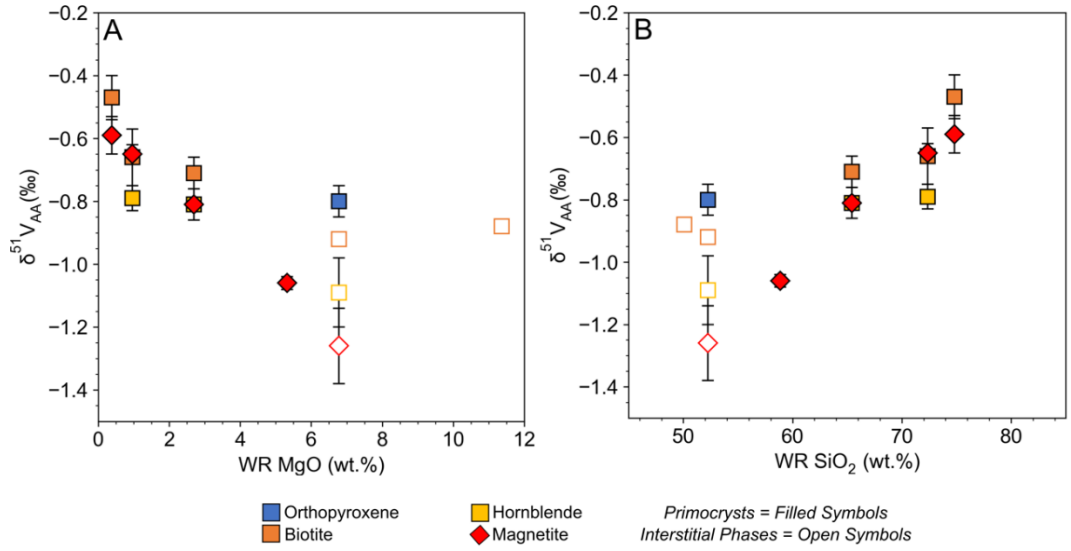

Figure 4.3. Variation in mineral separate $\delta^{51}V$ with WR MgO (A) and SiO_2 (B) content. Whole rock SiO_2 and MgO data are from Wyborn (1983). Minerals with interstitial morphologies are shown with open symbols, and primocrysts shown with filled symbols. Errors are plotted as 2SD of at least 3 individual measurements of each sample. When <3 analyses were made, errors are reported as the internal 2SE of an individual measurement, see Table 4.2.

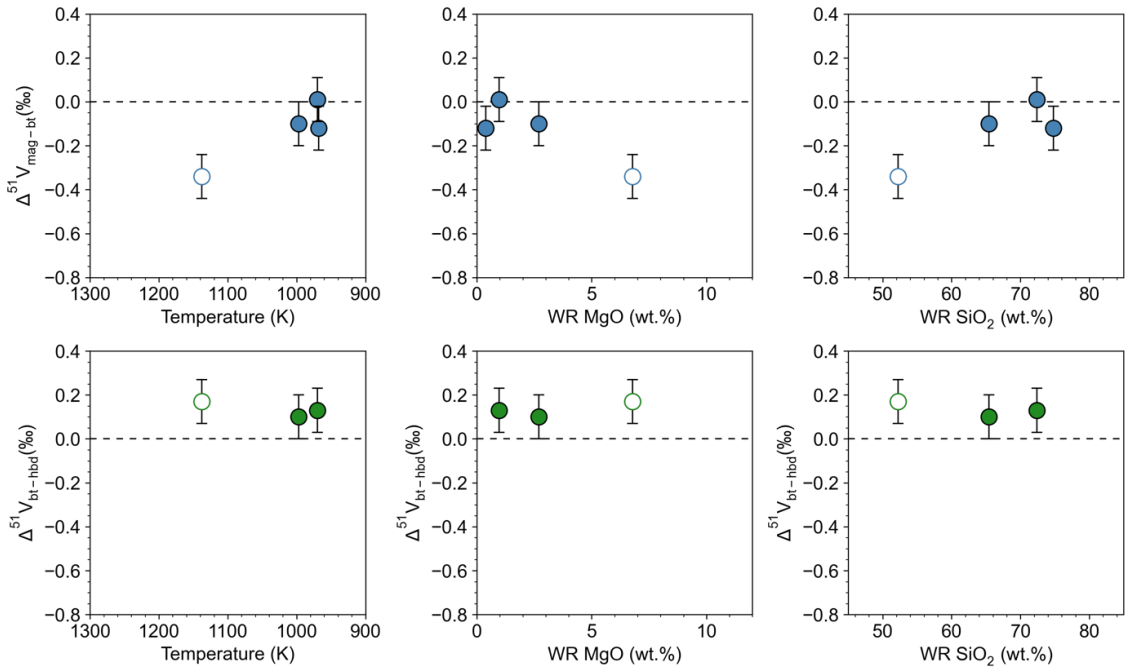

Figure 4.4. Inter-mineral fractionation factors in the BPZP. Whole rock SiO_2 and MgO data are from Wyborn (1983). Temperature values are from Chapter 3 and Stow et al. (2022). Minerals with interstitial morphologies are shown with open symbols, and primocrysts shown with filled symbols. Note that it is probable that interstitial phases have not crystallised in isotopic equilibrium. Errors are given as ±0.1‰, which is the typical analytical uncertainty (2SD). The dashed line shows $\Delta^{51}V_{min-min} = 0$, i.e. when mineral separates have identical isotopic compositions.

Table 4.1. Vanadium isotopic composition of BPZP whole rock powders. Isotopic compositions given relative to the AA standard. WR MgO data from Wyborn (1983). Errors are given as 2 standard deviations of the mean of at least 3 measurements of the sample. When fewer than 3 measurements were made, errors are reported as 2SE (*). The synthetic magnetite powder is an in-house standard, see Section 4.3.2 (+).

Sample	Rock Type	WR MgO (wt. %)	$\delta^{51}V_{AA}$ (‰)	2SD	n
BP34	Diorite	8.32	-0.94	0.03	3
BP1	Diorite	7.58	-0.98	0.06	3
BP39	Diorite	6.78	-1.04	0.06	3
BP40	Granodiorite	5.32	-0.85	0.11	3
	Replicate Digestion		-1.15	0.04	3
BP26	Granodiorite	4.48	-0.72	0.04	3
BP23	Granodiorite	3.56	-0.60	0.07	3
	Replicate digestion		-0.59	0.08	3
BP29	Granite	3.34	-0.90	0.10	4
BP22	Granite	2.69	-0.85	0.06	3
BP28	Granite	2.40	-0.79	0.06	3
	Replicate Digestion		-0.67	0.01	3
BP11	Granite	0.96	-0.81	0.07	3
BP12	Aplite	0.52	-0.71	0.04*	1
	Replicate digestion		-0.73	0.09	3
BP42	Aplite	0.38	-0.56	0.06	3
USGS reference Materials					
GSP-2			-0.58	0.06	4
BIR-1a			-0.90	0.04	5
BIR-1a			-0.98	0.06	5
Synthetic Magnetite Powder+			-0.96	0.07	3
Synthetic Magnetite Powder+			-0.85	0.06	5

Table 4.2. Vanadium isotopic composition of BPZP mineral separates. Isotopic compositions given relative to the AA standard. I and P denote whether the mineral is present as an interstitial phase (I) or primocryst (P). Errors are given as 2 standard deviations of the mean of at least 3 measurements of the sample. When fewer than 3 measurements were made, errors are reported as 2SE (*).

Sample	Mineral Phase	Texture	$\delta^{51}V_{AA}$ (‰)	2SD	n
BP41	Biotite	I	-0.88	0.11	3
BP39	Orthopyroxene	P	-0.80	0.05*	2
	Biotite	I	-0.92	0.05*	2
	Hornblende	I	-1.09	0.11	3
	Magnetite	I	-1.26	0.12	3
BP40	Magnetite	P	-1.06	0.02	3
BP22	Biotite	P	-0.71	0.05*	2
	Hornblende	P	-0.81	0.05*	2
	Magnetite	P	-0.81	0.05	3
BP11	Biotite	P	-0.66	0.09	3
	Biotite (Replicate)	P	-0.74	0.06	4
	Hornblende	P	-0.79	0.04*	2
	Magnetite	P	-0.65	0.03	3
BP42	Biotite	P	-0.47	0.07	3
	Magnetite	P	-0.58	0.11	3
	Magnetite (Replicate)	P	-0.59	0.06	5

4.4.2 Magnetite Trace Element Data

The trace element concentrations of the magnetite mineral separates are shown in Table 4.3, and the trace element concentrations of two different measurements of the *Synth. Mag* standard are reported in Table 4.4. It is important to note that magnetite samples were weighed then digested in 6M HCl so that any silicate inclusions would not be dissolved. Therefore, the total mass digested included some silicate material, so all concentrations determined here are minimum values.

The concentration of Fe in magnetite is much larger than all other elements, so samples must be heavily diluted before analysis. This means that the concentration of low abundance trace elements, including the Rare Earth Elements, cannot be measured

accurately. In Table 4.3, we report the concentrations of a selection of transition metals, which are shown in Figure 4.5. All other data can be found in Table 4.S1 (Chapter 4 Appendix). Concentrations of the transition metals Ti, V, Cr and Ni in magnetite decrease with WR MgO content, a proxy for degree of differentiation. Concentrations of Cu and Zn show less well-defined trends. The data fall on the same trend as values measured by LA-ICP-MS by Park et al. (2013) in a different set of samples from the BPZP.

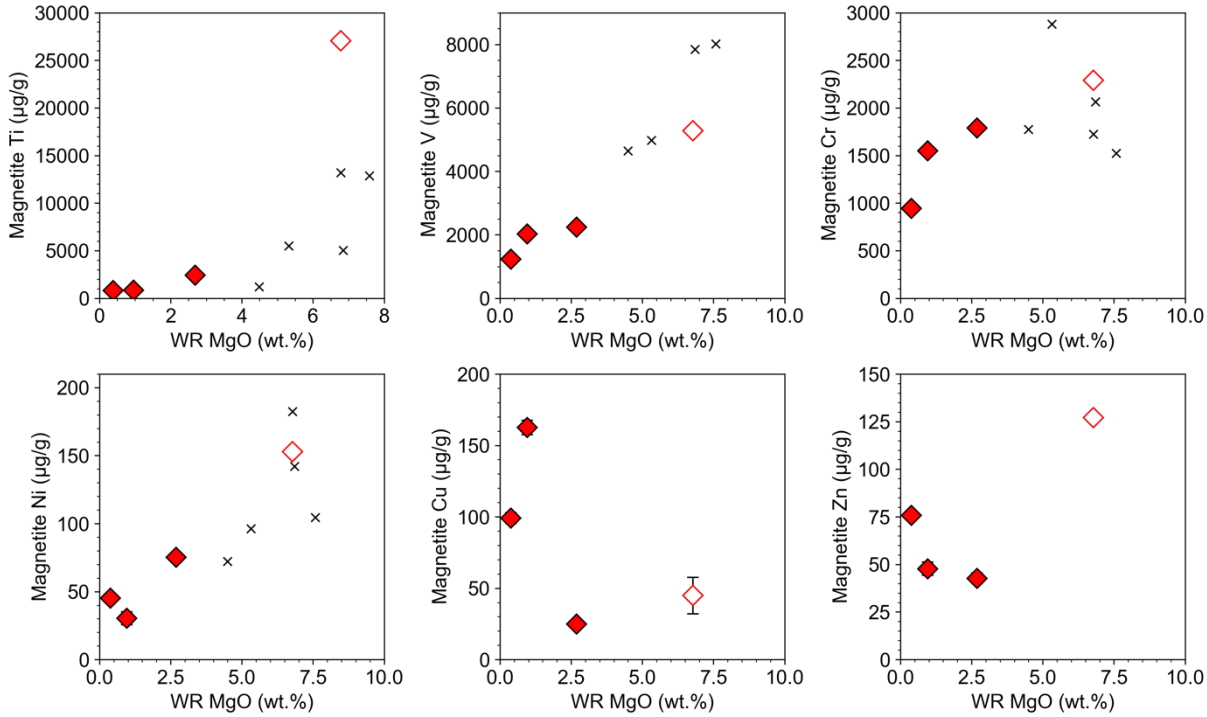

Figure 4.5. Trace element variations in magnetite measured by ICP-QQQ-MS. The BPZP samples are shown by the red diamonds. Interstitial magnetite is shown by open symbols, and primocrysts shown with filled symbols. WR MgO content is from Wyborn (1983). Errors are the within run RSD of an individual measurement of each sample, and are typically smaller than the size of the symbols. The crosses show the average concentration of Ti, V, Cr and Ni measured in magnetite using LA-ICP-MS by Park et al. (2013) from a different set of BPZP samples.

Table 4.3. Transition metal concentrations of magnetite mineral separates measured by ICP-QQQ-MS. Errors are given as the within run standard deviation (RSD). RSDs for Ti, V and Cu are typically <1%. RSDs for Ni, Cu and Zn are typically <10%, with the exception of Ni in BP11 and Cu in BP39. $Fe^{3+}/\Sigma Fe$ values, calculated stoichiometrically using EDS major element data, are also listed.

	BP42		BP11		BP22		BP39	
Element	**Conc (ug/g)**	**% RSD**	**Conc (ug/g)**	**% RSD**	**Conc (ug/g)**	**% RSD**	**Conc (ug/g)**	**% RSD**
Ti	827.7	1.0	844.9	0.5	2437.3	0.2	27042.3	0.01
V	1230.6	0.2	2030.0	0.2	2240.8	0.03	5281.2	0.04
Cr	942.9	0.2	1549.7	0.1	1787.3	0.1	2289.3	0.04
Ni	45.1	2.0	30.3	15.8	75.2	4.5	152.9	1.0
Cu	99.1	3.9	162.6	3.1	25.0	9.0	44.8	28.3
Zn	75.8	0.4	47.7	7.3	42.6	6.5	127.1	1.2
$Fe^{3+}/\Sigma Fe$	0.66		0.66		0.66		0.62	

Table 4.4. Transition metal concentrations of the synthetic magnetite powder measured by ICP-QQQ-MS. The synthetic magnetite powder (>96.8 wt.% Fe_3O_4) is an in-house standard obtained from Inoxia Ltd. The % RSD for Cr are high because of the low Cr concentration in the magnetite standard. Concentrations of all elements are lower by 10-20% the second time the magnetite standard was measured, which may be due to the cones becoming coated with Fe causing a reduction in sensitivity.

	Synth. Mag (Measurement 1)		Synth Mag (Measurement 2)	
Element	**Conc (ug/g)**	**% RSD**	**Conc (ug/g)**	**% RSD**
Ti	2383.7	0.1	2197.5	0.1
V	1036.3	0.1	920.0	0.3
Cr	9.1	34.2	7.0	27.3
Ni	188.9	2.8	149.1	1.1
Cu	13.9	19.0	11.0	4.7
Zn	51.0	1.9	41.0	8.5

A wide variety of trace elements can be incorporated into magnetite (O'Neill and Navrotsky, 1984). Trace element concentrations are influenced by temperature and fO_2 conditions at the time of crystallisation, which control the partition coefficients of trace elements between magnetite and melt (e.g. Toplis and Corgne, 2002; Sievwright et al., 2017). In addition, the concentration of the trace element in the magma or hydrothermal fluid from which the magnetite crystallises, and whether any other co-crystallising phases are competing for that element, also has an effect (Dare et al., 2014). Previous studies have shown that trace element contents of magnetite can be used as a petrogenetic indicator of ore formation processes and conditions (Dare et al., 2012; Dare et al., 2014; Nadoll et al., 2014).

The BPZP magnetite is plotted on the Ti versus Ni/Cr discrimination diagram (Dare et al., 2014) (Figure 4.6). Igneous and hydrothermal magnetite from the compilation of Canil and Lacourse (2020) is plotted for comparison. The BPZP magnetite has a similar composition to other igneous magnetite, and is chemically distinct from both hydrothermally altered magnetite and hydrothermally precipitated magnetite (Wen et al., 2017; Canil and Lacourse, 2020). This is further evidence that elemental and isotopic compositions of magnetite are not affected by late-stage hydrothermal processes in the BPZP. The BPZP magnetite does show lower Ti and Ni/Cr than other igneous magnetite. The most likely cause for the decreases in V, Ti, Cr and Ni in the BPZP magnetite during differentiation is that these elements are compatible in magnetite, and in biotite and hornblende. Hence, the BPZP magma is depleted in V, Ti, Cr and Ni during early fractionation of magnetite, biotite and hornblende, so later crystallising magnetite contains lower concentrations of these elements.

A major reason for analysing the trace element composition of the magnetite mineral separates processed for V isotope ratio measurements was to measure the Ti content of the bulk oxide separate to assess if we were sampling magnetite and/or ilmenite. All samples have very low Ti content (<0.5 wt.% TiO_2 with the exception of the interstitial magnetite from BP39 which has 4.5 wt.% TiO_2). Along with a lack of visible exsolution lamellae under reflected light in all samples, this suggests that the oxides measured in this study are magnetite, which has undergone little low T re-equilibration.

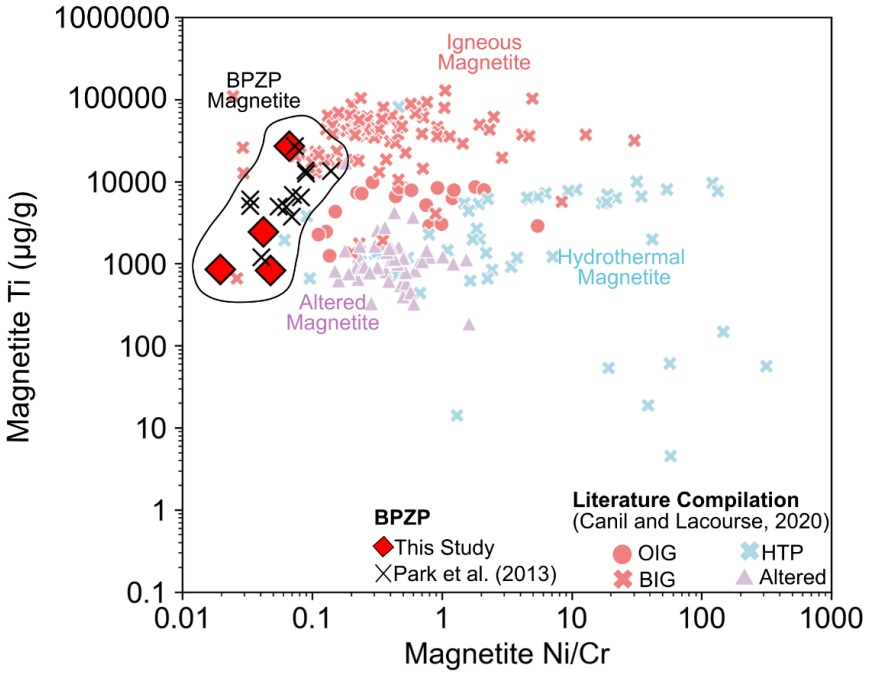

Figure 4.6. Ti-Ni-Cr magnetite discrimination diagram, based on Dare et al. (2014). The BPZP samples measured in this study are shown by the red diamonds. The crosses are values measured using LA-ICP-MS by Park et al. (2013) on a different set of BPZP samples. The literature data is from the compilation of Canil and Lacourse (2020), and is plotted using the same groupings. OIG = Ore-related igneous, BIG = barren igneous, HTP = hydrothermal porphyry. Altered magnetite is the Type 3 and 4 hydrothermally altered magnetite from Wen et al. (2017).

4.5 Causes of V isotopic variations in the Boggy Plain Zoned Pluton

In this section, we first discuss the causes of the variation in $\delta^{51}V$ in whole rock powders and mineral separates from the BPZP. We then describe an approach for reconstructing the V isotopic composition of the evolving melt at the time of crystallisation, because intrusive WR samples do not necessarily represent a true melt composition. This allows data to be compared more directly to extrusive lava suites. We then discuss the implications for our understanding of the V isotopic composition of the continental crust.

4.5.1 Explaining the scatter in WR $\delta^{51}V$ values

There is an overall, scattered increase in whole rock $\delta^{51}V$ with increasing WR SiO_2 and decreasing WR MgO content (Figure 4.2). Based on analysis of Nd, Fe and Zn isotopes within the BPZP, there is no evidence that isotopic trends within the pluton are affected by fluid exsolution, source heterogeneity or crustal assimilation (Ickert, 2010; Stow et al., 2022; Chapter 3). Therefore, the most likely explanation for this increase in whole rock $\delta^{51}V$ is fractional crystallisation.

Previous studies of extrusive lava suites have also shown increases in WR $\delta^{51}V$ during magmatic differentiation (e.g. Prytulak et al., 2017; Wu et al., 2018; Ding et al., 2020). However, the trends in extrusive lava suites are typically much better defined than those observed in the BPZP. It is important to consider what whole rock samples represent in extrusive and intrusive settings. Whereas a rapidly quenched, aphyric lava records the composition of the melt from which it crystallised, intrusive whole rock samples represent variable proportions of crystals and melt that may not have coexisted at equilibrium (e.g. Chappell and Wyborn, 2004). It is also likely that these crystals have been separated from coexisting melt by processes such as crystal settling and/or compaction (e.g. Bachmann and Bergantz, 2004; Holness, 2018). Therefore, the WR composition of an intrusive rock does not directly reflect melt composition. This is especially important for trace elements like V, which are concentrated in certain dense mineral phases. A variation in the modal abundance of these phases and in the amount of trapped interstitial melt could therefore have a large influence on WR $\delta^{51}V$. Hence, variations in WR $\delta^{51}V$ may not reflect true variations in the $\delta^{51}V$ of the evolving melt.

It is likely that some of the scatter in WR $\delta^{51}V$ in the BPZP is due to variations in modal mineralogy and the proportion of trapped interstitial melt. For example, in sample BP39, the isotopic composition of the constituent minerals spans a range of >0.4‰ (Figure 4.3). Biotite, hornblende and magnetite all show interstitial morphologies in BP39, and have likely crystallised from trapped patches of interstitial melt which do not have the same isotopic composition. Variation in the modal proportions of primocryst pyroxene and interstitial phases could therefore influence WR isotopic composition. This may explain the difference in $\delta^{51}V$ of two digestions of sample BP40 (-0.85±0.11‰ 2SD and -1.15±0.04‰ 2SD). Two different sample powders were made from the same 30 cm size BP40 whole rock sample. However, decimetre scale modal layering is observed in

samples in the field (Wyborn, 1983), and variations in modal mineralogy at this scale could influence the isotopic composition of different powders made from the same hand sample.

In the more felsic samples, primocryst biotite, hornblende and magnetite have similar isotopic compositions, within a range of 0.15‰, which is similar to the typical 2SD analytical precision of V isotope measurements. However, variation in the proportion of trapped, evolved interstitial melt with elevated $\delta^{51}V$ could also cause scatter in the WR $\delta^{51}V$ values of these samples.

4.5.2 Indistinguishable $\delta^{51}V$ of biotite, magnetite, and hornblende primocrysts in the same sample

Given the ambiguity in interpreting WR isotopic data in intrusive settings as discussed above, it may be more informative to focus on the isotopic compositions of mineral separates. Biotite, hornblende and magnetite mineral separates show well defined trends in $\delta^{51}V$ with WR MgO and WR SiO_2 (Figure 4.3). Notably, primocryst biotite and magnetite have identical V isotopic composition in the same sample, and hornblende is approximately 0.1‰ lighter than biotite, but within analytical error (Figure 4.4). This may be surprising given the different structures and chemical compositions of these minerals, as discussed below.

Fundamentally, the V isotopic composition of the minerals in the BPZP depends on the isotopic composition of the melt from which they crystallise, and the isotopic fractionation factor ($\Delta^{51}V_{min\text{-}melt}$) between that mineral and the melt. Fractionation factors are controlled by variation in valence state and bonding environment between mineral and melt, and external factors including temperature and fO_2 (e.g. Schauble, 2004). If biotite, magnetite and hornblende have indistinguishable $\delta^{51}V$ in an individual sample, this implies that $\Delta^{51}V_{min\text{-}melt}$ is also equal for all three minerals. This would suggest that the oxidation state and bonding environment of V is also similar in all three minerals.

Table 4.5 shows the most likely V substitutions, valence states and bond lengths in biotite, hornblende and magnetite. Vanadium can substitute as $^{VI}V^{3+}$ (0.640Å) for either $^{VI}Fe^{3+}$ (0.645Å) or $^{VI}Ti^{4+}$ (0.605Å) given their similar ionic radii (Shannon, 1976). There is the potential for some substitution of $^{VI}V^{4+}$, for example natural magnetite samples can

contain up to 10% V^{4+} (Balan et al., 2006). In addition, ^{VI}Fe-O (and hence ^{VI}V-O) bond lengths are similar in all phases. The type of neighbouring cations can also influence fractionation factors (e.g. Rabin et al., 2021) but this is difficult to quantify given the uncertainty about where V substitutes in minerals. Taken together, all three minerals appear to have similar bonding environments for V, so large inter-mineral fractionation factors are not expected, consistent with our observations.

There is still the potential that differences in the V^{4+}/V^{3+} ratio between mineral phases can influence isotopic composition. Based on bond valence theory, isotopically heavy V is predicted to concentrate in bonds containing V in a higher valence state, so minerals with higher V^{4+}/V^{3+} ratios would be isotopically heavier (e.g. Wu et al., 2015). There have been attempts to measure the valence state of V in spinel minerals and silicate melt using X-ray absorption near edge structure spectroscopy (XANES; Giuli et al., 2004; Sutton et al., 2005; Righter et al., 2006; Balan et al., 2006) but few studies on silicate minerals. This is because crystal orientation effects strongly influence the shape of the XANES spectra, and it is difficult to find appropriate standards for comparison (e.g. Papike et al., 2016). We can look at the ratio of Fe^{3+}/Ti^{4+} in silicate minerals as a proxy for V^{3+}/V^{4+} content, assuming the substitutions V^{3+} for Fe^{3+} and V^{4+} for Ti^{4+} on VI-sites only. In the BPZP, magnetite has the highest Fe^{3+}/Ti^{4+} and biotite has the lowest. Therefore, assuming only these substitutions, biotite would be expected to have the lowest V^{3+}/V^{4+} ratio of the three minerals, and isotopic enrichment would be expected in the order biotite > hornblende > magnetite if there was a valence control. However, this is not observed, and in most cases, hornblende is the isotopically lightest mineral in an individual sample.

In the BPZP, biotite, hornblende and magnetite have identical $\Delta^{51}V_{min\text{-}melt}$ values. The evidence discussed above suggests that the overwhelming control on inter-mineral V fractionation factors is mineral bonding environment, rather than variation in valence state.

Table 4.5. Structural formula and most likely V substitutions for magnetite, biotite and hornblende.

Mineral	Structural Formula	V substitution	$Fe^{3+}/\Sigma Fe$	Bond Lengths
Magnetite	Pure magnetite: $^{IV}(Fe^{3+})^{VI}(Fe^{3+}, Fe^{2+})O_4$ Ti substitutes following the reaction: $^{IV}Fe^{3+} + {}^{VI}Fe^{3+} = {}^{IV}Fe^{2+} + {}^{VI}Ti^{4+}$ Ti substitution causes unit cell distortion (longer T-O and shorter M-O bonds; Bosi et al. 2009).	Most likely **V^{3+} on VI sites** (O'Neill and Navrotsky, 1984) In titanomagnetite, some **V^{4+}** may be present, but would substitute on the **VI site** also, as its radius is too small for the IV site (Toplis and Corgne, 2002)	Pure magnetite = 0.66, and V^{3+}/V^{4+} ratio set to charge balance this by substitution $Fe^{2+} + V^{4+} = Fe^{3+} + V^{3+}$ (O'Neill and Navrotsky, 1984).	Magnetite: ^{VI}Fe-O = 2.068 ^{IV}Fe-O = 1.873 (Sossi and O'Neill, 2017)
Biotite	**$I\,M_{2\text{-}3}\,\square_{1\text{-}0}T_4O_{10}A_2$** I = Cs, K, Na, NH_4, Rb, Ba, Ca M = Li, Fe^{3+}, Fe^{2+}, Mg, Mn, Zn, Al, Cr, V, Ti $\square$ = vacancy T = Be, Al, B, Fe^{3+}, Si A = Cl, F, OH, O, S (Rieder et al., 1999)	**V^{3+} in VI-fold** coordination on the M layer (Zheng et al., 2019), most likely substituting for Fe^{3+}	BPZP = 0.1 – 0.2	Annite: ^{VI}Fe-O = 2.109 (Nie et al., 2021)
Hornblende	**$AB_2C_5T_8O_{22}W_2$** A = Na, K, Ca, Pb, Li B= Na, Ca, Mn^{2+}, Fe^{2+}, Mg, Li C = Mg, Fe^{2+}, Mn^{2+}, Al, Fe^{3+}, Mn^{3+}, Ti^{4+}, Li T = Si, Al, Ti^{4+}, Be W = OH, F, Cl, O (Hawthorne et al., 2012)	Most likely **V^{3+}** substituting for Fe^{3+} on **VI-fold** M2 or M3 (C) sites (Oberti et al., 2007).	BPZP = 0.2 – 0.25	Synthetic Amphibole: M_2-O = 2.107 M_3-O = 2.115 (Redhammer and Roth, 2002)

4.5.3 Drivers of the increase in $\delta^{51}V$ with differentiation

Both the WR samples and mineral separates show an overall increase in $\delta^{51}V$ with differentiation (Figures 4.3 and 4.3). Previous studies have attributed such increases in WR $\delta^{51}V$ during differentiation to crystallisation of isotopically light minerals, driving the residual magma to a heavier isotopic composition (Prytulak et al., 2017; Ding et al., 2020). Prytulak et al. (2017) proposed that the most likely phase driving this increase was (titano)magnetite, because V is highly compatible in magnetite (e.g. Toplis and Corgne, 2002) and thus magnetite can host a large proportion of the V in the system. Magnetite contains trivalent V in octahedral coordination (O'Neill and Navrotsky, 1984), whereas silicate melt contains IV- and V-fold V at higher redox state (Giuli et al., 2004; Sutton et al., 2005; Righter et al., 2006). Therefore, magnetite is theoretically predicted to be isotopically lighter than coexisting melt at equilibrium (e.g. Wu et al., 2015). This is supported by an experimental study of vanadium isotope fractionation between magnetite and melt, which consistently showed negative $\Delta^{51}V_{mag\text{-}melt}$ values (Sossi et al., 2018b). Recent work has also indicated that the specific mineralogy of the oxides will determine the extent of increase in WR $\delta^{51}V$. Comparisons of Fe-V-Ti isotopes in lavas from Kilauea Iki, Hekla and Anatahan hint that magnetite, Ti-rich ulvöspinel and ilmenite may have distinct $\Delta^{51}V_{min\text{-}melt}$ values (Ding et al., 2020), although this has not been tested directly using mineral separates.

However, in the BPZP, biotite and hornblende contain between 200 – 800 μg/g V (Wyborn, 1983), and both minerals have modal abundances of approximately 5-15% in samples spanning the differentiation sequence. Therefore, although the magnetite in the BPZP has the highest V concentration, mass balance calculations considering the proportion of phases and their V concentrations show that the silicate phases can account for 40-65% of the V budget in individual samples. As discussed in Section 4.5.2, biotite and hornblende predominantly host V^{3+} in VI-fold coordination, substituting for VI-fold Fe^{3+} which has a similar ionic radius (Shannon et al., 1976). Therefore, silicate minerals should also be isotopically lighter than coexisting melt at equilibrium.

The combined fractional crystallisation of isotopically light biotite, hornblende and magnetite can therefore drive an increase in melt $\delta^{51}V$. The next minerals which crystallise from this isotopically heavier melt then also have heavier $\delta^{51}V$. Hence, fractional crystallisation drives an increase in $\delta^{51}V$ of both melt and minerals. Whole rock

samples, which are collections of minerals and trapped interstitial melt, also show this increase in $\delta^{51}V$ during differentiation, but WR $\delta^{51}V$ values may not directly record the V isotopic composition of the evolving melt.

4.5.4 Trends in mineral separate V isotopic composition

The mineral separates also display relationships between mineral chemistry and mineral isotopic composition. Biotite $\delta^{51}V$ increases with increasing biotite FeO, $Fe^{3+}/\Sigma Fe$, and Na_2O content, and decreasing TiO_2, V, MgO content (Figure 4.7). Magnetite $\delta^{51}V$ increases with decreasing V, Cr and Ti content (Figure 4.8). These variations most likely reflect the overall changes in melt V isotopic composition and elemental concentrations during fractional crystallisation.

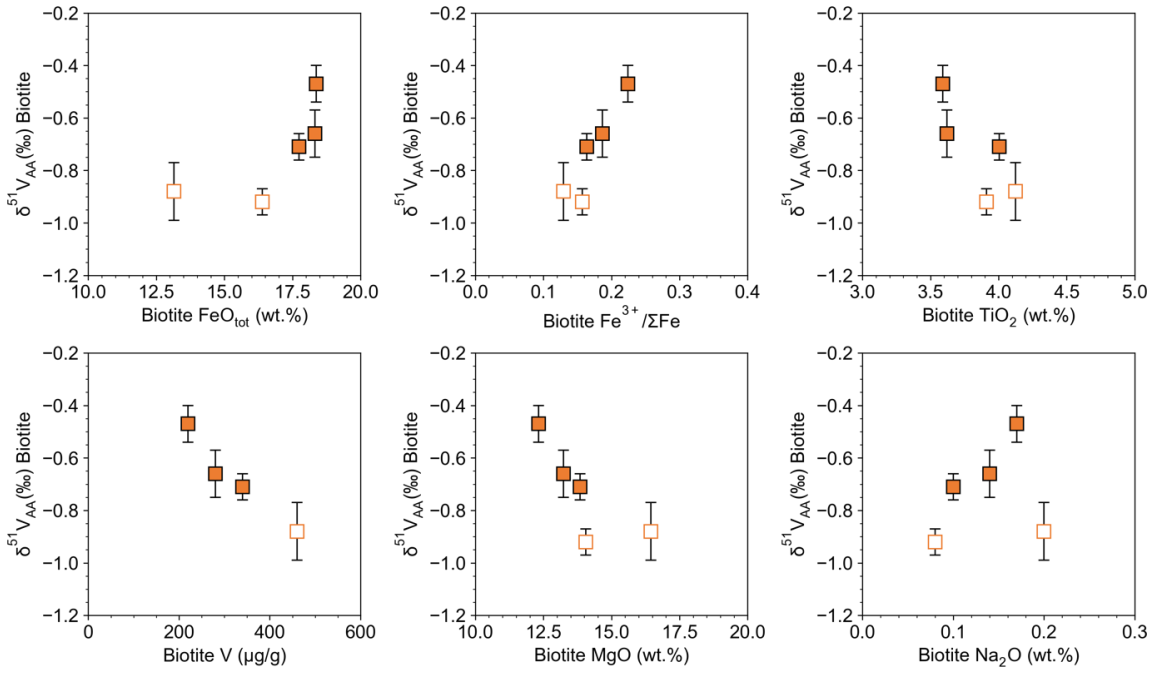

Figure 4.7. Variation in biotite V isotopic composition and chemistry. Biotite major and trace element data are from Wyborn (1983). Vanadium isotopic compositions are given in Table 4.2. Errors are 2SD of at least 3 measurements of an individual sample. Biotite with interstitial morphologies is shown with open symbols, and primocrysts shown with filled symbols.

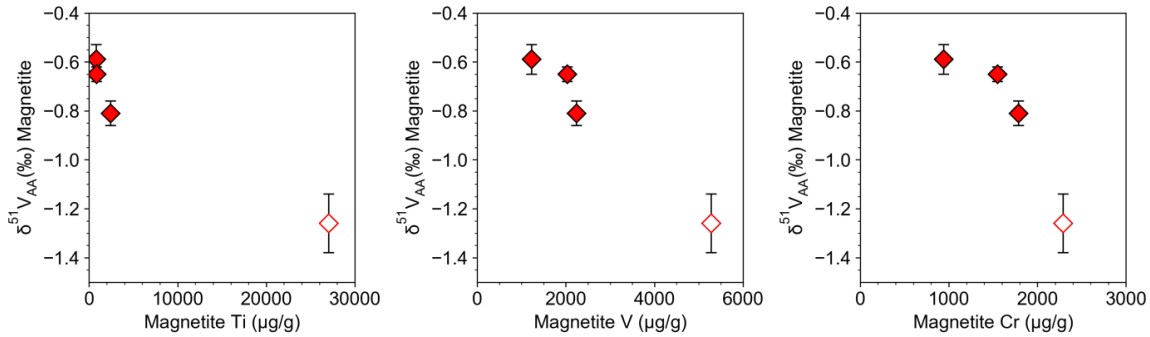

Figure 4.8. Variation in magnetite V isotopic composition and chemistry. Isotopic compositions are given in Table 4.2, trace element compositions are given in Table 4.3. For trace element concentrations, errors are the within run RSD of an individual measurement of each sample, and are normally smaller than the size of the symbols. Errors in $\delta^{51}V$ are 2SD of at least 3 measurements of an individual sample. Magnetite with interstitial morphologies is shown with open symbols, and primocrysts shown with filled symbols.

Notably, biotite and magnetite both show a trend of increasing $\delta^{51}V$ with WR $Fe^{3+}/\Sigma Fe$ content. Variation of magnetite $\delta^{51}V$ against WR $Fe^{3+}/\Sigma Fe$ content is shown in Figure 4.9. The data show a positive correlation with an R^2 value of 0.9962. If we were to assume that an increase in WR $Fe^{3+}/\Sigma Fe$ is recording an increase in magma fO_2, this trend could, at first glance, be interpreted as the V isotopic composition of the minerals directly recording variations in magma fO_2 (i.e. heavier isotopic composition at more oxidising conditions). However, this mechanism is unlikely when we consider the experimental work of Sossi et al. (2018b).

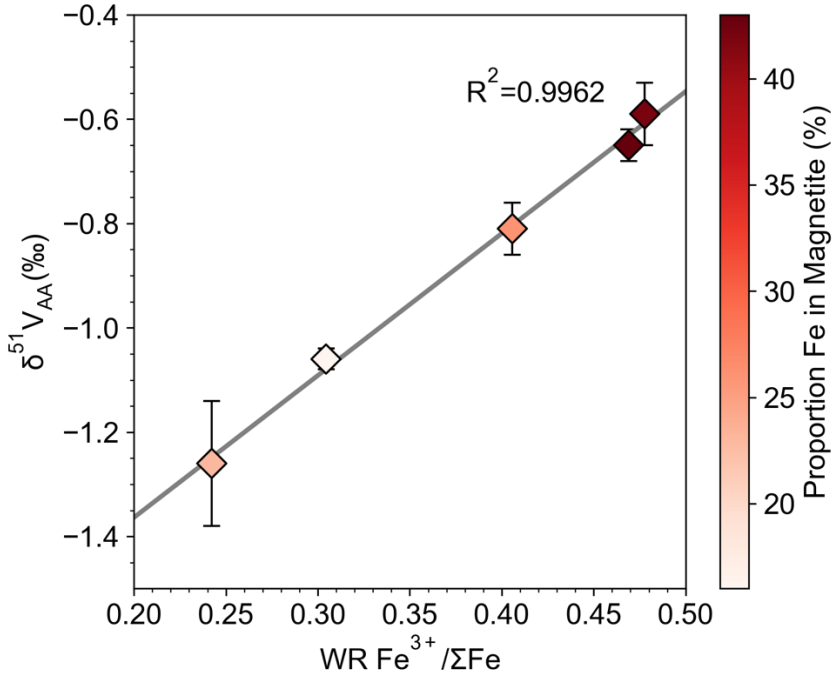

Figure 4.9. Vanadium isotopic composition of magnetite mineral separates plotted against WR $Fe^{3+}/\Sigma Fe$ from Wyborn (1983). Note that magnetite $\delta^{51}V$ is plotted against WR $Fe^{3+}/\Sigma Fe$ rather than magnetite $Fe^{3+}/\Sigma Fe$. This is because the magnetite has extremely low Ti concentration, so magnetite $Fe^{3+}/\Sigma Fe$ is controlled by stoichiometry and therefore has a value of approximately 0.66 across the whole pluton. The data show a positive correlation with an R^2 value of 0.9962. The colour of the symbols shows how much Fe is hosted in magnetite versus silicate phases. A darker red colour indicates a higher proportion of Fe hosted in magnetite. This is determined by a mass balance calculation considering the modal abundances of the different mineral phases and their Fe concentrations given in Wyborn (1983).

The experiments of Sossi et al. (2018b) were conducted over a fO_2 range of 6 log units, which encompasses and exceeds typical fO_2 values of terrestrial magmas. The temperature (800°C) and melt composition (hydrous haplogranite) at which the experiments were conducted are also geologically relevant to the crystallisation conditions of the BPZP (Sossi et al., 2018b; Wyborn, 1983). Quantitative determinations of oxygen fugacity are difficult for intrusive rocks like the BPZP, but estimates suggest initial magma fO_2 of approximately FMQ-1, and an increase of 1-2 log units during fractional crystallisation (Wyborn, 1983). For a fO_2 variation of 2 log units from FMQ-1 to FMQ+1, Sossi et al. (2018b) predict a variation in $\Delta^{51}V_{mag\text{-}melt}$ of approximately 0.1‰. Since the BPZP is an intrusive system, we do not have a coexisting melt phase to analyse, so cannot directly compare $\Delta^{51}V_{min\text{-}melt}$ values. However, we can consider the magnetite

mineral separates, which show a 0.6‰ range in $\delta^{51}V$ across the differentiation sequence. This range is much larger than the difference in $\Delta^{51}V_{mag\text{-}melt}$ predicted due to variation in magma fO_2, which highlights that although fO_2 variations may exert some influence on V isotope fractionation in the BPZP, it is not the primary control.

Instead, the increase in $\delta^{51}V$ of magnetite most likely reflects the increasing $\delta^{51}V$ of the evolving melt. As discussed in Section 4.5.3, crystallisation of isotopically light biotite, magnetite and hornblende causes an increase in magma $\delta^{51}V$, and thus the next minerals to crystallise also have heavier $\delta^{51}V$. This interpretation is supported by the other chemical variations in magnetite and biotite, such as decreasing TiO_2, V and MgO concentrations (Figure 4.8 and 4.9), which reflect the decreasing concentrations of these elements in the magma during fractional crystallisation (Wyborn, 1983; Figures 3.2 and 4.1).

However, the cause of the contemporaneous increase in WR $Fe^{3+}/\Sigma Fe$ is less intuitive. The span of WR $Fe^{3+}/\Sigma Fe$ in the BPZP is much larger than observed in lavas and glasses. For example, MORB glasses have $Fe^{3+}/\Sigma Fe = 0.16 \pm 0.01$ (Cottrell and Kelley, 2011) and arc lavas generally have $Fe^{3+}/\Sigma Fe$ values between 0.2 and 0.3 (Kelley and Cottrell, 2009; 2012; Brounce et al., 2014). In the BPZP, WR $Fe^{3+}/\Sigma Fe$ does not represent the $Fe^{3+}/\Sigma Fe$ of an evolving magma, but rather the mineralogy of the sample and whether Fe is hosted primarily as Fe^{3+} or Fe^{2+} in the different mineral phases. The increase in WR $Fe^{3+}/\Sigma Fe$ in the BPZP is due to an increased proportion of Fe hosted in magnetite ($Fe^{3+}/\Sigma Fe \sim 0.66$) in the more evolved samples, which has a higher $Fe^{3+}/\Sigma Fe$ than silicate phases like pyroxene, biotite and hornblende ($Fe^{3+}/\Sigma Fe$ values of ~0, 0.12-0.22 and 0.18-0.25 respectively; Wyborn, 1983). This is demonstrated by mass balance calculations considering modal abundance and Fe concentration of the minerals which make up each sample. In the more felsic samples, a greater proportion of Fe is hosted in magnetite relative to silicate minerals (dark red symbols in Figure 4.10). Therefore, the correlation between magnetite $\delta^{51}V$ and WR $Fe^{3+}/\Sigma Fe$ in the BPZP does not indicate a relationship between $\delta^{51}V$ and magma redox state. Instead, variations in $\delta^{51}V$ and WR $Fe^{3+}/\Sigma Fe$ are due to fractional crystallisation and subsequent changes in the modal mineralogy of samples. This highlights that in closed system differentiation sequences, although variations in T and fO_2 can influence the magnitude of mineral-melt fractionation factors

these are difficult to resolve, and isotopic trends in minerals will largely be controlled by variation in magma isotopic composition.

Sossi et al. (2018b) proposed that the V isotopic composition of magnetite from granites could potentially be used as an indicator of magma fO_2 during crystallisation, and that V isotopes in magnetite could be used more generally as a provenance tracer. This is because $\Delta^{51}V_{mag\text{-}melt}$ values increase (become more negative) at higher fO_2, so if two magmas with contrasting fO_2 had the same initial $\delta^{51}V$, magnetite crystallising from the magma with higher fO_2 should have a lighter isotopic composition (Sossi et al., 2018b). However, this work on the BPZP shows magnetite V isotopic composition cannot be easily used to track fO_2 variations in an individual pluton. Over a fO_2 range of 1-2 log units, $\Delta^{51}V_{mag\text{-}melt}$ is only predicted to vary by 0.1‰. This is a similar magnitude to typical analytical uncertainty on V isotope measurements, so variations in $\delta^{51}V$ are not resolvable over the fO_2 range of individual magmatic systems. Additionally, the isotopic composition of an individual magnetite crystal depends on the isotopic composition of the magma it crystallises from, which is primarily controlled by the extent of fractional crystallisation and subsequent removal of isotopically light phases in the suite. Therefore, magnetite $\delta^{51}V$ values are not necessarily distinctive between different settings.

4.6 Models of V Isotopic Variation

In this section, we investigate approaches for modelling V isotopic variations in the BPZP, with the caveat that WR samples do not necessarily record a true melt composition. We derive a new method to reconstruct the V isotopic composition of the evolving melt at the time of crystallisation from the mineral separate data. This overcomes the uncertainties with using WR analyses in intrusive settings, and allows data to be compared more directly to previous studies of extrusive suites.

4.6.1 Rayleigh models and reconstruction of melt isotopic composition

As discussed in Chapter 3, the most common approach for modelling isotopic variations during fractional crystallisation is to use Rayleigh equations (Equation 4.1). The underlying assumption is that WR $\delta^{51}V$ is equivalent to the $\delta^{51}V$ of the evolving magma at the time of crystallisation. The approach described in Chapter 3 (Section 3.7) and Stow et al. (2022) can, in principle, be used to model the V isotopic variations in the BPZP.

$$\delta^{51}V = \delta^{51}V_{initial} + (\Delta^{51}V_{min\text{-}melt} \times \ln fV) \qquad [4.1]$$

Equation 4.1 is used to calculate the bulk $\Delta^{51}V_{min\text{-}melt}$ that best describes the evolution in WR $\delta^{51}V$ during fractional crystallisation (See Chapter 3, section 3.7). Given the scatter in WR $\delta^{51}V$ in the mafic cumulate samples (Figure 4.2), a value of -0.9‰ is used for $\delta^{51}V_{initial}$, which is a value typical of mantle derived basalts (e.g. Prytulak et al., 2013; Wu et al., 2018). Figure 4.10 shows that a constant bulk mineral-melt fractionation factor of approximately -0.05‰ can describe the evolution of $\delta^{51}V$ in the WR samples. Given that biotite, hornblende and magnetite mineral separates have identical isotopic composition in individual samples, fractionation factors between biotite-melt, magnetite-melt and hornblende-melt would also be -0.05‰.

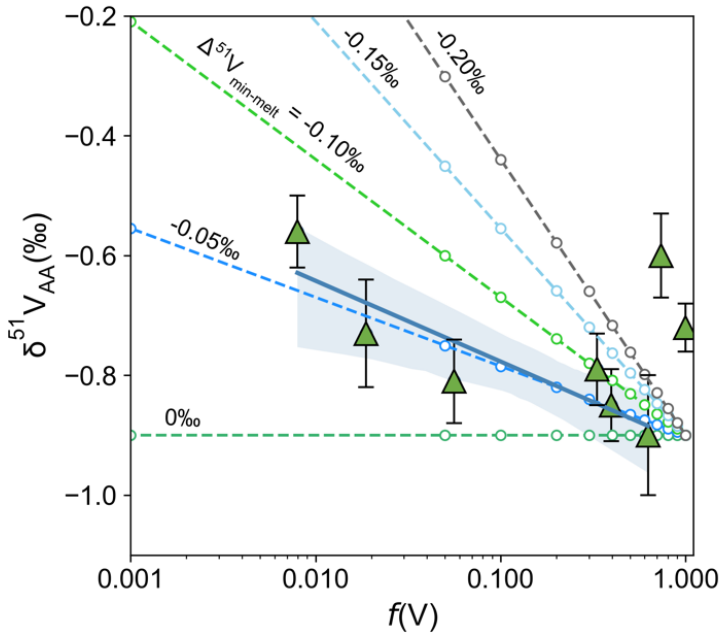

Figure 4.10. The $\delta^{51}V$ evolution of a melt undergoing fractional crystallisation (dashed lines). Melt $\delta^{51}V$ is modelled using the Rayleigh equation ($\delta^{51}V = \delta^{51}V_i + (\Delta^{51}V_{min\text{-}melt} \times \ln f(V)$; Equation 4.1) at constant $\Delta^{51}V_{min\text{-}melt}$. The starting magma composition ($\delta^{51}V_i$) was -0.90‰. The blue shaded area and dark blue solid line is a weighted linear regression of the BPZP data, omitting the two isotopically heavy samples at $fV \sim 0.8$. These two samples were omitted because they are obvious outliers to the general trend in WR $\delta^{51}V$, likely reflecting the presence of isotopically heavy trapped melt or mineral phases. This again highlights the uncertainties with using WR analyses in intrusive settings. The isotopic evolution of the BPZP magma can be described by a bulk $\Delta^{51}V_{min\text{-}melt}$ of approximately -0.05‰.

A bulk $\Delta^{51}V_{min\text{-}melt}$ value of -0.05‰ is much smaller than values determined for other magmatic systems. V isotopic variation in the Hekla and Anatahan differentiation suites requires $\Delta^{51}V_{min\text{-}melt}$ values of -0.4‰ to -0.5‰ (Prytulak et al., 2017), and trends at Kilauea Iki are described by $\Delta^{51}V_{min\text{-}melt}$ = -0.15‰ (Ding et al., 2020). The only individual mineral $\Delta^{51}V_{min\text{-}melt}$ values for comparison are the experimentally determined $\Delta^{51}V_{mag\text{-}melt}$ values from Sossi et al. (2018b), which are much larger, ranging from -0.63‰ at FMQ-1 to -0.92‰ at FMQ+5 at 800 °C.

It is possible that $\Delta^{51}V_{min\text{-}melt}$ values in the BPZP are truly smaller than in the differentiation sequences studied previously. However, an important distinction to make is that the previous studies were examining whole rock extrusive lava samples, whereas the whole rock samples from the BPZP are coarse grained, intrusive rocks. As discussed above, the whole rock samples from the BPZP most likely reflect the V isotopic composition of constituent mineral separates, rather than representing a true melt composition. Given that Rayleigh equations require the assumption that WR $\delta^{51}V$ is equivalent to melt $\delta^{51}V$ at the time of crystallisation, this approach cannot be used to accurately derive bulk $\Delta^{51}V_{min\text{-}melt}$ values in intrusive systems. Although we can theoretically construct Rayleigh models and choose appropriate $\Delta^{51}V_{min\text{-}melt}$ values which apparently describe the variation in WR $\delta^{51}V$ in intrusive systems, these models are not describing the variation in melt isotopic composition.

However, it may be possible to estimate the approximate composition of the evolving melt using the Boggy Plain mineral separate data and bulk $\Delta^{51}V_{min\text{-}melt}$ values from previous studies of lava suites. This is a suitable approximation for several reasons. Firstly, because biotite, hornblende and magnetite mineral separates have identical isotopic composition in individual samples (with current analytical precision), bulk $\Delta^{51}V_{min\text{-}melt}$ value should not be affected by variation in modal abundances during fractional crystallisation. Therefore, a single value can be used to describe the whole crystallisation sequence. Secondly, as discussed in Section 4.5.2, $\Delta^{51}V_{mag\text{-}melt}$ is only predicted to vary by about 0.1‰ across the entire fO_2 range of the BPZP (Sossi et al., 2018b), which is a similar magnitude to current analytical uncertainty. Therefore, is assumed that variations in fO_2 do not have to be considered in the model. Hence, at an individual point in the crystallisation sequence:

$$\text{Bulk } \Delta^{51}V_{\text{min-melt}} = \Delta^{51}V_{\text{mag-melt}} = \delta^{51}V_{\text{mag}} - \delta^{51}V_{\text{melt}} \qquad [4.2]$$

This can be rearranged to find melt $\delta^{51}V$ (Equation 4.3):

$$\delta^{51}V_{\text{melt}} = \delta^{51}V_{\text{mag}} - \Delta^{51}V_{\text{min-melt}} \qquad [4.3]$$

Bulk $\Delta^{51}V_{\text{min-melt}}$ values have been calculated previously for the Anatahan, Hekla and Kilauea Iki differentiation suites (Prytulak et al., 2017; Ding et al., 2020). However, since the type and chemistry of Fe-Ti oxides can influence bulk $\Delta^{51}V_{\text{min-melt}}$ values (Ding et al., 2020), it is most appropriate to choose a bulk $\Delta^{51}V_{\text{min-melt}}$ value from a suite with similar type and chemistry of Fe-Ti oxides as the BPZP. Therefore, the bulk $\Delta^{51}V_{\text{min-melt}}$ value of -0.45‰ from the Hekla differentiation suite is chosen, since titanomagnetite is the only crystallising oxide (Sigmarsson et al., 1992; Schuessler et al., 2009; Savage et al., 2011). The resultant $\delta^{51}V$ of the BPZP melt is shown by the yellow dashed line in Figure 4.11.

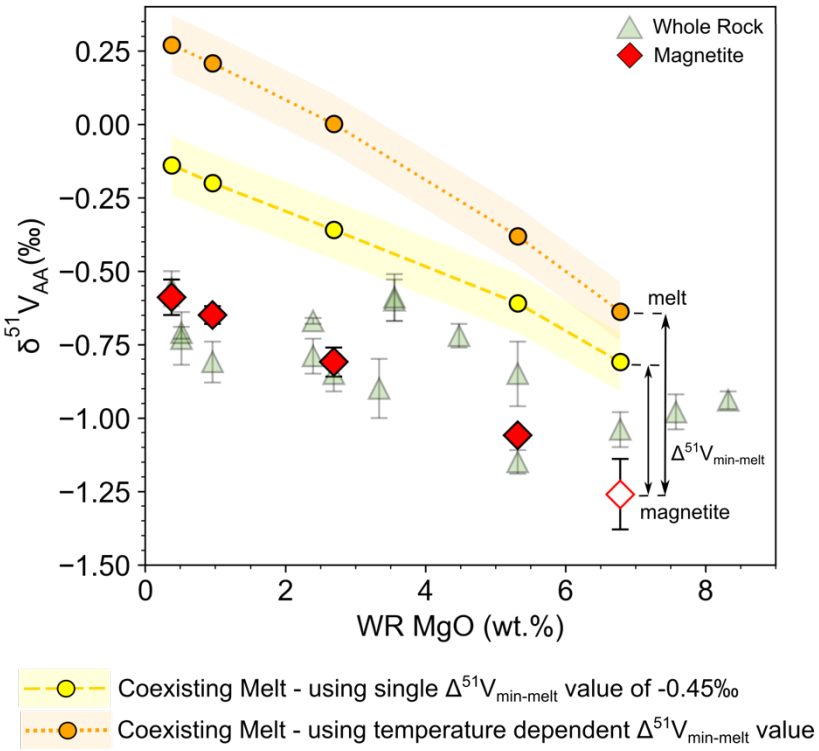

Figure 4.11. Calculation of the $\delta^{51}V$ of the BPZP melt from magnetite separate data. The theoretical V isotopic composition of the melt that the magnetite separates crystallised from is shown by the yellow and orange lines. The shaded area shows the error on the melt isotopic composition, which is taken to be ± 0.1‰, the long-term analytical uncertainty for V. Melt reconstruction 1 (yellow) uses a bulk $\Delta^{51}V_{\text{min-melt}}$ value of -0.45‰ as described in the text. Melt reconstruction 2 (orange) considers temperature variations, as described in the text.

An additional complication is that there is the potential for variation in $\Delta^{51}V_{min\text{-}melt}$ values with temperature, because Δ is proportional to $1/T^2$ (Schauble, 2004). Crystallisation temperatures span a range of 200°C across the BPZP differentiation sequence, decreasing from approximately 900°C to 700°C (Stow et al., 2022; Chapter 3). To demonstrate how this variation in temperature could influence magma $\delta^{51}V$, we assume an initial magma fO_2 equal to FMQ, and recast the $\Delta^{51}V_{mag\text{-}melt}$ measurements made at 800 °C by Sossi et al. (2018b) to the crystallisation temperatures of the individual BPZP samples given in Table 3.3, Chapter 3. This allows us to calculate an individual $\Delta^{51}V_{mag\text{-}melt}$ for each sample. Melt $\delta^{51}V$ is then calculated by subtracting this value from the value of magnetite $\delta^{51}V$ in that sample (Equation 4.3). The calculated melt $\delta^{51}V$ is shown by the orange dotted line in Figure 4.11. Therefore, there is the potential for a significant variation in $\Delta^{51}V_{min\text{-}melt}$ with temperature which needs to be better quantified, especially in intrusive settings where temperature can vary by several hundred degrees.

The yellow and orange lines and shaded areas on Figure 4.11 show the theoretical composition of the melt at the time of magnetite crystallisation. Melt compositions are isotopically heavier than the BPZP WR samples, and span a larger range in $\delta^{51}V$ when temperature variations are considered. However, the most evolved melts will have the lowest V concentrations, so even if isotopically heavy highly evolved melt were trapped within the crystallising pluton, such heavy $\delta^{51}V$ values would be difficult to detect in the WR samples. Note that the melt reconstructed from the interstitial magnetite in BP39 would reflect interstitial melt composition which may be distinct from the composition of the evolving magma body (e.g. Humphreys, 2011). Therefore, in situations where mineral separates have identical isotopic composition, it may be possible to reconstruct the isotopic composition of the coexisting (and now inaccessible) melt from mineral separate data. This is useful because it allows data from intrusive settings to be more directly compared to extrusive lava samples.

4.6.2. Smaller variation in modelled $\delta^{51}V_{melt}$ of the BPZP compared to extrusive lavas

We can compare the reconstructed melt V isotopic composition of the BPZP with extrusive lava samples from previous studies, shown in Figure 4.12. It is suggested that the distinctive trends observed in WR $\delta^{51}V$ in the different lava suites are driven by the modal abundance and mineralogy of oxides, and the timing of oxide saturation (Prytulak

et al., 2017; Ding et al., 2020). In terms of oxide mineralogy, Ding et al. (2020) hypothesise that:

> (1) $\Delta^{51}V_{ilm\text{-}melt}$ values are smaller (less negative) than $\Delta^{51}V_{mag\text{-}melt}$ values. This leads to the smaller increase in $\delta^{51}V$ in Kilauea Iki (ilmenite and magnetite fractionation) compared to Anatahan and Hekla (magnetite fractionation only).
>
> (2) $\Delta^{51}V_{mag\text{-}melt}$ values decrease (become less negative) with increasing Ti content in magnetite. A balance between the crystallisation of isotopically light magnetite and heavier Ti-rich ulvöspinel could explain the lack of variation in $\delta^{51}V$ in the Anatahan lavas immediately after initial oxide saturation (Group 2 in Williams et al., 2018).

In addition, there will be larger magnitude $\Delta^{51}V_{mag\text{-}melt}$ at lower temperatures (e.g. Urey, 1947; Schauble, 2004). However, if oxide petrology and temperature are the main control on magma $\delta^{51}V$ evolution, it is curious that the BPZP melt does not show as large or steep an increase in $\delta^{51}V$ as observed in the Hekla and Anatahan lavas over a similar MgO range (Prytulak et al., 2017), considering magnetite is the dominant oxide phase crystallising in all three suites, and the BPZP crystallises at a lower temperature than Hekla and Anatahan (Wyborn, 1983; Prytulak et al., 2017). This perhaps suggests that crystal-melt segregation processes are less efficient in silicic granites than in lavas, so melt isotopic evolution is not controlled by perfect Rayleigh fractional crystallisation. If some residual melt is trapped between crystallising minerals and not returned to the main magma body, this would result in smaller increases in $\delta^{51}V$ for the same $\Delta^{51}V_{min\text{-}melt}$ (e.g. Langmuir, 1989).

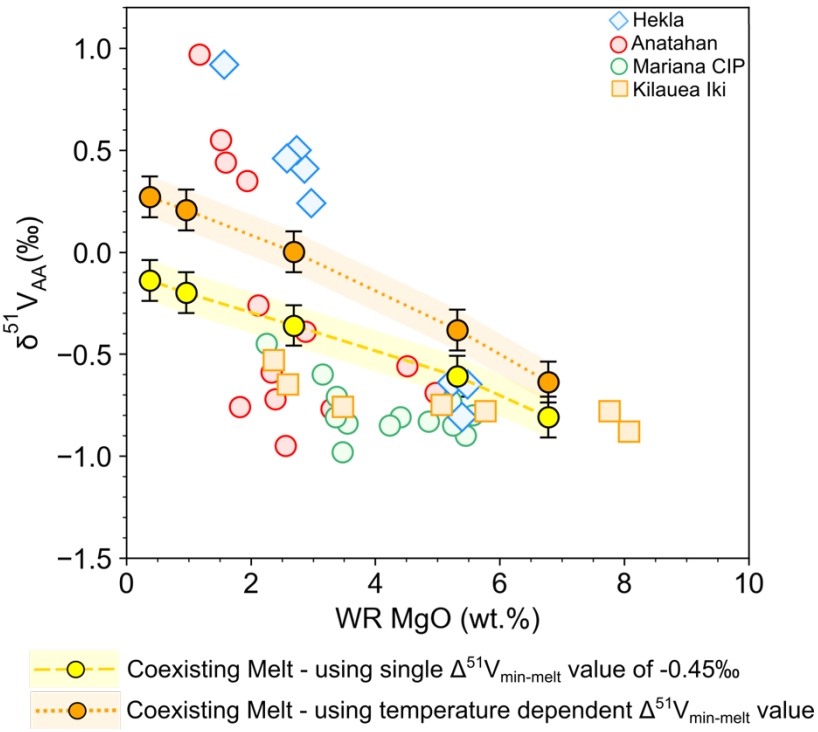

Figure 4.12. A comparison of the reconstructed BPZP melt and extrusive lava suites. The BPZP melt is shown by the yellow and orange filled circles. Errors are ± 0.1‰, the typical analytical uncertainty for V isotope measurements. The Anatahan, Mariana CIP and Hekla data are from Prytulak et al. (2017). The Kilauea Iki data are from Ding et al. (2020).

4.7 Pluton-scale isotopic heterogeneity and implications for the average isotopic composition of the continental crust

Erosion of the continental crust and transport of eroded material by rivers is the major source of V to the oceans (Shiller and Mao, 2000; Schuth et al., 2019). Therefore, it is important to understand the V isotopic composition of the continental crust, both in the present and through geological time, in order to assess possible variations in riverine and seawater isotopic composition over time. This is vital for the interpretation of ocean redox variations from the V isotopic signatures of black shales (e.g. Nielsen, 2020).

The whole rock samples from the BPZP span a wide range of isotopic composition from $\delta^{51}V$ = -1.15 ± 0.04‰ (2SD) to -0.56 ± 0.06‰ (2SD) (Figure 4.2), with the more silicic samples recording the heavier isotopic compositions. Biotite, hornblende and magnetite mineral separates also fall within this range. Assuming the BPZP is representative of a typical calc-alkaline differentiation sequence, a range in V isotopic composition of this magnitude could be expected in the other calc-alkaline plutons which make up a large

proportion of the upper continental crust. Ultimately, this means that deriving an average value for the V isotopic composition of the continental crust does not reflect the true isotopic variability present.

Additional studies of V isotopes in upper crustal plutons are required to assess how representative the BPZP is of the upper continental crust as a whole. However, compared to basaltic terranes, which thus far show $\delta^{51}V$ values clustering around -0.8‰ to -1.0‰ (Prytulak et al., 2013; Prytulak et al., 2017; Wu et al., 2018; Qi et al., 2019; Ding et al,. 2020; Novella et al., 2020), the V isotopic composition of intermediate to felsic plutonic rocks could be highly variable. Therefore, variation in the proportions of mafic to felsic material being eroded could influence the V isotopic composition of material delivered to the oceans. Additionally, given that the more felsic zones of the pluton have heavier $\delta^{51}V$, there is potential for an increase in the average $\delta^{51}V$ of the continental crust following the initiation of modern style plate tectonics and production of felsic crust, analogous to inferences made using the Ti isotope system (Greber et al., 2017).

Theoretically, variations in the average V isotopic composition of the upper continental crust through time could be determined by analysing clastic sedimentary samples like loess and diamictites. Loess and diamictites both form from material which has been physically eroded from the continental crust by glaciers. Loess is the wind-blown sediment sourced from glacial outwash plains or deserts (Taylor et al., 1983), whereas diamictites are unsorted, lithified glacial till (Gaschnig et al., 2014; 2016). However, it is not clear if the average V isotopic composition of the continental crust would be accurately sampled by clastic sediments. Firstly, there is potential for the chemical and isotopic compositions of loess and diamictites to be biased by preferential erosion of less resistant minerals during glaciation (Taylor et al., 1983), especially considering the large range in $\delta^{51}V$ in mineral separates measured here in just one pluton. Assuming all mineral phases are eroded equally, the average isotopic composition of sedimentary samples will be biased towards the minerals with the highest V concentrations, in this case magnetite. This study, and the work of Sossi et al. (2018b), show that magnetite can have extremely variable V isotopic compositions in crustal samples due to the combined influence of fractional crystallisation and fO_2 variations. Finally, particle sorting occurs during aeolian deposition of loess, and heavy minerals, such as Fe-Ti oxides, can be concentrated in certain fractions (Taylor et al., 1983; Sauzéat et al., 2015). Since Fe-Ti oxides host a large

proportion of the V in the system, particle sorting during deposition has the potential to bias results. In a similar manner, hydrodynamic sorting of Fe-Ti oxides during deposition has been shown to affect the Ti isotopic composition of marine sediments in the Eastern Mediterranean Sea (Klaver et al., 2021). Together, this means that it is very difficult to determine representative values for the V isotopic composition of the continental crust over geological time using clastic sediments. New methods are required to accurately determine if there are temporal variations the composition of the crust, before understanding the V isotopic mass balance between the crust, rivers and seawater over geological time.

4.8 Conclusions

To the best of our knowledge, this is the first investigation into V isotopic fractionation in intrusive settings. We present the first V isotope measurements of WR samples and their mineral separates from an approximately closed system calc-alkaline intrusive suite, representative of typical upper continental crust. The main conclusions are:

1. The $\delta^{51}V$ of WR samples and biotite, hornblende and magnetite mineral separates increase with fractional crystallisation. This is due to the crystallisation of isotopically light mineral phases (oxides and silicates), which drives an increase in $\delta^{51}V$ of the residual magma.
2. WR $\delta^{51}V$ values are highly scattered and reflect variations in the modal abundance of different mineral phases and/or amount of trapped interstitial melt. WR isotopic compositions do not represent a true magma composition and this caveat must be considered in future interpretation and modelling of intrusive samples. A new method is presented to reconstruct the isotopic composition of the evolving melt from mineral separate data to address this issue.
3. Primocryst magnetite, biotite and hornblende have identical $\delta^{51}V$ in individual samples, because they all host VI-fold coordinated V^{3+}. V isotopic fractionation is dominantly controlled by the bonding environment of V in minerals and melt, rather than variations in fO_2. Therefore, V isotopes in mineral separates are likely not a straightforward redox proxy.
4. The upper continental crust potentially has extremely variable V isotopic composition over small areas, which means that the average V isotopic

composition determined from the analysis of clastic sedimentary rocks will not capture the true isotopic variability present.

Chapter 4 Appendix

Table 4.S1. Magnetite trace element data measured by ICP-QQQ-MS. Errors are given as the within run standard deviation (RSD) of each individual analysis. % RSD errors are especially high on elements present in low concentrations in the magnetite, for example the rare earth elements. If %RSD > 15%, values are not reported (n.d.).

	BP42		BP11		BP22		BP39	
	Conc (µg/g)	% RSD	Conc (µg/g)	% RSD	Conc (µg/g)	% RSD	Conc (µg/g)	% RSD
Ti	827.7	1.0	844.9	0.5	2437.3	0.2	27042.3	0.0
V	1230.6	0.2	2030.0	0.2	2240.8	0.0	5281.2	0.0
Cr	942.9	0.2	1549.7	0.1	1787.3	0.1	2289.3	0.0
Co	18.2	6.9	n.d	n.d	26.4	12.7	64.3	3.2
Ni	45.1	2.0	30.3	15.8	75.2	4.5	152.9	1.0
Cu	99.1	3.9	162.6	3.1	25.0	9.0	44.8	28.3
Zn	75.7	0.4	47.7	7.3	42.6	6.5	127.1	1.2
Y	66.2	3.9	34.6	18.2	n.d	n.d	n.d	n.d
Zr	139.1	1.6	33.9	10.4	14.3	15.0	n.d	n.d
La	83.8	2.3	93.9	2.1	19.5	2.1	n.d	n.d
Ce	110.7	1.6	83.0	3.8	21.1	1.1	n.d	n.d
Pr	14.2	9.4	14.3	13.2	n.d	n.d	n.d	n.d
Nd	51.4	1.2	46.3	5.5	n.d	n.d	n.d	n.d
Pb	40.5	4.7	16.3	16.8	n.d	n.d	n.d	n.d
Th	76.9	4.2	100.0	3.3	n.d	n.d	n.d	n.d

Chapter 5: The influence of Fe-Ti Oxide mineralogy and crystallisation on V isotopic trends: comparison of a calc-alkaline and tholeiitic intrusion

5.0 Abstract

Cogenetic lavas show an increase in whole rock (WR) $\delta^{51}V$ during differentiation, which is primarily attributed to the fractional crystallisation of isotopically light Fe-Ti oxide minerals. Distinct trends of increasing WR $\delta^{51}V$ may reflect the timing of Fe-Ti oxide saturation, and the specific mineralogy of Fe-Ti oxides, both of which are related to magmatic composition and conditions. Knowledge of the magnitude of V isotope fractionation between isotopically lighter, V-rich Fe-Ti oxides and isotopically heavier coexisting melt is critical for accurate interpretation and modelling of V isotope data during differentiation processes. However, the V isotopic composition of Fe-Ti oxide mineral separates from natural samples is yet to be investigated, and thus quantitative Fe-Ti oxide-melt fractionation factors ($\Delta^{51}V_{oxide\text{-}melt}$) are lacking. To determine the extent of variability possible in fractionation factors and whether these can be usefully related to magmatic compositions and/or conditions, we examined titanomagnetite separates from two intrusive suites (the Red Hill intrusion in this chapter, and the Boggy Plain Zoned Pluton, Chapters 3 and 4) which show contrasting mineralogy, magma chemistry and fO_2, and timing of Fe-Ti oxide crystallisation.

Models of melt $\delta^{51}V$ evolution during fractional crystallisation demonstrate that typical tholeiitic (e.g. Red Hill intrusion) and calc-alkaline (e.g. Boggy Plain Zoned Pluton) differentiation sequences should show distinct trends in $\delta^{51}V$ during differentiation, with sharp increases in $\delta^{51}V$ only occurring after Fe-Ti oxide saturation. Larger increases in $\delta^{51}V$ are predicted at lower temperatures and during crystallisation of Ti-poor magnetite. However, the models demonstrate that the changes in temperature due to plutonic cooling can result in a similar range of $\Delta^{51}V_{oxide\text{-}melt}$ as changes in Fe-Ti oxide composition. Therefore, although future experimental and empirical studies could derive $\Delta^{51}V_{oxide\text{-}melt}$ values for specific Fe-Ti oxide phases and compositions, accurate temperature estimates

are vital for applying these fractionation factors to investigate V isotope fractionation across different intrusive settings.

It proved challenging to directly compare results from the tholeiitic Red Hill intrusion with data from the calc-alkaline Boggy Plain Zoned Pluton, given the textural complexities of intrusive samples and their differing thermal regimes. In hindsight, studying WR samples and mineral separates from intrusive settings was not the most appropriate way to assess the control of Fe-Ti oxide composition on V isotope fractionation. The challenges with this approach are discussed, and more promising methods for use in the future are proposed to fully understand the influence of Fe-Ti oxide chemistry on V isotope fractionation.

5.1 Introduction

Vanadium (V) is a multi-valent transition metal that shows resolvable isotopic fractionation during magmatic differentiation (e.g. Prytulak et al., 2013; 2017; Wu et al., 2018; Qi et al., 2019; Ding et al., 2020; Chapter 4). Isotopic fractionation is fundamentally driven by differences in the bonding environment and oxidation state of V in the melt and the crystallising mineral assemblage (e.g. Schauble, 2004; Prytulak et al., 2017; Ding et al., 2020). Thus, V isotopes have the potential to provide information about mineralogical and fO_2 variations during processes such as fractional crystallisation and, potentially, processes such as the formation of magmatic ore deposits.

Previous investigations of V isotope fractionation during magmatic differentiation have focussed on whole rock samples from cogenetic lava sequences (e.g. Hekla and Anatahan, Prytulak et al. 2017; Kilauea Iki, Ding et al. 2020). Thus far, all suites show an increase in WR $\delta^{51}V$ during differentiation, which has been attributed primarily to the crystallisation of the Fe-Ti oxide minerals titanomagnetite and ilmenite. Vanadium is highly compatible in Fe-Ti oxides (e.g. O'Neill and Navrotsky, 1984; Toplis and Corgne, 2002), and therefore Fe-Ti oxides are predicted to host large proportions of the V in magmatic systems. Fe-Ti oxides are also predicted to be isotopically lighter than coexisting melt, where V is hosted in a higher oxidation state and lower coordination (Giuli et al., 2004; Sutton et al., 2005; Righter et al., 2006).

A wide range of Fe-Ti oxide minerals are found in natural systems, but here we consider titanomagnetite (members of the magnetite:ulvöspinel solid solution series Fe_3O_4 : Fe_2TiO_4; substitution by $2Fe^{3+} = Ti^{4+} + Fe^{2+}$) and ilmenite ($FeTiO_3$), because they are the most common Fe-Ti oxide minerals in magmatic suites, particularly those discussed in this work. Although crystallisation Fe-Ti oxides is a key control on V isotope fractionation, there remains a lack of understanding about the natural variation in magnitude of V isotope fractionation expected between Fe-Ti oxides and melt at the temperatures and fO_2 conditions of magmatic systems. Thus far, there is only one experimental study which has determined magnetite-melt fractionation factors ($\Delta^{51}V_{mag\text{-}melt}$) at 800°C and fO_2 from FMQ-1 to FMQ+5 (Sossi et al., 2018b). These experiments were conducted in a Ti-free environment, so it is unknown how isotope fractionation may be influenced by variation in the Ti content of magnetite and presence of ilmenite. Currently, there are no published theoretical, natural or experimental titanomagnetite-melt or ilmenite-melt V isotope fractionation factors.

Variation in Fe-Ti oxide chemistry and speciation leads to resolvable differences in Fe-Ti oxide-melt fractionation factors in other isotope systems. For example, for Fe, theoretical calculations based on mineral bonding environment show that pure magnetite ($^{IV}Fe^{3+}\,{}^{VI}(Fe^{3+}, Fe^{2+})O_4$; $Fe^{3+}/\Sigma Fe = 0.66$) has higher bond force constant, larger $\Delta^{56}Fe_{ox\text{-}melt}$ and thus heavier Fe isotopic composition than Ti-rich ulvöspinel ($(Fe^{2+})_2TiO_4$); $Fe^{3+}/\Sigma Fe = 0$). This difference is driven by both the increase in Fe-O bond length (from 1.885Å to 1.933Å on IV sites; Rabin et al., 2021) and decrease in $Fe^{3+}/\Sigma Fe$ in ulvöspinel following Ti substitution (Bosi et al., 2009; Sossi and O'Neill, 2017; Rabin et al., 2021). In ilmenite ($Fe^{2+}TiO_3$), all Fe is hosted as Fe^{2+} on VI-sites, and therefore ilmenite has lower bond force constant, smaller $\Delta^{56}Fe_{ox\text{-}melt}$, and lighter isotopic composition, than magnetite and ulvöspinel which host Fe^{2+} and Fe^{3+} on both IV- and VI-fold sites (Sossi and O'Neill, 2017). The presence of other metal cations as impurities in Fe-Ti oxides may also influence isotopic compositions (Roskosz et al., 2015; Rabin et al., 2021). Likewise, the Ti isotopic composition of Fe-Ti oxide minerals varies with chemistry and oxide speciation. Titanium only occurs as Ti^{4+} in minerals and melt, so isotopic fractionation is driven by changes in bonding environment rather than redox variation (e.g. Millet et al., 2016). In the titanomagnetite-ulvöspinel solid solution series, there is an increase in the magnitude $\Delta^{49}Ti_{ox\text{-}melt}$ (the absolute value becomes more negative, since titanomagnetite with VI-fold coordinated Ti is always lighter than coexisting melt with V-fold

coordinated Ti) with increasing Ti content due to distortion of the crystal lattice during Ti substitution (Hoare et al., 2022). Titanomagnetite is also isotopically lighter than ilmenite in the same sample, owing to the longer Ti-O bond length in titanomagnetite compared to ilmenite (Hoare et al., 2022).

Therefore, it is predicted that different Fe-Ti oxide minerals have distinct V isotope mineral-melt fractionation factors ($\Delta^{51}V_{min\text{-}melt}$), which will influence the degree of $\delta^{51}V$ increase in the evolving melt. However, the effects of mineral chemistry and speciation are challenging to predict, because the structural position and substitutions of V in magnetite are not as well understood as for Fe and Ti. It is thought that V is most likely present as VI-fold coordinated V^{3+} and V^{4+} in titanomagnetite, substituting for Fe^{3+} and Ti^{4+} respectively (Toplis and Corgne, 2002). Therefore, V isotope fractionation will mostly be influenced by differences in V^{3+}/V^{4+} ratio and bonding environment between the different Fe-Ti oxide phases.

To address these uncertainties, Ding et al. (2020) compared the contrasting trends in WR $\delta^{51}V$ in lava suites which have different crystallising Fe-Ti oxide assemblages (Figure 5.1). In the Hekla (Iceland) samples, where titanomagnetite is the only crystallising Fe-Ti oxide mineral, there is a large increase in WR $\delta^{51}V$ with increasing SiO_2, requiring a $\Delta^{51}V_{mag\text{-}melt}$ value of approximately -0.4 to -0.5‰ (Prytulak et al., 2017). Lavas from Anatahan (Mariana Arc) and Kilauea Iki (Hawaii) show smaller initial increases in $\delta^{51}V$ compared to Hekla. Ding et al. (2020) proposed that this is because in these suites there is also crystallisation of Ti-rich ulvöspinel and ilmenite respectively, and therefore mineral-melt fractionation factors for ulvöspinel and ilmenite must be smaller ($\Delta^{51}V_{min\text{-}melt} \sim$ -0.15‰) than for magnetite.

However, these hypotheses have not yet been tested using Fe-Ti oxide mineral separates in natural samples. Therefore, we compare V isotopes in magnetite from the calc-alkaline Boggy Plain Zoned Pluton (BPZP; Chapter 4), with V isotopes in Fe-Ti oxides in the Red Hill intrusion, Tasmania, which has distinctly different chemistry and fO_2 conditions.

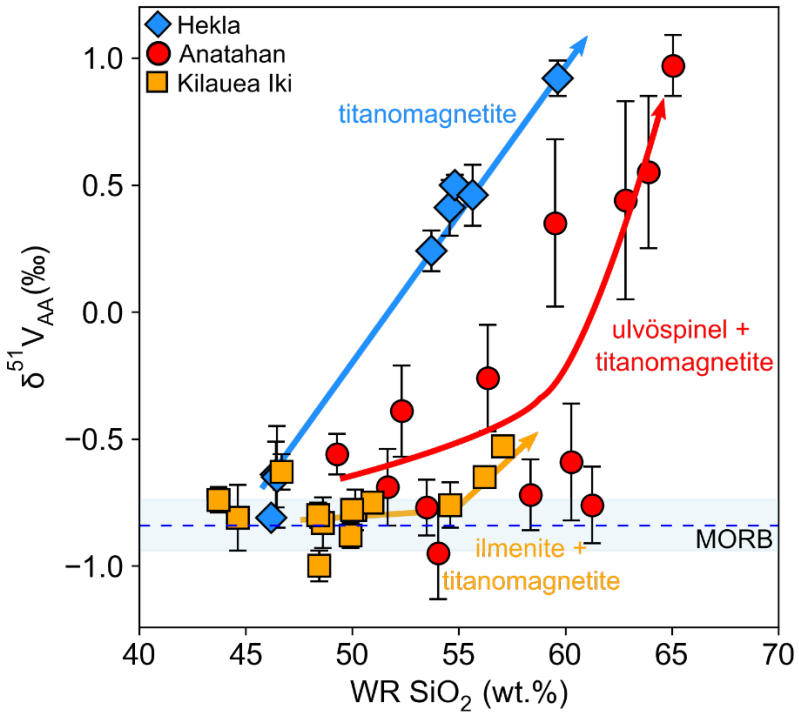

Figure 5.1. Variation in WR $\delta^{51}V$ of extrusive lava suites. Data for Hekla and Anatahan are from Prytulak et al. (2017). Data for Kilauea Iki are from Ding et al. (2020). The suites are labelled with the fractionating Fe-Ti oxide assemblage. All errors are as 2SD of at least 3 measurements of an individual sample. The blue dashed line and shaded area show the average $\delta^{51}V$ for MORB (-0.84 ± 0.10‰; Wu et al., 2018).

The well-characterised tholeiitic Red Hill intrusion was selected for several reasons. One advantage is that major element, trace element and Fe isotopic variations in the whole rock samples are thought to approximate the liquid line of descent of a crystallising tholeiitic magma (McDougall, 1962; Sossi; 2010; Sossi et al., 2012). There is an initial increase in WR $\delta^{56}Fe$ driven by crystallisation of isotopically light pyroxene, and then WR $\delta^{56}Fe$ decreases following titanomagnetite saturation. Critically, the chemistry and timing of Fe-Ti oxide saturation and the Fe isotopic variations are distinct from the BPZP (Chapter 3; Chapter 4; Stow et al., 2022), which suggests that it is likely that the two intrusions would show different V isotopic behaviour.

The same approach used successfully for understanding Fe-V-Zn isotopic variation in the BPZP (Chapters 3 and 4) was followed. The V isotopic compositions of whole rock

powders and the mineral separates which host the highest proportions of V in the system were analysed; in the Red Hill intrusion this is pyroxene and titanomagnetite. Additional Fe, Zn, Sr and Nd isotope analyses were conducted to assess other processes such as crustal contamination which may influence V isotopic compositions. Isotopic measurements were contextualised via petrographic examination of the mineralogy and textures of all samples.

Vanadium isotope data from the Red Hill intrusion and BPZP were compared to theoretical models of V isotopic variation in calc-alkaline and tholeiitic settings. We present a critical discussion of the significant challenges this method posed to investigate the control of Fe-Ti oxide chemistry and speciation on V isotopic fractionation, given the textural complexities and analytical challenges with the Red Hills intrusion specifically, and intrusive suites in general. We make suggestions of more effective methods for future work.

5.2 Geological Background

5.2.1 The Red Hill Intrusion, SE Tasmania

The Red Hill intrusion is part of the Tasmanian Dolerites, which intruded as horizontal, sheet-like bodies of magma into Permian and Triassic sedimentary rocks around 180Ma (McDougall, 1962; McDougall and Lovering, 1963; Schmidt and McDougall, 1977; Hergt et al., 1989), and are exposed over an area of approximately 30,000 km^2 (Hergt et al., 1989). Together with other tholeiitic rocks from South America, South Africa, Antarctica, and southern Australia, the Tasmanian Dolerites are part of the Ferrar large igneous province which formed during the breakup of Gondwana (Hergt et al., 1991; Hergt and Brauns, 2001).

The Red Hill intrusion is a 1.6km wide dyke which extends upward from the underlying dolerite sheet. It is unusual compared to most of the Tasmanian Dolerites because it shows the progressive differentiation of the tholeiitic magma from dolerite through quartz dolerite and fayalite granophyre to granophyre (McDougall, 1962). The most silicic rocks are exposed at the highest stratigraphic level at the top of Red Hill, Hickman's Hill and O'Brien's Hill (McDougall, 1962; Figure 5.2). Differentiation of the Red Hill intrusion is thought to be driven by approximately closed system fractional crystallisation.

Temperature estimates using bulk rock composition after Sisson and Grove (1993b) give crystallisation temperatures between approximately 950 – 1200°C (Sossi et al., 2012).

The samples used in this work are the exact same whole rock powders as used in Sossi (2010) and Sossi et al. (2012) to determine major element, trace element and Fe isotope compositions. Sample locations are shown on Figure 5.2.

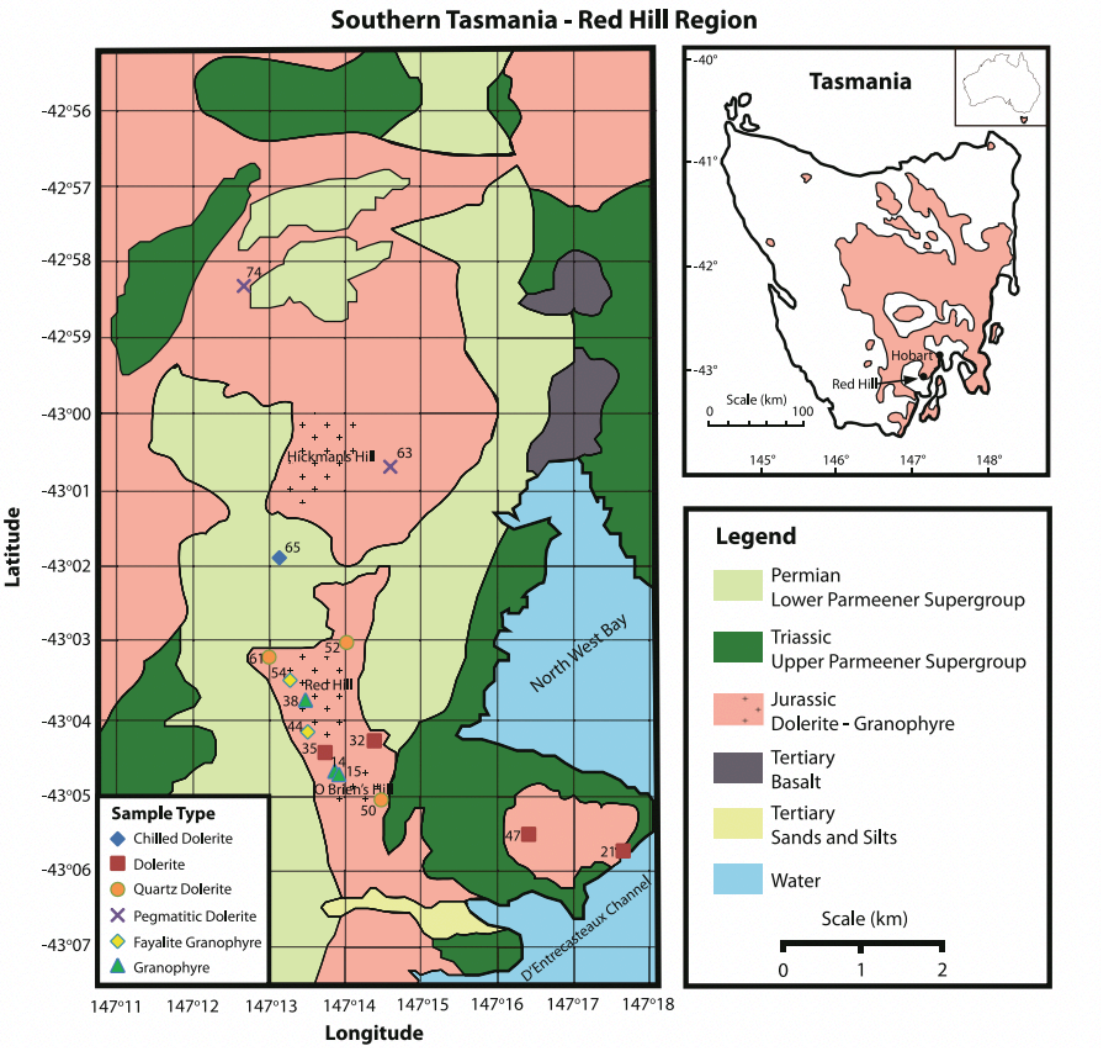

Figure 5.2. Geological Map of the Red Hill Intrusion. Figure reproduced from Sossi et al. (2012). The samples from Sossi et al. (2012) are the exact same samples used in this work. The dolerite and quartz dolerite are shown by the pink colour, and the granophyres are shown by the pink colour with crosses. The Permian and Triassic sedimentary rocks that the dolerite intruded into are shown by the green colours.

5.2.2 Whole Rock Chemical Variations

Whole rock major and trace element compositions show continuous trends with MgO and/or SiO_2 content (Figure 5.3), which are thought to approximate the liquid line of descent of the evolving magma (McDougall, 1962; Sossi et al., 2012).

The crystallisation sequence of the Red Hill magma can be separated into three distinct stages. In Stage 1 (8 – 3.2 wt.% MgO; Figure 5.3), the Red Hill magma follows a trend of early Fe-enrichment due to crystallisation of plagioclase and two pyroxenes (augite and pigeonite) as the main mineral phases. Whole rock TiO_2, Zn and Cu concentrations also increase during Stage 1 because these elements are relatively incompatible in pyroxene and plagioclase (e.g. Bédard, 2006; Bédard, 2007; Laubier et al., 2014). Whole rock V concentrations remain approximately constant due to minor incorporation of V into pyroxenes (e.g. Toplis and Corgne, 2002). During this stage, whole rock Cr falls sharply due to the high compatibility of Cr in pyroxene (e.g. Bédard, 2007; Lundstrom et al., 1998).

In Stage 2 (approximately 3.2 – 1.5 wt.% MgO; Figure 5.3), there is a sharp decrease in WR Cu concentration, which is most likely due to fractionation of Cu-bearing sulphide minerals such as chalcopyrite (McDougall and Lovering, 1963). Two different types of sulphide mineral were detected using EDS analysis (Section 5.2.4): individual grains of pyrite, and smaller, disseminated blebs of chalcopyrite.

Fractionation of Fe-Ti oxides, specifically titanomagnetite, occurs in Stage 3 (below 1.5 wt.% MgO; Figure 5.3). There is a decrease in WR Fe_2O_3, TiO_2, V and Cu concentrations, which are all highly compatible in magnetite (e.g. Sievwright et al., 2020). The occurrence of late Fe-Ti oxide fractionation is typical of low fO_2, tholeiitic magmas (e.g. Toplis and Carroll, 1996).

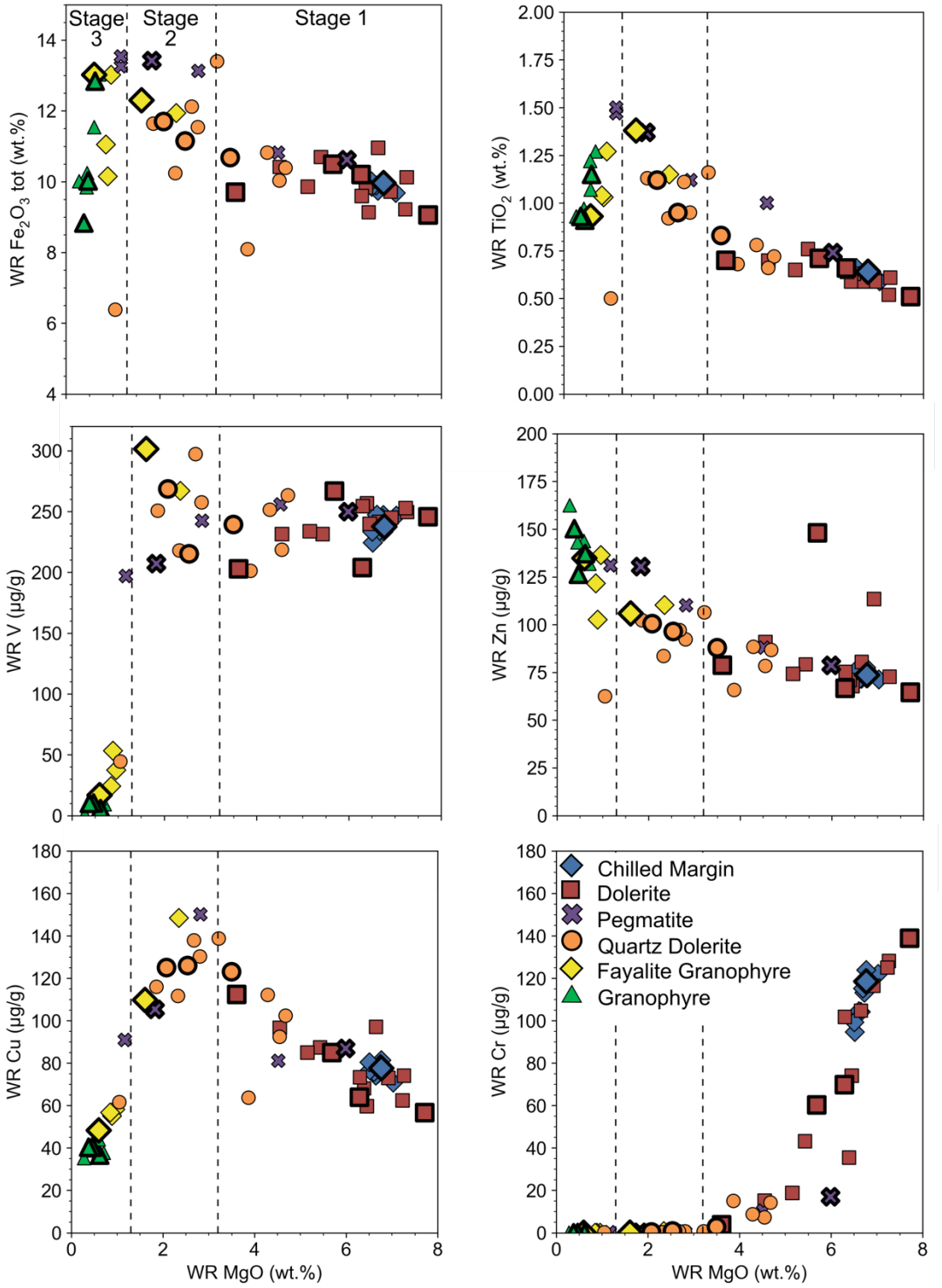

Figure 5.3. Chemical variations in the Red Hill Intrusion. Whole rock compositional data from Sossi (2010). Large symbols with bold outlines are those chosen for isotopic analysis in this study. The dashed line at 3.2 wt.% MgO indicates the onset of sulphide saturation, and the dashed line at 1.5 wt.% MgO indicates the onset of titanomagnetite crystallisation, inferred from the changes in slope of the major and trace element trends. Note that one anomalous Zn sample has Zn concentration of 280 µg/g at 7.23 wt.% MgO, but is not shown on the graph due to the y-axis scale.

5.2.3 Sample Petrography

The Red Hill intrusion shows the progressive differentiation of a tholeiitic magma, with lithologies grading from dolerite, through quartz dolerites to the most evolved granophyres which are present at the highest stratigraphic levels of the intrusion (McDougall, 1962). Thin section descriptions build on observations from McDougall (1962) and Sossi et al. (2012). Complete descriptions can be found in Electronic Appendix 5.

The outermost chilled margin (Sample 65; Figure 5.4A) consists of a fine-grained groundmass of pyroxene and plagioclase crystals with rare pyroxene phenocrysts >0.5mm. Inward from the chilled margin, the dolerite (Samples 21, 32, 35, 47; Figure 5.4B) typically contains two pyroxenes (pigeonite (20%) and augite (25%)) and plagioclase (>50%). Pyroxene occurs as individual tabular crystals 2-3mm in size, and can also display sub-ophitic textures, enveloping smaller plagioclase crystals. Plagioclase crystals show no defined orientation. Small (<0.5mm) Fe-Ti oxide grains (<1%) are found in interstitial sites between pyroxene and plagioclase. Both titanomagnetite and ilmenite are present. Backscatter electron images show that individual grains show ragged textures and have likely been altered by weathering processes. It is difficult to tell which are original crystals or exsolution features (e.g. Figure 5.5B).

Moving inwards from the dolerites to the quartz dolerites (Samples 50, 52, 61), there is a gradual increase in the proportion of interstitial quartz and K-feldspar intergrowths (5-10%), and a slight decrease in the proportions of plagioclase (<50%), pigeonite (15%), and augite (20%).

The quartz dolerites pass into fayalite bearing granophyres (Samples 44, 54; Figure 5.4C). The main mafic phases in the fayalite granophyres are Fe-rich olivine (<5%), which has been altered to iddingsite, and euhedral crystals of a pale brown coloured clinopyroxene (ferroaugite; 15%). Pale green amphibole can be found on the rims of some ferroaugite grains. Plagioclase crystals (30%) are 0.5mm long and show stubby morphologies. The majority of the rock is composed of quartz and K-feldspar (50%), either as equant grains or granophyric intergrowths. Titanomagnetite (<5%) becomes a major primocryst phase, indicated by the decrease in WR V and TiO_2 concentrations (Figure 5.3). Titanomagnetite grains are up to 0.5mm in size and all contain ilmenite exsolution lamellae.

Granophyres (Samples 14, 15, 38; Figure 5.4D) are only found at the highest stratigraphic levels of the intrusion. Fe-rich olivine disappears, and >60% of the rock is composed of quartz and K-feldspar. Quartz and K-feldspar can occur as individual crystals and granophyric intergrowths. Plagioclase (<25%) and clinopyroxene (10%) crystals have elongated, needle like morphologies. Titanomagnetite (2-4%) remains the main Fe-Ti oxide phase. Titanomagnetite grains are 0.1 – 0.2 mm in size, and only show very fine scale ilmenite exsolution lamellae.

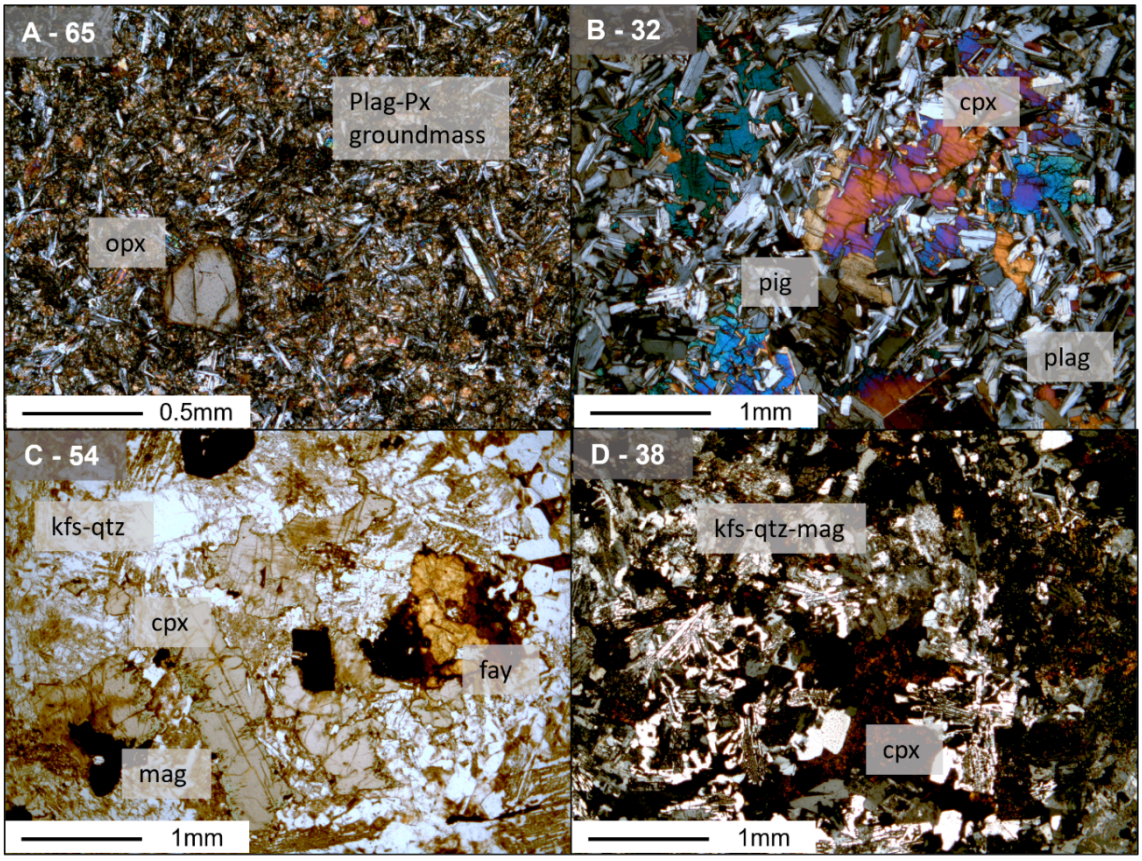

Figure 5.4. Petrography of the Red Hill intrusion. (A) Sample 65 (chilled margin of the intrusion) with fine grained plagioclase and pyroxene groundmass and individual 0.1mm orthopyroxene crystals. (B) Sample 32, a typical dolerite, containing tabular plagioclase crystals and two pyroxenes (pigeonite and augite). (C) Sample 54 (fayalite granophyre) containing fayalite (altered to iddingsite), ferroaugite, plagioclase, quartz, and K-feldspar. (D) Sample 38 (granophyre) containing fine grained granophyric intergrowths of quartz and K-feldspar. Clinopyroxene is highly altered. Abbreviations: px = pyroxene, cpx = clinopyroxene, opx= orthopyroxene, plag = plagioclase, pig = pigeonite, kfs = K-feldspar, qtz = quartz, mag = magnetite, fay = fayalite. Thin section scans can be found in Electronic Appendix 4.

There are coarse grained, decimetre scale pegmatite bodies throughout the intrusion (Samples 63, 74). The pegmatitic dolerites have similar mineralogy as finer grained

dolerites with similar WR MgO content, with the addition of 1-2% amphibole found at the margins of pyroxene grains. Samples fall on the same geochemical trends as the rest of the intrusion (Figure 5.3; purple crosses). The pegmatite bodies are thought to crystallise from volatile-rich regions of magma (McDougall, 1962).

5.2.4 Oxide and Sulphide Petrography

Fe-Ti oxides (e.g. magnetite and ilmenite) and sulphide minerals (e.g. pyrite, chalcopyrite) are major hosts of transition metals. Fe-Ti oxides contain large proportions of the Fe and V in the whole rock samples, and sulphide minerals can host considerable proportions of Fe and Zn. Oxide and sulphide minerals were examined under reflected light using a petrographic microscope, and using the Scanning Electron Microscope (SEM). Energy Dispersive X-ray Spectroscopy (EDS) was used to measure the major element chemistry of Fe-Ti oxides and sulphide minerals in order to determine approximate compositions and speciation by stoichiometry (see Chapter 4, Section 4.3.3 for the method). Typical 1σ errors for individual measurements based on counting statistics were 0.15 – 0.25 wt.% for Fe and 0.10 – 0.15 wt.% for Ti in Fe-Ti Oxides. For the sulphides, typical 1σ errors based on counting statistics were 0.15– 0.25 wt.% for Fe, 0.15 – 0.20 wt.% for S, 0.2 – 0.3 wt.% for Cu and 0.2 – 0.25 wt.% for Zn.

Fe-Ti Oxides

Compared to the Boggy Plain Zoned Pluton (Chapters 3 and 4) which contained low Ti magnetite (<0.5 wt.% TiO_2 in primocrysts) with no obvious exsolution features, the Fe-Ti oxides in the Red Hill intrusion show more complex textures and higher Ti concentrations. Ilmenite and minor titanomagnetite are present in the dolerites, as small (0.1-0.2 mm) interstitial grains between euhedral plagioclase and pyroxene crystals (Figure 5.5A and B). It is difficult to tell which grains are primary and which have formed by low temperature oxyexsolution (e.g. Frost and Lindsley, 1991), and grains are also variably altered as shown by their cloudy, ragged textures. However, given that the Fe-Ti oxides only occur as interstitial phases in the dolerites, they likely crystallised from trapped melt and thus their crystallisation did not influence overall bulk chemical or isotopic trends in the intrusion. For this reason, no Fe-Ti oxides were picked from the dolerites for isotopic analysis.

Fe-Ti oxide mineral separates were picked from the fayalite granophyres and granophyres (samples 50, 54 and 14) because whole rock Fe_2O_3, TiO_2 and V concentrations decrease dramatically in these samples (Figure 5.3), indicating the crystallisation of Fe-Ti oxide as a major cumulus phase. The only Fe-Ti oxide in these samples is a titanomagnetite containing extensive ilmenite exsolution arising from low temperature oxyexsolution (Figure 5.5E, F, G, H). Titanomagnetite separates were also picked from the pegmatitic dolerite (sample 74) because petrographic examination of these grains showed little evidence for low temperature oxyexsolution or alteration (Figure 5.5C and D). However, there is potential for isotopic compositions of this titanomagnetite to be influenced by volatiles or fluids during crystallisation. This caveat should be considered when interpreting data for the titanomagnetite and pyroxene from this sample.

The approximate Ti concentration of the bulk titanomagnetite at the time of crystallisation was determined using EDS. Firstly, a coarse raster over an entire grain was measured, which determines the average composition of an area consisting of host plus lamellae. Secondly, point analyses of the Ti concentrations of the titanomagnetite host and ilmenite lamellae were measured. The proportion (P) of host versus lamellae within grains was estimated using the Fiji ImageJ software, and then a bulk composition was calculated using a mass balance approach considering the concentration of Ti in the host and exsolved phase (Equation 5.1; Figure 5.6). The average TiO_2 content of primary, unexsolved titanomagnetite calculated using these methods is shown in Table 5.1. The Red Hill titanomagnetite contains on the order of 20 wt.% TiO_2.

$$Ti_{bulk} = \left(Ti_{mag} \times P_{mag}\right) + \left(Ti_{ilm} \times P_{ilm}\right) \qquad [5.1]$$

Figure 5.5. Oxide and sulphide petrography in the Red Hill intrusion. Figures are labelled with sample numbers. In the dolerites (A) and (B), ilmenite is the main Fe-Ti oxide and occurs as interstitial, altered grains between plagioclase crystals. Interstitial sulphides (pyrite) are also present. Given the interstitial nature of these grains, they do not affect the overall chemical evolution of the main magma body. Figures (C) and (D) show typical Fe-Ti oxides in sample 74 (pegmatite). The majority of the grains are magnetite with generally euhedral morphology, and extensive exsolution of ilmenite. Interstitial sulfides are also present. Titanomagnetite saturation occurs in the fayalite granophyres (E), (F), (G) and (H). Titanomagnetite in these samples also shows extensive exsolution of ilmenite. (E) is a backscatter electron image of a titanomagnetite grain in sample 50, and (F) is the same grain under reflected light. Pyrite and chalcopyrite are found in these samples. (G) is a larger titanomagnetite grain from the same sample. The granophyres (H) are fine grained and contain smaller (0.1-0.2mm) disseminated titanomagnetite grains. Abbreviations: ilm = ilmenite, mag = magnetite, py = pyrite, sul = sulfides (specific mineral not known).

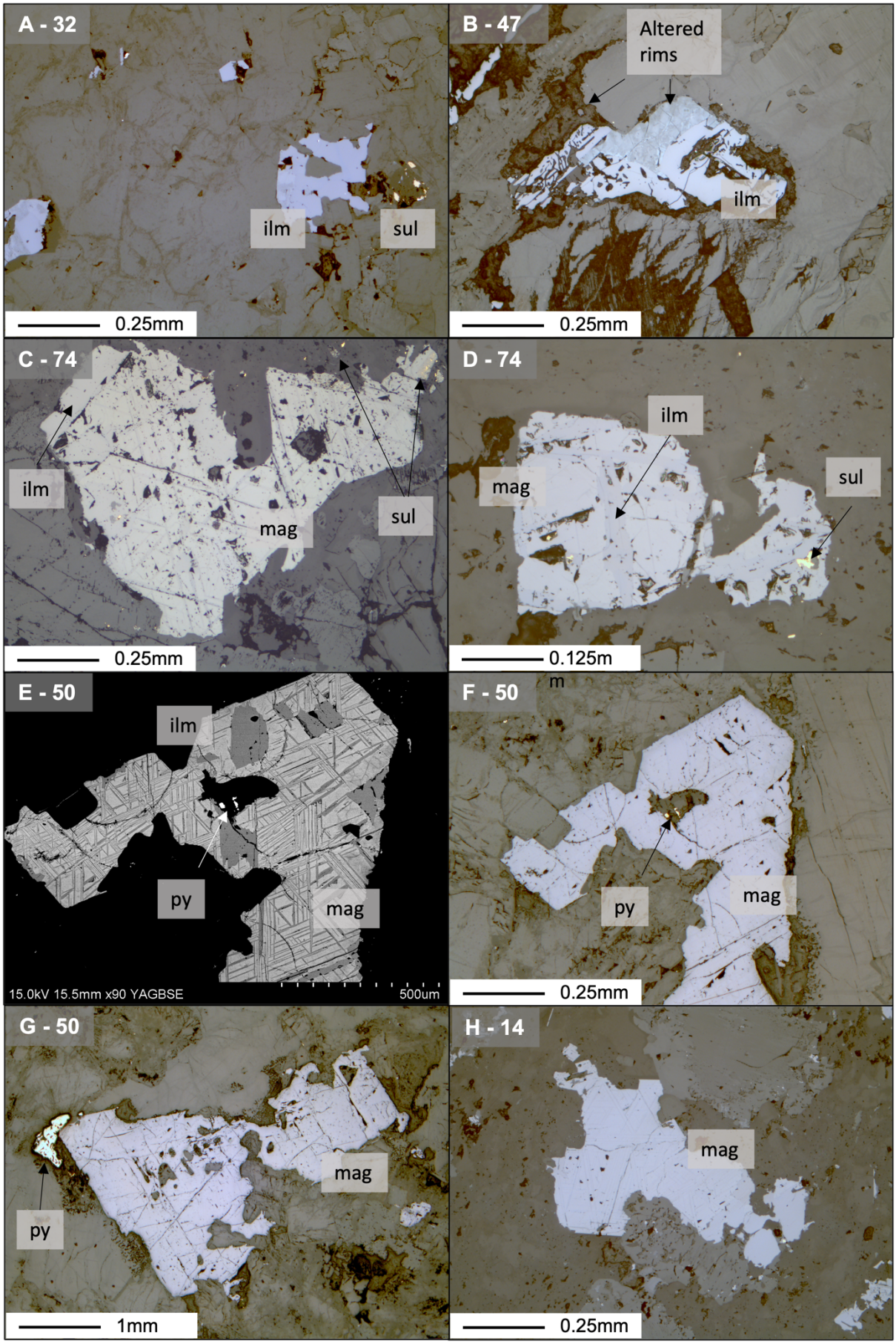
A - 32
ilm
sul
0.25mm
B - 47
Altered rims
ilm
0.25mm
C - 74
ilm
mag
sul
0.25mm
D - 74
ilm
mag
sul
0.125m
E - 50
ilm
py
mag
15.0kV 15.5mm x90 YAGBSE
500um
F - 50
m
py
mag
0.25mm
G - 50
mag
py
1mm
H - 14
mag
0.25mm

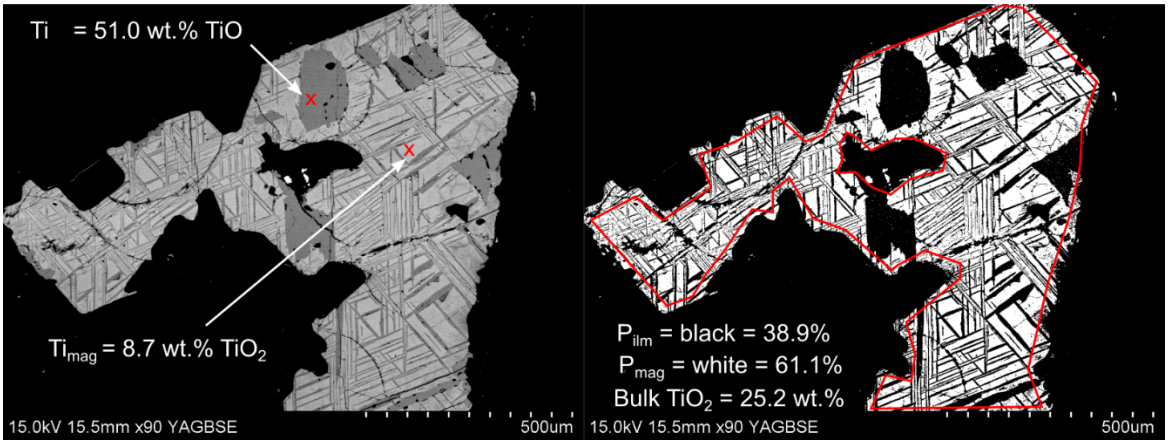

Figure 5.6. Schematic illustrating the method used to calculate bulk titanomagnetite TiO_2 concentration. Point analyses of the Ti content of the titanomagnetite host and exsolved ilmenite are measured by EDS (red crosses). The thresholding tool on ImageJ software is used to distinguish regions of titanomagnetite (white) and ilmenite (black) based on their colour in BSE images. ImageJ is then used to measure the proportions of each phase within a defined area (here defined by the red line). Equation 5.1 is then used to estimate the bulk TiO_2 concentration of the homogeneous grain before exsolution occurred.

Table 5.1. Titanomagnetite TiO_2 concentrations calculated using the mass balance approach and measured using EDS coarse rasters. Calculation (1) uses TiO_2 estimates for magnetite and ilmenite from EDS point analysis conducted in this study. Calculation (2) uses TiO_2 concentrations measured by EPMA by Sossi (2010). Errors are 2SD of all determinations of titanomagnetite TiO_2 concentration for that sample, and thus represent variation in the proportions of magnetite:ilmenite in different grains.

Sample	TiO_2 (wt.%) – Mass Balance Approach[1]	TiO_2 (wt.%) – Mass Balance Approach[2]	TiO_2 (wt.%) – Raster
14 - Titanomagnetite	21.1 ± 3.2 (n=3)	/	/
54 - Titanomagnetite	18.0 ± 4.2 (n=4)	18.6 ± 4.2 (n=4)	19.5
50 - Titanomagnetite	27.7 ± 6.7 (n=5)	28.5 ± 6.7 (n=5)	/

Although there has been extensive diffusion of Ti in the titanomagnetite during exsolution, given the low diffusion coefficient of V in magnetite (Sievwright et al., 2020), we do not expect V isotopes to be affected by diffusive re-equilibration. The bulk sampling approach of hand-picking entire grains should sample the host magnetite plus ilmenite lamellae, hence isotopic compositions should represent the composition of the magnetite at the time of crystallisation.

Sulphides

Sulphides are found in all lithologies of the intrusion. We conducted EDS analysis of Fe:Cu:S ratios in sulphide grains to identify the sulphide species present in the Red Hill intrusion (see Chapter 4 Section 4.3.3 for the method). The EDS analysis shows that there are two different types of sulphides, pyrite (FeS_2) and chalcopyrite ($FeCuS_2$) (Table 5.2). Pyrite is generally present as larger crystals along the margins of Fe-Ti oxide crystals (e.g. Figure 5.5G), whereas chalcopyrite appears as smaller, disseminated blebs throughout the samples. The chalcopyrite can also host considerable Zn; estimates from EDS are around 1 wt.%. Pyrite is present throughout the intrusion, but chalcopyrite only appears <3.5 wt.% MgO, causing the decrease in WR Cu content observed at this time (Figure 5.3; McDougall and Lovering, 1963). Given the low modal abundance of sulphide minerals (<<1%), it is unlikely that sulphide crystallisation has a resolvable effect on the Fe isotopic evolution of the Red Hill intrusion. However, there is potential for chalcopyrite crystallisation to influence Zn isotopes (see Section 5.5.2).

Table 5.2. Sulphide compositions measured by EDS. The sulphide grains in the sample generally show restricted compositional ranges. The average Fe, S, Cu and Zn concentrations of all sulphide grains in the sample (in wt.%) are listed in the table. n is the number of individual grains analysed in each sample, and the errors are 2SD of n measurements. The number of moles of S, Fe and Cu are calculated and used to identify sulphide species. Note that typical 1σ errors based on counting statistics are 0.15– 0.25 wt.% for Fe, 0.15 – 0.20 wt.% for S, 0.2 – 0.3 wt.% for Cu and 0.2 – 0.25 wt.% for Zn.

Sample	**14**	**54**	**50**	**50**
Lithology	**Granophyre**	**Fay. Gran.**	**Qtz. Dolerite**	**Qtz. Dolerite**
n	3	4	10	11
Average Concentration (wt.% ± 2sd)				
S	31.1 ± 1.6	32.1 ± 0.7	51.5 ± 3.4	32.0 ± 1.0
Fe	28.4 ± 1.1	28.7 ± 1.0	44.6 ± 2.2	28.1 ± 0.7
Cu	37.2 ± 1.1	37.1 ± 1.9	0.0	37.2 ± 1.1
Zn	1.2 ± 0.4	0.9 ± 0.3	0.0	0.9 ± 0.2
n	3	4	10	11
No. of moles				
S	0.97	1.00	1.61	1.00
Fe	0.51	0.54	0.80	0.50
Cu	0.59	0.58	0.00	0.59
mineral	chalcopyrite ($FeCuS_2$)	chalcopyrite ($FeCuS_2$)	pyrite (FeS_2)	chalcopyrite ($FeCuS_2$)

5.3 Methods

5.3.1 Iron, Zinc and Vanadium Isotopic Compositions

The Fe, Zn and V isotopic compositions of whole rock samples and magnetite and pyroxene mineral separates were measured as detailed previously in Chapters 2, 3 and 4. The whole rock samples are the exact same powders used in Sossi et al. (2012). In order to obtain enough Fe, V and Zn for analysis, a mass of 50-70 mg was digested for all samples with > 1 wt.% WR MgO. However, the granophyre samples with < 1 wt.% MgO contain 5-10 μg/g V (Figure 5.3). To obtain at least 3 isotopic measurements, a total of 1 μg/g V is required. Therefore, it was necessary to digest a mass of >100 mg. The digestion was split into separate aliquots of ~50 mg which were re-combined after column chemistry. However, several of these samples (15, 38 and 54) had V yields <50% after chemistry. It is possible that these low yields are due to inaccuracies in the V concentration measurements of these samples from Sossi (2010), given their low V concentrations. However, since we cannot confirm that the low yield is due to uncertainties in the V concentration of the samples, the data is not included in our interpretations.

For the mineral separates, a coarse gravel (>1cm size fraction) was crushed with a hammer and then sieved into several smaller size fractions. Magnetite and pyroxene mineral separates were hand-picked under binocular microscope from the 0.125 – 0.250 mm size fraction, taking care to avoid minerals with obvious alteration or inclusions where possible. Magnetite separates were initially roughly separated using a hand magnet before hand-picking. Mineral separates were then ground into fine powders by hand using an agate pestle and mortar, which was cleaned between samples with low Fe quartz sand.

Mineral separates and whole rock powders were digested as described in Chapters 2, 3 and 4. Ion exchange column chromatography and Fe, Zn and V isotopic measurements were carried out as detailed in Chapters 2, 3 and 4. However, note that the Fe isotopic measurements in this chapter were conducted using Ni-doping to correct for mass bias, and 2ml aliquots with 10 ug/g Fe concentration were doped to a concentration of 8 ug/g Ni (see Chapter 2 Section 2.5.2.2 for more details on this procedure). USGS reference materials BIR-1a and GSP-2 were measured during analytical sessions to assess machine

performance. Values are listed in Tables 5.3, 5.4 and 5.7, and agree within error with previously published values (see compilation in Tables 2.3, 2.11 and 2.18; Chapter 2).

5.3.2 Strontium and Neodymium Isotopic Analyses

The methods for Sr and Nd separation and isotopic analysis are described fully in Chapter 2, Section 2.6. To obtain enough Sr and Nd for analysis, approximately 50 mg of each whole rock powder was digested. Certified reference materials and USGS standards were measured throughout analytical sessions to assess machine performance. For Sr, the certified reference material NBS987 had an average $^{87}Sr/^{86}Sr$ of 0.710273 ± 0.000013 (2SD, n=8), and the USGS reference material BCR-2 had a $^{87}Sr/^{86}Sr$ value of 0.705005 ± 0.000007 (2SE), which is within error of published values (e.g. Jweda et al., 2016) and values reported on the GeoRem database. All Sr data was normalised to a NBS987 value of 0.710240. For Nd, the JNdi standard had an average $^{143}Nd/^{144}Nd$ of 0.512104 ± 0.000014 (n=8, 2SD), and USGS reference material BCR-2 had $^{143}Nd/^{144}Nd$ of 0.512633 ± 0.000013 (2SE), which agrees extremely well with published values (e.g. Weis et al., 2006; Jweda et al., 2016).

5.4 Results

5.4.1 Vanadium Isotopes

The V isotopic compositions of whole rock samples and mineral separates are shown in Table 5.3 and Figure 5.7. Whole rock $\delta^{51}V_{AA}$ increases from -1.05 ± 0.05‰ (2SD) to -0.56 ± 0.13‰ (2SD) with decreasing WR MgO content. Pyroxene mineral separates span a range in $\delta^{51}V_{AA}$ from -1.06 ± 0.07‰ (2SD) to -0.86 ± 0.03‰ (2SD) and have isotopically identical $\delta^{51}V_{AA}$ to their whole rock host. Magnetite mineral separates are isotopically lighter than whole rock samples and pyroxene mineral separates. Magnetite $\delta^{51}V_{AA}$ increases from -1.26 ± 0.10‰ (2SD) to -0.82 ± 0.06‰ (2SD) with decreasing WR MgO content. For the two samples where both magnetite and pyroxene mineral separates were analysed, magnetite separates are isotopically lighter than coexisting pyroxene by approximately 0.2‰.

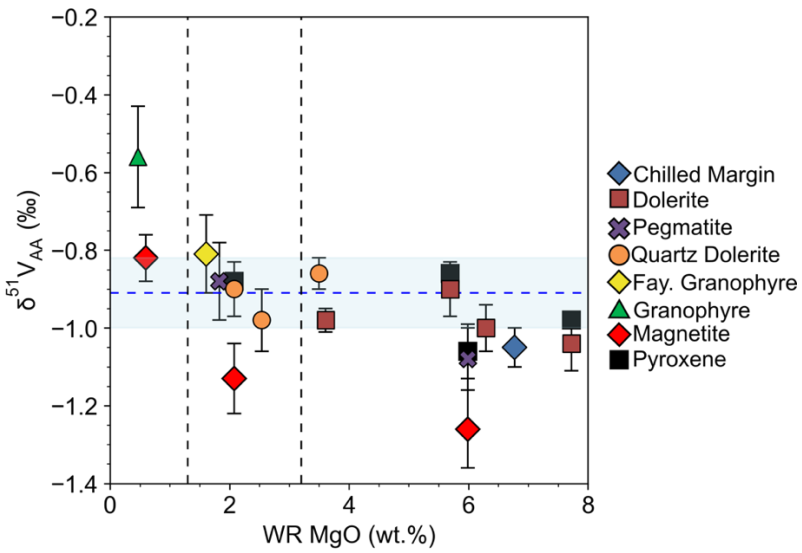

Figure 5.7. V isotopic composition of whole rock and mineral separates against WR MgO content. Errors are 2SD of at least three individual measurements of each sample. The blue shaded area is the average $\delta^{51}V_{AA}$ of the Bulk Silicate Earth (0.91 ± 0.09‰; Qi et al., 2019). The vertical lines show the timing of oxide and sulphide saturation, as in Figure 5.3.

Table 5.3. Vanadium isotopic compositions of whole rock and mineral separates from the Red Hills Intrusion. Errors are given as 2SD of at least 3 individual measurements of the sample. *If fewer than 3 measurements could be made, errors are given as internal 2SE. Abbreviations Peg. Dolerite = Pegmatitic Dolerite, Qtz Dolerite = Quartz Dolerite, Fay Gran = Fayalite Granophyre.

Sample	Lithology	WR MgO (wt. %)	Whole Rock			Pyroxenes			Magnetite		
			$\delta^{51}V_{AA}$ (‰)	2SD	n	$\delta^{51}V_{AA}$ (‰)	2SD	n	$\delta^{51}V_{AA}$ (‰)	2SD	n
65	Chilled Margin	6.77	-1.05	0.05	3						
32	Dolerite	7.72	-1.04	0.07	3	-0.98	0.01	3			
21	Dolerite	6.29	-1.00	0.06	3						
47	Dolerite	5.69	-0.90	0.07	3	-0.86	0.03	3			
35	Dolerite	3.61	-0.98	0.03	3						
74	Peg. Dolerite	5.99	-1.08	0.08	5	-1.06	0.07	3	-1.26	0.10	3
63	Peg. Dolerite	1.83	-0.88	0.10	5						
52	Qtz Dolerite	3.50	-0.86	0.04	3						
61	Qtz Dolerite	2.54	-0.98	0.08	3						
50	Qtz Dolerite	2.08	-0.90	0.07	3	-0.88	0.02*	2	-1.13	0.09	3
44	Fay. Gran.	1.61	-0.81	0.10	3						
54	Fay. Gran.	0.60							-0.82	0.06	3
14	Granophyre	0.47	-0.56	0.13	3						
USGS Reference Materials											
	GSP-2		-0.69	0.09	3						
	BIR-1a		-0.98	0.08	4						
	BIR-1a		-0.97	0.08	5						
	Synth Mag		-0.85	0.08	4						

5.4.2 Iron Isotopes

New Fe isotopic compositions of whole rock powers and magnetite and pyroxene mineral separates are shown in Tables 5.4, 5.5 and 5.6, and Figure 5.8. All samples show mass dependent behaviour (Figure 5.9). Whole rock samples show an overall increase in $\delta^{56}Fe_{IRMM\text{-}524B}$ from 0.014 ± 0.042‰ (2SD) to 0.152 ± 0.031‰ (2SD) with decreasing WR MgO content. Magnetite mineral separates show a decrease in $\delta^{56}Fe_{IRMM\text{-}524B}$ from 0.477 ± 0.080‰ (2SD) to 0.199 ± 0.074 ‰ (2SD) with decreasing WR MgO content. Pyroxene $\delta^{56}Fe_{IRMM\text{-}524B}$ increases from -0.111 ± 0.045‰ (2SD) to -0.008 ± 0.034‰ (2SD) with decreasing WR MgO content.

The Fe isotopic compositions of Red Hills whole rock powders and mineral separates were measured previously by Sossi et al. (2012). The exact same whole rock powders were used in this study. New magnetite and pyroxene mineral separates were handpicked from gravel chips made from the same whole rock samples used by Sossi et al. (2012). Since the column chemistry procedure used in this study separates Fe, V and Zn from the same sample digestion, the Fe fraction was collected and measured again to permit direct comparison between Fe, V and Zn isotope ratios from the exact same powder aliquot.

Tables 5.4, 5.5, and 5.6, and Figure 5.8 shows the Fe isotope data from this study compared to values from Sossi et al. (2012). Note that although data in this study is bracketed with the IRMM-524B standard, whereas the data in Sossi et al. (2012) is expressed relative to IRMM-014, these two reference materials are thought to be isotopically identical (Craddock and Dauphas, 2011). Although both studies show the same pattern of general increase in WR $\delta^{56}Fe$ of around 0.12‰ during fractional crystallisation, $\delta^{56}Fe$ values from this work are offset to lower values. The data from this work also do not show the large decrease WR $\delta^{56}Fe$ below 1 wt.% MgO, although the granophyres do show slightly lighter $\delta^{56}Fe$ than the fayalite granophyres (Figure 5.8). The $\delta^{56}Fe$ values for the mineral separates also vary between the two studies (Figure 5.8), although there is no systematic offset. Some of the discrepancy between the data from the two studies may be due to improvements in analytical techniques since 2012. However, since both studies show the same general increase in WR $\delta^{56}Fe$ during differentiation, the conclusions of Sossi et al. (2012) are not impacted. WR $\delta^{56}Fe$ initially increases due to

crystallisation of isotopically light, Fe^{2+} bearing pyroxene, then decreases below 1 wt.% MgO following the crystallisation of isotopically heavy titanomagnetite (Sossi et al., 2012). For the rest of this chapter, we only consider the Fe isotope data measured in this work.

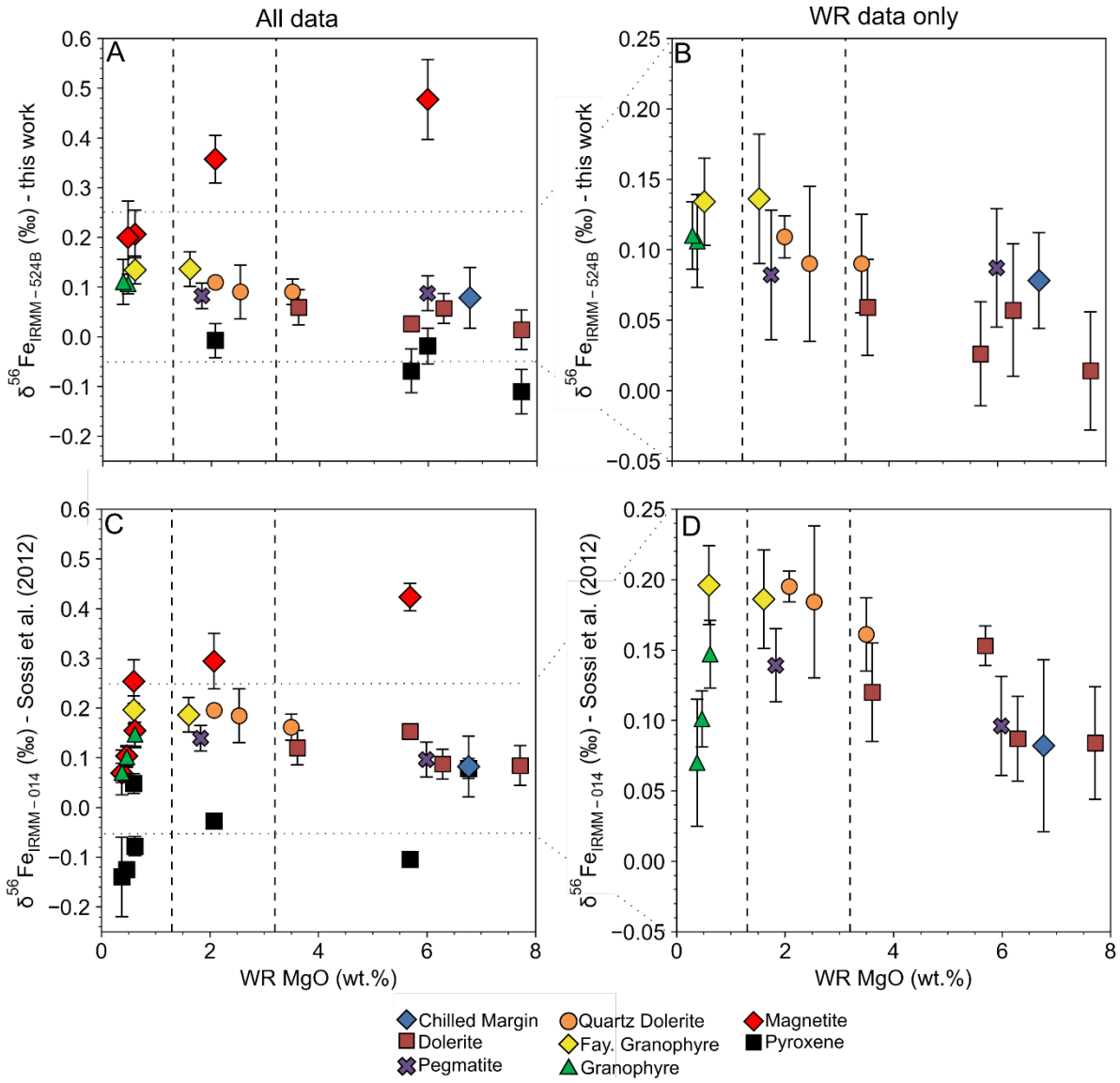

Figure 5.8. Comparison of Fe isotope data from this study (A and B) and Sossi et al. 2012 (C and D). The vertical dashed lines indicate the timings of sulphide and oxide saturation, as in Figure 5.3. The errors in the data from this study are given as 2SD of at least 3 measurements of an individual sample. Values from Sossi et al. (2012) given in tables 5.4, 5.5 and 5.6. The errors in Sossi et al. (2012) are given as 95% confidence intervals, calculated by the formula 95% s.e = t x s.d/√n, where t is the Student's t-factor.

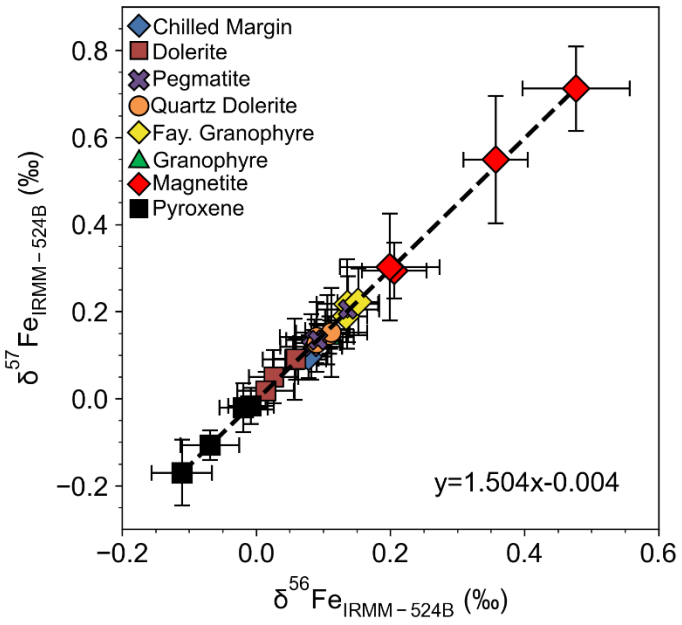

Figure 5.9. Three-isotope plot for Fe (δ^{56}Fe vs δ^{57}Fe). The slope of the linear regression (1.504) is consistent with the gradient predicted by mass dependent fractionation laws (i.e. ~1.5; Young et al., 2002). Errors are 2SD of at least 3 measurements of an individual sample.

Table 5.4. Whole Rock Fe isotopic compositions from this study, compared to values from Sossi et al. (2012). Note that although data in this study is bracketed with the IRMM-524B standard, whereas the data in Sossi et al. (2012) is expressed relative to IRMM-014, these two reference materials are thought to be isotopically identical (Craddock and Dauphas, 2011). Errors from this work are 2SD of at least 3 measurements of an individual sample. The errors from Sossi et al. (2012) are quoted as a 95% confidence interval on the mean ($2\sigma = t \times SD/\sqrt{n}$, where t is a multiplier depending on the number of repetitions and the confidence interval specified). Errors are recalculated as 2SD for direct comparison to this study (*), assuming that the t-value used is for the 95% confidence interval at n-1 degrees of freedom, as is appropriate when n <30 (e.g. Marsal, 1987). Abbreviations Peg. Dolerite = Pegmatitic Dolerite, Qtz Dolerite = Quartz Dolerite, Fay Gran = Fayalite Granophyre.

Sample	Lithology	WR MgO (wt. %)	Whole Rock (This Study)					*Whole Rock (Sossi et al. (2012)*			
			$\delta^{56}Fe_{IRMM-524B}$ (‰)	2SD	$\delta^{57}Fe_{IRMM-524B}$ (‰)	2SD	n	*$\delta^{56}Fe_{IRMM-014}$ (‰)*	*95% ci (2SE)*	*2SD**	*n*
65	Chilled Margin	6.77	0.078	0.034	0.096	0.049	4	*0.082*	*0.061*	*0.049*	*3*
32	Dolerite	7.72	0.014	0.042	0.018	0.043	5	*0.084*	*0.040*	*0.032*	*3*
21	Dolerite	6.29	0.057	0.047	0.09	0.093	4	*0.087*	*0.030*	*0.065*	*7*
47	Dolerite	5.69	0.026	0.037	0.05	0.061	3	*0.153*	*0.014*	*0.011*	*3*
35	Dolerite	3.61	0.059	0.034	0.091	0.047	3	*0.120*	*0.035*	*0.044*	*4*
74	Peg. Dolerite	5.99	0.087	0.042	0.135	0.046	3	*0.096*	*0.035*	*0.028*	*3*
	replicate		0.137	0.046	0.205	0.076	6				
63	Peg. Dolerite	1.83	0.082	0.046	0.119	0.075	4	*0.139*	*0.026*	*0.033*	*4*
	replicate		0.092	0.016	0.134	0.034	3				
52	Qtz Dolerite	3.50	0.090	0.035	0.127	0.045	4	*0.161*	*0.026*	*0.021*	*3*
61	Qtz Dolerite	2.54	0.090	0.055	0.141	0.08	4	*0.184*	*0.054*	*0.044*	*3*
	replicate		0.112	0.053	0.152	0.102	3				
50	Qtz Dolerite	2.08	0.109	0.015	0.146	0.043	3	*0.195*	*0.011*	*0.014*	*4*
44	Fay. Gran.	1.61	0.136	0.046	0.217	0.103	3	*0.186*	*0.035*	*0.056*	*5*
	replicate		0.152	0.031	0.222	0.077	3				
54	Fay. Gran.	0.60	0.134	0.031	0.189	0.030	3	*0.196*	*0.028*	*0.035*	*4*

14	Granophyre	0.47	0.106	0.033	0.158	0.079	3	*0.101*	*0.020*	*0.038*	*6*
15	Granophyre	0.38	0.110	0.024	0.147	0.032	3	*0.070*	*0.045*	*0.072*	*5*
USGS Reference Materials											
	GSP-2		0.171	0.055	0.241	0.088	4				
	BIR-1a		0.070	0.065	0.112	0.113	4				
	Synth Mag		0.107	0.085	0.150	0.134	3				

Table 5.5. Iron isotopic compositions of pyroxene mineral separates from this study, compared to values from Sossi et al. (2012). The errors from Sossi et al. (2012) are quoted as a 95% confidence interval on the mean ($2\sigma = t \times SD/\sqrt{n}$). Errors are recalculated as 2SD for direct comparison to this study (*).

Sample	Mineral	This Study					*Sossi et al. (2012)*			
		$\delta^{56}Fe_{IRMM-524B}$ (‰)	2SD	$\delta^{57}Fe_{IRMM-524B}$ (‰)	2SD	n	*$\delta^{56}Fe_{IRMM-014}$ (‰)*	*95% ci (2SE)*	*2SD**	*n*
32	Pyroxene	-0.111	0.045	-0.170	0.076	4				
47	Pyroxene	-0.069	0.044	-0.107	0.034	3	*-0.105*	*0.007*	*0.009*	*4*
74	Pyroxene	-0.019	0.036	-0.021	0.056	4				
50	Pyroxene	-0.008	0.034	-0.017	0.041	3	*-0.028*	*0.012*	*0.010*	*3*

Table 5.6. Iron isotopic compositions of magnetite mineral separates from this study, compared to values from Sossi et al. (2012). The errors from Sossi et al. (2012) are quoted as a 95% confidence interval on the mean ($2\sigma = t \times SD/\sqrt{n}$). Errors are recalculated as 2SD for direct comparison to this study (*).

Sample	Mineral	This Study					*Sossi et al. (2012)*			
		$\delta^{56}Fe_{IRMM-524B}$ (‰)	2SD	$\delta^{57}Fe_{IRMM-524B}$ (‰)	2SD	n	*$\delta^{56}Fe_{IRMM-014}$ (‰)*	*95% ci (2SE)*	*2SD**	*n*
74	Magnetite	0.477	0.080	0.712	0.097	5				
50	Magnetite	0.357	0.048	0.549	0.146	5	*0.294*	*0.056*	*0.045*	*3*
54	Magnetite	0.206	0.047*	0.294	0.064 *	2	*0.253*	*0.044*	*0.071*	*5*
14	Magnetite	0.199	0.074	0.302	0.123	5	*0.103*	*0.021*	*0.026*	*4*

5.4.3 Zinc Isotopes

The Zn isotopic composition of whole rock powders and mineral separates are shown in Table 5.7 and Figure 5.10. Whole rock $\delta^{66}Zn_{AA\text{-}ETH}$ values vary between -0.117 ± 0.027‰ (2SD) and 0.018 ± 0.063‰ (2SD). There is no overall trend with WR MgO content, but samples with higher WR MgO generally show more variation in $\delta^{66}Zn$ values (Figure 5.10). The overall range is similar to $\delta^{66}Zn$ of lavas from the Hekla differentiation sequence (-0.06±0.04‰ to +0.05±0.04‰ (2SD); Chen et al., 2013).

The pyroxene mineral separates are isotopically lighter than the WR samples, spanning a range in $\delta^{66}Zn_{AA\text{-}ETH}$ from -0.299 ± 0.018‰ (2SD) to -0.169 ± 0.039‰ (2SD), and showing a general increase with decreasing WR MgO content. The magnetite mineral separates are heavier than the whole rock samples and pyroxene mineral separates, and show the most variable Zn isotopic compositions, ranging from $\delta^{66}Zn_{AA\text{-}ETH}$ = 0.053 ± 0.046‰ (2SD) to 0.313 ± 0.013‰ (2SD). There is no overall trend in magnetite $\delta^{66}Zn$ with WR MgO content.

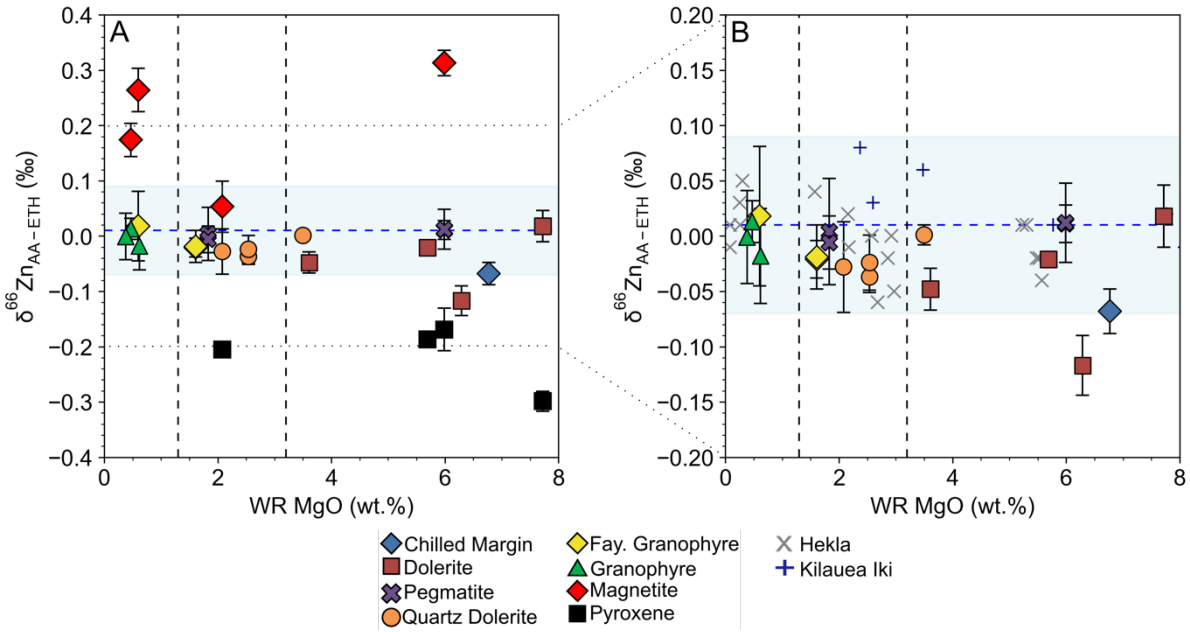

Figure 5.10. Zn isotopic composition of whole rock and mineral separates against WR MgO content. (A) shows the whole rock and mineral separate data. (B) is a magnified plot showing only the whole rock data in comparison to data from Kilauea Iki (blue crosses) and Hekla (grey crosses) from Chen et al. (2013). Errors are 2SD of at least three individual measurements of each sample. The blue shaded area is the average $\delta^{66}Zn$ of mantle derived magmas (0.01 ± 0.08‰ (2SD); Chen et al., 2013). The vertical lines show the timing of oxide and sulphide saturation, as in Figure 5.3.

Table 5.7. Zinc isotopic compositions of whole rock and mineral separates from the Red Hills Intrusion. Data is reported relative to the AA-ETH standard, but can be recast relative to the JMC-Lyon standard using the conversion of Archer et al. 2017 ($\delta^{66}Zn_{JMC\text{-}Lyon} = \delta^{66}Zn_{AA\text{-}ETH} + 0.28$). Abbreviations Peg. Dolerite = Pegmatitic Dolerite, Qtz Dolerite = Quartz Dolerite, Fay Gran = Fayalite Granophyre. Some of the WR samples do not show mass dependent $\delta^{66}Zn$ and $\delta^{68}Zn$. The WR samples were initially passed through only one ion exchange column. However, the replicate digestions were passed through two ion exchange columns and show mass dependent values. Both the original and replicate digestions show identical $\delta^{66}Zn$ values, so the $\delta^{66}Zn$ values from the mass independent samples are still correct and reliable.

Sample	Lithology		Whole Rock					Pyroxenes					Magnetite				
		WR MgO (wt. %)	$\delta^{66}Zn$ AA-ETH (‰)	2SD	$\delta^{68}Zn$ AA-ETH (‰)	2SD	n	$\delta^{66}Zn$ AA-ETH (‰)	2SD	$\delta^{68}Zn$ AA-ETH (‰)	2SD	n	$\delta^{66}Zn$ AA-ETH (‰)	2SD	$\delta^{68}Zn$ AA-ETH (‰)	2SD	n
65	Chilled Margin	6.77	-0.068	0.02	0.019	0.04	4										
32	Dolerite	7.72	0.018	0.028	0.036	0.011	3	-0.299	0.018	-0.593	0.057	3					
21	Dolerite	6.29	-0.117	0.027	-0.041	0.112	3										
47	Dolerite	5.69	-0.021	0.007	-0.038	0.057	3	-0.187	0.013	-0.381	0.043	3					
35	Dolerite	3.61	-0.048	0.019	-0.096	0.051	3										
74	Peg. Dolerite	5.99	0.011	0.017	0.047	0.029	3	-0.169	0.039	-0.340	0.011	3	0.313	0.013	0.598	0.033	3
	replicate		0.012	0.036	-0.023	0.058	3										
63	Peg. Dolerite	1.83	0.004	0.048	3.150	0.200	3										
	replicate		-0.006	0.024	-0.034	0.010	3										
52	Qtz Dolerite	3.50	0.001	0.009	-0.031	0.023	3										
61	Qtz Dolerite	2.54	-0.037	0.014	-0.088	0.068	3										
	replicate		-0.024	0.025	-0.073	0.026	3										
50	Qtz Dolerite	2.08	-0.028	0.041	-0.100	0.083	3	-0.205	0.010	-0.415	0.050	3	0.053	0.046	0.083	0.093	3
44	Fay. Gran.	1.61	-0.021	0.017	0.205	0.042	3										
	replicate		-0.019	0.029	-0.055	0.051	3										
38	Granophyre	0.62	-0.018	0.043	-0.071	0.100	3										
54	Fay. Gran.	0.60	0.018	0.063	0.634	0.065	3						0.264	0.039	0.495	0.026	3
14	Granophyre	0.47	0.013	0.019	4.647	0.265	3						0.174	0.030	0.320	0.032	3

15	Granophyre	0.38	-0.001	0.042	-0.013	0.072	3										
USGS Reference Materials																	
	BIR-1a		-0.012	0.036	-0.066	0.041	4										
	BIR-1a		-0.046	0.010	-0.106	0.033	3										
	Synth Mag		0.076	0.025	0.120	0.031	3										

5.4.4 Strontium and Neodymium Isotopes

To assess the potential for crustal contamination during differentiation of the Red Hill intrusion, strontium (Sr) and neodymium (Nd) isotope ratios were measured on a set of WR samples spanning the differentiation sequence.

Age corrections for the Sr and Nd isotope ratios are shown in Electronic Appendix 1. Present and initial epsilon values (εNd and εNd_i) were calculated using values of 6.54 x 10^{-12} for $\lambda^{147}Sm$ (Begemann et al., 2001) and values of 0.512630 and 0.1960 for the $^{143}Nd/^{144}Nd$ and $^{147}Sm/^{144}Nd$ of the chondritic uniform reservoir (CHUR) (Bouvier et al., 2008). The $^{87}Sr/^{86}Sr_i$ values were calculated using 1.42 x 10^{-12} for $\lambda^{187}Rb$ (Steiger and Jager, 1977). There have been several age determinations for the Tasmanian Dolerites. Brauns et al. (2000) obtained an age of 175.1 ± 5.4Ma using a Re-Os isochron method, which agrees with an earlier estimate using K-Ar dating by Schmidt and McDougall (1977) of 170.5 ± 8 Ma. Sossi (2010) calculated an age of 174 ± 10 Ma for the Red Hills intrusion specifically, using a Rb-Sr isochron method. The age estimate 174 ± 10 Ma is used in all age corrections for Sr and Nd isotopes. The measured $^{87}Sr/^{86}Sr$ and $^{143}Nd/^{144}Nd$ ratios for six samples measured by Sossi (2010) are recast to the ratios of the NBS987 and JNdi standards measured in this study (see Electronic Appendix and Section 5.3.2), and age corrected ratios are calculated as described above.

Figure 5.11 and Tables 5.8 and 5.9 show the age corrected Sr and Nd isotopic ratios. There is no significant variation in either εNd_i or $^{87}Sr/^{86}Sr_i$ with WR MgO content. The $^{87}Sr/^{86}Sr_i$ and εNd_i values agree within error with values for six samples measured by Sossi (2010). The Red Hill samples have $^{87}Sr/^{86}Sr_i$ values ranging from 0.710024 to 0.711642 and εNd_i values between -4.75 and -5.17. These values are higher and lower respectively than typical depleted MORB mantle (Salters and Stracke, 2004; Workman and Hart, 2005). Other samples from the Jurassic Ferrar Magmatic Province also show these distinctive radiogenic isotope signatures, which has been interpreted as incorporation of subducted sedimentary material into the mantle source of these magmas (Hergt et al., 1989; Hergt et al., 1991; Molzahn et al., 1996).

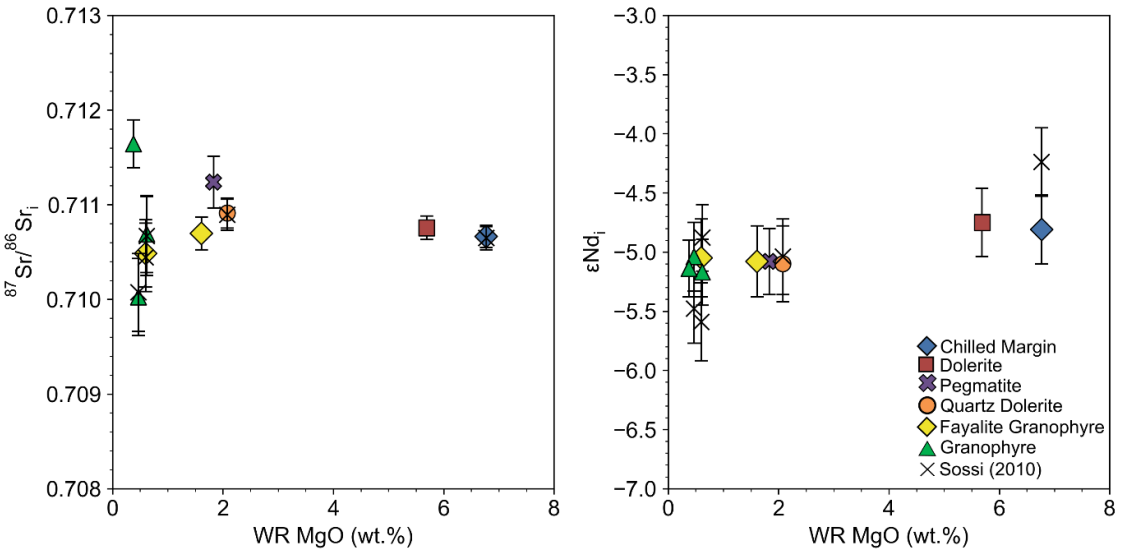

Figure 5.11. Initial Sr and Nd isotopic compositions in the Red Hill intrusion. Coloured symbols are values from this study. The values in Sossi (2010) are renormalised to the average isotopic compositions of the JNdi and NBS987 standards measured in this study, and shown by the black crosses. Errors are 2SE of the measured $^{87}Sr/^{86}Sr$ and $^{143}Nd/^{144}Nd$ ratios plus propagation of uncertainty in the age of the intrusion (174±10Ma; Sossi, 2010). The full age correction calculations are shown in Electronic Appendix 1.

Table 5.8. Neodymium isotopic composition of the Red Hills samples. Errors are internal 2SE of an individual measurement. *Sm and Nd concentrations are measured by ICP-MS, given in Sossi (2010). $^{143}Nd/^{144}Nd_i$ and εNd_i are calculated using the parameters listed in the text. Full calculations are in Electronic Appendix 1.

Sample	Lithology	Sm (µg/g)*	Nd (µg/g)*	$^{143}Nd/^{144}Nd$	2SE	$^{147}Sm/^{144}Nd$	$^{143}Nd/^{144}Nd_i$	εNd_i	2SE
65	Chilled Margin	2.93	12.38	0.512323	0.000011	0.143023	0.512160	-4.81	0.22
47	Dolerite	3.25	13.61	0.512328	0.000011	0.144306	0.512164	-4.75	0.22
63	Peg. Dolerite	6.8	29.58	0.512305	0.000011	0.138921	0.512147	-5.08	0.21
50	Qtz. Dolerite	4.89	21.25	0.512304	0.000012	0.139061	0.512145	-5.10	0.24
44	Fay. Gran.	5.32	22.97	0.512306	0.000012	0.139961	0.512147	-5.08	0.23
38	Granophyre	8.64	37.11	0.512302	0.000011	0.140695	0.512142	-5.17	0.21
54	Fay. Gran.	8.14	35.23	0.512307	0.000013	0.139627	0.512148	-5.05	0.26
14	Granophyre	8.64	38.3	0.512304	0.000011	0.136324	0.512149	-5.04	0.21
15	Granophyre	11.55	48.58	0.512307	0.000009	0.143675	0.512144	-5.14	0.18

Table 5.9. Strontium isotopic composition of the Red Hills samples. Errors are internal 2SE of an individual measurement. *Sr and Rb concentrations are measured by ICP-MS, given in Sossi (2010). $^{87}Sr/^{86}Sr_i$ is calculated using the parameters listed in the text. Full calculations are in Electronic Appendix 1.

Sample	Lithology	Rb (µg/g)*	Sr (µg/g)*	$^{87}Sr/^{86}Sr$	2SE	$^{87}Rb/^{86}Sr$	$^{87}Sr/^{86}Sr_i$
65	Chilled Margin	34.88	131.34	0.712565	0.000006	0.768625	0.710664
47	Dolerite	36.26	131.39	0.712731	0.000010	0.798744	0.710755
63	Peg. Dolerite	78.44	121.52	0.715861	0.000006	1.868808	0.711238
50	Qtz. Dolerite	55.55	150.88	0.713547	0.000007	1.065685	0.710911
44	Fay. Gran.	63.78	158.55	0.713576	0.000006	1.164384	0.710696
38	Granophyre	103.86	107.22	0.717628	0.000008	2.804932	0.710689
54	Fay. Gran.	97.31	115.1	0.716540	0.000007	2.447856	0.710484
14	Granophyre	105.56	109.35	0.716939	0.000009	2.795125	0.710024
15	Granophyre	111.08	186.76	0.715902	0.000007	1.721982	0.711642

5.5 Discussion

The aim of this chapter is to analyse the V isotopic composition of whole rock samples and mineral separates from the Red Hill intrusion to understand the drivers of V isotope fractionation in a tholeiitic intrusive suite. These findings are then compared to trends observed in the calc-alkaline Boggy Plain Zoned Pluton (Chapter 4).

Sossi et al. (2012) proposed that all Fe isotopic trends in the Red Hill intrusion are caused by approximately closed system fractional crystallisation of a tholeiitic magma. Initial crystallisation of isotopically light pyroxene drives the residual melt to a heavier Fe isotopic composition. The $\delta^{56}Fe$ of the residual melt then decreases following saturation of isotopically heavy titanomagnetite in evolved melts with < 1.5 wt.% MgO. However, before V isotope data can be interpreted within this framework, it is necessary to exclude other processes which could affect V isotopic compositions.

For this reason, Zn, Sr and Nd isotope ratios were also measured on the same set of samples. As with the Boggy Plain Zoned Pluton (Chapter 3), the Sr and Nd isotopic data were used to determine if the Red Hill intrusion formed from a single magma source, and to assess whether any crustal assimilation occurred during differentiation (Section 5.5.1). Zinc isotopes were used to check for late-stage fluid exsolution or alteration (e.g. Telus et al., 2012), and to investigate the potential influence of sulphide crystallisation on isotopic compositions (Section 5.5.2). The Fe isotope data from this study and from Sossi et al. (2012) were used to investigate if there is inter-mineral isotopic equilibrium between different minerals, or if disequilibrium processes such as diffusion could have affected isotopic compositions (Section 5.5.3). Once these processes are assessed, the drivers of V isotope fractionation in the Red Hill intrusion are investigated and compared to the calc-alkaline BPZP (Sections 5.5.4 and 5.5.5).

5.5.1 Radiogenic Sr-Nd values in the Red Hill intrusion

The Red Hill samples show higher $^{87}Sr/^{86}Sr_i$ and lower εNd_i that typical depleted MORB mantle (Salters and Stracke, 2004; Workman and Hart, 2005). However, there is no significant variation in εNd_i or $^{87}Sr/^{86}Sr_i$ with WR MgO content (Figure 5.11). This suggests that crustal assimilation occurred prior to crystallisation of the Red Hill intrusion

(Hergt et al., 1991; Molzahn et al., 1996). Therefore, assimilation would not have influenced V isotope trends within the intrusion. There is some variation in $^{87}Sr/^{86}Sr_i$ in the granophyres (Figure 5.11), which could possibly be caused by weathering processes, but the lack of resolvable V isotope fractionation during alteration or weathering documented thus far (Prytulak et al., 2013; Qi et al., 2022) means that this is unlikely to affect the V isotopic composition of these samples.

5.5.2 Zinc Isotopes in the Red Hill intrusion

Whole rock $\delta^{66}Zn$ varies by only 0.1‰ in the Red Hill intrusion, and there is no overall trend in WR $\delta^{66}Zn$ with differentiation. The variation in WR $\delta^{66}Zn$ in the Red Hill intrusion is of a similar magnitude to that observed in other differentiation sequences, such as Hekla (Chen et al., 2013), Kilauea Iki (Chen et al., 2013) and the Boggy Plain Zoned Pluton (Stow et al., 2022; Chapter 3), confirming a lack of resolvable Zn isotopic fractionation during fractional crystallisation. The lack of variation in WR $\delta^{66}Zn$ in the pegmatite samples and the granophyres with variable $^{87}Sr/^{86}Sr_i$ also suggests that samples have not been affected by fluid exsolution or alteration processes (Telus et al., 2012; Xia et al., 2017; Doucet et al., 2020).

In contrast to the WR data, the mineral separates in the Red Hill intrusion show extremely variable Zn isotopic compositions (Figure 5.10). Assuming that in titanomagnetite and pyroxene, VI-fold Zn^{2+} substitutes for VI-fold Fe^{2+} due to their similar ionic radii (0.74 Å and 0.78 Å respectively, Shannon, 1976), then theoretically titanomagnetite and pyroxene should have identical Zn isotopic composition. Previous studies have shown that hydrous silicates and oxide mineral separates have identical Zn isotopic compositions at equilibrium (Xu et al., 2019; Stow et al., 2022). However, titanomagnetite has heavier Zn isotopic composition than pyroxene in the same sample, and the titanomagnetite separates in particular have extremely variable $\delta^{66}Zn$.

There are several possibilities which could explain why titanomagnetite and pyroxene have different Zn isotopic compositions. Firstly, in normal spinel, Zn is hosted in IV-fold coordination (e.g. Marshall and Dollase, 1984; Yang et al., 2021). It is unclear what coordination Zn is found in inverse spinel like titanomagnetite, so if some Zn is also IV-fold coordinated in titanomagnetite, this may explain why titanomagnetite has a heavy Zn isotopic composition. In addition, Zn has a high diffusion rate in magnetite (Sievwright

et al., 2020), so the Zn isotopic composition of magnetite could be affected by diffusive re-equilibration.

The light Zn isotopic composition of the pyroxene separates may also be due to the specific coordination environment of Zn. In clinopyroxene, Zn^{2+} can substitute for Fe^{2+} in either VI-fold M1 sites, or distorted M2 sites with VI to VIII-fold coordination (Cameron and Papike, 1981; Morimoto, 1988). Therefore, if Zn^{2+} is found in higher coordination on the M2 sites, clinopyroxene may have a lighter Zn isotopic composition compared to other silicates which host only VI-fold Zn^{2+}.

Pyrite is found in all samples in the Red Hill intrusion, and chalcopyrite in samples with WR MgO < 3.2 wt.%. As shown in Figure 5.5, these sulphide inclusions are commonly associated with titanomagnetite grains. Considerable amounts of Zn can be hosted in sulphides (Kiseeva and Wood, 2015). The EDS analysis (Table 5.2) showed that chalcopyrite contains approximately 1 wt.% Zn, but Zn concentrations in pyrite were below detection limits. Sulphide minerals show highly variable $\delta^{66}Zn$ compared to silicates (e.g. Mason et al., 2005; John et al., 2008), although most previous measurements of Zn isotopes in sulphides have focused on hydrothermal and not magmatic systems. Therefore, if sulphides are found as inclusions or on the grain boundaries of these phases and sampled as part of the bulk mineral separate, this may explain some of the variation in $\delta^{66}Zn$ in the mineral separates.

It is unlikely that sulphides will influence V isotopic compositions because the partition coefficient of V between sulphide melt and silicate melt is low (Gaetani and Grove, 1997; Kiseeva and Wood, 2015). This inference is supported by the decoupling of Fe and V isotopic systems following sulphide saturation in Mariana arc lavas, where sulphide saturation causes an increase in $\delta^{56}Fe$ but no change in $\delta^{51}V$ (Williams et al., 2018). Therefore, V isotope variations in the Red Hill intrusion are most likely only influenced by the fractional crystallisation of silicate and oxide phases, as discussed below in Section 5.5.4. It is also unlikely that sulphide fractionation has a resolvable influence on $\delta^{56}Fe$ in the Red Hill intrusion, because although magmatic sulphides can show extremely variable $\delta^{56}Fe$ (Ding et al., 2019; Brzozowski et al., 2021), pyrite and chalcopyrite are present in low enough modal abundances (<0.01%) in the Red Hill intrusion that mass balance calculations show they host <0.1% of the total Fe budget. Hence, Fe isotopic trends are

dominantly controlled by pyroxene and titanomagnetite crystallisation (Sossi et al., 2012).

5.5.3 Assessing the attainment of inter-mineral isotopic equilibrium

An aim of this chapter is to investigate V isotope mineral-melt fractionation factors for Fe-Ti oxides in the Red Hill intrusion. Mineral-melt fractionation factors are only valid if minerals have crystallised in isotopic equilibrium with each other and the main magma body. Petrographic examination is needed to provide textural evidence for equilibrium and assess the effect of disequilibrium processes such as diffusion. In intrusive settings it is particularly important to understand which phases may have crystallised from isolated pockets of trapped interstitial melt, because these phases may not influence overall isotopic trends in the main evolving magma body (e.g. Stow et al., 2022; Chapter 3). Although the WR samples generally show well defined trends in Zn, V and Fe isotopic composition during magmatic differentiation, there is a large variation in the isotopic composition of mineral separates over the differentiation sequence (Figures 5.7, 5.8, 5.10).

In addition to petrographic examination (See Section 5.2.3 and petrographic descriptions in Electronic Appendix 5), the best means to determine whether there is inter-mineral isotopic equilibrium is to calculate the difference in isotopic composition between the two phases ($\Delta_{A\text{-}B} = \delta_A - \delta_B$) and compare this to theoretical estimates based on the vibrational properties of the minerals. Theoretical inter-mineral fractionation factors can be determined using either nuclear resonance inelastic X-ray scattering (NRIXS; e.g. Dauphas et al., 2012; Dauphas et al., 2014; Roskosz et al., 2015; Nie et al., 2021) or density functional theory calculations (DFT; e.g. Blanchard et al., 2009; Rabin et al., 2021). These methods are used to derive β-factors and bond force constants for different mineral phases. It is difficult to assess whether pyroxene and magnetite are in Zn and V isotopic equilibrium because relatively few pyroxene-magnetite mineral pairs were analysed, and there is a lack of mineral separate data from previous studies for comparison. Therefore, we assume if mineral pairs demonstrate inter-mineral Fe isotopic equilibrium, then they also are likely to be in V isotopic equilibrium, because V^{3+} and Fe^{3+} have similar diffusion rates, owing to the similarity in their charge and ionic radii (e.g. Zhang et al., 2010). There is some uncertainty if mineral pairs will be in Zn isotopic

equilibrium because Zn^{2+} diffusion rates are similar to those of Fe^{2+}, which are around 6 times faster than Fe^{3+} (e.g. Zhang et al., 2010).

For Fe, $\Delta^{56}Fe_{min\text{-}min}$ values can be calculated using equation 5.2 from Dauphas et al. (2014), as described in Chapter 3, Section 3.6.3.

$$\Delta^{56}Fe_{A-B} = 2853 \times \frac{<F_A> - <F_B>}{T^2} \qquad [5.2]$$

Figure 5.12 shows the Fe isotope fractionation factors between magnetite and pyroxene ($\Delta^{56}Fe_{mag\text{-}px} = \delta^{56}Fe_{mag} - \delta^{56}Fe_{px}$) measured in the Red Hill intrusion in this study, and by Sossi et al. (2012). Measured values are compared to theoretical estimates calculated using NRIXS and DFT data (blue and green curves). For $\Delta^{56}Fe_{mag\text{-}px}$ calculated using NRIXS data, force constants of 264±6 N/m (Roskosz et al., 2015) and 165±5 N/m (Jackson et al., 2009) are used for magnetite and pyroxene respectively. To calculate $\Delta^{56}Fe_{mag\text{-}px}$ using DFT data, force constants of 207.5 N/m and 127.8 N/m are used for magnetite and pyroxene respectively, with an error of ±5% (Rabin et al., 2021). Bond force constants determined using DFT calculations are systematically lower than those determined by NRIXS. A discussion of the reasons for the discrepancies between NRIXS and DFT data is given in Chapter 3, Section 3.6.3 (Stow et al., 2022). However, although the absolute values for force constants are different, the difference in force constant between the mineral pair is similar using both methods, so the theoretical estimates of $\Delta^{56}Fe_{mag\text{-}px}$ are within error (blue and green shaded areas on Figure 5.12).

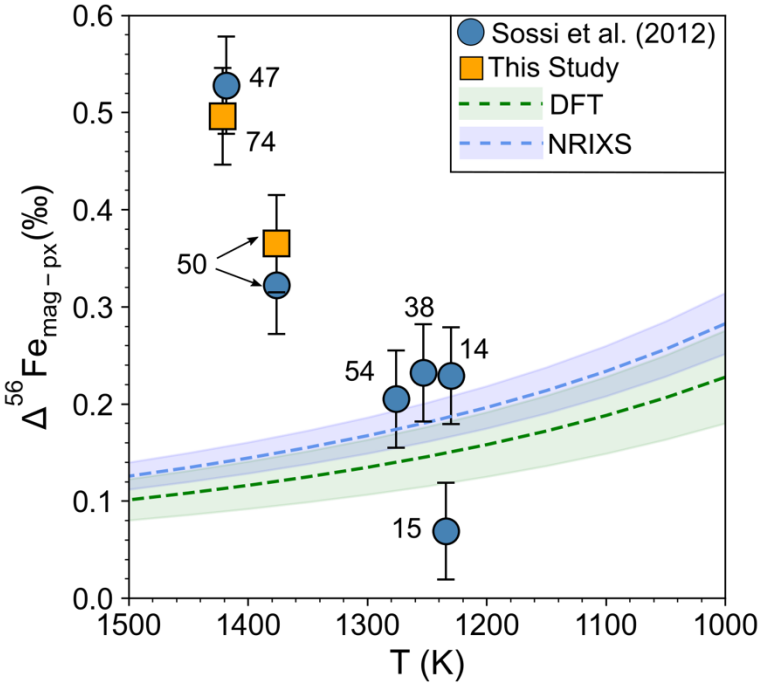

Figure 5.12. Measured $\Delta^{56}Fe_{mag\text{-}px}$ for the Red Hill samples against crystallisation temperature (K). Samples from this study are shown by the squares, and samples from Sossi et al. (2012) are shown by the circles. Temperature estimates are from Sossi et al. (2012) and are based on whole rock chemistry after Sisson and Grove (1993b). The blue and green lines and shaded areas show estimates of $\Delta^{56}Fe_{mag\text{-}px}$ derived using NRIXS and DFT data respectively, as described in the text. Note that $\Delta^{56}Fe_{mag\text{-}px}$ measured in sample 50 in this study is identical within error to the value measured by Sossi et al. (2012) on completely different mineral separate aliquots. This highlights that the differences in absolute $\delta^{56}Fe$ values between the two studies is likely a calibration issue and the overall magnitude and trends in $\delta^{56}Fe$ variation within the intrusion from both studies are comparable.

The samples with WR MgO <1.5 wt.% and crystallisation temperatures <1300K (Samples 14, 15, 38, 54) have $\Delta^{56}Fe_{mag\text{-}px}$ values within error of the NRIXS and DFT estimates. This suggests Fe isotopic equilibrium is attained between magnetite and pyroxene in the most evolved samples. However, it should be noted that the Red Hill titanomagnetite has high Ti content (Table 5.1), whereas the NRIXS and DFT data used to calculate the theoretical $\Delta^{56}Fe_{mag\text{-}px}$ is for pure magnetite (Roskosz et al., 2015; Rabin et al., 2021), so does not account for variation in Ti content. Sossi and O'Neill (2017) and Rabin et al. (2021) both calculate a smaller bond force constant for Ti-rich ulvöspinel (Fe_2TiO_4) compared to pure magnetite (Fe_3O_4), which suggests that increasing the Ti content may result in a smaller $\Delta^{56}Fe_{mag\text{-}px}$ value.

Samples 47, 50 and 74 show higher $\Delta^{56}Fe_{mag\text{-}px}$ values than predicted at equilibrium. The most likely explanation is that titanomagnetite and pyroxene did not crystallise in

equilibrium in these samples. Petrographic observations of anhedral, space-filling titanomagnetite grains (Figure 5.5) suggest that in the most mafic samples, titanomagnetite may have crystallised from trapped pockets of interstitial melt, which were isotopically heavy following the crystallisation of isotopically light pyroxene (Sossi et al., 2012). Therefore, measured $\Delta^{56}Fe_{mag\text{-}px}$ values would be larger than predicted at equilibrium. The caveat that magnetite and pyroxene may not have crystallised in equilibrium in these samples must be considered when interpreting the Zn and V isotope data.

5.5.4 Vanadium isotope trends in the Red Hill Intrusion

In the previous section, we established that source heterogeneity, crustal assimilation, fluid exsolution and sulfide crystallisation are unlikely to influence V isotopic trends. Therefore, we can interpret the data within the context of closed system fractional crystallisation of silicate and oxide minerals from a tholeiitic magma. The behaviour of V isotopes during fractional crystallisation of a tholeiitic intrusion is then compared to observations from the calc-alkaline Boggy Plain Zoned Pluton (BPZP; Stow et al., 2022; Chapter 4).

Vanadium isotopic trends during fractional crystallisation are largely controlled by the timing of oxide saturation, and the mineralogy of Fe-Ti oxide minerals (Prytulak et al., 2017; Ding et al., 2020), which are largely dictated by magma fO_2 and H_2O content (e.g. Sisson and Grove, 1993a; Toplis and Carroll, 1995; Feig et al., 2010). Vanadium isotopic fractionation reflects the contrast in bond coordination and V valence state between minerals and melt. Fe-Ti oxide minerals host V^{3+} and some V^{4+} in VI-fold coordination (O'Neill and Navrotsky, 1984). Therefore, Fe-Ti oxides are predicted to be isotopically lighter than coexisting silicate melt, which contains V at lower coordination and higher redox state (Giuli et al., 2004; Sutton et al., 2005; Righter et al., 2006). Upon saturation of isotopically light Fe-Ti oxides, the residual melt is driven to a heavier V isotopic composition (Prytulak et al., 2017; Sossi et al., 2018b; Wu et al., 2018; Ding et al., 2020). Fractionation of silicate phases may also contribute to the increase in $\delta^{51}V$ because silicate minerals are also predicted to host VI-fold coordinated V^{3+} (e.g. Toplis and Corgne, 2002; Wu et al., 2018; Chapter 4). Although silicate and Fe-Ti oxide phases are predicted to have similar $\delta^{51}V$ values based on theoretical valence and bonding environment

considerations, the pyroxene and titanomagnetite in samples 50 and 74 may have different $\delta^{51}V$ values because they did not crystallise in equilibrium.

The Red Hill magma has low fO_2 and H_2O content which delays magnetite saturation and promotes an early crystallising assemblage dominated by plagioclase and pyroxene, typical of other tholeiitic intrusions (e.g. Toplis and Carroll, 1995; McDougall, 1962; Sossi et al., 2012). Therefore, pyroxenes are the dominant V-bearing phase crystallising at high MgO content, and Ti-rich magnetite becomes the dominant V-bearing phase below 1.5 wt.% MgO. In contrast, in the Boggy Plain Zoned Pluton higher magma fO_2 and H_2O content promotes early saturation of magnetite (e.g. Sisson and Grove, 1993a). A Ti-poor magnetite occurs as a primocryst phase from ~5 wt.% WR MgO content, but the V budget is approximately evenly distributed between magnetite, biotite and hornblende (Stow et al., 2022; Chapters 3 and 4). Consequently, the two suites show different trends of WR V concentration with decreasing WR MgO (Figure 5.13). From these observations, it was likely that the Boggy Plain Zoned Pluton and Red Hill intrusion would show distinct V isotopic trends.

5.5.5 Modelling V isotope behaviour in calc-alkaline and tholeiitic magmas

Rayleigh fractional crystallisation models were developed to predict the evolution in melt $\delta^{51}V$ during crystallisation of the distinct mineral assemblages found in typical calc-alkaline and tholeiitic suites. Models are based on the observations of modal mineralogy in the Boggy Plain Zoned Pluton and Red Hill intrusion.

There was an attempt to model fractional crystallisation using the thermodynamic software Rhyolite-MELTS (Gualda et al., 2012; Ghiorso and Gualda, 2015). Theoretically, MELTS should be able to predict the crystallisation pathway of the anhydrous basaltic magma forming the Red Hill intrusion more accurately than for the hydrous magma forming the BPZP, given the limitations of calculating the phase stability of hydrous silicates using MELTS (Gualda et al., 2012; see discussion in Chapter 3 Appendix). However, there was no solution using realistic T, P and fO_2 input parameters (T ~ 1200°C; fO_2 ~ FMQ buffer; P~ 1-5kbars; Sossi, 2010; Sossi et al., 2012) where the modelled magma TiO_2, Fe_2O_3, and $Fe^{3+}/\Sigma Fe$ reproduced the Red Hill WR data. Since the timing of Fe-Ti oxide saturation is critical for modelling V isotopic variations, it was

decided that it was more representative to model the V isotopic evolution of the evolving melt using a Rayleigh approach.

Melt isotopic evolution is therefore modelled using Equation 5.3, where $\Delta^{51}V_{min\text{-}melt}$ is the bulk mineral-melt fractionation factor and *f*V is the fraction of V remaining.

$$\delta^{51}V = \delta^{51}V_{initial} + (\Delta^{51}V_{min\text{-}melt} \times \ln fV) \qquad [5.3]$$

Initial magma composition ($\delta^{51}V_{initial}$)

A value of $\delta^{51}V_{initial}$ = -1‰ was used as the initial melt composition. This is the isotopic composition of the Red Hill intrusion chilled margin (sample 65), and is a similar composition to other mantle derived basaltic magmas (e.g. Prytulak et al., 2013; Wu et al., 2018).

Estimating the fraction of V remaining (fV)

The V concentration of an evolving melt is modelled using Equation 5.4, where C and C_0 are the current and initial V concentration in the melt, D is the bulk partition coefficient of V between minerals and melt, and F is the melt fraction, which is varied in steps of 0.05. The D values were varied iteratively and values which best described the natural data were chosen.

$$C = C_0 \times F^{D-1} \qquad [5.4]$$

The change in V concentration in the BPZP can be modelled in a single step using an initial V concentration (C_0) of 149 µg/g and bulk D_{MgO} and D_V values of 2 and 1.8 respectively (Figure 5.13A).

In the Red Hill intrusion, V concentrations are initially highly scattered between 200 – 300 µg/g but show no obvious trend with decreasing MgO content. Below 1.5 wt.% MgO there is a sharp decrease in WR V to <50 µg/g (Figure 5.13B). Therefore, a two-stage model is required to reproduce the V concentration trend in the evolving magma. A value of 250 µg/g V was used for C_0, which is the average V concentration of the chilled margin and dolerite samples from Sossi (2010). Above 1.5 wt.% MgO, a bulk D_V value of 0.95

was used, and bulk D_V of 5 was used below 1.5 wt.% MgO. A bulk D_{MgO} value of 2 was used for both stages.

The fraction of V remaining (f(V)) in the melt is then calculated by Equation 5.5.

$$f(V) = (F \times C)/C_0 \qquad [5.5]$$

Deriving a bulk mineral-melt fractionation factor ($\Delta^{51}V_{min\text{-}melt}$)

The largest uncertainty for both models is choosing appropriate $\Delta^{51}V_{min\text{-}melt}$ values for the different mineral phases. This is because in comparison to other isotopic systems like Fe and Ti, there are a severe lack of empirical and theoretical $\Delta^{51}V_{min\text{-}melt}$ values for silicate and oxide minerals in the literature. The only mineral-melt fractionation factors determined thus far are from the experimental study of Sossi et al. (2018b), where $\Delta^{51}V_{mag\text{-}melt}$ values were calculated from experiments conducted in Ti-absent conditions at 800 °C, 0.5 GPa, and fO_2 buffered over the range FMQ–1 to FMQ+5. The relationship between $\Delta^{51}V_{mag\text{-}melt}$ and fO_2 at 800°C is given by Equation 5.6 (Sossi et al., 2018b).

$$\Delta^{51}V_{mag-melt} = -0.045(\Delta FMQ) - 0.70 \quad [5.6]$$

Expressed relative to the FMQ buffer (ΔFMQ), estimates of magma fO_2 in the BPZP and Red Hill intrusions range between approximately FMQ-1 to FMQ+1 (Wyborn, 1983; Sossi et al., 2012). Variation in fO_2 over two log units accounts for <0.1‰ change in $\Delta^{51}V_{mag\text{-}melt}$ (Equation 5.6; Sossi et al., 2018b). This is similar to typical analytical uncertainty for V isotope measurements, so for the purpose of this modelling the variation in $\Delta^{51}V_{min\text{-}melt}$ due to fO_2 is assumed to be negligible. For both systems, a ΔFMQ value of 0 (i.e. fO_2 equivalent to the FMQ buffer) is used in Equation 5.6.

In the BPZP, magnetite and hydrous silicates in the same samples have V isotopic compositions within error. Therefore, for this modelling it is assumed that $\Delta^{51}V_{mag\text{-}melt}$ and $\Delta^{51}V_{sil\text{-}melt}$ are equal, so $\Delta^{51}V_{mag\text{-}melt}$ calculated using Equation 5.6 can be used as the bulk $\Delta^{51}V_{min\text{-}melt}$ value in Equation 5.3. However, while this approximation stands for the BPZP, it may not be accurate for the Red Hill intrusion where no silicate and oxide pairs

in equilibrium have been measured. This approximation may need to be refined in the future as more $\Delta^{51}V_{min\text{-}melt}$ estimates for silicate phases become available.

Investigating the effect of temperature

The Red Hill intrusion and BPZP crystallised over different temperature ranges. Crystallisation temperatures in the Red Hill intrusion vary between approximately 1200 - 950°C (Sossi et al., 2012), whereas crystallisation temperatures are much lower, between around 900 – 700 °C, in the BPZP (Wyborn, 1983). Lower crystallisation temperatures are expected for H_2O saturated magmas like the BPZP (e.g. Sisson and Grove, 1993a).

We explore the effect of temperature on the magnitude of V isotope fractionation between magnetite and melt. Assuming a temperature dependence of $1/T^2$, we use Equation 5.6 to calculate $\Delta^{51}V_{mag\text{-}melt}$ values at 800°C and 1200°C, which gives $\Delta^{51}V_{mag\text{-}melt}$ values of -0.70‰ at 800°C and -0.31‰ at 1200°C (Figures 5.13C and D). This temperature range encompasses realistic crystallisation temperatures for most plutonic bodies.

Investigating the effect of oxide mineralogy/chemistry

While the experimentally derived $\Delta^{51}V_{mag\text{-}melt}$ values may be applicable to the Ti-poor magnetite in the Boggy Plain pluton, the Red Hill magnetite is extremely Ti rich (Table 5.1; Sossi, 2010; Sossi et al., 2012). Titanium substitution in magnetite occurs by the reaction $2Fe^{3+} = Fe^{2+} + Ti^{4+}$, although there is uncertainty over which crystallographic sites these substitutions occur on (e.g. Akimoto, 1954; Wechsler et al., 1984; Bosi et al., 2009). In addition, as magnetite Ti content increases, there is an increase in tetrahedral bond length and a slight decrease in octahedral bond lengths, causing distortion of the unit cell (Bosi et al., 2009). Variations in Ti content and bonding environment have previously been shown to affect Ti (Hoare et al., 2022) and Fe (Rabin et al., 2021) isotope fractionation between magnetite and melt. Since V^{3+} and V^{4+} can substitute for Fe^{3+} and Ti^{4+} in magnetite (Toplis and Corgne, 2002), Ti substitution may also affect the magnitude of $\Delta^{51}V_{mag\text{-}melt}$, although the exact change is difficult to quantify.

Ding et al. (2020) proposed that as Ti content increases, the magnitude of $\Delta^{51}V_{oxide\text{-}melt}$ decreases based on trends in WR lava samples from Anatahan volcano. Therefore, the

trend in magma $\delta^{51}V$ for the Red Hill intrusion calculated using the experimental magnetite-melt fractionation factors from Sossi et al. (2018b) is a maximum value (Figure 5.13D), and in reality, $\Delta^{51}V_{mag\text{-}melt}$ will be lower for titanomagnetite and ulvöspinel crystallisation.

Therefore, we also model magma $\delta^{51}V$ using bulk $\Delta^{51}V_{min\text{-}melt}$ values from other differentiation suites to evaluate the effect of variation in oxide compositions. Values of -0.45‰, which describes magnetite fractionation in the Hekla and Anatahan lavas (Prytulak et al., 2017), and -0.15‰ which describes coincident magnetite and ilmenite crystallisation at Kilauea Iki (Ding et al., 2020) are used. Rayleigh models of melt $\delta^{51}V$ using the different $\Delta^{51}V_{mag\text{-}melt}$ values are shown in Figures 5.13E and F.

Alternative Modelling of Melt Isotopic Composition

For comparison, melt $\delta^{51}V$ is also modelled using magnetite mineral separate data and $\Delta^{51}V_{mag\text{-}melt}$ values ($\delta^{51}V_{melt} = \delta^{51}V_{mag} + \Delta^{51}V_{mag\text{-}melt}$), as described in Chapter 4 Section 4.6.1 (Figure 5.13G and H). The assumption is made that all magnetite crystallised in equilibrium from the main magma body, which may not be true for the titanomagnetite in the most mafic samples from the Red Hill intrusion.

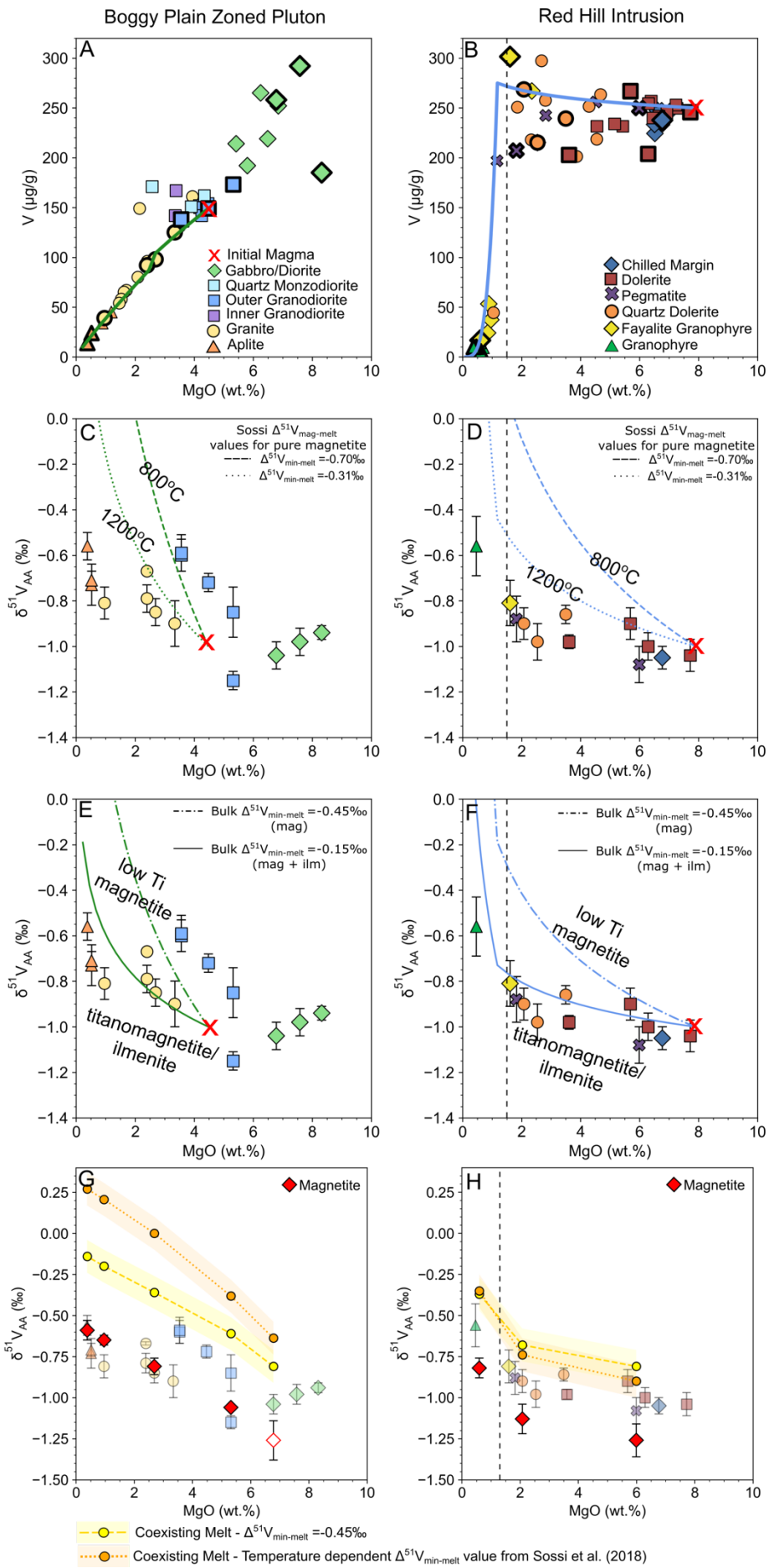
Boggy Plain Zoned Pluton
Red Hill Intrusion
A
B
C
D
E
F
G
H
V (µg/g)
MgO (wt.%)
Initial Magma
Gabbro/Diorite
Quartz Monzodiorite
Outer Granodiorite
Inner Granodiorite
Granite
Aplite
Chilled Margin
Dolerite
Pegmatite
Quartz Dolerite
Fayalite Granophyre
Granophyre
Sossi Δ51Vmag-melt values for pure magnetite
Δ51Vmin-melt =-0.70‰
Δ51Vmin-melt =-0.31‰
800°C
1200°C
δ51VAA (‰)
Bulk Δ51Vmin-melt =-0.45‰ (mag)
Bulk Δ51Vmin-melt =-0.15‰ (mag + ilm)
low Ti magnetite
titanomagnetite/ ilmenite
Magnetite
Coexisting Melt - Δ51Vmin-melt =-0.45‰
Coexisting Melt - Temperature dependent Δ51Vmin-melt value from Sossi et al. (2018)

Figure 5.13. Comparison of melt isotopic evolution in the Red Hill intrusion and Boggy Plain Zoned Pluton. Graphs A and B show Rayleigh models of melt V and MgO concentration. Graphs C to F show Rayleigh models of melt $\delta^{51}V$ variation using different bulk $\Delta^{51}V_{min\text{-}melt}$ values as described in the text. Graphs G and H show melt $\delta^{51}V$ calculated using magnetite mineral separate data as described in Chapter 4. WR MgO and V data for the BPZP is from Wyborn (1983). WR MgO and V data for the Red Hill intrusion is from Sossi (2010). Note that for the BPZP samples, sample BP41 with WR MgO of 11.37 wt.% is not shown due to the x-axis scale. The vertical dotted line shows the timing of titanomagnetite saturation in the Red Hill intrusion.

5.5.6 Discussion of model results

The aim of the modelling was to investigate the controls of mineralogy, timing of oxide saturation, and temperature on melt $\delta^{51}V$ evolution in calc-alkaline and tholeiitic magmas. The models demonstrate that changes in temperature and oxide mineralogy have a resolvable effect on melt $\delta^{51}V$. A larger overall increase in melt $\delta^{51}V$ is predicted at lower temperatures and lower magnetite Ti content (i.e. in the BPZP compared to the Red Hill intrusion). The timing of oxide saturation is also important, with the largest increases in $\delta^{51}V$ only occurring after Fe-Ti oxide saturation. This leads to distinct shaped trends in melt $\delta^{51}V$ evolution in the calc-alkaline and tholeiitic settings (Figure 5.13C to H)

It is then interesting that the Red Hill intrusion and BPZP show a remarkably similar magnitude of variation in WR $\delta^{51}V$ (symbols in Figure 5.13C and D) despite their different P-T-X-fO_2 conditions and crystallising assemblages. In both suites, WR $\delta^{51}V$ increases from approximately -1‰ to -0.6‰ during fractional crystallisation. While the Red Hill WR samples likely approximate the liquid line of descent of the evolving melt (Sossi et al., 2012), WR $\delta^{51}V$ in the BPZP is highly scattered and reflects variation in the modal abundance of mineral phases and trapped interstitial melt, rather than representing a true melt composition (Chapter 4). Therefore, it is probably coincidental that both suites show such similar WR $\delta^{51}V$, and this does not necessarily mean that melt $\delta^{51}V$ evolution is similar.

The models considered typical ranges in temperature that would be expected in natural igneous systems. Over this 400°C temperature range, $\Delta^{51}V_{mag\text{-}melt}$ values change by approximately 0.4‰ (Figure 5.13C and D). This difference is larger than the overall variation predicted due to changes in the composition of the fractionating Fe-Ti oxides (i.e. magnetite vs titanomagnetite vs ilmenite fractionation), which is around 0.3‰

(Figure 5.13E and F; Ding et al., 2020). Therefore, the total possible variation in the magnitude of $\Delta^{51}V_{min\text{-}melt}$ due to temperature is larger than the variations due to oxide mineralogy and composition. Although a logical step for future work would be to derive $\Delta^{51}V_{oxide\text{-}melt}$ fractionation factors for the different Fe-Ti oxide species and examine how these vary with composition, these fractionation factors alone are inadequate without accurate temperature estimates. This is especially important in high silica intrusions, such as those studied in this work, or magmatic-hydrothermal ore systems, where temperatures are lower (e.g. Hedenquist and Lowenstern, 1994) and thus fractionation factors will be larger (e.g. Urey, 1947; Schauble, 2004).

5.6 Complications and considerations for future work

The concept for this chapter was to compare two plutons which record relatively simple examples of calc-alkaline and tholeiitic magma differentiation in intrusive settings. This approach enabled exploration of the effect of contrasting mineralogy, chemistry and fO_2 conditions on V isotope fractionation in the two most common magmatic differentiation trends on Earth. The Red Hill intrusion was chosen specifically because $\delta^{56}Fe$ variation in WR powders and mineral separates (Sossi et al., 2012) were different from the trends observed in the Boggy Plain Zoned Pluton (Stow et al., 2022; Chapter 3). Therefore, it was likely that the two suites may also show contrasting V isotope behaviour.

The same approach which had proven successful for understanding Fe-V-Zn isotopic variations in the Boggy Plain Zoned Pluton (Chapters 3 and 4; Stow et al., 2022) was followed. Petrological examination of samples was combined with Fe-V-Zn isotopic analysis of mineral separates and WR powders. However, throughout this work it has become apparent that this may not have been the most appropriate approach for this system, and the specific chemistry and mineralogy of the Red Hill intrusion has presented a series of challenges.

1. Vanadium Concentration Trends

Above 1.5 wt.% MgO, WR V concentrations are scattered between 200 – 300 μg/g and show no obvious trend with WR MgO content. V concentrations then decrease sharply below 1.5 wt.% MgO following titanomagnetite saturation

(Figure 5.3). Therefore, the WR powders and mineral separates from samples with <1.5 wt.% MgO (i.e. the samples which record magnetite saturation) have extremely low V concentrations. For example, the pyroxene in sample 38, a typical granophyre, contains < 5 μg/g V (Sossi, 2010). Since at least 1 μg total V is required to make 3 isotopic measurements, this means that no pyroxenes could be feasibly analysed in the most felsic samples, and only one magnetite sample from sample 54 contained enough V for isotopic analysis. Mineral picking was also challenging in samples below 1.5 wt.% MgO because the granophyres are very fine grained (Figure 5.4).

2. Temperature Regimes

The Red Hill intrusion and BPZP have very different crystallisation temperatures. Estimates for the Red Hill intrusion are between approximately 950 – 1200°C (Sossi et al., 2012), whereas crystallisation temperatures for the BPZP are much lower, varying from approximately 700 – 900°C (Wyborn, 1983). Since the magnitude of isotopic fractionation between phases scales with $1/T^2$, this difference in temperature can account for significant differences in $\Delta^{51}V_{min\text{-}melt}$ before differences in mineral chemistry or fO_2 are even considered (see Figure 5.13).

3. Fe-Ti Oxides

Working with the Fe-Ti oxides is more complicated in the Red Hill intrusion than in the BPZP for several reasons. Firstly, the diorites contain both magnetite and ilmenite with anhedral morphologies (Figure 5.5) that have most likely crystallised from trapped interstitial melt. Theoretically, their crystallisation should not have affected the overall isotopic evolution of the main magma body. In these samples, it is difficult to tell whether magnetite and ilmenite are primary phases, or if they have formed through oxyexsolution processes, and oxides often appear altered. Therefore, magnetite separates were not picked from the most mafic samples.

It was also difficult to assess whether magnetite grains crystallised in isotopic equilibrium with the main magma body. In the BPZP, the occurrence of euhedral

grains was used as a criterion for assessing equilibrium crystallisation. However, although magnetite in samples 50 and 74 showed euhedral morphologies, Fe isotope data demonstrated that magnetite and pyroxene in these samples is not in isotopic equilibrium (section 5.5.3). It is likely that only the magnetite in samples with <1.5 wt.% MgO crystallised in equilibrium from the main magma body, because there is a decrease in WR V and TiO_2 concentrations at this point. Therefore, only magnetite separates in samples <1.5 wt.% MgO reflect V isotopic variations in the main magma body rather than pockets of trapped interstitial melt.

The magnetite in the Red Hill intrusion also shows extensive exsolution of ilmenite as blebs and lamellae (Figure 5.5), which can lead to uncertainties during sampling. The assumption in this work is that the isotopic composition of the hand-picked "bulk" magnetite fraction (magnetite plus ilmenite exsolution lamellae) is equivalent to the composition of magnetite at the time of crystallisation, before exsolution occurred. However, when samples are crushed and sieved before mineral picking, magnetite grains may be broken apart. When a magnet is used to separate magnetite from silicate minerals before handpicking, the magnetic fraction may potentially be biased towards fragments which contain less extensive ilmenite exsolution. Variation in the magnetite:ilmenite ratio would likely affect the Fe isotopic composition of the "bulk" magnetite separate (e.g. Dziony et al., 2014; Chen et al., 2014; Cao et al., 2019), and is also likely to affect V isotopic compositions (Ding et al., 2020).

The magnetite in the Red Hill intrusion also has a much higher Ti concentration than magnetite from the Boggy Plain Pluton (Table 5.1), which is likely to influence the magnitude of $\Delta^{51}V_{mag\text{-}melt}$, as discussed in Section 5.5.5. However, at this time the only magnetite-melt fractionation factors available for comparison were those determined in a Ti-free environment (Sossi et al., 2018b), which may not be appropriate for the Red Hill intrusion.

These complications raise several key considerations for future studies. Firstly, given the importance of Fe-Ti oxide fractionation in generating distinct trends in magma $\delta^{51}V$, the lack of empirically and experimentally determined oxide-melt fractionation factors at different T-X-fO_2 conditions is a major limitation for this work and future studies.

However, studying an intrusive system is not the most appropriate way to address this issue because of the lack of a coexisting melt phase to analyse to directly calculate $\Delta^{51}V_{min\text{-}melt}$ values. Isotopic analysis of coexisting Fe-Ti oxides and groundmass following the approach of Hoare et al. (2022) would be an effective method for obtaining a range of fractionation factors applicable to various magmatic conditions. Given the high partition coefficient of V in Fe-Ti oxides (e.g. Toplis and Corgne, 2002), oxides could potentially be sampled by micro-milling individual grains. It would also be informative to compare the difference in isotopic composition of milled Fe-Ti oxides and bulk separates to assess any bias due to sampling approaches.

However, variations in temperature exert a sizable influence on the magnitude of isotopic fractionation factors. Therefore, even if future studies derive fractionation factors for specific mineral phases and compositions, these have large uncertainties if they are not used in combination with accurate temperature estimates. A major problem in intrusive, coarse-grained rocks is the lack of appropriate geothermometers (e.g. Anderson et al., 2008). For this reason, it might be more beneficial to develop new mineral geothermometers for use in intrusive settings, which would allow fractionation factors for V (and other isotope systems) to be accurately used to investigate magmatic processes over a wider range of temperatures.

5.7 Conclusions

The aim of this chapter was to investigate the V isotopic composition of WR powders, magnetite and pyroxene mineral separates from the tholeiitic Red Hill intrusion, and compare trends to those in the calc-alkaline Boggy Plain Zoned Pluton, presented in Chapter 4. A multi-isotope approach (Fe, Zn, Sr, Nd) was used to assess secondary processes beyond closed system fractional crystallisation of a tholeiitic magma.

1. In the Red Hill intrusion, WR isotopic compositions approximate the liquid line of descent of an evolving melt. WR $\delta^{51}V$ increases from -1.05 ± 0.05‰ (2SD) to -0.56 ± 0.13‰ (2SD) during magmatic differentiation. Titanomagnetite and pyroxene mineral separates show increases in $\delta^{51}V$ during differentiation which mirror the WR trend.

2. The initial increase in WR $\delta^{51}V$ is driven by crystallisation of isotopically light pyroxene, followed by a sharp increase in WR $\delta^{51}V$ below 1.5 wt.% MgO, upon saturation of Ti-rich magnetite as a primocryst phase.
3. Rayleigh models demonstrate that calc-alkaline and tholeiitic differentiation sequences should display distinct trends in melt $\delta^{51}V$ due to variation in the timing of Fe-Ti oxide saturation and Fe-Ti oxide composition. However, the BPZP and Red Hill samples show similar ranges in WR $\delta^{51}V$ despite their disparate temperatures and fractionating assemblages. This most likely is because WR $\delta^{51}V$ in the BPZP does not represent a true melt composition, which highlights the uncertainties with a WR approach in intrusive settings.
4. The Rayleigh models show that variation in temperature can exert as large an influence on $\Delta^{51}V_{mag\text{-}melt}$ as changes in Fe-Ti oxide composition. This highlights the requirement for both composition specific mineral-melt fractionation factors and accurate temperature estimates for future work on more complex intrusive systems.

Chapter 6: Synthesis and Future Work

6.1 Synthesis and Conclusions

Within this thesis, the behaviours of transition metal stable isotopes in intrusive settings were investigated, using an integrated approach combining isotopic analysis (Fe, V and Zn) of mineral separates and whole rock powders and petrographic examination of samples. Two plutonic bodies were investigated, the calc-alkaline Boggy Plain Zoned Pluton, Australia (Wyborn, 1983) and the tholeiitic Red Hill intrusion, Tasmania (McDougall, 1962). The aims of the study were to:

1. Identify the main cause(s), magnitudes and directions of Fe, V and Zn isotope fractionation in intrusive settings.
2. Determine the effect of varying mineralogy, magma chemistry, fO_2 and temperature on Fe, V and Zn isotope fractionation. Assess the potential for Fe, V and Zn isotopes to be used as proxies for physical parameters or conditions during magmatic differentiation.
3. Develop methods for modelling isotopic variations in intrusive samples, based on the petrological understanding obtained from examination of crystal textures.
4. Extrapolate the findings from plutonic bodies to broader implications for the isotopic composition of the continental crust, and sediments eroded from it, over larger spatial and temporal scales.

Here, the main findings are summarised, and illustrated in Figure 6.1.

6.1.1 Advances in understanding the controls on Fe, V and Zn isotope fractionation in intrusive settings

Throughout Chapters 3, 4 and 5, the factors controlling the cause(s), magnitudes and directions of Fe, V and Zn isotope fractionation in intrusive settings were explored in two settings with contrasting mineralogy, magma chemistry, fO_2 and temperature. Advances in our understanding of the behaviour of each isotope system are summarised below.

Iron

As discussed in the Introduction (Chapter 1), Fe isotopes are currently the most extensively studied of all the transition metal isotope systems. At the start of this study, it was clear that during magmatic differentiation, the Fe isotopic composition of an evolving magma can be influenced by multiple processes including, but not limited to, fractional crystallisation, crustal contamination and fluid exsolution (e.g. see review in Dauphas et al., 2017). However, our understanding of the dominant controls on Fe isotope fractionation in intrusive settings was still incomplete. This was mainly due to limitations with the approaches previous studies have adopted when investigating intrusive settings. Firstly, studies often analysed the isotopic composition of whole rock powders without due consideration of petrological context (e.g. Poitrasson and Freydier, 2005; Heimann et al., 2008; Telus et al., 2012; Foden et al., 2015; Gajos et al., 2016; He et al., 2017; Wu et al., 2017; Wu et al., 2018). In addition, there were a lack of studies analysing the Fe isotopic composition of mineral separates in granitic intrusive rocks, with the majority of studies to date having measured mineral separates from individual, genetically unrelated intrusions (e.g. Heimann et al., 2008; Telus et al., 2012; Wu et al., 2017), which made it difficult to distinguish the exact controls of mineral-melt fractionation on isotopic trends.

The investigation of the BPZP in Chapter 3 (Stow et al., 2022) was the first study of the Fe isotopic composition of WR powders and mineral separates from a closed system calc-alkaline suite, which permitted a detailed examination on the controls of Fe isotope fractionation in intrusive settings. In this chapter, it was demonstrated that the overall trend in increasing WR δ^{56}Fe during differentiation was driven by fractional crystallisation, specifically the balance between crystallisation of isotopically heavy magnetite and isotopically light biotite and hornblende. This contrasts with the tholeiitic Red Hill intrusion where crystallisation of isotopically light pyroxene initially caused an increase in melt δ^{56}Fe, and then later crystallisation of isotopically heavy titanomagnetite led to a decrease in melt δ^{56}Fe (Sossi et al., 2012; Chapter 5). Therefore, fractional crystallisation of different mineral assemblages can cause distinct δ^{56}Fe variations in intrusive settings. The lack of correlation between WR Fe and Zn isotopic compositions in either extrusive suite demonstrated that Fe isotopes were not fractionated by late-stage fluid exsolution.

In Chapter 3, the first temperature dependent mineral-melt fractionation factors for magnetite, biotite and hornblende at relevant conditions for calc-alkaline differentiation trends were derived, which will be useful for future modelling. The approach in Chapter 3 also allowed investigation of equilibrium inter-mineral Fe isotope fractionation factors between different minerals in the BPZP. The order of heavy Fe isotope enrichment in the different minerals agrees with theoretical considerations of bonding environment and valence state, with the heaviest Fe isotopic compositions measured in magnetite which contains IV-fold and VI-fold coordinated Fe^{3+}. One key finding was that inter-mineral equilibrium Fe isotope fractionation, between biotite and magnetite ($\Delta^{56}Fe_{mag\text{-}bt}$) for example, is overwhelmingly influenced by variations in temperature. The $\Delta^{56}Fe_{mag\text{-}bt}$ values in the BPZP agree with both $\Delta^{56}Fe_{mag\text{-}bt}$ values calculated from theoretical studies (DFT calculations and NRIXS measurements), and values measured in a metamorphosed ironstone at different P-T-X-fO_2 conditions (Ye et al., 2020). This strong temperature dependence on equilibrium Fe isotope fractionation means that accurate temperature estimates are vital when modelling Fe isotopes in intrusive systems, and in investigating more complex systems such as ore-bearing intrusive rocks and large mushes.

Zinc

Previous work on extrusive lavas has demonstrated that fractional crystallisation alone causes negligible (<0.1‰) Zn isotopic fractionation (e.g. Chen et al., 2013). The studies of the BPZP and Red Hill intrusion in Chapters 3 and 5 were the first investigations of the Zn isotopic composition of WR powders and mineral separates from closed system intrusive plutons. There was no resolvable variation in $\delta^{66}Zn$ in the WR powders from either the BPZP (Chapter 3) or the Red Hill intrusion (Chapter 5), which confirmed that fractional crystallisation causes negligible Zn isotopic fractionation in intrusive settings. The aplite samples and their biotite separates from the BPZP had heavy Zn isotopic compositions, alongside petrographic evidence for the presence of Cl-rich fluids. This supports previous interpretations that isotopically light Zn binds to Cl ligands in magmatic fluids (e.g. Fujii et al., 2014), and exsolution of isotopically light Zn bearing fluids causes the heavy $\delta^{66}Zn$ values in some evolved rhyolites, granites and pegmatites (e.g. Telus et al., 2012; Xia et al., 2017). Such a finding may be useful to explore in the context of hydrothermal mineralisation in granitic systems.

Primocryst magnetite, biotite and hornblende mineral separates from the BPZP all had identical Zn isotopic compositions in individual samples, and showed no variation in isotopic composition during differentiation (Chapter 3). This lack of inter-mineral isotopic fractionation was not surprising since it is assumed that all phases host VI-fold coordinated Zn^{2+} (e.g. Shannon, 1976). From these findings, it was thought that the pyroxene and titanomagnetite mineral separates from the Red Hill intrusion (Chapter 5) would also have identical Zn isotopic compositions. However, pyroxene and titanomagnetite both showed extremely variable $\delta^{66}Zn$ across the Red Hill differentiation sequence, and there was approximately a 0.2‰ difference between titanomagnetite and pyroxene separates from the same sample. It is unclear if this variation was due to Zn^{2+} existing in different coordination in these minerals. For example, there is the potential for Zn^{2+} to be found in IV-fold coordination in titanomagnetite, and in distorted VI to VII-fold M2 sites in clinopyroxene (Cameron and Papike, 1981; Yang et al., 2021; see Chapter 1, Table 1.1). Alternatively, isotopic compositions could have been affected by diffusive re-equilibration of titanomagnetite grains (Sievwright et al., 2020), or by the presence of sulphide minerals with extremely variable $\delta^{66}Zn$ (e.g. Mason et al., 2005; John et al., 2008). This highlights that WR analysis alone can mask the complexities of the Zn isotope system, and a mineral separate approach permits a more detailed examination of the drivers of Zn isotope fractionation in intrusive settings.

Vanadium

Chapters 4 and 5 were the first investigations of the V isotopic composition of WR powders and mineral separates in intrusive igneous rocks. To date, studies of extrusive lavas have emphasised the importance of fractional crystallisation of isotopically light Fe-Ti oxide minerals in causing the increase in magma $\delta^{51}V$ during differentiation (e.g. Prytulak et al., 2017; Ding et al., 2020). However, the BPZP study in Chapter 4 demonstrated that the fractional crystallisation of the silicate phases biotite and hornblende can also cause significant V isotope fractionation. Although silicate phases contain lower concentrations of V compared to Fe-Ti oxides (e.g. Toplis and Corgne, 2002), silicate minerals are typically present in higher modal abundances, so can host considerable amounts of V in the system. In the BPZP, magnetite, biotite and hornblende mineral separates have analytically indistinguishable V isotopic compositions in individual samples (Chapter 4). This is most likely because all phases predominantly host

V^{3+} in VI-fold coordination (e.g. Toplis and Corgne, 2002; Shannon, 1976). Therefore, both Fe-Ti oxides and silicate phases should be isotopically lighter than the coexisting melt where V is present at higher oxidation state and lower coordination (e.g. Giuli et al., 2004; Sutton et al., 2005), and thus the combined fractional crystallisation of silicate and Fe-Ti oxide phases drives the increase in melt $\delta^{51}V$ during differentiation. This is the case in both the BPZP (magnetite, biotite and hornblende fractionation) and the Red Hill intrusion (pyroxene and titanomagnetite fractionation).

This work also explored two hypotheses from previous studies. Firstly, it has been proposed that the timing of Fe-Ti oxide saturation and the specific mineralogy of Fe-Ti oxides causes the variation in $\delta^{51}V$ between different cogenetic lava suites (Ding et al., 2020). Secondly, an experimental study has demonstrated that the magnitude of V isotope fractionation between magnetite and melt varies with magma fO_2 (Sossi et al., 2018b). However, these influences of fO_2 and mineral chemistry were yet to be explored in natural Fe-Ti oxide mineral separates.

In this work, we attempted to investigate the above hypotheses by studying two intrusive suites with contrasting fO_2 conditions, and thus contrasting crystallising assemblages and Fe-Ti oxide mineralogy. In terms of the influence of fO_2 on V isotope fractionation factors, there is approximately a 1-2 log unit difference in fO_2 between the BPZP and Red Hill magmas, and a similar variation within the entire BPZP pluton. According to the experimental results of Sossi et al. (2018b), such small fO_2 variations have a negligible influence on the magnitude of $\Delta^{51}V_{mag\text{-}melt}$ (<0.1‰ over 2 log units) and therefore there was no directly resolvable fO_2 control on $\delta^{51}V$ trends in these intrusions.

However, magma fO_2 fundamentally influences the crystallising assemblage, including the composition, abundance and timing of Fe-Ti oxide mineralisation (e.g. Sisson and Grove, 1993a; Toplis and Carroll, 1995). In Chapter 5, we used Rayleigh models to demonstrate that typical calc-alkaline and tholeiitic magmas will show distinct trends in $\delta^{51}V$. In tholeiitic suites, low fO_2 and H_2O cause early Fe enrichment and delay titanomagnetite saturation (e.g. Toplis and Carroll, 1995), and large increases in melt $\delta^{51}V$ only occur after titanomagnetite saturation. In comparison, early saturation of titanomagnetite in calc-alkaline magmas (e.g. Sisson and Grove, 1993a) leads to larger increases in melt $\delta^{51}V$ earlier in the crystallisation sequence. However, it proved challenging to directly compare model observations with isotope data from the BPZP and

Red Hill intrusions, given both the textural complexities of intrusive samples and the difference in temperature regime between the two suites (i.e. 700-900°C in the BPZP compared to 950 -1200°C in the Red Hill intrusion; Wyborn, 1983; Sossi et al., 2012).

In addition, although the Red Hill titanomagnetite (Chapter 5) has a much higher Ti concentration than the BPZP magnetite (Chapter 4), it was difficult to assess the effect of variation in Fe-Ti oxide chemistry on V isotopic trends in this work. This is because in intrusive settings there is no melt phase which can be analysed to directly calculate $\Delta^{51}V_{oxide\text{-}melt}$ values. Therefore, quantitative determinations of $\Delta^{51}V_{oxide\text{-}melt}$ for magnetite, Ti-rich ulvöspinel, and ilmenite are required for future work, as discussed in Section 6.2.

Overall conclusions

This work has demonstrated that the isotopic fractionation of V and Fe, two redox sensitive elements, is dominantly controlled by variations in bonding environment and temperature, rather than variations in valence state. This highlights that these redox sensitive isotopes are not direct tracers of magma fO_2 variations in magmatic settings, and the variation in $\delta^{51}V$ and $\delta^{56}Fe$ between different suites is largely down to the specific mineral assemblage, which is controlled by fO_2, and the temperature.

6.1.2 Complications with investigating isotopic variations in intrusive settings

To date, there are fewer studies on the behaviour of transition metal stable isotopes in intrusive plutons compared to extrusive lavas. Therefore, an aim of this thesis was to specifically investigate Fe, V and Zn isotopes in the plutonic rocks which make up large proportions of the continental crust. For studies of extrusive lavas, it is typical to analyse the isotopic composition of whole rock (WR) powders, and assume that WR isotopic compositions are equivalent to the liquid line of descent of an evolving magma (e.g. Schuessler et al., 2009; Chen et al., 2013; Prytulak et al., 2017; Xia et al., 2017; Ruttor et al., 2022). This approach has been commonly adopted in intrusive settings (e.g. Poitrasson and Freydier, 2005; Heimann et al., 2008; Sossi et al., 2012; Telus et al., 2012; Foden et al., 2015; Gajos et al., 2016; He et al., 2017; Wu et al., 2017; Wu et al., 2018). However, throughout this work, several key observations highlight specific issues which must be considered when interpreting and modelling isotopic data from intrusive settings.

Textural Considerations

Whole rock samples from intrusive settings are texturally complex. In the Boggy Plain Zoned Pluton (Chapters 3 and 4), WR samples are coarse grained and show decimetre scale modal layering. Samples are composed of euhedral primocrysts, which are thought to crystallise from the main magma body, and interstitial phases which are thought to crystallise from trapped interstitial melt. In the BPZP, WR V isotopic compositions are highly scattered (Chapter 4), which is thought to be due to variation in the modal abundances of mineral phases and/or trapped interstitial melt. Therefore, in the BPZP, WR isotopic composition is not equivalent to the composition of the evolving melt. However, WR isotopic trends in the Red Hill intrusion (Chapter 5) do appear to approximate the liquid line of descent of a crystallising magma, as suggested by Sossi et al. (2012). This distinction may reflect differences in the sizes and cooling timescales of the two intrusions, and also in mush structure (i.e. is efficient crystal-melt segregation occurring or is crystallisation occurring in-situ in a static environment; Holness et al., 2019). The Red Hill intrusion is a 1.6km wide, 300m thick vertical dyke extending from a flat underlying 400m thick sheet of doleritic magma (McDougall, 1962). However, the BPZP is a much larger intrusion, currently exposed over an area of 36km^2 (Wyborn, 1983). Therefore, cooling and crystallisation timescales are much longer in the BPZP, permitting formation of a long-lived crystal-rich, static mush. Therefore, whether a WR composition can be used as an approximation for melt composition in an intrusive setting must be considered in individual studies, and probably depends in part on the size of the intrusion and cooling timescales.

Textural considerations are also important for accurate modelling of isotopic variations in intrusive settings. Models typically require the modal abundances of fractionating mineral phases. However, it is important to assess whether phases are present as primocrysts, or as interstitial phases crystallised from trapped pockets of interstitial melt, because only crystallisation of primocryst phases is thought to influence the overall isotopic evolution of the residual melt (Chapter 3). In addition, when interpreting inter-mineral fractionation factors, it is important to consider that phases crystallising from trapped interstitial melt may not be in isotopic equilibrium with the main magma body, or with other minerals (Chapter 3).

The BPZP and Red Hill intrusion are also relatively simple, approximately closed system plutonic bodies. However, magma storage can also occur in open-system, mush-dominated, transcrustal magmatic systems (e.g. Cashman et al., 2017). In these types of system, processes such as additions of new batches of magma, mixing, assimilation, mush remobilization and reactive melt flow may be important (e.g. Cashman et al., 2017; Sparks et al., 2019; Weinberg et al., 2021). Therefore, further petrological observations, for example chemical mapping of samples, will be vital for interpreting the processes which have occurred within mushes prior to solidification that may influence isotopic trends.

Temperature Considerations

Unlike extrusive lavas, which undergo rapid cooling and crystallisation upon eruption, plutonic bodies exist at high temperatures over long periods of time and crystallise slowly. Crystallisation temperatures can be highly variable across a single pluton, for example the solidus-liquidus interval spans several hundred degrees in the BPZP (Wyborn, 1983). Thus, it is vital to use temperature dependent fractionation factors when modelling isotopic trends in intrusive settings, as demonstrated for Fe and V isotopes in this work.

Plutonic bodies also exist for substantial periods at subsolidus temperatures, and there is the potential for subsolidus re-equilibration of mineral phases. For example, low temperature re-equilibration of Fe-Ti oxides is common. Oxyexsolution of titanomagnetite leads to exsolution of ilmenite, and the extent and length scale of exsolution observed will depend on temperature, cooling rate and fO_2 as well as the initial TiO_2 content of the titanomagnetite (e.g. Buddington and Lindsley, 1964; Frost and Lindsley, 1991). In the BPZP, most Fe-Ti oxide grains only showed minor trellis exsolution lamellae of ilmenite (Chapters 3 and 4), typical of low temperature felsic plutonic rocks with low TiO_2 contents (e.g. Frost and Lindsley, 1991). However, exsolution was much more extensive in titanomagnetite from the Red Hill intrusion, which crystallised at higher temperature and was originally richer in TiO_2 (Chapter 5). Exsolved granules, sandwich and trellis exsolution of ilmenite are observed in all samples. Iron isotope fractionation has been documented during low temperature Fe-Ti oxide re-equilibration (e.g. Dziony et al., 2014; Chen et al., 2014; Cao et al., 2019). Therefore, subsolidus processes which may alter the isotopic composition of mineral separates must be considered when analysing mineral separates from plutonic suites.

Future Best Practice

A multitude of complex petrological processes can occur in intrusive systems before they solidify (e.g. fractional crystallisation, fluid exsolution, magma addition, crustal contamination, reactive flow; Cashman et al., 2017; Sparks et al., 2019; Weinberg et al., 2021), which results in texturally complex samples. Therefore, it is inappropriate to investigate intrusive systems in the same way as extrusive lavas by analysing WR powders alone. It is crucial to undertake detailed (e.g. thin section) examination of samples to assess petrological complexities and give isotopic data the necessary context they require for interpretation. The analysis of mineral separates is also necessary to explore the specific controls of mineral-mineral and mineral-melt isotopic fractionation.

It is also useful to analyse multiple isotope systems which can be fractionated by different processes. In this work, Fe, V, Zn, Sr and Nd isotopes were measured on the same samples, which allowed us to assess whether processes such as fluid exsolution, crustal assimilation or diffusion have influenced isotopic compositions. It is also beneficial to design column chemistry procedures so that all isotopes of interest can be obtained from the same sample digestion, because this limits uncertainty arising from sample scale modal heterogeneity.

6.1.3 Implications for the composition of the continental crust

Knowledge of Fe, V and Zn isotopes in two relatively simple plutons can be extrapolated to yield insight into the isotopic composition of the continental crust, which is assembled largely of plutonic complexes, and isotopic mass balance between different geological reservoirs. Chapters 3, 4 and 5 demonstrate the ranges in δ^{56}Fe, δ^{51}V and δ^{66}Zn in WR samples and mineral separates anticipated in typical calc-alkaline and tholeiitic plutons which have undergone fractional crystallisation.

For Fe and Zn, WR samples typically show ~0.2‰ range in isotopic composition within the individual intrusions (Chapters 3 and 5). The majority of mafic to felsic crustal igneous rocks have δ^{66}Zn and δ^{56}Fe within this 0.2‰ range (see Figures 1.2 and 1.3), with the exception of some highly silicic samples which have been affected by late-stage fluids

(e.g. Telus et al., 2012). Silicate and oxide minerals which crystallised in equilibrium have identical $\delta^{66}Zn$ values within error of WR $\delta^{66}Zn$ (Chapter 3), whereas Fe-Ti oxides have heavier Fe isotopic composition than coexisting silicate phases by ~0.2‰ (Chapter 3, Chapter 5).

In contrast, there are much larger ranges in V isotopic compositions in the BPZP and Red Hill intrusion, with variations of >0.6‰ measured in both the WR samples and mineral separates (Chapters 3 and 5). Larger variations in WR $\delta^{51}V$ of up to 2‰ have previously been observed in lavas (Prytulak et al., 2017) and at present it is unknown if other intrusive suites may also show such extreme ranges. Silicate and oxide minerals show identical $\delta^{51}V$ in individual samples at equilibrium, but $\delta^{51}V$ values can be highly variable for interstitial phases.

When crustal rocks are eroded to form clastic sediments, the average isotopic composition of the sediments will depend on the isotopic composition of the different mineral phases, and whether certain phases are preferentially eroded, altered or sorted during transport and deposition (e.g. Klaver at al., 2021). It has become popular to analyse the isotopic composition of clastic sediments such as wind-blown loess or glacial diamictites which, in theory, average the temporal variations in the isotopic composition of the continental crust over time, and relate changing isotopic signatures to global scale geological processes (e.g. Greber et al., 2017; Greaney et al., 2020; Klaver et al., 2021; Tian et al., 2021). The studies of the BPZP and Red Hill intrusion in this work demonstrated that there is a relatively restricted range in Fe isotopic composition of ~0.2‰ in typical upper crustal igneous rocks. This is reflected in loess samples from the Chinese Loess Plateau, which also show a restricted range in $\delta^{56}Fe$ between 0.06‰ and 0.12‰, and an average value of $\delta^{56}Fe$ of 0.09 ± 0.03‰ (2SD, n=32) for the upper continental crust (Gong et al., 2017).

However, the Red Hill intrusion and BPZP demonstrate that in the upper crust there can be large variations in $\delta^{51}V$ over small geographical areas that are generated internally without the need for external influences that might be invoked during large scale geologic processes. Therefore, although an average V isotopic composition of the continental crust can be inferred via analysis of clastic sedimentary deposits such as diamictites and loess, it will have an inherently large absolute range of variation, which may be further enhanced due to the preferential erosion of certain less resistant mineral phases. This is problematic

when attempting to determine if the V isotopic composition of the continental crust has changed over time, because the signal expected from processes such as the onset of plate tectonics (and therefore subduction) may be muted by the sheer range of small-scale natural variation in the isotope system.

Furthermore, material eroded from the continents is the major source of V to the oceans (e.g. Shiller and Mao, 2000; Schuth et al., 2019) and thus influences the V isotopic composition of the oceans over time (Schuth et al., 2019; Wu et al., 2019). It is very tempting to use an isotope system such as V to examine secular changes in ocean redox, as has been done for Mo (e.g. Arnold et al., 2004; Kendall et al., 2017 and references therein), Cr (e.g. Frei et al., 2009; 2011) and U (e.g. Montoya-Pino et al., 2010; Brennecka et al., 2011) for example, and a few studies have begun to explore this application via V isotopes (e.g. Nielsen, 2020; Wu et al., 2020; Fan et al., 2021). Clear challenges remain with estimating temporal variations in the V isotopic composition of the continental crust, the material eroded from it, and oceanic sediments such as black shales. Overall, accounting for the small-scale heterogeneous character of the continental crust, and the further heterogeneity likely introduced via preferential weathering of certain phases, remains a major obstacle to overcome in developing V isotope palaeoredox applications.

6.2 Future Work

6.2.1 Determining accurate mineral-melt fractionation factors

Throughout this work, it became apparent that a major current limitation in using transition metal stable isotopes to investigate magmatic processes is the lack of appropriate mineral-melt fractionation factors at relevant P-T-X-fO_2 conditions. This is especially true for V isotopes, because at present only $\Delta^{51}V_{mag\text{-}melt}$ values in a Ti-free environment have been determined (Sossi et al., 2018b). Therefore, it would be advantageous for future studies to determine new mineral-melt fractionation factors, either through partitioning experiments (e.g. Sossi et al., 2018b) or analysis of mineral separates and coexisting melt phases in natural samples (e.g. Hoare et al., 2022). In the case of V, given the major control of Fe-Ti oxide fractionation on V isotopic trends (Chapter 4 and 5), determining specific mineral-melt fractionation factors for magnetite, titanomagnetite and ilmenite is crucial for further work.

However, appropriate use of mineral-melt fractionation factors requires accurate temperature estimates. This is especially true in intrusive settings, where crystallisation temperatures can vary over hundreds of degrees within individual plutons (e.g. Wyborn, 1983), and in magmatic-hydrothermal ore systems where minerals can crystallise from fluids at temperatures as low as a few hundred degrees (e.g. Hedenquist and Lowenstern, 1994; Bodnar et al., 2014). Therefore, future work should also focus on establishing new mineral geothermometers which can be used in coarse grained samples where no coexisting melt phase is present.

6.2.2 Future investigations in intrusive settings

This thesis examined Fe, V and Zn isotope fractionation in two relatively simple, approximately closed system intrusive suites, with the hope of eventually using transition metal stable isotopes to understand the physical conditions and processes in more complex intrusive settings. Some examples which could be investigated in future work include:

- Larger felsic mush bodies: While the BPZP and Red Hill intrusion are both isolated, shallow level plutons, magma storage can occur in spatially extensive mush systems where petrogenetic processes are thought to be more complex (e.g. Cashman et al., 2017). Knowledge of the magnitude and direction of equilibrium isotopic fractionation between minerals and melt from this work could be used as a foundation to investigate whether fractional crystallisation does drive differentiation in these settings, or if disequilibrium processes such as reactive porous flow, diffusion, and magma injections (e.g. Cashman et al., 2017; Weinberg et al., 2021) are more important for generating geochemical trends. Relatively well-understood large-scale intrusions which could be investigated include the large granitic intrusions of the Western USA (e.g. Sierra Nevada and Peninsular Ranges batholiths; Silver and Chappell, 1988).
- Mafic Layered Intrusions: To date, there has been no examination of V isotopes in mafic plutonic rocks. Titanomagnetite in mafic intrusions can host considerable amounts of V, therefore there is the potential for extreme trends in $\delta^{51}V$ following titanomagnetite fractionation in these systems. Inter-mineral isotopic disequilibrium (e.g. Chen et al., 2014) may also lead to extremely variable $\delta^{51}V$

in mineral separates and WR samples. Layered mafic intrusions where Fe isotopic variations have previously been studied could be ideal suites to investigate (e.g. Bushveld Intrusion, Bilenker et al., 2017; Baima Intrusion, Chen et al., 2014; Windimurra Complex, Nebel et al., 2020).

- Ore-related granites: The BPZP and Red Hill intrusion are both barren felsic intrusions. A next step could be to investigate hydrothermal ore deposits related to granitic magmatism, for example porphyry deposits. Although there have been numerous studies using Fe isotopes to investigate the mineralization of porphyry deposits (e.g. Wawryk and Foden, 2017; He et al., 2020), an uncertainty in these studies is that Fe isotopes are fractionated by multiple processes, as discussed in this work. Therefore, a detailed study such as that conducted for the BPZP and Red Hill intrusions, combining analysis of several isotope systems with textural observations, may provide better understanding of the links between magmatic conditions in the intrusion (magma fO_2, temperature, mineralogy), fluid exsolution, and the concentration of critical metals in these deposits.

6.2.3 New approaches for modelling isotopic trends

In this work, and in most isotopic studies to date, isotopic variations during fractional crystallisation are modelled by Rayleigh equations. However, a Rayleigh approach assumes perfect fractional crystallisation (i.e. crystallisation and immediate separation of minerals and residual melt), which is not completely appropriate in intrusive mushes. Additionally, it is difficult to consider complexities such as additions of new batches of magma, melt migration and reactive porous flow. New mathematical approaches are necessary for representative modelling of isotopic variations in intrusive settings. The next step is the development of models which can integrate the physical processes occurring in magmatic reservoirs (e.g. Bergantz et al., 2015; Jackson et al., 2018; Cheng et al., 2020) with geochemical variations in the melt.

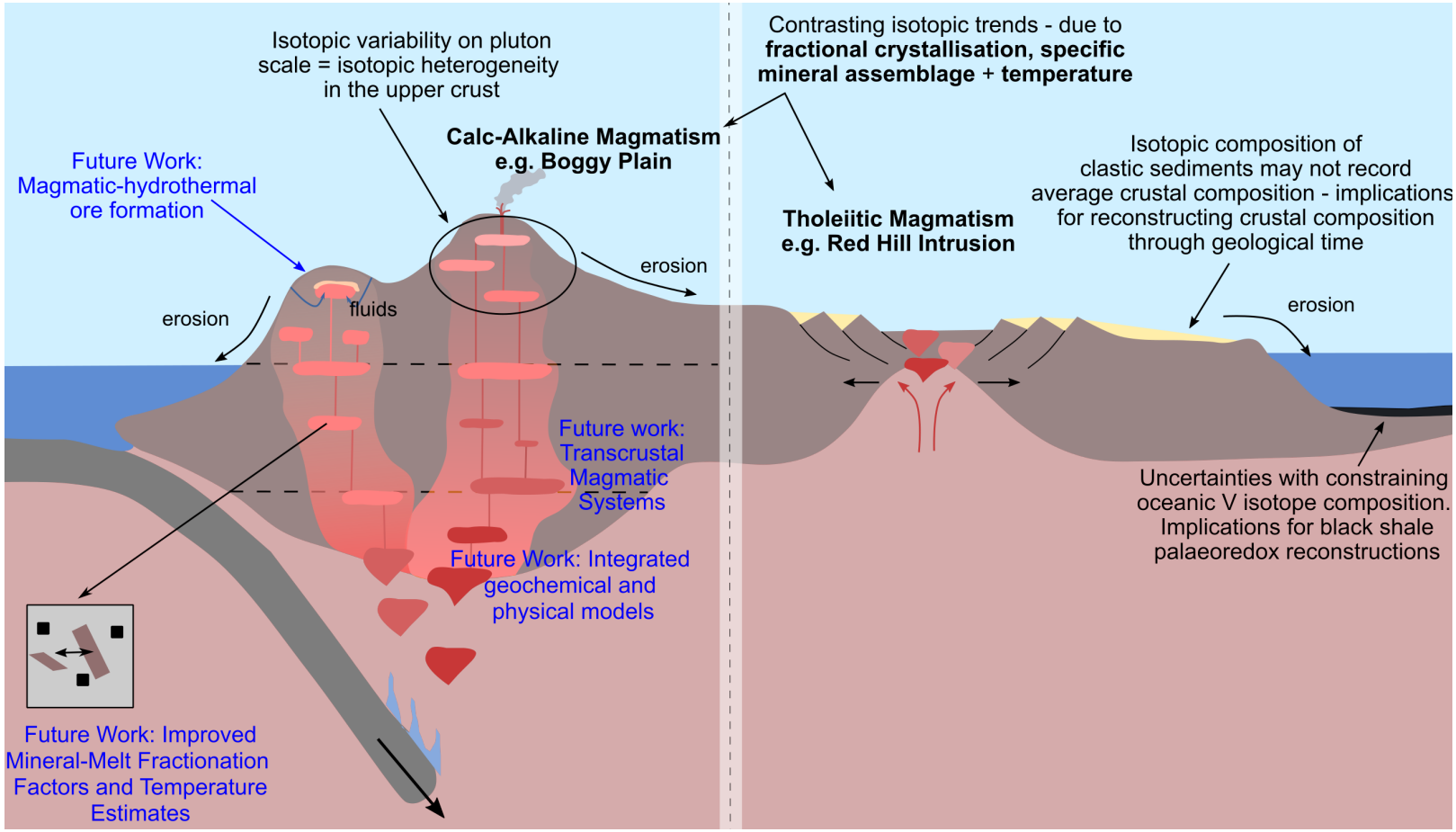

Figure 6.1. Summary diagram of concepts discussed in this thesis and ideas for future work.

References

Akimoto S. (1954) Thermo-Magnetic Study of Ferromagnetic Minerals Contained in Igneous Rocks. *J. Geomagn. Geoelectr.* **6**, 1-14.

Albarède F., Telouk P., Blichert-Toft J., Boyet M., Agranier A. and Nelson B. (2004) Precise and accurate isotopic measurements using multiple-collector ICPMS. *Geochim. Cosmochim. Acta* **68**, 2725–2744.

Anbar A. D., Roe J. E., Barling J. and Nealson K. H. (2000) Nonbiological Fractionation of Iron Isotopes. *Science* **288**, 126–128.

Anderson J. L., Barth A. P., Wooden J. L. and Mazdab F. (2008) Thermometers and thermobarometers in granitic systems. *Rev. Mineral. Geochemistry* **69**, 121–142.

Arató R. and Audétat A. (2017) Experimental calibration of a new oxybarometer for silicic magmas based on vanadium partitioning between magnetite and silicate melt. *Geochim. Cosmochim. Acta* **209**, 284–295.

Araújo D. F., Machado W., Weiss D., Mulholland D. S., Garnier J., Souto-Oliveira C. E. and Babinski M. (2018) Zinc isotopes as tracers of anthropogenic sources and biogeochemical processes in contaminated mangroves. *Appl. Geochemistry* **95**, 25–32.

Archer C. and Vance D. (2004) Mass discrimination correction in multiple-collector plasma source mass spectrometry: An example using Cu and Zn isotopes. *J. Anal. At. Spectrom.* **19**, 656–665.

Archer C., Andersen M. B., Cloquet C., Conway T. M., Dong S., Ellwood M., Moore R., Nelson J., Rehkämper M., Rehkämper R., Rouxel O., Samanta M., Shin K.-C., Sohrin Y., Takano S. and Wasylenki L. (2017) Inter-calibration of a proposed new primary reference standard AA-ETH Zn for zinc isotopic analysis. *J. Anal. At. Spectrom.* **32**, 415–419.

Arnold G. L., Anbar A. D., Barling J. and Lyons T. W. (2004) Molybdenum Isotope Evidence for Widespread Anoxia in Mid-Proterozoic Oceans. *Science* **304**, 87–90.

Arnold T., Schönbächler M., Rehkämper M., Dong S., Zhao J., Kirk G. J. D., Coles B. J. and Weiss D. J. (2010) Measurement of zinc stable isotope ratios in biogeochemical matrices by double-spike MC-ICPMS and determination of the isotope ratio pool available for plants from soil. *Anal Bioanal Chem* **398**, 3115–3125.

Bachmann O. and Bergantz G. W. (2004) On the Origin of Crystal-poor Rhyolites: Extracted from Batholithic Crystal Mushes. *J. Petrol.* **45**, 1565–1582.

Bachmann O. and Huber C. (2019) The Inner Workings of Crustal Distillation Columns; the Physical Mechanisms and Rates Controlling Phase Separation in Silicic Magma Reservoirs. *J. Petrol.* **60**, 3–18.

Bai Y., Su B. X., Xiao Y., Cui M. M. and Charlier B. (2021) Magnesium and iron isotopic evidence of inter-mineral diffusion in ultramafic cumulates of the Peridotite Zone, Stillwater Complex. *Geochim. Cosmochim. Acta* **292**, 152–169.

Balan E., De Villiers J. P. R., Eeckhout S. G., Glatzel P., Toplis M. J., Fritsch E., Allard T., Galoisy L. and Calas G. (2006) The oxidation state of vanadium in titanomagnetite from layered basic intrusions. *Am. Mineral.* **91**, 953–956.

Baldridge W S, McGetchin T R, Frey F A and Jarosewich E (1973) Magmatic Evolution of Hekla, Iceland. *Contrib. to Mineral. Petrol.* **42**, 245–258.

Balsiger H., Geiss J. and Lipschutz M. E. (1969) Vanadium isotopic composition in meteoritic and terrestrial matter. *Earth Planet. Sci. Lett.* **6**, 117–122.

Barboni M., Boehnke P., Schmitt A. K., Mark Harrison T., Shane P., Bouvier A. S. and Baumgartner L. (2016) Warm storage for arc magmas. *Proc. Natl. Acad. Sci.* **113**, 13959–13964.

Barnes C. G., Werts K., Memeti V. and Ardill K. (2019) Most Granitoid Rocks are Cumulates: Deductions from Hornblende Compositions and Zircon Saturation. *J. Petrol.* **60**, 2227–2240.

Beard B. L. and Johnson C. M. (1999) High precision iron isotope measurements of terrestrial and lunar materials. *Geochim. Cosmochim. Acta* **63**, 1653–1660.

Beard B. L., Johnson C. M., Skulan J. L., Nealson K. H., Cox L. and Sun H. (2003) Application of Fe isotopes to tracing the geochemical and biological cycling of Fe. *Chem. Geol.* **195**, 87–117.

Bédard J. H. (2006) Trace element partitioning in plagioclase feldspar. *Geochim. Cosmochim. Acta* **70**, 3717–3742.

Bédard J. H. (2007) Trace element partitioning coefficients between silicate melts and orthopyroxene: Parameterizations of D variations. *Chem. Geol.* **244**, 263–303.

Begemann F., Ludwig K. R., Lugmair G. W., Min K., Nyquist L. E., Patchett P. J., Renne P. R., Shih C. Y., Villa I. M. and Walker R. J. (2001) Call for an improved set of decay constants for geochronological use. *Geochim. Cosmochim. Acta* **65**, 111–121.

Belshaw N. S., Zhu X. K., Guo Y. and O'Nions R. K. (2000) High precision measurement of iron isotopes by plasma source mass spectrometry. *Int. J. Mass Spectrom.* **197**, 191–195.

Bergantz G. W., Schleicher J. M. and Burgisser A. (2015) Open-system dynamics and mixing in magma mushes. *Nat. Geosci.* **8**, 793–796.

Bermin J., Vance D., Archer C. and Statham P. J. (2006) The determination of the isotopic composition of Cu and Zn in seawater. *Chem. Geol.* **226**, 280–297.

Beunon H., Mattielli N., Doucet L. S., Moine B. and Debret B. (2020) Mantle heterogeneity through Zn systematics in oceanic basalts: Evidence for a deep carbon cycling. *Earth-Science Rev.* **205**, 103174.

Bigeleisen J. and Mayer M. G. (1947) Calculation of Equilibrium Constants for Isotopic Exchange Reactions. *J. Chem. Phys.* **15**, 261–267.

Bilenker L. D., VanTongeren J. A., Lundstrom C. C. and Simon A. C. (2017) Iron isotopic evolution during fractional crystallization of the uppermost Bushveld Complex layered mafic intrusion. *Geochemistry, Geophys. Geosystems* **18**, 956–972.

Blanchard M., Poitrasson F., Méheut M., Lazzeri M., Mauri F. and Balan E. (2009) Iron isotope fractionation between pyrite (FeS2), hematite (Fe2O3) and siderite (FeCO3): A first-principles density functional theory study. *Geochim. Cosmochim. Acta* **73**, 6565–6578.

Bodnar R., Lecumberri-Sanchez P., Moncada D. and Steele-MacInnis M. (2014). Fluid Inclusions in Hydrothermal Ore Deposits. In H. D. Holland and K. K. Turekian (Eds.), *Treatise on Geochemistry* (2nd ed., Vol. 13, pp. 119-142).

Böhlke J. K., de Laeter J. R., De Bièvre P., Hidaka H., Peiser H. S., Rosman K. J. R. and Taylor P. D. P. (2005) Isotopic Compositions of the Elements, 2001. *J. Phys. Chem. Ref. Data* **34**, 57–67.

Borrok D. M., Gieré R., Ren M. and Landa E. R. (2010) Zinc isotopic composition of particulate matter generated during the combustion of coal and coal + tire-derived fuels. *Environ. Sci. Technol.* **44**, 9219–9224.

Bosi F., Hålenius U. and Skogby H. (2009) Crystal chemistry of the magnetite-ulvöspinel series. *Am. Mineral.* **94**, 181–189.

Bouvier A., Vervoort J. D. and Patchett P. J. (2008) The Lu-Hf and Sm-Nd isotopic composition of CHUR: Constraints from unequilibrated chondrites and implications for the bulk composition of terrestrial planets. *Earth Planet. Sci. Lett.* **273**, 48–57.

Brauns C. M., Hergt J. M., Woodhead J. D. and Maas R. (2000) Os Isotopes and the Origin of the Tasmanian Dolerites. *J. Petrol.* **41**, 905–918.

Brennecka G. A., Herrmann A. D., Algeo T. J. and Anbar A. D. (2011) Rapid expansion of oceanic anoxia immediately before the end-Permian mass extinction. *Proc. Natl. Acad. Sci.* **108**, 17631–17634.

Brett A., Prytulak J., Hammond S. J. and Rehkämper M. (2018) Thallium Mass Fraction and Stable Isotope Ratios of Sixteen Geological Reference Materials. *Geostand. Geoanalytical Res.* **42**, 339–360.

Brounce M. N., Kelley K. A. and Cottrell E. (2014) Variations in Fe3+ / ΣFe of Mariana Arc Basalts and Mantle Wedge fO2. *J. Petrol.* **55**, 2513–2536.

Bryan A. L., Dong S., Wilkes E. B. and Wasylenki L. E. (2015) Zinc isotope fractionation during adsorption onto Mn oxyhydroxide at low and high ionic strength. *Geochim. Cosmochim. Acta* **157**, 182–197.

Brzozowski M. J., Good D. J., Wu C. and Li W. (2021) Iron isotope fractionation during sulfide liquid evolution in Cu–PGE mineralization of the Eastern Gabbro, Coldwell Complex, Canada. *Chem. Geol.* **576**, 120282.

Bucholz C. E., Stolper E. M., Eiler J. M. and Breaks F. W. (2018) A Comparison of Oxygen Fugacities of Strongly Peraluminous Granites across the Archean–Proterozoic Boundary. *J. Petrol.* **59**, 2123–2156.

Buddington A. F. and Lindsley D. H. (1964) Iron-Titanium Oxide Minerals and Synthetic Equivalents. *J. Petrol.* **5**, 310–357.

Burton-Johnson A., Macpherson C. G., Ottley C. J., Nowell G. M. and Boyce A. J. (2019) Generation of the Mt Kinabalu Granite by Crustal Contamination of Intraplate Magma Modelled by Equilibrated Major Element Assimilation with Fractional Crystallization (EME-AFC). *J. Petrol.* **60**, 1461–1487.

Cameron M. and Papike J. J. (1981) Structural and chemical variations in pyroxenes. *Am. Mineral.* **66**, 1–50.

Canil D. (1997) Vanadium partitioning and the oxidation state of Archaean komatiite magmas. *Nature* **389**, 842–845.

Canil D. and Lacourse T. (2020) Geothermometry using minor and trace elements in igneous and hydrothermal magnetite. *Chem. Geol.* **541**, 119576.

Cao Y., Wang C. Y., Huang F. and Zhang Z. (2019) Iron Isotope Systematics of the Panzhihua Mafic Layered Intrusion Associated With Giant Fe-Ti Oxide Deposit in the Emeishan Large Igneous Province, SW China. *J. Geophys. Res. Solid Earth* **124**, 358–375.

Cashman K. V, Sparks R. S. J. and Blundy J. D. (2017) Vertically extensive and unstable magmatic systems: A unified view of igneous processes. *Science* **355**.

Chapman J. B., Mason T. F. D., Weiss D. J., Coles B. J. and Wilkinson J. J. (2006) Chemical separation and isotopic variations of Cu and Zn from five geological reference materials. *Geostand. Geoanalytical Res.* **30**, 5–16.

Chappell B. W. and White A. J. R. (2001) Two contrasting granite types: 25 years later. *Aust. J. Earth. Sci.* **48**, 489-499.

Chappell B. W. and Wyborn D. (2004) Cumulate and Cumulative Granites and Associated Rocks. *Resour. Geol.* **54**, 227–240.

Chappell B. W., Bryant C. J. and Wyborn D. (2012) Peraluminous I-type granites. *Lithos* **153**, 142–153.

Chen H., Savage P. S., Teng F. Z., Helz R. T. and Moynier F. (2013) Zinc isotope fractionation during magmatic differentiation and the isotopic composition of the bulk Earth. *Earth Planet. Sci. Lett.* **369**, 34–42.

Chen L.-M., Song X.-Y., Zhu X.-K., Zhang X.-Q., Yu S.-Y. and Yi J.-N. (2014) Iron isotope fractionation during crystallization and sub-solidus re-equilibration: Constraints from the Baima mafic layered intrusion, SW China. *Chem. Geol.* **380**, 97–109.

Chen L.-M., Teng F.-Z., Song X.-Y., Luan Y., Yu S.-Y. and Kang J. (2021) Origins and implications of magnesium isotopic heterogeneity in Fe-Ti oxides in layered mafic intrusions. *Geochim. Cosmochim. Acta* **308**, 273–290.

Chen S., Liu Y., Hu J., Zhang Z., Hou Z., Huang F. and Yu H. (2016) Zinc Isotopic Compositions of NIST SRM 683 and Whole-Rock Reference Materials. *Geostand. Geoanalytical Res.* **40**, 417–432.

Chen S., Niu Y., Guo P., Gong H., Sun P., Xue Q., Duan M. and Wang X. (2019) Iron isotope fractionation during mid-ocean ridge basalt (MORB) evolution: Evidence from lavas on the East Pacific Rise at 10°30'N and its implications. *Geochim. Cosmochim. Acta* **267**, 227–239.

Chen Y., Niu Y., Duan M., Gong H. and Guo P. (2021) Fractional crystallization causes the iron isotope contrast between mid-ocean ridge basalts and abyssal peridotites. *Commun. Earth Environ.* **2**, 65.

Cheng L, Costa F and Bergantz G (2020) Linking fluid dynamics and olivine crystal scale zoning during simulated magma intrusion. *Contrib. to Mineral. Petrol.* **175**, 53.

Chin E. J., Shimizu K., Bybee G. M. and Erdman M. E. (2018) On the development of the calc-alkaline and tholeiitic magma series: A deep crustal cumulate perspective. *Earth Planet. Sci. Lett.* **482**, 277–287.

Clayton R. N., Grossman L. and Mayeda T. K. (1973) A Component of Primitive Nuclear Composition in Carbonaceous Meteorites. *Science* **182**, 485–488.

Collins W. J., Brendan Murphy J., Johnson T. E. and Huang H.-Q. (2020) Critical role of water in the formation of continental crust. *Nat. Geosci.* **13**, 331–338.

Condie K. C. (1993) Chemical composition and evolution of the upper continental crust: Contrasting results from surface samples and shales. *Chem. Geol.* **104**, 1–37.

Condie K. C. (2018) A planet in transition: The onset of plate tectonics on Earth between 3 and 2 Ga? *Geosci. Front.* **9**, 51–60.

Cottrell E. and Kelley K. A. (2011) The oxidation state of Fe in MORB glasses and the oxygen fugacity of the upper mantle. *Earth Planet. Sci. Lett.* **305**, 270–282.

Craddock P. R. and Dauphas N. (2011) Iron Isotopic Compositions of Geological Reference Materials and Chondrites. *Geostand. Geoanalytical Res.* **35**, 101–123.

Czamanske G. K. and Wones D. R. (1973) Oxidation During Magmatic Differentiation, Finnmarka Complex, Oslo Area, Norway: Part 2, The Mafic Silicates. *J. Petrol.* **14**, 349–380.

Dare S. A. S., Barnes S. J. and Beaudoin G. (2012) Variation in trace element content of magnetite crystallized from a fractionating sulfide liquid, Sudbury, Canada: Implications for provenance discrimination. *Geochim. Cosmochim. Acta* **88**, 27–50.

Dare S. A. S., Barnes S. J., Beaudoin G., Méric J., Boutroy E. and Potvin-Doucet C. (2014) Trace elements in magnetite as petrogenetic indicators. *Miner. Depos.* **49**, 785–796.

Dauphas N. and Schauble E. A. (2016) Mass Fractionation Laws, Mass-Independent Effects, and Isotopic Anomalies. *Annu. Rev. Earth Planet. Sci.* **44**, 709–783.

Dauphas N., Craddock P. R., Asimow P. D., Bennett V. C., Nutman A. P. and Ohnenstetter D. (2009a) Iron isotopes may reveal the redox conditions of mantle melting from Archean to Present. *Earth Planet. Sci. Lett.* **288**, 255–267.

Dauphas N., Janney P. E., Mendybaev R. A., Wadhwa M., Richter F. M., Davis A. M., van Zuilen M., Hines R. and Foley C. N. (2004) Chromatographic Separation and Multicollection-ICPMS Analysis of Iron. Investigating Mass-Dependent and -Independent Isotope Effects. *Anal. Chem.* **76**, 5863.

Dauphas N., John S. G. and Rouxel O. (2017) Iron Isotope Systematics. *Rev. Mineral. Geochemistry* **82**, 415–510.

Dauphas N., Pourmand A. and Teng F.-Z. (2009b) Routine isotopic analysis of iron by HR-MC-ICPMS: How precise and how accurate? *Chem. Geol.* **267**, 175–184.

Dauphas N., Roskosz M., Alp E. E., Golden D. C., Sio C. K., Tissot F. L. H., Hu M. Y., Zhao J., Gao L. and Morris R. V. (2012) A general moment NRIXS approach to the determination of equilibrium Fe isotopic fractionation factors: Application to goethite and jarosite. *Geochim. Cosmochim. Acta* **94**, 254–275.

Dauphas N., Roskosz M., Alp E. E., Neuville D. R., Hu M. Y., Sio C. K., Tissot F. L. H., Zhao J., Tissandier L., Médard E. and Cordier C. (2014) Magma redox and structural controls on iron isotope variations in Earth's mantle and crust. *Earth Planet. Sci. Lett.* **398**, 127–140.

De Moor J. M., Fischer T. P., Hilton D. R., Hauri E., Jaffe L. A. and Camacho J. T. (2005) Degassing at Anatahan volcano during the May 2003 eruption: Implications from petrology, ash leachates, and SO2 emissions. *J. Volcanol. Geotherm. Res.* **146**, 117–138.

De Vega C. G., Chernonozhkin S. M., Grigoryan R., Costas-Rodríguez M. and Vanhaecke F. (2020) Characterization of the new isotopic reference materials IRMM-524A and ERM-AE143 for Fe and Mg isotopic analysis of geological and biological samples. *J. Anal. At. Spectrom.* **35**, 2397–2782.

Deng J., He Y., Zartman R. E., Yang X. and Sun W. (2022) Large iron isotope fractionation during mantle wedge serpentinization: Implications for iron isotopes of arc magmas. *Earth Planet. Sci. Lett.* **583**, 117423.

Deng J., Wang C., Bagas L., Selvaraja V., Jeon H., Wu B. and Yang L. (2017) Insights into ore genesis of the Jinding Zn–Pb deposit, Yunnan Province, China: Evidence from Zn and in-situ S isotopes. *Ore Geol. Rev.* **90**, 943–957.

Deng Z., Chaussidon M., Savage P., Robert F., Pik R. and Moynier F. (2019) Titanium isotopes as a tracer for the plume or island arc affinity of felsic rocks. *Proc. Natl. Acad. Sci.* **116**, 1132–1135.

Ding X., Helz R. T., Qi Y. and Huang F. (2020) Vanadium isotope fractionation during differentiation of Kilauea Iki lava lake, Hawaii. *Geochim. Cosmochim. Acta* **289**, 114–129.

Ding X., Ripley E. M., Wang W., Li C. and Huang F. (2019) Iron isotope fractionation during sulfide liquid segregation and crystallization at the Lengshuiqing Ni-Cu magmatic sulfide deposit, SW China. *Geochim. Cosmochim. Acta* **261**, 327–341.

Doucet L. S., Laurent O., Ionov D. A., Mattielli N., Debaille V. and Debouge W. (2020) Archean lithospheric differentiation: Insights from Fe and Zn isotopes. *Geology* **48**, 1028–1032.

Doucet L. S., Laurent O., Mattielli N. and Debouge W. (2018) Zn isotope heterogeneity in the continental lithosphere: New evidence from Archean granitoids of the northern Kaapvaal craton, South Africa. *Chem. Geol.* **476**, 260–271.

Doucet L. S., Mattielli N., Ionov D. A., Debouge W. and Golovin A. V. (2016) Zn isotopic heterogeneity in the mantle: A melting control? *Earth Planet. Sci. Lett.* **451**, 232–240.

Droop G. T. R. (1987) A general equation for estimating Fe^{3+} concentrations in ferromagnesian silicates and oxides from microprobe analyses, using stoichiometric criteria. *Mineral. Mag.* **51**, 431–435.

Du D. H., Li W., Wang X. L., Shu X. J., Yang T. and Sun T. (2019) Fe isotopic fractionation during the magmatic–hydrothermal stage of granitic magmatism. *Lithos* **350**–**351**, 105265.

Du D.-H., Wang X.-L., Yang T., Chen X., Li J.-Y. and Li W. (2017) Origin of heavy Fe isotope compositions in high-silica igneous rocks: A rhyolite perspective. *Geochim. Cosmochim. Acta* **218**, 58–72.

Dziony W., Horn I., Lattard D., Koepke J., Steinhoefel G., Schuessler J. A. and Holtz F. (2014) In-situ Fe isotope ratio determination in Fe–Ti oxides and sulfides from drilled gabbros and basalt from the IODP Hole 1256D in the eastern equatorial Pacific. *Chem. Geol.* **363**, 101–113.

El Korh A., Luais B., Deloule E. and Cividini D. (2017) Iron isotope fractionation in subduction-related high-pressure metabasites (Ile de Groix, France). *Contrib. to Mineral. Petrol.* **172**, 41.

Fan H., Ostrander C. M., Auro M., Wen H. and Nielsen S. G. (2021) Vanadium isotope evidence for expansive ocean euxinia during the appearance of early Ediacara biota. *Earth Planet. Sci. Lett.* **567**, 117007.

Farquhar J., Bao H. and Thiemens M. (2000) Atmospheric Influence of Earth's Earliest Sulfur Cycle. *Science* **289**, 756–758.

Faure G. and Mensing T. M. (2005) *Isotopes: Principles and Applications*. 3rd ed., John Wiley and Sons.

Feig S. T., Jürgen Koepke and Snow J. E. (2010) Effect of oxygen fugacity and water on phase equilibria of a hydrous tholeiitic basalt. *Contrib. to Mineral. Petrol.* **160**, 551–568.

Foden J., Sossi P. A. and Nebel O. (2018) Controls on the iron isotopic composition of global arc magmas. *Earth Planet. Sci. Lett.* **494**, 190–201.

Foden J., Sossi P. A. and Wawryk C. M. (2015) Fe isotopes and the contrasting petrogenesis of A-, I- and S-type granite. *Lithos* **212**–**215**, 32–44.

Font L., Davidson J. P., Pearson, D. G., Nowell, G. M., Jerram, D. A. and Ottley, C. J. (2008) Sr and Pb Isotope Micro-analysis of Plagioclase Crystals from Skye Lavas: an Insight into Open-system Processes in a Flood Basalt Province. *J. Petrol.* **49**, 1449-1471.

Fourny A., Weis D. and Scoates J. S. (2016) Comprehensive Pb-Sr-Nd-Hf isotopic, trace element, and mineralogical characterization of mafic to ultramafic rock reference materials. *Geochemistry, Geophys. Geosystems* **17**, 739–773.

Frei R., Gaucher C., Døssing L. N. and Sial A. N. (2011) Chromium isotopes in carbonates - A tracer for climate change and for reconstructing the redox state of ancient seawater. *Earth Planet. Sci. Lett.* **312**, 114–125.

Frei R., Gaucher C., Poulton S. W. and Canfield D. E. (2009) Fluctuations in Precambrian atmospheric oxygenation recorded by chromium isotopes. *Nature* **461**, 250–253.

Frost B. R. and Lindsley D. H. (1991) Oxide Minerals: petrologic and magnetic significance. In D. H. Lindsley (ed) *Reviews in Mineralogy and Geochemistry* (pp. 433–468).

Fujii T., Moynier F., Blichert-Toft J. and Albarède F. (2014) Density functional theory estimation of isotope fractionation of Fe, Ni, Cu, and Zn among species relevant to

geochemical and biological environments. *Geochim. Cosmochim. Acta* **140**, 553–576.

Gaetani G. A. and Grove T. L. (1997) Partitioning of moderately siderophile elements among olivine, silicate melt, and sulfide melt: Constraints on core formation in the Earth and Mars. *Geochim. Cosmochim. Acta* **61**, 1829–1846.

Gajos N. A., Lundstrom C. C. and Taylor A. H. (2016) Spatially controlled Fe and Si isotope variations: an alternative view on the formation of the Torres del Paine pluton. *Contrib. to Mineral. Petrol.* **171**, 93.

Gao S., Luo T. C., Zhang B. R., Zhang H. F., Han Y. W., Zhao Z. D. and Hu Y. K. (1998) Chemical composition of the continental crust as revealed by studies in East China. *Geochim. Cosmochim. Acta* **62**, 1959–1975.

Gaschnig R. M., Rudnick R. L., McDonough W. F., Kaufman A. J., Hu Z. and Gao S. (2014) Onset of oxidative weathering of continents recorded in the geochemistry of ancient glacial diamictites. *Earth Planet. Sci. Lett.* **408**, 87–99.

Gaschnig R. M., Rudnick R. L., McDonough W. F., Kaufman A. J., Valley J. W., Hu Z., Gao S. and Beck M. L. (2016) Compositional evolution of the upper continental crust through time, as constrained by ancient glacial diamictites. *Geochim. Cosmochim. Acta* **186**, 316–343.

Ghiorso M. S. and Evans B. W. (2008) Thermodynamics of Rhombohedral Oxide Solid Solutions and a Revision of the Fe-Ti Two-Oxide Geothermometer and Oxygen-Barometer. *Am. J. Sci.* **308**, 957–1039.

Ghiorso M. S. and Gualda G. A. R. (2015) An H_2O–CO_2 mixed fluid saturation model compatible with rhyolite-MELTS. *Contrib. to Mineral. Petrol.* **169**, 53.

Giuli G., Paris E., Mungall J., Romano C. and Dingwell D. (2004) V oxidation state and coordination number in silicate glasses by XAS. *Am. Mineral.* **89**, 1640–1646.

Gleeson M. L. M., Gibson S. A. and Williams H. M. (2020) Novel insights from Fe-isotopes into the lithological heterogeneity of Ocean Island Basalts and plume-influenced MORBs. *Earth Planet. Sci. Lett.* **535**, 116114.

Gong H., Guo P., Chen S., Duan M., Sun P., Wang X. and Niu Y. (2020) A re-assessment of nickel-doping method in iron isotope analysis on rock samples using multi-collector inductively coupled plasma mass spectrometry. *Acta Geochim.* **39**, 355–364.

Gong Y., Xia Y., Huang F. and Yu H. (2017) Average iron isotopic compositions of the upper continental crust: constrained by loess from the Chinese Loess Plateau. *Acta Geochim* **36**, 125–131.

Greaney A. T., Rudnick R. L., Romaniello S. J., Johnson A. C., Gaschnig R. M. and Anbar A. D. (2020) Molybdenum isotope fractionation in glacial diamictites tracks the onset of oxidative weathering of the continental crust. *Earth Planet. Sci. Lett.* **534**, 116083.

Greber N. D. and Dauphas N. (2019) The chemistry of fine-grained terrigenous sediments reveals a chemically evolved Paleoarchean emerged crust. *Geochim. Cosmochim. Acta* **255**, 247–264.

Greber N. D., Dauphas N., Bekker A., Ptáček M. P., Bindeman I. N. and Hofmann A. (2017) Titanium isotopic evidence for felsic crust and plate tectonics 3.5 billion years ago. *Science* **357**, 1271–1274.

Groves D. I. and Bierlein F. P. (2007) Geodynamic settings of mineral deposit systems. *J. Geol. Soc. London.* **164**, 19–30.

Gualda G. A. R., Ghiorso M. S., Lemons R. V. and Carley T. L. (2012) Rhyolite-MELTS: a Modified Calibration of MELTS Optimized for Silica-rich, Fluid-bearing Magmatic Systems. *J. Petrol.* **53**, 875–890.

Hawkesworth C. J., Cawood P. A. and Dhuime B. (2020) The Evolution of the Continental Crust and the Onset of Plate Tectonics. *Front. Earth Sci.* **8**, 326.

Hawthorne F. C., Oberti R., Harlow G. E., Maresch W. V., Martin R. F., Schumacher J. C. and Welch M. D. (2012) Nomenclature of the amphibole supergroup. *Am. Mineral.* **97**, 2031–2048.

He Y., Ke S., Teng F. Z., Wang T., Wu H., Lu Y. and Li S. (2015) High-Precision Iron Isotope Analysis of Geological Reference Materials by High-Resolution MC-ICP-MS. *Geostand. Geoanalytical Res.* **39**, 341–356.

He Y., Wu H., Ke S., Liu S. A. and Wang Q. (2017) Iron isotopic compositions of adakitic and non-adakitic granitic magmas: Magma compositional control and subtle residual garnet effect. *Geochim. Cosmochim. Acta* **203**, 89–102.

He Z., Zhang X., Deng X., Hu H., Li Y., Yu H., Archer C., Li J. and Huang F. (2020) The behavior of Fe and S isotopes in porphyry copper systems: Constraints from the Tongshankou Cu-Mo deposit, Eastern China. *Geochim. Cosmochim. Acta* **270**, 61–83.

Hedenquist J. W. and Lowenstern J. B. (1994) The role of magmas in the formation of hydrothermal ore deposits. *Nature* **370**, 519–527.

Heimann A., Beard B. L. and Johnson C. M. (2008) The role of volatile exsolution and sub-solidus fluid/rock interactions in producing high $^{56}Fe/^{54}Fe$ ratios in siliceous igneous rocks. *Geochim. Cosmochim. Acta* **72**, 4379–4396.

Helz R. T. (1987) Differentiation behaviour of Kilauea Iki lava lake, Kilauea volcano, Hawaii: an overview of past and current work. *Geochemical Soc. Spec. Publ.* **1**, 241–258.

Helz R. T. and Thornber C. R. (1987) Geothermometry of Kilauea Iki lava lake, Hawaii. *Bull. Volcanol.* **49**, 651–668.

Hergt J. M. and Brauns C. M. (2001) On the origin of Tasmanian dolerites. *Aust. J. Earth Sci.* **48**, 543–549.

Hergt J. M., Chappell B. W., Mcculloch M. T., Mcdougall I. and Chivas A. R. (1989) Geochemical and Isotopic Constraints on the Origin of the Jurassic Dolerites of Tasmania. *J. Petrol.* **30**, 841–883.

Hergt J. M., Peate D. W. and Hawkesworth C. J. (1991) The petrogenesis of Mesozoic Gondwana low-Ti flood basalts. *Earth Planet. Sci. Lett.* **105**, 134–148.

Herzog G. F., Moynier F., Albarède F. and Berezhnoy A. A. (2009) Isotopic and elemental abundances of copper and zinc in lunar samples, Zagami, Pele's hairs, and a terrestrial basalt. *Geochim. Cosmochim. Acta* **73**, 5884–5904.

Hiebert R. S., Bekker A., Houlé M. G., Wing B. A. and Rouxel O. J. (2016) Tracing sources of crustal contamination using multiple S and Fe isotopes in the Hart komatiite-associated Ni–Cu–PGE sulfide deposit, Abitibi greenstone belt, Ontario, Canada. *Miner. Depos.* **51**, 919–935.

Hildreth W. (2004) Volcanological perspectives on Long Valley, Mammoth Mountain, and Mono Craters: Several contiguous but discrete systems. *J. Volcanol. Geotherm. Res.* **136**, 169–198.

Hoare L., Klaver M., Muir D. D., Klemme S., Barling J., Parkinson I. J., Lissenberg C. J. and Millet M.-A. (2022) Empirical and Experimental Constraints on Fe-Ti Oxide-Melt Titanium Isotope Fractionation Factors. *Geochim. Cosmochim. Acta*. **326**, 253-272

Hoare L., Klaver M., Saji N. S., Gillies J., Parkinson I. J., Lissenberg C. J. and Millet M. A. (2020) Melt chemistry and redox conditions control titanium isotope fractionation during magmatic differentiation. *Geochim. Cosmochim. Acta* **282**, 38–54.

Holland T. and Blundy J. (1994) Non-ideal interactions in calcic amphiboles and their bearing on amphibole-plagioclase thermometry. *Contrib. to Mineral. Petrol.* **116**, 433–447.

Holness M. B. (2018) Melt segregation from silicic crystal mushes: a critical appraisal of possible mechanisms and their microstructural record. *Contrib. to Mineral. Petrol.* **173**, 48.

Holness M. B., Stock M. J. and Geist D. (2019) Magma chambers versus mush zones: constraining the architecture of sub-volcanic plumbing systems from microstructural analysis of crystalline enclaves. *Philos. Trans. R. Soc. A* **377**.

Hopkins S. S., Prytulak J., Barling J., Russell S. S., Coles B. J. and Halliday A. N. (2019) The vanadium isotopic composition of lunar basalts. *Earth Planet. Sci. Lett.* **511**, 12–24.

Hoskin P. W. O., Kinny P. D., Wyborn D. and Chappell B. W. (2000) Identifying accessory mineral saturation during differentiation in granitoid magmas: An integrated approach. *J. Petrol.* **41**, 1365–1396.

Huang F., Zhang Z., Lundstrom C. C. and Zhi X. (2011) Iron and magnesium isotopic compositions of peridotite xenoliths from Eastern China. *Geochim. Cosmochim. Acta* **75**, 3318–3334.

Huang J. H., Huang F., Evans L. and Glasauer S. (2015) Vanadium: Global (bio)geochemistry. *Chem. Geol.* **417**, 68–89.

Huang J., Liu S. A., Gao Y., Xiao Y. and Chen S. (2016) Copper and zinc isotope systematics of altered oceanic crust at IODP Site 1256 in the eastern equatorial Pacific. *J. Geophys. Res. Solid Earth* **121**, 7086–7100.

Huang J., Zhang X. C., Chen S., Tang L., Wörner G., Yu H. and Huang F. (2018) Zinc isotopic systematics of Kamchatka-Aleutian arc magmas controlled by mantle melting. *Geochim. Cosmochim. Acta* **238**, 85–101.

Humphreys M. C. S. (2011) Silicate Liquid Immiscibility within the Crystal Mush: Evidence fromTi in Plagioclase from the Skaergaard Intrusion. *J. Petrol.* **52**, 147–174.

Ickert R. B., Williams I. S. and Wyborn D. (2011) Ti in zircon from the Boggy Plain zoned pluton: implications for zircon petrology and Hadean tectonics. *Contrib. to Mineral. Petrol.* **162**, 447–461.

Ickert R. B. (2010) U-Pb, Lu-Hf, and O isotope systematics of zircon from southeastern Australian Siluro-Devonian granites. PhD Thesis, Australian National University.

Iles K. A. (2017) Isotopic disequilibrium in granitic systems: the origins of heterogeneity in granites and implications for partial melting in the crust and petrogenetic models. PhD Thesis, University of Melbourne.

Inglis E. C., Debret B., Burton K. W., Millet M.-A., Pons M.-L., Dale C. W., Bouilhol P., Cooper M., Nowell G. M., McCoy-West A. J. and Williams H. M. (2017) The behavior of iron and zinc stable isotopes accompanying the subduction of mafic oceanic crust: A case study from Western Alpine ophiolites. *Geochemistry, Geophys. Geosystems* **18**, 2562–2579.

Inglis E. C., Moynier F., Creech J., Deng Z., Day J. M. D., Teng F. Z., Bizzarro M., Jackson M. and Savage P. (2019) Isotopic fractionation of zirconium during magmatic differentiation and the stable isotope composition of the silicate Earth. *Geochim. Cosmochim. Acta* **250**, 311–323.

Irvine T. N. (1982) Terminology for Layered Intrusions. *J. Petrol.* **23**, 127–162.

Jackson J. M., Hamecher E. A. and Sturhahn W. (2009) Nuclear resonant X-ray spectroscopy of (Mg,Fe)SiO3 orthoenstatites. *Eur. J. Mineral.* **21**, 551–560.

Jackson M. D., Blundy J. and Sparks R. S. J. (2018) Chemical differentiation, cold storage and remobilization of magma in the Earth's crust. *Nature* **564**, 405–409.

Jagoutz O. and Kelemen P. B. (2015) Role of Arc Processes in the Formation of Continental Crust. *Annu. Rev. Earth Planet. Sci.* **43**, 363–404.

Janoušek V. and Moyen J.-F. (2020) Whole-rock geochemical modelling of granite genesis: the current state of play. *Geol. Soc. London, Spec. Publ.* **491**, 267–291.

Jeong H., Ra K. and Choi J. Y. (2021) Copper, Zinc and Lead Isotopic Delta Values and Isotope Ratios of Various Geological and Biological Reference Materials. *Geostand. Geoanalytical Res.* **45**, 551–563.

John S. G., Rouxel O. J., Craddock P. R., Engwall A. M. and Boyle E. A. (2008) Zinc stable isotopes in seafloor hydrothermal vent fluids and chimneys. *Earth Planet. Sci. Lett.* **269**, 17–28.

Jweda J., Bolge L., Class C. and Goldstein S. L. (2016) High Precision Sr-Nd-Hf-Pb Isotopic Compositions of USGS Reference Material BCR-2. *Geostand. Geoanalytical Res.* **40**, 101–115.

Kehm K., Hauri E. H., Alexander C. M. O. and Carlson R. W. (2003) High precision iron isotope measurements of meteoritic material by cold plasma ICP-MS. *Geochim. Cosmochim. Acta* **67**, 2879–2891.

Kelley K. A. and Cottrell E. (2009) Water and the oxidation state of subduction zone magmas. *Science* **325**, 605–607.

Kelley K. A. and Cottrell E. (2012) The influence of magmatic differentiation on the oxidation state of Fe in a basaltic arc magma. *Earth Planet. Sci. Lett.* **329**–**330**, 109–121.

Kemp A. I. S., Hawkesworth C. J., Foster G. L., Paterson B. A., Woodhead J. D., Hergt J. M., Gray C. M. and Whitehouse M. J. (2007) Magmatic and crustal differentiation history of granitic rocks from Hf-O isotopes in zircon. *Science* **315**, 980–983.

Kendall B., Dahl T. W. and Anbar A. D. (2017) The Stable Isotope Geochemistry of Molybdenum. *Rev. Mineral. Geochemistry* **82**, 683–732.

Kiseeva E. S. and Wood B. J. (2015) The effects of composition and temperature on chalcophile and lithophile element partitioning into magmatic sulphides. *Earth Planet. Sci. Lett.* **424**, 280–294.

Klaver M., MacLennan S. A., Ibañez-Mejia M., Tissot F. L. H., Vroon P. Z. and Millet M. A. (2021) Reliability of detrital marine sediments as proxy for continental crust composition: The effects of hydrodynamic sorting on Ti and Zr isotope systematics. *Geochim. Cosmochim. Acta* **310**, 221–239.

Konter J. G., Pietruszka A. J., Hanan B. B., Finlayson V. A., Craddock P. R., Jackson M. G. and Dauphas N. (2016) Unusual δ^{56}Fe values in Samoan rejuvenated lavas generated in the mantle. *Earth Planet. Sci. Lett.* **450**, 221–232.

Langmuir C. H. (1989) Geochemical consequences of in situ crystallization. *Nature* **340**, 199–205.

Laubier M., Grove T. L. and Langmuir C. H. (2014) Trace element mineral/melt partitioning for basaltic and basaltic andesitic melts: An experimental and laser ICP-MS study with application to the oxidation state of mantle source regions. *Earth Planet. Sci. Lett.* **392**, 265–278.

Leake B. E., Woolley A. R., Arps C. E. S., Birch W. D., Gilbert, M. C., Grice J. D., Hawthorne F. C., Kato A., Kisch H. J., Krivovichev V. G., Linthout, K., Laird J., Mandarino J. A., Maresch W. V, Nickel E. H., Rock N. M. S., Schumacher J. C., Smith, D. C., Stephenson N. C. N., Ungaretti L., Whittaker E. J. W. and Youzhi, G (1997) Nomenclature Of Amphiboles: Report Of The Subcommittee On

Amphiboles Of The International Mineralogical Association, Commission On New Minerals And Mineral Names. *Can. Mineral.* **35**, 219–246.

Liao R., Zhu H., Deng J., Zhang L., Li H., Li C., Liu H. and Sun W. (2020) Zinc isotopic systematics of the South China Sea basalts and implications for its behavior during plate subduction. *Chem. Geol.* **541**, 119582.

Little S. H., Munson S., Prytulak J., Coles B. J., Hammond S. J. and Widdowson M. (2019) Cu and Zn isotope fractionation during extreme chemical weathering. *Geochim. Cosmochim. Acta*. **263**, 85-107

Liu P. P., Zhou M. F., Luais B., Cividini D. and Rollion-Bard C. (2014) Disequilibrium iron isotopic fractionation during the high-temperature magmatic differentiation of the Baima Fe-Ti oxide-bearing mafic intrusion, SW China. *Earth Planet. Sci. Lett.* **399**, 21–29.

Liu S. A., Li D., Li S., Teng F. Z., Ke S., He Y. and Lu Y. (2014) High-precision copper and iron isotope analysis of igneous rock standards by MC-ICP-MS. *J. Anal. At. Spectrom.* **29**, 122–133.

Liu S. A., Qu Y. R., Wang Z. Z., Li M. L., Yang C. and Li S. G. (2022) The fate of subducting carbon tracked by Mg and Zn isotopes: A review and new perspectives. *Earth-Science Rev.* **228**, 104010.

Liu S. A., Wang Z. Z., Li S. G., Huang J. and Yang W. (2016) Zinc isotope evidence for a large-scale carbonated mantle beneath eastern China. *Earth Planet. Sci. Lett.* **444**, 169–178.

Lodders K. (2003) Solar System Abundances and Condensation Temperatures of the Elements. *Astrophys. J.* **591**, 1220–1247.

Luck J.-M., Othman D. Ben and Albarède F. (2005) Zn and Cu isotopic variations in chondrites and iron meteorites: Early solar nebula reservoirs and parent-body processes. *Geochim. Cosmochim. Acta* **69**, 5351–5363.

Ludington S. (1978) The biotite-apatite geothermometer revisited . *Am. Mineral.* **63**, 551–553.

Lundstrom C. C., Shaw H. F., Ryerson F. J., Williams Q. and Gill J. (1998) Crystal chemical control of clinopyroxene-melt partitioning in the Di-Ab-An system: implications for elemental fractionations in the depleted mantle. *Geochim. Cosmochim. Acta* **62**, 2849–2862.

Makishima A., Zhu X.-K., Belshaw N. S. and Keith O'Nions R. (2002) Separation of titanium from silicates for isotopic ratio determination using multiple collector ICP-MS. *J. Anal. At. Spectrom.* **17**, 1290–1294.

Mann S., Geilenberg D., Broekaert J. A. C. and Jansen M. (1997) Digestion Methods for Advanced Ceramic Materials and Subsequent Determination of Silicon and Boron by Inductively Coupled Plasma Atomic Emission Spectrometry. *J. Anal. At. Spectrom.* **12**, 975–979.

Maréchal C. and Albarède F. (2002) Ion-exchange fractionation of copper and zinc isotopes. *Geochim. Cosmochim. Acta* **66**, 1499–1509.

Maréchal C. N., Télouk P. and Albarède F. (1999) Precise analysis of copper and zinc isotopic compositions by plasma-source mass spectrometry. *Chem. Geol.* **156**, 251–273.

Marsal D. (1987) *Statistics for Geoscientists*., Pergamon Press, Oxford.

Marshall C. P. and Dollase W. A. (1984) Cation arrangement in iron–zinc–chromium spinel oxides. *Am. Mineral.* **69**, 928–936.

Mason T. F. D., Weiss D. J., Chapman J. B., Wilkinson J. J., Tessalina S. G., Spiro B., Horstwood M. S. A., Spratt J. and Coles B. J. (2005) Zn and Cu isotopic variability

in the Alexandrinka volcanic-hosted massive sulphide (VHMS) ore deposit, Urals, Russia. *Chem. Geol.* **221**, 170–187.

Mason T. F. D., Weiss D. J., Horstwood M., Parrish R. R., Russell S. S., Mullane E. and Coles B. J. (2004) High-precision Cu and Zn isotope analysis by plasma source mass spectrometry part 1. Spectral interferences and their correction. *J. Anal. At. Spectrom.* **19**, 209–217.

McCammon C. (2005) The paradox of mantle redox. *Science* **308**, 807–808.

McCoy-West A. J., Fitton J. G., Pons M.-L., Inglis E. C. and Williams H. M. (2018) The Fe and Zn isotope composition of deep mantle source regions: Insights from Baffin Island picrites. *Geochim. Cosmochim. Acta* **238**, 542–562.

McCulloch M. T. and Woodhead J. D. (1993) Lead isotopic evidence for deep crustal-scale fluid transport during granite petrogenesis. *Geochim. Cosmochim. Acta* **57**, 659–674.

McDougall I. (1962) Differentiation of the Tasmanian Dolerites: Red Hill Dolerite-Granophyre Association. *Bull. Geol. Soc. Am.* **73**, 279–316.

McDougall I. and Lovering J. F. (1963) Fractionation of chromium, nickel, cobalt and copper in a differentiated dolerite-granophyre sequence at Red Hill, Tasmania. *J. Geol. Soc. Aust.* **10**, 325–338.

Millet M. A., Baker J. A. and Payne C. E. (2012) Ultra-precise stable Fe isotope measurements by high resolution multiple-collector inductively coupled plasma mass spectrometry with a 57Fe–58Fe double spike. *Chem. Geol.* **304**–**305**, 18–25.

Millet M. A., Dauphas N., Greber N. D., Burton K. W., Dale C. W., Debret B., Macpherson C. G., Nowell G. M. and Williams H. M. (2016) Titanium stable isotope investigation of magmatic processes on the Earth and Moon. *Earth Planet. Sci. Lett.* **449**, 197–205.

Mineev S. D., Polyakov V. B. and Permyakov, Y. V. (2007) Equilibrium iron isotope fractionation factors for magnetite from Mössbauer spectroscopy and inelastic nuclear resonant X-ray scattering data. *Geochim. Cosmochim. Acta* **71,** A669.

Moeller K., Schoenberg R., Pedersen R.-B., Weiss D. and Dong S. (2012) Calibration of the New Certified Reference Materials ERM-AE633 and ERM-AE647 for Copper and IRMM-3702 for Zinc Isotope Amount Ratio Determinations. *Geostand. Geoanalytical Res.* **36**, 177–199.

Molzahn M., Reisberg L. and Wörner G. (1996) Os, Sr, Nd, Pb, O isotope and trace element data from the Ferrar flood basalts, antarctica: evidence for an enriched subcontinental lithospheric source. *Earth Planet. Sci. Lett.* **144**, 529–545.

Montoya-Pino C., Weyer S., Anbar A. D., Pross J., Oschmann W., van de Schootbrugge B. and Arz H. W. (2010) Global enhancement of ocean anoxia during Oceanic Anoxic Event 2: A quantitative approach using U isotopes. *Geology* **38**, 315–318.

Morimoto N. (1988) Nomenclature of Pyroxenes. *Mineral. Petrol.* **39**, 55–76.

Moynier F., Beck P., Yin Q. Z., Ferroir T., Barrat J. A., Paniello R., Telouk P. and Gillet P. (2010) Volatilization induced by impacts recorded in Zn isotope composition of ureilites. *Chem. Geol.* **276**, 374–379.

Moynier F., Paniello R. C., Gounelle M., Albarède F., Beck P., Podosek F. and Zanda B. (2011) Nature of volatile depletion and genetic relationships in enstatite chondrites and aubrites inferred from Zn isotopes. *Geochim. Cosmochim. Acta* **75**, 297–307.

Moynier F., Vance D., Fujii T. and Savage P. (2017) The Isotope Geochemistry of Zinc and Copper. *Rev. Mineral. Geochemistry* **82**, 543–600.

Müntener O. and Baumgartner L. (2019) Comment on: 'Spatially controlled Fe and Si isotope variations: an alternative view on the formation of the Torres del Paine pluton' by Gajos et al. . *Contrib. to Mineral. Petrol.* **174**, 54.

Muxworthy A R (1998) Stability of magnetic remanence in multidomain magnetite. PhD Thesis, University of Oxford.

Nadoll P., Angerer T., Mauk J. L., French D. and Walshe J. (2014) The chemistry of hydrothermal magnetite: A review. *Ore Geol. Rev.* **61**, 1–32.

Nebel O., Sossi P. A., Bénard A., Arculus R. J., Yaxley G. M., Woodhead J. D., Rhodri Davies D. and Ruttor S. (2019) Reconciling petrological and isotopic mixing mechanisms in the Pitcairn mantle plume using stable Fe isotopes. *Earth Planet. Sci. Lett.* **521**, 60–67.

Nebel O., Sossi P. A., Bénard A., Wille M., Vroon P. Z. and Arculus R. J. (2015) Redox-variability and controls in subduction zones from an iron-isotope perspective. *Earth Planet. Sci. Lett.* **432**, 142–151.

Nebel O., Sossi P. A., Ivanic T. J., Bénard A., Gardiner N. J., Langford R. L. and Arculus R. J. (2020) Incremental Growth of Layered Mafic-Ultramafic Intrusions Through Melt Replenishment Into a Crystal Mush Zone Traced by Fe-Hf Isotope Systematics. *Front. Earth Sci.* **8**, 2.

Needham A. W., Porcelli D. and Russell S. S. (2009) An Fe isotope study of ordinary chondrites. *Geochim. Cosmochim. Acta* **73**, 7399–7413.

Nelson F., Murase T. and Kraus K. A. (1964) Ion exchange procedures. I. Cation exchange in concentration HCl and HClO4 solutions. *J. Chromatogr. A* **13**, 503–535.

Nie N. X., Dauphas N., Alp E. E., Zeng H., Sio C. K., Hu J. Y., Chen X., Aarons S. M., Zhang Z., Tian H.-C., Wang D., Prissel K. B., Greer J., Bi W., Hu M. Y., Zhao J., Shahar A., Roskosz M., Teng F.-Z., Krawczynski M. J., Heck P. R. and Spear F. S. (2021) Iron, magnesium, and titanium isotopic fractionations between garnet, ilmenite, fayalite, biotite, and tourmaline: Results from NRIXS, ab initio, and study of mineral separates from the Moosilauke metapelite. *Geochim. Cosmochim. Acta* **302**, 18–45.

Nielsen S. G. (2020) *Vanadium Isotopes: A Proxy for Ocean Oxygen Variations*., Cambridge University Press.

Nielsen S. G., Auro M., Righter K., Davis D., Prytulak J., Wu F. and Owens J. D. (2019) Nucleosynthetic vanadium isotope heterogeneity of the early solar system recorded in chondritic meteorites. *Earth Planet. Sci. Lett.* **505**, 131–140.

Nielsen S. G., Owens J. D. and Horner T. J. (2016) Analysis of high-precision vanadium isotope ratios by medium resolution MC-ICP-MS. *J. Anal. At. Spectrom.* **31**, 531–536.

Nielsen S. G., Prytulak J. and Halliday A. N. (2011) Determination of Precise and Accurate 51V/50V Isotope Ratios by MC-ICP-MS, Part 1: Chemical Separation of Vanadium and Mass Spectrometric Protocols. *Geostand. Geoanalytical Res.* **35**, 293–306.

Nielsen S. G., Prytulak J., Wood B. J. and Halliday A. N. (2014) Vanadium isotopic difference between the silicate Earth and meteorites. *Earth Planet. Sci. Lett.* **389**, 167–175.

Novella D., Maclennan J., Shorttle O., Prytulak J. and Murton B. J. (2020) A multi-proxy investigation of mantle oxygen fugacity along the Reykjanes Ridge. *Earth Planet. Sci. Lett.* **531**, 115973.

O'Neill H. S. C. and Navrotsky A. (1984) Cation distributions and thermodynamic properties of binary spinel solid solutions. *Am. Mineral.* **69**, 733–753.

Oberti R., Hawthorne F. C., Cannillo E. and Cámara F. (2007) Long-Range Order in Amphiboles. *Rev. Mineral. Geochemistry* **67**, 125–171.

Paniello R. C., Day J. M. D. and Moynier F. (2012) Zinc isotopic evidence for the origin of the Moon. *Nature* **490**, 376–379.

Papike J. J., Simon S. B., Burger P. V., Bell A. S., Shearer C. K. and Karner J. M. (2016) Chromium, vanadium, and titanium valence systematics in Solar System pyroxene as a recorder of oxygen fugacity, planetary provenance, and processes. *Am. Mineral.* **101**, 907–918.

Park J. W., Campbell I. H., Ickert R. B. and Allen C. M. (2013) Chalcophile element geochemistry of the Boggy Plain zoned pluton, southeastern Australia: A S-saturated barren compositionally diverse magmatic system. *Contrib. to Mineral. Petrol.* **165**, 217–236.

Paterson, S. R., Okaya, D., Memeti, V., Economos, R. and Miller, R.B. (2011) Magma addition and flux calculations of incrementally constructed magma chambers in continental margin arcs: Combined field, geochronologic and thermal modelling studies. Geosphere, **7**, 1439-1468.

Pelly I. Z., Lipschutz M. E. and Balsiger H. (1970) Vanadium isotopic composition and contents in chondrites. *Geochim. Cosmochim. Acta* **34**, 1033–1036.

Peters B. J., Shahar A., Carlson R. W., Day J. M. D. and Mock T. D. (2019) A sulfide perspective on iron isotope fractionation during ocean island basalt petrogenesis. *Geochim. Cosmochim. Acta* **245**, 59–78.

Petit J. C. J., de Jong J., Chou L. and Mattielli N. (2008) Development of Cu and Zn Isotope MC-ICP-MS Measurements: Application to Suspended Particulate Matter and Sediments from the Scheldt Estuary. *Geostand. Geoanalytical Res.* **32**, 149–166.

Poitrasson F. and Freydier R. (2005) Heavy iron isotope composition of granites determined by high resolution MC-ICP-MS. *Chem. Geol.* **222**, 132–147.

Poitrasson F., Delpech G. and Grégoire M. (2013) On the iron isotope heterogeneity of lithospheric mantle xenoliths: implications for mantle metasomatism, the origin of basalts and the iron isotope composition of the Earth. *Contrib. to Mineral. Petrol.* **165**, 1243–1258.

Poitrasson F., Halliday A. N., Lee D.-C., Levasseur, S. and Teutsch N. (2004) Iron isotope differences between Earth, Moon, Mars and Vesta as possible records of contrasted accretion mechanisms. *Earth Planet. Sci. Lett.* **223**, 253-266.

Poitrasson F., Levasseur S. and Teutsch N. (2005) Significance of iron isotope mineral fractionation in pallasites and iron meteorites for the core-mantle differentiation of terrestrial planets. *Earth Planet. Sci. Lett.* **234**, 151–164.

Polyakov V. B. and Mineev S. D. (2000) The use of Mossbauer spectroscopy in stable isotope geochemistry. *Geochim. Cosmochim. Acta* **64**, 849–865.

Polyakov V. B., Clayton R. N., Horita J. and Mineev S. D. (2007) Equilibrium iron isotope fractionation factors of minerals: Reevaluation from the data of nuclear inelastic resonant X-ray scattering and Mössbauer spectroscopy. *Geochim. Cosmochim. Acta* **71**, 3833–3846.

Pons M.-L., Debret B., Bouilhol P., Delacour A. and Williams H. (2016) Zinc isotope evidence for sulfate-rich fluid transfer across subduction zones. *Nat. Commun.* **7**, 13794.

Prytulak J., Nielsen S. G. and Halliday A. N. (2011) Determination of Precise and Accurate 51V / 50V Isotope Ratios by Multi-Collector ICP-MS, Part 2: Isotopic Composition of Six Reference Materials plus the Allende Chondrite and Verification Tests. *Geostand. Geoanalytical Res.* **35**, 307–318.

Prytulak J., Nielsen S. G., Ionov D. A., Halliday A. N., Harvey J., Kelley K. A., Niu Y. L., Peate D. W., Shimizu K. and Sims K. W. W. (2013) The stable vanadium isotope composition of the mantle and mafic lavas. *Earth Planet. Sci. Lett.* **365**, 177–189.

Prytulak J., Sossi P., Halliday A., Plank T., Savage P. and Woodhead J. (2017) Stable vanadium isotopes as a redox proxy in magmatic systems? *Geochem. Persp. Let* **3**, 75–84.

Putirka K. D. (2008) Thermometers and barometers for volcanic systems. *Rev. Mineral. Geochemistry* **69**, 61–120.

Putirka K. D. (2016) Amphibole thermometers and barometers for igneous systems and some implications for eruption mechanisms of felsic magmas at arc volcanoes. *Am. Mineral.* **101**, 841–858.

Qi Y. H., Gong Y. Z., Wu F., Lu Y., Cheng W., Huang F. and Yu H. M. (2022) Coupled variations in V-Fe abundances and isotope compositions in latosols: Implications for V mobilization during chemical weathering. *Geochim. Cosmochim. Acta* **320**, 26–40.

Qi Y. H., Wu F., Ionov D. A., Puchtel I. S., Carlson R. W., Nicklas R. W., Yu H. M., Kang J. T., Li C. H. and Huang F. (2019) Vanadium isotope composition of the Bulk Silicate Earth: Constraints from peridotites and komatiites. *Geochim. Cosmochim. Acta* **259**, 288–301.

Rabin S., Blanchard M., Pinilla C., Poitrasson F. and Gregoire M. (2021) First-principles calculation of iron and silicon isotope fractionation between Fe-bearing minerals at magmatic temperatures: The importance of second atomic neighbors. *Geochim. Cosmochim. Acta*., **304**, 101-118.

Raczek I., Stoll B., Hofmann A. W. and Peter Jochum K. (2001) High-Precision Trace Element Data for the USGS Reference Materials BCR-1, BCR-2, BHVO-1, BHVO-2, AGV-1, AGV-2, DTS-1, DTS-2, GSP-1 and GSP-2 by ID-TIMS and MIC-SSMS. *Geostand. Geoanalytical Res.* **25**, 77–86.

Redhammer G. J. and Roth G. (2002) Crystal structure and Mössbauer spectroscopy of the synthetic amphibole potassic-ferri-ferrorichterite at 298 K and low temperatures (80-110 K). *Eur. J. Miner.* **14**, 105–114.

Rehkämper M., Schönbächler M. and Stirling C. H. (2001) Multiple collector ICP-MS: Introduction to instrumentation, measurement techniques and analytical capabilities. *Geostand. Newsl.* **25**, 23–40.

Richter F. M., Davis A. M., DePaolo D. J. and Watson E. B. (2003) Isotope fractionation by chemical diffusion between molten basalt and rhyolite. *Geochim. Cosmochim. Acta* **67**, 3905–3923.

Richter F. M., Watson E. B., Mendybaev R. A., Teng F. Z. and Janney P. E. (2008) Magnesium isotope fractionation in silicate melts by chemical and thermal diffusion. *Geochim. Cosmochim. Acta* **72**, 206–220.

Rieder M., Cavazzini G., D'Yakonov Y.S., Frank-Kamenetskii V.A., Gottardi G., Guggenheim S., Koval P.V., Muller G., Neiva A. M. R., Radoslovich E. W., Robert J.-L., Sassi F. P., Takeda H., Weiss Z. and Wones D. R. (1999) Nomenclature of the micas. *Mineral. Mag.* **63**, 267–279.

Righter K., Sutton S. R., Newville M., Le L., Schwandt C.S., Uchida H., Lavina B. and Downs R. T. (2006) An experimental study of the oxidation state of vanadium in spinel and basaltic melt with implications for the origin of planetary basalt. *Am. Mineral.* **91**, 1643–1656.

Roskosz M., Dauphas N., Hu J., Hu M. Y., Neuville D. R., Brown D., Bi W., Nie N. X., Zhao J. and Alp E. E. (2022) Structural, redox and isotopic behaviors of iron in

geological silicate glasses: A NRIXS study of Lamb-Mössbauer factors and force constants. *Geochim. Cosmochim. Acta* **321**, 184–205.

Roskosz M., Sio C. K. I., Dauphas N., Bi W., Tissot F. L. H., Hu M. Y., Zhao J. and Alp E. E. (2015) Spinel-olivine-pyroxene equilibrium iron isotopic fractionation and applications to natural peridotites. *Geochim. Cosmochim. Acta* **169**, 184–199.

Rubin A. E., Cooper K. M., Till C. B., Kent A. J. R., Costa F., Bose M., Gravley D., Deering C. and Cole J. (2017) Rapid cooling and cold storage in a silicic magma reservoir recorded in individual crystals. *Science* **356**, 1154–1157.

Rudnick R. L. and Gao S. (2003) Composition of the Continental Crust. In H. D. Holland and K. K. Turekian (Eds.) *Treatise on Geochemistry* (1st ed., Vol. 3, pp.1–64).

Ruttor S., Nebel O., Nebel-Jacobsen Y., Norman M. D., Kendrick M. A., Rogers A. and Mather B. R. (2022) Iron isotope systematics during igneous differentiation in lavas from Kīlauea and Mauna Loa, Hawai'i. *Chem. Geol.* **606**, 120973.

Salters V. J. M. and Stracke A. (2004) Composition of the depleted mantle. *Geochemistry, Geophys. Geosystems* **5**, 5.

Sauzéat L., Rudnick R. L., Chauvel C., Garçon M. and Tang M. (2015) New perspectives on the Li isotopic composition of the upper continental crust and its weathering signature. *Earth Planet. Sci. Lett.* **428**, 181–192.

Savage P. S., Georg R. B., Williams H. M., Burton K. W. and Halliday A. N. (2011) Silicon isotope fractionation during magmatic differentiation. *Geochim. Cosmochim. Acta* **75**, 6124–6139.

Schauble E. A. (2004) Applying stable isotope fractionation theory to new systems. *Rev. Mineral. Geochemistry* **55**, 65–111.

Schmidt P. W. and McDougall I. (1977) Palaeomagnetic and potassium-argon dating studies of the tasmanian dolerites. *J. Geol. Soc. Aust.* **24**, 321–328.

Schoenberg R. and Von Blanckenburg F. (2005) An assessment of the accuracy of stable Fe isotope ratio measurements on samples with organic and inorganic matrices by high-resolution multicollector ICP-MS. *Int. J. Mass Spectrom.* **242**, 257–272.

Schoenberg R. and Von Blanckenburg F. (2006) Modes of planetary-scale Fe isotope fractionation. *Earth Planet. Sci. Lett.* **252**, 342–359.

Schoenberg R., Marks M. A. W., Schuessler J. A., von Blanckenburg F. and Markl G. (2009) Fe isotope systematics of coexisting amphibole and pyroxene in the alkaline igneous rock suite of the Ilímaussaq Complex, South Greenland. *Chem. Geol.* **258**, 65–77.

Schuessler J. A., Schoenberg R. and Sigmarsson O. (2009) Iron and lithium isotope systematics of the Hekla volcano, Iceland — Evidence for Fe isotope fractionation during magma differentiation. *Chem. Geol.* **258**, 78–91.

Schuiling R. D. and Feenstra A. (1980) Geochemical Behaviour of Vanadium in Iron-Titanium Oxides. *Chem. Geol.* **30**, 143–150.

Schuth S., Brüske A., Hohl S. V., Jiang S. Y., Meinhardt A. K., Gregory D. D., Viehmann S. and Weyer S. (2019) Vanadium and its isotope composition of river water and seawater: Analytical improvement and implications for vanadium isotope fractionation. *Chem. Geol.* **528**, 119261.

Schuth S., Horn I., Brüske A., Wolff P. E. and Weyer S. (2017) First vanadium isotope analyses of V-rich minerals by femtosecond laser ablation and solution-nebulization MC-ICP-MS. *Ore Geol. Rev.* **81**, 1271–1286.

Shahar A., Young E. D. and Manning C. E. (2008) Equilibrium high-temperature Fe isotope fractionation between fayalite and magnetite: An experimental calibration. *Earth Planet. Sci. Lett.* **268**, 330–338.

Shannon R. D. (1976) Revised Effective Ionic Radii and Systematic Studies of Interatomic Distances in Halides and Chalcogenides. *Acta Crystallogr. Sect. A* **32**, 751–767.

Shaw D., Cramer J., Higgins M. and Truscott M. (1986) Composition of the Canadian Precambrian shield and the continental crust of the earth. *Geol. Soc. Spec. Publ.* **24**, 275–282.

Shen J., Xia J., Qin L., Carlson R. W., Huang S., Helz R. T. and Mock T. D. (2020) Stable chromium isotope fractionation during magmatic differentiation: Insights from Hawaiian basalts and implications for planetary redox conditions. *Geochim. Cosmochim. Acta* **278**, 289–304.

Shiller A. M. and Mao L. (2000) Dissolved vanadium in rivers: effects of silicate weathering. *Chem. Geol.* **165**, 13–22.

Sievwright R. H., O'Neill H. S. C., Tolley J., Wilkinson J. J. and Berry A. J. (2020) Diffusion and partition coefficients of minor and trace elements in magnetite as a function of oxygen fugacity at 1150 ºC. *Contrib. to Mineral. Petrol.* **175**, 40.

Sievwright R. H., Wilkinson J. J., O'Neill H. S. C. and Berry A. J. (2017) Thermodynamic controls on element partitioning between titanomagnetite and andesitic–dacitic silicate melts. *Contrib. to Mineral. Petrol.* **172**, 62.

Sigmarsson O., Condomines M. and Fourcade S. (1992) A detailed Th, Sr and O isotope study of Hekla: differentiation processes in an Icelandic Volcano. *Contrib. to Mineral. Petrol.* **112**, 20–34.

Silver L. T. and Chappell B. W. (1988) The Peninsular Ranges Batholith: an insight into the evolution of the Cordilleran batholiths of southwestern North America. *Trans. R. Soc. Edinb. Earth Sci.* **79**, 105–121.

Sio C. K. I., Dauphas N., Teng F. Z., Chaussidon M., Helz R. T. and Roskosz M. (2013) Discerning crystal growth from diffusion profiles in zoned olivine by in situ Mg-Fe isotopic analyses. *Geochim. Cosmochim. Acta* **123**, 302–321.

Sisson T. W. and Grove T. L. (1993a) Mineralogy and Petrology Experimental investigations of the role of H20 in calc-alkaline differentiation and subduction zone magmatism. *Contrib. to Mineral. Petrol.* **113**, 143–166.

Sisson T. W. and Grove T. L. (1993b) Temperatures and H_2O contents of low-MgO high alumina basalts. Contrib. to Mineral. Petrol. **113**, 167-184.

Sleno L. (2012) The use of mass defect in modern mass spectrometry. *J. Mass Spectrom.* **47**, 226–236.

Soderman C. R., Matthews S., Shorttle O., Jackson M. G., Ruttor S., Nebel O., Turner S., Beier C., Millet M. A., Widom E., Humayun M. and Williams H. M. (2021) Heavy δ^{57}Fe in ocean island basalts: A non-unique signature of processes and source lithologies in the mantle. *Geochim. Cosmochim. Acta* **292**, 309–332.

Sossi P. (2010) The Northern Margin of the Ferrar Large Igneous Province: Petrogenesis and Differentiation of the Tasmanian Dolerites and Kangaroo Island basalts. Masters Thesis, University of Adelaide.

Sossi P. A. and O'Neill H. S. C. (2017) The effect of bonding environment on iron isotope fractionation between minerals at high temperature. *Geochim. Cosmochim. Acta* **196**, 121–143.

Sossi P. A., Foden J. D. and Halverson G. P. (2012) Redox-controlled iron isotope fractionation during magmatic differentiation: an example from the Red Hill intrusion, S. Tasmania. *Contrib. to Mineral. Petrol.* **164**, 757–772.

Sossi P. A., Halverson G. P., Nebel O. and Eggins S. M. (2015) Combined separation of Cu, Fe and Zn from rock matrices and improved analytical protocols for stable isotope determination. *Geostand. Geoanalytical Res.* **39**, 129–149.

Sossi P. A., Moynier F., Chaussidon M., Villeneuve J., Kato C. and Gounelle M. (2017) Early Solar System irradiation quantified by linked vanadium and beryllium isotope variations in meteorites. *Nat. Astron.* **1**, 0055.

Sossi P. A., Nebel O. and Foden J. (2016) Iron isotope systematics in planetary reservoirs. *Earth Planet. Sci. Lett.* **452**, 295–308.

Sossi P. A., Nebel O., O'Neill H. S. C. and Moynier F. (2018a) Zinc isotope composition of the Earth and its behaviour during planetary accretion. *Chem. Geol.* **477**, 73–84.

Sossi P. A., Prytulak J. and O'Neill H. S. C. (2018b) Experimental calibration of vanadium partitioning and stable isotope fractionation between hydrous granitic melt and magnetite at 800 °C and 0.5 GPa. *Contrib. to Mineral. Petrol.* **173**, 27.

Sparks R. S. J., Annen C., Blundy J. D., Cashman K. V., Rust A. C. and Jackson M. D. (2019) Formation and dynamics of magma reservoirs. *Philos. Trans. R. Soc. A Math. Phys. Eng. Sci.* **377**.

Steiger R. H. and Jäger E. (1977) Subcommission on geochronology: Convention on the use of decay constants in geo- and cosmochronology. *Earth Planet. Sci. Lett.* **36**, 359–362.

Stow M. A., Prytulak J., Humphreys M. C. S. and Nowell G. M. (2022) Integrated petrological and Fe-Zn isotopic modelling of plutonic differentiation. *Geochim. Cosmochim. Acta* **320**, 366–391.

Strelow F. W. E., Rethemeyer R. and Bothma C. J. C. (1965) Ion Exchange Selectivity Scales for Cations in Nitric Acid and Sulfuric Acid Media with a Sulfonated Polystyrene Resin. *Anal. Chem.* **37**, 106–111.

Su B. X., Teng F. Z., Hu Y., Shi R. D., Zhou M. F., Zhu B., Liu F., Gong X. H., Huang Q. S., Xiao Y., Chen C. and He Y. S. (2015) Iron and magnesium isotope fractionation in oceanic lithosphere and sub-arc mantle: Perspectives from ophiolites. *Earth Planet. Sci. Lett.* **430**, 523–532.

Sutton S. R., Karner J., Papike J., Delaney J. S., Shearer C., Newville M., Eng P., Rivers M. and Dyar M. D. (2005) Vanadium K edge XANES of synthetic and natural basaltic glasses and application to microscale oxygen barometry. *Geochim. Cosmochim. Acta* **69**, 2333–2348.

Taylor S. R. (1989) Growth of planetary crusts. *Tectonophysics* **161**, 147–156.

Taylor S. R., McLennan S. M. and McCulloch M. T. (1983) Geochemistry of loess, continental crustal composition and crustal model ages. *Geochim. Cosmochim. Acta* **47**, 1897–1905.

Telus M., Dauphas N., Moynier F., Tissot F. L., Teng F.-Z., Nabelek P. I., Craddock P. R. and Groat L. A. (2012) Iron, zinc, magnesium and uranium isotopic fractionation during continental crust differentiation: The tale from migmatites, granitoids, and pegmatites. *Geochim. Cosmochim. Acta* **97**, 247–265.

Teng F.-Z., Dauphas N. and Helz R. T. (2008) Iron Isotope Fractionation During Magmatic Differentiation in Kilauea Iki Lava Lake. *Science* **320**, 1620–1622.

Teng F.-Z., Dauphas N. and Watkins J. M. (2017) Non-Traditional Stable Isotopes: Retrospective and Prospective. *Rev. Mineral. Geochemistry* **82**, 1–26.

Teng F.-Z., Dauphas N., Huang S. and Marty B. (2013) Iron isotopic systematics of oceanic basalts. *Geochim. Cosmochim. Acta* **107**, 12–26.

Thirlwall M. F. (1991) Long-term reproducibility of multicollector Sr and Nd isotope ratio analysis. *Chem. Geol.* **94**, 85–104.

Tian S., Moynier F., Inglis E. C., Rudnick R. L., Huang F., Chauvel C., Creech J. B., Gaschnig R. M., Wang Z. and Guo J. L. (2021) Zirconium isotopic composition of the upper continental crust through time. *Earth Planet. Sci. Lett.* **572**, 117086.

Tindle A. G. and Pearce J. A. (1981) Petrogenetic Modelling of in situ Fractional Crystallization in the Zoned Loch Doon Pluton, Scotland. *Contrib. to Mineral. Petrol.* **78**, 196–207.

Toplis M. J. and Carroll M. R. (1995) An Experimental Study of the Influence of Oxygen Fugacity on Fe-Ti Oxide Stability, Phase Relations, and Mineral--Melt Equilibria in Ferro-Basaltic Systems. *J. Petrol.* **36**, 1137–1170.

Toplis M. J. and Carroll M. R. (1996) Differentiation of Ferro-Basaltic Magmas under Conditions Open and Closed to Oxygen: Implications for the Skaergaard Intrusion and Other Natural Systems. *J. Petrol.* **37**, 837–858.

Toplis M. J. and Corgne A. (2002) An experimental study of element partitioning between magnetite, clinopyroxene and iron-bearing silicate liquids with particular emphasis on vanadium. *Contrib. to Mineral. Petrol.* **144**, 22–37.

Urey H. C. (1947) The Thermodynamic Properties of Isotopic Substances. *J. Chem. Soc.*, 562–581.

Van der Walt T. N., Strelow F. W. E. and Verheij R. (1985) The Influence Of Crosslinkage On The Distribution Coefficients And Anion Exchange Behaviour Of Some Elements In Hydrochloric Acid. *Solvent Extr. Ion Exch.* **3**, 723–740.

Vernon R. H. and Collins W. J. (2011) Structural Criteria for Identifying Granitic Cumulates. *J. Geol.* **119**, 127–142.

Wagner L. J., Kleinhanns I. C., Weber N., Babechuk M. G., Hofmann A. and Schoenberg R. (2021) Coupled stable chromium and iron isotopic fractionation tracing magmatic mineral crystallization in Archean komatiite-tholeiite suites. *Chem. Geol.* **576**, 120121.

Wang K., Moynier F., Barrat J. A., Zanda B., Paniello R. C. and Savage P. S. (2013) Homogeneous distribution of Fe isotopes in the early solar nebula. *Meteorit. Planet. Sci.* **48**, 354–364.

Wang K., Savage P. S. and Moynier F. (2014) The iron isotope composition of enstatite meteorites: Implications for their origin and the metal/sulfide Fe isotopic fractionation factor. *Geochim. Cosmochim. Acta* **142**, 149–165.

Wang Z.-Z., Liu S.-A., Liu J., Huang J., Xiao Y., Chu Z.-Y., Zhao X.-M. and Tang L. (2017) Zinc isotope fractionation during mantle melting and constraints on the Zn isotope composition of Earth's upper mantle. *Geochim. Cosmochim. Acta* **198**, 151–167.

Wang Z.-Z., Liu S.-A., Liu Z.-C., Zheng Y.-C. and Wu F.-Y. (2020) Extreme Mg and Zn isotope fractionation recorded in the Himalayan leucogranites. *Geochim. Cosmochim. Acta* **278**, 305–321.

Wawryk C. M. and Foden J. D. (2017) Iron-isotope systematics from the Batu Hijau Cu-Au deposit, Sumbawa, Indonesia. *Chem. Geol.* **466**, 159–172.

Wechsler B. A., Lindsley D. H. and Prewitt C. T. (1984) Crystal structure and cation distribution in titanomagnetites (Fe3-x,TixO4). *Am. Mineral.* **69**, 754–770.

Wei F., Prytulak J., Xu J., Wei W., Hammond J. O. S. and Zhao B. (2017) The cause and source of melting for the most recent volcanism in Tibet: A combined geochemical and geophysical perspective. *Lithos* **288**–**289**, 175–190.

Weinberg R. F., Vernon R. H. and Schmeling H. (2021) Processes in mushes and their role in the differentiation of granitic rocks. *Earth-Science Rev.* **220**, 103665.

Weis D., Kieffer B., Maerschalk C., Barling J., de Jong J., Williams G. A., Hanano D., Pretorius W., Mattielli N., Scoates J. S., Goolaerts A., Friedman R. M. and Mahoney J. B. (2006) High-precision isotopic characterization of USGS reference materials by TIMS and MC-ICP-MS. *Geochemistry, Geophys. Geosystems* **7**.

Wells P. R. A. (1977) Pyroxene Thermometry in Simple and Complex Systems. *Contrib. to Mineral. Petrol.* **62**, 129–139.

Wen G., Li J. W., Hofstra A. H., Koenig A. E., Lowers H. A. and Adams D. (2017) Hydrothermal reequilibration of igneous magnetite in altered granitic plutons and its implications for magnetite classification schemes: Insights from the Handan-Xingtai iron district, North China Craton. *Geochim. Cosmochim. Acta* **213**, 255–270.

Weyer S. and Ionov D. A. (2007) Partial melting and melt percolation in the mantle: The message from Fe isotopes. *Earth Planet. Sci. Lett.* **259**, 119–133.

Weyer S. and Schwieters J. (2003) High precision Fe isotope measurements with high mass resolution MC-ICPMS. *Int. J. Mass Spectrom.* **226**, 355–368.

Weyer S., Anbar A. D., Brey G. P., Münker C., Mezger K. and Woodland A. B. (2005) Iron isotope fractionation during planetary differentiation. *Earth Planet. Sci. Lett.* **240**, 251–264.

Wilke M., Partzsch G. M., Bernhardt R. and Lattard D. (2005) Determination of the iron oxidation state in basaltic glasses using XANES at the K-edge. *Chem. Geol.* **220**, 143–161.

Wilkes E. B., Wasylenki L. E. and Anbar A. D. (2010) Zinc Finger Takes on a Whole New Meaning: Reducing and Monitoring Zinc Blanks in the Isotope Lab. In *AGU Fall Meeting Abstracts,* Abstract V51B-2183.

Williams H. M. and Bizimis M. (2014) Iron isotope tracing of mantle heterogeneity within the source regions of oceanic basalts. *Earth Planet. Sci. Lett.* **404**, 396–407.

Williams H. M., Peslier A. H., McCammon C., Halliday A. N., Levasseur S., Teutsch N. and Burg J.-P. (2005) Systematic iron isotope variations in mantle rocks and minerals: The effects of partial melting and oxygen fugacity. *Earth Planet. Sci. Lett.* **235**, 435–452.

Williams H. M., Prytulak J., Woodhead J. D., Kelley K. A., Brounce M. and Plank T. (2018) Interplay of crystal fractionation, sulfide saturation and oxygen fugacity on the iron isotope composition of arc lavas: An example from the Marianas. *Geochim. Cosmochim. Acta* **226**, 224–243.

Williams K. B., Krawczynski M. J., Nie N. X., Dauphas N., Couvy H., Hu M. Y. and Alp E. E. (2016) The Role Of Differentiation Processes In Mare Basalt Iron Isotope Signatures. In *47th Lunar and Planetary Science Conference,* 2779.

Wones D. R. (1981) Mafic Silicates as Indicators of Intensive Variables in Granitic Magmas. *Min. Geol.* **31**, 191–212.

Workman R. K. and Hart S. R. (2005) Major and trace element composition of the depleted MORB mantle (DMM). *Earth Planet. Sci. Lett.* **231**, 53–72.

Wu F., Owens J. D., Huang T., Sarafian A., Huang K.-F., Sen I. S., Horner T. J., Blusztajn J., Morton P. and Nielsen S. G. (2019) Vanadium isotope composition of seawater. *Geochim. Cosmochim. Acta* **244**, 403–415.

Wu F., Owens J. D., Scholz F., Huang L., Li S., Riedinger N., Peterson L. C., German C. R. and Nielsen S. G. (2020) Sedimentary vanadium isotope signatures in low oxygen marine conditions. *Geochim. Cosmochim. Acta* **284**, 134–155.

Wu F., Qi Y., Perfit M. R., Gao Y., Langmuir C. H., Wanless V. D., Yu H. and Huang F. (2018) Vanadium isotope compositions of mid-ocean ridge lavas and altered oceanic crust. *Earth Planet. Sci. Lett.* **493**, 128–139.

Wu F., Qi Y., Yu H., Tian S., Hou Z. and Huang F. (2016) Vanadium isotope measurement by MC-ICP-MS. *Chem. Geol.* **421**, 17–25.

Wu F., Qin T., Li X., Liu Y., Huang J. H., Wu Z. and Huang F. (2015) First-principles investigation of vanadium isotope fractionation in solution and during adsorption. *Earth Planet. Sci. Lett.* **426**, 216–224.

Wu H., He Y., Bao L., Zhu C. and Li S. (2017) Mineral composition control on inter-mineral iron isotopic fractionation in granitoids. *Geochim. Cosmochim. Acta* **198**, 208–217.

Wu H., He Y., Teng F. Z., Ke S., Hou Z. and Li S. (2018) Diffusion-driven magnesium and iron isotope fractionation at a gabbro-granite boundary. *Geochim. Cosmochim. Acta* **222**, 671–684.

Wyborn D. (1983) Fractionation Processes in the Boggy Plain Zoned Pluton. PhD Thesis, Australian National University.

Wyborn D., Chappell B. W. and James M. (2001) Examples of convective fractionation in high-temperature granites from the Lachlan Fold Belt. *Aust. J. Earth Sci.* **48**, 531–541.

Wyborn D., Turner B. S. and Chappell B. W. (1987) The Boggy Plain Supersuite: A distinctive belt of I-type igneous rocks of potential economic significance in the Lachlan Fold Belt. *Aust. J. Earth Sci.* **34**, 21–43.

Xia Y., Li S. and Huang F. (2017) Iron and Zinc isotope fractionation during magmatism in the continental crust: Evidence from bimodal volcanic rocks from Hailar basin, NE China. *Geochim. Cosmochim. Acta* **213**, 35–46.

Xu L. J., He Y., Wang S. J., Wu H. and Li S. (2017) Iron isotope fractionation during crustal anatexis: Constraints from migmatites from the Dabie orogen, Central China. *Lithos* **284**, 171–179.

Xu L. J., Liu S. A., Wang Z. Z., Liu C. and Li S. (2019) Zinc isotopic compositions of migmatites and granitoids from the Dabie Orogen, central China: Implications for zinc isotopic fractionation during differentiation of the continental crust. *Lithos* **324–325**, 454–465.

Yang C., Liu S.-A., Zhang L., Wang Z.-Z., Liu P.-P. and Li S.-G. (2021) Zinc isotope fractionation between Cr-spinel and olivine and its implications for chromite crystallization during magma differentiation. *Geochim. Cosmochim. Acta* **313**, 277–294.

Ye H., Wu C., Brzozowski M. J., Yang T., Zha X., Zhao S., Gao B. and Li W. (2020) Calibrating equilibrium Fe isotope fractionation factors between magnetite, garnet, amphibole, and biotite. *Geochim. Cosmochim. Acta* **271**, 78–95.

Young E. D., Galy A. and Nagahara H. (2002) Kinetic and equilibrium mass-dependent isotope fractionation laws in nature and their geochemical and cosmochemical significance. *Geochim. Cosmochim. Acta* **66**, 1095–1104.

Zajacz Z., Halter W. E., Pettke T. and Guillong M. (2008) Determination of fluid/melt partition coefficients by LA-ICPMS analysis of co-existing fluid and silicate melt inclusions: Controls on element partitioning. *Geochim. Cosmochim. Acta* **72**, 2169–2197.

Zambardi T., Lundstrom C. C., Li X. and McCurry M. (2014) Fe and Si isotope variations at Cedar Butte volcano; insight into magmatic differentiation. *Earth Planet. Sci. Lett.* **405**, 169–179.

Zhang Y., Ni H. and Chen Y. (2010) Diffusion Data in Silicate Melts. *Rev. Mineral. Geochemistry* **72**, 311–408.

Zhao X.-M., Zhang H.-F., Zhu X.-K., Zhu B. and Cao H. (2015) Effects of melt percolation on iron isotopic variation in peridotites from Yangyuan, North China Craton. *Chem. Geol.* **401**, 96–110.

Zheng Q., Zhang Y., Xue N., Liu T. and Huang J. (2019) Vanadium occupation and its leachability differences in trioctahedral and dioctahedral mica. *RSC Adv.* **9**, 27615.

Zhu C., Lu W., He Y., Ke S., Wu H. and Zhang L. (2018) Iron isotopic analyses of geological reference materials on MC-ICP-MS with instrumental mass bias corrected by three independent methods. *Acta Geochim.* **37**, 691–700.

Zhu Y., Li M., Wang Z., Zou Z., Hu Z., Liu Y., Zhou L. and Chai X. (2019) High-precision copper and zinc isotopic measurements in igneous rock standards using large-geometry MC-ICP-MS. *At. Spectrosc.* **40**, 206–214.

Zhu Z. Y., Jiang S. Y., Yang T. and Wei H. Z. (2015) Improvements in Cu-Zn isotope analysis with MC-ICP-MS: A revisit of chemical purification, mass spectrometry measurement and mechanism of Cu/Zn mass bias decoupling effect. *Int. J. Mass Spectrom.* **393**, 34–40.

Zimmer M. M., Plank T., Hauri E. H., Yogodzinski G. M., Stelling P., Larsen J., Singer B., Jicha B., Mandeville C. and Nye C. J. (2010) The role of water in generating the calc-alkaline trend: New volatile data for aleutian magmas and a new tholeiitic index. *J. Petrol.* **51**, 2411–2444.

Appendix 1: Preliminary Fe-Zn Isotope Data from the Fagradalsfjall Eruption, 2021

A1.1 Introduction

On the 19th March, 2021, an effusive basaltic eruption began in the Fagradalsfjall complex on the Reykjanes Peninsula, Iceland. The eruption lasted for approximately six months until September 2021 (e.g. Bindeman et al., 2022). The eruption site is located approximately 30km from the capital Reykjavik, which permitted high resolution temporal sampling of the lavas over the course of 6 months by a team from the University of Iceland.

The major element, trace element, and radiogenic isotope (Sr, Nd, Pb) compositions of the lavas in this work have been measured as part of a global collaborative study lead by researchers at the University of Iceland. This work has been accepted for publication, but has not yet been published at the time of submitting this thesis. However, major element, trace element, and oxygen isotope compositions of another set of lavas collected from the eruption have recently been published (Bindeman et al., 2022; Figure A1.1). The lavas show remarkable temporal variations in major element, trace element and radiogenic isotope compositions. Lavas become progressively enriched in incompatible elements over time, which is thought to represent variation in the depth and degree of mantle melting, or potentially melting of mantle sources with different composition (Bindeman et al., 2022; Marshall et al., 2022; Sigmarsson et al., 2022). Bindeman et al. (2022) proposed that the trace element variations are primarily due to the presence of different mantle source components, including pyroxenitic and peridotitic mantle, and ancient recycled E-MORB and OIB.

During my PhD, the opportunity arose to collaborate on this project and measure the Fe and Zn isotopic composition of lavas from the eruption. The main aim was to investigate if the clear trace element chemical variability of the lavas was reflected in the Fe and/or Zn isotopic compositions. Although it is debated, lithological heterogeneity (i.e. different

mantle mineralogy) may potentially be detected using stable isotopes, due to the difference in bond strength and thus isotopic composition of different minerals (e.g. Williams and Bizimis, 2014).

This work has been presented at the 2022 EGU conference, Vienna (Stow et al., 2022). The preliminary data is included as an Appendix to this thesis because Fe and Zn isotopes have been used throughout this thesis to investigate intrusive plutons. The same methods as described in Chapter 2 were used to separate Fe and Zn from sample matrices and measure Fe and Zn isotope ratios by MC-ICP-MS. Throughout this thesis, there has been an emphasis on the complexities with analysing and interpreting WR data from intrusive samples. However, this work demonstrates that a WR analysis is completely appropriate when investigating fresh, aphyric, rapidly quenched lavas.

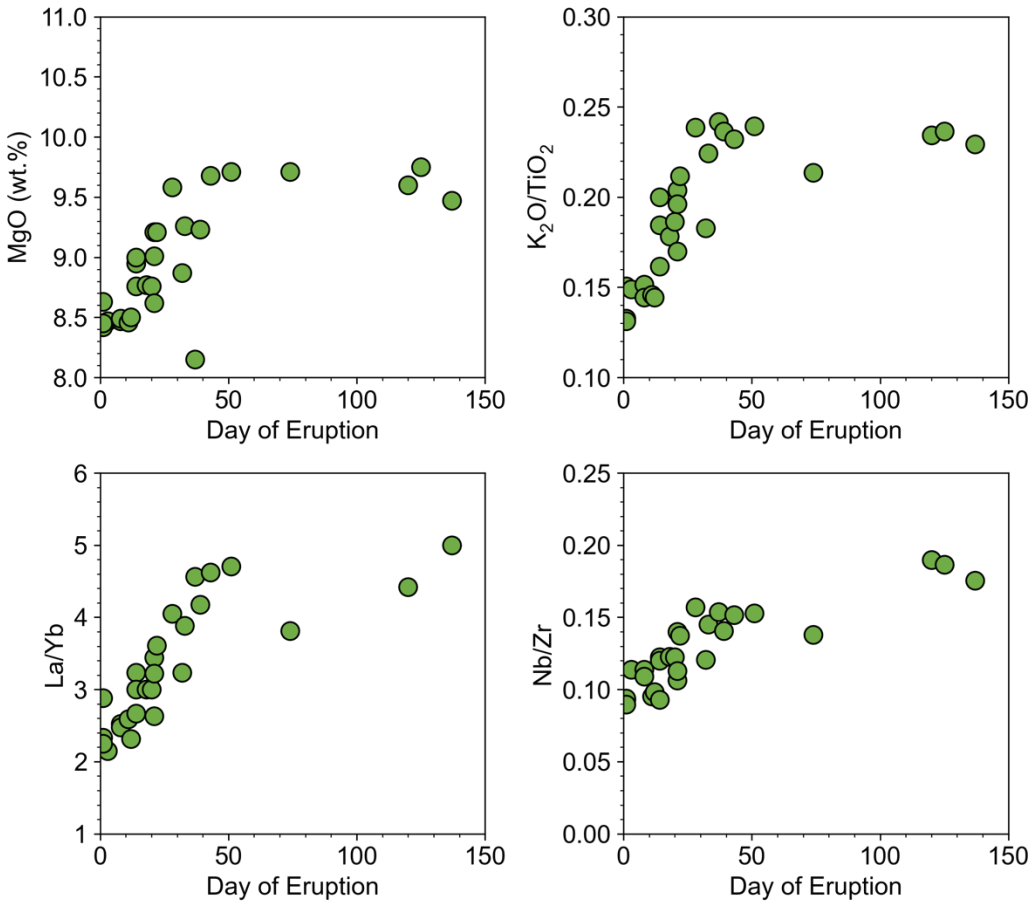

Figure A1.1. Temporal chemical variations in the Fagradalsfjall basalts. Data from Bindeman et al. (2022). Lavas become progressively enriched in incompatible elements over the first ~50 days of the eruption, and then compositions remain approximately constant until the end of the eruption.

A1.2 Fe and Zn isotope fractionation during mantle melting

The major element, trace element and radiogenic isotope data from the Fagradalsfjall eruption shows potential melting of a deeper, more enriched source over time (Marshall et al., 2022; Bindeman et al., 2022). Iron and Zn isotopes were used to determine whether or not the trace element heterogeneity was reflected in the isotopic composition, and thus potentially related to lithological variations in the mantle source.

The Fe isotopic compositions of peridotites and mantle derived basalts have been used to investigate mantle lithological heterogeneity, specifically the existence of enriched pyroxenite domains (e.g. Williams and Bizimis, 2014; Konter et al., 2016; Gleeson et al., 2020; Soderman et al., 2021). At equilibrium, Fe^{3+} bearing pyroxene should be enriched in heavy Fe isotopes compared to Fe^{2+} bearing olivine, so pyroxenite should be isotopically heavier than typical mantle peridotite (e.g. Williams and Bizimis, 2014; Sossi and O'Neill, 2017). Partial melting of isotopically heavy pyroxenite is thought to contribute to the heavy $\delta^{56}Fe$ signatures observed in some ocean island basalts (e.g. Konter et al., 2016; Nebel et al., 2019; Gleeson et al., 2020). However, there is debate if unrealistic proportions of pyroxenite would need to be melted to create these signatures (Soderman et al., 2021). There is also uncertainty in interpreting Fe isotope data because Fe isotopes can be fractionated by a multitude of processes in the mantle (Soderman et al., 2021).

Zinc isotopes are a useful complementary system to Fe isotopes. Zinc is only present as Zn^{2+} in terrestrial samples so Zn isotopes are not fractionated by changes in redox state which could potentially affect Fe isotopes (e.g. Moynier et al., 2017). Partial melting is thought to cause minor (~0.1‰) Zn isotopic fractionation and generate basalts that are isotopically heavier than the depleted mantle (Doucet et al., 2016; Wang et al., 2017; Sossi et al., 2018). The degree of Zn isotopic fractionation during mantle melting is thought to be controlled by the depth and degree of melting, and the specific lithology (i.e. isotopically light garnet bearing vs isotopically heavy spinel bearing; Doucet et al., 2016; Wang et al., 2017).

Therefore, although both Fe and Zn isotopes have been used to investigate mantle lithological heterogeneity, there is debate about how effective these systems are. The Fagradalsfjall lavas provide a unique time series where the trace element, major element,

and radiogenic isotope variations already suggest possible lithological heterogeneity. Therefore, the Fagradalsfjall lavas are an ideal sample set on which to test the efficacy of using Fe and Zn isotopes to track mantle lithological variations.

A1.3 Results

Figures A1.2 and A1.3 and Tables A1.1 and A1.2 show the Fe and Zn isotopic compositions of lavas collected over a 4-month time period between 21/03/21 and 29/07/21. The Fe and Zn isotopic compositions of the lavas are similar to basalts from the nearby Icelandic volcano Hekla, shown by the blue shaded areas on the figures (Schuessler et al., 2009; Chen et al., 2013). To date, there are no other published Fe or Zn isotope data for Icelandic basalts, but unpublished Fe data does show a range in δ^{56}Fe in different tectonic settings in Iceland (Simon Matthews, pers. comm.).

The Fe isotopic data spans a range of $\delta^{56}Fe_{NRM524}$ from 0.047 ± 0.042‰ (2SD) to 0.103 ± 0.055‰ (2SD), with an average isotopic composition of $\delta^{56}Fe_{NRM524}$ = 0.073 ± 0.033‰ (2SD, n= 14). There is no temporal variation in δ^{56}Fe in the lavas over the course of the eruption.

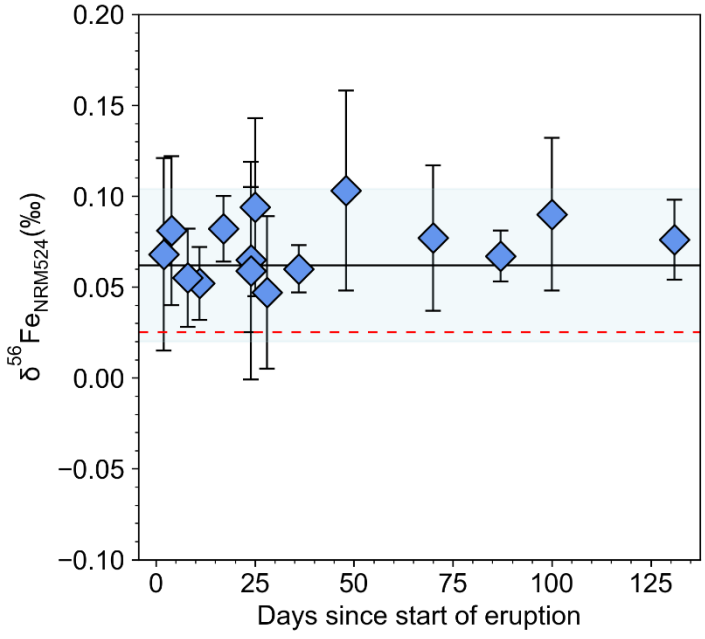

Figure A1.2. Iron isotopic composition of the Fagradalsfjall basalts. Error bars are 2SD of at least 3 measurements of each individual sample. The blue shaded area is the average isotopic composition of basalts from Hekla (0.062 ± 0.042‰; Schuessler et al., 2009). The red dashed line is the isotopic composition of the depleted MORB mantle (0.025 ± 0.025‰; Craddock et al., 2013).

The Zn isotopic composition of the lavas spans a range in $\delta^{66}Zn_{AA\text{-}ETH}$ from -0.059 ± 0.018‰ (2SD) to 0.013 ± 0.027‰ (2SD). There is a slight decrease in $\delta^{66}Zn$ around day 50, but there is not enough data from later in the eruption sequence to assess if this change is statistically significant.

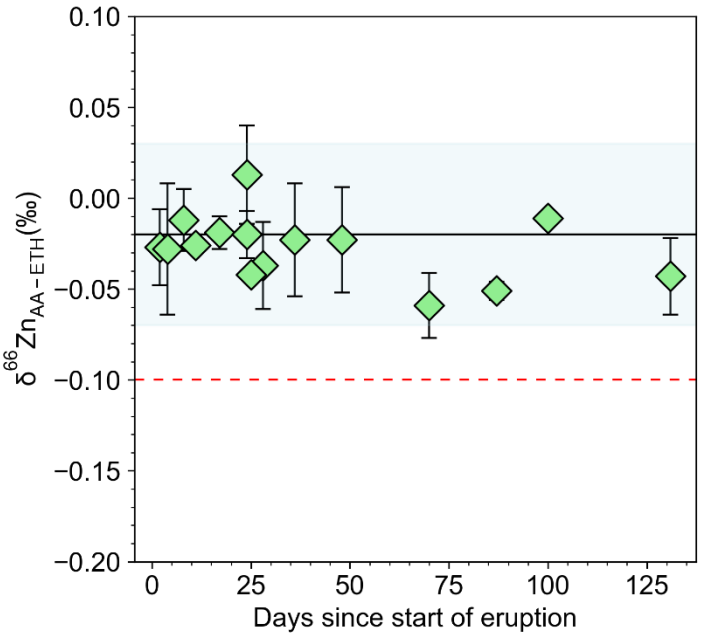

Figure A1.3. Zinc isotopic composition of the Fagradalsfjall basalts. Error bars are 2SD of at least 3 measurements of each individual sample. The blue shaded area is the average isotopic composition of basalts from Hekla ($\delta^{66}Zn_{AA\text{-}ETH}$ = -0.02 ± 0.05‰; Chen et al., 2013). The red dashed line is the composition of the depleted MORB mantle ($\delta^{66}Zn_{AA\text{-}ETH}$ = -0.10 ± 0.06‰; Wang et al., 2017).

Table A1.1. Iron isotope data for the Fagradalsfjall basalts relative to the NRM524 standard. Errors are given as 2 standard deviations of at least 3 measurements of an individual sample. Note that the sample names are the date the sample was taken, but eruption day refers to the day that the material was erupted.

Sample	Eruption Day	$\delta^{56}Fe_{NRM524}$ (‰)	2SD	$\delta^{57}Fe_{NRM524}$ (‰)	2SD	n
0321-2	2	0.068	0.053	0.108	0.086	3
0323-1	4	0.081	0.041	0.116	0.051	3
0330-2	11	0.052	0.020	0.086	0.05	3
0404-1	8	0.055	0.027	0.089	0.048	3
0405-1	17	0.082	0.018	0.108	0.029	3
0412-1	24	0.065	0.040	0.096	0.045	5
0412-2	24	0.059	0.060	0.106	0.089	6
0416-3	28	0.047	0.042	0.086	0.075	3
0416-4	25	0.094	0.049	0.135	0.059	6
0424-5	36	0.060	0.013	0.093	0.048	4
0511-2	48	0.103	0.055	0.138	0.089	6
0531-1	70	0.077	0.040	0.125	0.081	3
0616-1	87	0.067	0.014	0.108	0.086	3
0628-8	100	0.090	0.042	0.136	0.075	3
0729-1	131	0.076	0.022	0.123	0.014	3

Table A1.2. Zinc isotope data for the Fagradalsfjall basalts relative to the AA-ETH standard. Data can be recast relative to the JMC-Lyon standard using the correction of +0.28 (Archer et al., 2017). Errors are given as 2 standard deviations of at least 3 measurements of an individual sample. Note that the sample names are the date the sample was taken, but eruption day refers to the day that the material was erupted.

Sample	Eruption Day	$\delta^{66}Zn_{AA\text{-}ETH}$ (‰)	2SD	$\delta^{67}Zn_{AA\text{-}ETH}$ (‰)	2SD	n
0321-2	2	-0.027	0.021	-0.059	0.027	3
0323-1	4	-0.028	0.036	-0.074	0.029	3
0330-2	11	-0.026	0.003	-0.052	0.050	3
0404-1	8	-0.012	0.017	0.002	0.047	3
0405-1	17	-0.019	0.009	-0.024	0.013	3
0412-1	24	-0.020	0.013	-0.038	0.048	3
0412-2	24	0.013	0.027	-0.013	0.078	3
0416-3	28	-0.037	0.024	-0.066	0.043	3
0416-4	25	-0.042	0.003	-0.058	0.087	3
0424-5	36	-0.023	0.031	-0.028	0.031	3
0511-2	48	-0.023	0.029	-0.082	0.021	3
0531-1	70	-0.059	0.018	-0.121	0.070	3
0616-1	87	-0.051	0.005	-0.108	0.005	3
0628-8	100	-0.011	0.003	-0.043	0.070	3
0729-1	131	-0.043	0.021	-0.087	0.070	3

A1.4 Preliminary Conclusions

There is no resolvable variation in $\delta^{56}Fe$ in the Fagradalsfjall basalts during the eruption sequence. There may be a change in $\delta^{66}Zn$ around day 50, which should be investigated further alongside the trace element and radiogenic isotope data.

The lack of any overall variation in $\delta^{56}Fe$ and $\delta^{66}Zn$ throughout the eruption either suggests that the Fagradalsfjall basalts are not sampling any lithological heterogeneity in the mantle, and/or Fe or Zn isotopes are not sensitive enough to trace the presence of lithological heterogeneities. Once the full set of trace element, major element, radiogenic isotope, and stable isotope data is available, a clearer interpretation of the source and petrogenesis of the Fagradalsfjall basalts will be possible.

A1.5 References

Archer C., Andersen M. B., Cloquet C., Conway T. M., Dong S., Ellwood M., Moore R., Nelson J., Rehkämper M., Rehkämper R., Rouxel O., Samanta M., Shin K.-C., Sohrin Y., Takano S. and Wasylenki L. (2017) Inter-calibration of a proposed new primary reference standard AA-ETH Zn for zinc isotopic analysis. *J. Anal. At. Spectrom.* **32**, 415–419.

Bindeman I. N., Deegan F. M., Troll V. R., Thordarson T., Höskuldsson Á., Moreland W. M., Zorn E. U., Shevchenko A. V. and Walter T. R. (2022) Diverse mantle components with invariant oxygen isotopes in the 2021 Fagradalsfjall eruption, Iceland. *Nat. Commun.* **13**, 3737.

Chen H., Savage P. S., Teng F. Z., Helz R. T. and Moynier F. (2013) Zinc isotope fractionation during magmatic differentiation and the isotopic composition of the bulk Earth. *Earth Planet. Sci. Lett.* **369**, 34–42.

Craddock P. R., Warren J. M. and Dauphas N. (2013) Abyssal peridotites reveal the near-chondritic Fe isotopic composition of the Earth. *Earth Planet. Sci. Lett.* **365**, 63–76.

Doucet L. S., Mattielli N., Ionov D. A., Debouge W. and Golovin A. V. (2016) Zn isotopic heterogeneity in the mantle: A melting control? *Earth Planet. Sci. Lett.* **451**, 232–240.

Gleeson M. L. M., Gibson S. A. and Williams H. M. (2020) Novel insights from Fe-isotopes into the lithological heterogeneity of Ocean Island Basalts and plume-influenced MORBs. *Earth Planet. Sci. Lett.* **535**, 116114.

Konter J. G., Pietruszka A. J., Hanan B. B., Finlayson V. A., Craddock P. R., Jackson M. G. and Dauphas N. (2016) Unusual δ^{56}Fe values in Samoan rejuvenated lavas generated in the mantle. *Earth Planet. Sci. Lett.* **450**, 221–232.

Marshall, E., Rasmussen, M., Halldorsson, S., Matthews, S., Ranta, E., Sigmarsson, O., Robin, J., Barnes, J., Bali, E., Caracciolo, A., Guðfinnsson, G., and Mibei, G. (2022) An overview of the geochemistry and petrology of the mantle-sourced Fagradalsfjall eruption, Iceland, EGU General Assembly 2022, Vienna, Austria, 23–27 May 2022, EGU22-8304

Moynier F., Vance D., Fujii T. and Savage P. (2017) The Isotope Geochemistry of Zinc and Copper. *Rev. Mineral. Geochemistry* **82**, 543–600.

Nebel O., Sossi P. A., Bénard A., Arculus R. J., Yaxley G. M., Woodhead J. D., Rhodri Davies D. and Ruttor S. (2019) Reconciling petrological and isotopic mixing mechanisms in the Pitcairn mantle plume using stable Fe isotopes. *Earth Planet. Sci. Lett.* **521**, 60–67.

Sigmarsson, O., Marshall, E. W., Bosq, C., Auclair, D., Rasmussen, M. B., Kleine, B. I., Ranta, E. J., Matthews, S., Halldórsson, S. A., Jackson, M. G., Gudfinnsson, G. H., Bali, E., Stefánsson, A., and Gudmundsson, M. T. (2022) Basalt production controlled by mantle source fertility at Fagradalsfjall, Iceland, EGU General Assembly 2022, Vienna, Austria, 23–27 May 2022, EGU22-8479

Schuessler J. A., Schoenberg R. and Sigmarsson O. (2009) Iron and lithium isotope systematics of the Hekla volcano, Iceland - Evidence for Fe isotope fractionation during magma differentiation. *Chem. Geol.* **258**, 78–91.

Soderman C. R., Matthews S., Shorttle O., Jackson M. G., Ruttor S., Nebel O., Turner S., Beier C., Millet M. A., Widom E., Humayun M. and Williams H. M. (2021) Heavy δ^{57}Fe in ocean island basalts: A non-unique signature of processes and source lithologies in the mantle. *Geochim. Cosmochim. Acta* **292**, 309–332.

Sossi P. A., Nebel O., O'Neill H. S. C. and Moynier F. (2018) Zinc isotope composition of the Earth and its behaviour during planetary accretion. *Chem. Geol.* **477**, 73–84.

Sossi P. A. and O'Neill H. S. C. (2017) The effect of bonding environment on iron isotope fractionation between minerals at high temperature. *Geochim. Cosmochim. Acta* **196**, 121–143.

Stow, M., Prytulak, J., Burton, K., Nowell, G., Marshall, E., Rasmussen, M., Matthews, S., Ranta, E., and Caracciolo, A. (2022) Temporal Fe-Zn isotopic variations in the chemically heterogeneous Fagradalsfjall eruption, 2021, EGU General Assembly 2022, Vienna, Austria, 23–27 May 2022, EGU22-9846

Wang Z.-Z., Liu S.-A., Liu J., Huang J., Xiao Y., Chu Z.-Y., Zhao X.-M. and Tang L. (2017) Zinc isotope fractionation during mantle melting and constraints on the Zn isotope composition of Earth's upper mantle. *Geochim. Cosmochim. Acta* **198**, 151–167.

Williams H. M. and Bizimis M. (2014) Iron isotope tracing of mantle heterogeneity within the source regions of oceanic basalts. *Earth Planet. Sci. Lett.* **404**, 396–407.

Appendix 2: Copy of Stow et al. (2022)

Available online at www.sciencedirect.com

ScienceDirect

Geochimica et Cosmochimica Acta 320 (2022) 366–391

Geochimica et Cosmochimica Acta

www.elsevier.com/locate/gca

Integrated petrological and Fe-Zn isotopic modelling of plutonic differentiation

Madeleine A. Stow *, Julie Prytulak, Madeleine C.S. Humphreys, Geoffrey M. Nowell

Department of Earth Sciences, Durham University, Durham DH1 3LE, UK

Received 16 July 2021; accepted in revised form 17 December 2021; Available online 23 December 2021

Abstract

The upper continental crust is formed from chemically diverse granitic plutons. Active debate surrounds the range of physical conditions (P-T-X-fO_2) and differentiation processes which occur in mush bodies that solidify to form plutons. Transition metal stable isotopes are increasingly employed to trace magmatic processes in both extrusive lavas and intrusive plutonic suites, with a focus on analysis of whole rock powders. However, studies of plutonic suites often overlook the complex textures represented within coarse grained samples, and how these will influence whole rock isotopic compositions.

Here we examine the calc-alkaline Boggy Plain Zoned Pluton, SE Australia, which closely approximates closed system behaviour during magmatic differentiation. We combine petrological examination with Fe and Zn isotopic analysis of biotite, hornblende and magnetite mineral separates and whole rock powders. Whole rock Fe isotopic composition (as δ^{56}Fe) increases from 0.038‰ to 0.171‰ with decreasing MgO content, while mineral separates display heavy Fe isotope enrichment in the order magnetite > biotite = hornblende > pyroxene. A lack of correlation between whole rock Fe and Zn isotopic compositions suggests that the Fe isotopic variation is predominantly driven by closed system fractional crystallisation: specifically by the balance between crystallisation of isotopically heavy magnetite, and isotopically light silicates. To demonstrate this quantitatively, temperature dependent mineral-melt fractionation factors were derived from the mineral separate data ($\Delta^{56}Fe_{mag\text{-}melt} = 0.17 \times 10^6/T^2$ and $\Delta^{56}Fe_{bt/hbd\text{-}melt} = -0.12 \times 10^6/T^2$) and used to construct models that successfully reproduce the observed Fe isotopic variation during fractional crystallisation. These fractionation factors are compared to theoretical and empirical estimates from previous studies. We highlight that accurate determinations of temperature and modal mineralogy are critical when modelling Fe isotopic variations in plutonic suites. Successful interpretation of equilibrium Fe isotopic fractionation in a relatively simple calc-alkaline suite like the Boggy Plain Zoned Pluton paves the way for Fe isotopes to be used to investigate more complex mush bodies.

Keywords: Crystal mush; Granite; Differentiation; Transition metals; Fe-Zn stable isotopes

1. INTRODUCTION

It is now generally accepted that many crustal magma reservoirs are not melt-dominated systems, but instead are crystal-rich mushy regions where high melt fractions are present only transiently (e.g. Bachmann and Bergantz, 2004; Hildreth, 2004; Cashman et al., 2017; Sparks et al., 2019). The conceptual shift away from traditional melt-rich magma 'chambers' has generated new questions about storage conditions and differentiation processes in plutonic settings (e.g. Sparks et al., 2019). In melt dominated reservoirs, closed system in-situ fractional crystallisation was the intuitive differentiation mechanism to form chemically and lithologically zoned plutons (e.g. Tindle and Pearce, 1981; Wyborn et al., 1987). However, there is debate about how

* Corresponding author.
E-mail address: madeleine.a.stow@durham.ac.uk (M.A. Stow).

https://doi.org/10.1016/j.gca.2021.12.018
0016-7037/

Appendix

efficient crystal-liquid segregation processes are in evolved crystal mushes with a more viscous, low-density melt (Holness, 2018; Bachmann and Huber, 2019). Other processes such as magma recharge, mixing, assimilation and/or reactive porous flow (Jackson et al., 2018; Weinberg et al., 2021) may also be important controls on chemical variability. Despite these conceptual developments, chemical trends in plutonic suites are commonly modelled as the liquid line of descent of a liquid magma body undergoing fractional crystallisation and/or assimilation (e.g. Burton-Johnson et al., 2019), even though this may not be realistic.

The stable isotope variations of transition metals such as Fe are well established tracers of magmatic processes (e.g. see review in Dauphas et al., 2017). Equilibrium stable isotope fractionation in magmatic systems is fundamentally driven by differences in bond strength between minerals, melts and fluids. With Fe a major element constituent of melts and minerals, Fe isotopes can be a powerful tool to investigate processes such as partial melting (e.g. Williams et al., 2005; Weyer and Ionov, 2007; Williams and Bizimis, 2014; Xia et al., 2017; Xu et al., 2017), fractional crystallisation (e.g. Teng et al., 2008; Schuessler et al., 2009; Sossi et al., 2012; Du et al., 2017; He et al., 2017; Williams et al., 2018; Du et al., 2019) and fluid exsolution (e.g. Heimann et al. 2008; Telus et al., 2012). In minerals, Fe^{3+} preferentially enters tetrahedral sites whereas larger Fe^{2+} ions tend to be octahedrally coordinated. Tetrahedral Fe—O bonds are shorter and stiffer, and preferentially incorporate heavy Fe isotopes (Schauble, 2004). Variation in Fe oxidation state and coordination environment is thought to control the order of heavy Fe isotope enrichment in common rock forming minerals, such that: feldspar > magnetite > biotite, hornblende > pyroxene, olivine > ilmenite (Polyakov et al., 2007; Dauphas et al., 2012; Sossi et al., 2012; Sossi and O'Neill, 2017; Wu et al., 2017; Cao et al., 2019). In the coexisting melt, bond strength increases with $Fe^{3+}/\Sigma Fe$ ratio, and is greatest in high silica, polymerised, alkali rich melts (Dauphas et al., 2014). Fractionation factors (i.e. the difference in isotopic composition between phases) are also inversely proportional to T^2. Hence, equilibrium fractionation factors are controlled by mineral and melt chemistry, but also by intrinsic parameters such as temperature and fO_2. Taken together, this means that Fe isotopes could in principle address many important questions in petrology such as the relationship between melt redox state, crystallising assemblage and differentiation pathway. Conversely, processes such as additions of new batches of magma (Nebel et al., 2020), thermal diffusion (Zambardi et al., 2014; Gajos et al., 2016) and/or fluid exsolution (Poitrasson and Freydier, 2005; Heimann et al., 2008; Telus et al., 2012) may overprint these equilibrium isotopic fractionations.

Zinc and Fe isotopic compositions can be combined to further constrain magmatic processes and test the significance of possible overprinting processes. In contrast to Fe, Zn has relatively simple behaviour in magmatic systems (Telus et al., 2012; Moynier et al., 2017; Xia et al., 2017; McCoy-West et al., 2018). Zinc is a monovalent trace element present only as Zn^{2+}, so isotopic fractionation is not driven directly by changes in redox conditions. Numerous studies have demonstrated that negligible Zn isotope fractionation (<0.1‰) occurs during fractional crystallisation alone (Chen et al., 2013; Doucet et al., 2018; Huang et al., 2018). However, some high silica rhyolites, S-type granites and pegmatites have Zn isotopic compositions up to 0.6‰ heavier than mantle derived basalts (Telus et al., 2012; Xia et al., 2017; Doucet et al., 2018; Wang et al., 2020). Exsolution of isotopically light fluids (Telus et al., 2012; Wang et al., 2020) and/or enrichment of heavy Zn in the melt during partial melting (Doucet et al., 2018; Sossi et al., 2018a; Xu et al., 2019) are proposed to explain heavy Zn isotopic compositions in these evolved samples. Furthermore, extreme Zn isotopic compositions can be generated by chemical and/or thermal diffusion processes (e.g. McCoy-West et al., 2018). Doucet et al. (2020) discussed the principle of the coupled isotope systematics of Fe and Zn. Theoretically, since Fe and Zn are fractionated by different processes, Fe and Zn isotopes can be decoupled by interaction with fluids or sediments, and fO_2 variations during differentiation. However, a correlation between Fe and Zn isotopes in the same samples would imply that both are fractionated by the same processes. Hence, we employ a paired Fe-Zn approach in this study in order to better identify the causes of both Fe and Zn isotope fractionation in the BPZP.

Previous work on plutonic rocks has employed the isotopic composition of homogenous whole rock powders, in the absence of key information on petrographic textures (e.g. Poitrasson and Freydier, 2005; Schoenberg and von Blanckenburg, 2006; Heimann et al., 2008; Telus et al., 2012; Foden et al., 2015; Gajos et al., 2016; He et al., 2017; Du et al., 2019; Nebel et al., 2020). These types of studies make the implicit assumption that the whole rock composition is analogous to the evolving liquid composition. This may be valid for lavas, but is less appropriate for samples from coarse-grained, texturally complex plutonic suites. Plutonic rocks are typically formed of primocrysts surrounded by interstitial phases crystallised from trapped melt, so neighbouring phases in solidified samples were not necessarily in chemical equilibrium with each other. If chemical trends are generated by fractional crystallisation, samples have also experienced some degree of crystal-melt segregation. Therefore, whole rock composition of plutonic rocks is generally not equivalent to the melt composition at the time of crystallisation (Chappell and Wyborn, 2004; Vernon and Collins, 2011; Barnes et al., 2019).

It is crucial to consider this petrographic complexity when constructing geochemical models for plutonic suites. For example, it is common practice to choose the sample with the highest MgO content as the 'parental' magma composition for fractional crystallisation models of cogenetic lava suites, or to back-calculate a 'parental' magma composition from the most mafic sample in a suite (e.g. Sossi et al., 2016). However, this approach is problematic in plutonic settings where the most MgO rich samples are cumulates which do not represent real liquid compositions. Further, the competing controls on Fe isotope fractionation are generally difficult to distinguish using whole rock

Appendix

analyses alone. For example, a trend to increasingly heavy Fe isotopic composition with SiO_2 content is observed in a global compilation of igneous whole rocks, irrespective of tectonic setting. This variation has been ascribed to disparate processes such as fluid exsolution (Poitrasson and Freydier, 2005; Heimann et al., 2008; Telus et al., 2012), thermal diffusion (Zambardi et al., 2014; Gajos et al., 2016), fractional crystallisation and subsequent fO_2 variations (Sossi et al., 2012; Foden et al., 2015) and changing melt structure (Dauphas et al., 2014). It is critical to incorporate petrologic information, and, wherever analytically feasible, analyse individual mineral phases to help determine the cause of isotopic variation in a suite of related rocks.

Although intermediate to silicic plutons dominate the upper continental crust, only four previous studies have reported Fe isotopic compositions of mineral separates from granitoids (Heimann et al., 2008; Sossi et al., 2012; Telus et al., 2012; Wu et al., 2017). Of these, only Sossi et al. (2012) present mineral separates from a co-genetic plutonic suite (the low fO_2, tholeiitic Red Hills intrusion, Tasmania): there, fractionation of isotopically light pyroxene initially drives the residual magma to increasingly heavy Fe isotopic values. Upon saturation of isotopically heavy magnetite, the Fe isotopic composition of the residual magma decreases. However, these results are not necessarily directly applicable to the intermediate-silicic plutons which make up the majority of the continental crust. The continental crust is dominantly formed of I-type plutons, which crystallise from high fO_2 magmas derived from igneous protoliths, and crystallise mineral assemblages dominated by phases like biotite, hornblende and magnetite (e.g. Chappell and White, 2001).

Here, we present an integrated Fe and Zn isotope investigation of mineral separates and whole rocks from the I-type Boggy Plain Zoned Pluton, SE Australia, in order to unpick the controls on transition metal isotope fractionation in hydrous granites. The Boggy Plain Zoned Pluton formed via closed system fractional crystallisation of a calc-alkaline parent magma (Wyborn, 1983; Wyborn et al., 1987; Ickert, 2010). We combine textural and petrographic examination with Fe-Zn isotopic analysis of both whole rock powders and mineral separates for the main hosts of Fe and Zn (i.e. biotite, hornblende and magnetite). We construct temperature dependent models of isotopic fractionation that also take into account the effects of variation in modal mineralogy and fractionation factors. We consider how realistic different modelling approaches are in plutonic environments and provide a framework for further modelling of Fe isotopic variations in more complex mush settings.

2. GEOLOGICAL BACKGROUND

2.1. Boggy Plain Zoned Pluton

The Boggy Plain Zoned Pluton (BPZP) is a type example of a concentrically zoned pluton formed by closed system fractional crystallisation of a calc-alkaline magma (Wyborn, 1983; Wyborn et al., 1987; Hoskin et al., 2000; Wyborn et al., 2001; Chappell and Wyborn, 2004; Ickert, 2010; Ickert et al., 2011; Chappell et al., 2012; Park et al., 2013; Iles, 2017). The pluton outcrops over an area of 36 km^2 in the northern region of the Kosciuszko batholith in the Lachlan Fold Belt, SE Australia (Fig. 1A), and crystallised at 417 ± 2 Ma (Ickert, 2010). The BPZP is concentrically zoned, from minor gabbroic and dioritic cumulates at the rim, through granodiorite to granite, with lithologies becoming progressively more felsic towards the centre of the pluton. The granite is cut by late-stage aplitic dykes (Wyborn, 1983; Fig. 1B). Towards the centre of the pluton, there is increasing bulk rock and mineral Fe^{3+}/Fe^{2+}, decreasing proportions of ilmenite and increasing proportions of magnetite, all of which are evidence supporting an increase in magma fO_2 of >1 log unit during differentiation (Wyborn, 1983; Czamanske and Wones, 1973). Temperature estimates from two-pyroxene and biotite-apatite geothermometry give crystallisation temperatures ranging from 900 °C in the diorite to 700 °C in the felsic lithologies (Wyborn, 1983).

The continuous chemical trends in the BPZP were generated by *in situ* fractional crystallisation of a single body of intermediate magma in an upper crustal magma chamber (Wyborn, 1983; Wyborn et al., 1987). Recent isotopic studies (Nd, Hf, U-Pb, O; Ickert, 2010; Ickert et al., 2011; Iles, 2017) suggest minor amounts (10–20%) of crustal assimilation (consistent with our ancillary data, see Supplementary Information and later discussion). However, decoupling between major element and isotopic trends suggests this assimilation probably occurs prior to upper crustal magma differentiation (Ickert, 2010) which is the focus of our study. Therefore, we consider the Boggy Plain pluton to be as representative a candidate for closed system fractionation as is feasible in nature.

2.2. Whole rock chemical variations

Major and trace element compositions of whole rock samples typically show smooth, continuous trends with SiO_2 or MgO content, consistent with fractional crystallisation of a single parent magma (Wyborn, 1983; Fig. 2). Whole rock concentrations of highly incompatible elements (e.g. Rb) increase with differentiation, and concentrations of elements compatible in the crystallising bulk assemblage decrease with differentiation (e.g. Sr, compatible in plagioclase).

To understand the behaviour of Fe isotopes, the causes of variations in Fe concentration within the suite must first be understood. Variations in whole rock Fe_2O_3 and $Fe^{3+}/\Sigma Fe$ are plotted against MgO content in Fig. 2. Fe_2O_3 concentrations are scattered in samples with MgO > 4.5 wt.%. These higher MgO samples are petrographically identified as cumulates due to the presence of framework forming primocrysts and interstitial phases. Here "cumulate" is taken to mean that samples have experienced a concentration of crystals and/or crystal-melt segregation (e.g. Chappell and Wyborn, 2004). Therefore, the scatter in whole rock compositions of samples with MgO > 4.5 wt.% is likely due to variability in the modal mineralogy and amount of trapped interstitial melt, rather than representing variation

Appendix

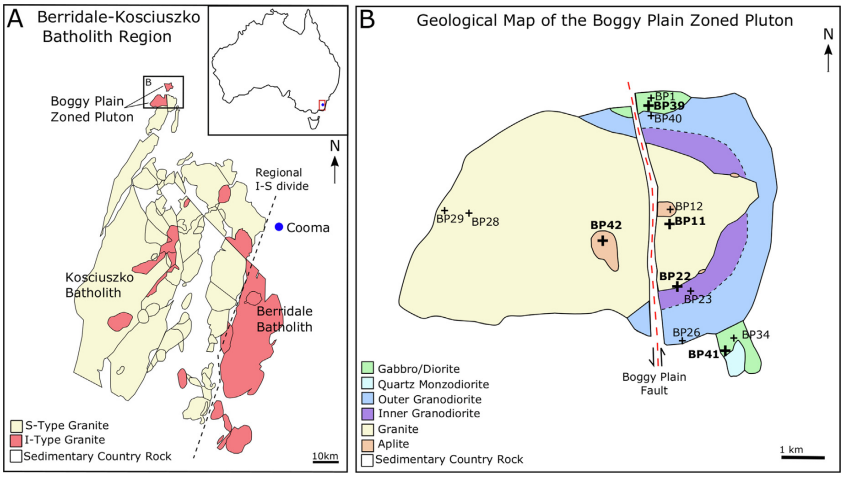

Fig. 1. (A) Map of the Berridale and Kosciuszko batholiths in the SE of the Lachlan Fold Belt (adapted from Ickert, 2010). The Boggy Plain Zoned Pluton is located in the North of the batholith. The sedimentary country rock is mostly Silurian-Ordovician aged turbidites and shales (Wyborn, 1983). (B) Geological map of the Boggy Plain Zoned pluton showing the concentric zonation from a gabbroic rim to a granitic core (adapted from Wyborn, 1983). The geological map is a reconstruction after subtracting 4.9 km left lateral strike slip motion on the Boggy Plain Fault (Wyborn et al., 1987). The black dashed line shows the boundary between the inner and outer granodiorite. Sample localities are indicated by crosses; those in bold are ones from which mineral separates were picked.

in liquid composition. For Fe_2O_3 the scatter is dictated by the proportion of interstitial magnetite, biotite and hornblende. Similar scatter is observed for TiO_2, Zn and Sr. Below 4.5 wt.% MgO, the Fe_2O_3 trend is smooth, reflecting crystallisation of magnetite, biotite and hornblende as part of the near-liquidus mineral assemblage. The whole rock compositions are therefore more representative of the fractionating magma when MgO is below 4.5 wt.%. Whole rock $Fe^{3+}/\Sigma Fe$ increases with differentiation, and together with increasing $Fe^{3+}/\Sigma Fe$ in both biotite and hornblende in more evolved samples is thought to reflect an increase in the magma fO_2 during differentiation (Wyborn, 1983).

3. SAMPLE SELECTION AND PETROGRAPHY

Based on major and trace element variations, samples or sampling localities from Wyborn (1983) were carefully selected to represent the complete range of lithologies observed in the BPZP. Samples were either those originally collected by Wyborn (1983), or from a field campaign in 2013 that resampled the same locations from Wyborn (1983).

We examined every sample petrographically, building on observations in Wyborn (1983) and Hoskin et al. (2000). A full description of all samples is given in Table S1. Two distinct textural groups of minerals were identified, primocrysts (i.e. euhedral crystals which likely crystallised unconfined from the magma) and interstitial phases (with anhedral morphologies which crystallised in confined spaces from the interstitial melt). In the context of the stable isotopic evolution of a cogenetic suite undergoing fractional crystallisation, we assume that only primocryst crystallisation will influence the isotopic composition of the evolving residual magma. However, the modal abundance of both primocryst and interstitial phases regulates the whole rock isotopic composition.

The lithologies in the BPZP progress from gabbro to monzodiorite to granodiorite to granite (Fig. 1). This is typical of a calc-alkaline differentiation sequence in showing early magnetite saturation and crystallisation of hydrous phases such as biotite and hornblende, interpreted as the result of high initial H_2O content and high fO_2 (e.g. Sisson and Grove, 1993; Zimmer et al., 2010). Gabbros and diorites form the outer rim of the pluton and are only exposed over an area of <2 km^2 (Fig. 1). Samples BP41 (gabbro) and BP39 (diorite) contain framework-forming primocrysts and interstitial phases, a texture typical of cumulate rocks (e.g. Irvine, 1982). In the gabbro, the main framework forming primocryst phases are plagioclase (An_{60}) (55%), clinopyroxene (15%), orthopyroxene (10%) and minor olivine (<10%) (Fig. 3A). Anhedral biotite (5%) occupies interstitial sites (Fig. 3B). Titanomagnetite (here referred to as magnetite) and ilmenite are rare (<1%) and found as inclusions within pyroxenes and as discrete grains associated with biotite in interstitial sites. In the diorite, the abundance of clinopyroxene is higher, and hornblende can be found with biotite in interstitial sites and as rims surrounding pyroxene crystals (Fig. 3C), sug-

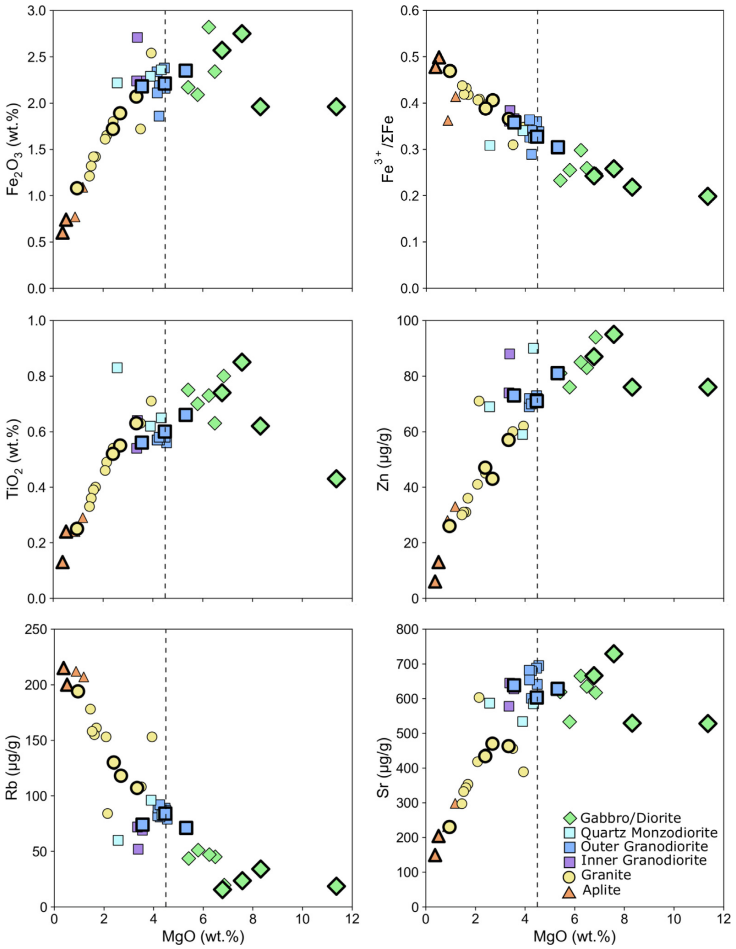

Fig. 2. Chemical variations in the BPZP. Whole rock compositional data from Wyborn (1983). Large symbols with bold outlines are those chosen for isotopic analysis in this study. The dashed line approximates the separation of liquids (<4.5 wt.% MgO) from cumulate rocks (>4.5 wt.% MgO; see text). The line also corresponds to the composition of sample BP26, which is used as the parental melt composition in subsequent models. The scatter in the granodiorite data (blue and purple squares) is attributed to the compositional zoning in the granodiorite. (For interpretation of the references to colour in this figure legend, the reader is referred to the web version of this article.)

gesting that both biotite and hornblende crystallised from melt films and trapped interstitial melt. Magnetite is almost exclusively associated with biotite and is therefore interpreted as an interstitial phase.

In more evolved samples, those with >58 wt.% SiO_2 and <4.5 wt.% MgO, biotite and hornblende replace orthopyroxene and clinopyroxene as the main ferromagnesian primocryst phases. Sample BP40 (5.32 wt.% MgO) shows the transition between the two textural regimes (Fig. 3D). Pyroxenes (20%) have irregular crystal habits whereas hornblende (15%) and biotite (5%) begin to show more prismatic shapes. Oxides (1%) are predominantly magnetite and exist mostly as inclusions within biotite and hornblende. Plagioclase (35%) remains a primocryst phase, and there is the first appearance of interstitial orthoclase (often poikilitic) (15%).

Appendix

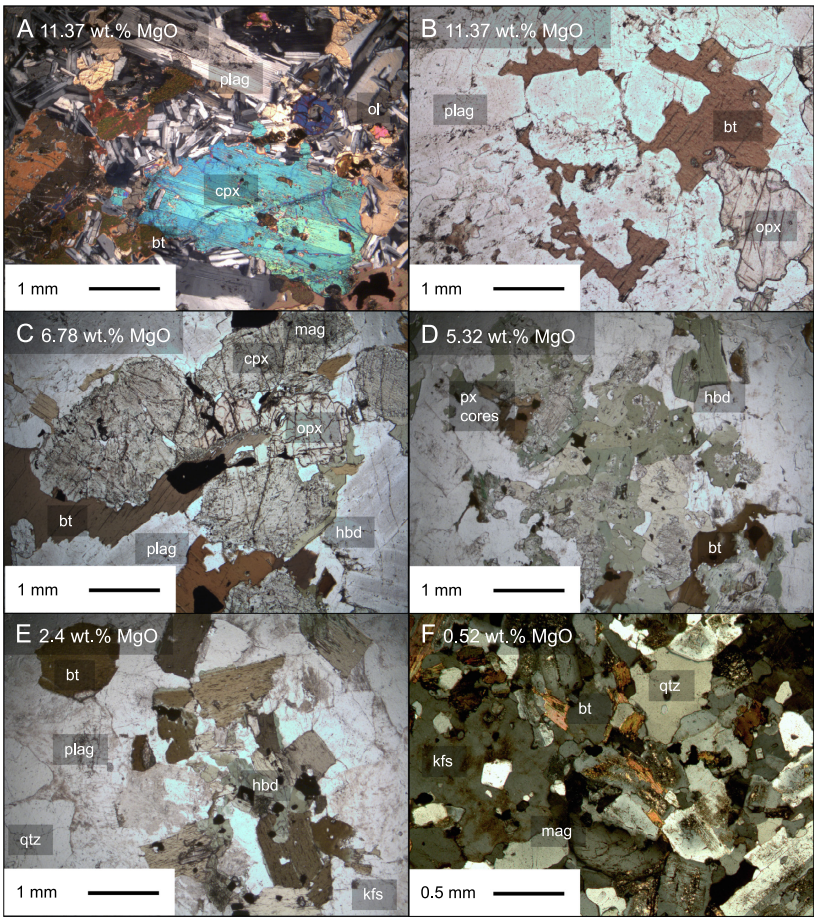

Fig. 3. Petrographic textures in the BPZP. (A) BP41 showing a typical cumulate texture, containing euhedral primocrysts of pyroxene and plagioclase, and minor interstitial biotite. (B) BP41 showing anhedral morphologies of interstitial biotite. (C) BP39 containing euhedral pyroxene primocrysts with biotite and hornblende rims. (D) BP40 transitional textures. Pyroxene cores surrounded by hornblende and biotite. (E) BP28 containing euhedral biotite and hornblende primocrysts, and no pyroxene present. (F) BP12 showing fine grained aplitic texture. Abbreviations opx = orthopyroxene, plag = plagioclase, ol = olivine, bt = biotite, hbd = hornblende, mag = titanomagnetite, kfs = K-feldspar. The BPZP samples are very coarse grained and therefore photomicrographs can show small scale features, but do not effectively demonstrate larger scale textural information. Full thin section scans are provided in the Supplementary Information.

In the granites (BP11, BP22, BP28 and BP29; Table S1), euhedral biotite (10%) and hornblende (15%) are the main ferromagnesian primocryst phases (Fig. 3E), interpreted to have fully replaced the pyroxenes. Quartz (20%), plagioclase (35%) and orthoclase (20%) are the most abundant phases. There is 1% magnetite and minor interstitial titanite (<1%).

A fine-grained aplite (BP42 and BP12) is found in the core of the pluton. Quartz, orthoclase and plagioclase make up over 95% of the modal mineralogy, with minor biotite and magnetite (<5% by volume; Fig. 3F). There is no hornblende present in the aplite. Biotite commonly shows a green colour along cleavage planes from chloritization by Cl-rich fluids.

Appendix

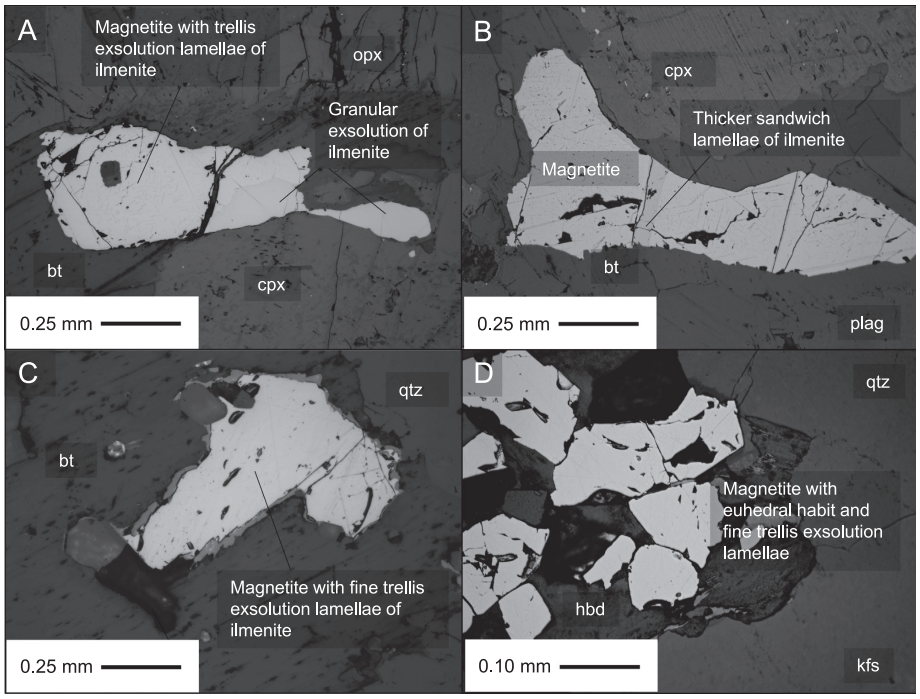

Fig. 4. Typical textures and morphologies of Fe-Ti oxides in the BPZP. (A) and (B) BP39 diorite, containing interstitial magnetite grains (white/yellow colour) with anhedral morphologies, showing granular exsolution of ilmenite and trellis exsolution of ilmenite (grey/brown colour). (C) and (D) BP22 granodiorites contain small, euhedral grains with very fine trellis exsolution lamellae. This is typical of magnetite grains in samples with WR MgO < 4.5 wt.%. (For interpretation of the references to colour in this figure legend, the reader is referred to the web version of this article.)

Fe-Ti oxide minerals such as titanomagnetite can host a large proportion of the Fe in the system. Low temperature oxyexsolution of titanomagnetite is common during slow cooling, resulting in exsolution of ilmenite (Frost and Lindsley, 1991). Exsolved ilmenite can occur as lamellae along {111} planes of the magnetite host (both thin trellis-type and thicker sandwich-type) or as anhedral granules on the edge of magnetite grains (Frost and Lindsley, 1991). The exchange of Fe and Ti between magnetite and ilmenite during oxyexsolution can alter the Fe isotopic composition of the oxide minerals (e.g. Dziony et al., 2014; Chen et al., 2014; Cao et al., 2019). In the mafic cumulates, there is evidence for low temperature re-equilibration of interstitial magnetite grains. Granular exsolution and trellis and sandwich exsolution lamellae of ilmenite are only present in the mafic diorites (Fig. 4A and B). In the more evolved samples, primocryst titanomagnetite only shows very fine trellis-type exsolution lamellae (Fig. 4C and D). There is no variation in exsolution style with grain size. The bulk magnetite separates were hand-picked from a 125–250 μm size fraction following an initial magnetic separation. This size fraction is much larger than the scale of exsolution features (Fig. 4), which permits sampling of magnetite grains in bulk with their hosted ilmenite lamellae. We are therefore confident that our approach allows us to determine the isotopic composition of bulk titanomagnetite at the time of crystallisation.

4. ANALYTICAL METHODS

Twelve whole rock samples, along with biotite, hornblende and magnetite mineral separates from five of the samples, were measured for Fe-Zn isotopic compositions. Biotite, hornblende and magnetite separates were chosen because they host the majority of Fe and Zn in the system, with modal proportions varying over the differentiation sequence. Mass balance calculations show that approximately 30% of total Fe is hosted in magnetite, and the remainder distributed equally between biotite and hornblende. In contrast, <5% of the total Zn is hosted in mag-

Appendix

netite, but up to 80% is hosted in biotite. Chemical purification and isotopic analysis were conducted at the Arthur Holmes Isotope Geology Laboratory, Durham University. Iron and Zn fractions were obtained from the same digestion. This reduces the amount of material required for isotopic analyses, which is beneficial when picking mineral separates. Since Fe is present at weight percent concentrations in all rock forming minerals, and Zn is a trace element with maximum concentrations of several hundred μg/g, the Zn concentration of mineral separates and whole rock powders dictated the mass of sample required for analysis. Biotite and hornblende mineral separates have Zn concentrations from 138 to 292 μg/g (Wyborn, 1983). Mass balance considerations based on whole rock and mineral separate Zn concentrations in Wyborn (1983) show that magnetite should contain 50–150 μg/g Zn. Approximately 1.5 μg total Zn is required to make at least three Zn isotopic measurements. Therefore, a minimum of 10–20 mg biotite and hornblende and 30–40 mg magnetite were handpicked under binocular microscope from a 125–250 μm size fraction, avoiding crystal fragments containing obvious inclusions. For whole rock analyses (9–95 μg/g Zn; Wyborn, 1983), approximately 50–70 mg of powder was required. The Nd isotopic compositions of four whole rock samples were also analysed in order to verify the absence of significant crustal assimilation (Ickert, 2010), as described in Section S2 of the Supplementary Information.

4.1. Chemical isolation

Mineral separates and whole rock samples were ground to homogenous powders using a Fritsch Pulverisette 0 agate motor and ball. Whole rock powders and silicate mineral separates were dissolved in 3 ml of Teflon Distilled (TD) 29 M HF and 1 ml of TD 16 M HNO_3 in Savillex beakers on a hotplate at 160 °C. The magnetite separates frequently contained silicate inclusions, which potentially have distinctive Fe and Zn isotopic compositions. Therefore, magnetite samples were dissolved in 5 ml TD 6 M HCl in Savillex beakers on a hotplate at 120 °C. This allowed full dissolution of the oxides, and the remaining insoluble silicates were separated by centrifugation.

Samples were refluxed in 1 ml TD 6 M HCl before being loaded onto anion exchange columns containing 2 ml Bio-Rad AG1-X8 resin (200–400 mesh) following the method of Sossi et al. (2015). The resin was initially pre-cleaned by shaking with TD 6 M HCl and MQ H_2O. Following this initial fines removal and pre-clean step, 20 ml of resin was further cleaned using a BioRad Econo-Pac column with 250 ml reservoir connected to a vacuum box. Cleaning involved eluting a sequence of 200 ml each of MQ H_2O, TD 3 M HCl, MQ H_2O, TD 3 M HNO_3, MQ H_2O. This was repeated three times. The cleaning steps were necessary to reduce Zn procedural blanks to below 20 ng total Zn.

Most matrix elements were eluted with 14 ml TD 6 M HCl, followed by Fe collection in 6 ml TD 0.5 M HCl, and finally Zn collection in 4 ml TD 3 M HNO_3. The isolated Zn fractions were passed through the same column procedure a second time. Column yields were consistently >95% for Fe and Zn, in agreement with Sossi et al. (2015). Total procedural blanks ranged from 10 to 30 ng for Fe and 10–20 ng for Zn during the course of the study.

4.2. Isotope ratio measurement

Iron isotopic measurements were carried out on a Neptune MC-ICP-MS in medium resolution mode ($m/\Delta m \sim 6000–8000$) to resolve Fe from isobaric molecular oxide and nitride interferences. Masses ^{53}Cr, ^{54}Fe, ^{56}Fe, ^{57}Fe, ^{58}Fe, ^{60}Ni and ^{61}Ni were measured on Faraday cups L4, L2, L1, C, H1, H2 and H4 respectively. ^{53}Cr was monitored in order to correct for the atomic interference of ^{54}Cr on ^{54}Fe. $10^{11}\Omega$ resistors were used on all cups with the exception of L1, where a $10^{10}\Omega$ resistor was connected to allow measurement of >50 V signals on ^{56}Fe. Standards and samples were run at a concentration of 8–10 μg/g Fe. Typical sensitivity with wet plasma in medium resolution was ~5 V/ppm on ^{56}Fe using a Savillex CF50 concentric flow nebuliser with 50 μl/min uptake rate connected to a Glass Expansion borosilicate glass Cinnabar microcyclonic spray chamber. An individual measurement was comprised of 1 block of 50 cycles with an integration time of 4.194 s per cycle, total analysis time around 3.5 minutes. Approximately 2 μg of Fe was consumed during one analysis at a concentration of 10 μg/g. Mass bias and instrument drift was corrected by standard sample bracketing with the IRMM-014 Fe standard and/or the isotopically indistinguishable IRMM-524 standard (Craddock and Dauphas, 2011).

Iron isotopic data are reported in delta notation relative to the IRMM-014 standard, where $\delta^X Fe = [(^X Fe/^{54}Fe)_{sample}/(^X Fe/^{54}Fe)_{IRMM\text{-}014} - 1] \times 10^3$ and X is mass 56 or 57. All samples show mass dependent behaviour (Fig. 5A). Samples were measured a minimum of three times, and errors are reported as 2SD of all individual measurements of the sample. USGS reference materials GSP-2, BHVO-2 and BIR-1a were processed and analysed alongside all unknowns, giving $\delta^{56}Fe$ values within the range of previous measurements (e.g. Craddock and Dauphas, 2011; Liu et al., 2014; Table 1). Long term reproducibility for Fe isotopic measurements was ±0.050‰ (n = 148, 2SD) based on measurement of an internal lab standard '*Romil Fe*' over the course of the study.

Zinc isotopic measurements were carried out on a Neptune Plus MC-ICP-MS in low resolution mode ($m/\Delta m \sim 400$). Masses ^{62}Ni, ^{63}Cu, ^{64}Zn, ^{65}Cu, ^{66}Zn, ^{67}Zn and ^{68}Zn were measured in Faraday cups L3, L2, L1, C, H1, H2 and H3 respectively, with $10^{11}\Omega$ resistors connected to all cups. ^{62}Ni was monitored to correct for the isobaric interference of ^{64}Ni on ^{64}Zn. ^{63}Cu and ^{65}Cu were used for mass bias corrections. Samples were run at concentrations of 0.750 μg/g Zn and doped with 0.375 μg/g Cu. Typical sensitivity with wet plasma was ~4 V/ppm on ^{66}Zn using the same introduction setup as for Fe. Mass bias and instrument drift was corrected by a combination of external element doping with Cu, and standard sample bracketing with the AA-ETH Zn solution (Archer et al., 2017). Data in this study is reported relative to AA-ETH, where

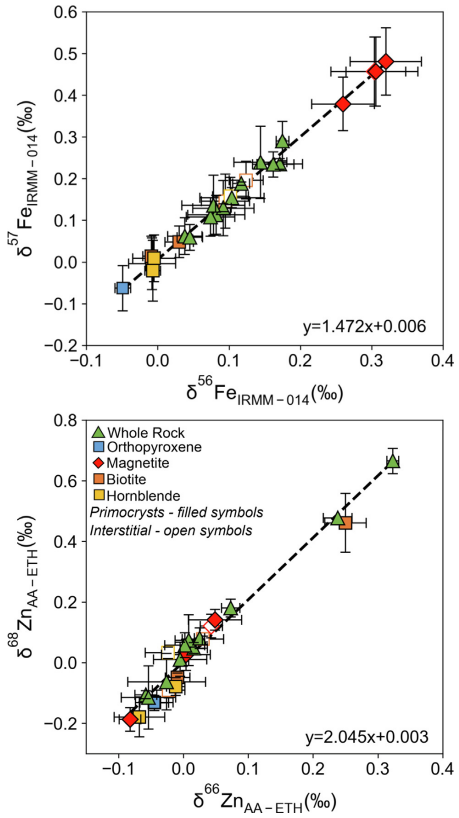

Fig. 5. Three-isotope plots for (A) Fe (δ^{56}Fe vs δ^{57}Fe) and (B) Zn (δ^{66}Zn vs δ^{68}Zn). The slopes of the linear regressions are 1.47 and 2.01 respectively, which are consistent with the gradients predicted by mass dependent fractionation laws (i.e. ~1.5 and 2; Young et al., 2002).

$\delta^{X}Zn = [(^{X}Zn/^{64}Zn)_{sample}/(^{X}Zn/^{64}Zn)_{AA\text{-}ETH} - 1] \times 10^{3}$ and X is mass 66, 67 or 68. All samples show mass dependent behaviour (Fig. 5B).

The AA-ETH Zn solution has an isotopic composition indistinguishable from the certified isotopic reference material IRMM-3702, while its δ^{66}Zn value is offset relative to the commonly used reference standard JMC 3-0749 L, also known as JMC Lyon Zn (Maréchal et al., 1999) by +0.28 ± 0.02‰ (Archer et al., 2017). The majority of previous studies report data relative to JMC Lyon, but the standard is no longer available. Data from this study is recast relative to JMC-Lyon for comparison, using the correction of Archer et al. (2017). The IRMM-3702 Zn standard was measured regularly throughout this study, giving an average isotopic composition of $\delta^{66}Zn_{AA\text{-}ETH} = 0.015 \pm 0.035$ ‰ (n = 83, 2SD), in agreement with Archer et al. (2017). Several USGS reference materials were processed and analysed alongside unknowns, giving δ^{66}Zn values which agree with previous measurements (e.g. Sossi et al., 2015; Chen et al., 2015; Table 1).

5. RESULTS

5.1. Iron isotopic data

Iron isotopic data for whole rock and mineral separates are shown in Tables 1 and 2. Major and trace element compositions for whole rocks and mineral separates are from Wyborn (1983) and are given in the Supplementary Information.

The whole rock δ^{56}Fe values vary with whole rock MgO content. δ^{56}Fe values increase from 0.038 ± 0.024‰ in the most mafic samples to a maximum value of 0.171 ± 0.032‰ at 0.52 wt.% MgO/73.07 wt.% SiO_2 (Fig. 6). This range is

Table 1
Iron and Zinc isotopic composition of BPZP whole rock samples and USGS reference materials. Whole rock (WR) MgO content from Wyborn (1983). Iron isotopic ratios are quoted relative to the IRMM 014 standard. Zinc isotopic ratios were measured relative to the AA-ETH standard. These are recast relative to the JMC-Lyon standard using the correction of +0.280‰ (Archer et al., 2017). Errors are quoted as 2 standard deviations of the mean of all measurements of the sample. If <3 analyses could be made, errors are reported as 2SE (+).

Sample	Rock Type	WR MgO (wt.%)	$\delta^{56}Fe_{IRMM-014}$ (‰)	2SD	$\delta^{57}Fe_{IRMM-014}$ (‰)	2SD	n	$\delta^{66}Zn_{JMC-Lyon}$ (‰)	$\delta^{66}Zn_{AA-ETH}$ (‰)	2SD	$\delta^{68}Zn_{AA-ETH}$ (‰)	2SD	n
BP34	Diorite	8.32	0.038	0.024	0.062	0.044	3	0.222	−0.058	0.017	−0.106	0.013	3
BP1	Diorite	7.58	0.045	0.018	0.059	0.031	3	0.226	−0.054	0.042	−0.115	0.104	3
BP39	Diorite	6.78	0.078	0.044	0.136	0.072	3	0.275	−0.005	0.041	0.011	0.056	3
BP40	Granodiorite	5.32	0.074	0.034	0.108	0.046	4	0.282	0.002	0.031	0.057	0.041	3
BP26	Granodiorite	4.48	0.092	0.043	0.129	0.066	5	0.288	0.008	0.021	0.074	0.084	3
BP23	Granodiorite	3.56	0.082	0.040	0.113	0.047	3	0.305	0.025	0.008	0.081	0.034	3
BP29	Granite	3.34	0.092	0.011	0.130	0.009	3	0.353	0.073	0.014	0.180	0.029	3
BP22	Granite	2.69	0.175	0.009	0.290	0.047	6	0.254	−0.026	0.060	−0.063	0.093	4
BP28	Granite	2.40	0.104	0.045	0.154	0.024	4	0.296	0.016	0.021	0.048	0.018	3
BP11	Granite	0.96	0.162	0.029	0.234	0.030	4						
BP12	Aplite	0.52	0.171	0.032	0.253	0.013	3	0.603	0.323	0.009	0.665	0.041	3
BP42	Aplite	0.38	0.144	0.037	0.239	0.087	4	0.518	0.238	0.022+	0.477	0.025+	2
	Replicate		0.117	0.012	0.188	0.004	3						
USGS Reference Materials													
GSP-2			0.150	0.033	0.217	0.034	13	0.956	0.676	0.059	0.954	0.104	3
BHVO-2			0.139	0.031	0.221	0.042	8						
BIR-1a			0.034	0.016	0.048	0.024	4	0.288	0.008	0.040	0.052	0.104	6

Table 2
Iron and Zinc isotopic composition of BPZP mineral separates. For mineral textures, I denotes interstitial phases, and P primocrysts. Iron isotopic ratios are quoted relative to the IRMM 014 standard. Zinc isotopic ratios were measured relative to the AA-ETH standard. These are recast relative to the JMC-Lyon standard using the correction of +0.280‰ (Archer et al., 2017). Errors are quoted as 2 standard deviations of the mean of all measurements of the sample.

Sample	Mineral Phase	Texture	$\delta^{56}Fe_{IRMM-014}$ (‰)	2SD	$\delta^{57}Fe_{IRMM-014}$ (‰)	2SD	n	$\delta^{66}Zn_{JMC-Lyon}$ (‰)	$\delta^{66}Zn_{AA-ETH}$ (‰)	2SD	$\delta^{68}Zn_{AA-ETH}$ (‰)	2SD	n
BP41	Biotite	I	0.124	0.024	0.196	0.045	3	0.310	0.030	0.032	0.078	0.010	3
BP39	Orthopyroxene	P	−0.049	0.011	−0.063	0.054	4	0.235	−0.045	0.022	−0.133	0.025	3
	Biotite	I	0.095	0.034	0.146	0.065	8	0.257	−0.023	0.025	−0.091	0.025	3
	Hornblende	I	0.102	0.025	0.158	0.045	3	0.256	−0.024	0.035	0.033	0.019	3
	Magnetite	I	0.304	0.061	0.457	0.083	3	0.323	0.043	0.017	0.121	0.039	3
BP22	Biotite	P	−0.008	0.033	−0.004	0.062	7	0.235	−0.045	0.029	−0.132	0.018	3
	Hornblende	P	−0.005	0.030	0.009	0.056	3	0.268	−0.012	0.014	−0.079	0.029	3
	Magnetite	P	0.260	0.044	0.379	0.064	5	0.329	0.049	0.041	0.141	0.034	3
BP11	Biotite	P	0.030	0.020	0.048	0.038	3	0.271	−0.009	0.019	−0.049	0.015	3
	Hornblende	P	−0.007	0.011	−0.021	0.073	4	0.212	−0.068	0.039	−0.179	0.066	3
	Magnetite	P	0.320	0.050	0.481	0.081	4	0.198	−0.082	0.017	−0.187	0.039	3
BP42	Biotite	P	−0.009	0.012	0.014	0.048	4	0.530	0.250	0.032	0.461	0.097	3
	Magnetite	P	0.306	0.042	0.457	0.083	4	0.284	0.004	0.038	0.026	0.051	3

similar to values previously measured in other I-type granitoids, which typically show maximum $\delta^{56}Fe \sim 0.21‰$ with differentiation (Foden et al., 2015).

5.1.1. Mineral-mineral fractionation factors

The Fe isotopic composition of the mineral separates is shown in Table 2. As expected, the mineral separates are enriched in ^{56}Fe relative to ^{54}Fe in the order magnetite > biotite = hornblende > orthopyroxene, in agreement with previous studies (e.g. Heimann et al., 2008; Sossi et al., 2012; Wu et al., 2017). This order of isotopic enrichment also supports observations from NRIXS and Mössbauer spectroscopy that β factors, and consequently $\delta^{56}Fe$ values, increase with $Fe^{3+}/\Sigma Fe$ (Polyakov and Mineev, 2000; Polyakov et al., 2007; Schoenberg et al., 2009).

The isotopically lightest mineral separate measured is the orthopyroxene, which contains octahedrally coordinated ferrous iron ($\delta^{56}Fe = -0.049 \pm 0.011‰$; n = 3). Magnetite ($^{IV}Fe^{3+}\ ^{VI}(Fe^{2+},Fe^{3+})\ O_4$) is the isotopically heaviest mineral phase measured. Magnetite $\delta^{56}Fe$ values are approximately constant across the differentiation sequence, varying from 0.260‰ to 0.320‰. Biotite and hornblende mineral separates have $Fe^{3+}/\Sigma Fe$ and $\delta^{56}Fe$ values between these extremes, consistent with a combination of Fe^{2+} and Fe^{3+} ions typically found in VI-fold coordination (e.g. Leake et al., 1997; Rieder et al., 1999). Biotite mineral separates span a range of $\delta^{56}Fe$ from −0.009‰ to 0.124‰ and hornblende separates from −0.007‰ to 0.102‰. Biotite and hornblende have identical isotopic compositions to each other in individual samples, with an average $\Delta^{56}Fe_{bt\text{-}hbd}$ of 0.009‰. However, biotite and hornblende separates from interstitial phases have heavier isotopic composition than primocrysts.

5.2. Zinc isotopic data

Zinc isotopic data for whole rock and mineral separates is presented in Tables 1 and 2. The Zn isotopic data is reported relative to the AA-ETH standard (Archer et al., 2017). With the exception of aplite samples BP12 and BP42, whole rock Zn isotopic compositions fall between $\delta^{66}Zn_{AA\text{-}ETH}$ of $-0.058 \pm 0.017‰$ and $0.073 \pm 0.014‰$ (Fig. 7). This is comparable to whole rock samples from the Hekla cogenetic lava suite ($\delta^{66}Zn_{AA\text{-}ETH}$ of −0.06‰ to +0.05‰; Chen et al. (2013)). With the exception of the aplites, samples are all within error of the average Zn isotopic composition of mantle derived magmas from Chen et al. (2013) of $\delta^{66}Zn_{AA\text{-}ETH} = 0.01 \pm 0.08‰$.

The silicate and oxide mineral separates from samples BP41, BP39, BP22 and BP11 have isotopic compositions within error of the average isotopic composition of basaltic magmas in Chen et al. (2013). Given that Zn^{2+} (0.74 Å) has a similar ionic radius to Fe^{2+} (0.78 Å) (Shannon, 1976), Zn^{2+} most likely substitutes for VI-fold coordinated Fe^{2+} in biotite, hornblende and magnetite. Silicate and oxide primocrysts from the same sample have Zn isotopic compositions that are indistinguishable within error, which is consistent with these theoretical considerations of bonding environment. Xu et al. (2019) also measured identical $\delta^{66}Zn$

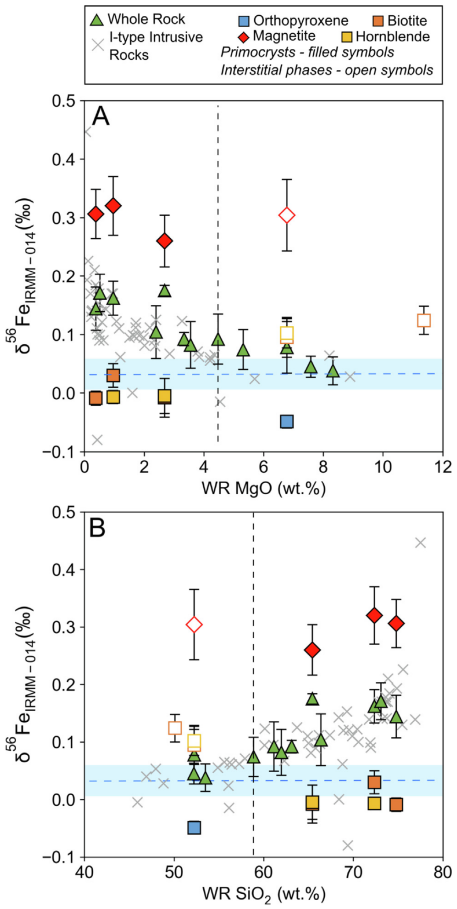

Fig. 6. Iron isotopic composition of whole rocks and mineral separates against WR MgO (A) and SiO_2 (B) content. Errors are plotted as 2SD of at least 3 individual measurements of each sample. A compilation of data from other plutonic I-type rocks is shown by the grey crosses (Poitrasson and Freydier, 2005; Schoenberg and von Blanckenburg, 2006; Heimann et al., 2008; Telus et al., 2012; Foden et al., 2015). The vertical dashed line shows the divide between cumulate samples and liquids as in Fig. 2. The blue shaded area is the estimate for the Bulk Silicate Earth from Sossi et al. (2016) of $\delta^{56}Fe = 0.033 \pm 0.027‰$. (For interpretation of the references to colour in this figure legend, the reader is referred to the web version of this article.)

in biotite, hornblende and magnetite separates from one melanosome from the Dabie Orogen, central China.

However, in the aplite sample (BP42), the magnetite has an isotopic composition within error of the other separates, but the biotite has a significantly heavier $\delta^{66}Zn_{AA\text{-}ETH}$ of 0.250 ± 0.032‰. The whole rock isotopic composition plots between the isotopic composition of biotite and magnetite, at a value of 0.238 ± 0.022‰ (2SE). The other aplite sample (BP12) also has a heavy whole rock isotopic composition of $\delta^{66}Zn_{AA\text{-}ETH} = 0.323 \pm 0.009‰$.

6. DRIVERS OF FE-ZN ISOTOPIC VARIATION IN THE BOGGY PLAIN ZONED PLUTON

Previous geochemical and petrographic work on the BPZP indicates that its evolution very closely approximates closed system fractional crystallisation (Wyborn, 1983; Wyborn et al., 1987; Wyborn et al., 2001). Fractional crystallisation is commonly proposed as the dominant control on Fe isotopic variation in both extrusive (e.g. Teng et al., 2008; Schuessler et al., 2009; Du et al., 2017; Xia

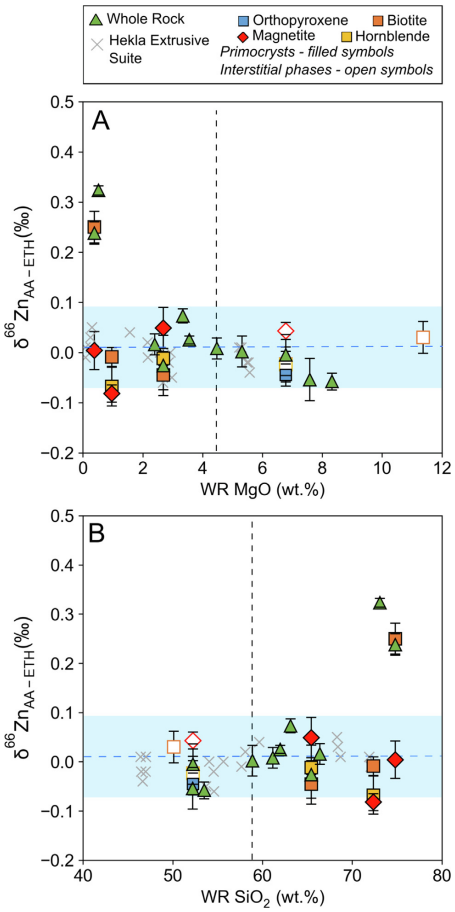

Fig. 7. Zinc isotopic compositions of whole rock and mineral separates against WR MgO (A) and SiO_2 (B) content. Errors are plotted as 2SD of at least 3 individual measurements of each sample. Grey crosses are co-genetic lavas from Hekla, Iceland (Chen et al., 2013). The vertical dashed line shows the divide between cumulate samples and liquids as in Fig. 2. Given that the pristine and depleted mantle have distinct Zn isotopic composition, and that heavy Zn isotopes can become concentrated in the melt during mantle partial melting (e.g. Wang et al., 2017; Huang et al., 2018; Sossi et al., 2018a), the average isotopic composition of mantle derived magmas from Chen et al., 2013 ($\delta^{66}Zn_{AA\text{-}ETH}$ of 0.01 ± 0.08‰) is shown by the blue shaded area for comparison.

et al., 2017) and plutonic (e.g. Telus et al., 2012; Sossi et al., 2012; Foden et al., 2015; Du et al., 2019) suites. However, Fe isotopes can be fractionated by multiple other processes, which are often difficult to distinguish using whole rock analyses alone (e.g. Soderman et al., 2021). In contrast, fractional crystallisation is thought to cause <0.1‰ Zn isotopic fractionation (e.g. Chen et al., 2013; Doucet et al., 2018; Huang et al., 2018), but there is the potential for larger magnitudes of Zn isotopic fractionation by fluid alteration (e.g. Telus et al., 2012; Wang et al., 2020). In this section we first exclude processes that do not contribute to Fe-Zn isotopic variations in the BPZP, then assess the controls on inter-mineral isotopic fractionation factors necessary for developing internally consistent, fully quantitative models of Fe isotopic variations in calc-alkaline magmas during fractional crystallisation.

Appendix

6.1. Impact of crustal assimilation and fluid exsolution on Fe-Zn isotopic compositions

Although the observed isotopic variation could, in part at least, reflect source mantle heterogeneity (e.g. Williams and Bizimis, 2014; He et al., 2017; Gleeson et al., 2020) or crustal contamination (e.g. Schoenberg and von Blanckenburg, 2006; Hiebert et al., 2016), we infer that these processes have had a negligible impact on the BPZP magma. Age-corrected whole rock εNd_i measured in this study show less than 2 epsilon unit variation (Table S2; Fig. S1), with values very similar to Ickert (2010) that are typical of magmas derived from an upper mantle source. The Nd isotopic data would be consistent with either the source of the BPZP being contaminated with ~10% crustal material or the parent magma from a homogenous source assimilating approximately 10% crustal material, with the exposed Ordovician-Silurian aged sedimentary country rock proposed as a possible assimilant (Ickert, 2010). However, irrespective of whether the Nd isotopic composition is inherited from a contaminated source or early assimilation of crust, the magma appears to subsequently evolve via closed system fractional crystallisation, without further assimilation. Therefore, the effect of crustal assimilation on the variation of Fe-Zn isotopic compositions within the BPZP magma is likely to be negligible.

There is variation in both Fe and Zn whole rock isotopic compositions across the BPZP differentiation sequence (Figs. 6 and 7). However, for Zn, this range is exaggerated by the presence of two isotopically heavy aplite samples. The remaining whole rock samples fall within a 0.13‰ range, with similar $\delta^{66}Zn$ values to the Hekla extrusive suite (Chen et al., 2013). Biotite, hornblende and magnetite separates also fall within this range. The mafic cumulates have the lightest $\delta^{66}Zn$ values, which may be due to the accumulation of isotopically light pyroxene which hosts the majority of Zn in these samples. There is no systematic variation in whole rock $\delta^{66}Zn$ with MgO content for the samples with <4.5 wt.% MgO, which are interpreted to be representative of evolving magma composition. This suggests that Zn isotopes are not significantly fractionated during fractional crystallisation of the BPZP, agreeing with the findings of previous studies (e.g. Chen et al., 2013; Huang et al., 2018).

The heavy Zn isotopic composition of the aplites is most likely due to fluid alteration. Zn can be mobilised as chloride complexes in magmatic fluids (e.g. Zajacz et al., 2008). Zn-chlorides are predicted to be enriched in ^{64}Zn (Fujii et al., 2014), and exsolution of isotopically light Zn bearing fluids may therefore explain the heavy Zn isotopic compositions up to $\delta^{66}Zn_{AA\text{-}ETH} = 0.60‰$ observed in some rhyolites and pegmatites (Telus et al., 2012; Xia et al., 2017; Doucet et al., 2020). Chloritized biotite present in the most felsic lithologies of the BPZP indicates the presence of Cl-rich fluids during late-stage crystallisation. Hence, the heavy $\delta^{66}Zn$ values for the aplites and the biotite separates from BP42 are most likely caused by loss of isotopically light Zn during the chloritization of the biotite grains.

Iron isotopes can also potentially be fractionated by fluids. Fluid exsolution has been invoked to explain the heavy Fe isotopic compositions of some granites and pegmatites (Poitrasson and Freydier, 2005; Heimann et al., 2008; Telus et al., 2012). Ferrous iron is predicted to complex strongly with chloride ions in magmatic fluids; the fluid should therefore be isotopically lighter than Fe^{3+} bearing silicate minerals and melt (Fujii et al., 2014). However, both aplite samples have whole rock $\delta^{56}Fe$ values similar to the other whole rock samples. Hence, we are confident that late-stage fluid exsolution or alteration has not led to fractionation of Fe isotopes in the BPZP.

In addition, there is no correlation between whole rock $\delta^{56}Fe$ and $\delta^{66}Zn$ in the BPZP (Fig. S2). The existence of coupled Fe-Zn isotope signatures in cratonic and mantle samples has previously been proposed to demonstrate that Fe and Zn isotopes are fractionated by the same processes during continental crust formation (Doucet et al., 2020). However, that co-variation is likely due to initial partial melting processes, rather than fractionation during magmatic evolution. Therefore, a lack of correlation supports the interpretation that Fe and Zn are not fractionated by the same processes in the BPZP.

Having interpreted the heavy Zn isotopic signatures as a consequence of fluid alteration, and given that there is no significant variation in $\delta^{66}Zn$ in the remainder of the whole rock data, we focus only on the Fe isotopic variations in the BPZP in the following sections.

6.2. Fe isotopic fractionation during fractional crystallisation

As demonstrated above, the Fe isotopic variation in the BPZP is not significantly influenced by source heterogeneity, crustal contamination or fluid exsolution. We therefore infer that the observed trend in whole rock $\delta^{56}Fe$ is driven by fractional crystallisation. The variation in magma $\delta^{56}Fe$ during fractional crystallisation is dependent on the fractionation of Fe between the melt and the crystallising assemblage. Fractionation factors are influenced primarily by temperature, Fe oxidation state and coordination environment (Polyakov and Mineev, 2000; Polyakov et al., 2007; Dauphas et al., 2014; Sossi and O'Neill, 2017), with the nature and number of surrounding cations exerting a minor control (Rabin et al., 2021).

In order to evaluate quantitatively the isotopic fractionation resulting from fractional crystallisation, we require accurate knowledge of mineral-melt fractionation factors. For the BPZP, we specifically require values for hydrous phases like biotite and hornblende, which host the majority of the Fe in the system. Fractionation factors can be determined experimentally (e.g. Shahar et al., 2008; Sossi and O'Neill, 2017) or empirically from mineral separates (e.g. Sossi et al., 2012; Wu et al., 2017; Ye et al., 2020; Nie et al., 2021). Alternatively, reduced partition function ratios (β factors) in relevant phases can be derived using spectroscopic techniques (e.g. Mössbauer and nuclear resonance inelastic X-ray scattering (NRIXS)), and used to theoretically determine bond force constants ($\langle F \rangle$) and fractionation factors (e.g. Polyakov et al., 2007; Dauphas et al., 2012; Roskosz et al., 2015; Dauphas et al., 2014; Nie et al., 2021). In addition, β factors and force constants can also be obtained from first principle calculations based

Appendix

on density functional theory (e.g. Blanchard et al., 2009; Rabin et al., 2021).

The strength of our BPZP dataset is that we report isotopic variations in mineral separates across a single closed system differentiation sequence, for which temperature and fO_2 estimates already exist. These mineral separate data can be used to derive accurate and internally consistent mineral-mineral and mineral-melt fractionation factors, as outlined below. These are reflective of natural variation in T-X-fO_2 conditions in calc-alkaline settings and include the first measurements for biotite and hornblende across a differentiation sequence within a single cogenetic pluton.

6.3. Controls on inter-mineral fractionation factors in the BPZP

Inter-mineral fractionation factors are expressed in the form $\Delta^{56}Fe_{min\text{-}min} = A \times 10^6/T^2$. Hence, accurate crystallisation temperature estimates are critical, given the temperature dependence of fractionation ($\Delta \propto 1/T^2$; Urey, 1947; Schauble, 2004). Crystallisation temperatures can be difficult to define given the wide solidus-liquidus interval for granites, and difficulty in determining the true composition of coexisting liquids. Ickert et al. (2011) calculated zircon crystallisation temperatures between 750 and 850 °C in all zones of the BPZP. However, given that zircon is one of the last phases to crystallise, these temperatures are not equivalent to the crystallisation temperatures of the Fe bearing primocrysts. We estimated primocryst crystallisation temperatures for the BPZP samples using multiple geothermometers (Table 3). These results indicate a 200 °C temperature range between the most primitive and evolved samples.

Biotite, hornblende and magnetite separates are divided into two textural groups: crystals with euhedral morphologies (primocrysts) assumed to crystallise from the main magma body, and anhedral crystals crystallised from trapped interstitial melt. Biotite, hornblende and magnetite are present as interstitial phases in the mafic cumulates, whereas they are primocrysts in samples with MgO < 4.5 wt.%. This is important for understanding isotopic fractionation because we assume that crystallisation of primocrysts will drive changes in the composition of the residual magma, whereas crystallisation of trapped interstitial melt will only drive local changes. Additionally, interstitial phases crystallised from isolated melt pockets may not have crystallised in chemical or isotopic equilibrium with each other, or the main magma body. Thus, mineral-mineral fractionation factors for interstitial phases may not reflect isotopic equilibrium.

Since primocryst biotite and hornblende have identical isotopic compositions in individual samples, and because biotite is present over a wider SiO_2 range than hornblende in the BPZP, we focus on variations in the magnetite-biotite fractionation factor ($\Delta^{56}Fe_{mag\text{-}bt}$) and assume this to be equal to $\Delta^{56}Fe_{mag\text{-}hbd}$. Within a cogenetic suite, variations in mineral-mineral fractionation factors can be controlled by variation in mineral composition, Fe coordination environment and/or temperature (e.g. Schauble, 2004). In the BPZP the $\Delta^{56}Fe_{mag\text{-}bt}$ increases with $Fe^{3+}/\Sigma Fe$ of biotite (values given in Wyborn, 1983), and this coincides with increasing SiO_2 content, increasing WR $Fe^{3+}/\Sigma Fe$ and decreasing crystallisation temperature (Figs. 8 and 9).

Fig. 9 shows the variation in $\Delta^{56}Fe_{mag\text{-}bt}$ of the BPZP samples with temperature, using the temperature estimates given in Table 3. Here we compare these values to temperature dependent biotite-magnetite fractionation factors derived by three different methods in previous studies. The red area represents the relationship derived by Ye et al. (2020) of $\Delta^{56}Fe_{mag\text{-}bt} = 0.28\ (\pm 0.07) \times 10^6/T^2$, from measurements of biotite and magnetite separates in a banded iron formation metamorphosed at a temperature of 538 ± 39 °C. The blue and green lines show $\Delta^{56}Fe_{mag\text{-}bt}$ derived theoretically using bond force constants ($\langle F \rangle$) obtained from NRIXS and *ab initio* studies respectively, following the method of Dauphas et al. (2014) (Eq. (1)).

$$\Delta^{56}Fe_{A-B} = 2853 \times \frac{\langle F_A \rangle - \langle F_B \rangle}{T^2} \quad (1)$$

Thus far, only Nie et al. (2021) have determined values for the bond force constant of biotite ($\langle F_B \rangle$). These values are for the biotite Fe endmember annite, and were determined by both NRIXS (188 ± 16 N/m) and DFT

Table 3
Temperature determinations for the BPZP. Calculations from [1]Putirka (2008, Eq. 27b at 1.5 kbar); [2]Holland and Blundy (1994, Edenite-richerite thermometer at 1.5 kbar); [3]Ludington (1978); [4]Wells (1977). Values using [3] and [4] are given in Wyborn (1983). All mineral chemistry is from Wyborn (1983) and given in the Supplementary Information. [+]A crystallisation temperature was then chosen by only considering estimates where phases were present as primocrysts. *Uncertainty estimates for the thermometers are given as quoted in the literature. Given the typical uncertainties for each thermometer, each chosen temperature has an uncertainty estimate of approximately ±50 °C. Mineral abbreviations as in Fig. 3.

Sample	Primocryst Mineralogy	Temperature Estimates (°C)				Chosen Temperature (°C)[+]
		Two-Feldspar[1]	Hornblende-Plagioclase[2]	Biotite-Apatite[3]	Two-Pyroxene[4]	
BP39	opx, cpx, plag		751		865	865
BP22	plag, cpx, bt, hbd	806	724			724
BP11	plag, bt, hbd, kfs, qtz	769	648	674		697
BP42	Plag, bt, qtz, kfs			695		695
Uncertainty (°C)*		±30	±35–40	n/a	±70	

Appendix

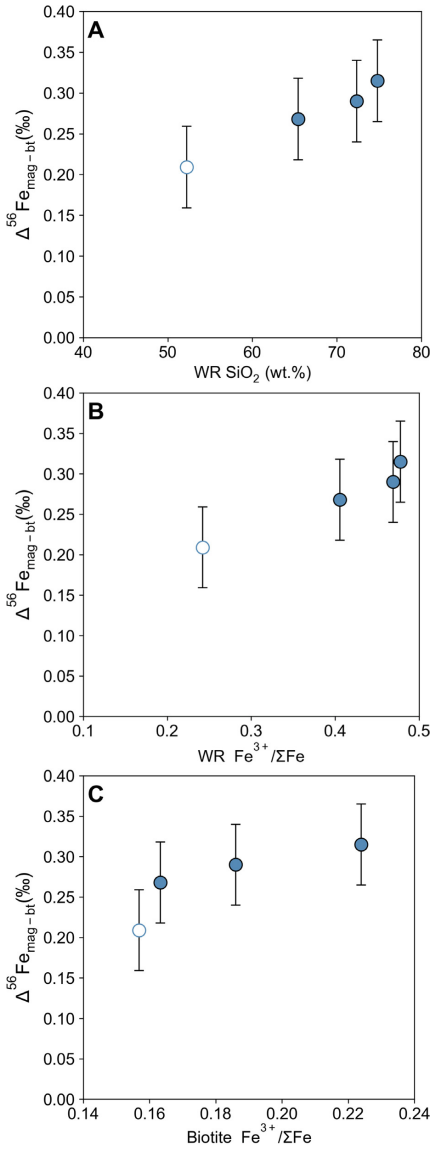

calculations (207 N/m). There are several published values for the bond force constant of magnetite ($\langle F_A \rangle$), ranging from 198 ± 15 N/m to 292 N/m (Polyakov et al., 2007; Mineev et al., 2007; Dauphas et al., 2012; Roskosz et al., 2015; Sossi and O'Neill, 2017; Rabin et al., 2021). The reason for this wide range of values is partly due to systematic variations between values derived using NRIXS, Mössbauer and *ab initio* calculations, as previously reported (e.g. Blanchard et al., 2009; Roskosz et al., 2015; Rabin et al., 2021). Hence, to accurately compare inter-mineral fractionation factors, it is more appropriate to use force constants determined by the same technique (Rabin et al., 2021), since it is the offset between, rather than the absolute force constant values, which will control the magnitude of Fe isotope fractionation.

The blue shaded area shows the $\Delta^{56}Fe_{mag\text{-}bt}$ calculated using force constants determined by NRIXS. For $\langle F_B \rangle$ in this equation, we correct the value of 188 ± 16 N/m (Nie et al., 2021) for the Fe^{3+} content of the BPZP biotite ($Fe^{3+}/\Sigma Fe \sim 0.18$; Wyborn, 1983) as described in Nie et al. (2021), giving a value of 172 ± 16 N/m. For consistency, we also chose a value for magnetite ($\langle F_A \rangle$) determined by NRIXS using the same analytical and processing procedures. Dauphas et al. (2012) and Polyakov et al. (2007) derived values of 230 ± 6 N/m and 228 ± 15 N/m respectively for the magnetite force constant. However, this data was collected over a smaller energy range than in more recent studies, which may have led to underestimation of $\langle F \rangle$ (Roskosz et al., 2015). Therefore, we chose to use the value of 264 ± 6 N/m for magnetite, derived from a regression of Al-bearing spinel (Roskosz et al., 2015).

The green shaded area shows $\Delta^{56}Fe_{mag\text{-}bt}$ calculated using force constants determined from *ab initio* calculations. Errors for force constants derived through *ab initio* calculations are thought to be on the order of ±5% (Rabin et al., 2021). The value of 207 N/m is used for biotite (Nie et al., 2021). Choosing an appropriate value for magnetite is more difficult, because the two studies which give *ab initio* values for the force constants of magnetite and ulvöspinel use different calculation approaches, resulting in different force constant values (292 N/m and 207.5 N/m for magnetite and 215 N/m and 151.8 N/m for ulvöspinel respectively; Sossi and O'Neill, 2017; Rabin et al., 2021). However, the force constant for magnetite of 207.5 N/m from Rabin et al. (2021) is identical to that of biotite from Nie et al. (2021). Given the large $\Delta^{56}Fe_{mag\text{-}bt}$ measured in the BPZP mineral separates, and difference in valence state and coordination environment between the two phases, it is unlikely that the force constants for biotite and magnetite are the same. Instead, this is likely an artifact of differences in the calculation method used. Hence, we chose to use the value of 292 N/m from Sossi

Fig. 8. Variation in magnetite-biotite fractionation factors with (A) WR SiO_2, (B) WR $Fe^{3+}/\Sigma Fe$ and (C) biotite $Fe^{3+}/\Sigma Fe$. Shaded symbols are when biotite and magnetite are both primocrysts. Open symbols are when biotite and magnetite are present as interstitial phases. Errors are the long term analytical uncertainty of ±0.05‰ (2SD) from measurement of solution standards.

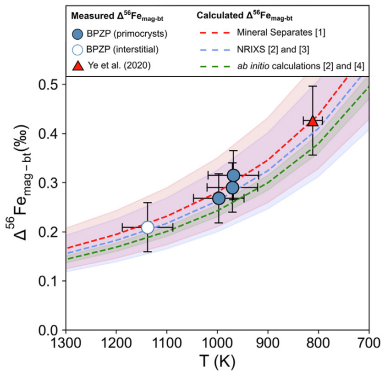

Fig. 9. Measured $\Delta^{56}Fe_{mag\text{-}bt}$ for the BPZP samples against crystallisation temperature (K). Filled circles are for primocryst biotite and hornblende. Open circles are interstitial biotite and hornblende. Errors in $\Delta^{56}Fe_{mag\text{-}bt}$ are given as ±0.05‰, the long-term analytical uncertainty for Fe. Errors in T as ±50 K, as discussed in the Table 3 caption. The red triangle shows the measured $\Delta^{56}Fe_{mag\text{-}bt}$ from a metamorphosed ironstone in Ye et al. (2020) [1]. The red line and shaded area show the relationship $\Delta^{56}Fe_{mag\text{-}bt} = 0.28\ (\pm 0.07) \times 10^6/T^2$ from Ye et al. (2020) [1]. The blue line and shaded area show a theoretical estimate of $\Delta^{56}Fe_{mag\text{-}bt}$ calculated using NRIXS data, using Eq. (1) after Dauphas et al. (2014). Values of 172 ± 16 N/m (Nie et al., 2021 [2]) and 264 ± 6 N/m (Roskosz et al., 2015 [3]) are used for the force constants of biotite and magnetite respectively, as discussed in the text. The green line and shaded area show a theoretical estimate of $\Delta^{56}Fe_{mag\text{-}bt}$ determined using values from *ab initio* calculations. Values of 207 N/m (Nie et al., 2021 [2]) and 292 N/m (Sossi and O'Neill, 2017 [4]) are used for the force constants of biotite and magnetite respectively, as discussed in the text. The error envelope considers a 5% error in the *ab initio* calculations. (For interpretation of the references to colour in this figure legend, the reader is referred to the web version of this article.)

and O'Neill (2017) for magnetite. To further support this choice, Nie et al. (2021) and Sossi and O'Neill (2017) calculate similar values for fayalite (178 N/m and 144 N/m) compared to the lower value of 99.6 N/m in Rabin et al. (2021), so the two studies are more directly comparable. We also chose to use values for magnetite rather than ulvöspinel, given the low Ti content of the BPZP magnetite (<0.7 wt.% TiO_2; Wyborn, 1983).

It is remarkable that an expression describing variation in $\Delta^{56}Fe_{mag\text{-}bt}$ with temperature, determined from ironstones metamorphosed <550 °C (red line), coincides with values for biotite and magnetite crystallising from the BPZP magma when extrapolated to temperatures >690 °C. These samples have experienced vastly different P-T-X-fO_2 conditions throughout their formation; for example, the biotite separates have different $Fe^{3+}/\Sigma Fe$ content: 0.13–0.22 for the BPZP (Wyborn, 1983) and 0.26–0.31 for the metamorphosed ironstone (Ye et al., 2020). The fractionation factors obtained from NRIXS data and *ab initio* calculations (blue and green lines) also show good agreement with the BPZP data. These findings demonstrate that temperature has a critical control on inter-mineral fractionation factors, in addition to variations in chemistry and/or fO_2. This highlights that accurate temperature estimates are essential when modelling Fe isotopic fractionation, especially in plutonic settings where temperature variations can be large.

7. MODELLING FE ISOTOPIC VARIATIONS IN PLUTONIC SETTINGS

In this section, we use our petrographic observations and mineral separate data to produce accurate and internally consistent models of Fe isotopic fractionation during fractional crystallisation of the BPZP. The whole rock samples with MgO > 4.5 wt.% consist of accumulated crystals and variable proportions of trapped interstitial melt, thus do not approximate a true melt composition. Hence, we chose to model only the $\delta^{56}Fe$ evolution of the BPZP below 4.5 wt.% MgO. From this point, whole rock isotopic composition approximates evolving magma composition. The mineral-mineral fractionation factors defined above are used to mathematically derive mineral-melt fractionation factors ($\Delta^{56}Fe_{min\text{-}melt}$). Fractional crystallisation is modelled incrementally using the Rayleigh equation (Eq. (2), after Sossi et al. (2012)) as the amount of residual Fe (fFe) in the system decreases:

$$\delta^{56}Fe = \delta^{56}Fe_{initial} + (\Delta^{56}Fe_{min-melt} \times \ln f Fe) \quad (2)$$

For this calculation, the Fe isotopic composition of the parent magma ($\delta^{56}Fe_{initial}$) must be known, and a bulk mineral-melt fractionation factor ($\Delta^{56}Fe_{min\text{-}melt}$) and fraction of Fe remaining (fFe) estimated for each model step. A series of models was produced to demonstrate how variations in modelling approaches, specifically estimates of mineral-melt fractionation factors, predict vastly different $\delta^{56}Fe$ trends in the residual magma.

7.1. Step 1: Estimating initial magma composition ($\delta^{56}Fe_{initial}$)

In lavas, the $\delta^{56}Fe$ of the most mafic sample is typically used to represent the isotopic composition of the parental magma ($\delta^{56}Fe_{initial}$). However, in plutonic settings like the BPZP, the most mafic samples are often cumulates (e.g. Chappell and Wyborn, 2004). The average $\delta^{56}Fe$ value of the mafic cumulates is 0.065‰. However, this value is most likely to reflect accumulation of isotopically light pyroxene, rather than reflect a primary melt composition. We therefore take the parental magma to be the most mafic granodiorite containing both primocryst biotite and hornblende (BP26; $\delta^{56}Fe = 0.092$‰), as this is assumed to be more representative of a liquid composition. Alternatively, if we assume that the interstitial biotite and hornblende in the mafic cumulates crystallised from trapped interstitial melt, it would also be appropriate to use the average isotopic composition of these interstitial phases (0.107 ± 0.030‰) as the parental melt composition.

Appendix

7.2. Step 2: Estimating fraction of Fe remaining (*f*Fe)

To estimate the fraction of Fe remaining (*f*Fe), we calculate the Fe content of the evolving magma (C) using Eq. (3), where C_0 is the initial FeO_{tot} concentration, F is the melt fraction, and D is the bulk mineral-melt partition coefficient for Fe.

$$C = C_0 \times F^{D-1} \quad (3)$$

The bulk partition coefficient for Fe was defined by modelling the major element trends for the BPZP whole rocks (e.g. MgO and FeO_{tot}) and selecting a bulk partition coefficient value which best reproduces the whole rock compositions ($D_{MgO} = 2$ and $D_{FeOtot} = 1.8$). The model was carried out over twenty steps, as F was varied in increments of 0.05. The fraction of Fe remaining at each model step is then calculated by $f(Fe) = (F \times C)/C_0$.

7.3. Step 3: Calculating mineral-melt fractionation factors

Inter-mineral fractionation factors determined directly from measurements of mineral separates (Section 6.3) are not directly used when modelling Fe isotopic evolution of a magma. Instead, mineral-melt fractionation factors are necessary to describe isotopic fractionation between the crystals and residual melt. Temperature dependent mineral-melt fractionation factors can be estimated using the Rayleigh equation (Eq. (2)), by iteratively selecting the $\Delta^{56}Fe_{min\text{-}melt}$ value which best fits the data (e.g. Sossi et al., 2012). Many studies use this method to estimate the bulk $\Delta^{56}Fe_{min\text{-}melt}$ which describes the entire isotopic evolution of the system rather than estimate mineral-melt fractionation factors for specific phases. For the BPZP, a bulk $\Delta^{56}Fe_{min\text{-}melt}$ of approximately −0.03‰ can describe the Fe isotopic evolution of the residual melt until 2% Fe remains (Fig. 10). However, this value does not capture the true variations in the mineral assemblage during the fractionation sequence.

However, a strength of the BPZP data set is that temperature dependent fractionation factors for all the individual phases in the fractionating assemblage can be calculated using the mineral separate data. Fractionation factors for each mineral are expressed in the form $\Delta^{56}Fe_{min\text{-}melt} = A \times 10^6/T^2$.

The bulk mineral-melt fractionation factor can be expressed by weighting (W) the fractionation factors for each mineral phase (p) by their Fe content ($[FeO_{tot}]$) and modal abundance (M).

$$\text{Bulk } \Delta^{56}Fe_{min-melt} = \Sigma(\Delta^{56}Fe^{p}{}_{min-melt} \times W^{p}) \quad (4)$$

$$\text{where } W^{p} = (M^{p} \times [FeO_{tot}]^{p})/\Sigma(M^{p} \times [FeO_{tot}]^{p}) \quad (5)$$

For the BPZP, this gives the expression:

$$\text{Bulk } \Delta^{56}Fe_{min-melt} = (\Delta^{56}Fe_{mag-melt} \times W_{mag}) + (\Delta^{56}Fe_{bt-melt} \times W_{bt}) + (\Delta^{56}Fe_{hbd-melt} \times W_{hbd}) \quad (6)$$

Biotite and hornblende have identical isotopic composition to each other across the differentiation sequence, so $\Delta^{56}Fe_{bt\text{-}melt} = \Delta^{56}Fe_{hbd\text{-}melt}$.

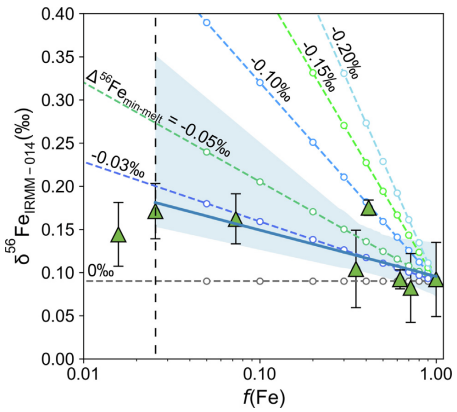

Fig. 10. Change in $\delta^{56}Fe$ of a magma undergoing fractional crystallisation (dashed lines), modelled using the Rayleigh equation ($\delta^{56}Fe = \delta^{56}Fe_i + (\Delta^{56}Fe_{min\text{-}melt} \times \ln f(Fe))$ at constant $\Delta^{56}Fe_{min\text{-}melt}$. BP26 was used as the starting magma composition. For the BPZP whole rock data (green triangles), *f*(Fe) is calculated based on changing MgO and FeO_{tot} content as described in the text. Previous studies have used the variation in concentration of incompatible elements (e.g. Rb, Th, U) to estimate F. However, concentrations of incompatible elements will also vary depending on the amount of trapped interstitial melt in the samples, so this method was not used. The blue shaded area is a weighted linear regression of the BPZP data from the start of the calculation until 2% Fe remains. This shows that the isotopic evolution for this part of the fractionation sequence can be described by a bulk $\Delta^{56}Fe_{min\text{-}melt}$ of approximately −0.03‰. (For interpretation of the references to colour in this figure legend, the reader is referred to the web version of this article.)

Appendix

$$\text{Bulk } \Delta^{56}Fe_{min-melt} = (\Delta^{56}Fe_{mag-melt} \times W_{mag}) + (\Delta^{56}Fe_{bt-melt} \times W_{bt}) + (\Delta^{56}Fe_{bt-melt} \times W_{hbd}) \quad (7)$$

The expression can therefore be expressed in terms of the relative weighting of silicate ($W_{sil} = W_{bt} + W_{hbd}$) and oxide phases ($W_{mag}$).

$$\text{Bulk } \Delta^{56}Fe_{min-melt} = (\Delta^{56}Fe_{mag-melt} \times W_{mag}) + (\Delta^{56}Fe_{bt-melt} \times W_{sil}) \quad (8)$$

For the BPZP, considerations of the modal abundances and FeO_{tot} concentrations of the fractionating assemblage show that $W_{sil} \sim 0.72$ and $W_{mag} \sim 0.28$ until 20% Fe remains. Therefore, $W_{sil} \sim 2.6 \times W_{mag}$.

$$\text{Bulk } \Delta^{56}Fe_{min-melt} = W_{mag}(\Delta^{56}Fe_{mag-melt} + 2.6\Delta^{56}Fe_{bt-melt}) \quad (9)$$

Substituting in the Bulk $\Delta^{56}Fe$ value of −0.03‰ obtained from Eq. (2) (Fig. 10), and the W_{mag} value of 0.28 gives the equation:

$$-0.107 = \Delta^{56}Fe_{mag-melt} + 2.6\Delta^{56}Fe_{bt-melt} \quad (10)$$

A second equation can be generated using the mineral separate data. Since at equilibrium, $\Delta_{a\text{-}c} = \Delta_{a\text{-}b} + \Delta_{b\text{-}c}$, then for the BPZP we can express the biotite-magnetite fractionation factor as:

$$\Delta^{56}Fe_{mag-bt} = \Delta^{56}Fe_{mag-melt} + \Delta^{56}Fe_{melt-bt} \quad (11)$$

This can be rearranged to:

$$\Delta^{56}Fe_{mag-bt} = \Delta^{56}Fe_{mag-melt} - \Delta^{56}Fe_{bt-melt} \quad (12)$$

Thus, using the magnetite-biotite fractionation factors at known temperatures (Fig. 9), we can then solve the values of $\Delta^{56}Fe_{mag\text{-}melt}$ and $\Delta^{56}Fe_{bt\text{-}melt}$ simultaneously, using Eqs. (10) and (12). The following values are calculated using the $\Delta^{56}Fe_{mag\text{-}bt}$ values for BP22, BP11 and BP42. A conservative error estimate is ±0.03‰, which is the average of the 2SD values reported for whole rock and mineral separate measurements.

$$\Delta^{56}Fe_{bt/hbd-melt} = -0.12 \times 10^6/T^2 \quad (13)$$

$$\Delta^{56}Fe_{mag-melt} = +0.17 \times 10^6/T^2 \quad (14)$$

The fractionation factors derived here do not explicitly consider the possible change in the bond force constant of ferrous iron in high silica melts (Dauphas et al., 2014), or variation in fractionation factor with mineral and melt chemistry. However, they are representative of T-fO_2 conditions in a calc-alkaline suite.

The only silicate mineral-melt fractionation factors for comparison are those from Sossi et al. (2012) for the tholeiitic Red Hills plutonic suite. Sossi et al. (2012) give a $\Delta^{56}Fe_{px\text{-}melt}$ value of $-0.17 \times 10^6/T^2$. The biotite-melt and hornblende-melt fractionation factors derived here are smaller ($\Delta^{56}Fe_{bt/hbd\text{-}melt} = -0.12 \times 10^6/T^2$). This supports theoretical considerations of valence and coordination environment. Biotite, hornblende and pyroxene all contain Fe in VI-fold coordination. However, the hydrous silicates have higher $Fe^{3+}/\Sigma Fe$. Therefore, Fe—O bonds should be stronger in hydrous silicates than pyroxenes, and thus there should be a smaller isotopic offset between hydrous silicates and coexisting melt at equilibrium. Additionally, the $\Delta^{56}Fe_{bt/hbd\text{-}melt}$ expression is similar to a $\Delta^{56}Fe_{bt\text{-}melt}$ value of −0.1‰ estimated from measurements of biotite separates and whole rock powders in Du et al. (2017).

Perhaps surprisingly, the $\Delta^{56}Fe_{mag\text{-}melt}$ value calculated for the BPZP is within error of the value of Sossi et al. (2012) for the Red Hills suite ($+0.13 \times 10^6/T^2$). Magma fO_2 in the calc-alkaline BPZP suite is higher than in the tholeiitic Red Hills suite (Wyborn, 1983; Sossi et al., 2012). Theoretically, differences in melt $Fe^{3+}/\Sigma Fe$ and subsequent variation in primary magnetite composition should lead to variation in $\Delta^{56}Fe_{mag\text{-}melt}$ values between the BPZP and Red Hills. The fact that $\Delta^{56}Fe_{mag\text{-}melt}$ values are within error in both suites suggest that bonding environment and temperature exert a more dominant control on Fe isotopic fractionation factors than melt redox state.

7.4. Step 4: Deriving a bulk mineral-melt fractionation factor ($\Delta^{56}Fe_{min\text{-}melt}$)

Deriving a bulk mineral-melt fractionation factor ($\Delta^{56}Fe_{min\text{-}melt}$, Eq. (4)) requires knowledge of the fractionating mineral assemblage. The variation in modal proportions of the fractionating assemblage over the differentiation sequence was approximated using a linear regression of the modal abundance of primocryst phases against sample MgO content. A bulk $\Delta^{56}Fe_{min\text{-}melt}$ value is then derived at each model step by multiplying the mineral-melt fractionation factors by a Fe weighting factor for each phase (Eqs. (4) and (5)). We use the mineral-melt fractionation factors calculated above for biotite, hornblende and magnetite, and the value of $\Delta^{56}Fe_{px\text{-}melt} = -0.17 \times 10^6/T^2$ for pyroxene, from Sossi et al. (2012). Temperature estimates were calculated based on a linear regression of the temperature estimates for the BPZP samples (Table 3) against MgO content.

The parameters discussed above were used to model the $\delta^{56}Fe$ of the residual magma using the Rayleigh equation (Eq. (2)). Calculated magma $\delta^{56}Fe$ is shown by the black solid line in Fig. 11. The blue shaded area shows the range in magma $\delta^{56}Fe$ when uncertainties of ±0.03‰ for the mineral-melt fractionation factors are considered. We consider this level of uncertainty to be intrinsic to such modelling and emphasise that errors in fractionation factors will always be amplified in the most silicic samples.

7.5. Model comparisons

Several studies use the thermodynamic modelling software Rhyolite-MELTS (Gualda et al., 2012; Ghiorso and Gualda, 2015) to model variation in Fe isotopic composition during fractional crystallisation (e.g. Dauphas et al., 2014; Foden et al., 2015; He et al., 2017; Xia et al., 2017). However, MELTS cannot accurately reproduce the stability of hydrous silicates like biotite and hornblende in calc-alkaline magmas (Gualda et al., 2012). Given that these are the main Fe bearing silicate phases in the BPZP and similar systems, the evolving magma chemistry and Fe iso-

Appendix

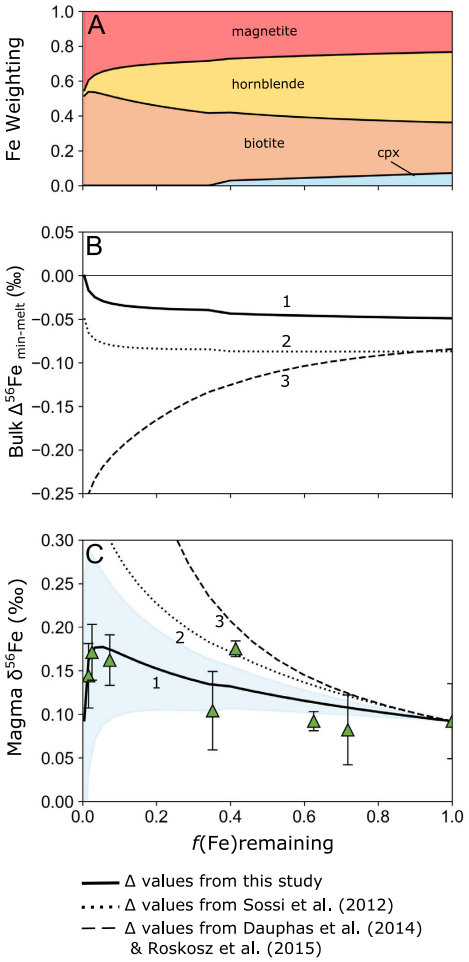

Fig. 11. Determinations of modal abundances (A), bulk $\Delta^{56}Fe_{min\text{-}melt}$ (B), and resulting magma $\delta^{56}Fe$ (C) from three Rayleigh models. Green triangles show the isotopic composition of the BPZP WR samples. *f*(Fe) is calculated as described in the text. The blue error envelope shows magma $\delta^{56}Fe$ considering an error of ±0.03‰ on the fractionation factor expressions. (For interpretation of the references to colour in this figure legend, the reader is referred to the web version of this article.)

topic composition cannot be accurately modelled this way (See Section 4 in Supplementary Information and Figs. S3 and S4). We therefore recommend that for I-type granites, modal abundances of the fractionating assemblage should be determined from petrographic observations, considering only the modal proportions of primocrysts and not interstitial phases. However, the choice of selected fractionation factors remains important.

Model 1 (Fig. 11) uses the fractionation factors calculated in this study (Eqs. (13) and (14)). For the first part of the differentiation sequence, isotopically light phases like biotite and hornblende host the majority of Fe in the system, causing an increase in the $\delta^{56}Fe$ of the evolving magma. However, below 1 wt.% MgO, when $f\text{Fe} < 0.1$, magnetite becomes the dominant Fe host and causes a decrease in $\delta^{56}Fe$ of the most silicic magma.

Appendix

In contrast, using fractionation factors for the tholeiitic Red Hills complex ($\Delta^{56}Fe_{mag\text{-}melt} = +0.13 \times 10^6/T^2$ and $\Delta^{56}Fe_{min\text{-}melt} = -0.17 \times 10^6/T^2$ for all silicate phases; Sossi et al., 2012), generates bulk $\Delta^{56}Fe_{min\text{-}melt}$ values of approximately −0.09‰ (Model 2; Fig. 11). The calculated increase in magma $\delta^{56}Fe$ in Model 2 is therefore larger than Model 1 and does not match the BPZP whole rock data. This reinforces the notion that fractionation factors for anhydrous silicates from a tholeiitic suite are not applicable to calc-alkaline settings where hydrous phases like biotite and hornblende are present.

Finally, we calculated fractionation factors using bond force constants (Model 3; Fig. 11). An average force constant ($\langle F \rangle$) was calculated for the melt and minerals at each step of the model, following the method in Dauphas et al. (2014). Given the scarcity of force constant measurements for biotite and hornblende, $\langle F \rangle$ values for silicate minerals were calculated as in Dauphas et al. (2014): a force constant for each mineral was calculated by weighting the force constants for ferrous (197 N/m) and ferric (255 N/m) Fe in olivine and glasses by mineral $Fe^{3+}/\Sigma Fe$. For example, biotite with a $Fe^{3+}/\Sigma Fe$ of 0.18 has a calculated $\langle F \rangle$ of 207 N/m. For magnetite, a force constant of 264 ± 6 N/m was adopted, the value determined by Roskosz et al. (2015). The bulk force constant for the minerals ($\langle F_{min} \rangle$) was calculated by multiplying the force constants for each phase by their Fe weighting (Eq. (5)). For the melt, the force constant for Fe^{2+} was calculated from $F^{Fe2+} = 199 + 41/(1 + e^{34\text{-}SiO2/2})$, and Fe^{3+} assigned a value of 351 N/m (Dauphas et al., 2014). $\langle F_{melt} \rangle$ was then calculated by weighting these force constants by the $Fe^{3+}/\Sigma Fe$ of the melt. Bulk $\Delta^{56}Fe_{min\text{-}melt}$ was then calculated using Eq. (1). The bulk $\Delta^{56}Fe_{min\text{-}melt}$ values calculated in this way (Model 3) are always negative. This is because the force constant estimates for Fe—O bonds in the melt (351 N/m for Fe^{3+} and between 200 and 240 N/m for Fe^{2+}) are always larger than in minerals. The bulk mineral-melt fractionation factor becomes more negative as the bond force constant of Fe^{2+} increases at high silica content (Dauphas et al., 2014), which drives an increase in $\delta^{56}Fe$ of the melt at more felsic compositions. However, the BPZP whole rock samples do not show this magnitude of $\delta^{56}Fe$ increase during differentiation. This suggests that there are uncertainties with extrapolating bond force constants measured in orthosilicates and glasses (Dauphas et al., 2014) to Fe^{3+} bearing silicates with more complex structures, like biotite and hornblende. This is demonstrated by the discrepancy between the bond force constant measured directly in biotite Fe endmember annite by NRIXS (188 ± 16 N/m at $Fe^{3+}/\Sigma Fe = 0.32$; Nie et al., 2021) and that calculated based on biotite $Fe^{3+}/\Sigma Fe$ content as above (216 N/m at $Fe^{3+}/\Sigma Fe = 0.32$). Additionally, this approach also assumes that force constants only vary with mineral $Fe^{3+}/\Sigma Fe$. However, variation in mineral composition and/or subsequent changes in Fe—O bond length will also affect force constants (Roskosz et al., 2015; Sossi and O'Neill, 2017; Rabin et al., 2021). Therefore, further work is needed to define force constants in hydrous silicates in order to accurately model fractional crystallisation in hydrous, I-type magmas in this way.

We conclude that there are several requirements for accurate modelling of Fe isotopic evolution in co-genetic plutonic settings, which differ from modelling of co-genetic extrusive lavas.

1. Accurate modal abundances. Only the modal abundance of primocryst phases crystallising from the main magma body will influence magma $\delta^{56}Fe$ and Fe content. Interstitial phases crystallised from trapped melt will influence bulk rock $\delta^{56}Fe$ but not magma $\delta^{56}Fe$ evolution. Modal abundance estimates from observations of samples are more accurate than those estimated from Rhyolite-MELTS, especially in I-type systems.
2. Accurate estimation of parental melt composition. In contrast to extrusive suites, the most mafic samples in plutonic bodies are often cumulates and do not reflect a true liquid or parental melt composition, so should not be used as such.
3. Temperature dependent mineral-melt fractionation factors. The use of temperature dependent fractionation factors is vital in plutonic settings where temperature variations can be large. It must also be considered that fractionation factors derived from *ab initio* calculations or NRIXS studies are not necessarily directly applicable to the specific chemistry and $Fe^{3+}/\Sigma Fe$ of the minerals in the suite being studied. Therefore, empirically derived fractionation factors at similar X-fO_2 conditions may be more appropriate.

Rayleigh models like those above assume perfect closed system fractional crystallisation. Although in practice the differentiation processes occurring in plutonic settings are more complex (e.g. Janoušek and Moyen, 2020), this straightforward approach can accurately reproduce the Fe isotopic trends in the BPZP.

8. IMPLICATIONS

I-type granitoids like the BPZP are the most abundant granite type in the upper continental crust (e.g. Kemp et al., 2007). In the BPZP, whole rock $\delta^{56}Fe$ is controlled by the balance between crystallisation of isotopically light silicates (biotite and hornblende) and isotopically heavy magnetite. Crystallisation drives a muted increase in $\delta^{56}Fe$ with differentiation, as demonstrated mathematically using the Rayleigh equation. Hence, this is the extent of Fe isotopic fractionation to be expected in a simple calc-alkaline system undergoing fractional crystallisation in the absence of additional processes (i.e. crustal contamination, fluid alteration, addition of new batches of magma). The restricted range in whole rock $\delta^{56}Fe$ observed and modelled in the BPZP matches the observation that I-type granitic rocks globally have low $\delta^{56}Fe$ values <0.2‰ (Foden et al., 2015).

Although the BPZP is interpreted to form by progressive fractional crystallisation of a liquid body of magma, it is likely that such liquid-dominant bodies of magma are rare in the crust. Instead, magma reservoirs are recognised to be "mushy" regions composed of non-eruptible crystal frame-

Appendix

works and interstitial melt (Bachmann and Bergantz, 2004; Hildreth, 2004). There remain questions surrounding the exact crystal-melt segregation and differentiation processes (e.g. Bachmann and Bergantz, 2004; Holness, 2018) and temperature regimes (e.g. Barboni et al., 2016; Rubin et al., 2017) in these mushes. However, if we consider that the larger, more complex mush bodies are formed of smaller plutonic units where magmatic processes are similar to the BPZP, this study provides a necessary baseline understanding of the behaviour of Fe isotopes to enable future investigation of more complex mushes.

A key finding from this study is that the $\Delta^{56}Fe_{mag\text{-}bt}$ values measured in the BPZP at temperatures >690 °C show close agreement with temperature dependent expressions derived from NRIXS and *ab initio* data (Fig. 9). Additionally, the $\Delta^{56}Fe_{mag\text{-}bt}$ values measured in the BPZP match temperature dependent expressions derived from mineral separates in a banded iron formation metamorphosed at 538 °C (Ye et al., 2020; Fig. 9). Hence, the BPZP study demonstrates the validity of these expressions when extended to higher temperatures. Mineral separates from a metamorphosed ironstone and an I-type granite will have experienced different P-T-X-fO_2 conditions during crystallisation. Therefore, the agreement between $\Delta^{56}Fe_{mag\text{-}bt}$ values from two vastly different geological settings suggests that inter-mineral fractionation factors between the same mineral pair in different samples is overwhelmingly controlled by temperature, rather than variations in chemical composition and/or fO_2.

The similarity between inter-mineral fractionation factors from a range of geological settings, temperatures, compositions and fO_2 conditions demonstrates the wide applicability of Fe isotopes to addressing problems in igneous geology. Specifically, in crystal mushes, inter-mineral fractionation factors between phases at equilibrium could be used to provide information about magma storage temperatures. This is especially useful in plutonic settings because of the lack of appropriate geothermometers when coexisting liquid composition cannot be easily determined (e.g. Putirka, 2016). If crystallisation temperature is known, inter-mineral fractionation factors can also be used to test for isotopic equilibrium between phases. Although the BPZP mineral separates obtain Fe isotopic equilibrium during fractional crystallisation, differentiation processes in larger mush bodies are thought to be more complex. Mush regions are often open systems, and if processes such as magma recharge, mixing, reactive porous flow and crustal assimilation occur, crystal scale isotopic disequilibrium may be expected. Therefore, the application of stable isotopic compositions to the investigation of more complex mushy systems to determine features like the range of storage temperatures and the extent of isotopic (dis)equilibrium during differentiation is a promising avenue of future research.

As Fe is present in multiple redox states, previous studies have investigated the potential link between Fe isotopic composition of mineral separates and/or whole rock powders and magma fO_2 during magmatic differentiation (e.g. Williams et al., 2005; Sossi et al., 2012; Foden et al., 2015). Although magma fO_2 will control the fractionating mineral assemblage, leading to distinct trends in whole rock $\delta^{56}Fe$ for I-, A- and S-type granites (Foden et al., 2015), this study has demonstrated that variation in mineral $Fe^{3+}/\Sigma Fe$ does not have a resolvable effect on Fe isotope fractionation factors between specific mineral pairs, suggesting limited use of Fe isotopes in mineral phases as a direct fO_2 proxy. A problem with Fe is that it is present as a major element in all silicate and oxide phases, and Fe isotopes are fractionated by a multitude of processes. However, the isotopic composition of trace elements concentrated in only one mineral may have potential as fO_2 proxies. A possibility is vanadium isotopes, where experimental studies suggest relationship between magnetite-melt V fractionation factors and magma fO_2 (Sossi et al., 2018b). Therefore, combining a well-studied isotope system of a major element like Fe with isotopes of a trace element like V may provide further understanding about P-T-X-fO_2 conditions during magmatic differentiation.

9. CONCLUSION

The Boggy Plain Zoned Pluton is a useful natural system for investigating Fe isotope fractionation during closed system fractional crystallisation of an I-type magma. This is the first time that the Fe isotopic composition of mineral separates have been measured in a closed system I-type suite. This has permitted the derivation of new mineral-melt fractionation factors which are representative of the X-T-fO_2 conditions in calc-alkaline settings.

1. In the BPZP, whole rock $\delta^{56}Fe$ increases from 0.038‰ to 0.171‰ with decreasing MgO content. Whole rock $\delta^{66}Zn$ is not affected by fractional crystallisation, but fluid alteration may cause the heavy $\delta^{66}Zn$ signal observed in aplite samples. A lack of coupling between $\delta^{56}Fe$ and $\delta^{66}Zn$ strongly suggests that Fe isotopes are not fractionated by fluid exsolution, thus Fe isotopic variation is dominantly controlled by fractional crystallisation.
2. Minerals show heavy Fe isotope enrichment in the order magnetite > biotite = hornblende > orthopyroxene. Mineral separates display inter-mineral Fe isotopic equilibrium. Inter-mineral fractionation factors match previous empirical and theoretical estimates from a range of P-T-X-fO_2 conditions.
3. Mineral separate data can be used to derive temperature dependent fractionation factors for magnetite and hydrous silicates in calc-alkaline settings: $\Delta^{56}Fe_{mag\text{-}bt} = 0.28 \times 10^6/T^2$, $\Delta^{56}Fe_{mag\text{-}melt} = 0.17 \times 10^6/T^2$ and $\Delta^{56}Fe_{bt/hbd\text{-}melt} = -0.12 \times 10^6/T^2$. These are used to construct internally consistent, temperature dependent models of Fe isotopic fractionation during fractional crystallisation of a calc-alkaline magma.
4. The strong temperature dependence on equilibrium Fe isotopic fractionation highlights future avenues of research for the use of Fe isotopes in investigating petrogenetic processes and physical conditions in crystal mush bodies.

Appendix

Declaration of Competing Interest

The authors declare that they have no known competing financial interests or personal relationships that could have appeared to influence the work reported in this paper.

ACKNOWLEDGEMENTS

This research was supported by a NERC IAPETUS Doctoral Training Programme (NE/L002590/1) studentship to MAS. Doone Wyborn and Hugh O'Neill are thanked for fieldwork assistance during JP's visit to ANU in 2013, funded by Australian Research Council Discovery Grant DP130101355 to H.St.C. O'Neill and JP. JP thanks Doone Wyborn and Bruce Chappell for many interesting discussions about granite petrogenesis during her 2013 visit. We appreciate the efficient editorial handling of M. Roskosz and thank Nicole Nie, Luc Doucet and one anonymous reviewer for constructive reviews which greatly improved the manuscript.

APPENDIX A. SUPPLEMENTARY MATERIAL

Supplementary data to this article can be found online at https://doi.org/10.1016/j.gca.2021.12.018.

REFERENCES

Archer C., Andersen M. B., Cloquet C., Conway T. M., Dong S., Ellwood M., Moore R., Nelson J., Rehkämper M., Rehkämper R., Rouxel O., Samanta M., Shin K.-C., Sohrin Y., Takano S. and Wasylenki L. (2017) Inter-calibration of a proposed new primary reference standard AA-ETH Zn for zinc isotopic analysis. *J. Anal. At. Spectrom.* **32**, 415–419.

Bachmann O. and Bergantz G. W. (2004) On the origin of crystal-poor rhyolites: Extracted from batholithic crystal mushes. *J. Petrol.* **45**, 1565–1582.

Bachmann O. and Huber C. (2019) The inner workings of crustal distillation columns; the physical mechanisms and rates controlling phase separation in silicic magma reservoirs. *J. Petrol.* **60**, 3–18.

Barboni M., Boehnke P., Schmitt A. K., Mark H. T., Shane P., Bouvier A. S. and Baumgartner L. (2016) Warm storage for arc magmas. *Proc. Natl. Acad. Sci.* **113**, 13959–13964.

Barnes C. G., Werts K., Memeti V. and Ardill K. (2019) Most granitoid rocks are cumulates: Deductions from hornblende compositions and zircon saturation. *J. Petrol.* **60**, 2227–2240.

Blanchard M., Poitrasson F., Méheut M., Lazzeri M., Mauri F. and Balan E. (2009) Iron isotope fractionation between pyrite (FeS_2), hematite (Fe_2O_3) and siderite ($FeCO_3$): A first-principles density functional theory study. *Geochim. Cosmochim. Acta* **73**, 6565–6578.

Burton-Johnson A., Macpherson C. G., Ottley C. J., Nowell G. M. and Boyce A. J. (2019) Generation of the Mt Kinabalu granite by crustal contamination of intraplate magma modelled by equilibrated major element assimilation with fractional crystallization (EME-AFC). *J. Petrol.* **60**, 1461–1487.

Cao Y., Wang C. Y., Huang F. and Zhang Z. (2019) Iron isotope systematics of the panzhihua mafic layered intrusion associated with giant Fe-Ti oxide deposit in the emeishan large igneous province, SW China. *J. Geophys. Res. Solid Earth* **124**, 358–375.

Cashman K. V., Sparks R. S. J. and Blundy J. D. (2017) Vertically extensive and unstable magmatic systems: A unified view of igneous processes. *Science* **355**.

Chappell B. W., Bryant C. J. and Wyborn D. (2012) Peraluminous I-type granites. *Lithos* **153**, 142–153.

Chappell B. W. and White A. J. (2001) Two contrasting granite types: 25 years later. *Aust. J. Earth Sci.* **48**, 489–499.

Chappell B. W. and Wyborn D. (2004) Cumulate and cumulative granites and associated rocks. *Resour. Geol.* **54**, 227–240.

Chen H., Savage P. S., Teng F. Z., Helz R. T. and Moynier F. (2013) Zinc isotope fractionation during magmatic differentiation and the isotopic composition of the bulk Earth. *Earth Planet. Sci. Lett.* **369**, 34–42.

Chen L.-M., Song X.-Y., Zhu X.-K., Zhang X.-Q., Yu S.-Y. and Yi J.-N. (2014) Iron isotope fractionation during crystallization and sub-solidus re-equilibration: Constraints from the Baima mafic layered intrusion, SW China. *Chem. Geol.* **380**, 97–109.

Chen S., Liu Y., Hu J., Zhang Z., Hou Z. and Yu H. (2015) Zinc isotopic compositions of NIST SRM 683 and whole-rock reference materials. *Geostand. Geoanaly. Res.* **40**, 417–432.

Craddock P. R. and Dauphas N. (2011) Iron isotopic compositions of geological reference materials and chondrites. *Geostand. Geoanaly. Res.* **35**, 101–123.

Czamanske G. K. and Wones D. R. (1973) Oxidation during magmatic differentiation, finnmarka complex, Oslo Area, Norway: Part 2, The mafic silicates. *J. Petrol.* **14**, 349–380.

Dauphas N., Roskosz M., Alp E. E., Golden D. C., Sio C. K., Tissot F. L. H., Hu M. Y., Zhao J., Gao L. and Morris R. V. (2012) A general moment NRIXS approach to the determination of equilibrium Fe isotopic fractionation factors: Application to goethite and jarosite. *Geochim. Cosmochim. Acta* **94**, 254–275.

Dauphas N., Roskosz M., Alp E. E., Neuville D. R., Hu M. Y., Sio C. K., Tissot F. L. H., Zhao J., Tissandier L., Médard E. and Cordier C. (2014) Magma redox and structural controls on iron isotope variations in Earth's mantle and crust. *Earth Planet. Sci. Lett.* **398**, 127–140.

Dauphas N., John S. G. and Rouxel O. (2017) Iron isotope systematics. *Rev. Mineral Geochem.* **82**, 415–510.

Doucet L. S., Laurent O., Mattielli N. and Debouge W. (2018) Zn isotope heterogeneity in the continental lithosphere: New evidence from Archean granitoids of the northern Kaapvaal craton, South Africa. *Chem. Geol.* **476**, 260–271.

Doucet L. S., Laurent O., Ionov D. A., Mattielli N., Debaille V. and Debouge W. (2020) Archean lithospheric differentiation: Insights from Fe and Zn isotopes. *Geology* **48**, 1028–1032.

Du D. H., Li W., Wang X. L., Shu X. J., Yang T. and Sun T. (2019) Fe isotopic fractionation during the magmatic–hydrothermal stage of granitic magmatism. *Lithos* **350–351**, 105265.

Du D.-H., Wang X.-L., Yang T., Chen X., Li J.-Y. and Li W. (2017) Origin of heavy Fe isotope compositions in high-silica igneous rocks: A rhyolite perspective. *Geochim. Cosmochim. Acta* **218**, 58–72.

Dziony W., Horn I., Lattard D., Koepke J., Steinhoefel G., Schuessler J. A. and Holtz F. (2014) In-situ Fe isotope ratio determination in Fe–Ti oxides and sulfides from drilled gabbros and basalt from the IODP Hole 1256D in the eastern equatorial Pacific. *Chem. Geol.* **363**, 101–113.

Foden J., Sossi P. A. and Wawryk C. M. (2015) Fe isotopes and the contrasting petrogenesis of A-, I- and S-type granite. *Lithos* **212–215**, 32–44.

Frost B. R. and Lindsley D. H. (1991) Oxide Minerals: Petrologic and magnetic significance. In *Reviews in Mineralogy and Geochemistry* (ed. D. H. Lindsley). pp. 433–468.

Fujii T., Moynier F., Blichert-Toft J. and Albarède F. (2014) Density functional theory estimation of isotope fractionation of Fe, Ni, Cu, and Zn among species relevant to geochemical and biological environments. *Geochim. Cosmochim. Acta* **140**, 553–576.

Appendix

Gajos N. A., Lundstrom C. C. and Taylor A. H. (2016) Spatially controlled Fe and Si isotope variations: An alternative view on the formation of the Torres del Paine pluton. *Contrib. Mineral. Petrol.* **171**, 93.

Ghiorso M. S. and Gualda G. A. R. (2015) An H_2O–CO_2 mixed fluid saturation model compatible with rhyolite-MELTS. *Contrib. Mineral. Petrol.* **169**, 53.

Gleeson M. L. M., Gibson S. A. and Williams H. M. (2020) Novel insights from Fe-isotopes into the lithological heterogeneity of Ocean Island Basalts and plume-influenced MORBs. *Earth Planet. Sci. Lett.* **535**, 116114.

Gualda G. A. R., Ghiorso M. S., Lemons R. V. and Carley T. L. (2012) Rhyolite-MELTS: A modified calibration of MELTS optimized for silica-rich, fluid-bearing magmatic systems. *J. Petrol.* **53**, 875–890.

He Y., Wu H., Ke S., Liu S. A. and Wang Q. (2017) Iron isotopic compositions of adakitic and non-adakitic granitic magmas: Magma compositional control and subtle residual garnet effect. *Geochim. Cosmochim. Acta* **203**, 89–102.

Heimann A., Beard B. L. and Johnson C. M. (2008) The role of volatile exsolution and sub-solidus fluid/rock interactions in producing high $^{56}Fe/^{54}Fe$ ratios in siliceous igneous rocks. *Geochim. Cosmochim. Acta* **72**, 4379–4396.

Hiebert R. S., Bekker A., Houlé M. G., Wing B. A. and Rouxel O. J. (2016) Tracing sources of crustal contamination using multiple S and Fe isotopes in the Hart komatiite-associated Ni–Cu–PGE sulfide deposit, Abitibi greenstone belt, Ontario, Canada. *Miner. Depos.* **51**, 919–935.

Hildreth W. (2004) Volcanological perspectives on Long Valley, Mammoth Mountain, and Mono Craters: Several contiguous but discrete systems. *J. Volcanol. Geotherm. Res.* **136**, 169–198.

Holland T. and Blundy J. (1994) Non-ideal interactions in calcic amphiboles and their bearing on amphibole-plagioclase thermometry. *Contrib. Mineral. Petrol.* **116**, 433–447.

Holness M. B. (2018) Melt segregation from silicic crystal mushes: A critical appraisal of possible mechanisms and their microstructural record. *Contrib. Mineral. Petrol.* **173**, 48.

Hoskin P. W. O., Kinny P. D., Wyborn D. and Chappell B. W. (2000) Identifying accessory mineral saturation during differentiation in granitoid magmas: An integrated approach. *J. Petrol.* **41**, 1365–1396.

Huang J., Zhang X. C., Chen S., Tang L., Wörner G., Yu H. and Huang F. (2018) Zinc isotopic systematics of Kamchatka-Aleutian arc magmas controlled by mantle melting. *Geochim. Cosmochim. Acta* **238**, 85–101.

Ickert R. B. (2010) U-Pb, Lu-Hf, and O isotope systematics of zircon from southeastern Australian Siluro-Devonian granites. Ph. D. thesis, Australian National University.

Ickert R. B., Williams I. S. and Wyborn D. (2011) Ti in zircon from the Boggy Plain zoned pluton: Implications for zircon petrology and Hadean tectonics. *Contrib. Mineral. Petrol.* **162**, 447–461.

Iles K. A. (2017) Isotopic disequilibrium in granitic systems: The origins of heterogeneity in granites and implications for partial melting in the crust and petrogenetic models. Ph. D. thesis, University of Melbourne.

Irvine T. N. (1982) Terminology for Layered Intrusions. *J. Petrol.* **23**, 127–162.

Jackson M. D., Blundy J. and Sparks R. S. J. (2018) Chemical differentiation, cold storage and remobilization of magma in the Earth's crust. *Nature* **564**, 405–409.

Janoušek V. and Moyen J.-F. (2020) Whole-rock geochemical modelling of granite genesis: The current state of play. *Geol. Soc. London, Spec. Publ.* **491**, 267–291.

Kemp A. I. S., Hawkesworth C. J., Foster G. L., Paterson B. A., Woodhead J. D., Hergt J. M., Gray C. M. and Whitehouse M. J. (2007) Magmatic and crustal differentiation history of granitic rocks from Hf-O isotopes in zircon. *Science* **315**, 980–983.

Leake B. E., Woolley A. R., Arps C. E. S., Birch W. D., Grice J. D., Hawthorne F. C., Kato A., Kisch H. J., Krivovichev V. G., Linthout K., Laird J., Mandarino J. A., Maresch W. V., Nickel E. H., Rock N. M. S., Schumacher J. C., Smith D. C., Stephenson N. C. N., Ungaretti L., Whittaker E. J. and Youzhi G. (1997) Nomenclature of amphiboles: Report of the subcommittee on amphiboles of the International Mineralogical Association, commission on new minerals and mineral names. *Can. Mineral.* **35**, 219–246.

Liu S. A., Li D., Li S., Teng F. Z., Ke S., He Y. and Lu Y. (2014) High-precision copper and iron isotope analysis of igneous rock standards by MC-ICP-MS. *J. Anal. At. Spectrom.* **29**, 122–133.

Ludington S. (1978) The biotite-apatite geothermometer revisited. *Am. Mineral.* **63**, 551–553.

Maréchal C. N., Télouk P. and Albarède F. (1999) Precise analysis of copper and zinc isotopic compositions by plasma-source mass spectrometry. *Chem. Geol.* **156**, 251–273.

McCoy-West A. J., Fitton J. G., Pons M.-L., Inglis E. C. and Williams H. M. (2018) The Fe and Zn isotope composition of deep mantle source regions: Insights from Baffin Island picrites. *Geochim. Cosmochim. Acta* **238**, 542–562.

Mineev S. D., Polyakov V. B. and Permyakov Y. V. (2007) Equilibrium iron isotope fractionation factors for magnetite from Mossbauer spectroscopy and inelastic nuclear resonant X-ray scattering data. *Geochim. Cosmochim. Acta* **71**(15), A669.

Moynier F., Vance D., Fujii T. and Savage P. (2017) The isotope geochemistry of zinc and copper. *Rev. Mineral. Geochem.* **82**, 543–600.

Nebel O., Sossi P. A., Ivanic T. J., Bénard A., Gardiner N. J., Langford R. L. and Arculus R. J. (2020) Incremental growth of layered mafic-ultramafic intrusions through melt replenishment into a crystal mush zone traced by Fe-Hf isotope systematics. *Front. Earth Sci.* **8**, 2.

Nie N. X., Dauphas N., Alp E. E., Zeng H., Sio C. K., Hu J. Y., Chen X., Aarons S. M., Zhang Z., Tian H.-C., Wang D., Prissel K. B., Greer J., Bi W., Hu M. Y., Zhao J., Shahar A., Roskosz M., Teng F.-Z., Krawczynski M. J., Heck P. R. and Spear F. S. (2021) Iron, magnesium, and titanium isotopic fractionations between garnet, ilmenite, fayalite, biotite, and tourmaline: Results from NRIXS, ab initio, and study of mineral separates from the Moosilauke metapelite. *Geochim. Cosmochim. Acta* **302**, 18–45.

Park J. W., Campbell I. H., Ickert R. B. and Allen C. M. (2013) Chalcophile element geochemistry of the Boggy Plain zoned pluton, southeastern Australia: A S-saturated barren compositionally diverse magmatic system. *Contrib. Mineral. Petrol.* **165**, 217–236.

Poitrasson F. and Freydier R. (2005) Heavy iron isotope composition of granites determined by high resolution MC-ICP-MS. *Chem. Geol.* **222**, 132–147.

Polyakov V. B., Clayton R. N., Horita J. and Mineev S. D. (2007) Equilibrium iron isotope fractionation factors of minerals: Reevaluation from the data of nuclear inelastic resonant X-ray scattering and Mössbauer spectroscopy. *Geochim. Cosmochim. Acta* **71**, 3833–3846.

Polyakov V. B. and Mineev S. D. (2000) The use of Mossbauer spectroscopy in stable isotope geochemistry. *Geochim. Cosmochim. Acta* **64**, 849–865.

Putirka K. (2016) Amphibole thermometers and barometers for igneous systems and some implications for eruption mechanisms of felsic magmas at arc volcanoes. *Am. Mineral.* **101**, 841–858.

Putirka K. D. (2008) Thermometers and barometers for volcanic systems. *Rev. Mineral. Geochem.* **69**, 61–120.

Appendix

Rabin S., Blanchard M., Pinilla C., Poitrasson F. and Gregoire M. (2021) First-principles calculation of iron and silicon isotope fractionation between Fe-bearing minerals at magmatic temperatures: The importance of second atomic neighbors. *Geochim. Cosmochim. Acta.* **304**, 101–118.

Rieder M., Cavazzini G., D'Yakonov Y. S. D., Frank-Kamenetskii V. A., Gottardi G., Guggenheim S., Koval P. V., Müller G., Neiva A. M. R., Radoslovich E. W., Robert J., Sassi F. P., Takeda H., Weiss Z. and Wones D. R. (1999) Nomenclature of the micas. *Mineral. Mag.* **63**, 267–279.

Roskosz M., Sio C. K. I., Dauphas N., Bi W., Tissot F. L. H., Hu M. Y., Zhao J. and Alp E. E. (2015) Spinel-olivine-pyroxene equilibrium iron isotopic fractionation and applications to natural peridotites. *Geochim. Cosmochim. Acta* **169**, 184–199.

Rubin A. E., Cooper K. M., Till C. B., Kent A. J. R., Costa F., Bose M., Gravley D., Deering C. and Cole J. (2017) Rapid cooling and cold storage in a silicic magma reservoir recorded in individual crystals. *Science* **356**, 1154–1157.

Schauble E. A. (2004) Applying stable isotope fractionation theory to new systems. *Rev. Mineral. Geochem.* **55**, 65–111.

Schoenberg R. and von Blanckenburg F. (2006) Modes of planetary-scale Fe isotope fractionation. *Earth Planet. Sci. Lett.* **252**, 342–359.

Schoenberg R., Marks M. A. W., Schuessler J. A., von Blanckenburg F. and Markl G. (2009) Fe isotope systematics of coexisting amphibole and pyroxene in the alkaline igneous rock suite of the Ilímaussaq Complex, South Greenland. *Chem. Geol.* **258**, 65–77.

Schuessler J. A., Schoenberg R. and Sigmarsson O. (2009) Iron and lithium isotope systematics of the Hekla volcano, Iceland — Evidence for Fe isotope fractionation during magma differentiation. *Chem. Geol.* **258**, 78–91.

Shahar A., Young E. D. and Manning C. E. (2008) Equilibrium high-temperature Fe isotope fractionation between fayalite and magnetite: An experimental calibration. *Earth Planet. Sci. Lett.* **268**, 330–338.

Shannon R. D. (1976) Revised effective ionic radii and systematic studies of interatomic distances in halides and chalcogenides. *Acta Crystallogr. Sect. A* **32**, 751–767.

Sisson T. W. and Grove T. L. (1993) Mineralogy and Petrology Experimental investigations of the role of H_2O in calc-alkaline differentiation and subduction zone magmatism. *Contrib. Mineral. Petrol.* **113**, 143–166.

Soderman C. R., Matthews S., Shorttle O., Jackson M. G., Ruttor S., Nebel O., Turner S., Beier C., Millet M. A., Widom E., Humayun M. and Williams H. M. (2021) Heavy δ^{57}Fe in ocean island basalts: A non-unique signature of processes and source lithologies in the mantle. *Geochim. Cosmochim. Acta* **292**, 309–332.

Sossi P. A., Foden J. D. and Halverson G. P. (2012) Redox-controlled iron isotope fractionation during magmatic differentiation: An example from the Red Hill intrusion, S. Tasmania. *Contrib. Mineral. Petrol.* **164**, 757–772.

Sossi P. A., Nebel O. and Foden J. (2016) Iron isotope systematics in planetary reservoirs. *Earth Planet. Sci. Lett.* **452**, 295–308.

Sossi P. A., Halverson G. P., Nebel O. and Eggins S. M. (2015) Combined separation of Cu, Fe and Zn from rock matrices and improved analytical protocols for stable isotope determination. *Geostand. Geoanalytical Res.* **39**, 129–149.

Sossi P. A. and O'Neill H. S. C. (2017) The effect of bonding environment on iron isotope fractionation between minerals at high temperature. *Geochim. Cosmochim. Acta* **196**, 121–143.

Sossi P. A., Nebel O., O'Neill H. S. C. and Moynier F. (2018a) Zinc isotope composition of the Earth and its behaviour during planetary accretion. *Chem. Geol.* **477**, 73–84.

Sossi P. A., Prytulak J. and O'Neill H. S. C. (2018b) Experimental calibration of vanadium partitioning and stable isotope fractionation between hydrous granitic melt and magnetite at 800 °C and 0.5 GPa. *Contrib. Mineral. Petrol.* **173**.

Sparks R. S. J., Annen C., Blundy J. D., Cashman K. V., Rust A. C. and Jackson M. D. (2019) Formation and dynamics of magma reservoirs. *Philos. Trans. R. Soc. A* **377**, 20180019.

Telus M., Dauphas N., Moynier F., Tissot F. L., Teng F.-Z., Nabelek P. I., Craddock P. R. and Groat L. A. (2012) Iron, zinc, magnesium and uranium isotopic fractionation during continental crust differentiation: The tale from migmatites, granitoids, and pegmatites. *Geochim. Cosmochim. Acta* **97**, 247–265.

Teng F.-Z., Dauphas N. and Helz R. T. (2008) Iron isotope fractionation during magmatic differentiation in Kilauea Iki Lava Lake. *Science* **320**, 1620–1622.

Tindle A. G. and Pearce J. A. (1981) Petrogenetic modelling of in situ fractional crystallization in the Zoned Loch Doon Pluton, Scotland. *Contrib. Mineral. Petrol.* **78**, 196–207.

Urey H. C. (1947) The thermodynamic properties of isotopic substances. *J. Chem. Soc.*, 562–581.

Vernon R. H. and Collins W. J. (2011) Structural criteria for identifying granitic cumulates. *J. Geol.* **119**, 127–142.

Wang Z.-Z., Liu S.-A., Liu J., Huang J., Xiao Y., Chu Z.-Y., Zhao X.-M. and Tang L. (2017) Zinc isotope fractionation during mantle melting and constraints on the Zn isotope composition of Earth's upper mantle. *Geochim. Cosmochim. Acta* **198**, 151–167.

Wang Z.-Z., Liu S.-A., Liu Z.-C., Zheng Y.-C. and Wu F.-Y. (2020) Extreme Mg and Zn isotope fractionation recorded in the Himalayan leucogranites. *Geochim. Cosmochim. Acta* **278**, 305–321.

Weinberg R. F., Vernon R. H. and Schmeling H. (2021) Processes in mushes and their role in the differentiation of granitic rocks. *Earth Sci. Rev.* **220**, 103665.

Wells P. R. A. (1977) Pyroxene thermometry in simple and complex systems. *Contrib. Mineral. Petrol.* **62**, 129–139.

Weyer S. and Ionov D. A. (2007) Partial melting and melt percolation in the mantle: The message from Fe isotopes. *Earth Planet. Sci. Lett.* **259**, 119–133.

Williams H. M., Peslier A. H., McCammon C., Halliday A. N., Levasseur S., Teutsch N. and Burg J.-P. (2005) Systematic iron isotope variations in mantle rocks and minerals: The effects of partial melting and oxygen fugacity. *Earth Planet. Sci. Lett.* **235**, 435–452.

Williams H. M., Prytulak J., Woodhead J. D., Kelley K. A., Brounce M. and Plank T. (2018) Interplay of crystal fractionation, sulfide saturation and oxygen fugacity on the iron isotope composition of arc lavas: An example from the Marianas. *Geochim. Cosmochim. Acta* **226**, 224–243.

Williams H. M. and Bizimis M. (2014) Iron isotope tracing of mantle heterogeneity within the source regions of oceanic basalts. *Earth Planet. Sci. Lett.* **404**, 396–407.

Wu H., He Y., Bao L., Zhu C. and Li S. (2017) Mineral composition control on inter-mineral iron isotopic fractionation in granitoids. *Geochim. Cosmochim. Acta* **198**, 208–217.

Wyborn D., Chappell B. W. and James M. (2001) Examples of convective fractionation in high-temperature granites from the Lachlan Fold Belt. *Aust. J. Earth Sci.* **48**, 531–541.

Wyborn D., Turner B. S. and Chappell B. W. (1987) The Boggy Plain Supersuite: A distinctive belt of I-type igneous rocks of potential economic significance in the Lachlan Fold Belt. *Aust. J. Earth Sci.* **34**, 21–43.

Wyborn D. (1983) Fractionation processes in the Boggy Plain Zoned Pluton. Ph. D. thesis, Australian National University.

Appendix

Xia Y., Li S. and Huang F. (2017) Iron and Zinc isotope fractionation during magmatism in the continental crust: Evidence from bimodal volcanic rocks from Hailar basin, NE China. *Geochim. Cosmochim. Acta* **213**, 35–46.

Xu L. J., He Y., Wang S. J., Wu H. and Li S. (2017) Iron isotope fractionation during crustal anatexis: Constraints from migmatites from the Dabie orogen, Central China. *Lithos* **284**, 171–179.

Xu L. J., Liu S. A., Wang Z. Z., Liu C. and Li S. (2019) Zinc isotopic compositions of migmatites and granitoids from the Dabie Orogen, central China: Implications for zinc isotopic fractionation during differentiation of the continental crust. *Lithos* **324–325**, 454–465.

Ye H., Wu C., Brzozowski M. J., Yang T., Zha X., Zhao S., Gao B. and Li W. (2020) Calibrating equilibrium Fe isotope fractionation factors between magnetite, garnet, amphibole, and biotite. *Geochim. Cosmochim. Acta* **271**, 78–95.

Young E. D., Galy A. and Nagahara H. (2002) Kinetic and equilibrium mass-dependent isotope fractionation laws in nature and their geochemical and cosmochemical significance. *Geochim. Cosmochim. Acta* **66**, 1095–1104.

Zajacz Z., Halter W. E., Pettke T. and Guillong M. (2008) Determination of fluid/melt partition coefficients by LA-ICPMS analysis of co-existing fluid and silicate melt inclusions: Controls on element partitioning. *Geochim. Cosmochim. Acta* **72**, 2169–2197.

Zambardi T., Lundstrom C. C., Li X. and McCurry M. (2014) Fe and Si isotope variations at Cedar Butte volcano; insight into magmatic differentiation. *Earth Planet. Sci. Lett.* **405**, 169–179.

Zimmer M. M., Plank T., Hauri E. H., Yogodzinski G. M., Stelling P., Larsen J., Singer B., Jicha B., Mandeville C. and Nye C. J. (2010) The role of water in generating the calc-alkaline trend: New volatile data for aleutian magmas and a new tholeiitic index. *J. Petrol.* **51**, 2411–2444.

Associate editor: Mathieu Roskosz

Appendix 3: Contents of Electronic Appendices

The following electronic appendices are submitted with this thesis.

- **Electronic Appendix 1** – Compilation of all isotopic (Fe, V, Zn, Sr, Nd), trace element and SEM data presented in this thesis (Excel File).
- **Electronic Appendix 2** – Thin Section Scans of the Boggy Plain Zoned Pluton samples (Chapters 3 and 4) (PDF Document).
- **Electronic Appendix 3** – Petrographic Descriptions of the Boggy Plain Zoned Pluton samples (Chapters 3 and 4) (PDF Document).
- **Electronic Appendix 4** – Thin Section Scans of the Red Hill Intrusion samples (Chapter 5) (PDF Document).
- **Electronic Appendix 5** – Petrographic Descriptions of the Red Hill Intrusion samples (Chapter 5) (PDF Document).